Unsteady simulations of liquid/gas interfaces in real gas flows using the Second Gradient theory

Davy Nayigizente

université
PARIS-SACLAY

Unsteady simulations of liquid/gas interfaces in real gas flows using the Second Gradient theory

Thèse de doctorat de l'Université Paris-Saclay

École doctorale n° 579, SMEMaG
Sciences mécaniques et énergétiques, matériaux et géosciences
Spécialité de doctorat: Énergétique
Unité de recherche: Université Paris-Saclay, CNRS, CentraleSupélec
Laboratoire EM2C, 91190, Gif-sur-Yvette, France
Référent: : CentraleSupélec

Thèse présentée et soutenue à Gif-sur-Yvette, le 1er avril 2021, par

Davy NAYIGIZENTE

Composition du jury:

Olivier DESJARDINS Professeur agrégé, Université Cornell, SSMAE	Président
Vincent GIOVANGIGLI Directeur de recherche, CNRS, CMAP	Rapporteur et Examinateur
Richard SAUREL Professeur des Universités, Aix-Marseille Université, LMA	Rapporteur et Examinateur
Bénédicte CUENOT Chef de projet, CERFACS	Examinatrice
Lionel MATUSZEWSKI Ingénieur de recherche, ONERA	Examinateur
Vincent MOUREAU Chargé de recherche, CNRS, CORIA	Examinateur
Sébastien DUCRUIX Directeur de recherche, CNRS, EM2C	Directeur
Thomas SCHMITT Chargé de recherche, CNRS, EM2C	Coencadrant
Didier JAMET Ingénieur de recherche, CEA	Invité

Thèse de doctorat

NNT: 2021UPAST025

Remerciements

Comme l'a si bien écrit Pierre Corneille dans Le Cid : *"A vaincre sans péril on triomphe sans gloire."*. Loin de moi l'idée de comparer la tenue de cette thèse au parcours héroïque de Don Rodrigue, je ne peux m'empêcher de penser qu'elle ne s'est pas faite sans son lot de péripéties. Et si aujourd'hui, après presque sept années, j'ai pu l'amener fièrement à son terme, cela n'aura été possible que grâce au concours d'un très grand nombre de personnes, sans doute trop nombreuses pour que je me rappelle de toutes et que puisse les nommer, mais que je voulais néanmoins dument joindre à cette réussite.

Je tiens en premier lieu à remercier le laboratoire EM2C à travers tous ses membres : chercheurs, enseignants, personnel technique et administratif, doctorants, post-doctorants et stagiaires. Je suis conscient de la chance d'avoir pu mener mes recherches dans un cadre aussi privilégié, entouré de personnes aussi passionnées que passionnantes, aussi motivées que motivantes et toujours prêtes à aider.
J'ai une pensée pour Frank Richecoeur et Olivier Gicquel qui ont su me séduire afin que je m'engage dans la voie de la thèse.
J'ai une autre pensée pour Alain, Dédit, Yannick et Érica qui ont toujours su se rendre disponibles afin que mes activités en soufflerie se passent pour le mieux.
Je salue chaleureusement tous les doctorants avec lesquels j'ai pu échanger de manière plus privilégiée, en particulier ceux qui ont eu la lourde tâche de devoir me supporter quotiennement dans leur bureau, à moins que ce ne fut le contraire... Je pense à Valentin le plus matheux des physiciens, à Chris le plus tatoué des australiens, au si souriant "longue serviette" Lantao, à Quentin le sportif de l'extrême, au génie incompris de Nicolas, au discret mais néanmoins chaleureux Giampi, à mon compagnon d'aventures Cédric, à la tornade d'énergie mexicaine Abi et surtout à Léo, le plus sage et rock'n'roll des brésiliens, à Lorellina et son sourire latin intarissable, à ma chère féministe émérite préférée Théa et bien sûr à Mindy ma chère "sista" de thèse.
Je n'oublie certainement pas la team Real Gas, Robin "Hood" et surtout Milan mon compagnon d'arme, avec lesquels j'ai partagé ces rêves de fusée autour d'un bon repas asiatique, ces tableaux noircis dans les tranchées de la thermodynamique, ces questionnements sans fin, ces blagues de scientifiques, cette grande camaraderie et ces franches rigolades.
Enfin, j'adresse une pensée toute particulière à Nathalie, Noï et Brigitte, les trois bonnes fées du laboratoire, les fourmis ouvrières, parfois oubliées à tort, sans qui toute cette machinerie ne tournerai plus rond et sans lesquelles réussir une thèse dans de si bonnes conditions aurait été impossible, pour moi, comme pour beaucoup d'autres.

Je tiens ensuite à remercier les membres de la communauté scientifique plus largement, qui, de manière plus ou moins importante, ont apporté leur pierre à l'édifice de cette thèse.
Je pense bien entendu aux membres de mon jury de soutenance qui ont montré un intérêt certain pour mon travail, dont les pertinentes questions et surtout les très chaleureuses remarques m'ont grandement touché. Je remercie en particulier les rapporteurs, Vincent et Richard, d'avoir accepté de relire ces quelques 500 pages dans un délai si court, du cœur qu'ils ont mis à l'ouvrage et des retours bienveillants qu'ils m'en ont fait. Je remercie également Didier Jamet d'avoir assisté à ma soutenance et d'avoir posé, en son temps, les premiers jalons, ô combien importants, sur lesquelles mon travail s'est appuyé sans retenue, ainsi que pour les nombreuses réponses qu'il a toujours su nous apporter lorsque parfois le chemin semblait bloqué.
Je pense également à nos collaborateurs au sein du projet ANR SubSuperjet : Pierre, Alexandre, Bénédicte avec son esprit scientifique aiguisé, sa bonne humeur communicative et sa motivation toujours renouvelée. J'adresse une pensé chaleureuse et toute particulière à Richard, qui aura su éclairer toutes ces sessions de travail d'une brillance scientifique qui n'est plus à démontrer, d'un regard toujours curieux et bienveillant, de conseils extrêmement avisés et d'une chaleur humaine que je n'oublierai pas.

Je tiens également à remercier toutes les autres personnes, en dehors du cadre scientifique, qui durant toutes ces années ont suivi activement mon travail.
Je salue mes collègues de la SNCF qui auront su me pousser à mener ce train à destination, fut-ce avec un peu de retard.
Je remercie "mes préférées", Claire et Lucie (et j'embrasse Alba), qui m'auront suivi toutes années sans jamais être avares de curiosité, d'empathie, d'encouragements et de mots pour me motiver.
Je remercie bien entendu mes Patounes : ma Estellou, mon Pedrito, ma Mamandine, el Hombre et mon Guacabro, jamais à court de vannes pour me rappeler les années passées sans soutenir, jamais à court de vin pour me remonter le moral et surtout jamais à court d'amitié pour me soutenir, sans faille.
Je remercie enfin mes proches pour leur patience, leur compréhension, leurs questions parfois ennuyeuses, leur inquiétude et leur bienveillance, qui je le sais, continuerons de m'accompagner dans la suite comme durant toutes ces années.

Je termine enfin en adressant ces derniers remerciements à mon directeur de thèse Sébastien Ducruix et mon encadrant de thèse Thomas Schmitt. Au-delà du privilège de travailler aux côtés de scientifiques de ce calibre, ils ont été, durant toutes ces années, deux piliers sur lesquels j'ai toujours pu compter et m'appuyer pour avancer dans mon travail. Face à un sujet aussi complexe, la confiance indéfectible qu'ils m'ont accordée depuis le premier jour jusqu'au dernier, leur savoir scientifique et technique, leur humanité, leur patience et leur compréhension, dans les bons comme dans les mauvais moments, sont des points essentiels qui m'ont permis d'arriver à bon port avec succès, un accomplissement qui est le leur tout autant que le mien.

Contents

Introduction **1**

1 Real gas thermodynamics **19**
1.1 Description and modeling of real gas thermodynamics . . . 20
1.1.1 The Virial expansion . . . 20
1.1.2 Molecular interactions and interatomic potentials . . . 21
1.1.3 The critical point . . . 23
1.2 Main thermodynamic results and cubic equations of state . . . 25
1.2.1 The corresponding states principle . . . 25
1.2.2 Cubic equations of state . . . 26
1.2.3 Departure values . . . 28
1.2.4 Transport properties for real gases . . . 31
1.3 Application to the Soave-Redlich-Kwong equation of state . . . 34
1.3.1 Departure values for cubic equations of state . . . 34
1.3.2 Application to the Soave-Redlich-Kwong equation of state . . . 34
1.4 Thermodynamic stability . . . 42
1.4.1 Stability criteria for isolated systems . . . 43
1.4.2 Liquid-vapor equilibrium . . . 44

I Review of interface simulation methods **49**

2 Sharp interface methods: Interface tracking **51**
2.1 Boundary Integral methods and Marker-and-Cell methods . . . 52
2.1.1 Boundary Integral methods . . . 52
2.1.2 Marker-and-Cell methods . . . 54
2.2 Front-Tracking methods . . . 62
2.2.1 Historical overview . . . 62
2.2.2 The computational setting . . . 64
2.2.3 The tracking of the interface . . . 66
2.2.4 Words on Glimm's methodology . . . 70
2.2.5 Tryggvason's methodology . . . 73

3 Sharp interface methods: Interface capturing **79**
3.1 Volume-of-Fluid methods . . . 80
3.1.1 Historical overview . . . 80

3.1.2 Modeling and equations . . . 82
3.1.3 VOF with Interface Reconstruction methods . . . 83
3.1.4 VOF with Flux Reconstruction methods . . . 92
3.2 Level-Set methods . . . 99
3.2.1 Historical overview . . . 99
3.2.2 Modeling and equations . . . 101
3.2.3 Reinitialization and extension . . . 107
3.2.4 Conservative Level-Set methods . . . 110

4 Diffuse interface methods 119
4.1 Phase-Field methods . . . 120
4.1.1 Historical overview . . . 120
4.1.2 Fundamental notions for the Phase-Field methods . . . 123
4.1.3 Cahn-Hilliard and Allen-Cahn equations . . . 127
4.1.4 Geometric approach to Phase-Field methods . . . 137
4.1.5 Phase-Field methods with Navier-Stokes equations . . . 140
4.2 Multi-Fluid methods . . . 149
4.2.1 Historical overview . . . 149
4.2.2 Out-of-equilibrium model . . . 150
4.2.3 Mechanical and kinematic equilibrium models . . . 151

5 The Second Gradient theory 159
5.1 Phenomenological approach to the capillary effects . . . 160
5.1.1 Molecular description of capillary phenomena . . . 160
5.1.2 Microscopic approach : Korteweg's model of capillarity . . . 163
5.1.3 Energetic approach to the Second Gradient model . . . 166
5.2 Conservation equations in the Second Gradient theory . . . 169
5.2.1 Virtual power principle . . . 169
5.2.2 First principle of thermodynamics . . . 172
5.2.3 Second principle of thermodynamics . . . 174
5.2.4 Equations in the Second Gradient theory . . . 176
5.3 Thermodynamic closure of the Second Gradient model . . . 178
5.3.1 Thermodynamic variables in the Second Gradient theory . . . 178
5.3.2 Application to the case $F_1 = \lambda \left(\boldsymbol{\nabla}\rho\right)^2 /2$ . . . 180
5.3.3 Words on multi-species cases . . . 181
5.4 Macroscopic characterization of a planar interface . . . 183
5.4.1 Existence and type of solutions . . . 183
5.4.2 Quantification of interface macroscopic values of interest . . . 189
5.4.3 Evaluation of the capillary coefficient λ . . . 196

II Implementation of the Second Gradient model in the solver AVBP 201

6 Presentation of the AVBP-RG solver 203
6.1 Main features of the AVBP solver . . . 204
6.1.1 Overwiew of the solver . . . 204
6.1.2 Residual distribution in the *Cell-Vertex* formulation . . . 205

6.2 Numerical schemes in AVBP . . . 208
6.2.1 Advection schemes . . . 208
6.2.2 Temporal integration . . . 212
6.2.3 Diffusive terms . . . 213
6.2.4 Numerical stabilization . . . 215
6.3 Boundary conditions in AVBP . . . 218
6.3.1 Hard boundary conditions . . . 218
6.3.2 Characteristic boundary conditions . . . 219

7 Numerical implementation of the Second Gradient model 221
7.1 Discretization of the Second Gradient equations . . . 222
7.1.1 Governing equations . . . 222
7.1.2 Numerical discretization . . . 224
7.1.3 Comparisons between the 2Δ and 4Δ discretizations . . . 229
7.2 Characterization of the Second Gradient equations . . . 235
7.2.1 Nature of the equations . . . 236
7.2.2 Boundary conditions . . . 243
7.2.3 Determination of a time step condition . . . 247

8 Numerical validation of the Second Gradient model 255
8.1 Validation cases in one dimension . . . 256
8.1.1 Stationary cases . . . 256
8.1.2 Isothermal 1D simulations . . . 258
8.1.3 Non isothermal 1D simulations . . . 260
8.1.4 Convergence orders . . . 274
8.2 Validation cases in two dimensions . . . 276
8.2.1 Oscillating planar interfaces . . . 276
8.2.2 Oscillating droplets . . . 290

III The Thickened Interface Method for the Second Gradient theory 303

9 Thickening strategies for the Second Gradient theory 305
9.1 The need for thickening strategies . . . 306
9.1.1 Adaptation of the Second Gradient theory to DNS meshes . . . 306
9.1.2 Thickening near the critical point . . . 308
9.1.3 Thermodynamically consistent thickening . . . 311
9.2 The Thickened Interface Method . . . 313
9.2.1 Modification of the thermodynamics . . . 314
9.2.2 Thermo-mechanical equation of the TIM . . . 319

10 Numerical validation of the Thickened Interface Method 325
10.1 Validation of the method in 1D configurations . . . 325
10.1.1 Isothermal 1D simulations with the TIM . . . 325
10.1.2 Non-isothermal 1D simulations with the TIM . . . 328
10.1.3 Convergence orders . . . 331
10.2 Validation of the method in 2D configurations . . . 334

10.2.1 Planar oscillating interface . . . 334
10.2.2 Oscillating droplets . . . 344

11 Application of the Thickened Interface Method 349
11.1 Colliding droplets . . . 349
11.1.1 General results for colliding droplets . . . 349
11.1.2 Numerical simulations . . . 352
11.1.3 Critical Weber identification . . . 356
11.2 Periodic liquid jets . . . 361
11.2.1 Numerical setup . . . 361
11.2.2 Impact of the jet velocity . . . 367
11.2.3 Impact of the spatial resolution . . . 371
11.2.4 Impact of the thickening coefficient . . . 376

Conclusion 385

A Usefull mathematical results 389
A.1 Results for linear and tensorial algebra . . . 389
A.1.1 Definitions . . . 389
A.1.2 Operations . . . 389
A.2 Result for differential calculus . . . 391
A.2.1 Differential operators . . . 391
A.2.2 Transport theorems . . . 392
A.2.3 Differential relationships . . . 393
A.3 Additional results . . . 395
A.3.1 Minimization of parametric integrals . . . 395
A.3.2 Cardan's method for 3^{rd} order equations . . . 399
A.4 Usefull relationships . . . 400
A.4.1 Linear/Tensorial algebra . . . 400
A.4.2 Differential operators . . . 400
A.4.3 Differential calculus . . . 401

B Complementary thermodynamic results 403
B.1 Brief results from general thermodynamics . . . 403
B.1.1 Global functions . . . 403
B.1.2 Volumetric functions . . . 404
B.1.3 Specific functions . . . 404
B.1.4 Maxwell's relations . . . 405
B.1.5 Partial derivatives . . . 406
B.2 Definition and derivation for real gas thermodynamics . . . 408
B.2.1 Residual values . . . 408
B.2.2 Other values . . . 413
B.2.3 Heat capacities . . . 413
B.3 Definition and derivation for cubic equations of state . . . 415
B.3.1 Departure values . . . 415
B.4 Thermodynamic modifications for the Thickened Interface Method . . . 418
B.4.1 Derivatives of saturation values . . . 419

C Additional developments on the Second Gradient theory **423**
C.1 Virtual power principle for the Second Gradient theory 423
C.1.1 Virtual power of the internal forces 424
C.1.2 Virtual power of the external forces 424
C.1.3 Virtual power of the acceleration forces 424
C.1.4 Virtual power theorems 425
C.1.5 Equations of motion 425
C.2 Gibbs equation 426
C.3 Entropy balance 427
C.4 Equilibrium conditions for an isothermal interface 429

Bibliography **433**

List of Tables

1 Specifications for the engines found on notable modern heavy launchers 5
2 Overview of experimental studies performed for cryogenic combustion, taken from Candel et al. (2006) and Rocchi (2014) 16

1.1 Values of the constants used in the principal cubic equations of state. 28

4.1 Pressure and capillary tensor divergence used in the literature for the incompressible Navier-Stokes PFM model. 143

5.1 Coefficients c_1 and c_2 used for the calculation of the capillary coefficient using Eq. (5.174). 198

7.1 List of high order derivatives terms in the SG equations 223
7.2 List of tested configurations depending on the discretization of the capillary terms 229
7.3 Simulation parameters used with N_2 for one and two dimensional comparisons for the implementation of the SG model in the solver AVBP 230
7.4 Simulation parameters used for the one dimensional N_2 uniform system to test the characteristic boundary conditions. 244
7.5 Simulation parameters used for the one dimensional N_2 uniform system to test the characteristic boundary conditions in presence of an interface. 246
7.6 Slope of Δt with respect to Δx in logarithmic scale for different values of λ . . 249
7.7 Slope of Δt with respect to λ in logarithmic scale for different values of Δx . . 249
7.8 Impact of the reduced temperature T_r on the time step Δt and several other main variables, with $\Delta x = 4.64 \cdot 10^{-5}$ m 250
7.9 Slope of Δt with respect to ρ_l in logarithmic scale for different elements 252

8.1 Simulation parameters used for the one dimensional N_2 planar interface in isothermal configurations solving Euler SG equations 259
8.2 Simulation parameters used for the one dimensional N_2 planar interface in non-isothermal configurations solving Euler/Navier-Stokes SG equations 261
8.3 Simulation parameters used for the one dimensional O_2 planar interface in non-isothermal configurations solving SG Navier-Stokes equations 268
8.4 Integrated energy E and entropy S balance for different interface configurations 272
8.5 Simulation parameters used for the first test case of an oscillating two dimensional N_2 planar interface 277
8.6 Simulation parameters used for the additional tests of an oscillating two dimensional N_2 planar interface 279

8.7 Interface and mesh resolutions used for the convergence study of an oscillating nitrogen interface initially at 100 K . . . 279
8.8 Oscillating periods and characteristic damping times extracted from the simulations, for an oscillating nitrogen interface at 100 K (eight points in the interface) for different values of dynamic viscosity solving isothermal Navier-Stokes equations . . . 282
8.9 Oscillating periods and characteristic damping times from the simulation of an oscillating nitrogen interface initially at 100 K (eight points in the interface) solving non-isothermal and isothermal Navier-Stokes equations for different values of dynamic viscosity . . . 283
8.10 Oscillating periods and characteristic damping times, from theory and simulations, for an oscillating isothermal nitrogen interface at 100 K (eight points in the interface) for different values of kinematic viscosity . . . 287
8.11 Simulation parameters used for the additional tests of an oscillating two dimensional O_2 planar interface with viscosity . . . 288
8.12 Oscillating periods and characteristic damping times, from theory and simulations, for an oscillating isothermal oxygen interface at 110 K (eight points in the interface) for different values of kinematic viscosity . . . 289
8.13 Simulation parameters used for the two dimensional 0_2 oscillating droplet . . . 290
8.14 Oscillation periods and characteristic damping times, from the simulation, the three-dimensional theory and the simplified two-dimensional correlation, for an oscillating isothermal oxygen droplet at 110 K (eight points in the interface) for different values of kinematic viscosity . . . 296
8.15 Interface, droplet and mesh resolutions used for the convergence study of an oscillating O_2 droplet . . . 297

10.1 Simulation parameters used for the one dimensional N_2 planar interface in isothermal configurations solving Euler SG equations modified by the TIM. w_0 is the interface thickness prior to the application of the thickening method. . . 326
10.2 Simulation parameters used for the two dimensional N_2 planar interface with the TIM . . . 334
10.3 Simulation parameters used for the two dimensional N_2 planar interface using the TIM with a non-isothermal initial solution . . . 337
10.4 Simulation parameters used for the additional tests of an oscillating two dimensional oxygen planar interface thickened with the TIM . . . 339
10.5 Laplace numbers and corresponding values of kinematic viscosity to perform simulation-theory comparisons for an oscillating isothermal oxygen interface at 110 K using different thickening factors in the TIM . . . 340
10.6 Oscillation periods and characteristic damping times, from theory and simulations, for an oscillating isothermal oxygen interface at 110 K (eight points in the interface) for different values of kinematic viscosity. Results obtained with a thickening factor F = 100 applied following the TIM. . . . 342
10.7 Oscillation periods and characteristic damping times, from theory and simulations, for an oscillating isothermal oxygen interface at 110 K (eight points in the interface) for different values of kinematic viscosity. Results obtained with a thickening factor F = 10000 applied following the TIM . . . 343

10.8 Simulation parameters used for the two dimensional isothermal oscillating oxygen droplets using the TIM . . . 344
10.9 Values of Laplace number and kinematic viscosity used for the two dimensional isothermal oscillating oxygen droplets using the TIM with thickening coefficients F = 100 and F = 10000 . . . 345

11.1 Parameters used for the three dimensional simulations of colliding O_2 droplets . 354
11.2 Values of the Weber We, Reynolds Re and Laplace La numbers of the collisions depending on the initial velocity of the droplets, with the corresponding figures 354
11.3 Number of satellite droplets created by colliding O_2 droplets as predicted by the model from Ko and Ryou (2005) in Eq. (11.14) . . . 361
11.4 Simulation parameters used for the two dimensional N_2 jets (reference mesh resolution and interface thickening leading to about nine points in the interface) 362
11.5 Simulation velocities and corresponding liquid Reynolds, Weber and Ohnesorge numbers used for the simulations of two dimensional N_2 jets with a liquid viscosity $\mu_l = 3.25 \cdot 10^{-4}$ kg $\cdot$ m$^{-1} \cdot$ s^{-1} . . . 362
11.6 Characteristic lengths, velocities and Reynolds numbers for the relevant scale to determine the critical conditions for the DNS (3D) of a liquid nitrogen jet at 100 K in its own vapor. . . . 364
11.7 Characteristic lengths, velocities and Reynolds number for the relevant scale to determine the critical conditions for the DNS (2D) of a liquid nitrogen jet at 100 K in its own vapor. . . . 366
11.8 Mesh resolutions and thickening factors used to study the impact of the interface resolution on the simulation results for a two-dimensional nitrogen jet in its own vapor . . . 366

B.1 Partial derivatives table for the density ρ . . . 406
B.2 Partial derivatives table for the temperature T . . . 406
B.3 Partial derivatives table for the pressure P . . . 406
B.4 Partial derivatives table for the specific sensible energy e_s . . . 407
B.5 Partial derivatives table for the specific enthalpy h . . . 407
B.6 Partial derivatives table for the specific entropy s . . . 407

List of Figures

1 Schematic representation of a rocket engine . . . 2
2 Schematic representation of the main components of the Ariane 5 launcher (type ECA) . . . 3
3 Ideal specific impulse of various oxidizer/fuel combinations, from Haidn (2008) 4
4 Main cycles used for liquid rocket engines . . . 6
5 Evolution of the thermodynamic regime during the early stages of an LRE ignition 7
6 Atomization regimes of a slow dense liquid jet by a fast light coaxial stream, taken from Marmottant and Villermaux (2004). From top left to bottom right the gas velocity is increased, the peeling of the liquid jet intensifies and surface instabilities further dominate the liquid disintegration. . . . 8
7 Breakup regimes in the parameter space $\mathrm{Re}_l - \mathrm{We}$ extracted for a water-air co-flow mixture, taken from Lasheras and Hopfinger (2000) . . . 9
8 Shadowgraphy imaging of liquid N_2 injected into room temperature nitrogen N_2 at different pressures, taken from Chehroudi et al. (2002). The bottom row contains magnified images of the top row in order to examine the shear layer. . . . 11
9 Shadowgraphy imaging of a liquid N_2 / gaseous He co-flow injection into quiescent gaseous He from Mayer et al. (1998), A:10 bar (subcritical pressure) and B:60 bar (supercritical pressure) . . . 12
10 Simulation of a three-dimensional liquid injection using the Front-Tracking method, taken from Bo et al. (2011) . . . 13
11 Simulation of a Diesel injection using a Volume-of-Fluid method with mesh refinement, from Fuster et al. (2009). Interface representation (top) and liquid fraction in a median plane (bottom). . . . 14
12 Simulation of the turbulent atomization of a liquid Diesel jet with the Accurate Conservative Level-Set method, from Desjardins et al. (2008) . . . 15
13 Simulation of a Diesel injection using a coupled Volume-of-Fluid/Level-Set approach, from Shinjo and Umemura (2010). The color indicates the axial velocity in $\mathrm{m.m}^{-1}$ . . . 15

1.1 Representation of the Morse, Exponential and Lennard-Jones potential curves with intermolecular distance in nondimensionalized coordinates . . . 22
1.2 Phase diagram schematics of a pure compound for temperature/pressure conditions. Inspired by Jessop and Leitner (2008) and Dahms and Oefelein (2013) 23
1.3 Clapeyron's diagram for pure oxygen O_2 with Andrew's isotherm curves for different regimes temperatures. Values taken from NIST thermodynamic database (Linstrom and Mallard (2001)). . . . 24

1.4 Evolution of the viscosity μ and the thermal conductivity k_{th} for nitrogen N_2 at subcritical and supercritical pressure ($P_c = 33.958$ Pa), from NIST online database Linstrom and Mallard (2001) 32
1.5 Isobaric curves of O_2 density ρ with respect to the temperature for the IG, vdW, PR and SRK EoSs. Reference values from NIST online database (Linstrom and Mallard (2001)) plotted for comparison 36
1.6 Isobaric curves of O_2 specific internal energy e_s with respect to the temperature for the IG, vdW, PR and SRK EoSs. Reference values from NIST online database (Linstrom and Mallard (2001)) plotted for comparison 36
1.7 Isobaric curves of O_2 specific isobaric heat capacity C_p with respect to the temperature for the IG, vdW, PR and SRK EoSs. Reference values from NIST online database (Linstrom and Mallard (2001)) plotted for comparison 37
1.8 Isobaric curves of O_2 sound speed c with respect to the temperature for the IG, vdW, PR and SRK EoSs. Reference values from NIST online database (Linstrom and Mallard (2001)) plotted for comparison 37
1.9 Isobaric curves of CH_4 density ρ with respect to the temperature for the IG, vdW, PR and SRK EoSs. Reference values from NIST online database (Linstrom and Mallard (2001)) plotted for comparison 38
1.10 Isobaric curves of CH_4 specific internal energy e_s with respect to the temperature for the IG, vdW, PR and SRK EoSs. Reference values from NIST online database (Linstrom and Mallard (2001)) plotted for comparison 38
1.11 Isobaric curves of CH_4 specific isobaric heat capacity C_p with respect to the temperature for the IG, vdW, PR and SRK EoSs. Reference values from NIST online database (Linstrom and Mallard (2001)) plotted for comparison 39
1.12 Isobaric curves of CH_4 sound speed c with respect to the temperature for the IG, vdW, PR and SRK EoSs. Reference values from NIST online database (Linstrom and Mallard (2001)) plotted for comparison 39
1.13 Isobaric curves of H_2 density ρ with respect to the temperature for the IG, vdW, PR and SRK EoSs. Reference values from NIST online database (Linstrom and Mallard (2001)) plotted for comparison 40
1.14 Isobaric curves of H_2 specific internal energy e_s with respect to the temperature for the IG, vdW, PR and SRK EoSs. Reference values from NIST online database (Linstrom and Mallard (2001)) plotted for comparison 40
1.15 Isobaric curves of H_2 specific isobaric heat capacity C_p with respect to the temperature for the IG, vdW, PR and SRK EoSs. Reference values from NIST online database (Linstrom and Mallard (2001)) plotted for comparison 41
1.16 Isobaric curves of H_2 sound speed c with respect to the temperature for the IG, vdW, PR and SRK EoSs. Reference values from NIST online database (Linstrom and Mallard (2001)) plotted for comparison 41
1.17 Schematic representation of the evaluation of the saturation pressure and densities for a given temperature with the SRK EoS 46
1.18 Evolution of the saturation pressure P^{sat} with the saturation temperature T^{sat} for different fluids. Comparison of vdW, PR and SRK equations of state. Reference values from NIST database plotted for comparison 47

2.1 Description of the time evolution of a vortex-sheet roll-up using a periodic distribution of vortices, taken from Rosenhead (1931) . . . 53
2.2 Staggered grid used in MAC methods, here in two dimensions . . . 55
2.3 Dissemination of markers in the fluid part of the domain . . . 56
2.4 Flagging of the cells used in MAC methods for single fluid simulations . . . 56
2.5 Time evolution of a water reservoir behind a sluice from Welch et al. (1965). The shape of the domain allows the water to break backwards toward the gate 59
2.6 Time evolution of a water droplet splashing into an initially quiescent water plane Amsden and Harlow (1970) . . . 60
2.7 Transient solution for two bubbles of different density rising in a third continuous phase, at different times, from De Sousa et al. (2004) . . . 61
2.8 Transient solution of a splashing drop falling into the free surface of a heavier and more viscous fluid, from De Sousa et al. (2004) . . . 61
2.9 Simulation of the cavity filling problem with two impacting water jets, from Raad and Bidoae (2005) . . . 62
2.10 Dual-mesh configuration used for calculations in FT methods . . . 64
2.11 Representation of two case of ill-fitted Lagrangian mesh for the interface: (a) points to far apart, (b) two high point concentration . . . 65
2.12 Schematic representation of the interface maintenance procedures: (a) addition of a new node, (b) removal of excess nodes by fusion. . . . 66
2.13 Riemann problem used in Glimm's methodology (see Glimm et al. (2001)) to create the ghost fluid values for the GFM. . . . 70
2.14 Interface representation between two fluids in early and late time steps in a simulation of Rayleigh-Taylor instabilities, taken from Glimm et al. (2001) . . . 72
2.15 Snapshots of density isosurface of 3D liquid jet injection at different times from Bo et al. (2011). Density ratio used ≈ 10, $Re \approx 2000$, $We \approx 2000$, Jet velocity $\approx 200\mathrm{m} \cdot \mathrm{s}^{-1}$ . . . 73
2.16 Schematic representation of the algebraic Fast-Marching method to determine interface normal vector in the fluid region from Terashima and Tryggvason (2009) 75
2.17 Snapshots of colliding and coalescing 3D droplets in two different impacting conditions from Nobari, Jan, and Tryggvason (1996) . . . 76
2.18 Snapshots of colliding 3D droplets in two extremes impacting conditions from Razizadeh, Mortazavi, and Shahin (2018) . . . 76
2.19 Snapshot of an air bubble in water (b) and a water cylinder in air (b) interacting with a shockwave Razizadeh, Mortazavi, and Shahin (2018). Upper:experiments, lower:simulation . . . 77
2.20 Evolution of a liquid/vapor interface during film boiling on a horizontal cylinder from Esmaeeli and Tryggvason (2004). . . . 77
2.21 Evolution of a saturated nucleate boiling from Sato and Ničeno (2013), the flow temperature is shown, the interface and the flow velocity field are depicted respectively on the right and left sides . . . 78

3.1 Typical cartesian mesh used in Volume-of-Fluid simulations using Interface Reconstruction methods . . . 83

3.2 Interface reconstruction using contant (SLIC) (b.1), (b2) and the piecewise linear PLIC (c) and quadratic (PROST) (d) methods from a reference volume fraction repartition (a) . . . 84
3.3 Result of different reconstruction methods depending on the order and regularity desired: (a) reference, (b) piecewise linear, (c) piecewise quadratic, (d) $\mathcal{C}^0$ continuous quadratic, (e) $\mathcal{C}^1$ continuous quadratic . . . 86
3.4 Principle of the Lagrangian split advection algorithm for Volume-of-Fluid methods, (a) and (b) are respectively the velocity determination and the volume advection respectively for the x-sweep, (c) and (d) represents the same steps for the y-sweep . . . 88
3.5 Principle of the Eulerian split advection algorithm for Volume-of-Fluid methods 89
3.6 Principle of the Lagrangian unsplit advection algorithms for Volume-of-Fluid methods . . . 90
3.7 Principle of the Eulerian unsplit advection algorithm EMFPA for Volume-of-Fluid methods from López et al. (2004) . . . 91
3.8 Snapshot of hollow-cone atomizer representative of automotive injection of isooctane from Fuster et al. (2009). Velocity norm used as color . . . 92
3.9 Snapshot of the atomization of a round water jet in a quiescent air from Le Chenadec and Pitsch (2013) . . . 93
3.10 Canonical 1D configuration used to construct the normalized variable diagram . 94
3.11 Example of a normalized variable diagram . . . 94
3.12 Impact of the Courrant number on the CBC (a) and example of the behavior the HRIC scheme from Muzaferija and Peric (1997) using the NVD for different values of CFL (b) . . . 95
3.13 Time evolution a three-dimensional water flow during the breaking of a damn with a secondary downstream obstacle from Issakhov and Imanberdiyeva (2019) 98
3.14 Snapshot of a three-dimensional hemisphere impacting an initially quiescent water plane with air above from Nguyen and Park (2017) . . . 99
3.15 Schematic representation of the Level-Set mechanics with function φ in a 2D setting: (a) the full surface defined with it zero level set, (b) the corresponding interface Γ . . . 102
3.16 Schematic representation of the Narrow Band approach; the extension, reinitialization and advection are only performed in the hatched area . . . 106
3.17 Simulations of inviscid air bubbles in water from Sussman et al. (1999). (a) Single bubble rising. (b) Interaction between two bubbles. . . . 111
3.18 Comparison between experiment and simulation of the head on collision of water droplets from Tanguy and Berlemont (2005). (a) Experimental results from Ashgriz and Poo (1990) (b) Simulation from Tanguy and Berlemont (2005). . . . 111
3.19 Simulation of the turbulent atomization of a liquid Diesel with the Accurate Conservative Level-Set method, from Desjardins et al. (2008) . . . 116
3.20 Simulation of a liquid-vapor flow in an annular cavity with gravitational effects from Mccaslin and Desjardins (2014). (a) $Re = 3370$, $We = 906$, $Fr = \infty$. (b) $Re = 3480$, $We = 967$, $Fr = 4.56$. (c) $Re = 3650$, $We = 1070$, $Fr = 1.20$. . . . 116
3.21 Simulation of a liquid droplet impacting a liquid pool of same nature from Shukla (2014). . . . 117

4.1 Free energy density F for an homogeneous system authorizing the existence of two stable phases . . . 125
4.2 Generic form of an interface in the PFM paradigm. . . . 125
4.3 Simulation of interface dynamics related configurations using the Cahn-Hilliard equation, taken from Brassel and Bretin (2011) . . . 129
4.4 Time evolution of the phase field during a spinodal decomposition and a coarsening simulated with the Cahn-Hilliard equation, taken from Kim et al. (2016) 130
4.5 Spinodal decomposition solving Cahn-Hilliard equation with a forced circular convection, taken from Kay et al. (2009) . . . 131
4.6 Return to a spherical shape of a liquid torus solving the non-conservative and conservative Allen-Cahn equations, taken from Brassel and Bretin (2011) . . . 132
4.7 Spinodal decomposition simulated using the conservative Allen-Cahn equations with different numbers of species, taken from Kim and Lee (2017) . . . 133
4.8 Water penetrating the air-filled gap between parallel plates with hydrophilic properties, taken from Takada et al. (2013) . . . 145
4.9 Time evolution of the concentration in a two-dimensional Rayleigh-Taylor instability for different Reynolds numbers ((a) $Re = 30$, (b) $Re = 150$, (c) $Re = 3000$, (d) $Re = 30000$), taken from Liang et al. (2014) . . . 146
4.10 Dynamic deformation of a liquid crystal drop immersed in a viscous fluid, taken from Shen and Yang (2014) . . . 146
4.11 Dynamic time evolution of a bubble rising into two layered non-miscible fluids of different characteristics, taken from Zhao et al. (2017) . . . 147
4.12 Simulation of a water droplet impacting a quiescent water film using a pseudo-conservative geometric approach for the phase-field equation, take from Chiu and Lin (2011) . . . 148
4.13 Comparison between experimental results form Layes and Le Métayer (2007) *(left images)* and simulations using the quick relaxing 6-equation model for a shock-bubble interaction configuration *(right images)*, taken from Saurel et al. (2009) . . . 152
4.14 Three dimensional simulation of a shock-bubble interaction with the 4-equation model, taken from Hejazialhosseini et al. (2013) . . . 153
4.15 Large Eddy Simulation with the 4-equation model of a reactive LO_x/GH_2 coaxial jet in transcritical injection conditions based in the Mascotte bench (see Habiballah et al. (1996); Vingert et al. (1999); Gicquel et al. (2001)) taken from Gaillard et al. (2016). Instantaneous temperature field in an axial cut plane (upper image) and temperature isosurface at $T = 1500\ K$ colored by the axial velocity (lower image). . . . 154
4.16 Simulation of the fragmentation of a liquid oxygen jet by a coaxial gaseous nitrogen co-flow solving the 3-equation model, taken from Chiapolino et al. (2017a). . . . 156
4.17 Large Eddy Simulation with the 3-equation model of a reactive LO_x/GH_2 coaxial jet in transcritical injection conditions based in the Mascotte bench (see Habiballah et al. (1996); Vingert et al. (1999); Gicquel et al. (2001)) taken from Pelletier (2019). Instantaneous fields in an axial cut plane, from top to bottom: O_2 mass fraction, OH mass fraction, H_2O mass fraction, temperature, axial velocity, density, stable **(red)**/unstable**(blue)** thermodynamic state. . . . 157

5.1 Schematic representation of the molecular interactions between to molecules . . 161
5.2 Schematic representation of a control volume $d\mathcal{V}$ and a remote volume $d\Omega$ to evaluate the modified momentum equation for a capillary fluid 164
5.3 Example of a profile W for $\rho_1 = \rho_v$. The figure shows remarkable densities: the saturation densities ρ_v and ρ_l; the metastable limit densities ρ_v^s and ρ_l^s 185
5.4 Intersection in 3D (left) and 2D (right) between the surface $\mathcal{S}(\rho, \rho')$ in grey and the plane $\mathcal{P}(\rho, \rho') = 0$ in blue for $\rho_1 < \rho_v$ 186
5.5 Example of a flat profile in the liquid phase 186
5.6 Intersection in 3D (left) and 2D (right) between the surface $\mathcal{S}(\rho, \rho')$ in grey and the plane $\mathcal{P}(\rho, \rho') = 0$ in blue for $\rho_v^s < \rho_1 < rho_l^s$ 187
5.7 Example of an unstable flat profile in the unstable densities region 187
5.8 Intersection in 3D (left) and 2D (right) between the surface $\mathcal{S}(\rho, \rho')$ in grey and the plane $\mathcal{P}(\rho, \rho') = 0$ in blue for $\rho_1 = \rho_v$ 188
5.9 Example of an interface profile between the vapor and liquid densities 188
5.10 Intersection in 3D (left) and 2D (right) between the surface $\mathcal{S}(\rho, \rho')$ in grey and the plane $\mathcal{P}(\rho, \rho') = 0$ in blue for $\rho_v < \rho_1 < \rho_v^s$ 189
5.11 Example of a soliton profile in the metastable densities region 189
5.12 Isothermal interface at equilibrium with the definition of its width w 190
5.13 Schematic representation of the excess volumetric free energy for the reference interface profile ρ^{r}. 192
5.14 Evolution of the interface thickness w and surface tension σ with the capillary coefficient λ for oxygen O_2 at different reduced temperature T/T_c. Results in logarithmic scale 196
5.15 Comparison of Lin's and our simplified correlations for the calculation of the capillary coefficient λ of nitrogen N_2 with the temperature T 198

6.1 Schematic representation of the meshes used for the three man formulations of Finite Volume methods 205
6.2 Schematic representation of the *Cell-Vertex* procedure : the residuals are calculated "at the cells" and are then redistributed to the cells vertices 207
6.3 Schematic representation of triangular volume of control (2D) with the faces (edges) normal $\boldsymbol{n}_{i,j}^e$ and the nodes normals $\boldsymbol{S}_j^e$ 207
6.4 Response of the filter F_N as a function of the normalized wavenumber for different numbers N of G-filter iterations, taken from Schmitt (2020) 216

7.1 Final density, pressure, temperature and velocity profiles of one dimensional isothermal nitrogen droplets after one crossing of the periodic domain to compare different discretizations of capillary fluxes terms 230
7.2 Final density, pressure, temperature and velocity profiles of one dimensional non-isothermal nitrogen droplets after one crossing of the periodic domain to compare different discretizations of capillary fluxes terms 231
7.3 Density profiles of two dimensional isothermal nitrogen droplets after one crossing of the periodic domain to compare different discretizations of capillary fluxes terms 232

7.4 Pressure profiles of two dimensional isothermal nitrogen droplets after one crossing of the periodic domain to compare different discretizations of capillary fluxes terms . . . 232
7.5 Density, pressure and temperature profiles of two dimensional non-isothermal nitrogen droplets after one crossing of the periodic domain to compare different discretizations of capillary fluxes terms . . . 233
7.6 Time evolution of density and velocity profiles for a one dimensional isothermal oxygen droplet using 2Δ and 4Δ configurations for the calculation of the Laplacian terms . . . 234
7.7 Evacuation of an acoustic wave in the SG system, non reflecting boundary conditions are used on both the left and right sides . . . 245
7.8 Evacuation of an entropic wave in the SG system, non reflecting boundary conditions are used on both the left and right sides . . . 246
7.9 Evacuation of an interface in the SG system, non reflecting boundary conditions are used on both the left and right sides . . . 247
7.10 Evolution, in log scale, of the limit time step: with respect to the mesh size for different capillary coefficients *(left)*, with respect to the capillary coefficient for different mesh sizes *(right)*. . . . 248
7.11 Evolution of the limit time step with respect to different variables impacted by the varying reduced temperature. . . . 251
7.12 Evolution, in log scale, of the limit time step with respect to the density gap $\Delta\rho$: for N_2 *(left)*, O_2 *(center)* and H_2 *(right)* . . . 251
7.13 Evolution, in log scale, of the limit time step with respect to the vapor density ρ_v: for N_2 *(left)*, O_2 *(center)* and H_2 *(right)* . . . 252
7.14 Evolution, in log scale, of the limit time step with respect to the liquid density ρ_l: for N_2 *(left)*, O_2 *(center)* and H_2 *(right)*. Red dotted lines for the log-linear regression. . . . 252
7.15 Evolution of the limit time step constant coefficient with respect to the reduced temperature. . . . 253
7.16 Comparative evolution, in semi-log scale, of the limit time steps for the Second Gradient (full line) and Brackbill (dashed line) models with respect to the temperature T: for N_2 *(left)*, O_2 *(center)* and H_2 *(right)* . . . 254

8.1 Comparison between the saturation densities calculated with the equilibrium criterion and predicted by the Second Gradient model for several single species. The relative errors for ρ_l and ρ_v are magnified. . . . 258
8.2 Density and pressure profiles of an isothermal N_2 interface convected at constant speed $u = 10\text{m} \cdot \text{s}^{-1}$. The plain lines show the calculation results and the dashed lines show the theoretical/ideal position of the interface. Non-reflecting velocity-temperature inlet (left) and pressure outlet (right) used. . . . 259
8.3 Density and pressure profiles of a static isothermal N_2 interface initially stretched by a factor 2. The plain lines show the calculation results and the dashed lines show the theoretical/ideal position of the interface. Non-reflecting pressure outlets (left and right) used. . . . 260

8.4 Density and pressure profiles of a static isothermal N_2 interface initially compressed by a factor 3. The plain lines show the calculation results and the dashed lines show the theoretical/ideal position of the interface. Non-reflecting pressure outlets (left and right) used. 260
8.5 Density and pressure profiles of an isothermal N_2 interface initially stretched by a factor 2 and convected at constant speed $u = 10\mathrm{m} \cdot \mathrm{s}^{-1}$. The plain lines show the calculation results and the dashed lines show the theoretical/ideal position of the interface. Non-reflecting velocity-temperature inlet (left) and pressure outlet (right) used. 261
8.6 Density, temperature, pressure and velocity profiles of a non isothermal N_2 interface interface initially stretched by a factor 2. The plain lines show the calculation results and the dashed lines show the theoretical/ideal position of the interface. Non-isothermal Euler SG equations (mass, momentum, energy) are solved. Non-reflecting pressure outlets (left and right) used. 262
8.7 Density, temperature, pressure and velocity profiles of a non isothermal N_2 interface interface initially stretched by a factor 2. Euler and Navier-Stokes SG equations (mass, momentum, energy) are solved. Non-reflecting pressure outlets (left and right) used. 263
8.8 Density, temperature, pressure and velocity profiles of a N_2 droplet convected at constant speed $u = 10\ \mathrm{m} \cdot \mathrm{s}^{-1}$. The plain lines show the calculation results and the dashed lines show the theoretical/ideal position of the interface. Periodic boundary conditions (left and right) used. Non isothermal SG Euler equations are solved, 8 points in the interface 264
8.9 Temperature profiles of a N_2 droplet convected at constant speed $u = 10\mathrm{m} \cdot \mathrm{s}^{-1}$. The plain lines show the calculation results and the dashed lines show the theoretical/ideal position of the interface. Periodic boundary conditions (left and right) used. Non isothermal SG Euler equations are solved for multiple higher mesh resolutions. 264
8.10 Density, temperature, pressure and velocity profiles of a N_2 droplet convected at constant speed $u = 10\mathrm{m} \cdot \mathrm{s}^{-1}$. Periodic boundary conditions (left and right) used. Non isothermal SG Euler equations are solved for multiple lower mesh resolutions 265
8.11 Density, temperature, pressure and velocity profiles of a N_2 droplet convected at constant speed $u = 10\mathrm{m} \cdot \mathrm{s}^{-1}$. Periodic boundary conditions (left and right) used. Non isothermal SG Navier-Stokes equations are solved with Chung's diffusion model, for multiple lower mesh resolutions 266
8.12 Density, temperature, pressure and velocity profiles of a N_2 droplet convected at constant speed $u = 10\mathrm{m} \cdot \mathrm{s}^{-1}$. Periodic boundary conditions (left and right) used. Non isothermal SG Navier-Stokes equations are solved with native AVBP artificial viscosity. 267
8.13 Density, temperature, pressure and profiles of a heated O_2 droplet with viscosity and thermal conduction. The dashed lines show the theoretical isothermal profiles at 110K and 140K, the plain lines show the calculation results. Isothermal boundary conditions at 140K are used on both sides. SG Navier-Stokes equations are solved, Chung model is used for the diffusive fluxes. 269

8.14 Density, temperature, pressure and profiles of a vanishing heated O_2 droplet with viscosity and thermal conduction (continuation of Fig. 8.13). The dashed lines show the theoretical isothermal profiles at 140K and 170K, the plain lines show the calculation results. Isothermal boundary conditions at 170K are used on both sides. SG Navier-Stokes equations are solved, Chung model is used for the diffusive fluxes. 270
8.15 Density, temperature, pressure and profiles of the creation of O_2 droplet with viscosity and thermal conduction. The dashed lines show the theoretical isothermal profiles at 170K and 140K, the plain lines show the calculation results. Isothermal boundary conditions at 140K are used on both sides. SG Navier-Stokes equations are solved, Chung model is used for the diffusive fluxes. 271
8.16 Density, temperature, pressure and profiles of a cooled O_2 droplet with viscosity and thermal conduction (continuation of Fig. 8.15). The dashed lines show the theoretical isothermal profiles at 140K and 110K, the plain lines show the calculation results. Isothermal boundary conditions at 140K are used on both sides. SG Navier-Stokes equations are solved, Chung model is used for the diffusive fluxes. 272
8.17 Density, temperature, pressure and profiles of an evaporating O_2 interface with viscosity and thermal conduction. An isothermal wall at 140K is used on the left side with a temperature relaxation condition while an non-reflecting outlet is used on the right boundary. SG Navier-Stokes equations are solved, Chung model is used for the diffusive fluxes. 273
8.18 Convergence orders of AVBP's GRK numerical scheme with the SG model implementation in 1D solving Euler isothermal, Euler non isothermal and Navier-Stokes (Chung model) equation. Results after after half a crossing of the domain. Logarithmic scale used for both axis. Interpolation slopes in legend. . . . 274
8.19 Convergence orders of AVBP's GRK numerical scheme with the SG model implementation in 1D solving Euler isothermal, Euler non isothermal and Navier-Stokes (Chung model) equation. Results after after one crossing of the domain. Logarithmic scale used for both axis. Interpolation slopes in legend. 275
8.20 Schematic representation of the computational setting for the oscillating planar interface 277
8.21 Time evolution of the density at the center of the domain for the oscillation of an initially harmonically perturbed plane nitrogen N_2 interface 277
8.22 Zoom on the normalized density gradient profiles at different instants for the oscillation of an initially harmonically perturbed plane N_2 interface 278
8.23 Comparison of the central density time evolution of a two-dimensional planar oscillating interface for different mesh resolutions. Isothermal Euler equations are solved using a selective numerical filter (coeff $1.0 \cdot 10^{-2}$). 279
8.24 Zoom on the normalized density gradient profiles at different instants for the oscillation of an isothermal N_2 interface. Comparison between a 4-point *(leftmost)* and a 8-point *(rightmost)* interface resolutions. 280
8.25 Comparison of the central density time evolution of a two-dimensional planar oscillating nitrogen interface for different mesh resolutions. Isothermal Navier-Stokes equations are solved with constant dynamic viscosity and no thermal conduction. A selective numerical filter (coeff $1.0 \cdot 10^{-2}$) is used. 281

8.26 Comparison of the central density time evolution of a two-dimensional planar oscillating nitrogen interface for different mesh resolutions. Non-isothermal Navier-Stokes equations are solved with constant dynamic viscosity and no thermal conduction. A selective numerical filter (coeff $1.0 \cdot 10^{-2}$) is used. 282
8.27 Comparison of the central density time evolution of a two-dimensional planar oscillating nitrogen interface for different mesh resolutions. Isothermal and non-isothermal Navier-Stokes equations are solved with constant viscosity and no thermal conduction, for different mesh resolutions. A selective numerical filter (coeff $1.0 \cdot 10^{-2}$) is used. 284
8.28 Comparison of the central density time evolution of a two-dimensional planar oscillating interface for different values of dynamic viscosity. Navier-Stokes equations are solved with constant viscosity and no thermal conduction in isothermal and non-isothermal settings. A selective numerical filter (coeff $1.0 \cdot 10^{-2}$) is used on the 8-point resolution mesh. 284
8.29 Comparison of the central density time evolution of a two-dimensional planar oscillating nitrogen interface for different sets of equations. Euler and Navier-Stokes equations are solved in isothermal and non-isothermal settings on the 8-point interface resolution mesh with different diffusive processes. 285
8.30 Comparison of the central density time evolution of a two-dimensional planar oscillating nitrogen interface at 100 K for different values of kinematic viscosity. Isothermal Navier-Stokes equations are solved with no thermal conduction. A selective numerical filter (coeff $1.0 \cdot 10^{-2}$) is used. 287
8.31 Comparison of the central density time evolution of a two-dimensional planar oscillating oxygen interface at 110 K for different values of kinematic viscosity. Isothermal Navier-Stokes equations are solved with no thermal conduction. A selective numerical filter (coeff $1.0 \cdot 10^{-2}$) is used. 288
8.32 Comparison between the theory and simulation results for the normalized displacement of a two-dimensional isothermal planar oscillating oxygen interface at 110 K for different values of kinematic viscosity. Isothermal Navier-Stokes equations are solved with no thermal conduction. A selective numerical filter (coeff $1.0 \cdot 10^{-2}$) is used. 289
8.33 Schematic representation of the computational setting for the oscillating droplet. *Not to scale* 290
8.34 Snapshots of the temporal evolution of the density for a non-viscous initially deformed O_2 droplet in an isothermal setting. 291
8.35 Temporal evolution of the total kinetic energy of a non-viscous oscillating O_2 droplet in an isothermal setting 292
8.36 Snapshots of the density, pressure, temperature and velocity magnitude field for an non-viscous initially deformed O_2 droplet in a non-isothermal setting before crash iteration. 292
8.37 Snapshots of the temporal evolution of the density for a viscous and initially deformed O_2 droplet. Isothermal Navier-Stokes equations are solved with a constant dynamic viscosity $\mu = 1.0 \cdot 10^{-5}$ Pa.s and no thermal conduction. . . . 293
8.38 Snapshots of the temporal evolution of the pressure for a viscous and initially deformed O_2 droplet. Isothermal Navier-Stokes equations are solved with a constant dynamic viscosity $\mu = 1.0 \cdot 10^{-5}$ Pa.s and no thermal conduction. . . . 294

8.39 Snapshots of the temporal evolution of the velocity field for a viscous and initially deformed O_2 droplet. Isothermal Navier-Stokes equations are solved with a constant dynamic viscosity $\mu = 1.0 \cdot 10^{-5}$ Pa.s and no thermal conduction. Velocity vectors (arrows) are superimposed over the normalized velocity amplitude in gray scale. . . . 294

8.40 Comparison of the temporal evolution of the total kinetic energy of a viscous ($\mu = 1.0 \cdot 10^{-5}$ Pa.s) oscillating O_2 droplet in isothermal and non-isothermal setting . . . 295

8.41 Comparison of the normal velocity at the maximal deformation point A in Fig. 8.33 following its movement in an oscillating isothermal oxygen droplet configuration for different values of kinematic viscosity. Isothermal Navier-Stokes equations are solved with no thermal conduction and a selective numerical filter (coeff $1.0 \cdot 10^{-2}$) is used. . . . 296

8.42 Impact of the spatial resolution on the temporal decay of the total kinetic energy of an oscillating O_2 droplet. Isothermal Navier-Stokes equations are solved with a constant dynamic viscosity and no thermal conduction. A selective numerical filter (coeff $1.0 \cdot 10^{-2}$) is used. . . . 298

8.43 Impact of the spatial resolution on the temporal decay of the total kinetic energy of an oscillating O_2 droplet. Non-isothermal Navier-Stokes equations are solved with a constant dynamic viscosity ($\mu = 1.0 \cdot 10^{-5}$ Pa.s, $La \approx 850$) and no thermal conduction. A selective numerical filter (coeff $1.0 \cdot 10^{-2}$) is used. . . . 298

8.44 Impact of the spatial resolution on the temporal decay of the total kinetic energy of an oscillating O_2 droplet. Non-isothermal simulations with the SG model solving Navier-Stokes equations, viscosity and thermal conduction coefficient calculated with Chung's method with a reduced factor applied to the diffusion coefficients μ and k_{th} . . . 299

9.1 Evolution of the interface width w with respect to the temperature T as predicted by the Second Gradient theory for pure oxygen, nitrogen, hydrogen and methane . . . 307

9.2 Example of an interface profile between the vapor and liquid densities . . . 308

9.3 Profile of the function $\mu_0 - \mu^{\text{sat}}$ relatively to the density in the vicinity of the critical point. . . . 309

9.4 Pressure, specific free enthalpy, specific internal energy and specific entropy of nitrogen N_2 at $T = 117$ K as modified by Eqs. (9.23), (9.20), (9.26) and (9.24) for different values of η . . . 317

9.5 Specific enthalpy, specific isobaric capacity, sound speed and isochoric heat capacity of nitrogen N_2 at $T = 117$ K as modified by Eqs. (9.27), (9.30), (9.31) and (9.32) for different values of η . . . 318

10.1 Density and pressure profiles of an isothermal N_2 interface convected at constant speed $u = 15\text{m}\cdot\text{s}^{-1}$. The plain lines show the calculation results and the dashed lines show the theoretical/ideal position of the interface. The interface has been thickened by a factor F = 10 using the TIM. . . . 326

10.2 Density and pressure profiles of an isothermal N_2 interface convected at constant speed $u = 15\text{m}\cdot\text{s}^{-1}$. The plain lines show the calculation results and the dashed lines show the theoretical/ideal position of the interface. Non-reflecting velocity-temperature inlet (left) and pressure outlet (right) used. The interface has been thickened by a factor F = 1000 using the TIM. 327

10.3 Density and pressure profiles of a static isothermal N_2 interface initially stretched by a factor 2. The plain lines show the calculation results and the dashed lines show the theoretical/ideal position of the interface. Non-reflecting velocity-temperature inlet (left) and pressure outlet (right) used. The interface has been thickened by a factor F = 10 using the TIM. 327

10.4 Density and pressure profiles of a static isothermal N_2 interface initially stretched by a factor 2. The plain lines show the calculation results and the dashed lines show the theoretical/ideal position of the interface. Non-reflecting pressure outlets (left and right) used. The interface has been thickened by a factor F = 1000 using the TIM. 328

10.5 Density and pressure profiles of a static isothermal N_2 interface initially compressed by a factor 3. The plain lines show the calculation results and the dashed lines show the theoretical/ideal position of the interface. Non-reflecting pressure outlets (left and right) used. The interface has been thickened by a factor F = 1000 using the TIM. 328

10.6 Density and pressure profiles of an isothermal N_2 interface initially stretched by a factor 2 and convected at constant speed $u = 5\text{m}\cdot\text{s}^{-1}$. The plain lines show the calculation results and the dashed lines show the theoretical/ideal position of the interface. Non-reflecting velocity-temperature inlet (left) and pressure outlet (right) used. The interface has been thickened by a factor F = 100 using the TIM. 329

10.7 Density and pressure profiles of an isothermal N_2 interface initially stretched by a factor 2 and convected at constant speed $u = 5\text{m}\cdot\text{s}^{-1}$. The plain lines show the calculation results and the dashed lines show the theoretical/ideal position of the interface. Non-reflecting velocity-temperature inlet (left) and pressure outlet (right) used. The interface has been thickened by a factor F = 1000 using the TIM. 329

10.8 Density, temperature, pressure and velocity profiles of a N_2 droplet convected at constant speed $u = 10\text{ m}\cdot\text{s}^{-1}$. The plain lines show the calculation results and the dashed lines show the theoretical position of the interface. Periodic boundary conditions (left and right) used. Non-isothermal SG+TIM Euler equations are solved with a eight-point interface resolution. The interface has been thickened by a factor F = 100 using the TIM. The high-order selective filter is used (coeff. $1.0 \cdot 10^{-4}$). 330

10.9 Density, temperature, pressure and velocity profiles of a N_2 droplet convected at constant speed $u = 10\text{m}\cdot\text{s}^{-1}$. Periodic boundary conditions (left and right) used. Non isothermal SG+TIM Navier-Stokes equations are solved with Chung's diffusion model, for multiple lower mesh resolutions. The interface has been thickened by a factor F = 100 using the TIM. The high-order selective filter is used (coeff. $1.0 \cdot 10^{-4}$). 331

10.10Density, temperature, pressure and velocity profiles of a N_2 droplet convected at constant speed $u = 10\text{m}\cdot\text{s}^{-1}$. Periodic boundary conditions (left and right) used. Non isothermal SG+TIM Navier-Stokes equations are solved with Chung's diffusion model, for multiple lower mesh resolutions. The interface has been thickened by a factor F = 10000 using the TIM. AVBP's artificial viscosity is used. The high-order selective filter is used (coeff. $1.0 \cdot 10^{-4}$). 332

10.11Convergence orders of AVBP's GRK numerical scheme with the SG model implementation in 1D isothermal and non-isothermal cases using the TIM with a thickening coefficient F = 100. Logarithmic scale used for both axis. Interpolation slopes in legend. 333

10.12Convergence orders of AVBP's GRK numerical scheme with the SG model implementation in 1D isothermal and non-isothermal cases using the TIM with a thickening coefficient F = 10000. Artificial viscosity from AVBP used for the calculations. Logarithmic scale used for both axis. Interpolation slopes in legend. 333

10.13Evolution of the initial density profiles for interfaces with different thickening factors, a fixed relative interface perturbation and a fixed geometry 335

10.14Evolution of the initial density profiles for interfaces with different thickening factors, a fixed relative interface perturbation and a proportionally expanded geometry 335

10.15Evolution of the interface oscillation period (normalized by $T_{\text{F}=1}$) with the thickening coefficient F (in log-log scale) for consistent and inconsistent thickening strategies, comparison between theoretical and numerical results using the inconsistent and TIM methods 336

10.16Comparison of the central density time evolution of a two-dimensional, initially isothermal, planar oscillating nitrogen interface for different thickening factors. Non-isothermal Euler equations are solved applying the TIM. A selective numerical filter (coeff $1.0 \cdot 10^{-2}$) is used but no artificial viscosity. 337

10.171D density *(left)* and temperature *(right)* profiles for an isobaric nitrogen N_2 interface at a reference temperature of 110 K 338

10.18Comparison of the central density time evolution of a two-dimensional, initially non-isothermal, planar oscillating nitrogen interface for different thickening factors. Non-isothermal Euler equations are solved applying the TIM. A selective numerical filter (coeff $1.0 \cdot 10^{-2}$) is used but no artificial viscosity. 338

10.19Evolution of the normalized interface oscillation period, with the thickening coefficient F (in log-log scale) for different types of initialization and equations solving 339

10.20Comparison of the central density time evolution of a two-dimensional planar oscillating oxygen interface for different values of kinematic viscosity. Isothermal Navier-Stokes equations are solved with constant kinematic viscosity and no thermal conduction. Different thickening factors F = 1, F = 100 and F = 10000 are applied following the TIM. A selective numerical filter (coeff $1.0 \cdot 10^{-2}$) is used. 341

10.21 Comparison between the theory and simulation results for the normalized displacement of a two-dimensional isothermal planar oscillating oxygen interface at 110 K for different values of kinematic viscosity. Isothermal Navier-Stokes equations are solved with no thermal conduction. A thickening factor F = 100 is applied following the TIM. A selective numerical filter (coeff $1.0 \cdot 10^{-2}$) is used. 342
10.22 Comparison between the theory and simulation results for the normalized displacement of a two-dimensional isothermal planar oscillating oxygen interface at 110 K for different values of kinematic viscosity. Isothermal Navier-Stokes equations are solved with no thermal conduction. A thickening factor F = 10000 is applied following the TIM. A selective numerical filter (coeff $1.0 \cdot 10^{-2}$) is used. 343
10.23 Schematic representation of the computational setting for the oscillating droplet. *Not to scale* . . . 344
10.24 Snapshots of the temporal evolution of the density field for a viscous and initially deformed O_2 droplet. Isothermal Navier-Stokes equations are solved with a constant kinematic viscosity $\nu = 1.0 \cdot 10^{-6}$ $m^2 \cdot s^{-1}$ and no thermal conduction. A thickening factor F = 10000 is applied following the TIM. A selective numerical filter (coeff $1.0 \cdot 10^{-2}$) is used. . . . 345
10.25 Snapshots of the temporal evolution of the velocity field for a viscous and initially deformed O_2 droplet. Isothermal Navier-Stokes equations are solved with a constant kinematic viscosity $\nu = 1.0 \cdot 10^{-6}$ $m^2 \cdot s^{-1}$ and no thermal conduction.A thickening factor F = 10000 is applied following the TIM. A selective numerical filter (coeff $1.0 \cdot 10^{-2}$) is used. Velocity vectors (arrows) are superimposed over the normalized velocity amplitude in gray scale. . . . 346
10.26 Comparison of the temporal evolution of the total kinetic energy for an oscillating oxygen droplet with different values of kinematic viscosity. Isothermal Navier-Stokes equations are solved with no thermal conduction and the addition of artificial viscosity. A thickening factor F = 100 is applied following the TIM. A selective numerical filter (coeff $1.0 \cdot 10^{-2}$) is used. . . . 347
10.27 Comparison of the temporal evolution of the total kinetic energy for an oscillating oxygen droplet with different values of kinematic viscosity. Isothermal Navier-Stokes equations are solved with no thermal conduction and the addition of artificial viscosity. A thickening factor F = 10000 is applied following the TIM. A selective numerical filter (coeff $1.0 \cdot 10^{-2}$) is used. . . . 347

11.1 Schematic representation of the configuration used to study the collision of two droplets . . . 349
11.2 Typical collision regimes observed in experiments depending on the Weber number and the impact parameter . . . 350
11.3 Example of liquid droplet collision regimes for different configurations, taken from Brenn (2011) adapted from Jiang et al. (1992) . . . 351
11.4 Initial solution used to study the collision of same sized initially isothermal oxygen droplets in their own vapor. The three-dimensional $\rho = 500$ $kg \cdot m^{-3}$ isosurface and the reference two dimensional density, pressure and normalize density fields are provided. . . . 353
11.5 Collision regimes in the parameter space $\delta - We$ extracted for same size droplets of water into air, taken from Ashgriz and Poo (1990) . . . 353

11.6 Head-on collision of liquid droplets, simulation results with oxygen droplets at $We = 20$ ($Re_l = 556$) using the TIM 355
11.7 Head-on collision of liquid droplets, simulation results with oxygen droplets at $We = 46$ ($Re_l = 840$) using the TIM 355
11.8 Head-on collision of liquid droplets, comparison between experiments with water droplets at $We = 23$ from Ashgriz and Poo (1990) and simulation results with oxygen droplets at $We = 40$ ($Re_l = 790$) using the TIM 356
11.9 Head-on collision of liquid droplets, comparison between experiments with water droplets at $We = 40$ from Ashgriz and Poo (1990) and simulation results with oxygen droplets at $We = 80$ ($Re_l = 1100$) using the TIM 357
11.10 Critical Weber numbers separating different collision regimes for hydrocarbons droplets in air, taken from Jiang et al. (1992) 357
11.11 Head-on collision of liquid droplets, simulation results with oxygen droplets at $We = 192$ ($Re_l = 1720$) using the TIM 359
11.12 Schematic representation of the density field for the simulation configuration of a periodic liquid jet in its vapor 362
11.13 Breakup regimes for liquid round jets in the parameter space $\mathrm{Re}_l - \mathrm{Oh}$ extracted for a hydrocarbons-air configuration, taken from Shimasaki and Taniguchi (2011) 363
11.15 Evolution in time of the density profiles for two-dimensional periodic Nitrogen liquid jets in their vapor. Four cases have been carried out with the reference spatial resolution and thickening factor F = 1000 for different Reynolds numbers, from left to right: $Re = 460$ (412), $Re = 730$ (1030), $Re = 1040$ (2080) and $Re = 1470$ (4150) 368
11.16 Evolution in time of the temperature profiles for two-dimensional periodic Nitrogen liquid jets in their vapor. Four cases have been carried out with the reference spatial resolution and thickening factor F = 1000 for different Reynolds numbers, from left to right: $Re = 460$ (412), $Re = 730$ (1030), $Re = 1040$ (2080) and $Re = 1470$ (4150) 369
11.17 Evolution in time of the pressure profiles for two-dimensional periodic Nitrogen liquid jets in their vapor. Four cases have been carried out with the reference spatial resolution and thickening factor F = 1000 for different Reynolds numbers, from left to right: $Re = 460$ (412), $Re = 730$ (1030), $Re = 1040$ (2080) and $Re = 1470$ (4150) 370
11.18 Evolution in time of the density profiles for two-dimensional periodic Nitrogen liquid jets in their vapor. Three cases have been carried out for $Re = 1470$ ($We = 4150$) with the reference thickening factor F = 1000 and three different spatial resolutions (*left*: reference $r = 1$, *center*: coarse $r = 1/2$, *right*: very coarse $r = 1/3$). 372
11.19 Evolution in time of the density profiles for two-dimensional periodic Nitrogen liquid jets in their vapor. Three cases have been carried out at $Re = 730$ ($We = 1030$) with the reference thickening factor F = 1000 and three different spatial resolutions (*left*: reference $r = 1$, *center*: coarse $r = 1/2$, *right*: very coarse $r = 1/3$) 373

11.20Evolution in time of the temperature profiles for two-dimensional periodic Nitrogen liquid jets in their vapor. Three cases have been carried out for $Re = 1470$ ($We = 4150$) with the reference thickening factor F = 1000 and three different spatial resolutions (*left*: reference $r = 1$, *center*: coarse $r = 1/2$, *right*: very coarse $r = 1/3$) 374
11.21Time evolution of liquid nitrogen jets thermodynamic regime in a temperature-density diagram for different Reynolds numbers using three different spatial resolutions (*left*: reference $r = 1$, *center*: coarse $r = 1/2$, *right*: very coarse $r = 1/3$) 375
11.22Time evolution of liquid nitrogen jets thermodynamic regime in temperature-density diagram for $Re = 1470$ ($We = 4150$) using three different spatial resolutions (*left*: reference $r = 1$, *center*: coarse $r = 1/2$, *right*: very coarse $r = 1/3$) 375
11.24Evolution in time of the density profiles for two-dimensional periodic Nitrogen liquid jets in their vapor. Three cases have been carried out at $Re = 1470$ (4150) with the reference spatial resolution and three different thickening factors (*left*: large F = 1000, *center*: medium F = 500, *right*: low F = 333) 377
11.26Evolution in time of the temperature profiles for two-dimensional periodic Nitrogen liquid jets in their vapor. Three cases have been carried out at $Re = 1470$ (4150) with the reference spatial resolution and three different thickening factors (*left*: large F = 1000, *center*: medium F = 500, *right*: low F = 333) . . . 378
11.28Evolution in time of the pressure profiles for two-dimensional periodic Nitrogen liquid jets in their vapor. Three cases have been carried out at $Re = 1470$ (4150) with the reference spatial resolution and three different thickening factors (*left*: large F = 1000, *center*: medium F = 500, *right*: low F = 333) 379
11.30Evolution in time of the density profiles for two-dimensional periodic Nitrogen liquid jets in their vapor. Four cases have been carried out with the reference spatial resolution and a reduced thickening factor F = 333, for different Reynolds numbers, from left to right: $Re = 460$ ($We = 412$), $Re = 730$ ($We = 1030$), $Re = 1040$ ($Re = 46080$) and $Re = 1470$ ($We = 4150$) . . . 380
11.32Evolution in time of the density profiles for two-dimensional periodic Nitrogen liquid jets in their vapor at $Re = 1470$ ($We = 4150$). Two thickening factors and two mesh resolutions are used to get the same interface resolutions of five points (F = 500 / $r = 1/2$, *left images*) and three points (F = 333 / $r = 1/3$, *right images*) 382

Introduction

Technological framework

The last decade has seen a renewed and steadily growing interest in space exploration. Whether it is to accommodate the increasing demand in satellites, to carry space probes for future scientific programs, to transport cargo and crews to the International Space Station and, in a foreseeable future, open space travel to tourism activities, the need in efficient and reliable space launchers has never been so high. It has fostered intense academic research, industrial activities and the creation of multiple companies.

A space launcher uses the thrust generated by its engines to accelerate its payload until it reaches the desired orbit at the right velocity.
At its core, the principle behind the functioning of a rocket engine is rather straightforward and can be summed up by Fig. 1: an oxidant (usually oxygen) and a fuel are combined together in a combustion chamber to achieve a strongly exothermic chemical reaction; the energy generated is used to heat up and accelerate the reaction products that are then exhausted through a convergent-divergent nozzle.
The thrust T generated by this process can be estimated with Eq. (1) where $\dot{m}$ is the mass flow rate of the propellant, u_e is the velocity of the exhaust gases, P_a is the ambient pressure outside the engine and P_e and A_e are respectively the exit pressure and exit area of the nozzle.

$$\mathrm{T} = \dot{m} u_e + (P_e - P_a) A_e \tag{1}$$

In typical operating conditions, the thrust can be expressed as depending solely on the pressure in the combustion chamber P_c and the cross section at the nozzle throat A_c as shown in Eq. (2)

$$\mathrm{T} \approx A_c P_c \tag{2}$$

Building more efficient and, above all, more powerful engines requires the master of several processes such as the choice of the propellant, the design of the injection system and the nozzle and the fine tuning of combustion conditions. However a rule of thumb hinted by Eq. (2) is that to increase the power of the engine, the combustion pressure should get higher. This trend has been consistently followed in the past half century.
As a side note, it should be noticed that this increase can also be observed for aircraft engines (see Koff (2004)). Indeed, they similarly require to reach a higher pressure in the combustion chamber to accommodate the cleaner combustion regimes imposed by safety and environmental regulations.

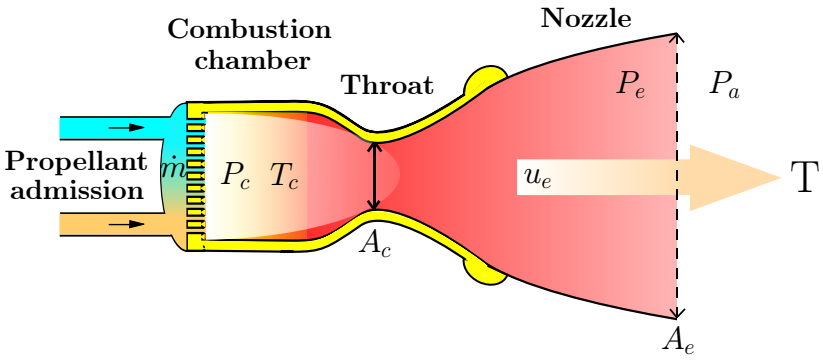

Figure 1: *Schematic representation of a rocket engine*

There exist a plethora of available rocket engine designs but for the most part, they can be classified into two categories depending on the fuel they use.
Solid rocket engines, commonly called boosters, rely on the combustion of a solid grain that produces accelerated exhaust gases to generate thrust. Once ignited, solid rockets cannot be extinguished because the solid grain contains both the fuel and the oxidant necessary to sustain the combustion. Of a lesser efficiency and maneuverability, solid rockets generate a formidable amount of thrust and for these reasons they are usually used as small launchers for very light payloads or as boosters for heavier launchers. For instance, in the space launcher Ariane 5, shown in Fig. 2, operated by ArianeSpace, the two lateral boosters each generate a thrust of about 7070 kN during their two minutes of combustion when compared to the merely (but still impressive) 1390 kN thrust of the main engine.
Liquid rocket engines (LRE) use fuel and oxidant that are both in a liquid form. Thanks to their fairly high density in this form, the propellants can be stored using reasonably small tanks. By adding a pressurization system (using a pressured inert gas or a turbo-pump, as shown in Fig. 4) to inject the propellants into the combustion chamber at the required high mass flux rate, they can be stored at relatively low pressures thus not requiring reinforced tanks which would drastically reduce the propellant-to-structure mass ratio of the rocket due to the added matter.

A special type of LRE known as cryogenic rocket engine uses oxidizer and/or fuel that are gases which have been liquefied at very low temperatures. Semi-cryogenic engines use only liquefied oxygen (LOx) for the oxidizer whereas the fuel, such as methane, kerosene or hydrazine, naturally remains liquid at ambient temperature. Fully cryogenic engines use LOx as an oxidizer but also liquefied hydrogen (LH_2) as a fuel.
These types of propellants require dedicated tanks to preserve them at the right temperature along with dedicated feeding lines and insulation usually making them more difficult to maintain and more complex to operate. However, cryogenic engines make up for the added complexity by offering a very seductive efficiency when compared to other configurations.

The efficiency of a rocket engine is evaluated using the specific impulse I_{sp} which is defined as the thrust generated per mass unit of propellant consumed per time unit, expressed in second. A higher I_{sp} implies that the propellant is better used to generate thrust relatively to how

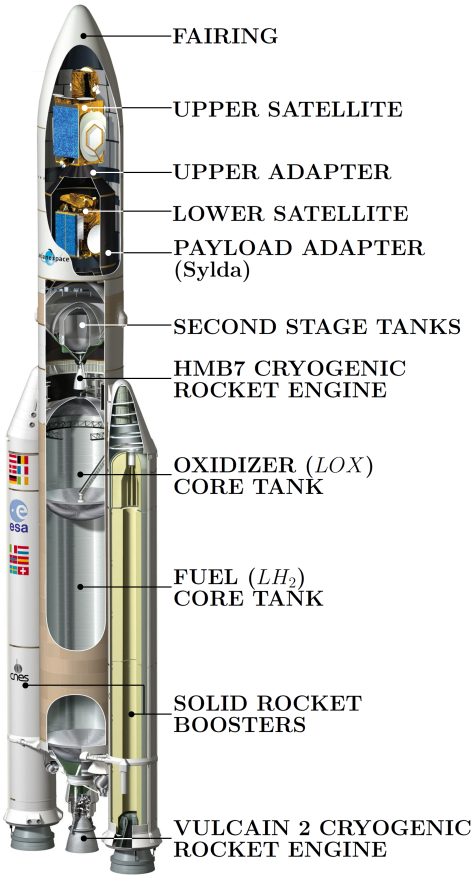

Figure 2: *Schematic representation of the main components of the Ariane 5 launcher (type ECA)*

fast it is consumed, which is favored by a high exhaust gas temperature (i.e. a high heat of combustion) and by the generation of exhaust gases with a very low molecular weight.
Fig. 3 presents the ideal specific impulses in vacuum for several oxidizer/fuel combinations and showcases the superiority of the LOx/LH_2 pair which ideally meets the conditions previously mentioned. Additionally, the product of combustion of the pair is simply clean water that can be ejected through the nozzle in a vapor state, a significantly much cleaner exhaust then those typically encountered for other rocket engines.

In practice, cryogenic engines are preferred on heavy launchers capable of delivering massive payloads. Among the main heavy launchers currently under exploitation/development, the vast majority resort to fully cryogenic engines. For instance Ariane 6 first stage Vulcain 2 and second stage Vinci engines both operate with LOx/LH_2. Likewise both YF-77 and YF-75D mounted on the first and second stages of the Chinese heavy launcher Long March 5 operate with LOx/LH_2, which is also the case for the Japanese launcher H3 which will be equipped with the fully cryogenic engines LE-9 and LE-5 on its first and second stages respectively. The Space Launch System developed by NASA will reinvest the RS-25 engine created for the late Space Shuttle, which is also fully cryogenic. The only noticeable variations are the BE-4 and Merlin engines, installed respectively on the second stage of Blue Origin's New Glenn heavy

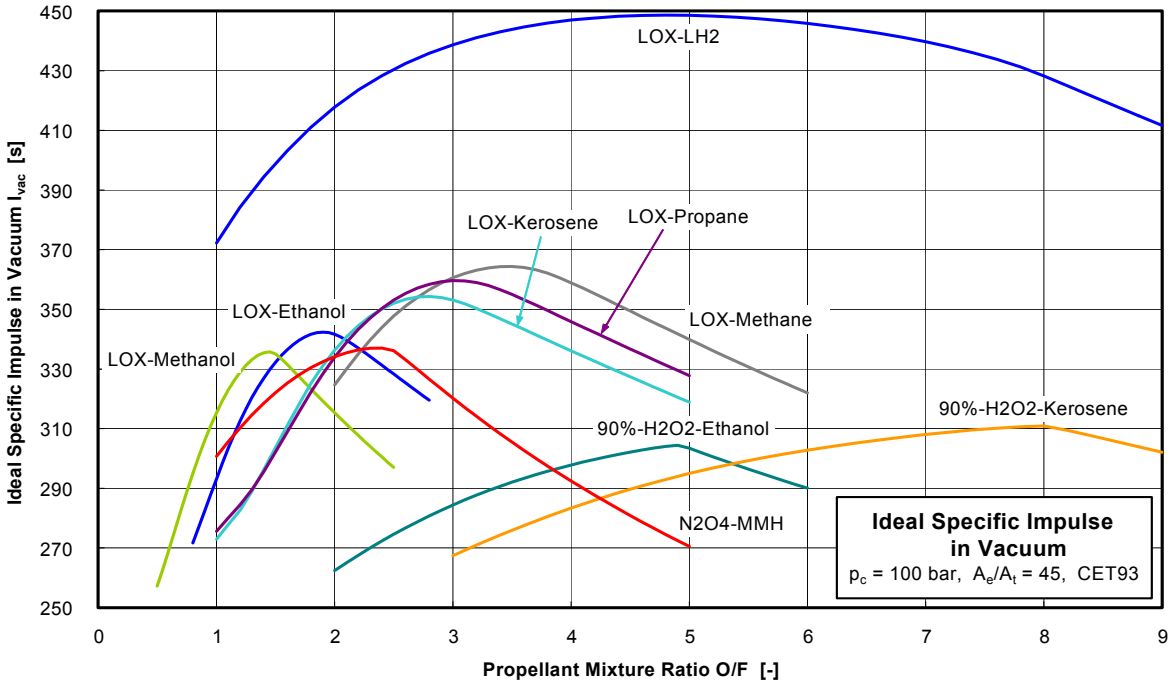

Figure 3: *Ideal specific impulse of various oxidizer/fuel combinations, from Haidn (2008)*

launcher and on all the launchers developed by Space-X, in particular the Falcon Heavy, which both operate with a $LOx/RP1$ pair, $RP1$ being a variant of kerosene. Tab. 1 summarizes the specifications of several engines used or planed to be used, on current and future heavy launchers.

To sustain the high mass flow rate of propellant required by such engines, the liquid fuel and oxidizer must be accelerated by increasing their pressure. Small engines that operate at low combustion chamber pressures are compatible with pressurized tanks which rely on an inert pressurizing gas (helium in general) that is expanded through a heat exchanger with the combustion chamber and/or the nozzle as presented in Fig. 4.
For more powerful engines, turbo-pumps become indispensable to deliver the necessary quantity of propellant. These turbo-pumps are integrated into different operating cycles for LRE. The main cycles are recalled in Fig. 4.

The most simple cycle, called the Expander (or sometimes Closed Expander) cycle, uses in a first time the cold fuel to cool down the nozzle and/or the combustion chamber (most of the time, the materials used for its conception, to limit the mass of the engine, cannot sustain on their own the high temperatures of the exhaust gases) causing it to expand and to experience a phase change. The heated and accelerated gaseous fuel is then used in the turbine that powers the fuel and oxidizer pumps before being injected into the combustion chamber to be burned as well.
The Expander Bleed is another cycle that deviates from the classic Expander by using only a small part of the heated fuel to power the turbine. This fuel is then vented outside without going through the combustion chamber.

Name	Launcher	Stage	Cycle	Thrust in vac. (on gr.)	Prop.	I_{sp} in vac. (on gr.)	Press. chamber
BE-4	New Glenn	1^{st}	Staged combustion	- (2 450 kN)	LOx/CH_4	- (-)	134 bar
BE-3U	New Glenn, Vulcan	2^{nd}	Expander bleed	710 kN	LOx/LH_2	-	-
LE-9	H3	1^{st}	Expander bleed	1470 kN (-)	LOx/LH_2	426 s (-)	100 bar
LE-5B	H3	2^{nd}	Expander bleed	137 kN	LOx/LH_2	447 s	35.8 bar
Merlin 1D	Falcon Heavy, Falcon 9	Booster 1^{st} , 2^{nd}	Gas-generator	981 kN (854 kN)	$LOx/RP-1$	311 s (282 s)	97 bar
RS-68A	Delta IV Heavy	1^{st}	Gas-generator	3560 kN (3137 kN)	LOx/LH_2	414 s (366 s)	109 bar
RL-10B	Delta IV Heavy	2^{nd}	Expander	110 kN	LOx/LH_2	464 s	44 bar
RS-25 (SSME)	Space Shuttle, SLS	Main stage	Staged combustion	2279 kN (1860 kN)	LOx/LH_2	452 s (366 s)	206 bar
Vulcain 2	Ariane 5 Ariane 6	1^{st}	Gas-generator	1 350 kN (939 kN)	LOx/LH_2	434 s (318 s)	115 bar
Vinci	Ariane 6	2^{nd}	Expander	180 kN	LOx/LH_2	467 s	61 bar
YF-77	Long March 5	1^{st}	Gas-generator	700 kN (510 kN)	LOx/LH_2	430 s (310 s)	102 bar
YF-75	Long March 5	2^{nd}	Expander	88 kN	LOx/LH_2	442 s	41 bar

Table 1: *Specifications for the engines found on notable modern heavy launchers*

For even more powerful engines, the Expander cycle cannot provide enough power to the pumps as the volume of fuel to be injected increases much faster than the volume that can be heated up by contact with the nozzle.
In those cases, part of both the fuel and the oxidizer are injected into a smaller combustion chamber which operates with a high mixture ratio and a high enough pressure to ensure that its exhaust gases reach a sufficiently high enough temperature. These highly energetic gases are then used to power the turbine. Depending on the final destination of the exhaust gases, one can distinguish between two cycles in a fashion somewhat similar to the Expander and Expander Bleed cycles:
- the Gas-Generator cycle simply vents these gases outside using a separate exhaust system; this calls for a simple installation and leads to lighter engines but lacks in efficiency due to the lost propellant.
- the Staged Combustion cycle injects the turbine exhaust gases together with the exhaust

gases from the main combustion chamber; of a higher complexity and requiring the turbine to work with higher pressure, it however offers the highest efficiency for a LRE.

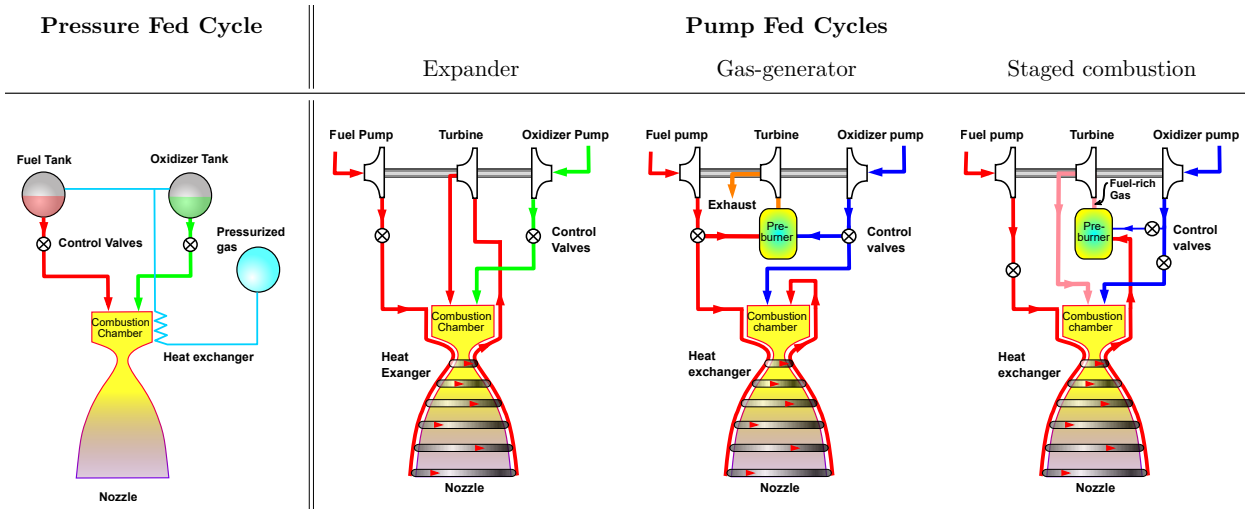

Figure 4: *Main cycles used for liquid rocket engines*

Scientific framework

The design of a cryogenic rocket engine or any LRE or more broadly any type of combustion chamber conceived to operate with a liquid propellant at very high pressures requires the master over several and very complex physical phenomena.

In the combustion chamber, the propellant must evaporate prior to burning and the rate of evaporation directly correlates with the surface of liquid propellant available to be heated. A manner to maximize this surface is by atomizing the liquid into a spray to create small droplets that vaporize much faster: the better the atomization, the more efficient the combustion. One peculiar effect of working at very high pressures is that the manner in which the liquid jet behaves and possibly atomizes radically changes throughout the ignition process as the pressure increases and the thermodynamic regime goes from subcritical to supercritical, as exposed in the phase diagram of Fig. 5.

This evolution of the thermodynamic regime and its impact on the jet behavior during the injection has been the focal point of several studies for the past years.
The progresses made over the last decades have been fostered by numerous experimental studies enhanced by the design of more advanced optical diagnostics such as OH^* chemiluminescence, Planar Laser Induced Fluorescence (PLIF) and many other methods extensively described in Section VI.1.1 of Gaillard (2015).
However, the pivotal role of numerical simulation, supported by theoretical modeling, must also be emphasized on as it has permitted to gain precious insight into these complex phenomena, often complicated and expensive to study experimentally. A brief overview of the major results with both experimental and numerical strategies, complementary by nature, is proposed in the

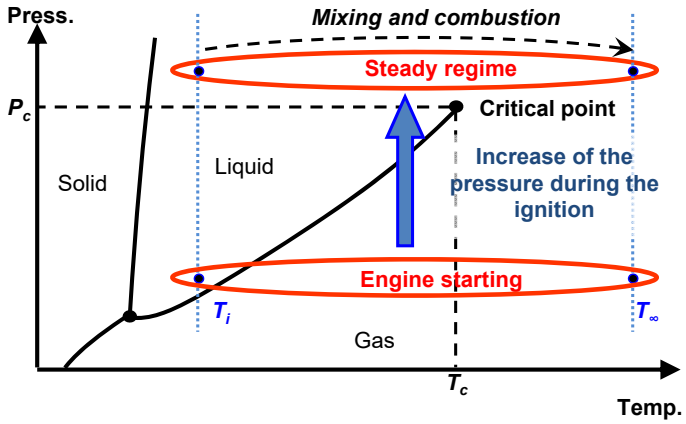

Figure 5: *Evolution of the thermodynamic regime during the early stages of an LRE ignition*

next paragraphs.

Experimental studies

Generic results on liquid jets

In subcritical conditions, the liquid injected is characterized by the presence of surface tension that makes the fluid resists the extension of its surface. The external forces, through shear stress, must overcome surface tension to atomize the liquid.
The first experimental and theoretical studies regarding liquid jets can be traced back to the 1800's through the work of Bidone (1829); Plateau (1873) or Rayleigh (1878); Rayleigh (1879). A systematic review of the most notable experiments performed in the 1900's and the addition of several experiments of their own allowed the authors in Faeth (1991); Hsiang and Faeth (1992); Hsiang and Faeth (1993); Wu and Faeth (1993); Faeth (1996) to identify the main regimes of atomization occurring for a round jet of liquid injected into a quiescent gas.
Following the early experiments performed by Hoyt and Taylor (1977a); Hoyt and Taylor (1977b) of liquid jets with a gaseous co-flow, the authors in Hopfinger and Lasheras (1994); Hopfinger (1998); Lasheras et al. (1998); Lasheras and Hopfinger (2000) have extended the results previously established for quiescent gases.

Overall, the process of atomization of a liquid jet can be separated into two main mechanisms. The first one, known as *primary breakup* is initiated by the shear strain caused by the differential velocity between the liquid and the gas. A tangential force is created at the interface and disturbs it through a phenomenon called Rayleigh instabilities (see Rayleigh (1878)). This disturbance, when strong enough, gives birth to complex structures such as membranes and ligaments which are then ejected from the jet through a peeling-like action.
The biggest chunks of liquid that have been ejected are further shattered by the cross wind from the gaseous flow to form small droplets ready to evaporate for combustion, a mechanism known as *secondary breakup*.
In Faeth (1991) and later in Lasheras et al. (1998); Lasheras and Hopfinger (2000); Marmottant and Villermaux (2003); Marmottant and Villermaux (2004), the main regimes of

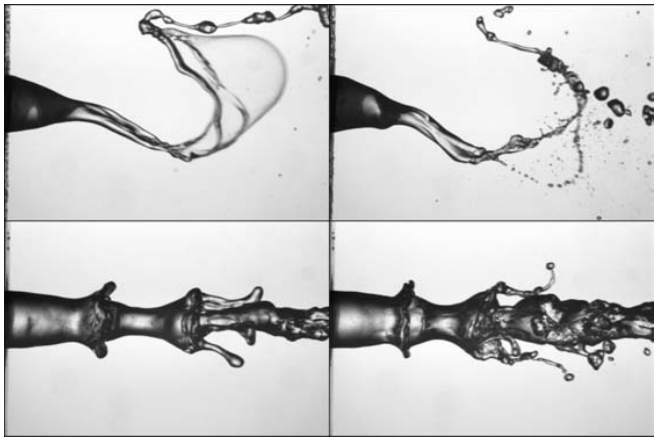

Figure 6: *Atomization regimes of a slow dense liquid jet by a fast light coaxial stream, taken from Marmottant and Villermaux (2004). From top left to bottom right the gas velocity is increased, the peeling of the liquid jet intensifies and surface instabilities further dominate the liquid disintegration.*

atomization, some of which are displayed in Fig. 6, have been identified. These regimes are mostly controlled by the dimensionless Reynolds Re and Weber We numbers defined as follows:

$$Re_l = \frac{\rho_l D U_l}{\mu_g} = \frac{\text{aerodynamic forces}}{\text{gaseous viscosity forces}} \tag{3}$$

$$We = \frac{\rho_g D \left(U_g - U_l\right)^2}{\sigma} = \frac{\text{aerodynamic forces}}{\text{surface tension forces}} \tag{4}$$

and also to a lesser extend by the Ohnsorge Oh and Froude Fr numbers, (Fr only when gravity is taken into account) defined with:

$$Oh_l = \frac{\mu_l}{\sqrt{\rho_l D \sigma}} = \frac{\text{liquid viscosity forces}}{\sqrt{\text{aerodynamic forces} \times \text{surface tension forces}}} \tag{5}$$

$$Fr_l = \frac{u_l^2}{gD} = \frac{\text{liquid inertial forces}}{\text{gravitational forces}} \tag{6}$$

In Lasheras and Hopfinger (2000), the authors present a detailed cartography, shown in Fig. 7, of the different regimes for co-axial round jets depending on both Re_l and We. In particular, for the typically very high Re and We values encountered in LRE, the observations are consistent with the fiber-type atomization described by the authors.
Two other key parameters have been identified in Hopfinger and Lasheras (1994); Lasheras et al. (1998); Favre-Marinet and Schettini (2001) as having a strong impact on the liquid jet behavior and the mixing between the liquid and the gas. They are namely the density ratio R_ρ and the momentum flux ratio J defined respectively by Eq. (7) and Eq. (8).

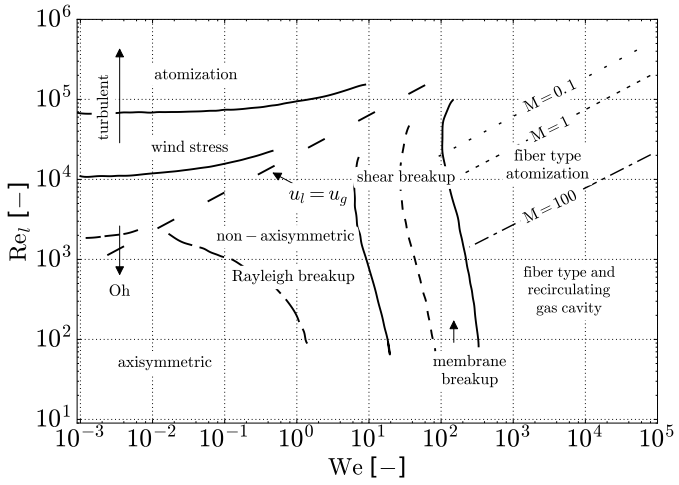

Figure 7: *Breakup regimes in the parameter space* $\mathrm{Re}_l - \mathrm{We}$ *extracted for a water-air co-flow mixture, taken from Lasheras and Hopfinger (2000)*

$$\mathrm{R}_\rho = \frac{\rho_l}{\rho_g} \tag{7}$$

$$\mathrm{J} = \frac{\rho_g u_g^2}{\rho_l u_l^2} \tag{8}$$

In particular, the length L of the liquid core during the atomization has been shown in Lasheras et al. (1998) to behave like $L \propto \mathrm{J}^{-\frac{1}{2}} u_l^{-\frac{3}{2}} D$ and the spray angle θ has been shown to follow the trend $\theta \approx \frac{\pi}{4} - \tan^{-1}\left(\sqrt{\mathrm{J}}/12\right)$.

The main results from these different studies can be broadly summarized by saying that a good atomization of the liquid jet requires a great velocity from either the liquid or the gas to create an important velocity differential and promote shear stresses. However, a great gas velocity has the benefit to allow a much easier atomization for larger liquid jets.

Results for non-reactive cryogenic jets

Experiments on spray atomization specifically dedicated to LRE in supercritical conditions were initiated in Newman and Brzustowski (1971) where the authors studied pure CO_2 and CO_2/N_2 mixtures injected into a chamber of pure gaseous N_2 operating at both subcritical and supercritical temperatures and pressures.
Since then, substantial advances have been permitted by the creation of test benches on several facilities capable of injection and combustion of cryogenic material at high temperature and pressure under subcritical or supercritical conditions.
Most of the results have been produced at the German Aerospace Center (DLR) equipped with the M3 (see Mayer et al. (1996)) and P8 (see Sternfeld et al. (1995); Koschel and Haidn (1998); Haberzettl et al. (2000)) benches, at the French Aerospace Laboratory (ONERA)

equipped with the bench Mascotte (see Habiballah et al. (1996); Vingert et al. (1999); Gicquel et al. (2001)) and at the Air Force Research Laboratory (AFLR) in the United States also equipped with such a bench EC-4 (see Chehroudi et al. (1999); Chehroudi et al. (2000)).

Owing to the proximity of its molecular mass and critical values (temperature and pressure) to that of O_2, nitrogen N_2 is generally used as a substitute in experiments to study non-reactive cases.
In Chehroudi et al. (2002), the authors studied the effect of the pressure on a liquid jet of N_2 injected into a quiescent gaseous N_2 chamber, as exposed in Fig. 8.
In subcritical conditions $P < P_c$, a typical spray behavior is observed where big droplets and ligaments formed by the primary breakup are further broken into small droplets through the secondary breakup mechanism.
In reasonably supercritical conditions $P > P_c$, this behavior disappears as droplets are no longer observed. They are instead replaced by comb-like structures appearing at the surface, caused by the local existence of a mixing layer. These structures are rapidly diffused into the gas. Additionally, the separation between the liquid and vapor phases is no longer clear-cut and the interface seems to be smeared out. These observations hint at the disappearance of surface tension effects.
Under strongly supercritical conditions $P \gg P_c$, liquid atomization altogether ceases to be observed and the jet behaves like a dense gas. Strong density gradients are still present at the extremely smeared out transition between the core jet and the outside gas but observations confirm that capillary effects either vanish or can be neglected.
Similar results have been obtained in Mayer et al. (1996); Mayer et al. (2003), also for pure liquid N_2 injection into pure gaseous N_2.

Multi-species experiments have also been performed in Mayer et al. (1996); Mayer et al. (2000) where liquid N_2 was injected into a gaseous He chamber for which pictures are given in Fig. 9.
The results were similar to that of the single species cases: at subcritical pressure (relatively to the critical pressure of nitrogen) a typical spray behavior is retrieved whereas no droplets and only a rapid diffusion of the dense core are observed once the pressure becomes supercritical. This further confirms that the behavior of the liquid jet at supercritical pressures can be treated as that of a dense gas with no significant capillary effects.

Additional experiments have been carried out with an external acoustic forcing imposed on the liquid jet in Chehroudi and Talley (2002); Davis and Chehroudi (2007). Yet again, a noticeable difference as been noted depending on the injection regime.
Below the critical pressure, the liquid jet displays a strong response that grows stronger as the pressure approaches its critical value. This response mostly vanishes once the pressure becomes supercritical relatively to the liquid critical pressure.
Finally, in Mayer et al. (1998); Mayer et al. (2001) the authors investigated the impact of the pressure on the critical temperature of the mixture and on the surface tension. Other than noting the sensitivity of fluid behavior near the pseudo-boiling point (see Banuti and Hannemann (2014)), the authors found that the critical temperature decreases with an increasing pressure. More importantly, they also observed that surface tension could still exist in a LOx/H_2 injection for pressures above the critical pressure of pure O_2.

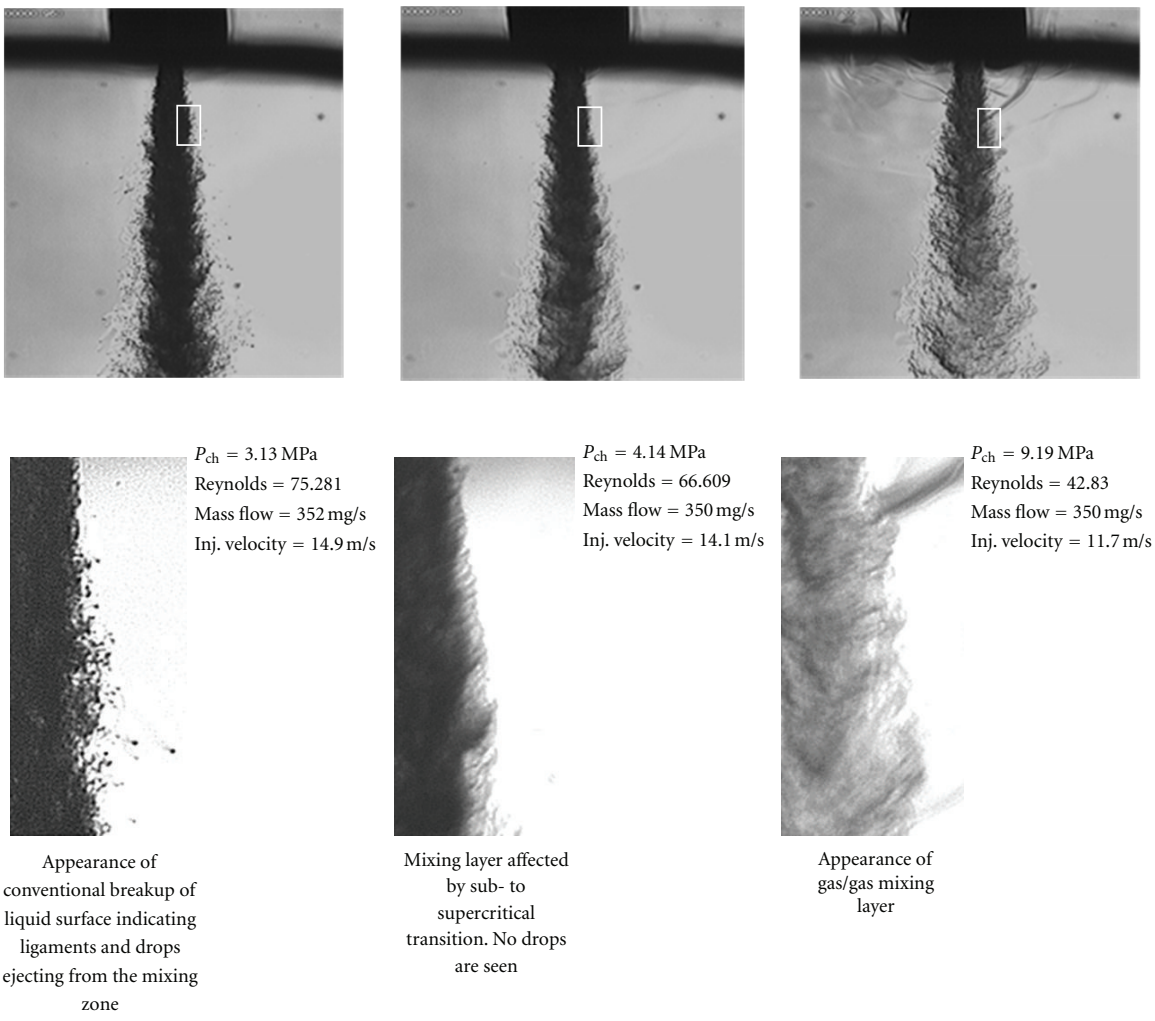

Figure 8: *Shadowgraphy imaging of liquid N_2 injected into room temperature nitrogen N_2 at different pressures, taken from Chehroudi et al. (2002). The bottom row contains magnified images of the top row in order to examine the shear layer.*

Numerical studies

Generic two-phase flows simulations

A wide variety of numerical techniques have been designed to address simulations involving two-phase flows and interfaces. Most of them consider, and rightfully so in most cases, that the interface can be treated as a surface separating two constituents. The ways in which each technique decides to track the interface movements in time allow to separate them into three classes as suggested in Sethian (2001).
To do so, it is assumed that the interface is a two dimensional curve $\Gamma(t)$ (the considerations developed in the following carry over to three dimensions without loss of generality) that is transported by a velocity field $\mathbf{v} = (u, v)$.

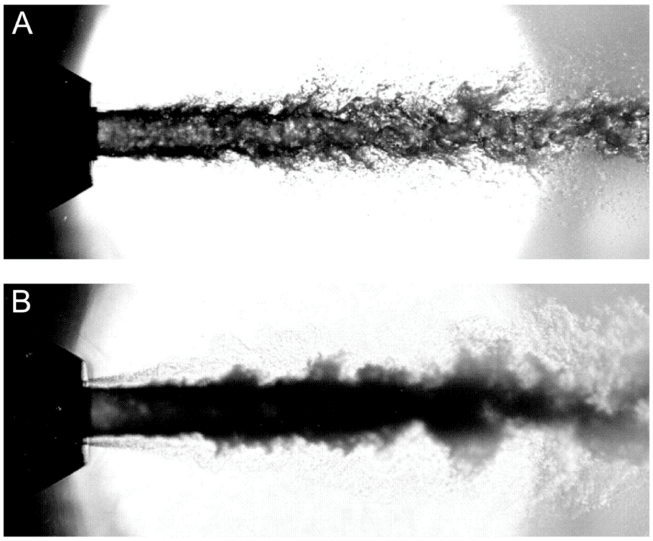

Figure 9: *Shadowgraphy imaging of a liquid N_2 / gaseous He co-flow injection into quiescent gaseous He from Mayer et al. (1998), A:10 bar (subcritical pressure) and B:60 bar (supercritical pressure)*

The geometric view consists in describing the interface using a specific set of points $\Gamma(t) = (x_\Gamma(t), y_\Gamma(t)) = \boldsymbol{x}(t)$. The interface is tracked by solving the ordinary differential equation:

$$\frac{dx_\Gamma}{dt} = \mathbf{v}_\Gamma \tag{9}$$

This characterization of the interface, where the underlying fixed Eulerian coordinate system has been discarded, has produced methods based on a Lagrangian representation such as Marker-and-Cell (Harlow et al. (1965); Welch et al. (1965); Amsden and Harlow (1970)) or Front-Tracking methods (Glimm et al. (1981); Unverdi and Tryggvason (1992); Bo et al. (2011)). Fig. 10 provides an example where Front-Tracking is applied to simulate a complex liquid injection.

The set theoretic view considers the characteristic function $\chi(\boldsymbol{x}, t)$ defined in all the domain and which equals one in a reference phase and zero in the other. This function is advected with the flow following the partial differential equation:

$$\frac{\partial \chi}{\partial t} = -\mathbf{v} \cdot \boldsymbol{\nabla} \chi \tag{10}$$

This second approach has produced Volume-of-Fluid methods (Hirt and Nichols (1981); Youngs (1982); Owkes and Desjardins (2014)) where the computational cells are filled with values representative of the characteristic function χ which actually accounts for the volume fraction of either of the phase. Cells with volume fractions different from zero or one are then assumed to contain portions of the interface, that must later be geometrically reconstructed. Fig. 11 provides an example where Volume-of-Fluid has been combined to a mesh refinement technique to simulate a three-dimensional Diesel injection.

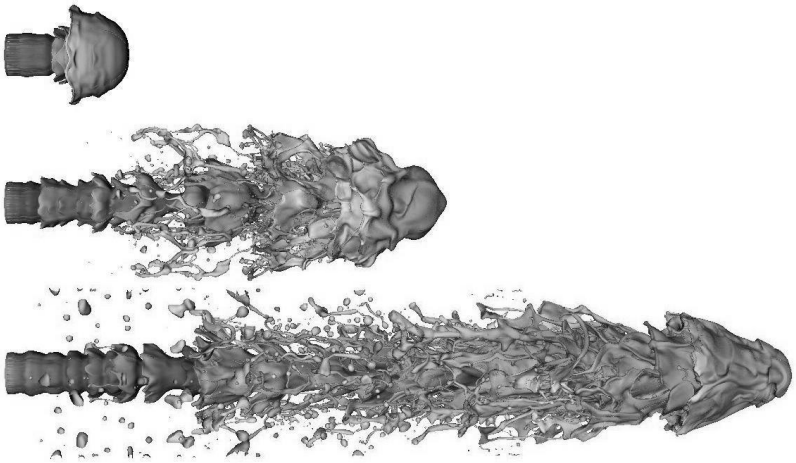

Figure 10: *Simulation of a three-dimensional liquid injection using the Front-Tracking method, taken from Bo et al. (2011)*

The analysis view defines the interface as a level-set, often the zero-level, of a continuous function φ defined over the whole domain. This function is also advected with the flow following the partial differential equation:

$$\frac{\partial \varphi}{\partial t} + \mathbf{v} \cdot \boldsymbol{\nabla} \varphi = 0 \tag{11}$$

At any given moment, the position of the interface can be evaluated by retrieving the zero-level set of φ. This third approach has brought forth techniques such as Level-Set methods (Osher and Sethian (1988); Sussman et al. (1994); Desjardins et al. (2008)) and, to a lesser degree, Phase-Field methods. In either case, the particularity is that the interface is always slightly numerically spread on the mesh to facilitate the calculations of high order derivatives.
Fig. 11 provides an example where an advanced version of the Level-Set technique has been used to simulate the turbulent atomization of a three-dimensional Diesel injection.

All three points of view have their pros and cons, further explored in Chap. 2 and Chap. 3. Lately, different points of view have been combined to take advantage of their respective virtues and reduce the impact of their individual drawbacks. This is especially true for Volume-of-Fluid and Level-Set methods, particularly suited to work in unison. Fig. 13 provides an example where both techniques have been combined to produce a very complex Diesel injection simulation in three dimensions.
The visual examples provided hereinbefore fall under Direct Numerical Simulation. It seems worth noticing that Large-Eddy simulations of such configurations are starting to be produced, such as in Xiao et al. (2013); Xiao et al. (2014) where water jets have been simulated in various configurations, coupling Volume-of-Fluid and Level-Set techniques.

Some physical phenomena, especially the ones that will be addressed in the present work, are not compatible with a sharp interface approach. Indeed, in near critical conditions, the interface between the different phases starts to be smeared out and eventually finally disappears

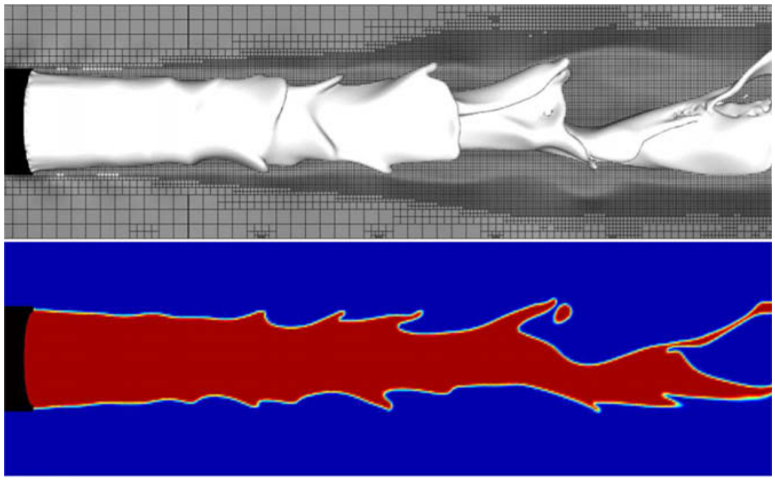

Figure 11: *Simulation of a Diesel injection using a Volume-of-Fluid method with mesh refinement, from Fuster et al. (2009). Interface representation (top) and liquid fraction in a median plane (bottom).*

when supercritical conditions are reached.
The matter of describing the fluid in supercritical conditions is an whole new task in itself, briefly reviewed in the next paragraph. However, even in subcritical conditions, the fact that the interface physically thickens calls for different techniques known as Diffuse Interface methods (in contrast with the Sharp Interface methods mentioned before).

Among these techniques, two main classes can be identified: the Phase-Field approach and its variants and the Multi-Fluid methods. Both are further reviewed in Chap. 4 but in a few words, they can be differentiated as follows:
- Phase-Field methods have been historically derived in a physically driven fashion. Indeed, the natural thickening of the interface is interpreted as a modification of the thermodynamics of the fluid, of which description is modified accordingly to model this new behavior. The free energy of the fluid is added new terms, depending on the gradient of key variables such as density or concentration. These terms cause the equations to asymptotically transform into their sharp interface counterparts but to drastically depart from them near critical conditions.
- Multi-Fluid methods, on the other hand, are rather numerically driven in their construction as they were initially introduced to simulate all sort of discontinuities inside the flow (shocks, contact discontinuities, etc...). The two phases are described using different sets of equations, better suited to their individual behavior (particularly the equation of state) and the interface is modeled as a zone where these two fluids encounter and mix together.

Both these approaches have been recently used in the context of cryogenic injection. In Gaillard (2015), the author used a variant of the Phase-Field approach to study the subcritical to supercritical transition of LOx during injection in a LOx/H_2 and used the Multi-fluid approach the perform Large Eddy Simulations (LES) of supercritical LOx/H_2 flames. A multi-fluid method has also been used in Chiapolino et al. (2017a) to simulate the evaporation of oxygen in a LOx/H_2 2D injection.

Figure 12: *Simulation of the turbulent atomization of a liquid Diesel jet with the Accurate Conservative Level-Set method, from Desjardins et al. (2008)*

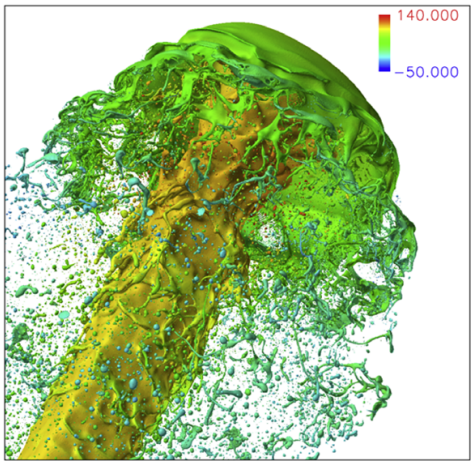

Figure 13: *Simulation of a Diesel injection using a coupled Volume-of-Fluid/Level-Set approach, from Shinjo and Umemura (2010). The color indicates the axial velocity in* $\mathrm{m.m^{-1}}$

Cryogenics jets

The work in Oefelein and Yang (1998); Bellan (2000); Yang (2000); Okong'o and Bellan (2002) has pioneered the modeling and simulation of supercritical injection for LRE configurations. One key aspect of the work presented in this document was the use of an appropriated thermodynamic description of the fluid via specially designed equations of state (EoS) known as real gas EoS. The comprehensive review of Direct Numerical Simulations of unsteady non-reacting mixing layers done in Bellan (2006) allowed to asses the effect real gas EoS on the turbulent mixing in supercritical conditions:

- the transport and diffusion coefficients strongly differ from those obtained using an ideal gas modeling; this modification strongly impacts the mixing,
- the density gradient stabilizes the jet and causes large velocity fluctuations leading to a better redistribution of the turbulent kinetic energy in the mixing layer,

- the non linearity of the real gas EoS requires modified and additional terms associated with the filtering process of Reynolds Averaged Navier-Stokes (RANS) and LES approaches.

Using a RANS approach, the authors in Mayer et al. (2003); Cheng and Farmer (2006); Kim and Moin (2011) were able to retrieve the mean density profiles observed in the experiments with pure N_2 injection.

The teachings from Bellan (2006) have been successfully applied to numerous LES simulations of cryogenic injection. In Zong et al. (2004); Schmitt et al. (2010) the authors simulated round jets of N_2 injected into quiescent gaseous N_2, in Schmitt et al. (2012) the acoustic perturbation of a pure N_2 coaxial jet was numerically investigated, a co-flow injection with liquid O_2 and gaseous CH_4 was studied in Zong and Yang (2005); Zong and Yang (2006), in Ruiz (2012) a thorough numerical analysis of a O_2/H_2 mixing layer from a co-flow injection was performed.
All these simulations showed acceptable to very great agreement with previous experimental studies.

Phenomenon	References for experiments	Benches
Flame structure	Candel et al. (1998) Cessou et al. (1998) Herding et al. (1995); Herding et al. (1998) Juniper et al. (2000) Snyder et al. (1997)	Mascotte (ONERA)
	Mayer and Tamura (1996)	(DLR)
Injection parameters	Snyder et al. (1997)	Mascotte (ONERA)
	Mayer and Tamura (1996)	(DLR)
Impact of pressure	Juniper et al. (2000); Juniper et al. (2001b) Singla et al. (2005); Singla et al. (2006)	Mascotte (ONERA)
	Mayer et al. (1998)	(DLR)
	Smith (2007); Smith (2007)	P8 (DLR)
Flame stabilization	Herding et al. (1996) Juniper et al. (2000)	Mascotte (ONERA)
	Mayer et al. (1998)	(DLR)
Impact of recess	Juniper et al. (2001a) Kendrick et al. (1998); Kendrick et al. (1999) Tripathi et al. (1999)	Mascotte (ONERA)
Ignition	De Rosa et al. (2006) Schmidt et al. (2003); Schmidt et al. (2004) Gurliat et al. (2003)	M3 (DLR)
	Mayer and Tamura (1996); Mayer et al. (2001)	M3 & P8 (DLR)

Table 2: *Overview of experimental studies performed for cryogenic combustion, taken from Candel et al. (2006) and Rocchi (2014)*

Words on reactive cases

The vast majority of the literature referenced so far only involves non-reactive cases as they are the main concern of the work presented in this document. However, no LRE can function without burning its propellant and combustion experiments to that effect are plenty.
A non-exhaustive but thorough review of experimental studies regarding cryogenic rocket engines has been done in Candel et al. (2006) and is summarized in Tab. 2.
Likewise, substantial reviews of numerical simulations in reactive cases can be found in Section 1.3 of Schmitt (2009), in Section 1.2.3 of Ruiz (2012), in Section 2.5 of Rocchi (2014) and in the introduction of Gaillard et al. (2016).

Structure of the document

The objective of this document is to assess the capability of the Second Gradient theory to permit simulations representative of the early stages of a cryogenic rocket engine ignition, more specifically the injection process. So far, although the simulation of cryogenic engines has been met with success, it has been essentially limited to supercritical conditions, as apparent from the reference provided in the previous paragraphs. Studies dedicated to subcritical simulations of such configurations are not numerous and include, for instance Dahms and Oefelein (2013); Dahms (2015); Gaillard et al. (2016); Chiapolino et al. (2017b); Pelletier (2019). This scarcity is due to the fact that modeling the thermodynamic behavior of a cryogenic fluid, over a wide range of temperatures and pressures while accounting for capillary phenomena and evaporation is no mean feat and represents a hurdle quite intricate to combine with the more established methods designed to handle flows with both liquid and vapor phases. Moreover, most of the thermodynamic models that have been developed to deal with fluids in conditions typical of LRE fails to propose a unified description of said fluids when multiple phases coexist in subcritical conditions. This thesis has been motivated by the promising features of a different model, which despite its relative old age when compared to other more well know methods, has only recently resurfaced in the context of numerical simulation involving multiphase real gas flows. The Second Gradient (SG) is a model built on the work of van der Waals (1893) and Korteweg (1901) which has been later completed by Cahn and Hilliard (1958) and various new authors. It is a Diffuse Interface model which, at its core, considers the interface to be a transitional region with a finite thickness. It offers a complete mechanical and thermodynamic description of the interfacial region which allows to evaluate key macroscopic variables such as the interface width and the associated surface tension.
The established work on the theoretical and numerical behavior of the method has been systematically studied, reformulated and expanded upon. Although a dense literature has already been produced to lay the theoretical foundations of the method, very few documents have been dedicated to assessing the applicability of said method to practical simulations. The present work is a straight continuation of these pioneering studies and as such, it has required a series of understandable simplifying hypotheses, mostly, the limitation to single species and non-reactive configurations.
The model has been implemented into the academic solver AVBP used in the industry to perform simulations on academic and semi-industrial configurations. The presentation of our work articulates around three main parts. They are preceded, in Chap. 1 by a theoretical and numerical presentation of real-gas thermodynamics as it is central to most of the other notions

explored in the rest of the document.

The first part, rather independent of the two others, is dedicated to an in-depth review of the main numerical methods used to deal with two-phase flows. The main sharp interface methods, i.e Volume-of-Fluid, Front-Tracking and Level-Set methods are described in Chapters 2 and 3, along with more historical but nonetheless insightful methods such as the Boundary Integral and Marker-and-Cell methods. Diffuse Interface methods, i.e. Phase-Field and Multi-Fluid are also explored in Chap. 4 as they appear more suitable four our matter at hands given the real gas thermodynamics to be used in our simulations. For each method that is presented, efforts have been made to outline its historical development, its current capabilities and usages but also its limitations and disparities with other methods.
The theoretical foundations of the Second Gradient theory are then thoroughly presented in Chap. 5.

The second part focuses on systematically laying down the elements necessary to perform simulations with the native Second Gradient model. The emphasis is put on justifying as mush as possible the theoretical developments that have been done and the numerical choices that have been made to produce our results.
To do so, the AVBP solver used for the calculations is described in Chap. 6 with an emphasis on the available numerical methods. Chap. 7 describes how the SG model has been implemented into the solver. The limitation of theoretical arguments to justify some of the implementation choices has fostered a systematic practical investigation of said choices on simplified cases to ensure the correct numerical behavior of the model. The final implementation is then tested in Chap. 8 to validate both its success and consistency in the AVBP solver and the correct thermodynamic behavior of the model on canonical cases specifically designed to trigger capillary phenomena.

The third part is dedicated to the presentation of a new method used to thicken the interface in the framework of the SG theory, a process, as it will be shown in the document, that is necessary to simulate realistic configurations at a reasonable computational cost. The theoretical derivation of the new thickening method is presented in Chap. 9. The strategy is then validated on simplified cases in Chap. 10 and tested on three dimensional colliding droplets and two-dimensional periodic jets in Chap. 11, a configuration mildly representative of an LRE injection.

Chapter 1

Real gas thermodynamics

The following chapter is dedicated to the presentation of the models used to describe the behavior of the fluids considered in this document within the different thermodynamic regimes they experience. The results are limited to the simplified case of a single species since all the theoretical and numerical investigations of this present work are limited to single species configurations. Thorough descriptions of multi-species thermodynamics, with its added complexity, can be found in Gaillard (2015); Pelletier (2019)

Indeed, as it is explained in Sec. 1.1, the assumptions made to derive the ideal gas law, usually used for fluid simulations, are no longer valid in the near critical and supercritical regimes that are investigated to qualify cryogenic LRE.

The generic strategies used to overcome these shortcomings are briefly detailed in Sec. 1.2, in particular the emphasis is put on the cubic equations of state (EoS), staple equations to model fluids in real gas conditions.

The results provided by the cubic EoS are particularized to the Soave-Redlich-Kwong (SRK) equation (Redlich and Kwong (1949); Soave (1972)) for which the expressions of the principal thermodynamic variables are provided together with illustrative graphics.

Eventually, the question of thermodynamic stability, pivotal when addressing phase change and therefore of a major importance for this work, is discussed in Sec. 1.4.

The results presented in this chapter, either formulas, graphics or general thoughts and conclusions, are abundantly employed in the rest of the document. Consequently, the reader not accustomed to the notions generically used when dealing with real gas flows is strongly encouraged to precociously read this chapter beforehand.
Additional mathematical and physical results are also available in App. A and App. B with a more in depth presentation of the different derivations used to obtain the main formulas.

1.1 Description and modeling of real gas thermodynamics

1.1.1 The Virial expansion

The starting assumption to derive the ideal gas law is to consider that every molecules constituting the fluid are somehow isolated and only interact through collisions to exchange momentum, kinetic and internal energy. For these assumptions to be valid, the density of the fluid must remain low enough to keep a large enough mean distance between particles. For higher densities, the remote interactions between the constituents are non longer negligible and must be accounted for by modifying accordingly the EoS.

The first major step towards the derivation of more realistic EoSs was the introduction of the virial theorem by Clausius (1870). This theorem states that, independently of the form of the considered intermolecular interactions, the time-average kinetic energy $\bar{K}_i$ of a molecule i submitted to a force F_i is equal to the time-average virial of the force $\bar{\mathcal{V}}_i = -\mathbf{r}_i \cdot \mathbf{F}_i/2$ applied on that molecule. This statement, once extended to a set of molecules, results in the fundamental relation in Eq. (1.1).

$$\bar{\mathcal{V}} = \sum_i \bar{\mathcal{V}}_i = \sum_i -\frac{1}{2}\mathbf{r}_i \cdot \mathbf{F}_i/2 = \sum_i \bar{K}_i = \bar{K} \tag{1.1}$$

Using this theorem, in van der Waals (1873), the author derived a new EoS expressed by Eq. (1.3) and named after himself.
He assumed that for a mole of fluid in a closed volume V at a pressure of P, the time-average kinetic energy $\bar{K}$ was equal to $3RT/2$ and the time-average virial of the external forces $\bar{\mathcal{V}}_{(e)}$ was equal to $3PV_m$, with V_m the molar volume.
To fully apply the virial theorem, he also needed to express the time-average virial of the internal forces $\bar{\mathcal{V}}_{(i)}$. He showed that, at the first order, it could be expressed by:

$$\bar{\mathcal{V}}_{(i)} = \sum_i \sum_j r_{ij}\phi_{ij} \tag{1.2}$$

with r_{ij} the distance between molecules i and j, and ϕ_{ij} the magnitude of the attraction forces between the two molecules. Van der Waals then showed that $\bar{\mathcal{V}}_{(i)}$ was proportional to the squared density of the fluid. With additional considerations, he eventually derived the complete equation:

$$P = \frac{RT}{V_m - B} - \frac{A}{{V_m}^2} \tag{1.3}$$

Classically, the terms of (1.3) are interpreted as follow s:

- The term containing A, the molar internal pressure constant, accounts for the attractive forces experienced by the molecules when located at large distances from one another. It is responsible for the cohesion of the fluid.
- The denominator with B, the molar covolume, accounts for the short range repulsive forces in the fluid. Experimentally, it is observed that once the molecules are close enough to one another, they start to repel. B also numerically embodies the fact that there is a certain density that the fluid cannot exceed because of molecular inter-penetration.

No specific assumptions were made by van der Waals regarding the actual form of the interactions between the molecules. In his derivation, he mostly included their observable impact on the fluid thermodynamics.
Heike Kamerlingh Onnes built upon the van der Waals EoS, initially using a polynomial series development to better fit experimental data. He later modified this first attempt and derived what is now know as the virial EoS given by Eq. (1.4).
This equation is expressed as an infinite polynomial series of the inverse molar volume $1/V_m$.

$$\frac{P}{RT} = \frac{1}{V_m} + \frac{B(T)}{V_m^2} + \frac{C(T)}{V_m^3} + \frac{D(T)}{V_m^4} + \cdots \tag{1.4}$$

where $B(T)$, $C(T)$, $D(T)$, etc... are called the second, third, fourth, etc... virial coefficients and depend only on the fluid temperature. Using the kinetic theory of gas, see Dymond and Smith (1980), it can be shown that $B(T)$ corresponds to pair molecular interactions, $C(T)$ corresponds to trio molecular interactions and so forth. When the molar volume V_m is high enough, the additional terms of the expansion can be neglected and the expression reduces to the ideal gas law.

1.1.2 Molecular interactions and interatomic potentials

Multiple analytical results have been proposed to account for the short/mid range molecular interactions. They are generally expressed in terms of the intermolecular potential $U(r)$ between two molecules separated by a distance r. The most often used are arguably the Morse, the Exponential and especially the Lennard-Jones potentials which all allow a fairly good representation of the repulsive interactions at closed range and attractive interactions at longer range. Their expressions are given hereunder and the corresponding curves are shown in Fig. 1.1.

The Morse potential is expressed by Eq. (1.5) where r_m is the equilibrium bound length (where the potential is minimal), D_e is the dissociation energy (energy required to completely separate the two molecules) and w characterizes the width of the potential well.

$$U_M(r) = D_e\left(e^{-2w(r-r_m)} - 2e^{2w(r-r_m)}\right) \tag{1.5}$$

The Exponential potential is expressed through Eq. (1.6) where r_m is the equilibrium bound length, ε characterizes the depth of the potential well (the minimal interaction potential or the maximal attraction energy) and η is a scaling parameter (usually taken equal to 13.772 to give the same curvature as the Lennard-Jones potential at $r = r_m$).

$$U_E(r) = \frac{\varepsilon}{\eta - 6}\left(6e^{\eta\left(1-\frac{r_m}{r}\right)} - \eta\left(\frac{r_m}{r}\right)^6\right) \tag{1.6}$$

The Lennard-Jones potential is expressed with Eq. (1.7) where σ is the collision diameter (the distance at which the potential is equal to zero). An expression of the first virial coefficients (along with the physical assumptions to derive them) can be found in Wu and Aaron (2015) using this particular form of potential.

$$U_{LJ}(r) = 4\varepsilon\left(\left(\frac{\sigma}{r}\right)^{12} - \left(\frac{\sigma}{r}\right)^6\right) \tag{1.7}$$

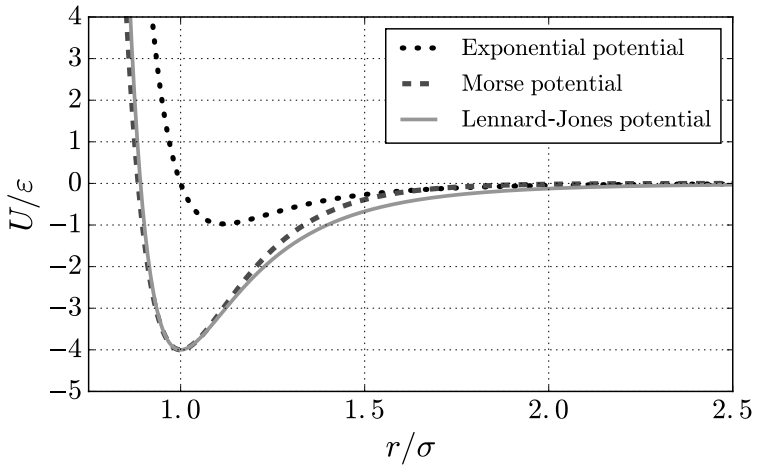

Figure 1.1: *Representation of the Morse, Exponential and Lennard-Jones potential curves with intermolecular distance in nondimensionalized coordinates*

The existence of such intermolecular potentials also implies that in a mixture composed of different species, each one has to be treated in interaction with the other and not independently as it is done for ideal gases (since molecules do not interact through potentials). Different species may interact differently and thus impact the overall behavior of the mixture.
For instance, the interaction potential U_{ij} between two different species i and j can be described by adapting the Lennard-Jones potential to get:

$$U_{LJ_{ij}}(r) = 4\varepsilon_{ij}\left(\left(\frac{\sigma_{ij}}{r}\right)^{12} - \left(\frac{\sigma_{ij}}{r}\right)^{6}\right) \tag{1.8}$$

where the collision diameter σ_{ij} Eq. (1.9) and the energy ε_{ij} Eq. (1.10) are expressed using the values σ_k and ε_k associated to the species k:

$$\varepsilon_{ij} = \sqrt{\varepsilon_i \varepsilon_j} \tag{1.9}$$

$$\sigma_{ij} = \frac{1}{2}(\sigma_i + \sigma_j) \tag{1.10}$$

This interdependency of the intermolecular potentials will in turn impact the parameters of the EoS used to describe the fluid. For instance, in the Virial EoS, the second virial coefficient will be expressed as:

$$B(T) = \sum_{i,j}^{N} X_i X_j B_{ij}(T) \tag{1.11}$$

with X_i, X_j being the molar fractions of the species i and j, and $B_{ij}(T)$ being the crossed virial coefficient between these two species (calculated using Eq. (1.8)). Other EoSs will have to implement mixing rules as well to describe correctly heterogeneous mixtures. One major impact of these results is that the values of partial thermodynamic variables for a given species in the mixture depend on the other species too, which is not the cases for a mixture of ideal gases.

1.1.3 The critical point

Intermolecular potentials allow to intuitively interpret the different states in which classic matter can be encountered, as presented in the phase diagram Fig. 1.2. From a molecular point of view, the overall energy of the fluid will result from a balance between the potential energy of interaction and the kinetic energy due to thermal agitation.

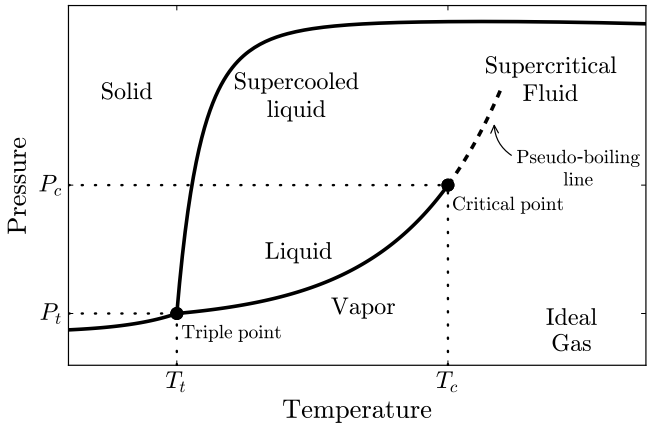

Figure 1.2: *Phase diagram schematics of a pure compound for temperature/pressure conditions. Inspired by Jessop and Leitner (2008) and Dahms and Oefelein (2013)*

Classically at very high pressures for low to moderate temperatures, the material is in a solid state, which will not be addressed here. When focusing on the fluid phases, one can notice the existence of five cases: the pure liquid and pure gaseous phases, the two-phase regime where liquid and vapor coexist along the saturation line, the ideal gas and the supercritical phase.

In the vapor phase, the inter-molecular distance is high, leading to low attractive forces combined with an important thermal agitation, thus a high kinetic energy.
When the temperature is even higher, thermal agitation completely undermines the potential interactions and the fluid behaves like an ideal gas.
Conversely, in the liquid, the attraction forces become much higher and overcome the kinetic energy.
By increasing the pressure even more, it is possible to obtain a liquid with an extremely high density, so much so that it actually behaves like a solid to some extent. Such a fluid is called a supercooled liquid.
Starting from a vapor phase, when the inter-molecular distance decreases, due to a pressure (thus, a density) increase, if the temperature is low enough, the kinetic energy gets lower than the interaction potential energy. This causes the molecules to stabilize at a distance r_{eq} which, when applied to a portion of the fluid, results in a condensation and the appearance of a liquid form.
However, there exists a certain temperature above which the condensation will not occur no matter what the pressure applied to the system. Indeed, if the temperature is high enough, the kinetic energy will be higher than the maximal interaction potential ε impeding any condensation. This temperature is called the critical temperature T_c of the fluid and the critical pressure P_c is the minimal pressure to apply to the fluid at its critical temperature to trigger

condensation for a molar volume V_c. Together, T_c, P_c and V_c define the critical point of the fluid.

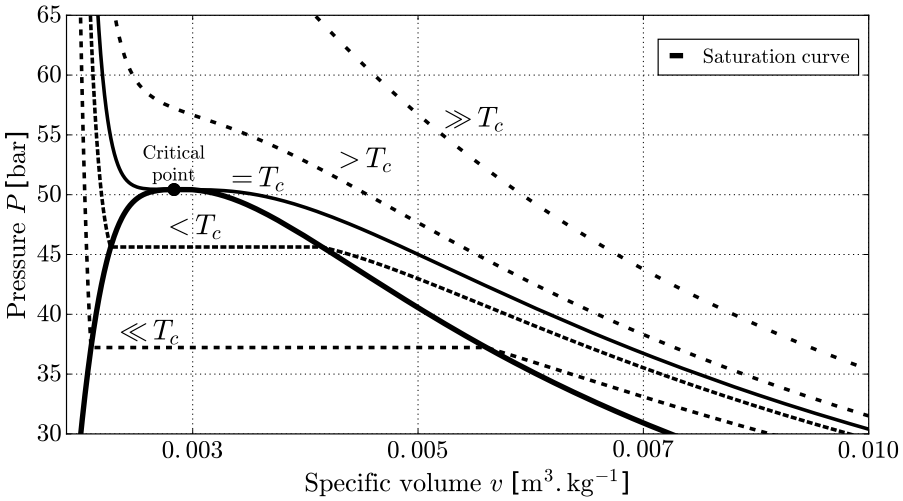

Figure 1.3: *Clapeyron's diagram for pure oxygen O_2 with Andrew's isotherm curves for different regimes temperatures. Values taken from NIST thermodynamic database (Linstrom and Mallard (2001)).*

The critical point is also present in the Clapeyron's diagram Fig. 1.3 where the variations of the pressure P with the specific volume v are given for different isothermal curves. In the liquid, the volume does not vary much with the pressure, as liquids usually have a very low compressibility whereas it is the opposite in the vapor phase. Between the two bulk phases there is a transition zone were liquid and vapor phases coexist as the fluid transit from one phase to the other. This transition admittedly occurs at a constant pressure, the saturation pressure $P_{\text{sat}}(T)$.
When the two phases coexist, the molecules in the vapor near the interface will perceive a much stronger attraction coming from the liquid phase than its surrounding vapor phase and will be attracted in that direction. The interaction potentials are no longer balanced in that region, leading to a residual energy locally condensed at the interface and usually referred to as surface tension. This unbalance is the source of capillary phenomena.

The saturation pressure increases with the temperature. As the latter gets closer to its critical value T_c, the vapor phase starts to display a behavior closer to that of the liquid. In particular, the fluid density in both phases becomes extremely sensitive to pressure and/or temperature variations, so do other characteristic values of the fluid.
During this temperature increase, the unbalance between the energies of the liquid and vapor phases reduces. This causes the surface tension to diminish and eventually vanish at the critical point when the phases becomes indistinguishable. In Fig. 1.3, one can even see that the critical point is characterized by an inflection point in the isothermal curve for $T = T_c$

which translates mathematically into:

$$\left(\frac{\partial P}{\partial v}\right)_T\Big|_{T_c,P_c} = \left(\frac{\partial^2 P}{\partial v^2}\right)_T\Big|_{T_c,P_c} = 0 \tag{1.12}$$

Finally, when the temperature is far over T_c, the isothermal curves display a tendency in $1/v$ typical of an ideal gas.

1.2 Main thermodynamic results and cubic equations of state

1.2.1 The corresponding states principle

Following the derivation of its EoS, van der Waals also noticed that constants A and B, that were apparently a cause for loosing the universality of the EoS, could actually be linked to the critical parameters of the fluid by:

$$T_c = \frac{8A}{27RB} \tag{1.13a}$$

$$P_c = \frac{1}{27B^2} \tag{1.13b}$$

$$V_c = 3B \tag{1.13c}$$

From that observation, he decided to express the EoS using the reduced quantities $T_r = T/T_c$, $P_r = P/P_c$ and $V_r = V/V_c$ thus moving from a formulation $P(T, V)$ to the formulation $P_r(T_r, V_r)$:

$$P_r = \frac{8T_r}{3V_r - 1} - \frac{3}{V_r} \tag{1.14}$$

The formulation in Eq. (1.14) allows the EoS to retrieve some sense of universality.
Van der Waals went further and enunciated a thermodynamic principle that has become a foundation in modern thermodynamic derivations, especially when oriented towards simulation. In the author's own words from van der Waals (1873), the original Corresponding States Principle (CSP) is written as:

If we express the pressure in terms of the critical pressure, the volume in terms of the critical volume and the absolute temperature in terms of the critical temperature, the isothermal curves for all bodies become the same[...] This result no longer contains any reference to the specific properties of various bodies, the specifics have disappeared.

It is worth mentioning that this principle makes the expression of a (well-enunciated) EoS universal but does not nor qualify neither improve the intrinsic quality of the EoS regarding its propensity to fit on experimental data.
For instance, as explained in Poling et al. (2001), using only two parameters (T_c and P_c following van der Waals framework) for the CSP implies that all the species have the same critical compressibility $Z_c = P_c V_c/(RT_c)$. For the van der Waals EoS, this value is for instance 0.375. Unfortunately, the critical compressibility Z_c varies for all fluids and takes values between 0.15 and 0.3 for most organic compounds.

To gain accuracy, EoSs based on the CSP must use additional parameters to describe the fluids. The acentric factor ω is such a parameter and is the most commonly used. Introduced in Pitzer et al. (1955) and Pitzer and Curl Jr (1957) and defined by Eq. (1.15), it allows to take into account the fact that the fluid particles are not spherical and/or the fact that they may be polar.

$$\omega = -\ln\left(P_{r\text{sat}}\left(T_r = 0.7\right)\right) - 1 \tag{1.15}$$

Here, $P_{r\text{sat}}\left(T_r = 0.7\right)$ is the reduced saturation pressure for a reduced temperature of 0.7.

Indeed, the CSP as expressed by van der Waals is valid only under other strong assumptions besides an universal value of critical compressibility Z_c. The particles have to be spherical, non-polar and have an interaction potential curve that complies to an universal shape, what most materials do not verify.
An updated version of the principle including ω is necessary. In its new form, it asserts that all materials can be described by an EoS written in terms of:

$$P_r = P_r\left(T_r, V_r, \omega\right) \tag{1.16}$$

And more generally, other thermodynamic variables, written in a nondimensionalized form, also tend to be expressed as functions of the inputs P_r, T_r, V_r and ω. Some examples are given for the heat conduction in Roy and Thodos (1968), the viscosity in Chung et al. (1988) or the surface tension in Pitzer (1995).

To further increase the accuracy of the EoSs, multiple strategies have been implemented and are described in Poling et al. (2001). One of them is for instance adding a new parameter to the corresponding state principle or using two (or more) reference fluids with different values ω_1, ω_2,..., ω_n of acentric factors. However, no correlations have given satisfactory results with this strategy so far.
Another strategy is to use non-analytical EoSs like the Benedict-Webb-Rubin EoS from Benedict et al. (1940). One issue with such EoSs is that the gain in accuracy is unfavorably balanced by a much greater complexity. In particular, the determination of the density from the temperature and the pressure requires to solve a non-linear, usually high order polynomial equation that cannot be solved analytically, thus calling for a numerical resolution, often costly.

1.2.2 Cubic equations of state

From a theoretical point of view, the Virial EoS allows to demonstrate the impact and the influence of molecular interactions but it lacks in accuracy relatively to its complexity, in particular when compared to more simple yet more accurate analytical EoSs used in practice. This is mostly because the expansion is often truncated to the second or third coefficient limiting its use for high density values.
As already mentioned, one practical restriction on the EoS is the nature of the equation $\rho = f\left(P, T\right)$ to solve in order to retrieve the density from the pressure and the temperature. Strongly non-linear equations are prohibited and an analytical resolution is only possible up to the 4^{th} order for polynomial equations, thus limiting the complexity of analytical EoS that are affordable in practice.

However, for the Andrew's isothermal curves to display the correct behavior in the different regimes of Fig. 1.3, in particular have an inflection point for (T_c, P_c), the equation must at least be 3$^{\text{rd}}$ order polynomial in the density. These observations provide the most simple expression possible for a polynomial-analytical EoS.

EoSs that have a third order polynomial development with respect to the density are called cubic EoS. A wide variety of cubic EoS have been developed in the past decades and a non exhaustive list can be found in Poling et al. (2001). It is worth mentioning that the van der Waals EoS Eq. (1.3) also falls under that classification. In the following, we will only focus on the cubic EoS of which general expression can be written as in Eq. (1.17) since this form encompasses the most often used ones, namely the van der Waals EoS from van der Waals (1873), the Peng-Robinson EoS from Peng and Robinson (1976) and the Soave-Redlich-Kwong EoS Redlich and Kwong (1949); Soave (1972). In particular, the Peng-Robinson and the Soave-Redlich-Kwong EoSs are the ones used in AVBP-RG, a specific version of the solver AVBP dedicated to real gas simulations.

$$P = \frac{\rho r T}{1 - b\rho} - \frac{a\left(T\right)\rho^2}{1 + e_1 b\rho + e_2 b^2 \rho^2} \tag{1.17}$$

Here e_1 and e_2 are the coefficients characterizing the cubic EoS, a is a function of the temperature depending on the fluid, r is the constant of the fluid given by $r = R/M$ and b is also a constant depending on the fluid. More precisely, for a single species, a and b are given by:

$$a\left(T\right) = \Phi_c \Psi\left(T\right)^2 \tag{1.18}$$

$$\Psi\left(T\right) = 1 + c\left(1 - \sqrt{T/Tc}\right) \tag{1.19}$$

$$\Phi_c = \phi \frac{\left(rT_c\right)^2}{P_c} \tag{1.20}$$

$$b = \varphi \frac{rT_c}{P_c} \tag{1.21}$$

$$c = \gamma_0 + \gamma_1 \omega + \gamma_2 \omega^2 \tag{1.22}$$

In multi-species configurations, a and b are obtained using mixing rules involving the species mass fractions and intrinsic values of critical variables. In some occurrences, $\Psi\left(T\right)$ is set to 0 for temperatures T above the critical temperature T_c, although it is not a requisite. Additionally, γ_0, γ_1, γ_2, ϕ and φ are constants depending on the EoS. The values all of these coefficients are given Tab. 1.1 for the van der Waals, Peng-Robinson and Soave-Redlich-Kwong EoSs. It can be shown, see Michelsen et al. (2008), that coefficients ϕ and φ are actually dependent of the choices for e_1 and e_2 and are obtained by solving a 3$^{\text{rd}}$ order polynomial equation.
The calculation of the density ρ from the temperature T and the pressure P is done by solving the 3$^{\text{rd}}$ order polynomial equation:

$$a_0 + a_1\rho + a_2\rho^2 + a_3\rho^3 = 0 \tag{1.23}$$

Constants	van der Waals	Peng-Robinson	Soave-Redlich-Kwong
e_1	0	2	1
e_2	0	-1	0
ϕ	27/64	0.457236	0.077796
φ	1/8	0.427480	0.086640
γ_0	0	0.37464	0.48508
γ_1	0	1.54226	1.5517
γ_2	0	- 0.26992	- 0.15613

Table 1.1: *Values of the constants used in the principal cubic equations of state.*

of which coefficients a_0, a_1, a_2 and a_3 are given by:

$$a_0 = -P \tag{1.24a}$$
$$a_1 = (1 - e_1)\, Pb + rT \tag{1.24b}$$
$$a_2 = (e_2 - e_1)\, Pb^2 + e_1 rTb - a \tag{1.24c}$$
$$a_3 = e_2 Pb^3 + e_2 rTb^2 + ab \tag{1.24d}$$

The calculation of the temperature T from the density ρ and the pressure P is done by solving the 2$^{\text{nd}}$ order polynomial equation:

$$b_0 + b_1\sqrt{T} + b_2 T = 0 \tag{1.25}$$

where coefficients b_0, b_1 and b_2 are given by:

$$b_0 = -(1+c)^2 \rho^2 \phi_c - P\left(1 + e_1 b\rho + e_2 b^2 \rho^2\right) \tag{1.26a}$$
$$b_1 = 2c\,(1+c)\,\rho^2 \Phi_c \tag{1.26b}$$
$$b_2 = \frac{\rho r\left(1 + e_1 b\rho + e_2 b^2\rho^2\right)}{1 - b\rho} - c^2\rho^2\Phi_c \tag{1.26c}$$

Eqs. (1.23) and (1.25) can happen to have multiple real solutions. To discriminate between them, it is necessary to find the admissible solutions leading to stable thermodynamic states and possibly choose the more stable one. Doing so requires the calculation of the fugacity f described in more details in the next paragraph, in particular in Eqs. (1.34) and (1.35). The stable solution is the one leading to the minimal fugacity.
For Eq. (1.25) with the temperature, it can be shown that the stable solution is always given by the smallest real positive value of $\sqrt{T}$ found during the resolution.
For Eq. (1.23) with the density, the admissible solutions (real positive solutions smaller than $1/b$) have first to be extracted. If there is more than one admissible solution, the one among them leading to the smallest fugacity is the stable one. If two admissible solutions share the same smallest fugacity, even though this case is unlikely to occur during a computation, there is a coexistence of two phases characterized by the two different values of density.

1.2.3 Departure values

To express the other thermodynamic variables, in particular the thermodynamic potentials, the standard approach is to separate the contributions from the low density state where only

the individual molecular energies matter (translation, rotation, vibration) given by the ideal gas modeling and from the high density (or high pressure) state taking into account the non-kinetic molecular interactions. For a state variable χ, the separation is written as:

$$\chi^{\mathrm{EoS}} = \chi^0 + \Delta\chi \tag{1.27}$$

where χ^0 is the ideal gas reference and $\Delta\chi$, called the departure value of the variable χ, is the gap between the low and high density/pressure states. For the three basic thermodynamic variables T, P and ρ are not independent, there are two ways to define the departure value $\Delta\chi$, as explained in Vidal (1997). Indeed, the ideal gas and the real fluid can be considered to share the same temperature and density (in which case their pressures will differ, i.e. $P^{\mathrm{EoS}}(T,\rho) \neq P^0(T,\rho)$), the departure value is given in that case by Eq. (1.28). Conversely, they can be considered to share the same pressure and temperature (in which case their densities will differ, i.e. $\rho^{\mathrm{EoS}}(T,P) \neq \rho^0(T,P)$), the departure is given this time by Eq. (1.29).

$$\Delta^{\rho}\chi(T,\rho) = \chi^{\mathrm{EoS}}(T,\rho) - \chi^0(T,\rho) = \int_0^{\rho} \left[\left(\frac{\partial \chi^{\mathrm{EoS}}}{\partial \varrho} \right)_T - \left(\frac{\partial \chi^0}{\partial \varrho} \right)_T \right] d\varrho \tag{1.28}$$

$$\Delta^{P}\chi(T,P) = \chi^{\mathrm{EoS}}(T,P) - \chi^0(T,P) = \int_0^{P} \left[\left(\frac{\partial \chi^{\mathrm{EoS}}}{\partial \mathrm{P}} \right)_T - \left(\frac{\partial \chi^0}{\partial \mathrm{P}} \right)_T \right] d\mathrm{P} \tag{1.29}$$

In most cases, these two definitions are not equivalent. Since in practice, temperature and pressure are the more reliably measured variables, they usually are chosen as reference. Following this clarification, if not mentioned otherwise, we will retain the definition of departure value from reference pressure and temperature as defined in Eq. (1.29). From the form of Eq. (1.29), the explicit formulation of the departure values strongly relies on the differential relationships between the state variables, known as the Maxwell relationships, which are compiled in App. B. A difficulty is caused by the formulation of most EoS that gives explicitly the pressure from the temperature and the density. To overcome this impediment, it is suitable to turn the integral in the pressure variable P of (1.29) into an integral in the density variable ϱ. Additionally, partial derivatives of the pressure must be explicitly introduced in the integrand preferably to that of the temperature or the density. All the corresponding mathematical manipulations are detailed in App. B. The expressions of the departure values are given for the specific state variables: the internal energy e_s,the free energy f, the entropy s and the

isochoric heat capacity C_v :

$$\Delta^P e_s = \int_0^\rho \left[\frac{P}{\varrho^2} - \frac{T}{\varrho^2} \left(\frac{\partial P}{\partial T} \right)_\varrho \right] d\varrho \tag{1.30}$$

$$\Delta^P f = \int_0^\rho \left[\frac{P}{\varrho^2} - \frac{rT}{\varrho} \right] d\varrho - rT \ln \left(\frac{P}{\rho r T} \right) \tag{1.31}$$

$$\Delta^P s = \int_0^\rho \left[\frac{r}{\varrho} - \frac{1}{\varrho^2} \left(\frac{\partial P}{\partial T} \right)_\varrho \right] d\varrho + r \ln \left(\frac{P}{\rho r T} \right) \tag{1.32}$$

$$\Delta^P C_v = \int_0^\rho -\frac{T}{\varrho^2} \left(\frac{\partial^2 P}{\partial T^2} \right)_\varrho d\varrho \tag{1.33}$$

The fugacity f is defined by the differential relationship Eq. (1.34) where $g = \mu$ is the specific free enthalpy (or equivalently the chemical potential) of the fluid. It is another variable that quantifies the deviation of the fluid thermodynamics from the ideal gas model.

$$dg = rT\, d(\ln \mathrm{f}) \tag{1.34}$$

Of a moderate interest for a single fluid, for a mixture it extends the notion of partial pressure to real gases. In a mixture of ideal gases, each fugacity f_i would be equal to the partial pressure P_i. That is not the case for a mixture of real gases due to the inter-species interactions. For two phases φ_1 and φ_2 to coexist, their fugacities f_{φ_1} and f_{φ_2} must be equal.
Most of the time, the fugacity is tedious to manipulate and one rather defines the fugacity coefficient $\phi = \mathrm{f}/P$. However in practice, $\mathcal{F} = rT \ln \phi$ is the value employed for calculations because the straightforward definition given Eq. (1.35) renders it particularly easy to use.

$$\mathcal{F} = rT \ln \phi = \Delta^P g = \Delta^P f + \frac{P}{\rho} - rT \tag{1.35}$$

Granted that the pressure and the temperature of the systems under comparison are the same, the equality of the fugacities f amounts to the equality of the values $\mathcal{F}$. Remarkably, this is particularly the case when discriminating between the solutions of the cubic equation to find the density or to calculate saturation values at a given temperature.

Finally, the internal energy e_s, the free energy f and the isochoric heat capacity C_v are linked to the enthalpy h, the free enthalpy g, the chemical potential μ and the isobaric heat capacity C_p through Eqs. (1.36), (1.37) and (B.67).

$$h = e_s + \frac{P}{\rho} \tag{1.36}$$

$$g = \mu = f + \frac{P}{\rho} \tag{1.37}$$

$$C_p = C_v + \frac{T\alpha^2}{\rho\beta} \tag{1.38}$$

where α is the thermal expansion coefficient defined in Eq. (1.39) and β is the isothermal compressibility coefficient defined in Eq. (1.40).

$$\alpha \quad \hat{=} \quad -\frac{1}{\rho}\left(\frac{\partial \rho}{\partial T}\right)_P \quad = \quad \frac{1}{\rho}\left(\left(\frac{\partial P}{\partial \rho}\right)_T\right)^{-1}\left(\frac{\partial P}{\partial T}\right)_\rho \tag{1.39}$$

$$\beta \quad \hat{=} \quad \frac{1}{\rho}\left(\frac{\partial \rho}{\partial P}\right)_T \quad = \quad \frac{1}{\rho}\left(\left(\frac{\partial P}{\partial \rho}\right)_T\right)^{-1} \tag{1.40}$$

The thermodynamic sound speed c can also be calculated thanks to:

$$c^2 \hat{=} \left(\frac{\partial P}{\partial \rho}\right)_s = \frac{1}{\rho\beta}\frac{C_p}{C_v} \tag{1.41}$$

1.2.4 Transport properties for real gases

1.2.4.1 Transport properties for ideal gases

The dynamic viscosity μ and the thermal conduction coefficient k_{th} are also impacted by the non-idealistic nature of the real gas. This translates physically by a dependency of these variables on the fluid density. The model most often used for the dynamic viscosity of an ideal gas is an exponential law expressed in Eq. (1.42) where μ only varies with the temperature.

$$\mu\left(T\right) = \mu_0\left(\frac{T}{T_0}\right)^a \tag{1.42}$$

Here, μ_0 is reference value for the dynamic viscosity, usually acquired experimentally, at a reference temperature T_0 and a is the exponential constant depending on the fluid. The thermal conduction coefficient k_{th} is then obtained with the hypothesis of a constant Prandtl number Pr (i.e. independent of the temperature and of the composition for a mixture) to give:

$$k_{\text{th}} = \frac{\mu C_p}{Pr} \tag{1.43}$$

where C_p is the specific isobaric heat capacity of the fluid.

1.2.4.2 Transport properties for simple diluted gases

For real gases, the first noticeable difference is that the dynamic viscosity μ no longer varies monotonously with the temperature, in particular in the vicinity of and above the critical point. As shown in Fig. 1.4, the viscosity of the dense liquid-like phase diminishes with the temperature whereas the opposite occurs for the light gas-like fluid.

Multiple methods have been proposed to evaluate the viscosity of a real gas but in essence, all of them rely either on the Corresponding States Principle or the Chapman-Enskog developments from Chapman (1954) and Chapman and Cowling (1970) or occasionally on both principles simultaneously. From the Chapman-Enskog theory, the viscosity of the fluid can be written as:

$$\mu^{\text{CH}}\left(T\right) = \frac{2.669 \cdot 10^{-8}\sqrt{M}}{\Theta\left(T\right)\sigma^2}\sqrt{T} \tag{1.44}$$

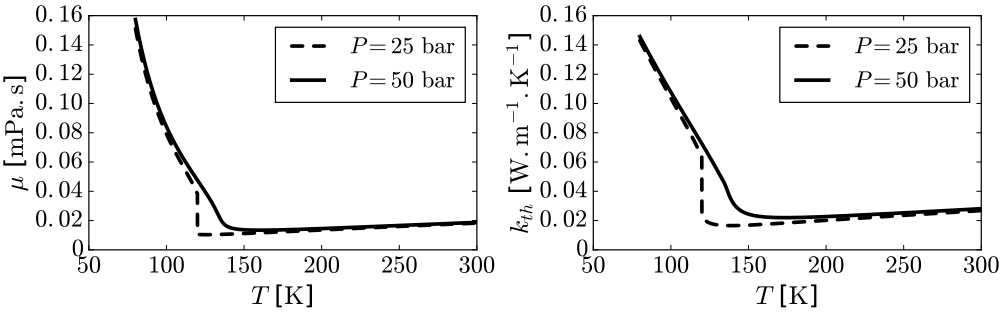

Figure 1.4: *Evolution of the viscosity μ and the thermal conductivity k_{th} for nitrogen N_2 at subcritical and supercritical pressure ($P_c = 33.958$ Pa), from NIST online database Linstrom and Mallard (2001)*

where M is the molar mass of the fluid in g.mol^{-1}, T its temperature in K, σ is the collision diameter introduced in Eq. (1.7) in nm and $\Theta(T)$ is the collision integral of which expression depends on the form chosen for the intermolecular potential to describe the non-kinetic interactions within the fluid.
The Lennard-Jones potential given by Eq. (1.7), the most often used, leads to the following expression for the collision integral (from Neufeld et al. (1972)):

$$\begin{aligned}\Theta(T_*) = 1.16145\ T_*^{-0.14874} + 0.52487\ e^{-0.77320\ T_*} + 2.16178\ e^{-2.43787\ T_*} \\ -6.435\ T_*^{0.14874} \sin\left(18.0323\ T_*^{-0.76830} - 7.27371\right)\end{aligned} \tag{1.45}$$

where $T_* = Tk_B/\varepsilon$ with $k_B = 1.38064852 \cdot 10^{-23}$m^2.kg.s^{-2}.K^{-1} the Boltzmann constant and ε the minimal interaction potential introduced Eq. (1.7). The last component of Eq. (1.45) with the sine function is often discarded for numerical applications.
The expression has been further simplified by Chapman & Enskog noticing the quasi-linear dependency of Θ in $1/\sqrt{T_*}$ to eventually lend the commonly used formulas:

$$\Theta = \frac{1.604}{\sqrt{T_*}} \tag{1.46}$$

$$\mu^{\mathrm{CH}}(T) = \frac{526.191\sqrt{M}}{\sigma^2\sqrt{\frac{\varepsilon}{k_B}}}T \tag{1.47}$$

This approach only holds for simple, non-polar and usually monoatomic molecules. For more complex gases, the authors in Chung et al. (1988) describe a new method based on the CSP. It consists in evaluating the reference viscosity μ^{CH} from the Chapman-Enskog theory and then apply a corrective factor F_c as follows:

$$\mu^{\mathrm{Ch,lowP}} = \mu^{\mathrm{CH}} F_c(T, \rho, T_c, V_c, \omega) \tag{1.48}$$

where T_c, V_c, ω are the critical temperature, critical molar volume and acentric factor of the fluid, F_c the corrective factor. For a mixture, the different critical values used when applying the CSP to obtain Eq. (1.48) have to be formally replaced by "mixture" critical values $T_{c,\mathrm{mix}}$, $V_{c,\mathrm{mix}}$, ω_{mix}, etc.. of which expressions are given in Poling et al. (2001).
The corrective factor is given by:

$$F_c = 1 - 0.2756\omega + 0.059035\vartheta_r^4 + k \tag{1.49}$$

where k is a corrective factor for molecules with strong hydrogen bounding effects, ω is the acentric factor and ϑ_r is the dimensionless dipole moment expressed from the dipole moment ϑ in Debye with:

$$\vartheta_r = 0.1313 \frac{\vartheta}{\sqrt{V_c T_c}} \tag{1.50}$$

For complex fluids, the relation between the viscosity $\mu_{\text{lowP}}^{\text{Ch}}$ and the thermal conductivity coefficient $k_{\text{th}}^{\text{Ch,lowP}}$ can no longer be described with Eq. (1.43). The new correlation is:

$$k_{\text{th}}^{\text{Ch,lowP}} = 31.179 * \frac{M \mu^{\text{Ch,lowP}}}{\Psi\left(T_r, \omega, C_v^0\right)} \tag{1.51}$$

where $k_{\text{th}}^{\text{Ch,lowP}}$ is calculated in $\text{W.m}^{-1}\text{.K}^{-1}$, the molar mass M expressed in g.mol^{-1} and Ψ is a coefficient depending on the reduced temperature $T_r = T/T_c$, the acentric factor ω and the corresponding ideal gas molar isochoric heat capacity C_v^0.
The value of Ψ can be calculated using the following formulas:

$$\Psi\left(T_r, \omega, C_v^0\right) = 1 + \kappa \frac{0.215 + 0.28288\kappa - 1.061\eta + 0.26665Z}{0.6366 + \eta Z + 1.061\kappa\eta} \tag{1.52a}$$

$$\kappa = \frac{C_v^0}{R} - \frac{3}{2} \tag{1.52b}$$

$$\eta = \frac{\mu}{0.77320\rho} \tag{1.52c}$$

$$Z = 2.0 + 10.5T_r^2 \tag{1.52d}$$

In practice, coefficient η is rather expressed through correlation as a function of ω.

1.2.4.3 Transport properties for dense gases

When the temperature and the pressure increase, their effects on the viscosity and thermal conduction coefficient must be accounted for. To do so, additional corrective correlation are proposed in Chung et al. (1988) and can be summarized by Eqs. (1.53a)-(1.53b).

$$\begin{cases} \mu^{\text{Ch}} = \mu^{\text{Ch,lowP}} \text{C}_\mu + \mu^{\text{corr,highP}} \text{D}_\mu & \text{(1.53a)} \\ k_{\text{th}}^{\text{Ch}} = k_{\text{th}}^{\text{Ch,lowP}} \text{C}_{k_{\text{th}}} + k_{\text{th}}^{\text{corr,highP}} \text{D}_{k_{\text{th}}} & \text{(1.53b)} \end{cases}$$

where $\mu^{\text{corr,highP}}$ and $k_{\text{th}}^{\text{corr,highP}}$ are high-pressure corrective viscosity and thermal conductivity coefficient expressed by Eqs. (1.54a) and (1.54b), C_μ, D_μ, $\text{C}_{k_{\text{th}}}$ and $\text{D}_{k_{\text{th}}}$ are intricate corrective coefficients depending on the quantity $y = \rho V_c/6$, the acentric factor ω, the reduced dipole moment ϑ_r and coefficient k introduced in Eq. (1.49).

$$\mu^{\text{corr,highP}} = 3.6334 \cdot 10^{-10} \frac{M^{\frac{1}{2}} T_c^{\frac{1}{2}}}{V_c^{\frac{2}{3}}} \tag{1.54a}$$

$$k_{\text{th}}^{\text{corr,highP}} = 1271 \cdot 10^{-3} \frac{T^{\frac{1}{2}}}{M^{\frac{1}{2}} V_c^{\frac{2}{3}}} \tag{1.54b}$$

To the best of our knowledge, the validity of this method (or any other relying on the combination Chapman-Enskog/Corresponding States Principle) has never been discussed for unstable thermodynamic regimes as we encounter in the Second Gradient theory. For this reason, in this study, no modification has been applied when calculating μ and k_{th} inside the saturation curve, particularly in the spinodal region.
A special attention has been given to the values taken by the thermal conduction coefficient and the viscosity in this region as the correlation from Chung et al. (1988) is known to possibly lead to unphysical values. No such situation was encountered in our applications.

1.3 Application to the Soave-Redlich-Kwong equation of state

1.3.1 Departure values for cubic equations of state

When applied to the cubic equations of state described by Eq. (1.17), the departure values expressions in Eqs. (1.30)-(1.33) can be simplified. The derivatives of the quantity $a(T)$ come into play as well as the quantity $\mathcal{I}(e_1, e_2, \rho)$ defined in Eq. (1.55). The calculation of $\mathcal{I}(e_1, e_2, \rho)$ is done App. B.3 and its final expression, more easily written in terms of specific volume $\mathrm{v} = 1/\rho$, is given by Eq. (B.78).

$$\mathcal{I}(e_1, e_2, \rho) = \int_0^{\rho} \frac{d\varrho}{1 + e_1 b\varrho + e_2 b^2 \varrho^2} \tag{1.55}$$

$$\mathcal{I}(e_1, e_2, \rho) = \frac{1}{\mathrm{v}_+ - \mathrm{v}_-} \ln\left(\frac{\mathrm{v} - \mathrm{v}_-}{\mathrm{v} - \mathrm{v}_+}\right) \tag{1.56}$$

$$\mathrm{v}_{+/-} = \frac{b}{2}\left(-e_1 + /- \sqrt{{e_1}^2 - 4e_2}\right) \tag{1.57}$$

The resulting departure values are given by:

$$\Delta^P e_s = \left(T\frac{da}{dT}(T) - a(T)\right)\mathcal{I}(e_1, e_2, \rho) \tag{1.58}$$

$$\Delta^P f = -a(T)\,\mathcal{I}(e_1, e_2, \rho) - rT\ln\left(\frac{P(1-b\rho)}{\rho r T}\right) \tag{1.59}$$

$$\Delta^P s = \frac{da}{dT}(T)\,\mathcal{I}(e_1, e_2, \rho) + r\ln\left(\frac{P(1-b\rho)}{\rho r T}\right) \tag{1.60}$$

$$\Delta^P C_v = T\frac{d^2 a}{dT^2}(T)\,\mathcal{I}(e_1, e_2, \rho) \tag{1.61}$$

1.3.2 Application to the Soave-Redlich-Kwong equation of state

In this paragraph, as an application example, the expression of thermodynamic variables are detailed using the SRK EoS of which formula is recalled in Eq. (1.62) and is obtained with the values $e_1 = 1$ and $e_2 = 0$.

$$P(T, \rho) = \frac{\rho r T}{1 - b\rho} - \frac{\rho^2 a(T)}{1 + b\rho} \tag{1.62}$$

This EoS has been preferably chosen to perform all the calculations presented in this document because relatively to its simplicity, it offers a pretty good agreement with experimental data over a wide range of temperatures and pressures. When compared to the Peng-Robinson EoS, it tends to be less accurate near the critical point, which is usually a challenge for all EoS especially the cubic ones. However, it is overall more precise, in particular in the dense phase which was of a primary interest for our simulations.
The cubic equation to retrieve the density from P and T becomes:

$$\rho^3 [ab] + \rho^2 \left[Pb^2 + rTb - a\right] + \rho [rT] - P = 0 \tag{1.63}$$

With $v_+ = 0$ and $v_- = -b$, the value of $\mathcal{I}(e_1, e_2, \rho)$ is given by:

$$\mathcal{I}(e_1, e_2, \rho) = \frac{1}{b} \ln(1 + b\rho) \tag{1.64}$$

From that, the specific internal energy, free energy, entropy, isochoric heat capacity and also the fugacity coefficient can be obtained:

$$e_s(T, \rho) = e_s^0(T) + \frac{1}{b}\left(T\frac{da}{dT} - a\right)\ln(1 + b\rho) \tag{1.65}$$

$$f(T, \rho) = f^0(T) + -\frac{a}{b}\ln(1 + b\rho) - rT\ln\left(\frac{P(1 - b\rho)}{\rho rT}\right) \tag{1.66}$$

$$s(T, \rho) = s^0(T) + r\ln\left(\frac{P(1 + b\rho)}{\rho rT}\right) + \frac{da}{dT}\frac{1}{b}\ln(1 + b\rho) \tag{1.67}$$

$$C_v(T, \rho) = C_v^0(T) + \frac{T}{b}\frac{d^2a}{dT^2}\ln(1 + b\rho) \tag{1.68}$$

$$rT\ln\phi = \frac{P}{\rho} - rT - \frac{a}{b}\ln(1 + b\rho) - rT\ln\left(\frac{P(1 - b\rho)}{\rho rT}\right) \tag{1.69}$$

as well as the thermal expansion coefficient α and the isothermal compressibility coefficient β.

$$\alpha = \frac{\left(1 - b^2\rho^2\right)\left(r(1 + b\rho) - \dfrac{\partial a}{\partial T}\rho(1 - b\rho)\right)}{rT(1 + b\rho)^2 - a(T)\rho(2 + b\rho)(1 - b\rho)^2} \tag{1.70}$$

$$\beta = \frac{\left(1 - b^2\rho^2\right)^2}{\rho rT(1 + b\rho)^2 - a(T)\rho(2 + b\rho)(1 - b\rho)^2} \tag{1.71}$$

Figs. 1.5 to 1.16 compare isobaric profiles of thermodynamic variables obtained for different values of pressure using the Ideal Gas (IG) law and the three main cubic EoSs, namely the van der Waals (vdW) EoS, the Peng-Robinson (PR) EoS and the Soave-Redlich-Kwong (SRK) EoSs. The variables are evaluated for oxygen O_2 ($T_c = 154.58$ K, $P_c = 50.43$ bar, Figs. 1.5-1.8), methane CH_4 ($T_c = 190.564$ K, $P_c = 45.992$ bar, Figs. 1.9-1.12) and hydrogen H_2 ($T_c = 33.145$ K, $P_c = 12.964$ bar, Figs. 1.5-1.8), They are compared to reference values extracted from the NIST database for fluid properties (see Linstrom and Mallard (2001)). The perfect gas reference values ($e_s^0(T)$, $s^0(T)$, $C_v^0(T)$, etc.) have been computed using the NASA 9-coefficient non-linear polynomial correlations from McBride et al. (2002).

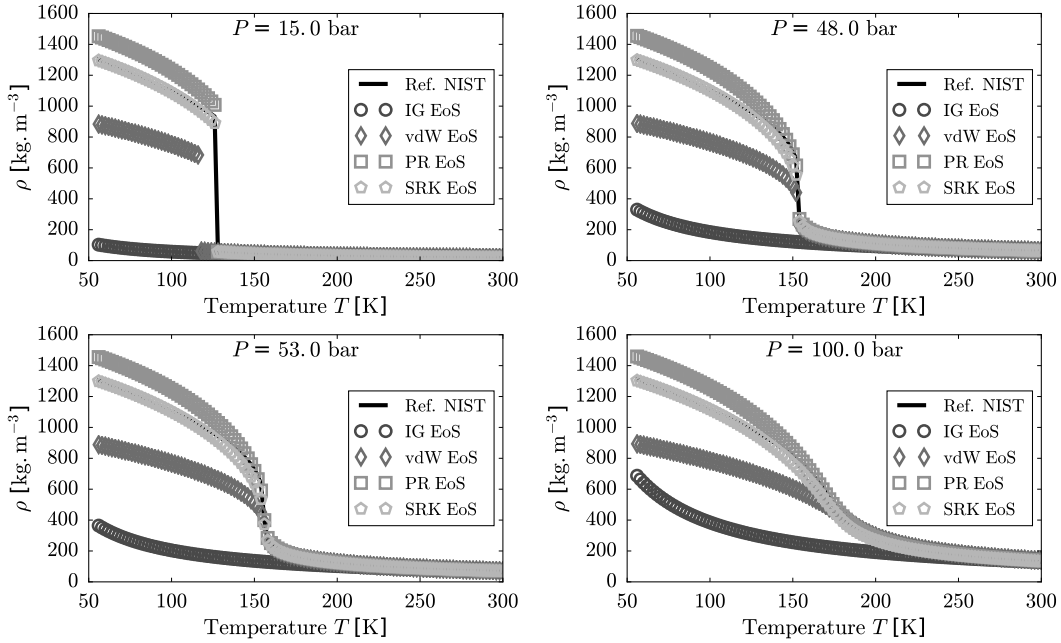

Figure 1.5: *Isobaric curves of O_2 density ρ with respect to the temperature for the IG, vdW, PR and SRK EoSs. Reference values from NIST online database (Linstrom and Mallard (2001)) plotted for comparison*

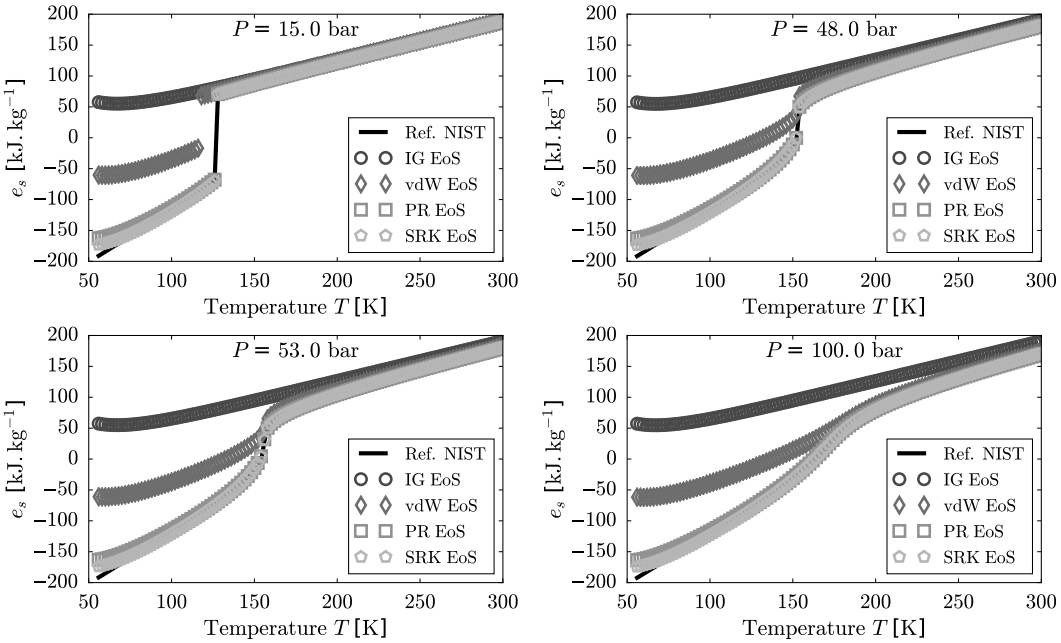

Figure 1.6: *Isobaric curves of O_2 specific internal energy e_s with respect to the temperature for the IG, vdW, PR and SRK EoSs. Reference values from NIST online database (Linstrom and Mallard (2001)) plotted for comparison*

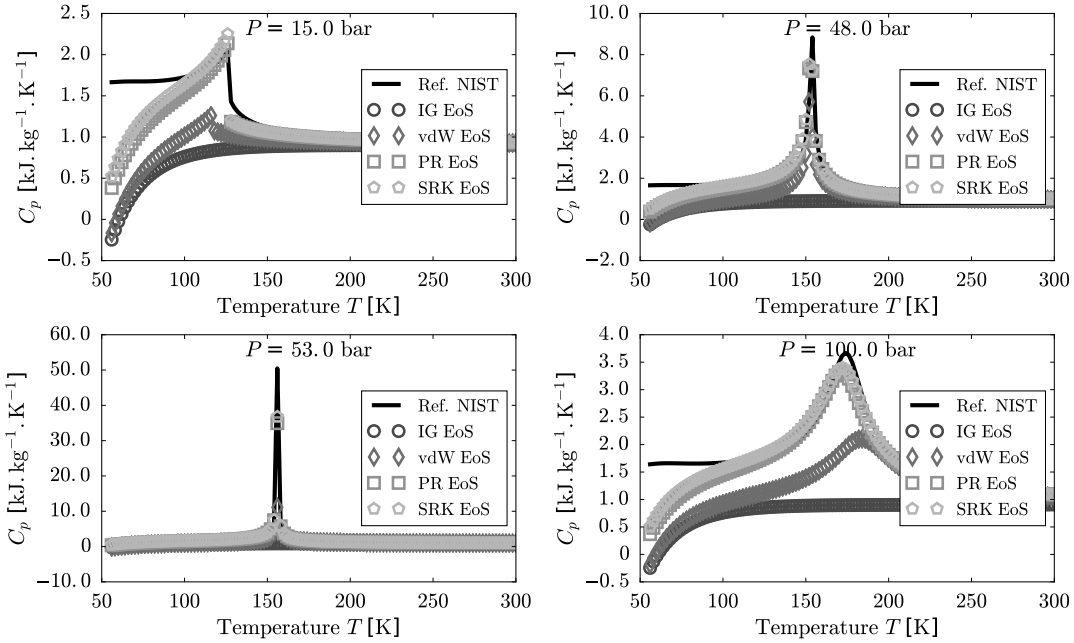

Figure 1.7: *Isobaric curves of O_2 specific isobaric heat capacity C_p with respect to the temperature for the IG, vdW, PR and SRK EoSs. Reference values from NIST online database (Linstrom and Mallard (2001)) plotted for comparison*

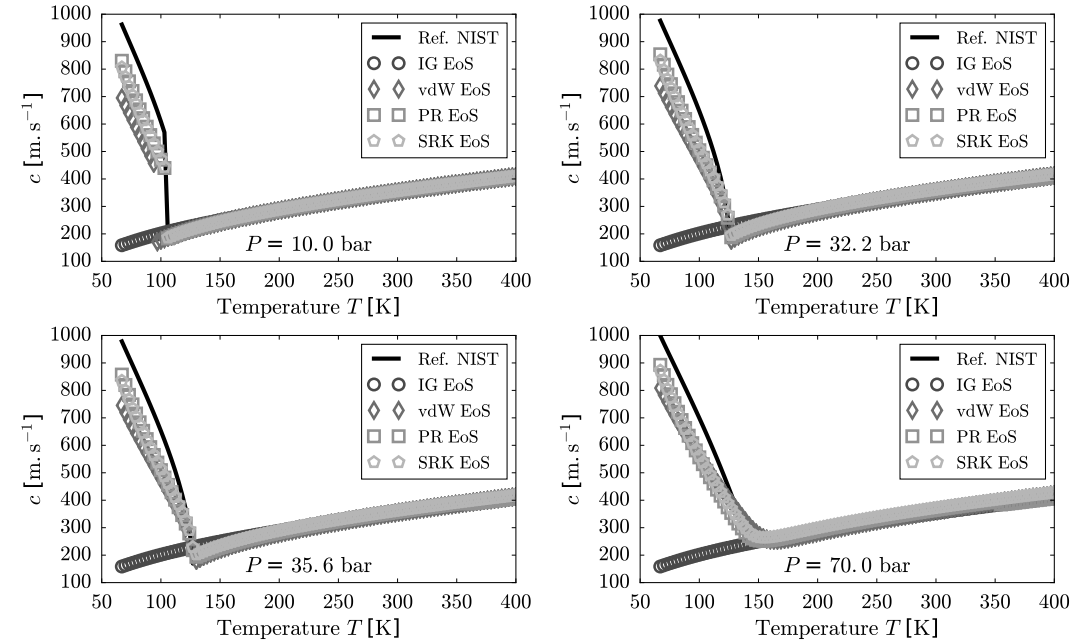

Figure 1.8: *Isobaric curves of O_2 sound speed c with respect to the temperature for the IG, vdW, PR and SRK EoSs. Reference values from NIST online database (Linstrom and Mallard (2001)) plotted for comparison*

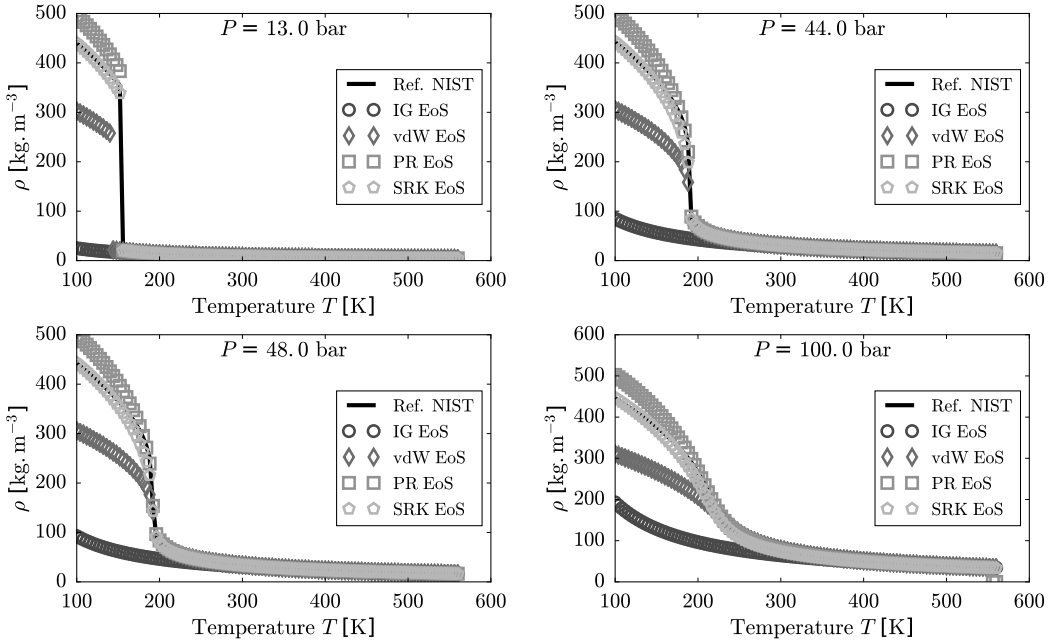

Figure 1.9: *Isobaric curves of CH_4 density ρ with respect to the temperature for the IG, vdW, PR and SRK EoSs. Reference values from NIST online database (Linstrom and Mallard (2001)) plotted for comparison*

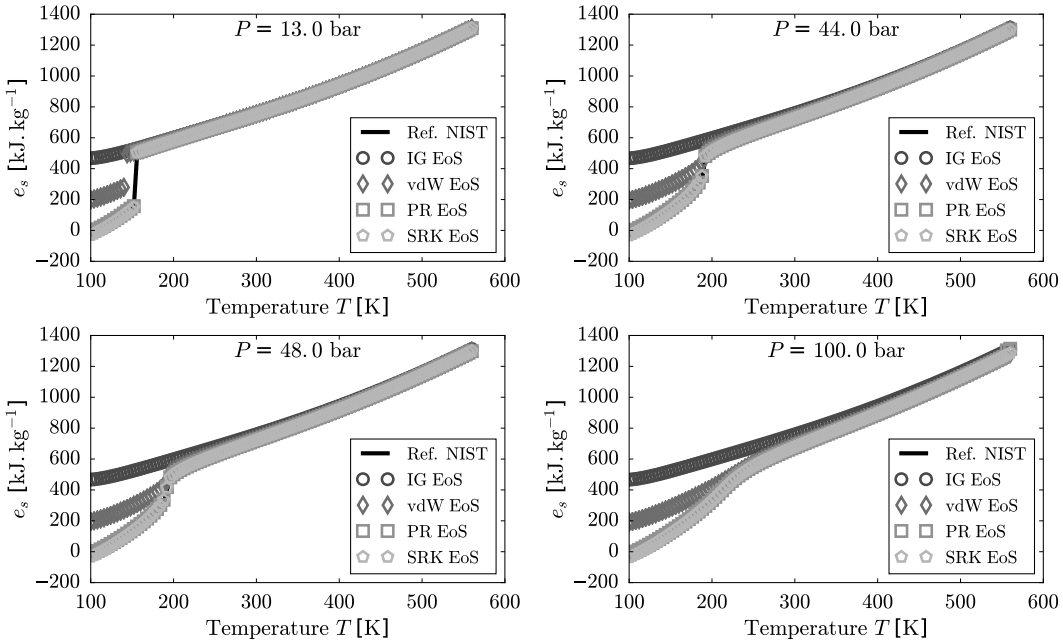

Figure 1.10: *Isobaric curves of CH_4 specific internal energy e_s with respect to the temperature for the IG, vdW, PR and SRK EoSs. Reference values from NIST online database (Linstrom and Mallard (2001)) plotted for comparison*

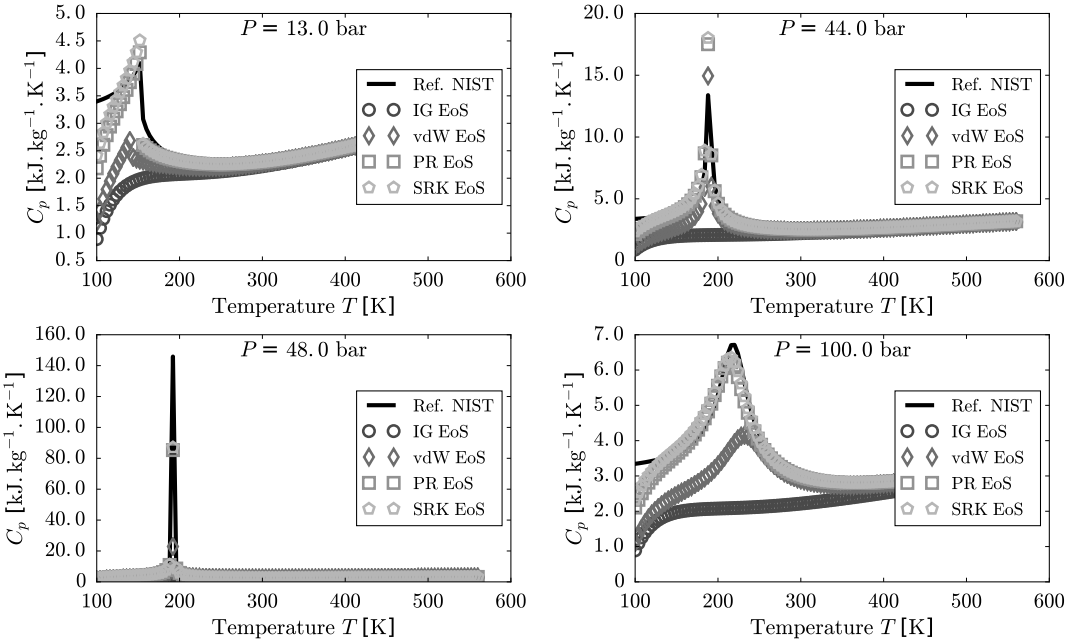

Figure 1.11: *Isobaric curves of CH_4 specific isobaric heat capacity C_p with respect to the temperature for the IG, vdW, PR and SRK EoSs. Reference values from NIST online database (Linstrom and Mallard (2001)) plotted for comparison*

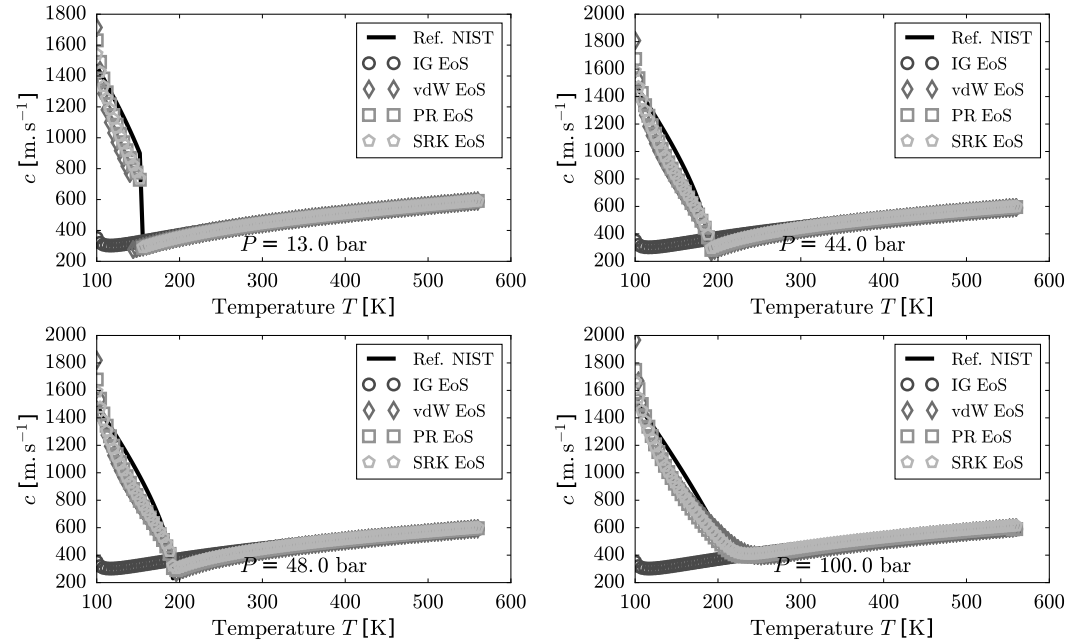

Figure 1.12: *Isobaric curves of CH_4 sound speed c with respect to the temperature for the IG, vdW, PR and SRK EoSs. Reference values from NIST online database (Linstrom and Mallard (2001)) plotted for comparison*

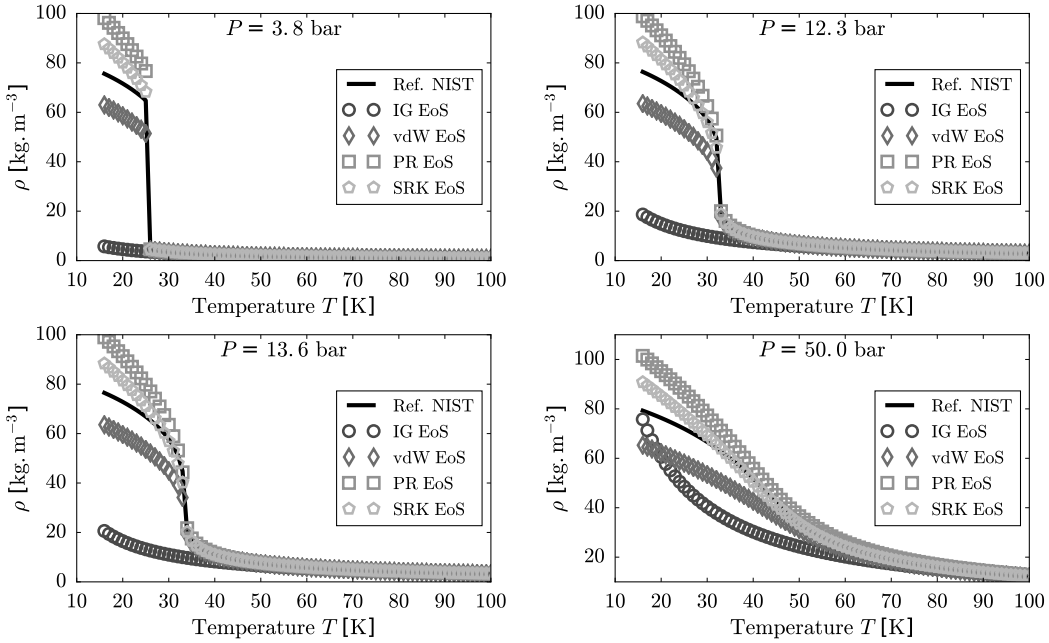

Figure 1.13: *Isobaric curves of H_2 density ρ with respect to the temperature for the IG, vdW, PR and SRK EoSs. Reference values from NIST online database (Linstrom and Mallard (2001)) plotted for comparison*

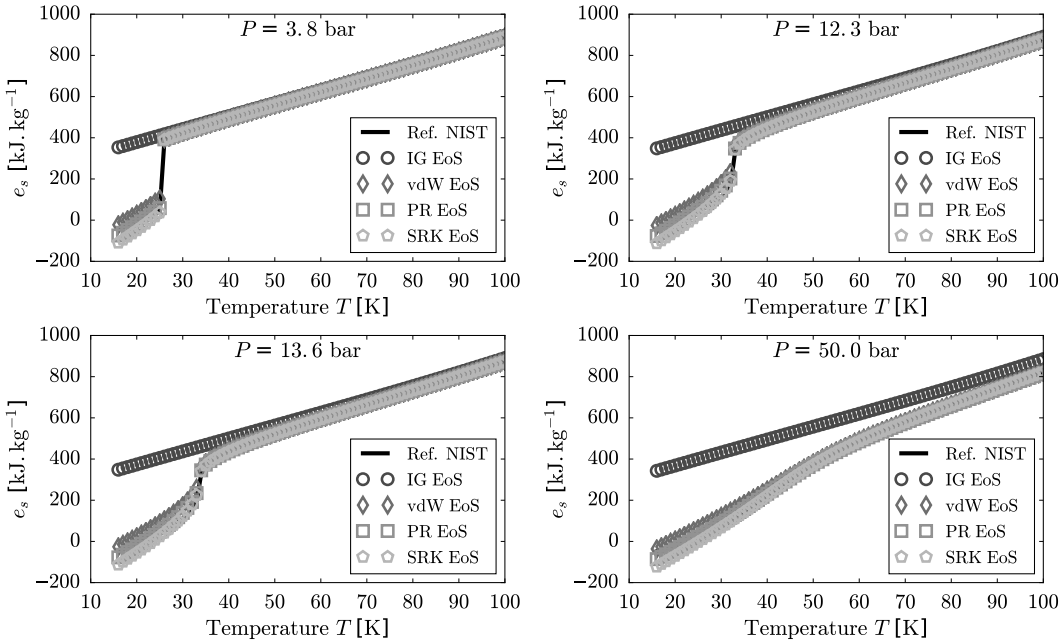

Figure 1.14: *Isobaric curves of H_2 specific internal energy e_s with respect to the temperature for the IG, vdW, PR and SRK EoSs. Reference values from NIST online database (Linstrom and Mallard (2001)) plotted for comparison*

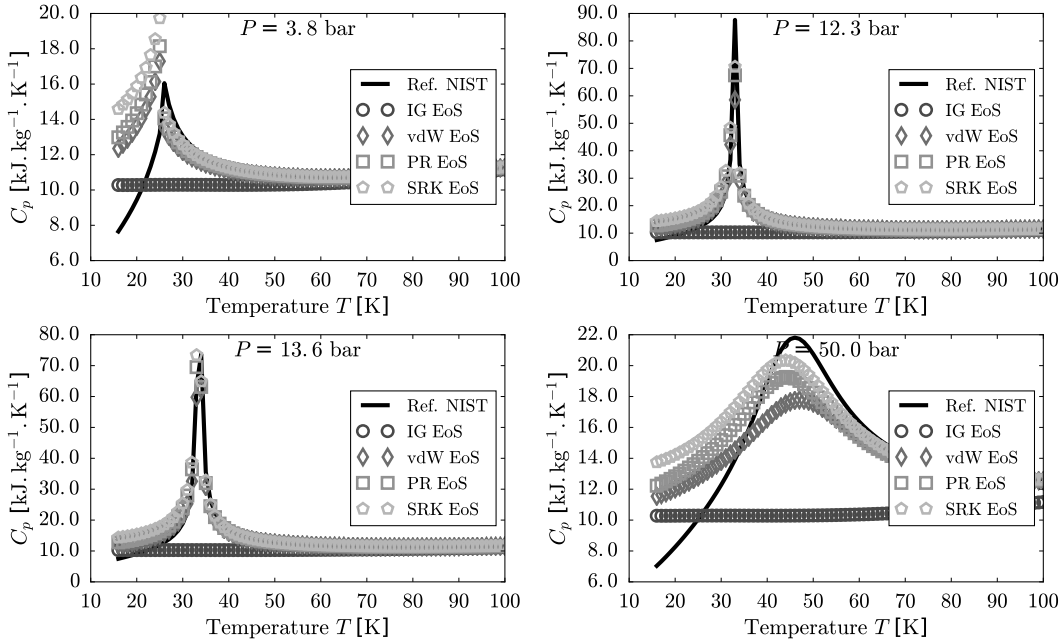

Figure 1.15: *Isobaric curves of H_2 specific isobaric heat capacity C_p with respect to the temperature for the IG, vdW, PR and SRK EoSs. Reference values from NIST online database (Linstrom and Mallard (2001)) plotted for comparison*

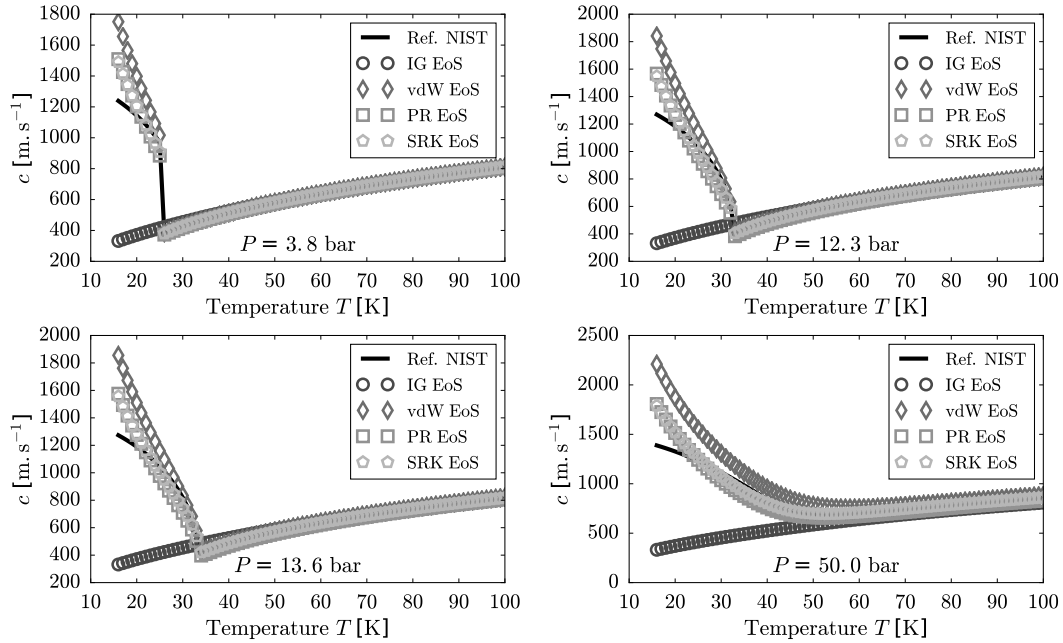

Figure 1.16: *Isobaric curves of H_2 sound speed c with respect to the temperature for the IG, vdW, PR and SRK EoSs. Reference values from NIST online database (Linstrom and Mallard (2001)) plotted for comparison*

All curves display the same behavior traits:

- The cubic EoSs allow to get the correct trends for the high density/high pressure regions
- In particular, the transition between the discontinuous thermodynamics at subcritical pressures and the continuous one at supercritical pressures is observed
- All the different curves converge for high temperatures as the ideal gas law hypotheses start to be justified
- The van der Waals EoS, despite showing an appropriate behavior, lacks in precision when compared to the two other cubic EoSs
- The Peng-Robinson EoS is more precise near the critical point whereas the Soave-Redlich-Kwong allows for an accurate mean description over a wider range of temperature values
- For very low temperatures, all numerically calculated curves suffer the discrepancies coming from the ideal gas reference correlations from NASA

The results given by the PR and SRK EoSs are particularly satisfactory for oxygen and lead to a fairly good agreement for methane. Noticeably, the quality of the fit is strongly reduced for hydrogen, which is notoriously hard to model, as visible in Figs. 1.5-1.8. This contrast is caused by the peculiar behavior of hydrogen due, in part, to its extremely low molecular weight when compared to much heavier fluids and also its propensity to be the subject of strong molecular and quantum effects.

1.4 Thermodynamic stability

One aspect of real gas flows particularly relevant for the study presented in this document is the notion of thermodynamic stability. Practically, as shown in Fig. 1.2, a fluid can exist in different states. Sometimes two of these states can coexist (solid-liquid or liquid-vapor) and at the triple point, solid, liquid and vapor phases exist at the same time.
Studying the thermodynamic stability of a fluid consists in two tasks. The first is determining the different states the fluid can access depending on the conditions enforced upon him. Such states are known as equilibrium states. The second is, given a specific equilibrium state, evaluating the ability of the fluid to persist in that state when perturbations are applied to said fluid.

Numerous experiments have been carried out in order to tackle these two tasks. They have permitted the creation of extensive databases (such as the NIST online database, see Linstrom and Mallard (2001)) compiling, for a handful list of fluids, their most stable state for a wide range of temperatures and pressures.
Such experiments naturally led researchers to investigate the equilibrium between different phases, in particular the liquid-vapor coexistence at the heart of the present work. Likewise, extensive quantitative data is available regarding the saturation values of a wide variety of fluids.

By construction, an EoS provides a list of potential equilibrium states for a fluid in a given set of conditions (temperature, and/or pressure and/or density). The selection of the most stable, and therefore physical, state is done using the minimal fugacity criterion. In this section, a slightly more detailed discussion is proposed regarding the derivation of stability conditions for real-gas/cubic EoSs. In particular, due to their analytic formulation, cubic EoSs allow

to theoretically investigate thermodynamic regimes not accessible in experiments due to their instability.

1.4.1 Stability criteria for isolated systems

The thermodynamic stability of a fluid is ruled by the first and the second principles of thermodynamic which state that the entropy of a closed system must increase with time while its energy is conserved. These principles translate into a stability criterion for the entropy : the latter must be concave relatively to the pertinent variables used to describe the system. For a closed system, these variables are classically the density ρ and the specific internal energy e_s.

1.4.1.1 Local stability

Locally, the concavity constraint on the entropy can be reformulated as follows: the Hessian matrix $\mathbb{H}_{\rho,e_s}(s)$ of the specific entropy s relatively to ρ and e_s must be negative semi-definite. The symmetric Hessian matrix of s relatively to ρ and e_s is defined by:

$$\mathbb{H}_{\rho,e_s}(s) = \begin{pmatrix} \dfrac{\partial^2 s}{\partial \rho^2} & \dfrac{\partial^2 s}{\partial e_s \partial \rho} \\ \dfrac{\partial^2 s}{\partial \rho \partial e_s} & \dfrac{\partial^2 s}{\partial {e_s}^2} \end{pmatrix} \tag{1.72}$$

In Giovangigli and Matuszewski (2012), the authors prove that for a single fluid this condition can be expressed in the equivalent and more convenient form given by Eqs. (1.73a)-(1.73b).

$$\left(\frac{\partial e_s}{\partial T}\right)_\rho > 0 \tag{1.73a}$$

$$\left(\frac{\partial P}{\partial \rho}\right)_T > 0 \tag{1.73b}$$

Eq. (1.73a) represents a thermal stability condition: increasing the temperature of the fluid while maintaining its volume should lead to an increase in its energy. Eq. (1.73b) is a mechanical stability condition: to reduce the volume (or increase the density) of the fluid while maintaining its temperature, the pressure must be increased.
For a system with multiple species, chemical conditions must be added to account for the interactions between the different constituents. In the case of a single species, these additional conditions reduce and become equivalent to the mechanical stability condition.

1.4.1.2 Global stability

It must be emphasized that satisfying Eqs. (1.73a)-(1.73b) only grants a local stability for the fluid. By definition, the global stability require to analyze at once all the states accessible to the system to extract the globally stable regions, i.e. regions where the entropy is globally concave. Practically, the global stability is lost when the hypersurface $\Gamma_s = \{s(\rho, e_s) \,|(\rho, e_s) \in \text{admissible states}\}$ diverges from its concave envelope.

For general cases with multiple species, the global stability criterion is virtually impossible to derive. The actual description of the hypersurface Γ_s cannot be done without additional hypotheses. For such cases, even the local stability criterion can prove tedious to specify analytically.

For a single species, as the system can be described with only two variables, the analytical derivation strongly simplifies but for a generic EoS, only the local stability criterion is easily accessible.
Broadly speaking, global stability always implies local stability. However the opposite is not true. Thermodynamic states that are locally stable but outside the global stability region are referred to as metastable and can sometimes be accessed in practice. A common occurrence is that of supercooled water which (in subcritical conditions) can be cooled down several degrees below its fusion point without solidifying. The precariousness of this local stability causes the water to freeze instantly when submitted to an outside perturbation such as a light shock.

1.4.1.3 Case of cubic EoS

By definition of the specific isochoric heat capacity C_v, the condition from Eq. (1.73a) is actually strictly equivalent to $C_v > 0$. Applying the generic definition of Eq. (1.27) to C_v by injecting its departure value calculated for a cubic EoS in Eq. (1.61), it comes the expression:

$$C_v{}^{\mathrm{EoS}}(\rho, T) = C_v{}^{0}(\rho, T) + T\frac{d^2a}{dT^2}(T)\,\mathcal{I}(e_1, e_2, \rho) \tag{1.74}$$

The reference values of $C_v{}^0$, taken constant or extracted from a database, must be always positive if well defined for an ideal gas. The positivity of $C_v{}^{\mathrm{EoS}}$ is therefore tied to the positivity of its rightmost term.

Given the expression from Eq. (1.19) used in Eq. (1.18) to define coefficient a, its second derivative can be expressed:

$$\frac{d^2a}{dT^2}(T) = \frac{1}{T}\frac{\Phi_c c\,(1+c)}{\sqrt{TT_c}} \tag{1.75}$$

This term is trivially positive knowing $c > 0$.

Regarding $\mathcal{I}(e_1, e_2, \rho)$ of which expression is given by Eq. (B.78), it can also be shown to be positive. Indeed, from their respective definitions in Eq. (1.57) it comes that $0 \geqslant \mathrm{v}_+ \geqslant \mathrm{v}_-$. Therefore, $0 \geqslant \mathrm{v}_+ \geqslant \mathrm{v}_-$ and for a positive specific volume v one has $v - \mathrm{v}_- \geqslant v - \mathrm{v}_+$, in particular $\ln\left[(v - \mathrm{v}_-)/(v - \mathrm{v}_+)\right] \geqslant 0$. Combining these two inequalities into Eq. (B.78) shows the positivity of $\mathcal{I}$.

Ultimately, the positivity of the isochoric heat capacity is always satisfied for a cubic EoS and the local stability criterion reduces to Eq. (1.24) i.e. for a single species, the local thermodynamic stability is equivalent to the local mechanical stability.

1.4.2 Liquid-vapor equilibrium

As already mentioned, metastable states can be experimentally produced but are difficult to maintain. Unstable states, by definition, cannot be observed. In practice, an unstable

state spontaneously gives birth to an equilibrium between two new states. A metastable state leads to the same outcome after a perturbation. These two new stable states, called phases, lay in the thermodynamically stable regions and the mix of these two phases leads to same amount of mass and energy in the system albeit with a higher total entropy. It should be noticed however that unstable states can be stabilized by adding new contributions to the thermodynamic description of the fluid, for instance density gradient, as it is done in the Second Gradient theory presented in Chap. 5.

1.4.2.1 Equilibrium conditions between two phases

It is interesting to investigate the conditions these two phases must satisfy in order to coexist. To that affect, the global entropy of both phase 1 and phase 2 can be expressed by $\mathcal{S}_1 = \mathcal{S}_1(\mathcal{E}_1, \mathcal{M}_1)$ and $\mathcal{S}_2 = \mathcal{S}_2(\mathcal{E}_2, \mathcal{M}_2)$ where $\mathcal{E}_i$ and $\mathcal{M}_i$ are the global energy and the mass of phase i. The total entropy of the system $\mathcal{S} = \mathcal{S}_1 + \mathcal{S}_2$ can be differentiated using Gibbs identity Eq. (B.1) to get:

$$d\mathcal{S} = d\mathcal{S}_1 + d\mathcal{S}_1 = \frac{1}{T_1}\, d\mathcal{E}_1 + \frac{P_1}{T_1}\, d\mathcal{V}_1 - \frac{\mu_1}{T_1}\, d\mathcal{M}_1 + \frac{1}{T_2}\, d\mathcal{E}_2 + \frac{P_2}{T_2}\, d\mathcal{V}_2 - \frac{\mu_2}{T_2}\, d\mathcal{M}_2 \tag{1.76}$$

where P_i, T_i, μ_i and $\mathcal{V}_i$ are the pressure, temperature, free enthalpy and volume of phase i. For a (locally) closed system, the energy, mass and volume are conserved providing the relations:

$$\begin{cases} d\mathcal{E} = d\mathcal{E}_1 + d\mathcal{E}_2 = 0 & \rightarrow \quad d\mathcal{E}_2 = -\,d\mathcal{E}_1 & \text{(1.77a)} \\ d\mathcal{M} = d\mathcal{M}_1 + d\mathcal{M}_2 = 0 & \rightarrow \quad d\mathcal{M}_2 = -\,d\mathcal{M}_1 & \text{(1.77b)} \\ d\mathcal{V} = d\mathcal{V}_1 + d\mathcal{V}_2 = 0 & \rightarrow \quad d\mathcal{V}_2 = -\,d\mathcal{V}_1 & \text{(1.77c)} \end{cases}$$

which, once injected into Eq. (1.76) lead to the new expression of $d\mathcal{S}$:

$$d\mathcal{S} = \left(\frac{1}{T_1} - \frac{1}{T_2}\right) d\mathcal{E}_1 + \left(\frac{P_1}{T_1} - \frac{P_2}{T_2}\right) d\mathcal{V}_1 - \left(\frac{\mu_1}{T_1} - \frac{\mu_2}{T_2}\right) d\mathcal{M}_1 \tag{1.78}$$

For a stable state, the differential of the entropy $d\mathcal{S}$ must be null, which is achieved if each of its components is also null, i.e.:

$$\frac{1}{T_1} = \frac{1}{T_2} \qquad \frac{P_1}{T_1} = \frac{P_2}{T_2} \qquad \frac{\mu_1}{T_1} = \frac{\mu_2}{T_2} \tag{1.79}$$

The condition can be simplified to retrieve the classic equilibrium conditions between two stable phases:

$$\begin{cases} T_1 = T_2 & \text{(1.80a)} \\ P_1 = P_2 & \text{(1.80b)} \\ \mu_1 = \mu_2 & \text{(1.80c)} \end{cases}$$

For a given set $(\mathcal{E}, \mathcal{V}, \mathcal{M})$ or equivalently (ρ, e_s), the total entropy of the mix is maximized if each phase lays at the boundary of its own stability region.

1.4.2.2 Saturation curves

The equalities in Eqs. (1.80a)-(1.80c) allow to define the notions of saturation temperature T^{sat} and pressure P^{sat} that are the temperature and pressure shared by the two phases in a liquid-vapor equilibrium. The process of describing this equilibrium consists in, for a couple (T, P), to determine whether two states, defined by two densities ρ_1 / ρ_2, exist and lead to the same chemical potential $\mu_1 = \mu_2$.
As explained in Eq. (1.2.2), cubic EoSs are built such as beyond critical conditions ($T > T_c$ and/or $P > P_c$) one single density is admissible. In strictly subcritical conditions, one, two or three densities can be found admissible while solving Eq. (1.23). Only when three such densities are found, two of them, the maximal and minimal, are susceptible to share the same chemical potential. In that case, the system, depending on its energy, may be constituted by a mix of liquid and vapor phases at equilibrium.

Practically, one is rather interested in determining, for a given subcritical temperature T (or subcritical pressure P) the possible values of pressure $P(T)$ (or temperature $T(P)$) that lead to the existence of ρ_1 and ρ_2 such as $\mu(\rho_1, T) = \mu(\rho_2, T)$.
It can be shown that for cubic EoSs, such a pressure $P(T)$ (or temperature (T)) always exists and the task reduces to only finding its value. This can be achieved by classic means using a root-finding algorithm. It provides access to the complete set of saturation variables T^{sat}, P^{sat}, ρ_l and ρ_v. The process is coarsely represented in Fig. 1.17.

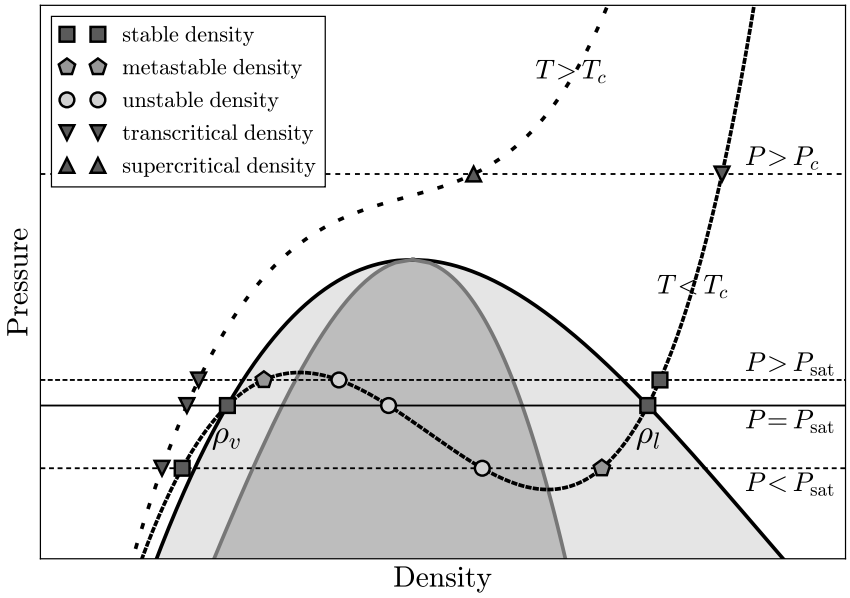

Figure 1.17: *Schematic representation of the evaluation of the saturation pressure and densities for a given temperature with the SRK EoS*

For a reference subcritical isothermal curve, when the trial pressure is either too high or too low, one single density possesses the smallest chemical potential, be it a high liquid density or a small vapor density depending on the pressure. For the exact saturation pressure P^{sat}, the

vapor and liquid density are matched in chemical potential.
For the supercritical isothermal curve, only one density solution exists, even for subcritical pressure, meaning that only a single phase is defined. Likewise, no matter the temperature, if a supercritical trial pressure in used, a single density solution exists with the same implications. By calculating the saturation values for several temperatures, the saturation curve from Fig. 1.3 can be constructed.

In the special case of a single fluid, further numerical investigations can show that the saturation curve actually demarcates the global stability region.
This region is indeed more restrictive than the local stability region of which limits lay below the saturation curve. The region between the saturation and local stability curve, i.e. the zone for metastable states and represented in light gray in Fig. 1.17, is called the binodal region. The strictly unstable region, represented in dark gray in Fig. 1.17, is called the spinodal region.

Fig. 1.18 compile comparative plots of the correlation curves $P^{\text{sat}}\left(T^{\text{sat}}\right)$ for different fluids where the results from several cubic EoS are compared to reference values from NIST database (Linstrom and Mallard (2001)).
Such as it was the case for classic variables, results from PR and SRK EoSs show a very good agreement with experimental measurements. The vdW EoS, while still capturing the right trend, induces results that diverge noticeably from the reference.

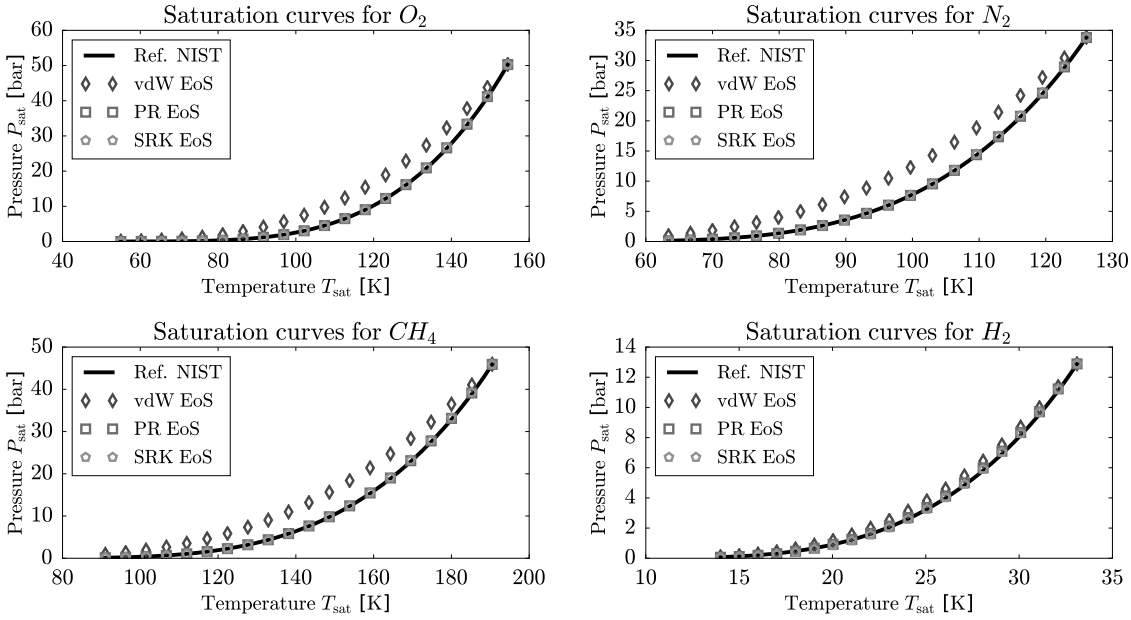

Figure 1.18: *Evolution of the saturation pressure P^{sat} with the saturation temperature T^{sat} for different fluids. Comparison of vdW, PR and SRK equations of state. Reference values from NIST database plotted for comparison*

Part I

Review of interface simulation methods

Chapter 2

Sharp interface methods: Interface tracking

The following chapter focuses on sharp interface methods commonly labeled as interface tracking methods that share the feature of having a specific numerical structure dedicated to the localization of the interface. This structure usually consists in a set of markers with specific attributes (vortices, massless particles, fluid particles, Lagrangian mesh nodes, etc...) of which positions directly relate to the interface position, the latter being obtained merely through geometrical reconstruction by "linking" adequately the markers together.

A variety of methods fall under the previous description.
The Boundary Integral (BI) and Marker-in-Cell (MAC) methods bear a major historical importance as they, together with the Volume-of-Fluid methods, can arguably be considered as the first methods designed to deal with multi-fluid and/or multiphase flows. Almost all modern sharp interface methods directly stem or substantially borrow from these three. As such, it seemed relevant to us to provide some insight into the BI and MAC methods.
Although not initially designed to address multiphase simulations, Front-Tracking methods have steadily evolved to become a standard for such configurations. As they are now the most often used sharp interface tracking methods, this study would feel incomplete without addressing them as well.
Other methodologies worth mentioning are the Vortex-in-Cell methods which are modified and particularized versions of the BI methods detailed in Meng and Thomson (1978); Couet et al. (1981); Anderson (1985); Cottet and Poncet (2004) and the Particle-in-Cell methods explored in Harlow (1964); Amsden (1966); Brackbill and Ruppel (1986); Kelly et al. (2015), variant versions of the early MAC method which, as it so happens, has underwent a wide variety of modifications and developments.

This presentation aim at providing two types of information: the historic of their creation with the underlying motivations and difficulties, the physical and numerical framework within which the methods operate and when relevant, with the main steps to implement them. Throughout and whenever possible the major and/or recent results permitted by these methods along with discussion regarding their current limitations are also provided.

2.1 Boundary Integral methods and Marker-and-Cell methods

The Boundary Integral methods and Marker-and-Cell methods present an important historical value as they have laid the grounds for the more modern interface modeling methods which have borrowed, to a various degree, different ideas from these early methods.
As their use in contemporary work is very limited, due their restricted range of application, a lesser emphasis is put on their description in the main core of this document. Only a historical overview and a rapid description of their mechanics is provided, which can help to get a better insight into the functioning of the more modern methods.

2.1.1 Boundary Integral methods

2.1.1.1 Potential flows

The Boundary Integral (BI) methods have been introduced in the work of Rosenhead (1931), later expanded upon in Birkhoff (1955); Birkhoff and Fisher (1959); Birkhoff (1962). These methods are deeply related to potential flows, defined as two-dimensional incompressible flows with no diffusion nor viscosity that are additionally supposed to be irrotational. The theory of potential flows has been formalized in Kellogg (1929) and many of its applications to canonical cases can be found in Lamb (1975).

The complete behavior of a potential flow can be described using two specific functions: the stream function ψ and the potential function φ, linked to the flow velocity and defined by means of differential equations.
These two functions satisfy a simple Poisson equation, i.e. $\mathbf{\Delta}\psi = 0$ and $\mathbf{\Delta}\varphi = 0$, which is quiet conventional in fluid dynamics and for which plethora of numerically efficient methods have been designed.

The link between potential flows and interfaces lays in the fact the isolines of the stream function ψ define virtual frontiers that cannot be crossed by the particles in the flow. This property, in absence of diffusion (mechanical by viscosity, thermal by conduction and chemical by species diffusion), is an adequate representation for an interface.
All the stakes behind BI methods are therefore to find the proper stream and potential functions ψ and φ that represent correctly the initial state of the flow and the initial position of the interface. Afterwards, during the computation, the time evolution of the corresponding isolines of ϕ allows to track the position of the interfaces.

2.1.1.2 Interface representation

The task of finding the proper functions ψ and φ to represent a flow with arbitrary shaped interfaces is actually intricate. Practically, it is done by combining several canonical flows corresponding to more simple configurations.
Kellogg's theory allows to define multiple elementary potential flows such as uniform flows, mass sources and sinks, vortices, etc... that can be combined, thanks to the linearity of the equations, in order to generate more complex configurations.

One such configuration is formed by a collection of elementary vortices, which is particularly

suitable to model flow with a discontinuity in the tangential velocity. A vortex sheet is defined as a surface separating two regions where the fluid is essentially irrotational and across which a discontinuity of the fluid velocity occurs: the tangential velocity is discontinuous whereas the normal component remains continuous. This tangential velocity discontinuity implies that the flow has an infinite vorticity on a vortex sheet.
This last observation provides a strong foundation for the theory to evolve towards interfaces simulation. Indeed, an interface is, among other things, characterized by a tangential velocity discontinuity. This description is suited when studying the interface between two incompressible and non-miscible liquids, between incompressible gas and liquid (like air and water) or between two phases of the same incompressible element with the absence of evaporation/liquefaction.

This modeling has been used early on, in particular in Rosenhead (1931) to study Helmholtz instabilities and vortex-sheet roll-up which is the formation of a spiral in the shape of an evolving vortex sheet. Helmholtz instabilities appear in configurations where two flows with the same properties, initially separated by a planar boundary, are put into movement with opposite parallel velocities. A numerical simulation of such a configuration and the ensuing vortex-sheet roll-up, from Rosenhead (1931), is shown in Fig. 2.1.
It is worth mentioning that the study of this phenomenon remains a substantial analytical and numerical challenge almost a century later.

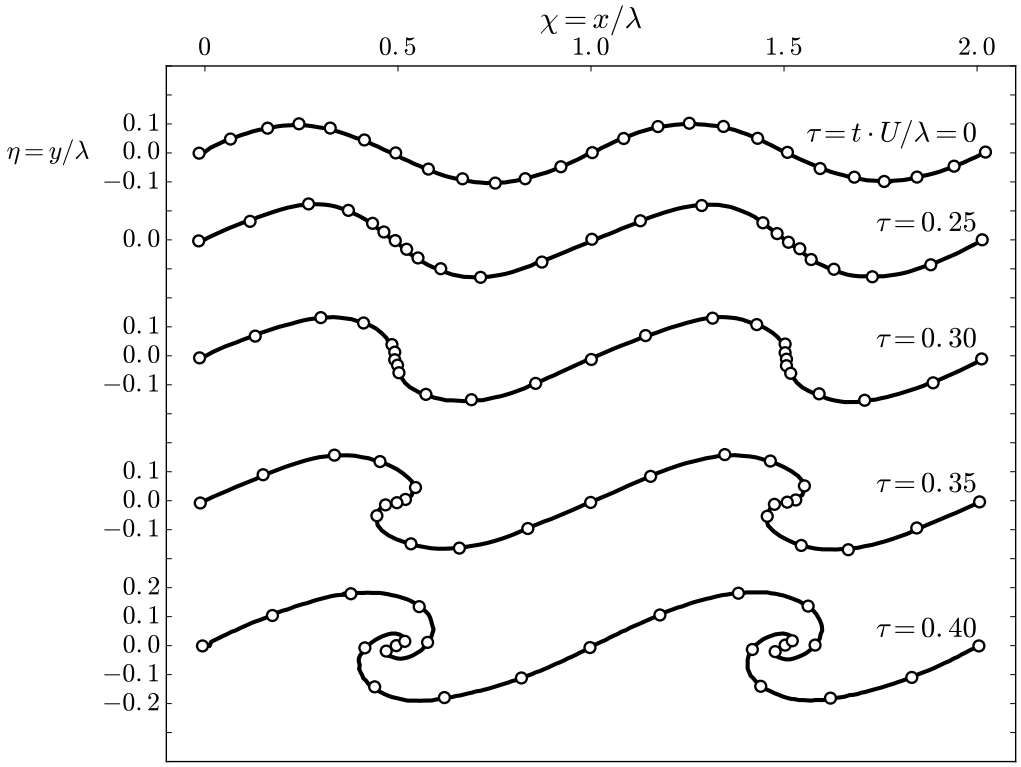

Figure 2.1: *Description of the time evolution of a vortex-sheet roll-up using a periodic distribution of vortices, taken from Rosenhead (1931)*

Later, through multiple studies proposed by Birkhoff in Birkhoff (1955); Birkhoff and Fisher (1959); Birkhoff (1962) and supplemented by the additional work in Hama and Burke (1960); Fink and Soh (1976); Zalosh (1976), it was shown that the discrete approach used by Rosenhead was not suitable. One of its major flaw is the fact that it introduces an artificial surface tension that stabilizes the vortex sheet. Using more points with an irregular distribution of the vortices and adding both viscosity and surface tension provides more physical results.
However, these investigations eventually served to cement the use of a continuous approach to deal with vortex sheets. Although this approach was already used, for instance to study fluid-rigid body interactions, Birkhoff initiated the systematic use of the Boundary Integral method to deal with fluid-fluid interfaces.

2.1.2 Marker-and-Cell methods

2.1.2.1 Historical perspective

The original Maker-and-Cell method was introduced at Los Alamos Laboratories in the early 1960's by Harlow et al. (1965) and Welch et al. (1965), its main purpose was to study free surface for viscous incompressible flows in 2D planar or 2D axisymmetric configurations. A distinctive feature of this method is the use of a staggered grid and a finite-difference spatial scheme, so much so that nowadays the MAC acronym is often employed as a mean to refer to the use of this type of mesh, often but not necessarily in conjunction with a finite-difference spatial scheme, even for calculations not involving any free surface or interface. The use of this staggered had been initially motivated by the work of Lebedev (1964).

Over more than half a century, the initial MAC method underwent several modifications leading to various methods being named after it. Although they are too numerous to all be discussed in details, the arguably more relevant are briefly presented in Sec. 2.1.2.4.

Its creation aside, four principal milestones can be identified for the familly of MAC methods. In 1970, in Amsden and Harlow (1970) was proposed a new strategy to simplify the Poisson equation associated with the determination of the pressure, the method being known as the Simplified Marker-and-Cell (SMAC). In the rest of the 1970's, a specific attention was given to the treatment of the free surface/interface, mostly the proper evaluation of the pressure imposed on it to ensure consistent stress contributions on either sides. This problematic had been shown to lead to poor results for free-surface/interface undergoing strong deformations and the effort in Chan et al. (1971) and Easton (1972) , Nichols and Hirt (1971), among others, allowed qualitative and quantitative improvements. It is worth noticing that based on Gawain and Pritchett (1970) an ambitious attempt at addressing turbulent flows with the MAC was made in Pritchett (1970) and lead to encouraging results though efforts in that direction seems to have faded since then, other methods being privileged. The third big step occurred in the late 1980's/early 1990's where attempts were made to expand the methods to more complex geometries where so far they were limited to boundaries following the cartesian mesh or, at the very best, parallel to the mesh directions.
Although the mesh remained cartesian in essence, the method in Viecelli (1969), based on the original MAC method (refereed to as the ABMAC for Arbitrary external Boundaries MAC), and the one in Tomé and McKee (1994), based on the SMAC method (referred to as GENSMAC for General domain SMAC), allow simulations for any geometry of the boundaries.

Noticeably, the GENSMAC has even been extended to non-Newtonian fluids in Tomé et al. (1996).
For the same purpose, but using an opposite strategy, in Kashiwa (1986) was described an adaptation of the MAC philosophy to a Finite Volume paradigm in order to use arbitrarily shaped cells and thus arbitrarily shaped boundaries. It appears as though methods derived from the original MAC method rather than the SMAC have been discarded in the latest works. Indeed, since the 2000's, most numerical results have been obtained by increasingly improving the GENSMAC method of Tomé and McKee (1994) to extend it to axisymmetric flows Tomé et al. (2000), to try implicit time-stepping Oishi et al. (2004), to add surface tension Mangiavacchi et al. (2005) and to extend it to three dimensions De Sousa et al. (2004), McKee et al. (2008).

In the following, the Maker-and-Cell methods will be presented in a two dimensional planar configuration on a structured Eulerian grid if not mentioned otherwise.

2.1.2.2 The MAC paradigm

2.1.2.2.1 The staggered grid

To discretize the Navier-Stokes equations, the MAC method relies on a staggered grid, the scalars and vectors are defined at different locations of the computational grid. This allows to minimize errors when calculating the fluxes in the momentum equation. As shown in Fig. 2.2 , the scalars (pressure $P_{i,j}$, kinematic viscosity $\nu_{i,j}$, etc...) are defined at the center of the cells , the x-components of the vectors (horizontal velocity $u_{i+\frac{1}{2},j}$, etc...) are defined in the middle of the horizontal faces of the cells and the y-components of the vectors (vertical velocity $v_{i,j+\frac{1}{2}}$, etc...) are defined in the middle of the vertical faces of the cells. Sometimes, these quantities need to be calculated at locations different from where they are attributed to. To that effect, averaging procedures are to be used.

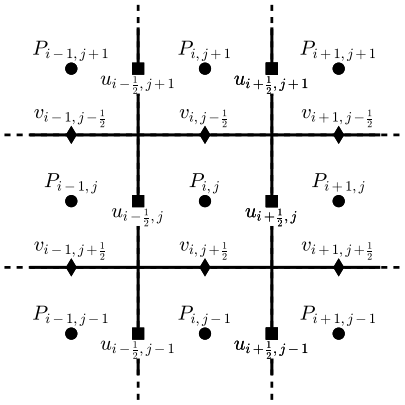

Figure 2.2: *Staggered grid used in MAC methods, here in two dimensions*

2.1.2.2.2 The flagged domain

To track the fluid, massless markers are used Fig. 2.3. Their initial position must be prescribed by the user. During the calculation, they are transported by the fluid motion.

In the original method, these markers served only to differentiate the fluid from the void to track free surfaces. In the latest methods, the definition of these markers has been modified to accommodate multi-fluid or liquid-vapor calculations with eventual interfaces and free surfaces.

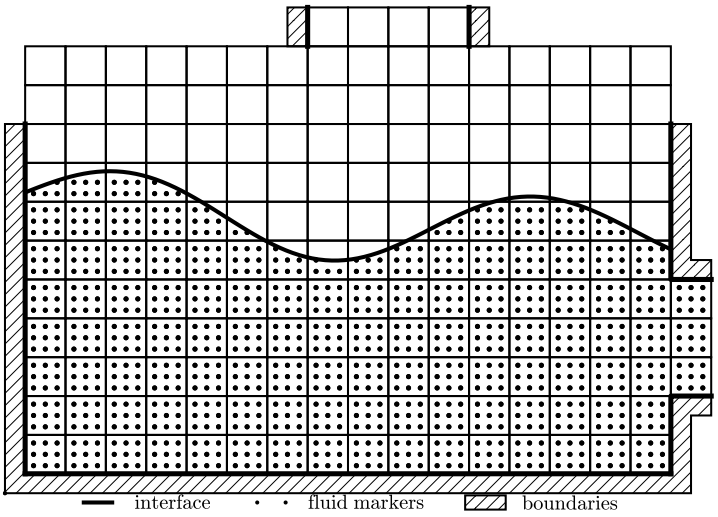

Figure 2.3: *Dissemination of markers in the fluid part of the domain*

The ability to locate said interfaces is primordial since they require a specific treatment in terms of flux determination. This matter is even more important when surface tension, mass fluxes or heat fluxes are authorized at the discontinuities. In general, the enforcement of these conditions requires the specification of a precise pressure at the discontinuities and possibly the determination of a surface normal vector and a surfce curvature. To do so, every cell in the domain is attributed a flag characterizing its composition, as depicted in Fig. 2.4 below.

E	E	E	E	E	E	E	E	I	I	I	I	E	E	E	E	E	E
E	E	E	E	E	E	E	E	E	E	E	E	E	E	E	E	E	E
E	E	E	E	E	E	E	E	E	E	E	E	E	E	E	E	E	E
B	E	E	E	E	E	E	E	E	E	E	E	E	E	E	E	E	B
B	S	S	S	S	S	E	E	E	E	E	E	S	S	S	E	E	B
B	F	F	F	F	S	S	E	E	E	S	S	S	F	S	S	S	B
B	F	F	F	F	F	S	S	S	S	S	F	F	F	F	F	S	B
B	F	F	F	F	F	F	F	F	F	F	F	F	F	F	F	F	O
B	F	F	F	F	F	F	F	F	F	F	F	F	F	F	F	F	O
B	F	F	F	F	F	F	F	F	F	F	F	F	F	F	F	F	O
B	F	F	F	F	F	F	F	F	F	F	F	F	F	F	F	F	B
B	F	F	F	F	F	F	F	F	F	F	F	F	F	F	F	F	B
B	B	B	B	B	B	B	B	B	B	B	B	B	B	B	B	B	B

Figure 2.4: *Flagging of the cells used in MAC methods for single fluid simulations*

Single fluid flagging

For a single fluid calculation, as shown in Fig. 2.4, the different flags used are:

- BOUNDARY (B): a cell with more than half of its volume outside the calculation domain is considered as a boundary cell, this flag is reserved to solid walls
- INFLOW (I), OUTFLOW (O): these flags extend the boundary flag to eventual inflows and outflows using the same discrimination method
- EMPTY (E): a cell is considered EMPTY if it does not contain any marker and is not part of any type of boundary
- SURFACE (S): a cell is considered to contain a surface if it is not a boundary cell, if it contains marker and if it has at least one neighboring cell flagged as empty
- FLUID (F): a cell is considered to be full of fluid if it is not a boundary cell, if it contains markers and all its neighboring cells also contain markers

This flagging procedure must be performed after each time iteration but since the time step is restricted by a CFL type condition, markers cannot move farther than one cell away. This means that the free surfaces and interfaces move at most one cell at each time step. Therefore, the update in the cells flagging it only necessary in the vicinity of the interface and surface cells.

2.1.2.3 The original MAC method

2.1.2.3.1 The equation discretization

As mentioned, the original MAC method in Welch et al. (1965) was designed to numerically solve the Navier-Stokes equations for viscous and incompressible flows in a single fluid framework. For such a flow, the mass and momentum equations are:

$$\frac{\partial u}{\partial x} + \frac{\partial v}{\partial y} = 0 \tag{2.1}$$

$$\frac{\partial u}{\partial t} + \frac{\partial u^2}{\partial x} + \frac{\partial uv}{\partial y} = -\frac{\partial \mathcal{P}}{\partial x} + \nu\left(\frac{\partial^2 u}{\partial x^2} + \frac{\partial^2 u}{\partial y^2}\right) + g_x \tag{2.2}$$

$$\frac{\partial v}{\partial t} + \frac{\partial uv}{\partial x} + \frac{\partial v^2}{\partial y} = -\frac{\partial \mathcal{P}}{\partial y} + \nu\left(\frac{\partial^2 v}{\partial x^2} + \frac{\partial^2 v}{\partial y^2}\right) + g_y \tag{2.3}$$

where u,v are the horizontal and vertical components of the velocity, $\mathcal{P} = P/\rho$ is the reduced pressure, ν the kinematic viscosity and $\boldsymbol{g} = (g_x, g_y)$ accounts for the body forces acceleration.

With the conventions 2.1.2.2.1, the Eqs. (2.1) to (2.3) are discretized using a central finite-difference scheme. The mass equation, in its discretized form, becomes:

$$D_{i,j} = \frac{u_{i+\frac{1}{2},j} - u_{i-\frac{1}{2},j}}{\Delta x} + \frac{v_{i,j+\frac{1}{2}} - v_{i,j-\frac{1}{2}}}{\Delta x} = 0 \tag{2.4}$$

while the momentum equation can be split in two along the x and y directions to get:

$$\frac{\partial u_{i+\frac{1}{2},j}}{\partial t} = F_x\left(u, v, \mathcal{P}, \nu\right) \tag{2.5}$$

$$\frac{\partial v_{i,j+\frac{1}{2}}}{\partial t} = F_y\left(u, v, \mathcal{P}, \nu\right) \tag{2.6}$$

where F_x and F_y are the numerical functions to calculate the momentum fluxes divergence in both directions. The time integration strategy can be adapted to gain more precision, for instance using high order Runge-Kutta methods. Most of the time, an explicit time stepping is used meaning that the right hand sides of Eq. (2.5) and Eq. (2.6) are calculated with the known values at iteration n ($F_x\left(u^n, v^n, \mathcal{P}^n, \nu^n\right)$ and $F_y\left(u^n, v^n, \mathcal{P}^n, \nu^n\right)$) to evaluate the new velocity at iteration $n+1$.

To achieve accurate results, the numerical velocity divergence $D_{i,j}$ must be equal to zero to agree with the continuity equation Eq. (2.1) (or Eq. (2.4) when discretized). However, due to numerical errors and computational imprecisions, this condition may not be satisfied in practice. Since the quality of the calculations relies on this condition, the strategy of the MAC method is to enforce it using the pressure as a pivot value. It can be viewed as a self-correction procedure which avoids the propagation of errors from one iteration to the other and thus their accumulation. This idea has even been expanded beyond the scope of the MAC method in Hirt and Harlow (1967) to deal with initial-value problems. Using the definition of $D_{i,j}$ and discretizing Eqs. (2.5) and (2.6), one can write:

$$\frac{D_{i,j}^{n+1} - D_{i,j}^{n}}{\Delta t} = Q_{i,j}^{n} - \frac{\mathcal{P}_{i+1,j}^{n} - 2\mathcal{P}_{i,j}^{n} + \mathcal{P}_{i-1,j}^{n}}{\Delta x^2} - \frac{\mathcal{P}_{i,j+1}^{n} - 2\mathcal{P}_{i,j}^{n} + \mathcal{P}_{i,j-1}^{n}}{\Delta y^2} + W_{i,j}^{n} \tag{2.7}$$

where $Q_{i,j}^{n}$ and $W_{i,j}^{n}$ are functions of the discrete velocity components and the viscosity known at iteration n. With the constraint that $D_{i,j}^{n+1} = 0$ in Eq. (2.7) one can then write:

$$\frac{\mathcal{P}_{i+1,j}^{n} - 2\mathcal{P}_{i,j}^{n} + \mathcal{P}_{i-1,j}^{n}}{\Delta x^2} - \frac{\mathcal{P}_{i,j+1}^{n} - 2\mathcal{P}_{i,j}^{n} + \mathcal{P}_{i,j-1}^{n}}{\Delta y^2} = \frac{D_{i,j}^{n}}{\Delta t} Q_{i,j}^{n} + W_{i,j}^{n} \tag{2.8}$$

which is a Poisson equation that can be solved by means of classic Poisson solvers. However, this equation is not to be solved in all the domain indifferently : a specific pressure is to be enforce at the surface/interface cells (S flag) and at the boundaries (B, O and I flags) as well.

The solving procedure

The original MAC method solving procedure articulates around the following steps:

1. At the end of iteration n, the velocity components and the viscosity are known in all the domain and the cells have been properly flagged. Wherever it is needed (mostly around the boundaries and at the free surfaces), the velocity values are modified to ensure physical consistency. This allows to calculate the values $D_{i,j}^{n}$, $Q_{i,j}^{n}$, $W_{i,j}^{n}$ and determine the right hand side of Eq. (2.8)
2. With the current flagging, the areas where Eq. (2.8) is to be solved and the areas where the pressure is to be enforced are identified. The procedure then follows trough with the corresponding calculations to get the discrete values of $\mathcal{P}$, taking into account the specific boundary conditions, in particular at the free surfaces.
3. With the discrete values of $\mathcal{P}$ known everywhere, the right-hand side of Eq. (2.5) and Eq. (2.6) can be evaluated and the velocity components for the iteration $n+1$ can be determined.
4. With the updated velocities, the markers can be advanced. To do so, a Euler forward method is used so that $x_k^{n+1} = x_k^n + \Delta t u_k^{n+1}$, $y_k^{n+1} = y_k^n + \Delta t v_k^{n+1}$ where (x_k, y_k) denotes the position of the k-th marker. The marker velocity components u_k^{n+1}, v_k^{n+1} are obtained from the fluid velocity after its update, through linear interpolation.

5. After the markers position is updated, the cell flagging can be updated as well as other output values if needed and the procedure cycles back.

Two types of boundary conditions have to be included into the MAC method: the solid boundary condition where the fluid is un contact with solid wall and the free surface condition where surface cells S and empty cells E interact. They mostly rely on the use of ghost cells with carefully chosen velocity and pressure values to numerically match the prescribed conditions. An extensive description can be found in Welch et al. (1965). Over the years, numerous sophisticated methods have been devised, using markers and adequate interpolation strategies, in order to tackle the issue of boundary conditions.

With the above described method, the authors in Welch et al. (1965) were successfully able to simulate several configurations such as a dam breaking, a wave evolving above a reef or water in a reservoir behind a sluice gate, shown in Fig. 2.5, pioneering results at that time.

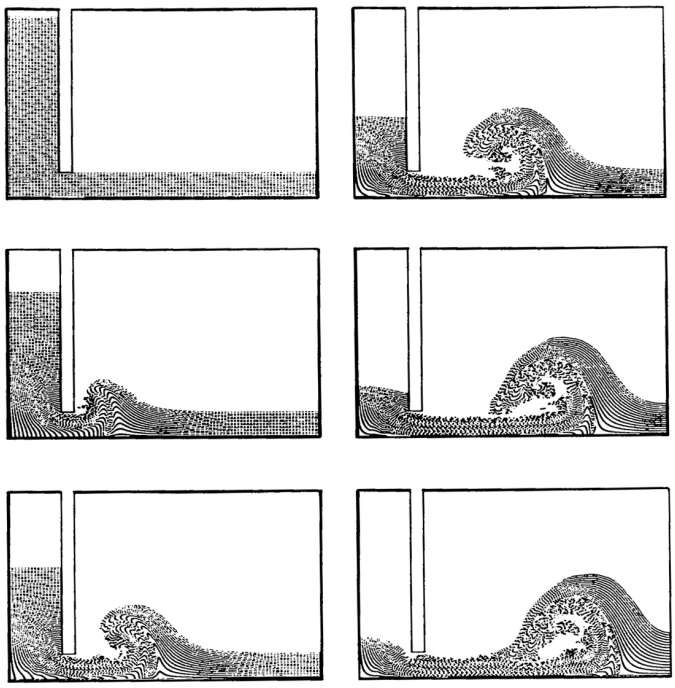

Figure 2.5: *Time evolution of a water reservoir behind a sluice from Welch et al. (1965). The shape of the domain allows the water to break backwards toward the gate*

2.1.2.4 Improvements on the original method

Since the work in Welch et al. (1965), the original method has undergone several improvements but only the major modifications due to these improvements are recalled here.

The SMAC method

The simplified MAC method (SMAC), introduced in Amsden and Harlow (1970), gets rid of the Poisson equation to access the pressure by using a predicted reduced pressure field $\tilde{\mathcal{P}}$ which

natively satisfies the correct boundary conditions, in particular at the interface, to find the velocity. This new velocity is then used to correct the pressure field and obtain $\mathcal{P}$.
With these modifications, the authors in Amsden and Harlow (1970) presented, among others, the simulation of an impacting drop of which images are given in Fig. 2.6.

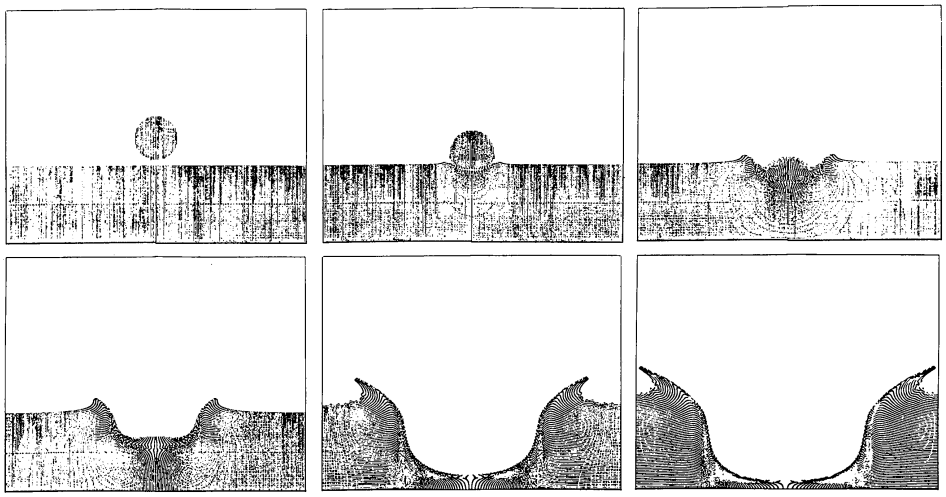

Figure 2.6: *Time evolution of a water droplet splashing into an initially quiescent water plane Amsden and Harlow (1970)*

The GENSMAC method

The General domain SMAC, introduced by Tomé and McKee (1994), represents a major shift if the way MAC methods are designed. Indeed, the classic markers disseminated all other the fluid are traded for less numerous markers only used to delimit the interfaces and free surfaces. To some extent, this method is analogous to the familly of Front-Tracking methods presented in Sec. 2.2.
In particular, the markers at the interface can be used to evaluate its curvature and therefore introduce surface tension in a more consistent and precise manner.

Work on the GENSMAC has spanned over a decade with the sequential improvements provided in Tomé et al. (2000); Oishi et al. (2004); Mangiavacchi et al. (2005); De Sousa et al. (2004); McKee et al. (2008).
Thanks to these efforts, very promising results have been produced such as the non-symmetrical rising of two different bubbles in a third fluid, shown in Fig. 2.7 or the splashing of a droplet onto a denser more viscous fluid, shown in Fig. 2.8.

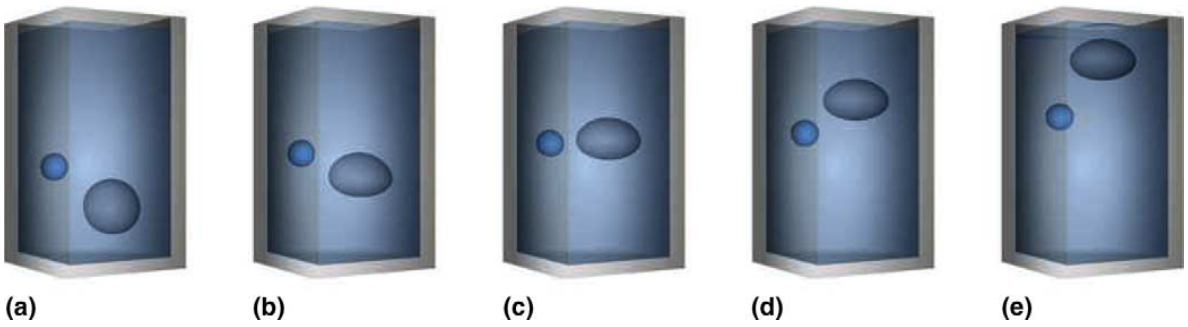

Figure 2.7: *Transient solution for two bubbles of different density rising in a third continuous phase, at different times, from De Sousa et al. (2004)*

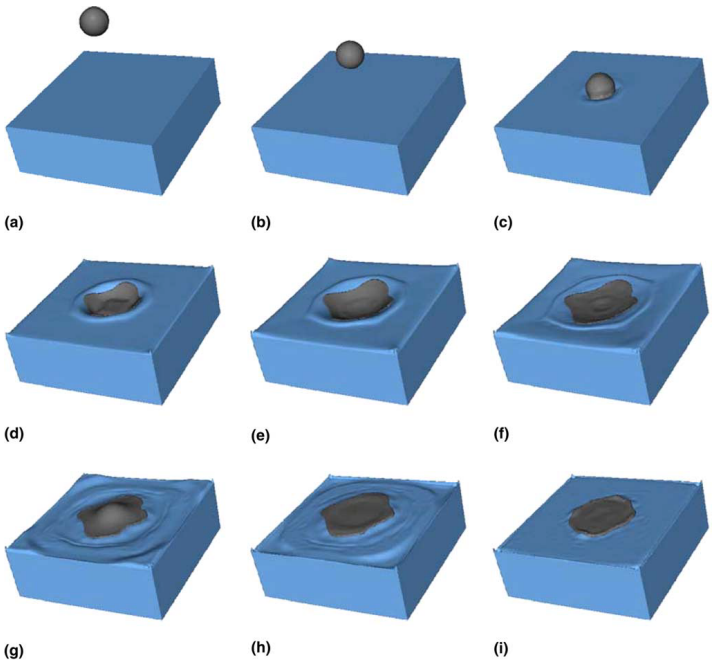

Figure 2.8: *Transient solution of a splashing drop falling into the free surface of a heavier and more viscous fluid, from De Sousa et al. (2004)*

The Micro-Cell methods

With the same idea of using interface/surface makers rather than fluid markers, another category of MAC methods has been introduced by trying to evaluate more precisely the fluxes at the interface.

The Surface-Marker and Micro-Cell method (SMMC) from Chen et al. (1997) and the Eulerian-Lagrangian Marker and Micro-Cell (ELMMC) from Raad and Bidoae (2005) both rely on a local mesh refinement to deal with cases involving more than one interface in one cell. Eponymous micro-cells are created by dividing a local cell following a process similar to automatic mesh refinement techniques. These new micro-cells are then flagged and treated using the classic MAC paradigm. This approach offers a better handling of interface separation and merging and a better evaluation of interfacial fluxes.

Using these modifications, the authors in Raad and Bidoae (2005) have provided results for, among others, the filling of a rectangular cuboid using two initially impacting jets, as shown in Fig. 2.9.

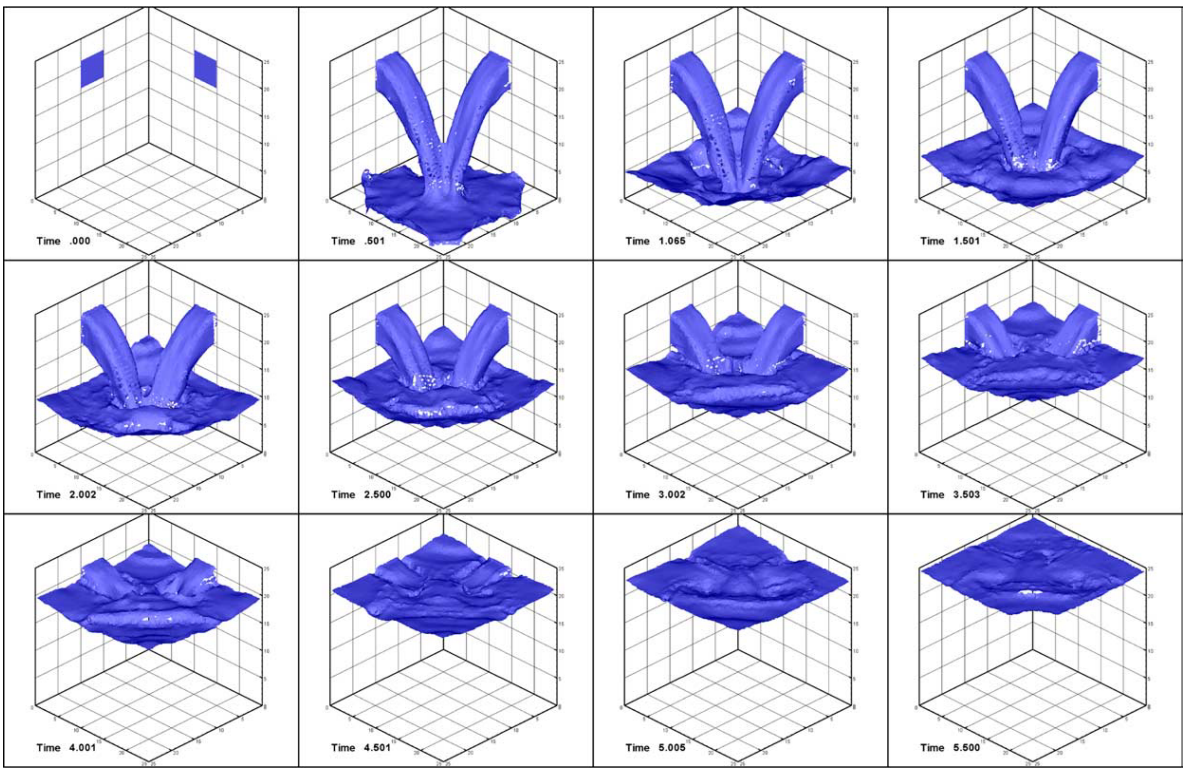

Figure 2.9: *Simulation of the cavity filling problem with two impacting water jets, from Raad and Bidoae (2005)*

2.2 Front-Tracking methods

2.2.1 Historical overview

The Front-Tracking (FT) methods are some of the oldest and most popular approaches to perform computations involving boundaries between different materials. Although in the prospect of this document, only the liquid-vapor configurations are of interest, it should be noted that FT methods are inherently designed to track any kind of discontinuity in a flow.
This includes shocks as well as contact discontinuities such as interfaceS between non-miscible fluids or bi-variate density fluids. More recently, they also have been extended to compressible and/or miscible fluids with the added capability to address phase change. The first occurrences of such methods trace back to the late 1960's.

The idea was originally proposed in Richtmyer and Morton (1967) to study the movement of a shock in an initially undisturbed material. The authors exposed the principle of using a specific grid (a linear grid in two dimensions) composed of points and curves linking them to accurately locate the shock front.

The name Front-Tracking originates from this original study, although no practical implementation of the method was presented there. The first reference to a practical use of a dedicated mesh to track an interface between two fluidS is found in Daly and Pracht (1968) and Daly (1969) where the authors used specific markers additionally to the initial makers from the MAC method.
From that, they performed very early calculations of density-current cases, see Daly and Pracht (1968), and studied the evolution of Rayleigh-Taylor instabilities, see Daly (1969), involving two incompressible viscous fluids. The front markers were introduced in the MAC calculations as a mean to accurately evaluate the interface curvature and normals.

The growth of Front-Tracking as a self-sustained method, through practical implementation, is largely due to the work of the American mathematician James Glimm, spanning over three decades, in particular by way of the code *FronTier*, see Du et al. (2006). This work was initiated in Glimm et al. (1981) to improve upon the Random Choice Method (see Chorin (1976); Glimm et al. (1980); Glimm et al. (1980); Glimm et al. (1981)) used at that time as a predominant tool to track discontinuities (i.e. shocks or interfaces) in hyperbolic equations. In Glimm et al. (1981), the authors established the foundations of the method, namely, the use of a specific mesh of one lesser dimension to track a discontinuity in the flow as shown in Fig. 2.10. This mesh is used to reconstruct the front via appropriate interpolationS, to calculate relevant physics such as surface tension and fluxes and is advected in a Lagrangian fashion once the specific velocity of the front has been determined.

Since then, the method has been extensively studied and improved through successive studies, most notably: in Glimm et al. (1985) an in depth study of the 2D Riemman problem used to evaluated the front speed is performed, in Glimm and Mcbryan (1985) a data structure and a computational model is devised specifically for FT simulations, in Glimm et al. (1988) an algorithm is proposed to solve front intersection by creating topology bifurcations, in Glimm et al. (1998) the method is successfully extended in three dimensions, in Glimm et al. (2003) a method is presented to achieve better local conservation in the front vicinity and in Bo et al. (2011) a hybrid method combining FT and Ghost-Fluid methods is described and applied to the study of primary breakup in liquid jetS.

In spite of being historically the first to be introduced and still being used until recently, the method developed by Glimm and his coworkers is often overshadowed by the one introduced in Unverdi and Tryggvason (1992). Although it essentially deriveS from Glimm's, this method is solely dedicated to the simulation of multiphase flows with interfaceS (and not any other type of front). Moreover, in its first formulation, it gleaned substantially from Peskin's Immersed Boundary Method (IBM) (see Peskin (1977)). Besides, like Glimm's, it has sustained regular and relevant improvements, most notably: in Juric and Tryggvason (1998) the authors allow for a non-isothermal formulation with phase change and mass transfer at the front, in Tryggvason et al. (2001) a more robust manipulation of the interface grid and a more precise manner to account for surface tension are presented and in Terashima and Tryggvason (2009) yet another hybrid method combining FT and Ghost-Fluid Method (GFM) was proposed allowing for simulations involving compressible flows. Noticeably, the method has even been extended to reactive cases such as reactive bubbles in Koynov et al. (2005) and premixed flames in Qian et al. (1998).

Lastly, several other FT methods have been developed in the literature, the most noticeable (excluding the two already mentioned) for multiphase flow studies being the ELAFLINT method of Udaykumar and coworkers, see Udaykumar et al. (1996); Udaykumar et al. (1997); Udaykumar et al. (1999). For the use of FT methods in aeronautics, the reader can refer to the early review in Moretti (1987) or the studies in Witteveen et al. (2007); Paciorri and Bonfiglioli (2009); Witteveen (2010). FT methods have even been adapted to non-Newtonian fluids as presented in Izbassarov and Muradoglu (2015).

The rest of the section will essentially expands upon Tryggvason's approach, which is the preferred one in most contemporary simulations performed with FT methods. Moreover, in their modern formulations, some of the differences between Glimm's and Tryggvason's approaches tend to smear out as they start sharing specific numerical tools to answer similar needs. In this presentation, the numerical schemes employed to solve the Navier-Stokes/Euler equation are not treated in order to focus on the interface treatment. A similar approach is taken in Chap. 3 to address Level-Set and Volume-of-Fluid methods who share, with FT methods, a need for classic numerical tools. These tools are referenced throughout the description of the different methods and only expanded upon when needed to ensure the clarity of the presentation.

2.2.2 The computational setting

In the FT methods, two grids are used. The primary grid is an Eulerian mesh, not necessarily but most often orthogonal, upon which the Euler or Navier-Stokes equations are solved in a undifferentiated manner for the two phases (or fluids). The interface is tracked using a second grid, Lagrangian in nature as it is composed by markers which are to be convected in the flow with the velocity of the interface. This setting is presented in Fig. 2.10.

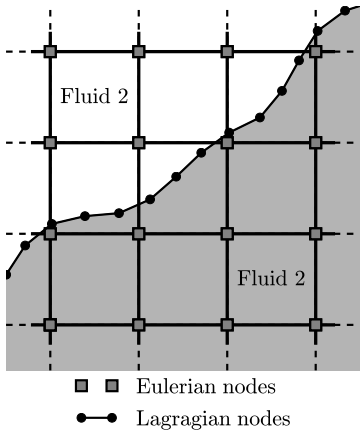

Figure 2.10: *Dual-mesh configuration used for calculations in FT methods*

In the FT methods, the front usually refers to the set of markers representing the interface but also includes additional information regarding the physics at the interface and its geometrical properties.

2.2.2.1 The data representation

The choices made to represent the front, from a computational point of view, has a direct impact on the efficiency of the calculations. This is especially true in 3D cases which represent a significant increase in the level of complexity regarding the handling of the front. The implementation used will impact the calculation of the interface values needed for the computation (normals, surface tension, pressure jumps, interface velocity, etc...) as well as the maintenance of the front when time comes to add or remove markers, as explained in the next paragraphs. Any data structure can be made efficient with relative ease for 2D cases. It is however not the case for 3D cases where the overall efficiency of the method will strongly rely on said structure. In both cases, it possible to represent the interface using structured and unstructured arrays. Structured arrays benefit from their simplicity and straightforwardness of implementation. They are particularly suited for two-dimensional cases. Unstructured arrays come as overreaching for 2D cases, but are sometimes used due to their specific perks. They are however a must go for three-dimensional cases, and despite being noticeably more complex to implement, they make up for it by their relative ease to maintain and modify.

2.2.2.2 The interface maintenance

Low quality interface tracking

To ensure sufficient precision during the computation, the structure of the interface must undergo a maintenance process. Indeed, following the advection of the interface, the different markers can settle in peculiar positions ill-fitted to perform correct calculations. Two main phenomena occur that are to be avoided and are represented in Fig. 2.11.

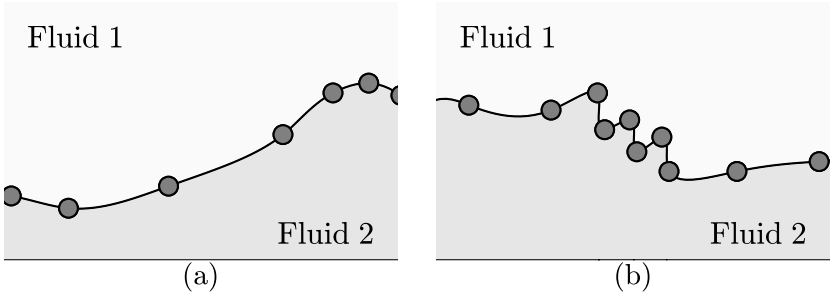

Figure 2.11: *Representation of two case of ill-fitted Lagrangian mesh for the interface: (a) points to far apart, (b) two high point concentration*

The first and most obvious case, showed in Fig. 2.11. (a), occurs when markers drift away from one another. This leads locally to a poor resolution of the interface and the inability to resolve topologically complex deformations. This issue is solved by adding new points in the interface.

The second case, displayed in Fig. 2.11. (b) is more treacherous and corresponds to an overabundance of points in a given region. It should not be intrinsically an issue since more points usually implies more precision. But two drawbacks rise from this situation. Firstly, it leads to an unnecessary overload in the calculation time since the local precision granted by the extra points is not consistent with the order of precision of the interface reconstruction at other locations of the interface. Secondly, for inviscid calculations, or for moderate and high

Reynolds numbers, it can lead to the appearance of undulations smaller than a cell size much like those observed in MAC simulations. This case can be addressed in two different ways. The most straightforward is by removing "unnecessary" points, what reduces the number of points where to perform calculation and the propensity to generate unphysical oscillations. The second is to smooth the interface (which only mitigates the oscillations but does not reduce the number of computational points) in a similar fashion as done with the TSUR in Sousa et al. (2007) for the MAC method. The standard method, know as Front-Tracking Interface Smoothing (FTIS), has been described in Toutant et al. (2012).

Node addition and removal

To control the activation of the addition/removal procedure, a node per length/surface density is usually prescribed with upper and lower thresholds. Whenever, locally, the distance between two nodes goes bellow the upper threshold, a new node is created in-between them. Conversely, if two nodes become closer than the lower threshold, they are fused into one node. These two processes are displayed in Fig. 2.12.

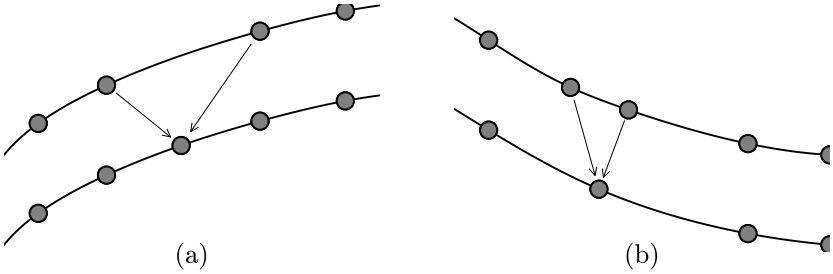

Figure 2.12: *Schematic representation of the interface maintenance procedures: (a) addition of a new node, (b) removal of excess nodes by fusion.*

Both node addition and node removal call for the creation of a new point. The precision of these processes strongly depends on how the position of this new point is chosen. The two principal strategies consist in using the barycenter of the two reference node as the position for the new point or relying on the interpolation used to geometrically reconstruct the interface in the first place.

The front maintenance involves changing the neighborhood of multiple points in the simulation. It proves more efficient to locate all the problematic points in the interface beforehand and then apply the maintenance procedures on all of them at once. Sometimes, it can even be necessary to perform multiple rounds of maintenance on the front, especially when the number of problematic regions is very important.

2.2.3 The tracking of the interface

2.2.3.1 Different philosophies for interface tracking

In FT methods, the interface is advected using the velocity field known on the fixed Eulerian grid. Conversely, near the interface, the numerical fluxes expressed on the Eulerian grid requires physical terms (surface tension, pressure jumps, mass fluxes, etc...) known on the front Lagrangian grid. From that, it ensues that FT methods require an exchange of information between the Lagrangian and Eulerian grids. This transfer has been performed in numerous

ways throughout the development of FT methods and the manner in which the two grids interact is essentially what distinguishes the various FT methods. With no regard for the specifics, all the methods can somehow be assembled under two main philosophies. Independently of the chosen approach, the final purpose is being able to define, on the one hand the interface velocity so it can be advected and on the other hand to update the physical state in all the domain solving the Euler/Navier-Stokes equations. These operations are however performed in different ways depending on the chosen philosophy.

The first methodology is inherited from Glimm's work: the interface is treated as sharply as possible using dedicated formulations so as to keep an actual discontinuity between two well defined domains. It strongly relies on the Ghost-Fluid Method from Fedkiw et al. (1999) and the resolution of Riemann problems which stand as a classic mathematical description of sharp discontinuities.
Conversely, in the second one, partly due to the work of Tryggvason, the front is smoothed as the interface is considered to be a narrow transitional region between the two domains. The approach relies on interpolation rules from the Immersed Boundary Method in Peskin (1977) to approximate the unknown values such as the velocity. The approach also introduces a marker function I, reminiscent of a Heavyside function, in order to delimit the two regions bordering the interface.

Both approaches where initially designed for isothermal incompressible cases (non-miscible liquid-liquid / liquid-solid / liquid-vapor) for which densities (and possible viscosities) values are constant and uniform on either side of the interface. In particular, the continuity equation reduces to $\boldsymbol{\nabla} \cdot \boldsymbol{u} = 0$ where $\boldsymbol{u}$ is the fluid velocity. For all intents and purposes, the solved equations are similar to that of the MAC methods presented in Sec. 2.1.2.3. For such cases, the study "essentially" simplifies since it only "suffices" to advect the interface at each steps. Once the new interface location is known, the densities (and eventual viscosities) can be updated, followed by the velocity and pressure fields, usually involving a projection method and a Poisson equation. However, as FT methods progressed and cases of interest got more complex, the need to simulate compressible, miscible and/or conductive systems arose, motivating the search for new strategies to solve such cases. The solution came from the introduction of the Ghost-Fluid method, first presented in Fedkiw et al. (1999) and later detailed in Fedkiw et al. (1999) and Fedkiw (2002). This method, somewhat inspired by the the early work in Glimm et al. (1981), renders possible to simulate discontinuities in compressible flows. The method was used in Hu and Khoo (2004); Bo et al. (2011) with Glimm's approach and, in its more popular installment, in Terashima and Tryggvason (2009) with Tryggvason's approach.

Both the Immersed Boundary Method (IBM) and the Ghost-Fluid Method (GFM) are further detailed in Peskin (1977); Peskin and McQueen (1989); Peskin (2002) and Glimm et al. (1981) respectively. In the next paragraph, the emphasis is put on the manner in which these two support techniques are incorporated into the FT methods framework. In particular, their precise historical derivation will be omitted here so as to focus on their modern versions.

2.2.3.2 The marker function

The GFM (and to a lesser extent the IBM) requires not only the ability to locate the interface but also to discriminate which type of fluid is located on either sides of the interface. Yet, this information is not readily available in the core formulation of FT methods. Noticeably, the Level-Set or Volume-of-Fluid methods, also used jointly with the GFM, do not suffer this drawback since the signed distance function for the former and the volume fraction for the latter, allows at the same time to locate the interface and identify the different fluids.
Arguably, reconstructing a Level-Set signed function or a Volume-of-Fluid volume fraction (a discussion about the construction of a volume fraction function to locate the interface can be found in section 6.5.2 of Tryggvason et al. (2011)) would allow to benefit their respective perks but would also mean composing with their drawbacks. Besides, this would negate the founding principle of the FT-GFM methodology for which only the location of the phase should be required. The solution comes in the form of a so called marker function I, reminiscent of a Heaviside function, taking the value 0 in one phase and 1 in the other (if multiple fluids/phase are present, multiple marker functions should be used).
Contrary to the Level-Set signed distance function or the Volume-of-Fluid function, the marker function is never used to attribute any value to a fluid property at some location but only to locate the position of the different phases. As such, it does not require to be reinitialized at every time steps or to satisfy any physical constraint as it is merely a numerical tool. Its only constraint is to be properly advected with the flow. To create this marker function, one could devise an algorithm which, for a given point close to the interface, compares its previous state and the movement of the interface between two time steps to determine whether the point remained on the same side or not.
This approach is simple and straightforward but suffers a major drawback as if the interface passes more than one time in a cell, knowing on which side of the interface one point actually is becomes near impossible to do accurately. This goes to show that relying on a point to point approach in not sufficient. A global approach is achieved using a contour function in the form of an integral.

For a closed contour $\mathcal{C}$ and a point (x, y) in the computational domain, the contour integral is:

$$I(x,y) = \oint_{\mathcal{C}} \frac{\boldsymbol{r}_{x,y}(s) \cdot \boldsymbol{n}(s)}{r_{x,y}^2(s)} w(r_{x,y}(s))\, ds \tag{2.9}$$

where s in the curvilinear abscissa on the curve $\mathcal{C}$, $\boldsymbol{r}_{x,y} = \boldsymbol{x}_{\mathcal{C}}(s) - \boldsymbol{x}(x,y)$ is the vector between the point at $\boldsymbol{x}$ and the point on the curve $\mathcal{C}$ at abscissa s, $r_{x,y}$ being its norm and w a weighting function who takes values in $[0, 1]$. Classically, $w(r)$ is taken constant equal to 1 what results in I being the contour number equal to 1 if the point $\boldsymbol{x}$ inside $\mathcal{C}$ and 0 otherwise. Numerically, it is preferable to smooth the transition between the inside and outside of the contour using a smoother weighting function w. Practically, this approach is not suited since the evaluation of the integral is numerically onerous. However, its is possible to take advantage of the numerical properties of I, especially its gradient, to design an alternative way to evaluate it. Indeed, in the ideal case $w(r) = 1$, the gradient of the marker function $I(x, y)$ becomes:

$$\boldsymbol{\nabla} I(x,y) = \oint_{\mathcal{C}} [I]\, \boldsymbol{n}(s)\, \delta(r_{x,y}(s))\, ds \tag{2.10}$$

where δ is a Dirac function centered on the contour and $[I]$ is the jump of the maker function across the contour, normally equal to 1. The discrete version of Eq. (2.10) implies approximating the Dirac function, which requires a smooth enough approximation for numerical stability but a sharp enough approximation to preserve accuracy. The actual formula is given by:

$$(\boldsymbol{\nabla} I)_{i,j} = \frac{1}{\Delta x \Delta y} \sum_{k=1}^{N_{\text{interface}}} [I]_{i,j}\, w_{i,j}^{k} \boldsymbol{n}_k\, d(s)_k \tag{2.11}$$

where Δx and Δy are the constant mesh sizes in the directions x and y, index k identifies the markers on the interface, $\boldsymbol{n}_k$ is the normal vector to the interface at the marker k, $d(s)_k$ the discretized interface partial length and $w_{i,j}^{k}$ is a weighting factor for the node (i,j) respectively to the marker k. Figuratively, the weights $w_{i,j}^{k}$ represent the way the interface is "distributed" on the Eulerian grid. A more in-depth discussion regarding their actual meaning and values can be found in Peskin (2002).
Trough Eq. (2.11), one can notice that $(\boldsymbol{\nabla} I)$ is not actually an unknown value of the system, therefore it can be used to reconstruct the values of the marker function I. One possible way to do so would be to integrate the values of $(\boldsymbol{\nabla} I)$ starting from points where the values of I are known. As shown in Tryggvason et al. (2011) Sec. 6.5.1, this is strictly equivalent to solving the equation Eq. (2.12) which can actually be derived by taking the divergence of Eq. (2.11) to get:

$$\boldsymbol{\Delta} I = \boldsymbol{\nabla} \cdot (\boldsymbol{\nabla} I) \tag{2.12}$$

Granted that $(\boldsymbol{\nabla} I)$ is known, Eq. (2.12) is merely a Poisson equation which, once solved, provides a marker function I approximatively constant in each phases with a transition of finite thickness from one side to the other of the interface.
This later aspect, of a critical importance in the early implementation of Tryggvason's methodology, as I was used to reconstruct the values of the density (and viscosity) in the whole domain, is now dismissed as the values of I are only used to locate the ghost fluid regions in order to apply the GFM steps. Eq. (2.12) can be solved using a classic Poisson solver, it is however not necessary in most cases since only a narrow band, centered on the interface, has to be accurately located to create the ghost fluid regions and calculate the ghost values. Therefore, only iterating for a fews steps starting near the interface is sufficient enough to grant a good convergence in its vicinity. This can be done by flagging all the cells crossed by the interface (potentially, adjacent cells may need also to be flagged depending on the width of the band where I is to be calculated) in a one-directional linked list. Eq. (2.12) is then solved cascading through the list.
All modern implementations of FT-GFM solvers use this principle to locate the interface and the ghost regions, regardless of whether Glimm's or Tryggvason's methodology is used. This means that the two approaches are not actually differentiated by this localization step of the GFM but rather by the advection and the ghost mapping steps, as discussed hereinafter.

2.2.3.3 Mechanical equations

Such as in Volume-of-Fluid and Level-Set method,s the interface tracking serves as a support to then solve the actual mechanical equations. Classically, FT simulations involve two incom-

pressible non-miscible fluids. In either of this fluid, the Navier-Stokes equations is written:

$$\boldsymbol{\nabla} \cdot \mathbf{v} = 0 \tag{2.13}$$

$$\rho \frac{d\mathbf{v}}{dt} = -\boldsymbol{\nabla} P + \boldsymbol{\nabla} \cdot \left(\mu \left(\boldsymbol{\nabla} \mathbf{v} + \boldsymbol{\nabla} \mathbf{v}^{\mathrm{T}} \right) \right) + \rho \boldsymbol{g} \tag{2.14}$$

where classically ρ, μ, P and $\mathbf{v}$ are the fluid density, viscosity, pressure and velocity and $\boldsymbol{g}$ represents the potential body forces. Using the marker function I, it is possible to introduce extended variables, defined in the whole domain, resulting into a description similar to that of a single fluid :

$$\rho(\boldsymbol{x}, t) = I(\boldsymbol{x}, t)\, \rho_1 + (1 - I(\boldsymbol{x}, t))\, \rho_2 \tag{2.15a}$$

$$\mu(\boldsymbol{x}, t) = I(\boldsymbol{x}, t)\, \mu_1 + (1 - I(\boldsymbol{x}, t))\, \mu_2 \tag{2.15b}$$

$$c_p(\boldsymbol{x}, t) = I(\boldsymbol{x}, t)\, c_{p_1} + (1 - I(\boldsymbol{x}, t))\, c_{p_2} \tag{2.15c}$$

$$\dots$$

When I is updated, the newly calculated physical variables allow to solve Eqs. (2.13)-(2.14), usually by means of a projection method for incompressible flows. With the early Tryggvason's methodology, the solving is done at once in all the computational domain. If one rather use the Ghost-Fluid method, the equations have to be solved twofold, once in each fluid.

2.2.4 Words on Glimm's methodology

2.2.4.1 Riemman problem in one dimension

In Glimm's methodology, designed from its inception with compressible applications in mind, the advection and ghost mapping steps are performed at once by means of Riemann problems. The left W_l and right W_r states of the flows, defined by the two fluids/phases, serve as inputs for the Riemann problem while the interface is being treated as a contact discontinuity. This principle is shown in Fig. 2.13.

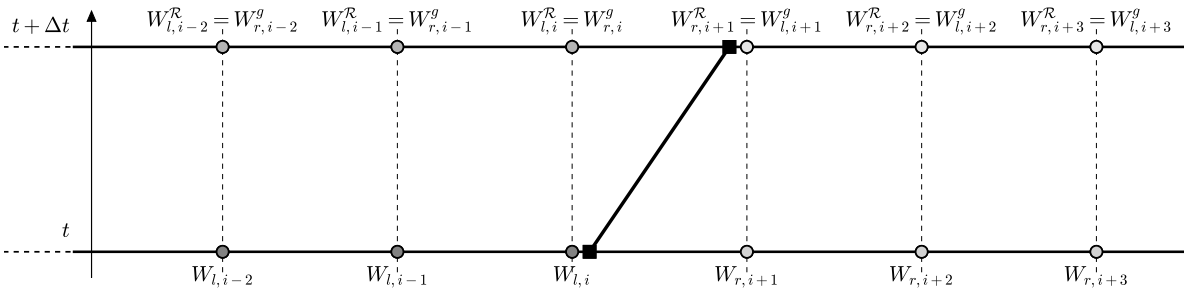

Figure 2.13: *Riemann problem used in Glimm's methodology (see Glimm et al. (2001)) to create the ghost fluid values for the GFM.*

After solving the Riemann problem, two new states $W_l^{\mathcal{R}}$ *(left)* and $W_r^{\mathcal{R}}$ *(right)* are found on either side of the interface. Although the interface may experience a displacement ensuing the solving of the Riemann problem, the time step Δt is chosen to ensure that the interface do not move for more than one computational cell, meaning that at most one point may have

changed side after the Riemann problem is solved.

The results states $W_l^{\mathcal{R}}$ and $W_r^{\mathcal{R}}$ are then used as ghost values to solve the Navier-Stokes equations. When the real fluid/phase on the left is considered, i.e. the state W_l, the ghost values used in the right region are those provided by $W_r^{\mathcal{R}}$. This notion is represented in Fig. 2.13 with the equalities $W_{r,i+1}^{\mathcal{R}} = W_{l,i+1}^{g}$, $W_{r,i+1}^{\mathcal{R}} = W_{l,i+1}^{g}$, etc ... where the superscript g is used to mark the ghost values. Conversely, when the real fluid/phase on the right side is considered with W_r, the ghost values are given by the solution of the Riemann problem on the left side as represented by the equalities $W_{r,i-1}^{\mathcal{R}} = W_{l,i-1}^{g}$, $W_{r,i}^{\mathcal{R}} = W_{l,i}^{g}$, etc ... It is the solving of the Riemann problem that ensures the proper handling of the interface even in presence of compressible fluids. In order to remain consistent with the sharp modeling of the interface, the authors in Bo and Grove (2014) propose to introduce surface tension by incorporating a pressure jump constraint directly in the Riemann problem.

To advect the interface, the Lagrangian equation (2.16) needs to be solved where $\boldsymbol{x}_k$, $\boldsymbol{v}_k$ are the position and velocity of the marker k on the interface.

$$\frac{d\boldsymbol{x}_k}{dt} = \boldsymbol{v}_k \tag{2.16}$$

The velocity $\boldsymbol{v}_k$ of the marker is obtained by solving a new Riemann problem. The left and right values for this new problem are those provided after the application of the GFM and the solving of Navier-Stokes equations. This means that the density and velocity are known everywhere in the fluid. Still considering the interface as a contact discontinuity, its velocity is obtained by solving the Riemann problem. The velocity of the corresponding marker is thus assimilated to that of the contact discontinuity. The GFM has since been improved by the likes of Fedkiw et al. (1999), Liu et al. (2005) or Bo et al. (2011).

2.2.4.2 Extension to multidimensional cases

Practically, the previous method needs to be transposed to 2D (and 3D) cases, what reveals to be a tedious task depending on the level of accuracy the user desires.
A straightforward way to address the matter is to solve the Riemann problem directly in two dimensions. This however is easier said than done since this topic is still raising fundamental questioning and is still a major problematic in applied mathematics. Example of applications can be found in Lax and Liu (1998); Kurganov and Tadmor (2002); Zheng (2012) that are however completely dedicated to the resolution of the Riemann problem without regard for an implementation into a bigger solving framework. Given its inherent complexity and difficulties of implementation, already discussed during the genesis of FT methods, as evidenced by the work in Glimm et al. (1985), this strategy is essentially never used for FT applications.
A second manner to tackle the issue is by analytically expressing the solution of the 1D Riemann problem and make the formal dependency to the geometry disappear. This is done in Hu and Khoo (2004), where the ghost fluid variables are expressed only using the interface state (ρ_I, ν_I, P_I) where ν_I now represent the normal velocity at the interface. In their paper Hu and Khoo (2004), the authors relied on a specific implementation of their algorithm and had a signed distance function to the interface ϕ, similar to that of the Level-Set methods, easily allowing to define a generalized normal with $\boldsymbol{n} = \boldsymbol{\nabla}\phi/|\boldsymbol{\nabla}\phi|$. It is possible, although not

practical, to recalculate a signed function to apply this formula. Another solution, adopted in Terashima and Tryggvason (2009), is to use an algebraic fast-marching method to incrementally populate the nodes of the narrow band with a normal vector created from the nodes where the normal vector is already known.
The problem can be solved in a third fashion, by recreating the 1D Riemann problem for each point on the interface, as done in Glimm et al. (2001) for instance.

Application of Glimm's methodology
The methodology introduced by Glimm and further developed through its collaborations has been successfully applied to incompressible flows, viscid or not, especially Rayleigh-Taylor instabilities, an example of which is given in Fig. 2.14.

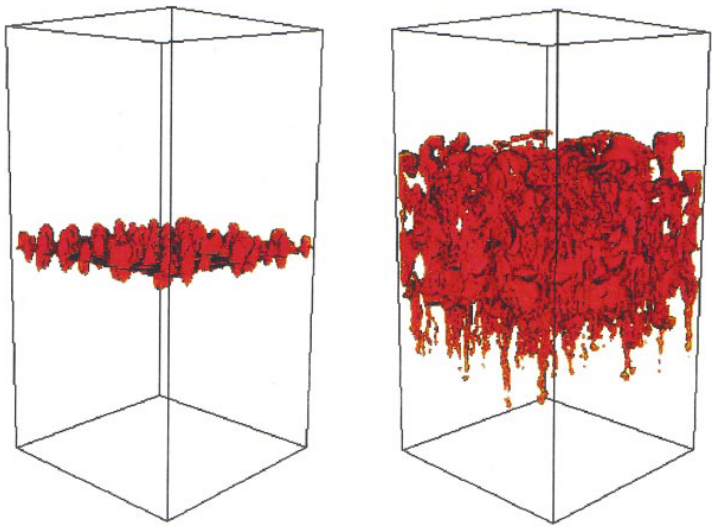

Figure 2.14: *Interface representation between two fluids in early and late time steps in a simulation of Rayleigh-Taylor instabilities, taken from Glimm et al. (2001)*

Impressive numerical results, shown in Fig. 2.15, have been achieved in Bo et al. (2011) where the authors have simulated the primary breakup of a liquid jet into a light gaseous atmosphere. The appearance of initial Kelvin-Helmholtz instabilities due to inflow turbulence and the breakup of large films into filaments further breaking into droplets is faithfully captured.
Based on the information provided by the literature, especially in Hu and Khoo (2004), it seems that this strategy only applies in the absence of heat transfer or mass exchange through the interface. However, since later studies (see Houim and Kuo (2013) for instance) have suggested methods to introduce mass and heat fluxes at the interface by means of jump conditions in the Riemann problem, it can be argued that these methods could be applied to Glimm's methodology, even more so since they are specifically designed to work within the GFM paradigm.
Regarding their conservative properties, FT methods, because of the way they typically advect the interface, are not conservative by construction as noted in Glimm et al. (2001); Glimm et al. (2002); Glimm et al. (2003). The modifications proposed in Glimm et al. (2003), although providing substantial improvements in that prospect, seem not to have been reprized in the following studies.

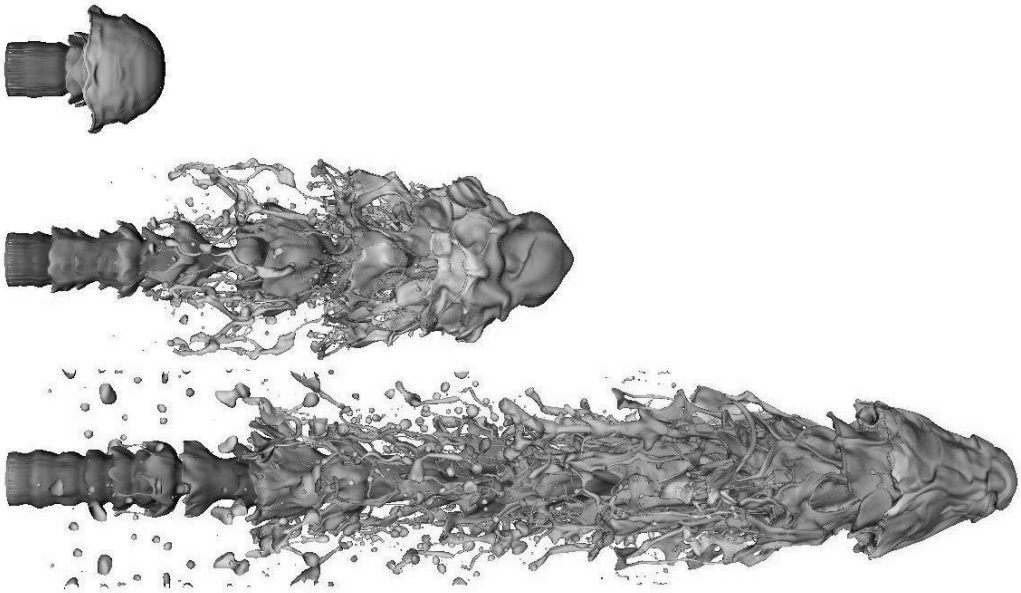

Figure 2.15: *Snapshots of density isosurface of 3D liquid jet injection at different times from Bo et al. (2011). Density ratio used* ≈ 10*, Re* ≈ 2000*, We* ≈ 2000*, Jet velocity* $\approx 200\text{m} \cdot \text{s}^{-1}$

This may, in part, explain why Tryggvason methodology, described in te next subsection, is favored in modern implementations of FT methods, at least for liquid-vapor simulations.

2.2.5 Tryggvason's methodology

2.2.5.1 Interface advection

For the advection and ghost mapping steps, Tryggvason's methodology takes full advantage of the Immersed Boundary Method (IBM), presented in Peskin (1977); Peskin and McQueen (1989); Peskin (2002), that allows the Eulerian flow mesh and the Lagrangian interface grid to communicate. Using an interpolation formula, the velocity can be calculated at the all the interface markers from the known velocity in the fluid, following Eq. (2.17). The same method can be applied to evaluate any other variable that needs to be defined at the interface (markers) while not readily being so.

$$\boldsymbol{v}_k = \sum_{i,j} w_{i,j}^k \boldsymbol{v}_{i,j} \tag{2.17}$$

The markers velocity $\boldsymbol{v}_k$ can be injected into the Lagrangian equation Eq. (2.16) which is solved using the same time integration scheme as the one used to integrate the Eulerian equations, usually high-order Runge-Kutta schemes as explained in Terashima and Tryggvason (2009), completing the advection step of the GFM.

2.2.5.2 Ghost mapping and extension of the normal vector

In Tryggvason's methodology, the advection step is the first of the three GFM steps to be executed. Once the interface position has been updated (to be understood as once the Runge-Kutta sub-iteration has been applied to Eq. (2.16)), the ghost regions can be generated using Eq. (2.12) of the localization step. Eventually, the ghost mapping step, described hereinafter, brings the process to a close.
In its revised version of the GFM, Fedkiw (2002), the author reinvested the method introduced in Adalsteinsson and Sethian (1999) to extend the real fluid values to the ghost fluid regions, namely solving the advection equation:

$$\frac{\partial \psi}{\partial \tau} = \boldsymbol{n} \cdot \boldsymbol{\nabla} \psi \tag{2.18}$$

where ψ in the variable to extend in the ghost fluid regions and $\boldsymbol{n}$ is the interface normal vector. ψ is supposed to be known in the real fluid region (density, velocity, entropy, pressure, etc...) and Eq. (2.18) allows to progressively extend it to the ghost fluid regions.
This method patently requires to define the normal vector $\boldsymbol{n}$ outside the interface, particularly within a narrow band centered on said interface. Since the GFM was initially introduced in a Level-Set setting, the authors used a signed distance function that readily provided means to evaluate the normal $\boldsymbol{n}$ anywhere in the calculation domain.

For reasons already mentioned, resorting to reconstructing a signed distance function in the framework of FT-GFM methods is a discarded option. One needs a different strategy to propagate the interface normal vector from the maker points to the Eulerian grid nodes in the ghost regions. To do so, the Fast-Marching method of Sethian (1996) can be used. Formally, starting from nodes where the normal vector has been evaluated beforehand (with a zero initial value everywhere else), one solves the pseudo-time partial differential equation Eq. (2.19)

$$\frac{\partial n_i}{\partial \tau} = |\boldsymbol{\nabla} n_i| \tag{2.19}$$

where $i = x$ or $i = y$ to denote the x or y component of the normal vector. Practically, as applied in Terashima and Tryggvason (2009), rather than solving Eq. (2.19), the Fast-Marching procedure can be applied algebraically.
Another solution, adopted in Terashima and Tryggvason (2009), is to use an algebraic fast-marching method to incrementally populate the nodes of the narrow band with a normal vector created from the nodes where the normal is already known. First the nodes of cells containing the interface are attributed the same normal values as that of the closest interface nodes. Alternatively, at those nodes, a more sophisticated averaging procedure can be used. This precisely amounts to spreading an interfacial value to the Eulerian node. For consistency, the same weighting rules must be applied, particularly the same weights must be used. Overall, to define a value over the Eulerian mesh, the formula is:

$$\psi_{i,j} = \sum_k w_{i,j}^k \psi^k \frac{ds_k}{\Delta x \Delta y} \tag{2.20}$$

where Δx and Δy are the constant mesh sizes in the directions x and y, k identifies the markers on the interface, ψ^k the known value at the marker k, ds_k the discretized interface partial length and $w_{i,j}^k$ is a weighting factor for the node (i, j) respectively to the marker k.

Then, using all the nodes where the normal vector has already been calculated, labeled as "known points", the cells can be classified according to the number of know points they are formed with. For cells with exactly three known points, the normal value at the fourth point is expressed as the average of the values on the tree known points. For cells with two known points, the same value of normal vector is affected to the two far points and is expressed as the average of the values at the two known points.
This process is performed by iterations, as shown in Fig. 2.16, until the narrow band is fully populated of known points, preferring whenever possible configurations with three know points and limiting two known points configurations to unavoidable cases. The simplicity of this averaging procedure facilitates the implementation of this strategy. Besides, it capitalizes as much as possible on the values known at the interface and limits the number of hypothesis made to extend the definition of the normal vector beyond the interface.

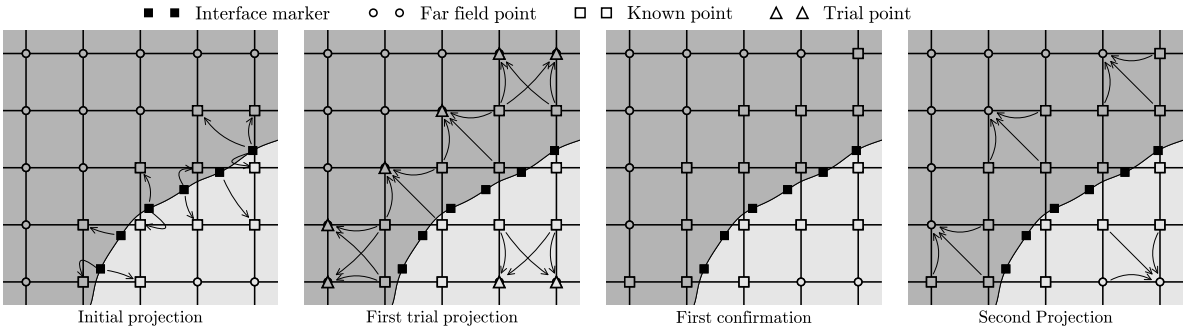

Figure 2.16: *Schematic representation of the algebraic Fast-Marching method to determine interface normal vector in the fluid region from Terashima and Tryggvason (2009)*

Either formally or algebraically, Eq. (2.19) is solved until the narrow interfacial band has been filled. The authors in Terashima and Tryggvason (2009) precise that the algebraic resolution offers more robustness than its formal counterpart using the advection equation, especially when faced with complex deformations. The authors justify this result by the explicit tracking induced by the algebraic approach, although this statement would benefit from further and in depth analysis.

Application of Tryggvason's methodology
Similarly to Glimm's methodology, Tryggvason's has permitted and still is permitting to achieve impressive calculations. For incompressible flows, a substantial number of studies focused on droplet dynamics such as in Nobari, Jan, and Tryggvason (1996); Tryggvason, Bunner, Esmaeeli, Juric, Al-Rawahi, Tauber, Han, Nas, and Jan (2001); Tryggvason, Esmaeeli, Lu, and Biswas (2006); Hua, Stene, and Lin (2008); Muradoglu and Tryggvason (2008); Bayareh and Mortazavi (2011); Razizadeh, Mortazavi, and Shahin (2018). Examples of very early and very recent results are depicted respectively in Fig. 2.17 and in Fig. 2.17.

Most compressible cases where Tryggvason's methodology is used almost systematically involve thermal conduction. Non-conductive cases are mostly focused on bubble/drop - shock interactions such as in Terashima and Tryggvason (2009); Terashima and Tryggvason (2010); Lu, Zhao, and Wang (2016).

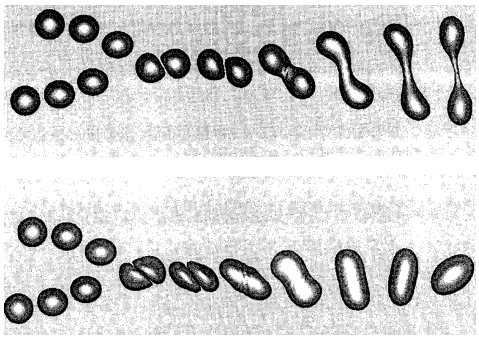

Figure 2.17: *Snapshots of colliding and coalescing 3D droplets in two different impacting conditions from Nobari, Jan, and Tryggvason (1996)*

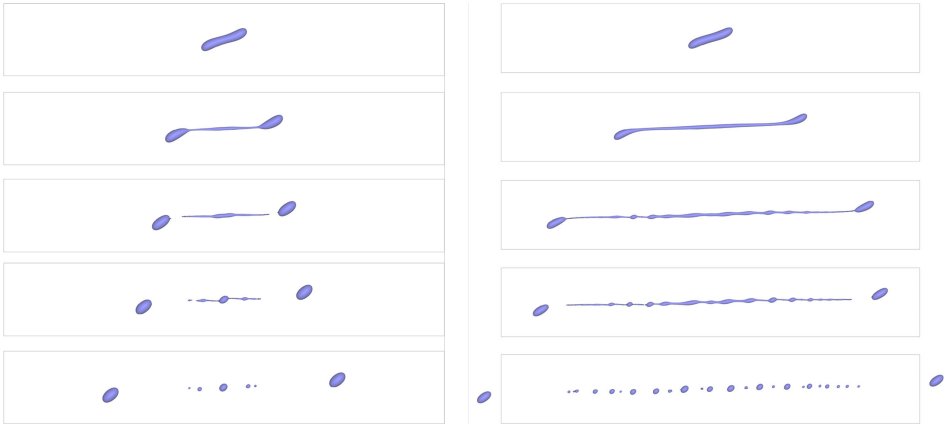

Figure 2.18: *Snapshots of colliding 3D droplets in two extremes impacting conditions from Razizadeh, Mortazavi, and Shahin (2018)*

In Fig. 2.19 (a), a plane shock wave, propagating in water from right to left with a Mach number $M = 1.72$ has collided with an upstream air bubble, inducing a motion of the interface especially through the late water jet penetration coinciding with the collapse of the bubble. In Fig. 2.19 (b), still a planar shock, traveling from left to right with a Mach number $M = 1.47$ in quiescent air disrupts a water droplet.

To address conductive cases, the methodology presented in Esmaeeli and Tryggvason (2004) is generally favored. It has been extensively used to study film boiling problems, droplet evaporation as in Irfan and Muradoglu (2017) and more recently has even been applied to the study combustion of a n-heptane droplet in Irfan and Muradoglu (2018).

In Fig. 2.21 are presented cases of water film boiling on a horizontal cylinder. A fairly similar case is presented in Fig. 2.21 where a horizontal hot wall, placed at the bottom of the domain, is used to repeatedly generate bubbles in a quiescent water pool.

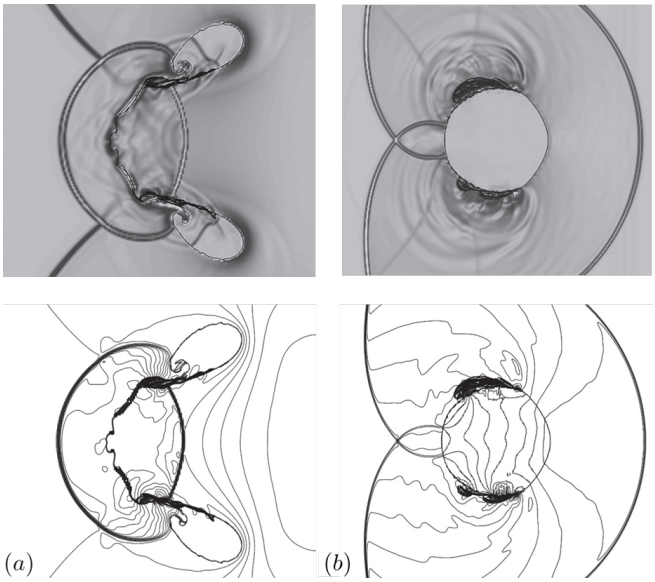

Figure 2.19: *Snapshot of an air bubble in water (b) and a water cylinder in air (b) interacting with a shockwave Razizadeh, Mortazavi, and Shahin (2018). Upper:experiments, lower:simulation*

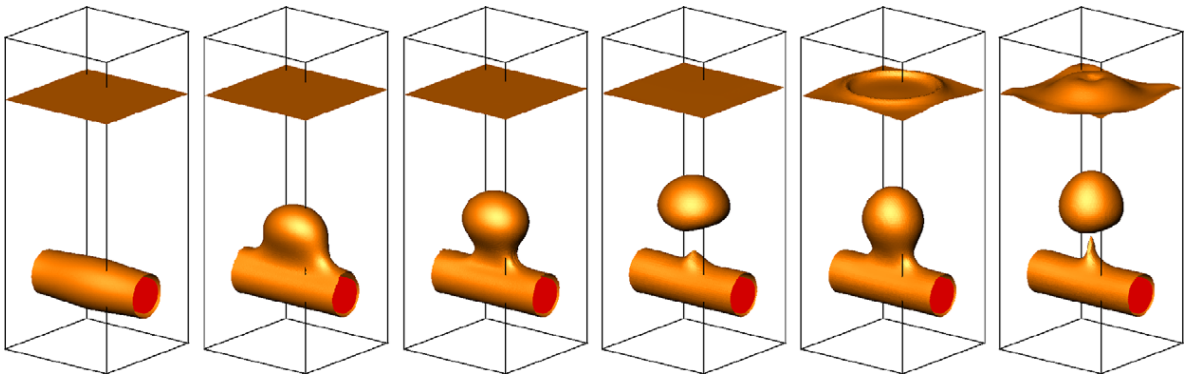

Figure 2.20: *Evolution of a liquid/vapor interface during film boiling on a horizontal cylinder from Esmaeeli and Tryggvason (2004).*

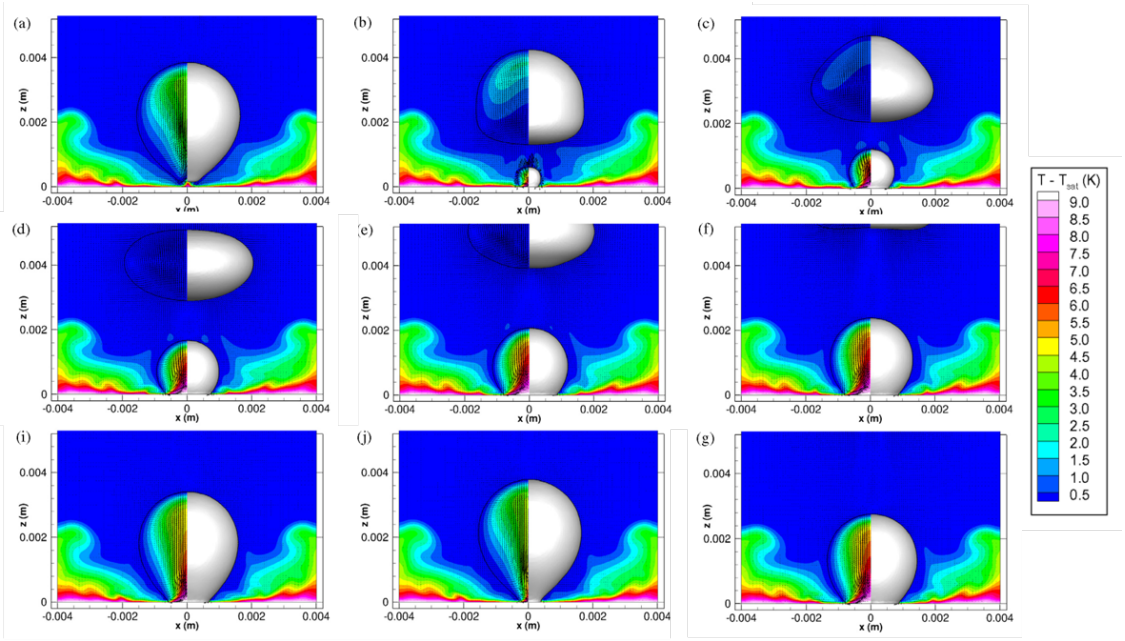

Figure 2.21: *Evolution of a saturated nucleate boiling from Sato and Ničeno (2013), the flow temperature is shown, the interface and the flow velocity field are depicted respectively on the right and left sides*

Chapter 3

Sharp interface methods: Interface capturing

The following chapter focuses on sharp interface methods commonly labeled as interface capturing methods. These methods share the feature of embedding the structure of the interface within a carefully selected continuous function.
By doing so, they do not require a specific numerical structure to track the interface, this task is performed by solving an additional transport equation. Additionally, they are automatically and implicitly treated unlike in FT methods.
In return, they must settle for an implicit description of the interface geometry which is merely "captured" rather than actually "tracked". In practice, this means that these methods require an additional treatment to reconstruct the interface from the embedding function.

The two main classes of sharp interface capturing methods are the Volume-of-Fluid (VOF) and the Level Set (LS).

In VOF methods, the information regarding the interface is carried by the eponymous volume function that track the volume of one of the two fluid in each cell of the domain.
These methods are conservative by nature, contrary to FT or LS but require often complex procedures to properly reconstruct the interface and/or intricate numerical scheme to evaluate the fluxes. This makes this kind of methods hard to extend to more complicated mesh design, particularly in 3D.
In particular, they are deemed to offer as less precise description of the interface topology.

LS method, on the contrary, offer a precise but most importantly easy treatment of the interface geometry by defining it as the zero level set of a continuous function. Thanks to this modeling, the level set methods can be transposed to any number of dimensions and any type of mesh structure with virtually little to no change.
This however comes at the cost of mass conservation. Besides, the level set must be carefully maintained throughout the simulation to achieve precise results.

It should be noticed that these two classes of methods are rather frameworks designed to follow

the movement of a discontinuity rather than actual schemes to solve mechanical equations such as Navier-Stokes or Euler, just as it is the case. This claim is supported by the fact that these methods have been used way beyond the scope of fluid mechanics.
In particular, when navigating the vast literature available on FT, LS and VOF methods, the numerical strategies used to solve the fluid equations fall under two categories: they either are extremely specific to one case or extremely classic. The strategies in the first category are too numerous to all be listed and those in the second category are already extremely well documented.
For these reasons, the numerical schemes used to solve the Navier-Stokes/Euler equations are purposely omitted in this chapter, as done for the FT methods in Sec. 2.2, in order to focus on the treatment of the interface.

Finally, given the complementary qualities and drawbacks of VOF and LS method, it was inevitable that combinations of the two would be attempted. This lead to the apparition of promising hybrid methods, not explored here, such as the coupled level set and volume-of-fluid (CLSVOF) in Sussman and Puckett (2000), the mass-conserving level-set (MCLS) in Van der Pijl et al. (2005) or more recently the coupled volume-of-fluid and level set (VOSET) method in Sun and Tao (2010).

3.1 Volume-of-Fluid methods

3.1.1 Historical overview

With the Level-Set methods, the Volume-of-Fluid (VOF) methods are arguably the most often used to perform numerical simulation with free surfaces and interfaces. It is an Eulerian method introduced in Nichols and Hirt (1975) and more explicitly in Hirt and Nichols (1981) drawing from the previous work of Ramshaw and Trapp (1976) and Noh and Woodward (1976).

A first motivation for creating these methods stems from the important computational cost of Lagragian interface tracking methods when compared to their relative accuracy, especially when strong topological changes occur. In practical terms, unless a very high amount of markers is used, interface tracking methods tend to offer a coarse description of the interface position while still requiring the tracking of all these markers throughout time. If one is to settle for a coarse description of the interface position, it can be taken advantage of to design a computationally efficient method.
A second motivation being the growth of VOF methods is the ability to conserve mass by design, a feature missing in Front-Tracking and Level-Set methods. Understandably, some applications (reactive cases, combustion, phase change) may require a precise mass conservation rather than an accurate interface localization. The early VOF method aimed at modeling free surface but rapidly evolved to achieve multi-species simulations accounting for surface tension.

However, this strength of VOF methods to preserve mass acts also as a potential threat. Indeed, the volume in order to preserve a bounded volume fraction throughout the simulation, the typical numerical schemes that one would use to solve the interface advection equation are know to be highly diffusive and would lead to a smearing of the interface, what is in total contradiction with the sharp nature of VOF methods.

To solve this issue, several techniques have been designed and they are the main subject of the discussions to come. From the founding articles referenced at the beginning, two main philosophies emerged regarding the advection of the interface and all modern installations of VOF method can be put in either of these two categories.

The first category rely on a geometrical reconstruction of the interface as initially done with the SLIC method in Noh and Woodward (1976). Starting from a simple reconstruction using vertical and horizontal lines, they evolved and became more complicated as the order of the reconstruction increase to gain accuracy. The PLIC, the first piecewise linear construction method introduced in Youngs (1982) spawned a series of other linear reconstruction strategies as found in Ashgriz and Poo (1991); Puckett (1991); Pilliod (1992); Puckett and Saltzman (1992); Parker and Youngs (1992); Scardovelli and Zaleski (2003). First instances of piecewise quadratic reconstruction in Poo and Ashgriz (1989) lead to several other approaches in Kim and No (1998); Price et al. (1998); Price (1998); Renardy and Renardy (2002); López et al. (2004) and even $\mathcal{C}^1$ continuous reconstruction in Diwakar et al. (2009).

The second category of methods, that grew in parallel, builds on the approach introduced in Hirt and Nichols (1981) where the focus the volume of fluid fluxes rather than the geometry itself. Specific numerical schemes are designed and combined to ensure that the interface is not smeared while the volume of fluid remains properly bounded. Likewise the PLIC for the interface reconstruction method, the Acceptor-Donor scheme of Hirt spawned plethora of other schemes such as in Lafaurie et al. (1994); Ubbink and Issa (1999); Darwish and Moukalled (2006); Tsui et al. (2009); Patel and Natarajan (2015)

The research for new interface or flux reconstruction method is still ongoing to this date.
Meanwhile, effort have been made to extend VOF method to arbitrary mesh such as in Jasak (1996); Ubbink and Issa (1999); Owkes and Desjardins (2014); Ivey and Moin (2017)
One specific weakness of VOF method seems the difficulty to extend them to compressible flows, even though we found no specific argument arguing for or against. This conclusion is drawn from the scarcity of results in that sense in the literature as only a very few examples are available, such as in de Niem et al. (2007) or Wemmenhove et al. (2015).

The rest of the section is dedicated to the description of the most relevant aspects regarding the Volume-of-Fluid methods. The key points of the modeling, such as the characterization of the interface and the equations to be solved, are first detailed.
As done for the Front-Tracking in 2.2 and the Level-Set methods in 3.2, the actual solving of the Navier-Stokes/Euler equations are omitted, for reasons detailed in the introduction of this chapter, so as to focus on the interface advection.
The two strategies to advect the interface are then further detailed: the main interface reconstruction paradigms are illustrated with some graphical examples and the philosophy behind flux reconstruction methods is explored, here again with some examples used clarify their mechanics.

3.1.2 Modeling and equations

In the following, it is supposed that studied system is composed of two non miscible fluids or a single fluid in its liquid and vapor form. The first and second components (the liquid and vapor phase if so) are referred to with the subscripts 1 ans 2 respectively. Initially, the Navier-Stokes equations solved for an incompressible, inviscid fluid are:

$$\boldsymbol{\nabla} \cdot \mathbf{v} = 0 \tag{3.1}$$

$$\rho \frac{d\mathbf{v}}{dt} = -\boldsymbol{\nabla} P + \boldsymbol{\nabla} \cdot \left(\mu \left(\boldsymbol{\nabla} \mathbf{v} + \boldsymbol{\nabla} \mathbf{v}^{\mathrm{T}} \right) \right) + \rho \boldsymbol{g} \tag{3.2}$$

where classically ρ, μ, P and $\mathbf{v}$ are the fluid density, viscosity, pressure and velocity and $\boldsymbol{g}$ represents the potential body forces.
The set of Eqs. (3.1)-(3.2) have been solved using a wide variety of discretization and numerical methods which will not be expanded upon here since, for the most part, they do not directly relate with the specificity of the VOF method. The curious reader can referrer to the different sources cited in this section for concrete cases.
The novelty of the VOF methods is to trade the marker function I of FT methods for a color function ϕ, usually a volume fraction of one on the specie or one of the phase, to follow the interface. The color/phase function ϕ is convected with the flow following the equation:

$$\frac{\partial \phi}{\partial t} + \mathbf{v} \cdot \boldsymbol{\nabla} \phi = 0 \tag{3.3}$$

with the additional hypothesis that the flow is incompressible, Eq. (3.3) can be written in the conservative form:

$$\frac{\partial \phi}{\partial t} + \boldsymbol{\nabla} \cdot (\mathbf{v} \phi) = 0 \tag{3.4}$$

The function ϕ allows to locate the two phases in the flow as well as the interface. For instance, for a liquid-gas simulation, ϕ is often defined as the liquid volume fraction and the discrete values $\phi_{i,j}$ represent the mean values of ϕ over a mesh cell. In the liquid phase $\phi = 1$, in the vapor phase $\phi = 0$ and the cells with $0 \leqslant \phi \leqslant 1$ contain an interface.
In that case the fluid density ρ, mechanical viscosity μ, specific heat capacity c_p and specific thermodynamic potential (e, h, s, etc...), are defined as a ϕ-averaged of the same quantities over all the phases:

$$\rho(\boldsymbol{x}, t) = \phi(\boldsymbol{x}, t) \rho_l + (1 - \phi(\boldsymbol{x}, t)) \rho_v \tag{3.5a}$$

$$\mu(\boldsymbol{x}, t) = \phi(\boldsymbol{x}, t) \mu_l + (1 - \phi(\boldsymbol{x}, t)) \mu_v \tag{3.5b}$$

$$c_p(\boldsymbol{x}, t) = \phi(\boldsymbol{x}, t) c_{p_l} + (1 - \phi(\boldsymbol{x}, t)) c_{p_v} \tag{3.5c}$$

$$\dots$$

The quality of VOF methods simulations strongly depends on how well Eq. (3.4) is solved since ϕ bears almost alone the information about the phases location and the interface position. It is even more so if interfacial boundary conditions have to be applied such as mass or energy fluxes between the two phase phases or surface tension that additionally requires an

estimation of the interface curvature and normal vector. Since their initial introduction, VOF methods underwent numerous improvements regarding the solving of the advection equation Eq. (3.4) which will be the essential focus of the section.

These methods can be separated into two categories. The first category, referred to as Interface Reconstruction methods here, aim at creating a geometrical reconstruction of the interface in the mesh cell using available information from the discretized version of ϕ. The second category, referred to as Flux Reconstruction methods, aim at calculating directly the numerical fluxes in the discretized version Eq. (3.4). Both philosophies have their advantages and drawbacks and both, still to this day, foster substantial theoretical and numerical studies in the community.

3.1.3 VOF with Interface Reconstruction methods

The principle of Interface Reconstruction is arguably a building block of the VOF methods in itself. The principle, introduced by DeBar (1974), Ramshaw and Trapp (1976) and Noh and Woodward (1976), served as a premise for the so called original VOF method from Hirt and Nichols (1981). Since then, multiple variants have been proposed and although too many to be all explored in detail, the principal ones will be briefly presented here to allow a grasp of both the advantages of this philosophy and its inherent numerical difficulties.
To present these methods, a two-dimensional structured cartesian mesh is considered as shown in Fig. 3.1. The horizontal and vertical step sizes Δx and Δy, though different, are constant for all the mesh.

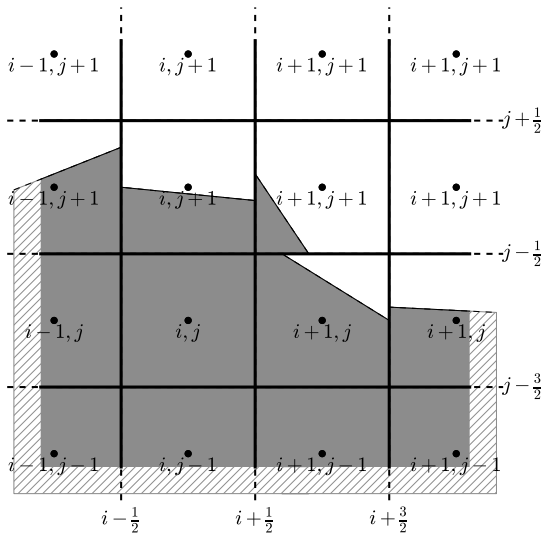

Figure 3.1: *Typical cartesian mesh used in Volume-of-Fluid simulations using Interface Reconstruction methods*

3.1.3.1 Interface reconstruction

The different reconstruction methods can be first and foremost separated according the order of the curve used to represent the interface in each cell. Although there exist no theoretical limit to the order that can be used, the increase in the method complexity associated with this order augmentation acts as practical deterrent. For most application, only zeroth, first and second order reconstruction are contemplated. The different results that can be obtained from these orders of reconstruction are exemplified in Fig. 3.2 where constant, linear and quadratic paradigms are represented. Intuitively, the higher the order is, the more accurate the representation of the interface becomes.

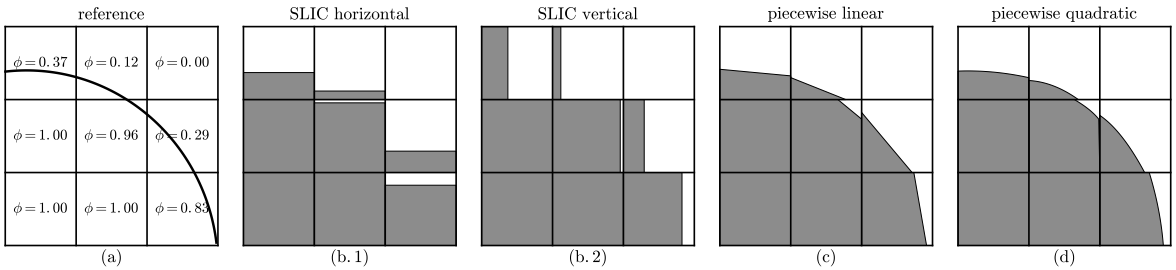

Figure 3.2: *Interface reconstruction using contant (SLIC) (b.1), (b2) and the piecewise linear PLIC (c) and quadratic (PROST) (d) methods from a reference volume fraction repartition (a)*

Constant reconstruction

The Simple Line Interface Calculation (SLIC), introduced in Noh and Woodward (1976), is the oldest and most simple reconstruction method but is still used today nonetheless.
The SLIC reconstructs the interface using only horizontal or vertical line. The reconstruction is done in both directions separately and the fluxes are evaluated accordingly. After the cells that containing both fluids/phase are localized, the SLIC choses between a list of pre-identified configuration to determine how the interface should be laid down. These configurations depend on the surrounding values of the volume fraction function and allow to decide which fluid is on which side of the interface. Once the disposition of the fluid is know in an interface cell, the exact position of the interface is adjusted so as to get the correct volume fraction.
Fig. 3.2 shows an example of reconstruction using the SLIC method, both horizontal (b.1) and vertical (b.2) reconstructions are provided. One can notice that the formulation of the SLIC seems to retrain it to cartesian meshes but actually attempts have been made to extend the method to unstructured grids. However the SLIC seems limited to two dimensional triangular grids Huang et al. (2010), it already provides encouraging results for an adaptation to arbitrary grids.

Piecewise linear reconstruction

The precision with which the interface geometry is described can be substantially increased by using a linear reconstruction in each cell as noted by the authors in Youngs (1982) when designing the Piecewise Linear Interface Calculation (PLIC) method as shown in Fig. 3.2 (c). The original PLIC method spawned a wide variety of methods which in spite of their name

still consist in a piecewise linear reconstruction of the interface. A certain ambiguity has grow around the acronym PLIC as, depending on the material, it can be used either to reference to the original method in Youngs (1982) or any other linear reconstruction method regardless of its actual implementation. Here, the acronym is exclusively used to refer to the original method, any other method will be referenced by its own specific name.
Piecewise linear are generally the go-to reconstruction methods as they are substantially more precise than the SLIC for a limited computational cost overhead. They also has been successfully applied to arbitrary structured and unstructured meshes as demonstrated in Ivey and Moin (2015); Ivey and Moin (2017).

A criterion used to compare these methods is evaluating their order of convergence. No extensive survey has been done in that sense to the best of our knowledge but partial comparisons can be found in Pilliod and Puckett (2004) or Tryggvason et al. (2011). A simple test, that can usually be performed analytically, is to assess the ability of a given method to reconstitute a straight line in a cell, a native feature for a methods with second order convergence but not ensured for those with only a first order of convergence Another test, however harder to perform, consists in evaluating the ability of the method to reconstitute a continuous interface as continuous, feature that also ensure a higher degree of precision.

Noticeable piecewise linear methods include, apart from the original PLIC, the KRAKEN, an heuristic method introduced in DeBar (1974), the FLAIR of Ashgriz and Poo (1991) that can be perceived to some extend as an improvement of both the PLIC and the KRAKEN where the segments are not defined within the cells but rather at the boundaries, the LVIRA method proposed by Puckett (1991) which a upgraded version of the PLIC were a specific norm is minimized, the ELVIRA from Pilliod (1992) which reinvest and simplifies the minimization process of the LVIRA method by creating a preselection of possible normal vectors and the The Least-square fit method devised in Scardovelli and Zaleski (2003) that actually showcase a second order convergence on canonical cases.
Some methods, such as the Center of Mass from Puckett and Saltzman (1992) or the Parker-Youngs method Parker and Youngs (1992), although of a historical interest, are usually dismissed for they are unable to properly reproduce a straight line interface.
In spite of a better geometrical representation of the interface, piecewise linear methods suffer the inability to inherently offer a continuous description of the interface unless global optimization process are used. This, in part, motivates the use of higher order of reconstruction.

Quadratic reconstruction method
To further increase the precision of the reconstruction, second order polynomials can be used in each cells.
The first instance of using a quadratic reconstruction in conjunction with a volume fraction function appears in Poo and Ashgriz (1989) where a philosophy similar to that of the SLIC or the LVIRA method is used: possible configurations of the interface are exhaustively listed and the volume fraction repartition over a certain zone (a 3x3 macro-cell) is used to chose the most suitable among them. Different adjustments adjustments are made to respect the volume fraction in each cells. In Poo and Ashgriz (1989), the quadratic representation is not so much used to reconstruct the interface rather than to estimate the interface curvature.
In Price et al. (1998); Price (1998) and Kim and No (1998), a piecewise quadratic reconstruc-

tion of the interface is actually used were different strategies, always based on the local volume fraction repartition, are employed to select the correct shape of the interface and evaluate the associated fluxes.
Later methods such as the spline reconstruction in López et al. (2004) and the Parabolic Reconstruction of Surface Tension (PROST) in Renardy and Renardy (2002) can be viewed as improved version of those in Poo and Ashgriz (1989) and Price et al. (1998) respectively. For all these methods, the principle is always to perform a first linear reconstruction using an arbitrary piecewise linear method and then use the obtained segment to generate the quadratic interpolation.

The Quadratic Spline based Interface (QUASI), an ever mode advanced method has been developed in Diwakar et al. (2009) and allows to perform a quadratic interpolation but constrary to the previously cited methods, an order $\mathcal{C}^0$ or even $\mathcal{C}^1$ continuity can be enforced upon the reconstructed interface.
The differences between piecewise linear, piecewise quadratic, $\mathcal{C}^0$ QUASI and $\mathcal{C}^1$ QUASI reconstruction is exposed

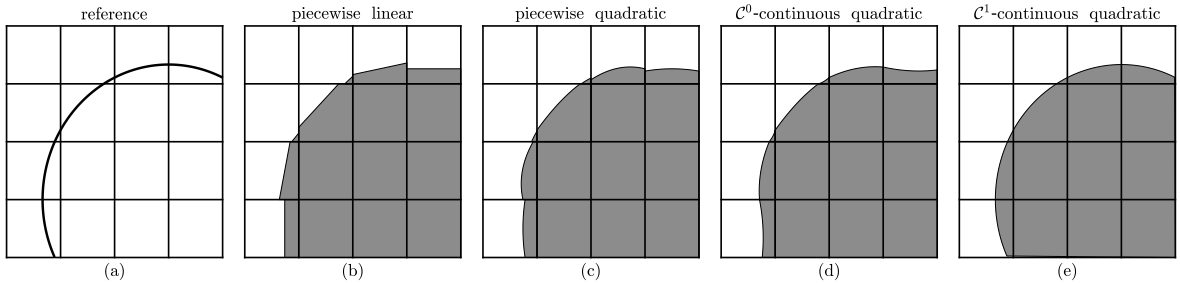

Figure 3.3: *Result of different reconstruction methods depending on the order and regularity desired: (a) reference, (b) piecewise linear, (c) piecewise quadratic, (d) $\mathcal{C}^0$ continuous quadratic, (e) $\mathcal{C}^1$ continuous quadratic*

A case for the piecewise linear reconstruction methods
Piecewise linear method remain to this date the most commonly used reconstruction methods despite their apparent oldness, for three mains reasons beyond the intuitive interpretation they permit. The first is the substantial ease with which they can be implemented when compared to more modern and precise methods. The second reasons stem from the first, as numerical power increases, the ability to diminish mesh sizes grows and these methods, on fine enough meshes, offer sufficient enough precision relatively to its low computational cost. Moreover, in modern application where several physical phenomenon are usually coupled and studied at once, refining meshes becomes more often a requirement while the ability to same computational time remain a key issue. Piecewise linear methods are particularly suited to accommodate with these constraints. Finally the third reason is their propensity to be easily declined over to different advection scheme, explicit or implicit, Eulerian and Lagrangian, split or unsplit, which is not the case of other reconstruction methods. In particular, when one wishes to update an already existing code in order to perform two-phase flow calculation with a VOF interface reconstruction method, these two method are the most likely to interfere with the numerical methods already implemented.

However, the limitations af these two methods, in particular their precision, must be kept in mind when they are used and specific configurations or simulation need may call for the use of more sophisticated methods which, all things being equal, are usually more precise.

3.1.3.2 Interface advection

Once the interface has been reconstructed in the concerned cells, the advection equation Eq. (3.4) must be solved to update the values of ϕ in the computational domain. The problem can be enunciated in those terms: knowing the values of the phase function ϕ^n and the velocity $\mathbf{v}^n$ in all the domain at a time iteration n, how one can estimate the the values of the phase function ϕ^{n+1} at the next time iteration $n+1$. The method to perform this advection are usually fall under of the two following classes: the split methods and the unsplit (or multidimensional) methods

The split methods perform the advection iteratively in each direction of the mesh. For each direction, a specific volume of fluid to advect is determined in each cell and then distribute it: they are simple and straightforward but usually of low order and pron to errors.
The unsplit methods determine the volumes of fluid to advect and perform the distribution in all the directions at once: they tend to be more complicated to implement but offer more precision and accuracy.

Independently of the split or unsplit nature of the advection, the algorithms can also be separated in two different categories: Eulerian and Lagrangian methods. The specificities of these two categories will be expanded upon in the following paragraphs.

Split methods
In a two-dimensional case as represented in Fig. 3.4, the split methods will update the phase function ϕ performing an advection first in x direction and then in the y direction, or the other way around. The advection in one direction in called a sweep. By alternating the order of the sweep direction, it is possible to increase the order of the advection algorithm. For regular grids, the principal issues faced by the split methods are: the possibility to advect more fluid than physically available in one cell, advect a volume of fluid multiple times, creating non-physical values of ϕ after advection such as $\phi > 1$ or $\phi < 0$. For unstructured/non-conformant grids, additional issues arise such as the possibility to miss the advection of a certain volume of fluid or to advect a volume of fluid in the wrong cell. These issues are well documented in Ivey and Moin (2017). In that respect, split methods require additional treatment to overcome these shortcomings.

Lagrangian split algorithms
The first Lagragian split advection algorithm is arguably the one used by DeBar (1974) for the KRAKEN code. The same methodology is used by Li (1995) and has been extended to three-dimensional cases in Gueyffier et al. (1999). Simulations performed in Ashgriz and Poo (1991) and Scardovelli and Zaleski (2003) rely on this type of algorithm. The essential features of the method are depicted Fig. 3.4.
For a sweep in the x direction, the horizontal velocity on the two vertical boundaries of the

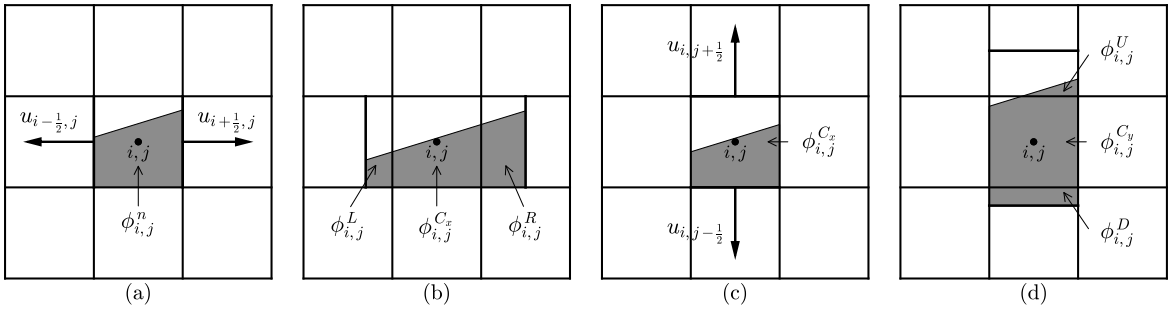

Figure 3.4: *Principle of the Lagrangian split advection algorithm for Volume-of-Fluid methods, (a) and (b) are respectively the velocity determination and the volume advection respectively for the x-sweep, (c) and (d) represents the same steps for the y-sweep*

cell i, j (the velocities can be accessed directly if a staggered MAC grid is used or calculated through averaging/interpolation procedures) is assumed to be constant. It is worth noticing that the incompressibility condition (3.1) does not negate the presence of a velocity gradient $\partial u/\partial x$ which may cause an expansion. The left and right boundaries are than convected at once causing a compression/expansion of the 'dark' volume of fluid. In particular, this volume of fluid may overflow on the left and right neighboring cells. Using geometrical argument the left $\phi^L_{i,j}$, right $\phi^R_{i,j}$ and central $\phi^{C_x}_{i,j}$ volumes of fluid can be easily accessed. The phase function in the cell i, j can than be updated as follow:

$$\phi^*_{i,j} = \phi^{C_x}_{i,j} + \phi^R_{i-1,j} + \phi^L_{i+1,j} \tag{3.6}$$

The notation $\phi^*_{i,j}$ is used to denote that this update is only partial. The same procedure is to be applied in the vertical direction to determine up $\phi^U_{i,j}$, down $\phi^D_{i,j}$ and central $\phi^{C_y}_{i,j}$ volumes of fluid for the sweep. The update can be completed with:

$$\phi^{n+1}_{i,j} = \phi^{C_y}_{i,j} + \phi^U_{i,j-1} + \phi^D_{i,j+1} \tag{3.7}$$

It is important to remember that the triplet of volumes for the x sweep and for the y sweep must be calculated one after another and not simultaneously to avoid convecting some parts of the fluid two times. In practice, Lagrangian split methods suffer more important mass conservation issues, in particular the condition $0 \leqslant \phi \leqslant 1$ may be violated.These issues are mostly due to the fact that the discrete velocity field is not exactly divergence free. Additional local and global algorithm are usually required to redistribute excessive mass among the cells.

Eulerian split algorithms

Eulerian advection methods integrate the equation Eq. (3.3) directly evaluating the boundary fluxes. Classically horizontal fluxes are denoted F and vertical fluxes G. The discrete integration of Eq. (3.3) writes:

$$\phi^*_{i,j} = \phi^n_{i,j} + \frac{\Delta t}{\Delta x}\left(F^n_{i-\frac{1}{2},j} - F^n_{i+\frac{1}{2},j}\right) \tag{3.8a}$$

$$\phi^{n+1}_{i,j} = \phi^*_{i,j} + \frac{\Delta t}{\Delta y}\left(G^n_{i,j-\frac{1}{2}} - G^n_{i,j+\frac{1}{2}}\right) \tag{3.8b}$$

The superscript * refers to a partial update after first direction sweep. As it was the case for Lagrangian methods, the update for the second direction sweep must be carried out carefully in order to limit volume conservation errors. On a cartesian mesh, the fluxes are evaluated by calculating the volume of fluid present in sub-rectangles adjacent to the considered boundary. For instance in Fig. 3.5, the left and right flux are given by $F^n_{i-\frac{1}{2},j} = u_{i-\frac{1}{2},j}\Delta t \phi_{i-\gamma,j}$ where $\gamma = 1$ if $u_{i-\frac{1}{2},j} > 0$ and $\gamma = 0$ if $u_{i-\frac{1}{2},j} < 0$ and $F^n_{i+\frac{1}{2},j} = u_{i+\frac{1}{2},j}\Delta t \phi_{i+\gamma,j}$ with $\gamma = 0$ if $u_{i+\frac{1}{2},j} > 0$ and $\gamma = 1$ if $u_{i+\frac{1}{2},j} < 0$. The same consideration are used to determine the vertical fluxes for the y sweep. The order of the sweep are switched at every time iteration for better accuracy.

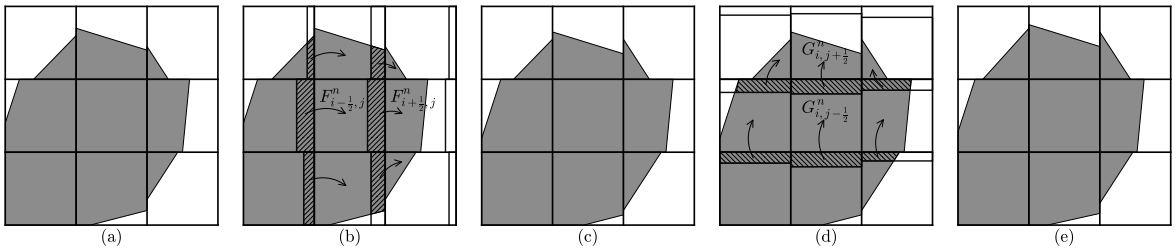

Figure 3.5: *Principle of the Eulerian split advection algorithm for Volume-of-Fluid methods*

Unsplit methods

For many problem, the split methods, handled properly, offer convenient second order accuracy. However, for some cases, a "stair-ification" of the interface occurs due to the multistep sweeps, known as "push-pull" phenomenon. For such problematic cases, unsplit advection methods are to be used. Whether Eulerian or Lagrangian methods are considered, the main idea is to evaluate at once the modifications needed to update the phase function. Though more complicated in essence, unsplit algorithms, once carefully expressed, translate more naturally to unstructured non-cartesian grids explaining their preferential use in modern literature. On summarized survey of the existing unsplit methods and the associated difficulties can be found in Comminal et al. (2015) and Ivey and Moin (2017).

Lagrangian unsplit algorithms

In Lagrangian unsplit algorithms, all remarkable points of a given cell are convected at once by solving the equation. By noting $\boldsymbol{x}$ the position of such a point, the advection done along the characteristic lines solving the motion equation $\partial \boldsymbol{x}_i / \partial t = \boldsymbol{v}_i(\boldsymbol{x}_i, t)$. The local velocity $\boldsymbol{v}_i$ of the point is obtained through interpolation of the fluid velocity defined on the calculation grid. As shown in Fig. 3.6 for a regular grid, the advected points are the four corners of the cell and the point limiting the position of the two fluid in the cell. The position of the newly created polygon allows to evaluate the volumes of fluid distributed in the eight possible neighboring cells $\phi^{\mathrm{L}}_{i,j}, \phi^{\mathrm{R}}_{i,j}, \phi^{\mathrm{U}}_{i,j}, \phi^{\mathrm{D}}_{i,j}, \phi^{\mathrm{LU}}_{i,j}, \phi^{\mathrm{LD}}_{i,j}, \phi^{\mathrm{RU}}_{i,j}, \phi^{\mathrm{RD}}_{i,j}$ (with $\mathrm{L}, \mathrm{R}, \mathrm{U}, \mathrm{D}$ standing for Left, Right, Up and Down) as well as the volume of fluid remaining in the considered cell $\phi^{\mathrm{C}}_{i,j}$. The evaluation of these volumes is merely a geometrical problem. Once evaluated, the volumes are used to update the phase function for the next iteration is the same fashion as in Eqs. (3.6)-(3.7) but

at once following:

$$\phi_{i,j}^{n+1} = \phi_{i,j}^{\mathrm{C}} + \phi_{i+1,j}^{\mathrm{L}} + \phi_{i-1,j}^{\mathrm{R}} + \phi_{i,j-1}^{\mathrm{U}} + \phi_{i,j+1}^{\mathrm{D}}, \\ \phi_{i+1,j-1}^{\mathrm{LU}} + \phi_{i+1,j+1}^{\mathrm{LD}} + \phi_{i-1,j-1}^{\mathrm{RU}} + \phi_{i-1,j+1}^{\mathrm{RD}} \tag{3.9}$$

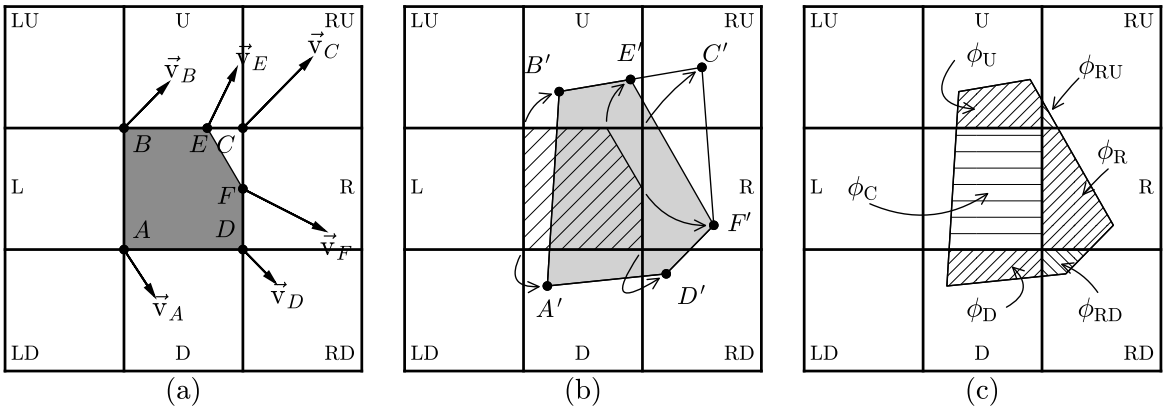

Figure 3.6: *Principle of the Lagrangian unsplit advection algorithms for Volume-of-Fluid methods*

As in the Lagrangian split method, the advection of the whole cell suffer errors in the mass conservation due to numerical errors in the velocity interpolation, motion equation integration, deformation of straight lines by high order integration methods and the fact that the divergence of the numerical velocity field does not exactly nullify. Local and global mass redistribution may be necessary to satisfy $0 \leqslant \phi \leqslant 1$ in all cells.

Eulerian unsplit algorithms

The design of an Eulerian unsplit algorithm is particularly complicated because it requires, for each faces of the computational cell, to determine at once the correct quantity of fluid that is advected while paying attention not to convect the same volume multiple times and not to forget to convect a volume that should have been.

An early method has been proposed in Rider and Kothe (1998) but it lacked the conservation properties previously mentioned. The method has been improved in López et al. (2004) which gave birth to the Edge-Matched Flux Polyhedron Advection (EMFPA). The principle behind this algorithm is presented in Fig. 3.7

In this example, the face delimited by points A and B is considered and the objective is to determine the flux that is injected into cell $\mathrm{C}_{i,j}$ from the surrounding cells. To that effect, much like in Fig. 3.5, a fictive cell is created which contains the volume to consider in order to evaluate the flux F_{A-B} entering (or leaving) through segment $A - B$.

This volume is a polygon formed by points A and B and two additional points A' and B'. A series of conditions allow to determined the positions of A' and B'. These conditions, listed hereunder in Eqs. (3.10a)-(3.10d), render the matter of finding A' and C', and therefore F_{A-B}

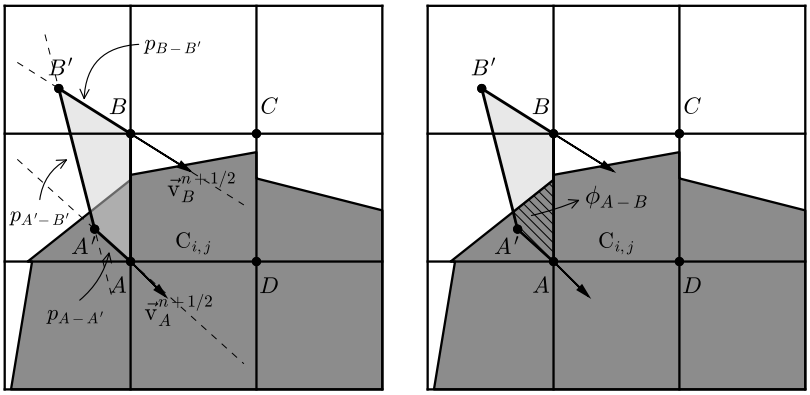

Figure 3.7: *Principle of the Eulerian unsplit advection algorithm EMFPA for Volume-of-Fluid methods from López et al. (2004)*

a purely geometrical problem.

$$p_{A-A'} = \frac{v_A^{n+1/2}}{u_A^{n+1/2}} \tag{3.10a}$$

$$p_{B-B'} = \frac{v_B^{n+1/2}}{u_B^{n+1/2}} \tag{3.10b}$$

$$p_{A'-B'} = \frac{x_A - x_B - \left(u_A^{n+1/2} - u_B^{n+1/2}\right)\Delta t}{y_A - y_B - \left(v_A^{n+1/2} - v_B^{n+1/2}\right)\Delta t} \tag{3.10c}$$

$$\mathcal{V}_{A-B-B'-A'} = \frac{1}{2}\left(u_A^{n+1/2} + u_B^{n+1/2}\right)\Delta y \Delta t \tag{3.10d}$$

where $p_{P_1-P_2}$ is the slope of the segment between arbitrary points P_1 and P_2, $u_P^{n+1/2} = \left(u_P^n + u_P^{n+1}\right)/2$ is the interpolated horizontal velocity at instant $t + \Delta t/2$ at arbitrary point P of the mesh and $\mathcal{V}_{A-B-B'-A'}$ is the volume of the polygon delimited by points A, B, B' and A'.
Of course, Eqs. (3.10a)-(3.10d) must be adapted if an horizontal edge is considered or negative velocities are involved. Special cases leading to infinite slopes (i.e. vertical lines) must also be dealt with specific care, but for the most part, the difficulty is more computational than conceptual.

Once the exact positions of A' and B' are known, the volume of fluid that is intercepted by the polygon $ABB'A'$ is exactly the amount of fluid that is to be advected toward cell $C_{i+1/2,j+1/2}$. This volume is signified by ϕ_{A-B} in Fig. 3.7 (b).
By repeating this process on all the edges of $C_{i,j}$, the volume of fluid can be updated as follows:

$$\phi_{i,j}^{n+1} = \phi_{A-B} + \phi_{B-C} + \phi_{C-D} + \phi_{D-A} \tag{3.11}$$

The authors in Ivey and Moin (2017) have further improved the EMFPA, in particular its

application to unstructured mesh, which, even theoretically possible, was never expanded upon in López et al. (2004).

3.1.3.3 Numerical results

Here are provided two examples of impressive numerical results obtained using VOF method with interface reconstruction techniques. Both are based on PLIC reconstruction, results applied to industrial configurations with higher orders of reconstruction still lacking in the literature.

Fig. 3.8 shows the disintegration of a liquid jet injected with an outward swirl opening. The injection at 100 bar into a 1 bar domain, with $Re = 10^4$ and $We = 10^3$, is performed with fluid properties so as to be representative of automotive injection. The downstream propagation of jet instabilities, fostered by the initial rotational velocity, can clearly be seen up to the breakup process which creates fuel droplets.

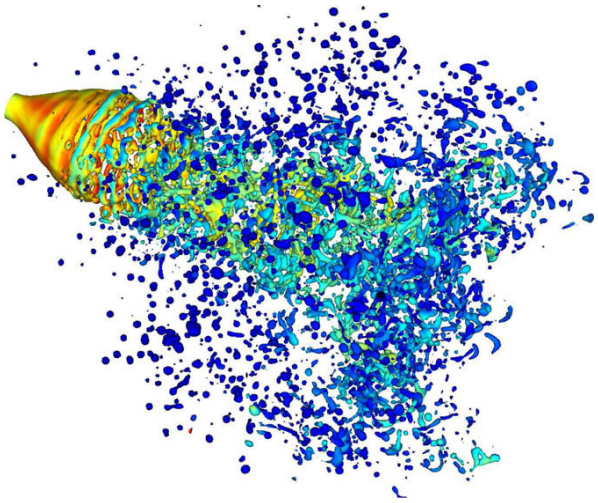

Figure 3.8: *Snapshot of hollow-cone atomizer representative of automotive injection of iso-octane from Fuster et al. (2009). Velocity norm used as color*

Fig. 3.9 depicts the injection of a water jet into a quiescent air with a density ratio of 800. The regime obtained with $Re = 5000$ and $We = 60,000$ allows to get a strong destabilization of the jet leading to primary a secondary breakup phenomena. The liquid sheets, ligaments and droplet are faithfully retrieved.

3.1.4 VOF with Flux Reconstruction methods

As numerical methods progressed and computational power increased, the will to address more complex configurations emerged. Such configurations usually involve intricate geometries, tree-dimensional aspects and often reveals hard to tackle using homogeneous regular cartesian meshes. A vast majority of the Interface Reconstruction methods are limited to such type of meshes. Beside, for some of these methods, usually the most accurate, the level of complexity of the rules used to reconstruct the interface is already important even for two-dimensional configurations. Effort have thus been made to develop methods to overcome this

Figure 3.9: *Snapshot of the atomization of a round water jet in a quiescent air from Le Chenadec and Pitsch (2013)*

previous shortcomings.

The derivation of these methods relies on the previously made observations but also on the hereunder considerations. At their core, VOF methods try to preserve a sharp description of the interface as the simulations are carried out while preventing the smoothing effect of the usual advection schemes. Besides, the geometry of the interface is usually not a final unknown of the system to be determine but rather a intermediary to access to evaluate the volume-of-fluid fluxes. Therefore, its precise reconstruction does not appear that compulsory outside of display purposes granted that other values of interest are correctly calculated. Moreover, the discrimination between split/unsplit methods and Euler/Lagrangian approaches in volume reconstruction to better suit a simulation often lack proper motivations despite having a possibly strong impact on the simulation results.

For all these reasons, Flux Reconstruction methods provide a direct discretization of the volume-of-fluid fluxes without reconstructing the interface. For these methods, the volume fraction fluxes at faces of the volumes of control are directly expressed with restrained geometrical information. This discretization is carried out so as to get bounded values of the volume fraction while limiting the diffusion or the smearing of the interface.
The bounding constraint is most often enforced through the hypothesis that a value of ϕ in a given cell should lay between the extremal values of its surrounding cells after a time step iteration. As for the interface diffusion, it should be limited to at most the width of a computational cell.

3.1.4.1 Construction of a Flux Reconstruction method

The normalized variable diagram
Modern Flux Reconstruction technique use the normalized variable diagram (NVD). Indeed, at first order, the boundedness of ϕ can be insured using a upwind scheme. By using the upstream values of ϕ, the upwind scheme is unconditionally stable and bounded, it however is strongly diffusive. On the other hand, the downwind scheme uses the downstream values

of ϕ and by doing so insures the preservation of a sharp interface. However, by doing so, it introduces a negative numerical diffusion that makes this scheme unconditionally unstable.

The NVD allows to devise and analyze schemes that blend the qualities of these two simple schemes to moderate their respective flaws.
To construct the NVD, a one dimensional setting is used, comprised of three cells (upstream (U), central (C) and downstream U) as shown in Fig. 3.10 where $\mathbf{v}$ is the velocity vector.

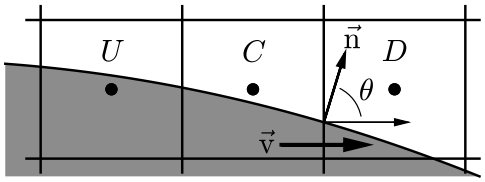

Figure 3.10: *Canonical 1D configuration used to construct the normalized variable diagram*

The normalized volume fraction $\tilde{\phi}$ for the central cell is then introduced by:

$$\tilde{\phi}(\boldsymbol{x}, t) = \frac{\phi(\boldsymbol{x}, t) - \phi_U}{\phi_D - \phi_U} \tag{3.12}$$

where $\boldsymbol{x}$ is the position vector, t the time, ϕ_U and ϕ_D the value of ϕ respectively in the upstream and downstream cells.
The NVD compares the reduced value predicted by the scheme at the central cell upwind face, noted $\tilde{\phi}_f$ with the current value at the center of the central face $\tilde{\phi}_C$, as shown in Fig. 3.11.

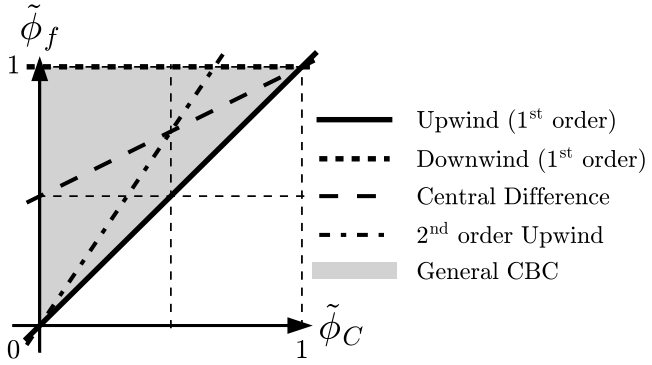

Figure 3.11: *Example of a normalized variable diagram*

If for any value of $\tilde{\phi}_C$ one has $\tilde{\phi}_f = 1$, one is using the first order downwind scheme. Conversely, if $\tilde{\phi}_f = \tilde{\phi}_C$ for any value of $\tilde{\phi}_C$, the first order upwind scheme is being used. These two configurations are displayed in Fig. 3.11 (a).
It can be shown (see Gaskell and Lau (1988)) that in order to be bounded, a one-dimensional implicit differencing scheme must remain within the gray area in Fig. 3.11 of which bounds are given by Eq. (3.13). This region is said to satisfy the convection boundedness criteria (CBC).

$$\begin{cases} \tilde{\phi}_C \leqslant \tilde{\phi}_f \leqslant 1 \text{ for } 0 \leqslant \tilde{\phi}_C \leqslant 1 \\ \tilde{\phi}_f = \tilde{\phi}_C \text{ for } \tilde{\phi}_C < 1 \text{ or } \tilde{\phi}_C > 1 \end{cases} \tag{3.13}$$

For a one-dimensional explicit scheme, the Courant number CFL intervenes. The corresponding region is colored in gray in Fig. 3.12 and its boundaries are given by:

$$\begin{cases} \tilde{\phi}_C \leqslant \tilde{\phi}_f \leqslant \min\left(1, \dfrac{\tilde{\phi}_C}{CFL}\right) \text{ for } 0 \leqslant \tilde{\phi}_C \leqslant 1 \\ \tilde{\phi}_f = \tilde{\phi}_C \text{ for } \tilde{\phi}_C < 1 \text{ or } \tilde{\phi}_C > 1 \end{cases} \tag{3.14}$$

Another effect that must be integrated in dimensions higher than one is the fact that the downwind scheme tends to artificially align the interface perpendicularly to the velocity of the flow. This occurs even for configurations where the interface is initially tangent to the flow velocity.
To manage this unphysical behavior of the scheme, the angle θ between the interface and the velocity, as shown Fig. 3.10, must be accounted for. For nearly right angle $\theta \approx \pi/2$, the downwind scheme allows to maintain a sharp interface.
Conversely, going back to an upwind scheme for low angles will prevent the wrinkling of the interface without diffusion, the latter being essentially tangent to the velocity. This angle is calculated by evaluating the volume fraction gradient and is defined by $\theta = (\widehat{\mathbf{v}, \boldsymbol{\nabla}\phi})$. The impact of this treatment has been early noticed in Hirt and Nichols (1981), initially investigated in Lafaurie et al. (1994) and proven to be of a major importance in Ubbink (1997).

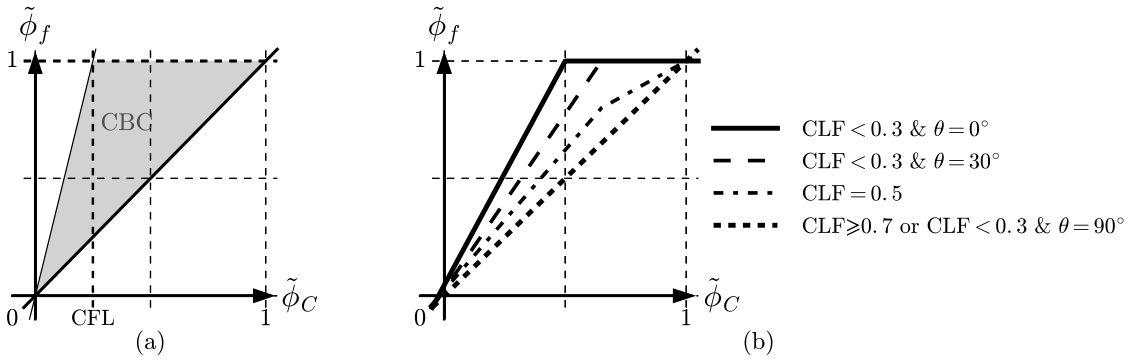

Figure 3.12: *Impact of the Courrant number on the CBC (a) and example of the behavior the HRIC scheme from Muzaferija and Peric (1997) using the NVD for different values of* CFL *(b)*

Additional treatment must be performed to ensure the correct bounding of the volume fraction values. Essentially, once the volume fraction are determined in the volumes of control faces, one must ensure that a cell does not transfer more volume of any phase than it contains.
Using all these criteria, especially Eq. (3.14) for explicit schemes, the main Flux Reconstruction methods can described using three main steps: First a compressive (upwind like) and a high order/anti-diffusive scheme must be chosen, using the NVD in Fig. 3.11, thus generating

temporary values $\tilde{\phi}_{\text{Comp}}$ and $\tilde{\phi}_{\text{HR}}$. The two predicted values are then mixed using a blending factor $\omega(\theta)$ depending on the angle θ for create a new prediction $\tilde{\phi}_\theta$. Eventually, the impact of the Courant number is injected in the last step and it usually involves the use of an intricate function f using as arguments CFL, $\tilde{\phi}_\theta$ and possibly other values such as $\tilde{\phi}_C$, $\tilde{\phi}_D$ or $\tilde{\phi}_U$. The overall process is summarized with Eqs. (3.15a)-(3.15b)

$$\tilde{\phi}_\theta = \omega(\theta)\,\tilde{\phi}_{\text{Comp}} + (1-\omega(\theta))\,\tilde{\phi}_{\text{HR}} \tag{3.15a}$$

$$\tilde{\phi}_f = f\left(\text{CFL}, \tilde{\phi}_\theta, \cdots,\right) \tag{3.15b}$$

The last step allows to evaluate the final value $\tilde{\phi}_f$ which in turn can be used to evaluate the actual volume fraction flux crossing the face between cells C and U of Fig. 3.10 by mean of Eq. (3.16).

$$\phi_f = \tilde{\phi}_f\,(\phi_D - \phi_U) + \phi_D \tag{3.16}$$

Examples of Flux Reconstruction method

The Acceptor-Donor algorithm, introduced by Johnson (1970) can be used as an example for its simplicity. Beside, it is the flux reconstruction method used in the original VOF method introductory paper Hirt and Nichols (1981). Its characteristics are given in Eqs. (3.17a)-(3.17d) The chosen compressive scheme is the first order upwind and the anti-diffusive scheme is the first order downwind. A simple cut-off value of 45° is chosen for the angle θ to switch between the two scheme. Finally, the Courant number is not taken into account.

$$\tilde{\phi}_{\text{Comp}} = \tilde{\phi}_C \tag{3.17a}$$

$$\tilde{\phi}_{\text{HR}} = 1 \tag{3.17b}$$

$$\omega(\theta) = \begin{cases} 1 \text{ if } \theta \leqslant 45° \\ 0 \text{ if } \theta > 45° \end{cases} \tag{3.17c}$$

$$\tilde{\phi}_f = \tilde{\phi}_\theta = \begin{cases} \tilde{\phi}_C \text{ if } \theta \leqslant 45° \\ 1 \text{ if } \theta > 45° \end{cases} \tag{3.17d}$$

This original method presents several shortcomings. Firstly, despite this simple formulation, it lacks flexibility as it is restrained to Cartesian grids. Secondly, the choice of the cut-off angle is purely empirical and lacks justification. It can be shown, see Ubbink (1997), that a constant value 45° is not suitable for most cases. Thirdly, the switch between the upwind and downwind formulation is not done smoothly and results in a deformation of the interface. It can be shown that this deformation originates from the non compliance of the switching method with the local boundedness criteria for the volume fraction. In particular, the authors in Lafaurie et al. (1994) realized that the important question was not so much how than when to switch. Beside, they also demonstrated that the first upwind scheme is the worst possible scheme to switch because of it excessive diffusivity, in particular when the interface is parallel to the flow direction

The High Resolution Interface Capturing (HRIC) presented in Muzaferija and Peric (1997) is used as more consequent example of which characteristics are given (3.18a)-(3.18d). The chosen compressive scheme is still the first order upwind, but the high-order scheme is not more intricate and additionally the Courant number actually impact the final flux evaluation.

$$\tilde{\phi}_{\text{Comp}} = \tilde{\phi}_C \tag{3.18a}$$

$$\tilde{\phi}_{\text{HR}} = \begin{cases} \tilde{\phi}_C \text{ if } \tilde{\phi}_C < 0 \\ 2\tilde{\phi}_C \text{ if } 0 \leqslant \tilde{\phi}_C < 0.5 \\ 2\tilde{\phi}_C \text{ if } 0 \leqslant \tilde{\phi}_C < 0.5 \\ \tilde{\phi}_C \text{ if } 1 < \tilde{\phi}_C \end{cases} \tag{3.18b}$$

$$\omega(\theta) = \sqrt{|\cos\theta|} \tag{3.18c}$$

$$\tilde{\phi}_f = \begin{cases} \tilde{\phi}_\theta \text{ if CFL} < 0.3 \\ \tilde{\phi}_C + \left(\tilde{\phi}_\theta - \tilde{\phi}_C\right) \dfrac{0.7 - \text{CFL}}{0.7 - 0.3} \text{ if } 0.3 \leqslant \text{CFL} \leqslant 0.7 \\ \tilde{\phi}_C \text{ if } 0.7 < \text{CFL} \end{cases} \tag{3.18d}$$

A non exhaustive list of such methods include SURFER Lafaurie et al. (1994), CICSAM Ubbink and Issa (1999), STACS Darwish and Moukalled (2006), FBICS Tsui et al. (2009), CUIBS Patel and Natarajan (2015) for which furter details can be found in their respective article.

3.1.4.2 Interface advection

It should be noticed that all the characteristics embedded in the combination of compressive and high-order anti-diffusive schemes, in particular the boundedness, are exclusively established in 1D configuration and the transition to higher dimension is not guaranteed to preserve them. For this reason, a double sweeping mechanism similar to the one used in Eqs. (3.8b)-(3.8b) is usually employed to carry out the interface advection.
Interestingly, using the projection method in Jasak (1996), the methods can be adapted to arbitrary meshes it however requires the ability to move pass the splitting technique. Several results have been produced since then using reconstruction methods on non-cartesian meshes but unfortunately, no mentions to the exact strategy used to perform the actual advection are proposed. The predictor-corrector algorithm presented in Ubbink and Issa (1999) is, to the best of our knowledge, the only strategy proposed so far that clarifies in detail a manner to tackle this issue.

3.1.4.3 Numerical results

Even if, per say, flux reconstruction methods as numerical techniques are as old as interface reconstruction methods, their comprehensive integration into fully coupled VOF solver present a lesser maturity. This explains in part the scarcity of numerical results involving industrial configuration. Plethora of comparative simulations have been performed to assess the performance of these methods two and one dimensional settings, mostly on canonical configuration such as Zalesak's disc, shear advection test or Rayleigh-Taylor instabilities.

Nonetheless, the two recent results are exposed here prove the viability of reconstruction techniques for VOF methods as numerical tool to address complex two phase flows

Fig. 3.13 presents a breaking dam simulation, perfomed with the CICSAM flux reconstruction method. The broken dam is represented by a wall with a partial hole and secondary obstacle is placed downstream of the dam. The simulation manages to capture the collision between the backward flow created after the water impacts the downstream wall and the water retained by the trapezoidal obstacle and the obstacle itself.

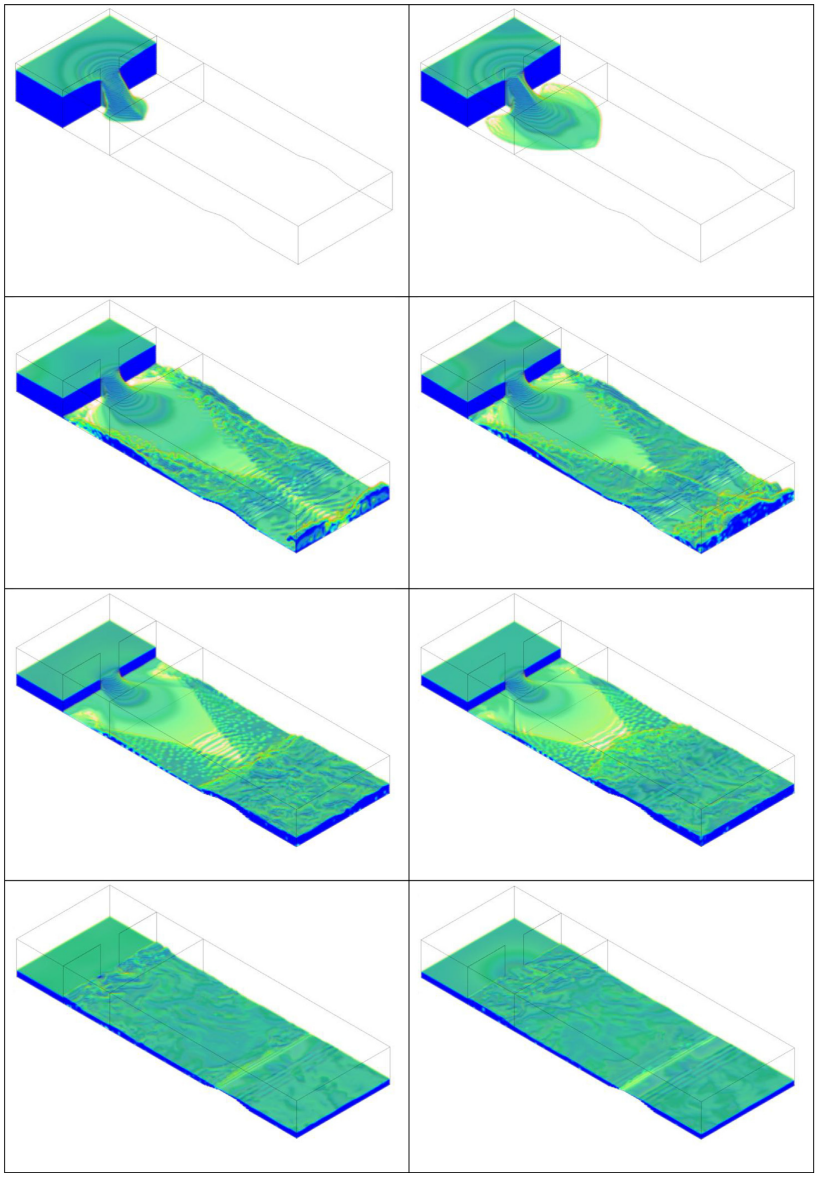

Figure 3.13: *Time evolution a three-dimensional water flow during the breaking of a damn with a secondary downstream obstacle from Issakhov and Imanberdiyeva (2019)*

Fig. 3.14 displays the time evolution of a water-air interface when the lower liquid is impacted

by a solid hemisphere in three dimensions. In particular, the velocity and penetration depth of the solid present a particularly good agreement with experiments, more so than theoretical results. A modified version if the HRIC method, developed in Heyns et al. (2013) is used as to perform the flux reconstruction.

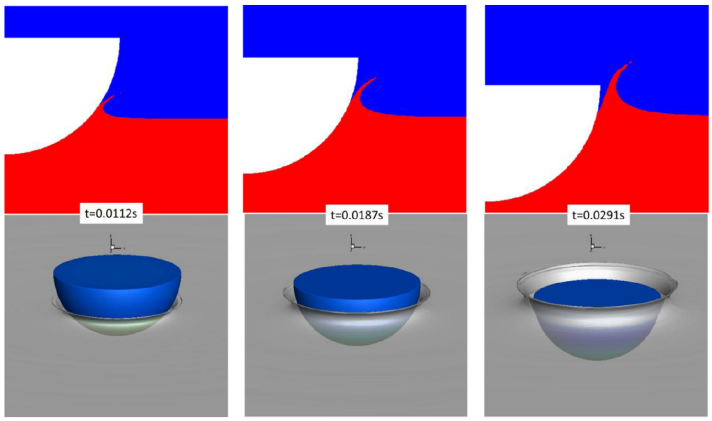

Figure 3.14: *Snapshot of a three-dimensional hemisphere impacting an initially quiescent water plane with air above from Nguyen and Park (2017)*

3.2 Level-Set methods

3.2.1 Historical overview

The foundations of the Level-Set methods have been laid down in the late 1980's and early 1990's upon the preliminary work of mathematician James Albert Sethian developed in the early 1980's, see Sethian (1982); Sethian (1984); Sethian (1985).
Similarly to Front-Tracking methods, the Level-Set methods are not inherently designed to tackle problem involving multiphase flows but find usage in areas spanning from boiling flows Son and Dhir (1998); Sussman (2003); Tanguy et al. (2007), three-phase flows Yap et al. (2017), crystal growth and dendrite solidification Sethian and Straint (1992); Chen et al. (1997); Ohtsuka et al. (2015), flames and shocks propagation Stewart et al. (1995); Aslam et al. (1996); Osher and Fedkiw (2006) to image analysis and computer vision Malladi et al. (1995); Zhang et al. (2010); Wu and He (2015). In the rest of the current section the focus is however placed onto multiphase flows application and more specifically two-phase flows cases with an emphasis regarding liquid-gas configurations.

The viability of Level-Set is deeply rooted in both the notion of viscosity solution, thoroughly investigated in Crandall and Lions (1983); Crandall et al. (1984); Crandall and Lions (1984a); Crandall and Lions (1984b) and its links to curve and surface evolution theory (see Sethian (1985)) front propagation (see Sethian (1982); Sethian (1987)) and hyperbolic laws conservation (see Sethian (1984)). All these previous aspects have been merged to achieve the basis for the Level-Set methods in Osher and Sethian (1988) where first was introduced the idea to track a discontinuity as a specific level-set of a smooth enough (Lipschitz continuous) function, referred to as φ in this section. As it is further explored in Sec. 3.2.2.4 and Sec. 3.2.3.1,

Level-Set methods essentially formulate the interface propagation problem in terms of a time-dependent initial value problem for the level-set function φ.

From Osher and Sethian (1988), the ensuing works during the 1900's focused on improving the methods to solve this problem. A preliminary improvement was introduced in Chopp (1991), at that time for image processing, to limit the calculations involving φ to a restrained region of interest in order to reduce computational cost. The first major adding came in Sethian and Straint (1992) where the authors noticed the necessity to extend interfacial variable (most of the time the velocity), to the rest of the domain. A second major modification came in Sussman et al. (1994) where the authors introduced a new method to reinitialize φ as signed distance throughout the calculations. These three main ideas were then first combined in Malladi et al. (1994) and clarified in Adalsteinsson and Sethian (1995) where the Narrow Band approach was introduced. The overall method has been successfully applied to two-phase flows Sussman et al. (1994); Chang et al. (1996), flame propagation Rhee et al. (1995) and crystal growth Chen et al. (1997). It should be noticed that different strategies are used to extend the interfacial velocity depending on the physics to be simulates
The introduction of the Fast Marching method in Sethian (1996) provided a powerfull tool to solve stationary boundary-dependent that is used jointly with the Narrow Band to greatly simplify and diminish the cost the velocity update. In Adalsteinsson and Sethian (1999), a new strategy was proposed to extend the velocity so as to ensure that φ doest not require reinitialization. This new strategy can be applied, in principle, arbitrarily to any type of physics.

In parallel of these improvements, the extensive work in Evans et al. (1991); Evans and Spruck (1992a); Evans and Spruck (1992b); Evans et al. (1991); Evans et al. (1991); Evans and Spruck (1995) allowed to further ground the theoretical legitimacy of the Level-Set approach. One interesting result is that the motion obtaind with LS methods is the asymptotic motion that would be obtained using a Phase-Field modeling that no superfluous stiffness is required with LS. In particular, Phase-Field models have better odds to ill-behave on poorly resolved meshes, contrary to their LS counterparts.
The design of the Ghost-Fluid method in Fedkiw et al. (1999) has allowed the LS method to drastically increase the precision of the simulations as it prevents the smearing of the interface caused by conventional bounded numerical scheme. It has been consistently employed for incompressible simulation ever since and has even permitted to contemplate compressible simulation as the study of droplet motion induced by Stefan flow in Tanguy et al. (2007) or the droplet-shock interaction in Houim and Kuo (2013), greatly improving upon the early attempts at compressible flow simulation with LS method such as in Mulder et al. (1992)

Starting the 2000's, Level-Set methods have been extensively used, in particular for two phase flow simulations. As LS methods are known to face issues regarding mass conservation, a crucial point for fluid simulations, efforts have been made in order to alleviate this drawback. Several approaches rely primarily on the choice of specific advection schemes. For instance a custom finite volume scheme is employed in Shepel and Smith (2006) where as mixing and exchange rules are used to evaluate the fluxes in Hu et al. (2006).
In Enright et al. (2002), the authors combine a LS approach with particle markers that allow to correct error convection *a posteriori* by locally modifying the values of φ

The most preeminent strategy has been introduced in Olsson and Kreiss (2005); Olsson et al. (2007) where a smeared Heaviside function is favored over the classic signed distance to act as the level set function. This strategy was reinvested in and adapted by the authors in Desjardins et al. (2008) using a finite difference framework and later a Discontinuous Galerkin approach in Owkes and Desjardins (2013). A new reinitialization procedure, adapted to the new level set function, has been proposed in Mccaslin and Desjardins (2014).
In Zhao et al. (2014), the authors decided to combine the smeared Heaviside function of Olsson for its conservative properties with the classic signed distance function for its geometrical precision.
Lately, a new procedure based on the local curvature of the interface appeared in Luo et al. (2015) which, in principle, should ensure an absolute mass conservation of the liquid phase.
Contrary to the VOF methods, no formulation of the LS method inherently ensure mass conservation and even if most studies settle with the smeared Heaviside function of Olsson, this problem remains a modeling challenge to this date.

In the rest of this section, building blocks of the Level-Set methods are explored. First, the representation of the interface is detailed along with its advection equation, as well as the complete modeling of the fluid.
As done for the Front-Tracking and the Volume-of-Fluid methods, the actual resolution of the Navier-Stokes/Euler equations are omitted, for reasons detailed in the introduction of this chapter, so as to focus on the interface advection.
The strategies used for the reinitialization and extension problem are then presented as these steps are primordial to achieves correct simulation.
Lastly, some of the methods to improve mass conservation are discussed.

3.2.2 Modeling and equations

3.2.2.1 The Level-Set function

The Level-set methods track the movement of an hypersurface (a line in two dimensions, a surface in three dimensions) Γ by embedding the later in the level set of a function φ, usually the zero contour, such as the time evolution of Γ is described by:

$$\Gamma(t) = \{\boldsymbol{x} \in \Omega \mid \varphi(\boldsymbol{x}, t) = 0\} \tag{3.19}$$

Eq. (3.19) implies that φ is a space and time dependent function over the whole spatial domain Ω. The corresponding situation is illustrated Fig. 3.15.
As the zero contour of φ represent the interface, in a two-phase flow configuration with fluid 1 and fluid 2, the different constituent of the flows are characterized through the properties:

$$\begin{cases} \varphi(\boldsymbol{x}, t) > 0 \text{ for } \boldsymbol{x} \in \text{ fluid 1} & \text{(3.20a)} \\ \varphi(\boldsymbol{x}, t) = 0 \text{ for } \boldsymbol{x} \in \Gamma & \text{(3.20b)} \\ \varphi(\boldsymbol{x}, t) > 0 \text{ for } \boldsymbol{x} \in \text{ fluid 2} & \text{(3.20c)} \end{cases}$$

As such, following Γ through time merely mounts to tracking the zero contour of φ. Conveniently, φ can also be used to evaluated interfacial geometric quantities such as the normal

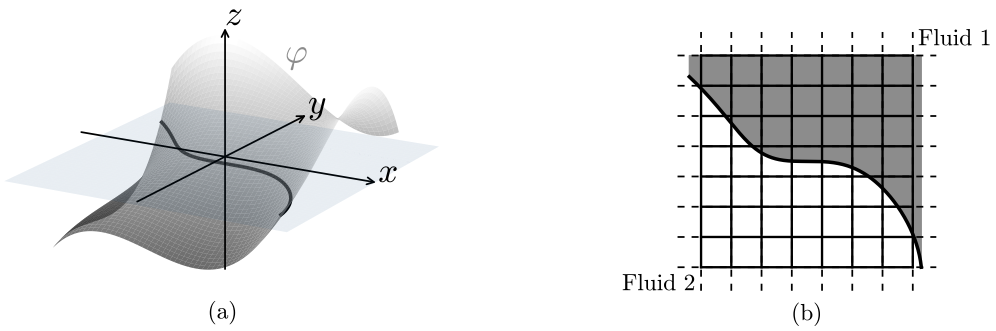

Figure 3.15: *Schematic representation of the Level-Set mechanics with function φ in a 2D setting: (a) the full surface defined with it zero level set, (b) the corresponding interface Γ*

vector $\boldsymbol{n}$ and the mean curvature κ using Eqs. (3.21a)-(3.21b).

$$\boldsymbol{n} = \frac{\boldsymbol{\nabla}\varphi}{|\boldsymbol{\nabla}\varphi|} \tag{3.21a}$$

$$\kappa = \boldsymbol{\nabla}\cdot\boldsymbol{n} = \boldsymbol{\nabla}\cdot\left(\frac{\boldsymbol{\nabla}\varphi}{|\boldsymbol{\nabla}\varphi|}\right) \tag{3.21b}$$

3.2.2.2 Mechanical equations

We consider here, in a first approach, a system composed of two non miscible fluids or a single fluid in its liquid and vapor form. The first and second components (the liquid and vapor phase if so) are referred to with the subscripts 1 ans 2 respectively. Initially, the Navier-Stokes equations solved for an incompressible, inviscid fluid are given Eqs. (3.22)-(3.23) where ρ, μ, P and $\mathbf{v}$ are the fluid density, viscosity, pressure and velocity and $\boldsymbol{g}$ represents the potential body forces.

$$\boldsymbol{\nabla}\cdot\mathbf{v} = 0 \tag{3.22}$$

$$\rho\frac{d\mathbf{v}}{dt} = -\boldsymbol{\nabla}P + \boldsymbol{\nabla}\cdot\left(\mu\left(\boldsymbol{\nabla}\mathbf{v} + \boldsymbol{\nabla}\mathbf{v}^{\mathrm{T}}\right)\right) + \rho\boldsymbol{g} \tag{3.23}$$

The properties of the fluid are accessed on either sides on the interface using the marker function I in FT methods or the volume of fluid ϕ in VOF methods. This can be emulated in LS method by introducing a indicator function Φ that should intuitively be defined as a Heaviside function H such as:

$$\Phi(\boldsymbol{x},t) = H(\varphi(\boldsymbol{x},t)) = \begin{cases} 0 & \text{if } \varphi(\boldsymbol{x},t) < 0 \\ \dfrac{1}{2} & \text{if } \varphi(\boldsymbol{x},t) = 0 \\ 1 & \text{if } \varphi(\boldsymbol{x},t) > 0 \end{cases} \tag{3.24}$$

and the physical variable then read:

$$\rho(\boldsymbol{x},t) = \Phi(\boldsymbol{x},t)\,\rho_l + (1-\Phi(\boldsymbol{x},t))\,\rho_v \tag{3.25a}$$
$$\mu(\boldsymbol{x},t) = \Phi(\boldsymbol{x},t)\,\mu_l + (1-\Phi(\boldsymbol{x},t))\,\mu_v \tag{3.25b}$$
$$c_p(\boldsymbol{x},t) = \Phi(\boldsymbol{x},t)\,c_{p_l} + (1-\Phi(\boldsymbol{x},t))\,c_{p_v} \tag{3.25c}$$
$$\dots$$

However, this sharp representation can cause numerical difficulties and is prone to produce numerical oscillation in the simulation unless very specific numerical schemes are used.
For this reason, a smoothed Heaviside function H_ε is preferred, as developed in Eq. (3.26) where coefficient ε permits to control the width of the interface (similarly to PF method) and thus allows to ensure that the interface is always resolved on the mesh. Indeed, with this definition of H_ε, the interface has approximatively a width given by Eq. (3.27).

$$H_\varepsilon(\varphi) = \begin{cases} 0 & \text{if } \varphi < -\varepsilon \\ \frac{1}{2}\left[1 + \frac{\varphi}{\varepsilon} + \sin\left(\frac{\pi\varphi}{\varepsilon}\right)\right] & \text{if } |\varphi| \leqslant \varepsilon \\ 1 & \text{if } \varphi > \varepsilon \end{cases} \tag{3.26}$$

$$w = \frac{2\varepsilon}{|\boldsymbol{\nabla}\varphi|} \tag{3.27}$$

The physical values in Eqs. (3.25a),... are remplaced in the Navier-Stokes equations (3.22)-(3.23) by their smoothed counterparts ρ_ε, μ_ε, etc... with $\rho_\varepsilon = \Phi_\varepsilon(\boldsymbol{x},t)\,\rho_l + (1-\Phi_\varepsilon(\boldsymbol{x},t))\,\rho_v$ and $\Phi_\varepsilon = H_\varepsilon(\varphi)$.
For possible quantities concentrated at the interface such as the surface tension or the interfacial heat flux when considered, the formulation also allows to define a smoothed delta function δ_ε as follows:

$$\delta_\varepsilon(\varphi) = \frac{dH_\varepsilon}{d\varphi} \tag{3.28}$$

As already evoked, the wide variety of discretization and numerical methods which used to solve these equation are not expanded upon here and curious reader can refer to the different sources cited in this section for concrete cases.
The emphasis is thus put on the different steps that allow to properly update the level-set function with provide all the information needed to solve the mechanical equations.

Compressible simulations
In the framework of LS methods, the treatment of compressible fluids entirely rely on the Ghost-Fluid method (GFM) introduced in Fedkiw et al. (1999); Fedkiw (2002) which was designed from the beginning as a support strategy for LS methods to evolves towards compressible simulations.
Nowadays, the GFM is used in combination within a much wider variety of numerical framework.

3.2.2.3 The interface advection

The motion of Γ is induced by an interfacial velocity field $\boldsymbol{v}_I$ that usually depends on the time and position at which the observation is done. It however can be defined in a more complex fashion, depending on the geometry of the interface such its curvature, normal and/or tangent vectors) as well as external physical parameters (pressure jump, density jump, etc...). As shown in Osher and Sethian (1988), the time evolution of φ can be tracked using the partial differential equation Eq. (3.29a) along with an initial condition Eq. (3.29b).

$$\frac{\partial \varphi}{\partial t} + \mathbf{v}_I \cdot \boldsymbol{\nabla} \varphi = 0 \tag{3.29a}$$

$$\varphi(\boldsymbol{x}, 0) = \varphi_0(\boldsymbol{x}) \tag{3.29b}$$

By defining the normal velocity at the interface $\mathrm{v}_n = \boldsymbol{n} \cdot \mathbf{v}_I$, Eq. (3.29a) can be reformulated in a more convenient form:

$$\frac{\partial \varphi}{\partial t} + \mathrm{v}_n \left| \boldsymbol{\nabla} \varphi \right| = 0 \tag{3.30}$$

In the specific cases where $\mathrm{v}_n = \mathrm{v}_n(\boldsymbol{n})$, Eq. (3.30) becomes a first order Hamilton-Jacob equation for which plenty of theoretical justification (see Evans et al. (1991); Evans and Spruck (1992a); Evans and Spruck (1992b); Evans and Spruck (1995)) as well as numerical result (see Evans and Spruck (1992b)) have since been produced.

3.2.2.4 Requirement for an efficient LS method

Whereas Front-Tracking, Volume-of-Fluid and Phase-Field methods have foster approaches with fundamental differences, Level-Set methods share a very consistent basis which make them substantially easier, both to describe but also to actually implement them numerically. Early on in the development of the Level-Set methods, several key points have been identified as critical and they transpire through the description made in the previous paragraphs.

Firstly, an appropriate numerical scheme, with theoretical background, must be chosen to solve Eq. (3.30). In particular, when the smoothness of the solution is lost, the correct weak solution, of which existence in ensured by hyperbolic conservation laws and studied in Sethian (1982); Sethian (1984); Sethian (1985), must effectively be selected.

Secondly, since the level set approach above requires an additional space dimension to carry the embedding of the interface Γ, it can be computationally inefficient for many problems. This is can be by limiting the region over which level set interface calculation are performed, such as in Adalsteinsson and Sethian (1995)

Thirdly, whereas the level set function φ is intrinsically defined over the whole physical domain, this is not often the case for the interface velocity $\boldsymbol{v}_I$ depended on the physical phenomenon that is studied. If need be, one must be able to expand the definition of the interfacial velocity (and potentially other relevant interfacial variables) to the whole domain as well, or at least, to the whole region over which Eq. (3.29a) is solved.

Finally, as the interface width directly depends on the gradient of the level set function by virtue of Eq. (3.27), it can be advantageous, if not necessary, to maintain this gradient constant (by convenience, equal to 1). Doing so amounts to ensuring that the level set function remains a signed distance throughout the simulation, which unfortunately can not be ensured intrinsically by the advection scheme. Therefore a method has to be designed to rectify the drift of ϕ from a proper signed distance function.

The first point is put to rest for this description for reasons already mentioned, the second and fourth points are briefly evoked hereinunder, the third point is however treated in separate paragraph it is a crucial element that further detailing be adequately explained.

The Narrow Band approach

Regarding the limitation of the interfacial calculations to the vicinity of Γ, a similar issue is also encountered, to a smaller scaler, for the FT and VOF methods. By design, these two classes of methods already have a limited area over which interfacial calculations are done: FT methods already have markers on the interface and VOF methods, either by interface of by flux reconstruction, literally need to perform calculation only at the interface. The matter of limiting the calculation area, when it does, only occurs for the solving of the mechanical equation but not for the interface advection.

However, this is not the case for LS method since Eq. (3.30) is solved as it is. Obviously, having φ defined provides non negligible advantages such as the faculty to evaluate the interface normal and curvature everywhere in the domain and not solely at the interface (where FT methods must deploy strategies such as Fast Marching methods to extend these two quantities from the interface). The price to pay however is to have to solve Eq. (3.30) well.

Of course, this leads to unnecessary additional computational time and this issue was spotted early on and addressed in Chopp (1991). The method was improved in Malladi et al. (1994) and to some extent finalized in Adalsteinsson and Sethian (1995) as most modern installments of LS method rely on the approach this later work introduced known as the narrow band approach.

The method is pretty straightforward and consists in defining a "narrow band" around the interface of a fixed width as depicted in Fig. 3.16 and to perform level set advection, distance reinitialization and velocity extension only in this band.

The width of the band is predicated on the cases to be treated and on the numerical schemes that are used because it has at least to accommodate the stencil of the schemes plus a safety length. The wider the band, the greater the point where calculation must be done, the more precise the reinitialization and extension processes are and thus the less often they need to be performed as the quality of the approximated φ and $\boldsymbol{v}_I$ deteriorates slowly. Conversely, narrowing the band will reduce the calculations to be done at one iteration but will augment the frequency at which they have to be done. A balance must be found by the user.

Of course, this requires the ability to locate the interface. Granted that its initial position is none, the calculations are usually done such as the interface cannot move for more than a computational mesh cell, therefore from one time iteration to the other, only a limited number of position have to verified the interface.

It must be emphasized that the Narrow band is not a fancy addition to the method but constitute a real source of saving in terms of computational power. Some simulations, in

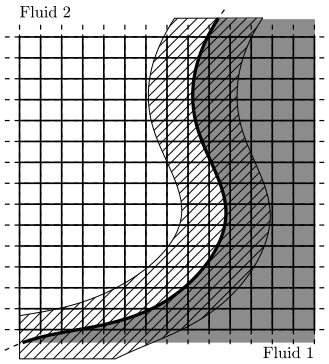

Figure 3.16: *Schematic representation of the Narrow Band approach; the extension, reinitialization and advection are only performed in the hatched area*

particular in 3D configuration, are only conceivable thanks to this approach.

Variable extension from the interface

In most problem addressed with LS methods, the interface velocity $\mathbf{v}_I$ is only defined at the interface and little to no direct link with the components surrounding it. For such cases, it is necessary to extend the velocity to the rest of the domain to solve the advection equation for φ.
In fluid simulation it is not the cases as the interface velocity directly relates to the flow velocity and $\mathbf{v}_I$ can and must be readily used in Eq. (3.29a).
However, a brief overview of the different methods available to perform this task seemed beneficial to the present description. Moreover, depending on the physics treated, other variables than the velocity may be needed in the rest of the computational domain, even for fluid simulations.

Classically, three approaches exist to extend a variable f from the interface.
The first one, used in Malladi, consists in finding the point of the interface the closest of the point where f must be evaluated and use a simple extrapolation. Noticeably, this method requires to locate the interface and thus can be onerous despite a limited accuracy.
A more precise method, introduced in Chen et al. (1997) consists in solving the partial differential equation up to a steady state. This generate a extended variable f^{ext} that evolves normally to the interface and the smears out rapidly as the distance to the interface grows.

$$\frac{\partial f}{\partial \tau} + S(\varphi)\frac{\boldsymbol{\nabla}\varphi}{|\boldsymbol{\nabla}\varphi|} \cdot \boldsymbol{\nabla} f^{\text{ext}} = 0 \tag{3.31}$$

The last method is exclusively dedicated to the velocity extension and is closely related to the distance reinitialization problem. It is presented in the paragraph **Extension velocity correction**.

3.2.3 Reinitialization and extension

3.2.3.1 Distance initialization and reinitialization

When it comes to the initial conditions in Eq. (3.29b), any sufficiently smooth function φ satisfying the conditions Eqs. (3.20a)-(3.20c) can be used. A common and sound choice is usually to define φ_0 as signed distance function to the interface, i.e., given a norm $\|\cdot\|$ defined for $\mathbb{R}^N$ (N being the number of dimensions of the problem), a distance function $d^{\Gamma}_{\|\cdot\|}$ to Γ is defined as:

$$\forall \boldsymbol{x} \in \Omega,\ d^{\Gamma}_{\|\cdot\|}(x) = \min\left\{\|\boldsymbol{x} - \boldsymbol{x}_{\Gamma}\| \,\|\boldsymbol{x}_{\Gamma} \in \Gamma\right\} \tag{3.32}$$

Classically the euclidian norm is used with the associated euclidian distance d^{Γ}. The signed distance φ_0 can consequently be defined by:

$$\begin{cases} \varphi_0(\boldsymbol{x}) & = +d^{\Gamma}(x) \text{ for } \boldsymbol{x} \in \text{ fluid 1} \\ \varphi_0(\boldsymbol{x}) & = 0 \text{ for } \boldsymbol{x} \in \Gamma \\ \varphi_0(\boldsymbol{x}) & = -d^{\Gamma}(x) \text{ for } \boldsymbol{x} \in \text{ fluid 2} \end{cases} \tag{3.33}$$

Although it may seem arbitrary, the choice of initializing φ_0 as a signed distance proves particularly efficient from a theoretical as well as a practical point of view. Ideally, one would like φ to preserve the qualities of signed distance function, which means that at any time the Eikonal equation Eq. (3.34) must be satisfied.

$$|\boldsymbol{\nabla}\varphi(\boldsymbol{x}, t)| = 1 \tag{3.34}$$

As it so happen, the authors in Barles et al. (1993) formally proved that Eq. (3.30) and Eq. (3.34), that is to say a level set function, even perfectly advected using Eq. (3.30) has no reason whatsoever to remain a signed distance function. Ever since, substantial efforts have been made to overcome this issue. Those are motivated by several reasons.
Firstly, a signed distance function is usually very regular and smooth, in particular in the vicinity of the interface. This reduces the numerical difficulties associated to the advection of said function. It also ensures that the normal vector in Eq. (3.21a) and the interface curvature in Eq. (3.21b) can be calculated accurately
Secondly, the use of the Narrow Band approach can cause a lost in accuracy if a proper signed distance function is not used. Indeed, since the calculations are concentrated near the interface, one has to ensure that this reduced amount of calculations are conducted as precisely as possible. Thirdly, if φ remains a signed signed distance function then by definition $|\boldsymbol{\nabla}\varphi| = 1$ which should ensure that the interface keeps a designated width.

The necessity to reinitialize the level set function was first introduced in Chopp (1993) for image processing purposes. The author used a direct approach where the signed distance function was calculated from scratch whenever the treatment was needed using Eq. (3.32), this lead to very precise calculations. The major difficulty associated with this approach is that the actual zero level set of φ must be retrieve in order to compute the distances. It goes without saying that this approach was very time consuming, even more so if the reinitialization was performed at every time step. In practice, the author greatly reduced the computational overload by using a narrow band approach for his simulations.

Pseudo-time correction

Reinvesting some results from Rouy and Tourin (1992), the authors in Sussman et al. (1994) proposed a new method that does not require to formally locate the interface. By solving the partial differential equation Eq. (3.35) for a function $f(\boldsymbol{x}, t)$ and a time invariant function g up to a steady state ($\tau \to \infty$), the solution respects $|\boldsymbol{\nabla} f_0| = g(\boldsymbol{x})$

$$\frac{\partial f}{\partial \tau} + |\boldsymbol{\nabla} f| = g(\boldsymbol{x}) \tag{3.35}$$

Applied to the signed distance function, of which sign must be preserved and using $g(\boldsymbol{x}) = 1$, the equation becomes:

$$\frac{\partial \eta}{\partial \tau} + S(\varphi_0)(|\boldsymbol{\nabla}\eta| - 1) = 0 \tag{3.36a}$$

$$\eta(\tau = 0) = \varphi_0 = \tilde{\varphi}(\boldsymbol{x}, t) \tag{3.36b}$$

where S is the sign function and $\tilde{\varphi}$ is the "incorrect" level set function, after advection. Solving Eq. (3.36a) leads to a solution φ that satisfies $|\boldsymbol{\nabla}\varphi|$ and such as $\{\boldsymbol{x}|\varphi(\boldsymbol{x}, t) = 0\} = \{\boldsymbol{x}|\tilde{\varphi}(\boldsymbol{x}, t) = 0\}$, in other word, it creates a level-set function which is a signed distance and which preserves the sign and the zero level of $\tilde{\varphi}$ as predicted by the advection.
This approach is very effective as long as the prediction $\tilde{\varphi}$ is smooth enough which is sadly not always the case. In Sussman et al. (1994), it is proposed to use a smoothed sign function S_α as presented Eq. (3.37) to smear out the defaults of $\tilde{\varphi}$.

$$S_\alpha(\varphi_0) = \frac{\varphi_0}{\sqrt{\varphi_0^2 + \alpha^2}} \tag{3.37}$$

where α is a small smoothing coefficient, usually taken equal to the mesh size Δx. Eq. (3.36a) becomes:

$$\frac{\partial \eta}{\partial \tau} + S_\alpha(\varphi_0)(|\boldsymbol{\nabla}\eta| - 1) = 0 \tag{3.38}$$

The idea was even improved on in Peng et al. (1999) who proposed Eq. (3.40) where the smeared sign function S_α in Eq. (3.39) is actually applied directly to η. The authors show that this formulation offers much better results when $\tilde{\varphi}$ is very far of a sign function.

$$\bar{S}_\alpha(\eta) = \frac{\eta}{\sqrt{\eta^2 + |\boldsymbol{\nabla}\eta|^2 \alpha^2}} \tag{3.39}$$

$$\frac{\partial \eta}{\partial \tau} + \bar{S}_\alpha(\eta)(|\boldsymbol{\nabla}\eta| - 1) = 0 \tag{3.40}$$

In most studies, Eq. (3.38) is preferred despite is lesser precision for computational reasons. Indeed, when solving Eq. (3.38) in pseudo-time τ, $S_\alpha(\varphi_0)$ has to be evaluated only one time at the beginning whereas in (3.38), $\bar{S}_\alpha(\eta)$ bust be calculated at eat sub-iterations.

Although the position of the interface should not be modified by solving, Eq. (3.38) or Eq. (3.40), the numerical errors in practice often cannot be neglected and can lead to a small deformation of the zero level set predicted by $\tilde{\varphi}$.

For fluid mechanics purposes where the conservative nature of a method is paramount it can constitute a important source of errors.

A first attempt to improve conservation was introduce in Chang et al. (1996) where the author traded Eq. (3.38) for Eq. (3.41) where $\mathcal{A}_0 = \mathcal{A}(\varphi_0)$ and $\mathcal{A}(\eta)$ are the total areas associated to the predicted $\tilde{\varphi}$ and the iteratively corrected η level set functions, κ the curvature defined Eq. (3.21b) and c is a positive constant used to stabilize the calculations.

$$\frac{\partial \eta}{\partial \tau} + (\mathcal{A}_0 - \mathcal{A}(\eta))(-c + \kappa)|\boldsymbol{\nabla}\eta| = 0 \tag{3.41}$$

This method caused a significant increase in the mass conservation for number of iterations slightly higher to similar when compared to more classic reinitialization methods.
Yet another strategy was designed in Sussman et al. (1999) where the authors still modified Eq. (3.39) but this time they ensured a local conservation in each cell by writing:

$$\frac{\partial \eta}{\partial \tau} + S_\alpha(\varphi_0)(|\boldsymbol{\nabla}\eta| - 1) = L\delta_\varepsilon(\eta)|\boldsymbol{\nabla}\eta| \tag{3.42}$$

where the balancing factor l is given in each cell $\Omega_{i,j}$:

$$L_{i,j} = \frac{\int_{\Omega_{i,j}} S_\alpha(\varphi_0)(|\boldsymbol{\nabla}\eta| - 1)\delta_\varepsilon(\eta)\, d\boldsymbol{x}}{\int_{\Omega_{i,j}} |\boldsymbol{\nabla}\eta|\,\delta_\varepsilon(\eta)^2\, d\boldsymbol{x}} \tag{3.43}$$

Another method to ensure conservation was proposed in Russo and Smereka (2000), it requires to locale the position of the interface with $\tilde{\varphi}$ and solve two simpilfied advection equations instead of Eq. (3.38), the first inward, the second backward and ensure everytime that the stencil used in the discretization does not cross the interface, canceling the interaction between the two sides of the interface. Although appealling, this method requires more calculations than the previous one and so far the gain in accuracy has been shown to be limiting and strongly dependend on the scheme used to perform the inward and outward advections.

Extension velocity correction
Another method can be used to ensure that φ remains a distance function. The principle is to embed this condition within the advection equation Eq. (3.29a). By using a specific extension velocity, it is possible to ensure that the properties of φ are preserved. Indeed, if one is to generate a extension velocity ${\mathbf{v}_I}^{\text{ext}}$ such as at any time iteration Eq. (3.44) is respected, it can be shown that the initial distance function φ will remain as such.

$${\mathbf{v}_I}^{\text{ext}} \cdot \boldsymbol{\nabla}\varphi = 0 \tag{3.44}$$

This idea was firstly introduced in Zhao et al. (1996); Peng et al. (1999) as a consequence of using a the limit case of the Narrow Band of Adalsteinsson and Sethian (1995) where the with was of only once cell. Using the Fasting Marching method of Sethian (1996), the authors in Adalsteinsson and Sethian (1999) a fast and efficient method to generate this extension velocity by solving the eikonal equation Eq. (3.44).

It should be noticed that in the prospect of a fuid simulation, this method cannot be applied since the velocity field is already defined in the whole demain Ω by default. The same observation applies for any physical simulation where the velocity cannot be chosen arbitrarily.

Although it is not expanded upon, this approach seemed worth mentionning for is originality and efficiency and for the fact that is it usually a go-to when it can be applied, even for more recent applications.

Overall the matter of distance reinitialization is still a topic actively investigated as demonstrated by the recent studies in Hartmann et al. (2008); Chopp (2009); Hartmann et al. (2010).

3.2.3.2 Early results

Contrary to VOF methods, LS methods have not inherently been designed to simulate two-phase flows. Rather, can virtually be to capture any type of surface (in three dimensions) that evolves in time according to a prescribed equation. It is particularly used in image processing and computer graphics. In that aspect, they stand closer to FT methods that can also theoretically be used for several purposes other than two-phase flow simulation, for instance to follow shocks.
For these reasons, early papers treating about LS methods often focus on their mathematical description, characterization and improvements. Actual applications to two-phase flow modeling became noticeable in the late 1990's and early 2000's, of which two results are presented here.

Fig. 3.17 shows an early fully three-dimensional result studying the behavior of water bubbles in water with different configurations. The fluids are considered inviscid and the density ratio is 816:1 with $We \approx 200$. Configuration (a) focuses on the rise of a single bubble whereas configuration (b) displays the interactions between two bubbles.

Fig. 3.18 presents a comparison between the experimental results from Ashgriz and Poo (1990) and the numerical simulation in Tanguy and Berlemont (2005) of a head-on collision between water droplets. Both the experimental and physical settings involve a density ratio of about 800 with $We = 23$ with bubble radius equal to 400 μm. A very good qualitative agreement is obtained by the simulation, in particular when it comes to predicting the full separation of the droplets without creation of smaller satellites.

3.2.4 Conservative Level-Set methods

3.2.4.1 Strategies to reduce mass loss for Level-Set simulation

The poor mass conservation of the LS methods when compared to VOF methods that are conservative by construction or even FT methods, especially in regard to fluid simulations, is a well known and documented issue, see Chang et al. (1996); Sussman et al. (1998); Tornberg and Engquist (2000); Pai et al. (2009) for some examples.

To address this problem, multiple strategies have been devised throughout the years as LS methods developed. We found that these strategies, for the most part, can be classified into six categories. These six categories are further detailed hereafter but we wanted to draw the attention of the reader on the often possible misleading meaning of the term *conservative* attached to some of the LS methods that can be found in the literature.

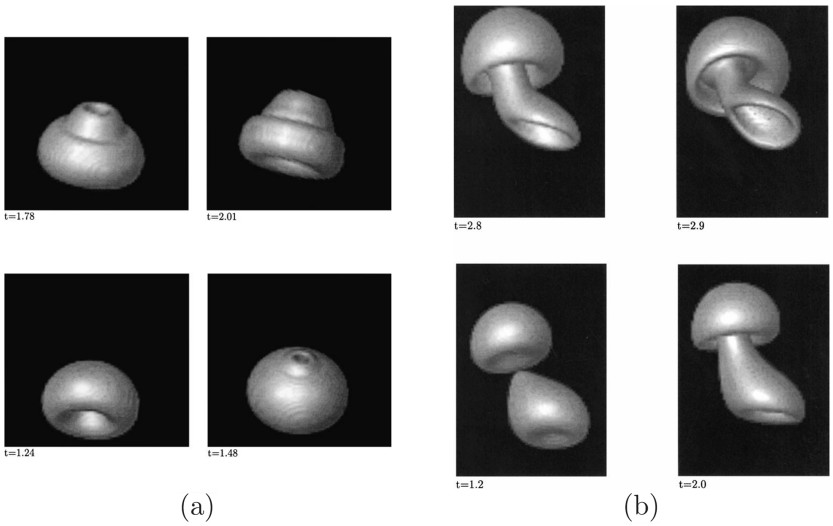

Figure 3.17: *Simulations of inviscid air bubbles in water from Sussman et al. (1999). (a) Single bubble rising. (b) Interaction between two bubbles.*

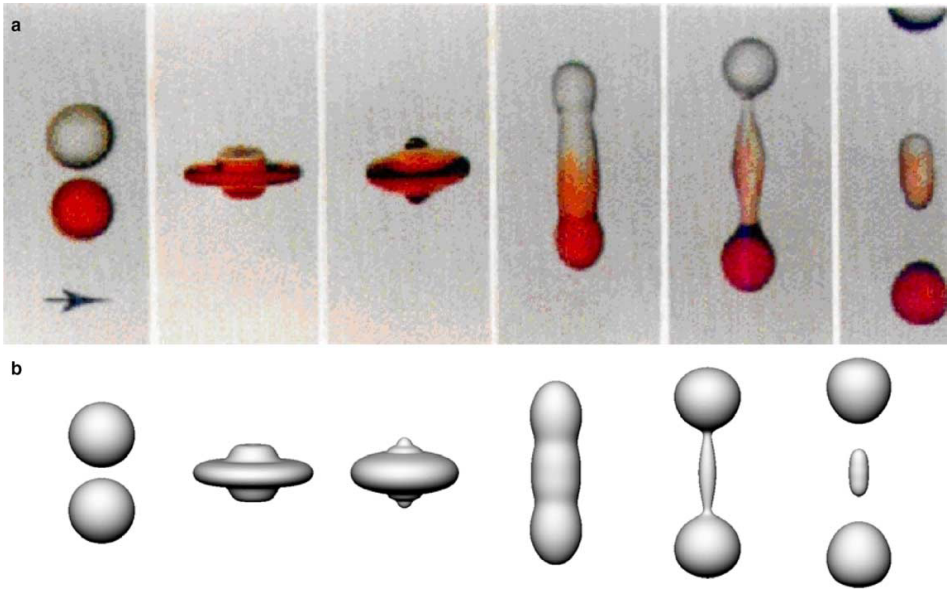

Figure 3.18: *Comparison between experiment and simulation of the head on collision of water droplets from Tanguy and Berlemont (2005). (a) Experimental results from Ashgriz and Poo (1990) (b) Simulation from Tanguy and Berlemont (2005).*

Although substantial improvements have been achieved in the direction of mass loss limitation, no LS method produced to this day is conservative by nature in the sense that VOF methods are. The term *conservative* associated to some LS methods is used in reference to the numerical scheme chosen to advance the level set function in time.

The first method to diminish the mass loss is to increase the mesh resolution. Of course, the narrow band method is still used to limit the area over which the resolution must be increased

to greatly reduce the cost of this approach.
Some approaches are original to the LS community such as the the Adaptive Level Set (ALS) approach from Sussman et al. (1999), the Refined Level Set Grid (RLSG) method in Herrmann (2008), the Accurate Adaptive Level Set (AALS) method found in Kim and Liou (2011) or the Spectrally Refined Interface approach presented in Desjardins and Pitsch (2009)
Some others reinvest in already existing strategies such as the structured adaptive mesh refinement technology used in Nourgaliev et al. (2005) or the adaptation of the octree structure used in Losasso et al. (2006).
For all the improvement they permits, these methods still fall short on mass reduction in region where the interface is not properly resolved and when compared to the others, remain relatively costly in computation power.

A second strategy to reduce mass loss is the use of better numerical schemes for the transport of the level set function. The different schemes that have been used for the discretization of Eq. (3.30) are to numerous to be listed. Some of the most advanced includes high-order weighted essentially nonoscillatory (WENO) schemes used in Nourgaliev et al. (2005); Salih and Moulic (2009), the accurate semi-Lagrangian advection schemes used in Strain (1999); Enright et al. (2005) and the Discontinuous Galerkin schemes employed in Chopp (2009); Owkes and Desjardins (2013).
Still, even high order schemes struggle to offer proper conservation for LS methods.

Some attempts have been made, understandably so, to capitalize of other two-phase flow simulation methods that display better conservation properties the LS methods. They constitute the third category.
The coupled level set and volume-of-fluid (CLSVOF) in Sussman and Puckett (2000) and the coupled volume-of-fluid and level set (VOSET) method in Sun and Tao (2010) are two successful instances where LS and VOF approached have been combined together. The volume of fluid is used to transport the interface in a conservative way and a level set function is then reconstructed to accurately locate the interface and evaluate the normals and curvature. A common critic against these two methods is their complexity especially regarding the reconstruction the level set function from the already geometrically reconstructed interface, a process that lacks accuracy.
The mass-conserving level-set (MCLS) in Van der Pijl et al. (2005) offers another combination of VOF and LS that does not require a geometrical reconstruction of the interface. More recently, the LS approach has also been couple to the Moment-of-Fluid (MOF) method (see Dyadechko and Shashkov (2005)) to design the coupled level set-moment of fluid method (CLSMOF) in Jemison et al. (2013).
Another approach have been used in Enright et al. (2002); Enright et al. (2005); Hieber and Koumoutsakos (2005) where massless particles are used in conjunction with the level set function. By detecting the particles that have crossed the zero level set after a time iteration, it is possible to locate regions where the interface is wrongly reconstructed by the advection and to correct its shape in a theoretically conservative fashion.
All the mentioned methods drastically diverge from the simplicity of the original LS method and generally requires a substantial amount of supplementary calculations since two methods are actually used at once, even if efforts have been made to alleviate this computational cost.

All the previously mentioned categories where focused into applying an "exterior" modification to the LS methods in order to improve their mass conservation capability. Other studies have focused on modifying the internal process of the LS method to achieve the same goal. Presumably, these types of approach should preserve the relative simplicity of implementation and interface topology management associated with the LS method in the first place.
To that effect, a fourth method, already discussed, stem from the improvement of the reinitialization step in LS method. Indeed, theoretically, if a conservative scheme were to be used to solve Eq. (3.30), the fluid volume should be correctly preserved. The actually mass loss occurs during the reinitialization which, if not done carefully, displaces the zero level set of φ and destroys conservation. The reader can refer to Sec. 3.2.3.1 to see the improvements achieved for this approach.
Methods in the fifth category rely on a better expression of the extension velocity and are closely related to that of the fourth category for reasons already mentioned in Sec. 3.2.3.1. An interesting novelty proposed in Ovsyannikov et al. (2012); Sabelnikov et al. (2014) is the addition of a source term to the transport equation of φ that depends on the extension velocity. This new equation embeds the condition of the eikonal equation Eq. (3.44) and since the new source term vanishes at the interface, the zero level set is not affected by its addition. For fluid applications, as previously explained, methods that rely on manipulating the extension velocity can not be used since the advection speed of the level function is already given everywhere by the fluid velocity.
The sixth category builds on a shift in the paradigm used to define the level set function which is no longer a signed distance but rather an smeared Heaviside function, as introduced by Olsson and Kreiss (2005). This approach has a strong impact on the way the other steps of the LS method are applied, it is further explained in the next paragraph. This approach has several appeals: it builds strongly on the already existing LS approach, it comes at a moderate additional computational price and most importantly, it can easily be applied to fluid simulations even in compressible settings.

3.2.4.2 The Accurate Conservative Level-Set method

A new level set function

In a limit case where φ was to be an Heaviside function, if one was able to accurately transport it using Eq. (3.30) with a conservative numerical scheme the area bounded by φ would be exactly preserved and the mass would be conserved. This cannot be achieved for hyperbolic equation such as Eq. (3.30), however, as hinted in Olsson and Kreiss (2005), using a smeared version of an Heaviside function such as H_ε and by defining the interface as the isoline (or isosurface) or value 0.5, a conservative numerical scheme should allow to preserve the shape of the interface and thus to avoid mass conservation errors.

Building from this idea, the authors in Olsson and Kreiss (2005) have designed a new approach for their LS method. In this approach, the level set function ψ is defined as follows:

$$\psi(\boldsymbol{x},t)\begin{cases}0 & \text{if } d^{\Gamma}_{+/-}(\boldsymbol{x}) < -\varepsilon \\ \dfrac{1}{2}\left[1+\dfrac{d^{\Gamma}_{+/-}(\boldsymbol{x})}{\varepsilon}+\sin\left(\dfrac{\pi d^{\Gamma}(\boldsymbol{x})}{\varepsilon}\right)\right] & \text{if } |\varphi| \leqslant \varepsilon \\ 1 & \text{if } d^{\Gamma}_{+/-}(\boldsymbol{x}) > \varepsilon \end{cases} \tag{3.45}$$

where ε is still a factor used to define the interface width and $d^{\Gamma}_{+/-}$ the signed distance function to the interface. In Desjardins et al. (2008), the authors used a similar function given by:

$$\psi(\boldsymbol{x},t) = \frac{1}{2}\left[\tanh\left(\frac{d^{\Gamma}_{+/-}(\boldsymbol{x})}{2\varepsilon}\right)+1\right] \tag{3.46}$$

In either case, the level set function can be used directly to reconstruct the physical variables:

$$\rho(\boldsymbol{x},t) = \psi(\boldsymbol{x},t)\,\rho_l + (1-\psi(\boldsymbol{x},t))\,\rho_v \tag{3.47a}$$
$$\mu(\boldsymbol{x},t) = \psi(\boldsymbol{x},t)\,\mu_l + (1-\psi(\boldsymbol{x},t))\,\mu_v \tag{3.47b}$$
$$c_p(\boldsymbol{x},t) = \psi(\boldsymbol{x},t)\,c_{p_l} + (1-\psi(\boldsymbol{x},t))\,c_{p_v} \tag{3.47c}$$
$$\dots$$

and it will follow the transport equation Eq. (3.30) which, granted that the velocity field used to advance it respects $\boldsymbol{\nabla}\cdot\mathbf{v}_I = 0$ (which is automatically satisfied in a incompressible fluid simulation), can be written in the conservative form:

$$\frac{\partial\psi}{\partial t} + \boldsymbol{\nabla}\cdot(\mathbf{v}_I\psi) = 0 \tag{3.48}$$

A new reinitialization strategy

Just as φ could not be maintained as a signed distance function solving Eq. (3.30) a has to be reinitialized, ψ has to be reinitialized in a corrective step after being advected with Eq. (3.48) so as to maintain its width. In the original presentation of Olsson and Kreiss (2005), the reinitialization of ψ is done by solving the system (3.49a)-(3.49b) in pseudo time until a steady state is achieved.

$$\frac{\partial\eta}{\partial\tau} + \boldsymbol{\nabla}\cdot(\eta(1-\eta)\,\boldsymbol{n}) = \varepsilon\boldsymbol{\Delta}\eta \tag{3.49a}$$
$$\eta(\tau=0) = \psi_0 = \tilde{\psi}(\boldsymbol{x},t) \tag{3.49b}$$

where $\tilde{\psi}$ is the level set function incorrectly transported with Eq. (3.48). This equation is comprise of a compressive flux $\eta(1-\eta)\,\boldsymbol{n}$ on the left hand side that counteracts the numerical smearing of ψ and a diffusive term on the right hand side which prevents the apparition of discontinuities that naturally develop in compressive hyperbolic equations. The balance between the two terms permits to maintain the new level set function ψ to a width close to is initial one of approximatively 2ε.

On the one hand, ε has to be small enough to limit the smearing of the physical values and reduce conservation errors while on the other hand, it has be large enough to ensure that the interface is still properly resolved on the mesh. Usually the choice $\varepsilon = \Delta x$ leads to the most satisfactory results.

In their follow up study Olsson et al. (2007), the authors noticed the discrepancy in Eq. (3.49a) between the compressive term that acts only in the direction normal to the interface and the isotropic diffusion term acting in all direction leading to unbalanced contributions in

the direction tangent to the interface. From that observation, they corrected the reinitialization equation into:

$$\frac{\partial \eta}{\partial \tau} + \boldsymbol{\nabla} \cdot (\eta\,(1-\eta)\,\boldsymbol{n}) = \varepsilon \boldsymbol{\nabla} \cdot ((\boldsymbol{\nabla}\eta \cdot \boldsymbol{n})\,\boldsymbol{n}) \tag{3.50}$$

Where the smeared Heaviside function used for ψ offers better conservation properties, it lacks the regularity of a signed distance function, in particular when in come to reconstructing the geometric properties of the interface. In Eqs. (3.49a) and (3.50), the normal vector is calculated using Eq. (3.51a). Likewise, when needed, the curvature is calculated with Eq. (3.51b).

$$\boldsymbol{n} = \frac{\boldsymbol{\nabla}\psi}{|\boldsymbol{\nabla}\psi|} \tag{3.51a}$$

$$\kappa = \boldsymbol{\nabla} \cdot \left(\frac{\boldsymbol{\nabla}\psi}{\|\boldsymbol{\nabla}\psi\|} \right) \tag{3.51b}$$

However, as shown in Desjardins et al. (2008), spurious oscillation in the ψ-field can lead to poorly calculated normals that can jeopardize the quality of the reinitialization step from Eq. (3.50). In comparison, given the inherent smoothness of a signed distance function, even poorly reconstructed, it leads to better normals calculations. This comparison is even more important in the first sub-iterations of the reinitialization when ψ is still lacking a proper reconstruction. From the observation that a not so precise signed distance function is a better choice than an average quality Heaviside function, the authors Desjardins et al. (2008) suggest to calculate the normals and curvature using Eqs. Eq. (3.52a)-Eq. (3.52b) where ϕ is a signed distance function reconstructed from ψ using a Fast Marching Method algorithm, as again, the quality of ϕ does not need to be optimal.

$$\boldsymbol{n} = \frac{\boldsymbol{\nabla}\phi}{|\boldsymbol{\nabla}\phi|} \tag{3.52a}$$

$$\kappa = \boldsymbol{\nabla} \cdot \left(\frac{\boldsymbol{\nabla}\phi}{\|\boldsymbol{\nabla}\phi\|} \right) \tag{3.52b}$$

The authors noticed a drastic improvement in quality of the ψ reconstruction. In theory, ϕ should be reconstructed at each sub-iteration of Eq. (3.50) for every new and best reinitialized $\psi_k(\boldsymbol{x})$. This would lead to substantial increase in the computational time despite the FMM and as observed on practical case, using only the first value of the ψ reconstruction, namely $\psi_0 = \tilde{\psi}(\boldsymbol{x}, t)$ actually leads to very satisfactory results.

The method designed by Olsson & Kreiss is known as the Conservative Level Set (CLS) and the method instigated in Desjardins et al. (2008) is referred to as the Accurate Conservative Level-Set (ACLS).
With the latter, the author where able to perform the impressive simulation of a turbulent injection representative of Diesel engines, with a density ratio of 40, $Re = 3000$ and $We = 10,000$. This configuration foster the apparition of complex break-up phenomena, droplets and filaments creation and disintegration that the model is able to capture.

It should be noted that, even with the ACLS method, a 3% mass loss is observed in the simulation, which, despite representing a great improvement, remain far from the capacity of natively conservative methods such as VOF or PF.

Figure 3.19: *Simulation of the turbulent atomization of a liquid Diesel with the Accurate Conservative Level-Set method, from Desjardins et al. (2008)*

Recent updates

In the past few years, some attempts at improving the reinitialization step in the context have been proposed. While pointing out that they do no enjoy the same amount of practical test than the CLS or ACLS methods, these methods can prove particularly efficient as they gain maturity.

In Mccaslin and Desjardins (2014), the authors introduced a factor that controls locally the degree up to which the distance function needs to be reinitialized. They used this approach to study the gravitational effects in a horizontal annular liquid-gas flow for several condition as presented in Fig. 3.20. The impact of gravity is notable, especially when comparing cases (a) and (c), in the latter droplet and filaments cannot persist in time are forced back downwards into the main flow.

Figure 3.20: *Simulation of a liquid-vapor flow in an annular cavity with gravitational effects from Mccaslin and Desjardins (2014). (a)* $Re = 3370$, $We = 906$, $Fr = \infty$. *(b)* $Re = 3480$, $We = 967$, $Fr = 4.56$. *(c)* $Re = 3650$, $We = 1070$, $Fr = 1.20$.

In Shukla (2014), the author modified the ACLS method by adopting a gradient formulation and introducing a non-linear mapping allowing to work on the signed distance function, easier to discretized than the smeared Heaviside function. This strategy was used to simulate the impact of liquid droplet on a initially quiescent pool of the same liquid while the upper domain is filled with gas for a density ratio of 1000 and $Wb = 2000$. The strong deformation of the droplet and the pool, shown in Fig. 3.21, in particular the creation of the aftershock ring, are well captured by the method.
Unfortunately the conservation error of the method is not evaluated by the authors for this configuration. For one-dimensional test of shock tubes, the order of convergence in terms of mass conservation is shown to increase by 50% when compared to more classic formulations.

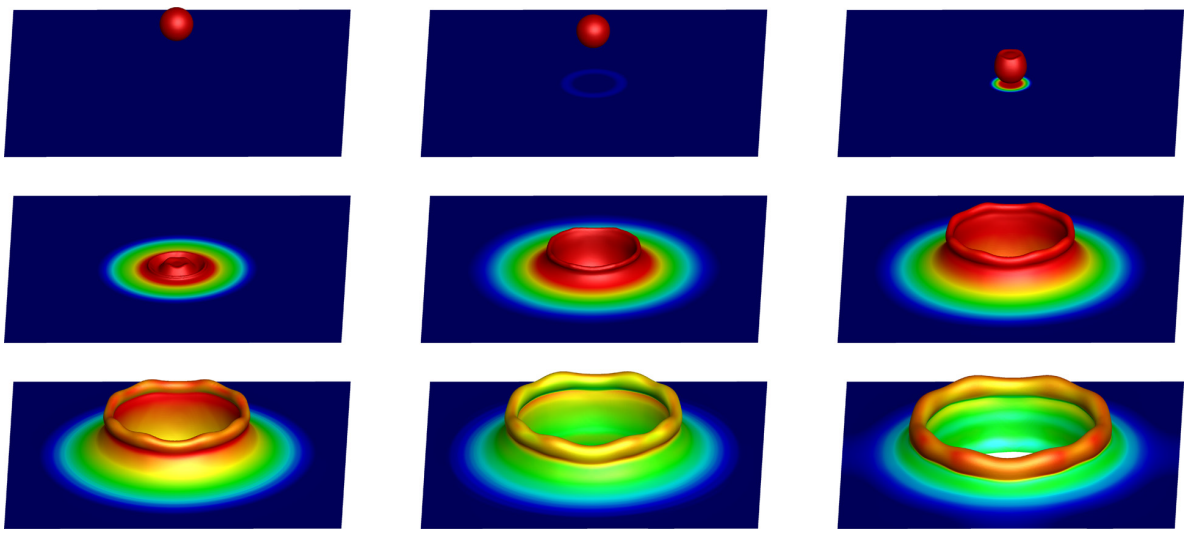

Figure 3.21: *Simulation of a liquid droplet impacting a liquid pool of same nature from Shukla (2014).*

In Wacławczyk (2015), the authors returned to a conservative formulation of the reinitialization equation and determined through extensive numerical investigation the optimal mapping to used between ψ and ϕ to facilitate the calculations.
In Chiodi and Desjardins (2017), the author introduced in compressive term in the non-linear mapping between ψ and ϕ to alleviate the impact of transport errors of ϕ when calculating ψ, preferred to evaluate the interface normal.

Chapter 4

Diffuse interface methods

Chapters 2 and 3 are devoted to the description of several Sharp Interface methods for which an interface is interpreted as a line/surface of discontinuity within the flow where key variables experience a jump in their values. This description is well fitted for a wide variety of applications where the characteristic size of the system is orders of magnitude greater than the scale at which interfacial phenomena occur. In such cases, the interface is assumed to have a zero thickness and is endowed with physical properties such as surface tension, intrinsic interfacial viscosity and thermal conduction that are incorporated within the models by enforcing specific boundary conditions at the interface, for instance a pressure jump for the surface tension following the Young-Laplace equality.
However, in some cases that have been the subject of a growing interest in the last century, the discontinuous point of view introduced by Monge (1787); Young (1805); De Laplace (1806); De Laplace (1807); Gauss (1877) cannot be used to model the interface. Three main reasons can explain a necessary shift in the way the interface is modeled. The first and somewhat less prominent reason is the complex modification of the interface shape that is associated with local phenomena such as capillary and thermal effects. This difficulty is handled to some extent in Sharp Interface methods but the tools introduced to circumvent it can be perceived as *ad hoc*. A second reason comes with the study of intrinsically local phenomena such as the interactions between interfaces and solid walls to determine contact angles. The third reason, of a great interest for this study, is the existence of situations where the interface is actually physically thick, namely for near-critical fluids. All three reasons involve situations where the characteristic length of the physical phenomenon that is studied is comparable to the interface scale, a setting where the sharp approach breaks down.

To address such cases, a new family of methods, the Phase-Field methods (PFM) has emerged in the last decades. The fundamental hypothesis of these methods is to consider that the interface is rather a region of non-zero but finite thickness over which the flow variables evolve rapidly but continuously. The interface is thus said to have been "diffused" in the domain. In PFM, this diffusion of the interface is justified by physical means and is embedded in their formulation. Another family as also been used building on the principle of diffusing the interface, the Multi-Fluid methods (MFM). The latter tends to treat the interface as a heterogeneous region where the different phases mix together. However, it is important to mention that in MFM, the interface is diffused numerically, i.e. the variable used to describe

the interface in the equation are diffused, but physically, the interface is still considered to be sharp. PFM and MFM share similarities with the LS and VOF methods respectively and can be viewed, to some extent, as more physically driven versions of these two sharp approaches. For these reasons, PFM and MFM are often associated together into the class commonly referred to as Diffuse Interface methods (DIM) and are the main focus of this fourth chapter. In opposition to the very localized modeling of Sharp Interface methods, in the eponymous DIM approach, the interface is "diffused" in space. This new perception of the interface has been instigated over a century ago by the likes of Poisson (1831); Gibbs (1878); Rayleigh (1879); van der Waals (1891). If both MFM and PFM are Eulerian by nature, the manner in which the interface is "diffused" allows to separate these two types of methods. In the PFM, an order parameter ϕ, analogous to the level-set function used in LS methods, is introduced to localize the different phases. This parameter varies smoothly in the interface. The difference between LS and PFM comes from the way in which the order parameter ϕ is introduced. Indeed, this introduction is physically motivated for PFM rather than being a mathematical tool to localize the interface while spreading it on a few computational cells as in LS methods. Conversely, MFM use an approach more comparable to the VOF methods where a volume fraction of one of the phase is used to write the different transport equations (mass, momentum, energy) of both phase in the whole domain. A specific transport equation is solved to evolve the volume fraction in time. Yet again, this volume fraction is used in a physically motivated fashion as the set of transport equations that are used take into account the disparities than can exist between the values of the thermodynamic variables for the two phases. The latter can possibly have different velocities, pressures, temperatures and chemical potentials.

As their descriptions show, in Sec. 4.1 and 4.2 respectively, PFM and MFM only share the "diffuse" point of view on the interface and have more aspects in common with their respective Sharp Interface Capturing methods counterparts, LS and VOF methods respectively, than between themselves.
As such, this chapter tries to establish insightful comparisons and connections between the Diffuse and Sharp Interface approaches in general and between their respective representative methods in particular.

4.1 Phase-Field methods

4.1.1 Historical overview

Modern Phase-Field methods are the results of reflections started in the late 1800's and early 1900's regarding the physical nature and the mathematical modeling of phase transition.

Following his work on the thermodynamic description of real fluids, van der Waals proposed an updated theory of capillarity in van der Waals (1891) with an energetic approach building upon the work in Gibbs (1878) where the notion of interfacial excess values was first introduced. In Gibbs and van der Waals theory, surface tension is but the macroscopic manifestation of an energy accumulated at the interface. Additionally, van der Waals reckoned in van der Waals (1893) that the presence of the interface manifested also by the necessity to adopt a higher order of modeling by using an additional independent variable, the density gradient in his work, to describe the thermodynamic variables of the flow. Using his newly found EoS and

the previous considerations, van der Waals proposed a proper formulation for the free energy of a fluid in presence of an interface and evaluated the corresponding excess energy from which the surface tension steamed. In particular, he observed that the excess energy was equally contributed to by the out-of-equilibrium free energy, departing from the free energy of the bulk phases, and the additional energy contribution due to the introduction of the density gradient as an independent thermodynamic variable.
These early thermodynamic considerations have then been consolidated using molecular theory in Rocard (1952) and have been extended by introducing mechanical considerations in Korteweg (1901); Germain (1972); Casal and Gouin (1985) to give birth to the so called Gradient Theory of fluid or the Second Gradient theory.

All the work in the vein of van der Waals early results seem to be essentially devoted to the modeling of liquid-gas interface as they remain closely related to the notion of phase change and often focus on the description of a single fluid flow with a variable density.
However in parallel, another series of Phase-Field methods have emerged in the footsteps of the foundation work in Cahn and Hilliard (1958); Cahn (1959); Cahn and Hilliard (1959) where the authors presented a method initially devoted to the description of phase separation in binary alloys which straightforwardly evolved as a method to study any type of unstable binary mixture forced out of equilibrium.
The method reinvests the key argument presented by van der Waals but uses one component concentration rather than the fluid density as the new independent thermodynamic variable. Therefore, in the Cahn-Hilliard model, the surface tension also results from an accumulation of free energy over a volumetric transition zone where the composition evolves rapidly but continuously and this free energy is composed by both the classic free energy of the components and an additional contribution due to the gradient of the composition. Moreover, the authors also proposed an equation to track the time evolution of the composition.

The theoretical arguments for this equation can be found in the work of Landau (1937); Ginzburg and Landau (1950) who were the first to properly describe the notion of an additional order parameter ϕ and how it could be used to expand the description of the free energy of a given substance to account for complex molecular interactions. In particular, the ensuing equation for the order parameter is based on the assumption that the system will evolve to minimize its total free energy as already established in Gibbs (1878).
This early model has been enriched to study spinodal decomposition in Cahn (1961); Cahn and Hilliard (1971) and crystal growth in Cahn (1961); Kikuchi and Cahn (1962); Cahn and Kikuchi (1966). It has then been adapted in Langer and Sekerka (1975) to study solidification.
A few years later, a complementary model has been introduced in Allen and Cahn (1979), building upon Smoluchowski (1951); Turnbull (1952), to describe the motion of grain boundaries, i.e. defect interfaces that create between small crystallites in a polycrystalline material. The order parameter used is the concentration of one the metallic alloy composing the material. The Allen-Cahn (AC) model offers a simpler alternative to the Cahn-Hilliard (CH) equation, trading a fourth-order space derivative for only a second order but at the expanse of conservative properties. The well-posedness of AC has been first established in Rubinstein and Sternberg (1992) and is linked to the general theory of semilinear parabolic equations detailed in Henry (2006). The inability of the AC model, contrary to the CH model, to conserve the order parameter has been addressed in several work, see Rubinstein and Sternberg (1992);

Bronsard and Stoth (1997); Brassel and Bretin (2011), through the introduction of different Lagrange multipliers to enforce mass conservation, leading to somewhat more complicated models.

The physical properties of AC and CH models have been explored for instance in Carr and Pego (1989); Rubinstein et al. (1989); Heida et al. (2012a) and Novick-Cohen and Segel (1984); Penrose and Fife (1990); Alikakos et al. (1991); Bates and Fife (1993); Ward (1996); Heida et al. (2012b) respectively. The corresponding mathematical properties have also been extensively studied in de Mottoni and Schatzman (1990); Owen and Sternberg (1992); Feng and Prohl (2003); Garcke et al. (2008); Brassel and Bretin (2011) for the AC model and Elliott (1989); Blowey and Elliott (1991); Du and Nicolaides (1991); Debussche and Dettori (1995); Novick-Cohen (1998) for the CH model respectively. A special care has been given in comparing the behavior of said models to more conventional discontinuous descriptions in the limit of very small interface thickness for instance in Modica (1987); Sternberg (1988), more particularly in Fife (1988); Chen (1992); Kohn et al. (2006); Kohn et al. (2007); Zhang and Du (2009) for the AC model and in Pego (1989); Alikakos et al. (1994); Anderson and McFadden (1997); Lowengrub and Truskinovsky (1998) for the CH model. These papers show that both approaches consistently converge towards well studied discontinuous models for the interface such as mean curvature flows or Hele-Shaw flows. Some papers, mainly focusing on binary alloys, have merged the AC and CH equations to produce a more complete model that can been found in Cahn and Novick-Cohen (1994); Dal Passo et al. (1999); Novick-Cohen (2000); Gokieli and Marcinkowski (2003).
Both models have been used to study disparate physical phenomena: dendidric growth in Wheeler et al. (1993), solidification in Elder et al. (1994), flow coarsening in Diepers et al. (1999), grain growth in Krill Iii and Chen (2002), spinodal decomposition in Chen and Shen (2016), crack propagation in Karma et al. (2001), dual-permeability porous medium in Amiri and Hamouda (2013) or even image processing in Beneš et al. (2004). Comprehensive lists of such applications can be found in the review studies Anderson and McFadden (1997); Boettinger et al. (2002); Chen (2002); Kim (2012); Mehrabian (2014)

The combination of AC and CH models with hydrodynamic effects has been addressed early on by the likes of Siggia et al. (1976); Hohenberg and Halperin (1977) in the context of critical dynamics of binary fluid, giving birth to the so-called model H. The model has been extended to shear flow in critical fluids in Onuki and Kawasaki (1979), to polymer solutions in Helfand and Fredrickson (1989) and to spinodal decomposition in Koga and Kawasaki (1991).
Specifically for fluid applications, the native models needed to be combined with Euler or Navier-Stokes equations in a consistent fashion. This has been dove by several authors, essentially for the CH model in Antanovskii (1995); Jacqmin (1995); Gurtin et al. (1996); Anderson and McFadden (1997); Lowengrub and Truskinovsky (1998); Blesgen (1999); Jacqmin (1999); Yue et al. (2004) and more recently for the AC model in Yang et al. (2006); Heida et al. (2012b); Ding et al. (2013); Chen and Guo (2017); Ma et al. (2017).

In the past decades, a new approach to PFM has been proposed in Beckermann et al. (1999); Folch et al. (1999) and studied in Boettinger et al. (2002); Sun and Beckermann (2007); Takada et al. (2013); Chai et al. (2018). These new models depart from the purely thermodynamic approach of model H and focus on creating sets of equations that naturally derive

from and remain as close as possible to the Sharp Interface equations. The new approach, referred to is this document as geometric, is to be compared in the following section with the thermodynamic approach introduced early on.

Finally, for the past two decades, PFM have seen a strong renewed interest in the two-phase flow community with the multiplication of both theoretical (see Abels et al. (2012); Lee et al. (2012); Abels et al. (2013a); Kou and Sun (2014); Kou et al. (2015); Kou and Sun (2016); Lee and Kim (2016)) and numerical (see Ding et al. (2007); Mehrabian (2014); Guo and Lin (2015); Lee and Kim (2015); Li et al. (2016); Strait et al. (2017); Yang and Ju (2017)) studies casting PFM back onto the main stage of two-phase flow modeling.
This section focuses on the description of the Cahn-Hilliard and the Allen-Cahn methods, the main considerations used during their inception, the different evolutions that have undergone, their integration within fluid dynamics frameworks, the late bifurcations that occurred in their regard and the noticeable numerical results they have permitted.
PFM dedicated to the simulation of pure fluid of variable density, i.e. the Second Gradient theory, is the central focus of this P.h.D. thesis and as such benefits from a completely dedicated in description in chapter Chap. 5. A number of subtleties separate AC and CH models from the SG theory despite their undeniable proximity. The information provided in this section aims at offering a better insight into the whole range of fluid dynamics related PFMs.

4.1.2 Fundamental notions for the Phase-Field methods

4.1.2.1 Free energy of a non homogeneous system

The starting point of all Phase-Field methods is the definition of an extended free energy that takes into account the local anisotropy of the fluid caused by the presence of the interface. This idea, introduced early on by van der Waals to study liquid-vapor equilibrium, has been extended by Landau (1937); Ginzburg and Landau (1950) to study other sources of anisotropy (solidification, magnetic field, atomic interactions, etc...) and more notoriously in Cahn and Hilliard (1958) to study the equilibrium and the spinodal decomposition of density matched non-miscible fluids.
In all these papers, the idea is to use a specific variable φ, that can be defined physically or not, referred to as a phase field or order parameter, dedicated to the monitoring of the interface. Much like the level-set function in LS methods, the phase field variable takes definite values in the bulk phases, usually $[0, 1]$ or $[-1, +1]$ and varies continuously from one phase to the other. However, the variable is used to enrich the thermodynamic description of the fluid and through this it allows to derive the proper thermo-mechanical equations to account for the presence of the interface. This is in opposition with the level-set function which is essentially a mathematical tool used to facilitate the tracking of the interface but that does not bear an intrinsic physical meaning. In particular, as it is shown in the following paragraphs, the equation to describe the time evolution of the phase field is physically motivated and derived based on thermodynamic consistency whereas the one for the level-set function is just a classic advection equation (aside from the modifications generated by the reinitialization problematic, see Sec. 3.2.3.1).

In PFM, the expression of the total free energy of a non-homogeneous system in the domain

Ω writes:

$$\mathcal{F} = \int_{\Omega} \left[F_0 \left(\boldsymbol{\xi}, \varphi \right) + \frac{\alpha}{2} \left| \boldsymbol{\nabla} \varphi \right|^2 \right] d\mathcal{V} \tag{4.1}$$

where F_0 is the free energy density of the homogeneous system which depends on the order parameter φ and eventually on another set of variables $\boldsymbol{\xi}$, most of the time the temperature. The term $(\boldsymbol{\nabla}\varphi)^2$ vanishes in the bulk phases but has a strong impact in the vicinity of the interface where φ varies rapidly. Its impact is controlled by the gradient coefficient α, also called capillary coefficient for its relation to the surface tension which is explored in later paragraphs.

The choice of the order parameter φ is dictated by the physics that is studied: the fluid density for hydrodynamics, the concentration of one component in density matched non-miscible mixtures, the total magnetization in transitioning ferromagnetic systems, etc... In some instances, no physical interpretation can be given to the order parameter. It is nonetheless used primarily for the thermodynamic description of the system rather than as a tracking device for the interface.

Consequently to Eq. (4.1), a total volumetric free energy F_{PF} can be introduced as follows:

$$F_{\mathrm{PF}} \left(\boldsymbol{\xi}, \varphi \right) = F_0 \left(\boldsymbol{\xi}, \varphi \right) + \frac{\alpha}{2} \left| \boldsymbol{\nabla} \varphi \right|^2 \tag{4.2}$$

A justification for the form of the local gradient contribution $(\alpha/2) \left| \boldsymbol{\nabla} \varphi \right|^2$ is given in Cahn and Hilliard (1958) using one component concentration as the order parameter. It rests upon adopting a higher order of modeling to account for the molecules short range interactions and the resulting macroscopic anisotropy of the flow characteristics in the vicinity of the interface. The methodology of the associated derivation is recalled and applied to the case $\varphi = \rho$ in Sec. 5.1.3.
From Gibbs (1878), in the homogeneous case where the free energy density is given by $F_0 \left(\boldsymbol{\xi}, \varphi \right)$, the necessary condition for the existence of two stable phases in regards to φ is that F_0, as a function of φ, presents two local minima sharing the same tangent line. This situation is schematized in Fig. 4.1. When the interface is represented as a discontinuity, φ jump from the value φ_{min} to φ_{max} and vice versa.

4.1.2.2 Diffuse interface in the Phase-Field methods

In Cahn and Hilliard (1958); Modica (1987); Elliott (1989), the authors show that when the complete form in Eq. (4.2) is used, the phase field spatially varies smoothly between its extreme values φ_{min} and φ_{max} as exemplified in Fig. 4.2.
To obtain such a result, the previously mentioned authors rely on the condition established by Gibbs which states that for the system to be at equilibrium, its total free energy must be minimized, i.e. the equilibrium phase field φ_{eq} needs to satisfy:

$$\mathcal{F} \left(\varphi_{\mathrm{eq}} \right) = \min_{\varphi} \mathcal{F} \left(\varphi \right) \tag{4.3}$$

Using the notion of functional derivative $\delta\mathcal{F}/\delta\varphi$ described in App. A.3.1.1 and in particular the vectorial version of the result in Eq. (A.45), it comes that finding φ_{eq} that satisfies Eq.

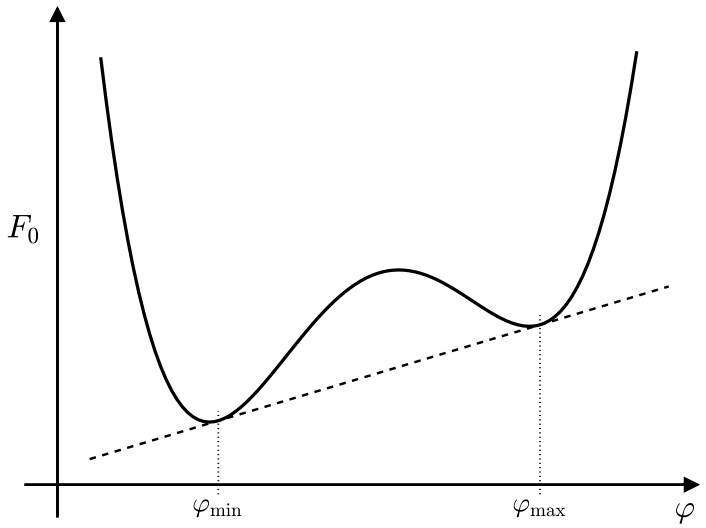

Figure 4.1: *Free energy density F for an homogeneous system authorizing the existence of two stable phases*

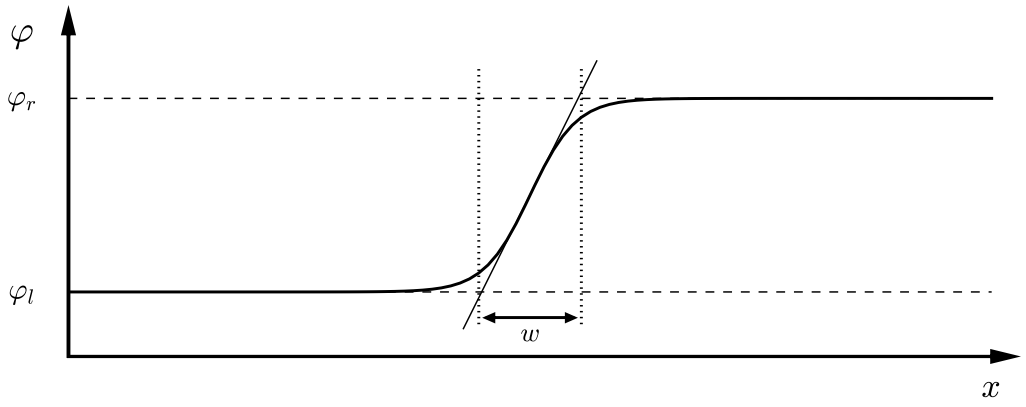

Figure 4.2: *Generic form of an interface in the PFM paradigm.*

(4.3) equates to solving the differential equation:

$$\left(\frac{\partial F_{\mathrm{PF}}}{\partial \varphi}\right)_{\boldsymbol{\xi},\boldsymbol{\nabla}\varphi} - \boldsymbol{\nabla}\cdot\left(\left(\frac{\partial F_{\mathrm{PF}}}{\partial \boldsymbol{\nabla}\varphi}\right)_{\boldsymbol{\xi},\varphi}\right) = 0 \tag{4.4}$$

which, using the form $\mathcal{F}$ in Eq. (4.1) and the notations in Eq. (4.2), can be written in the form:

$$\underbrace{\left(\frac{\partial F_0}{\partial \varphi}\right)_{\boldsymbol{\xi}} - \boldsymbol{\nabla}\cdot(\alpha\boldsymbol{\nabla}\varphi)}_{\mu_{\mathrm{PF}}} = 0 \tag{4.5}$$

The left-hand side of Eq. (4.5) is usually defined as the chemical potential μ_{PF} of the non-homogeneous system while $\mu_0 = (\partial F_0/\partial\varphi)_{\boldsymbol{\xi}}$ is its homogeneous counterpart.

In Jamet (2010), using the density as the phase variable, the author used another method based on the maximum entropy principle. He enforced a mass and a total energy upon the system with Lagrange multipliers and arrived to the same condition as in Eq. (4.5); Additionally, he proved that such an interface was necessarily isothermal.

With the notion of interfacial excess energy introduced by Gibbs (1878) (see Edwards et al. (1991) for an updated description) and thanks to the equilibrium relation in Eq. (4.5), the surface tension σ of a one dimensional interface can be introduced. It is defined as the excess free energy of the system and can be expressed (the complete derivation for the case $\varphi = \rho$ is given in Sec. 5.4.2.2) with the relation:

$$\sigma = \int_{\varphi_l}^{\varphi_r} \alpha \frac{\partial \varphi_{\text{eq}}}{\partial x}\, d\varphi \tag{4.6}$$

where φ_l and φ_r are the left and right values of the phase field, as presented in Fig. 4.2.

One remarkable result obtained with PFM, visible through Eq. (4.5) which also writes $(\partial F_0/\partial \varphi)_{\boldsymbol{\xi}} = \boldsymbol{\nabla} \cdot (\alpha \boldsymbol{\nabla} \varphi)$, is that the inherent spatial variations of the phase field (through the variations of $\boldsymbol{\nabla}\varphi$) and the free energy from the bulk phases (through the variations of F_0) participate equally to the surface tension. This shared contribution is absent from the purely geometric interpretation of the surface tension through interface curvature introduced by the Continuum Surface Force of Brackbill et al. (1992) and the Distributed Convected Force of Unverdi and Tryggvason (1992).

4.1.2.3 Expression for the homogeneous free energy density F_0

The exact shape of the equilibrium interface in Fig. 4.2 depends on the value of α, considered in the following to be constant, but more importantly on the expression of F_0. Many such expressions exist in the literature, for which a non-exhaustive list is given is Eqs. (4.7a) - (4.7d). Most of these formulas are not physically justified but are rather chosen the satisfy the conditions in Fig. 4.1 with the most simple form that allows to obtain physically relevant results.

$$F_0(\varphi) = \Delta F \varphi^2 (1-\varphi)^2 \qquad (\varphi \text{ in } [0,1]) \tag{4.7a}$$

$$F_0(\varphi) = \Delta F \left(1-\varphi^2\right)^2 \qquad (\varphi \text{ in } [-1,1]) \tag{4.7b}$$

$$F_0(\varphi) = \Delta F \sin^2(\pi\varphi) \qquad (\varphi \text{ in } \mathbb{R}) \tag{4.7c}$$

$$F_0(\varphi) = \Delta F \left(1-\varphi^2\right) + \mathrm{I}(\varphi) \qquad (\varphi \text{ in } \mathbb{R}), \quad \text{with } \mathrm{I}(\varphi) = 0 \text{ if } |\varphi| \leqslant 1,\ \mathrm{I}(\varphi) = +\infty \text{ if } |\varphi| > 1 \tag{4.7d}$$

Eqs. (4.7a) and (4.7b) represent the classic double-well potential used in the majority of the studies involving PFM. ΔF is a reference value for the energy differential "to be paid" when transitioning from one phase to the other. Eq. (4.7c) has been introduced in Wang et al. (2001) as a crystalline energy to study dislocation dynamics and Eq. (4.7d) in Oono and Puri (1988) to simulate the phase separation of a quenched system. With the classic choices of (4.7a) or (4.7b), it can be shown that the equilibrium profile of a planar interface is given by:

$$\varphi(x) = \frac{1}{2}\left[1 + \tanh\left(\frac{x}{2\delta}\right)\right] \tag{4.8}$$

where x is the space coordinate and δ is the characteristic interfacial thickness expressed in Eq. (4.9). Its expression also illustrates the fact the equilibrium profile for the interface results from a specific balance between the bulk phase contributions (represented by ΔF in Eq. (4.9)) and its intrinsic geometry thanks to the added gradient term in the free energy (represented by α in Eq. (4.9)).

$$\delta = \sqrt{\frac{\alpha}{2\Delta F}} \tag{4.9}$$

The previous expressions of F_0 are dedicated to isothermal systems and as such, they cannot be used to address thermocapillary effects such as liquid solidification or vaporization. To that effect, the authors in Cahn and Hilliard (1958) have introduced in their ground work an expression for the free energy that incorporate a contribution from the temperature, given in Eq. (4.10) where k_B in the Boltzmann constant. In particular, the existence and the impact of a critical temperature T_c on the fluid behavior is accounted for.

$$F_0(T,\varphi) = k_B T\left[\varphi \ln(\varphi) + (1-\varphi)\ln((1-\varphi)\right] - 2k_B T_c \varphi(1-\varphi) \qquad (\varphi \text{ in }]0,1[) \tag{4.10}$$

The authors in Caginalp (1989) have also introduced an expression for F_0 that recognizes the change in the fluid behavior passed the characteristic temperature T_m of the studied phenomenon, namely the melting temperature for solidification and the saturation temperature for vaporization. A more comprehensive method to derive an expression for $F_0(T,\varphi)$ in the perspective of similar thermocapillary applications can be found in Boettinger et al. (2002). The original formulation from Caginalp (1989) is given in Eq. (4.11a) and a more recent result following Boettinger et al. (2002) is shown in Eq. (4.11b) (γ is an energy constant)

$$F_0(T,\varphi) = \Delta F\left(1-\varphi^2\right)^2 + \gamma(T-T_m)\varphi \quad (\varphi \text{ in } [-1,1]) \tag{4.11a}$$

$$F_0(T,\varphi) = \Delta F\varphi^2(1-\varphi)^2 + \gamma\varphi^3\left(10-15\varphi+6\varphi^2\right)(T-T_m) \quad (\varphi \text{ in } [0,1]) \tag{4.11b}$$

A different class of more intricate formulas with thermal components has also been introduced by the likes of Penrose and Fife (1990); Kobayashi (1991); Wang et al. (1993). These formula are derived consistently from the entropy to ensure the satisfaction of the second thermodynamic principle. In the case of real gas flows, the free energy expression is readily available from, and for that matter is even imposed by the equation of state chosen to model the fluid behavior. As shown in Chap. 5, the additions from the PFM allow to unify the description of the fluid in the whole subcritical domain where the sole real gas EoSs normally lead to unstable states in the binodal region.

It should be emphasized that for all the previously presented expressions of F_0, a significant amount of literature has been devoted to proving the existence and unicity of an equilibrium solution to the problem in Eq. (4.5). The reader is referred to the affiliated work mentioned in the introduction of this section 4.1.1 for further details.

4.1.3 Cahn-Hilliard and Allen-Cahn equations

4.1.3.1 The Cahn-Hilliard equation

The previous study of the equilibrium profile of planar interface had already been performed, for the most part, by van der Waals in the late 1800's using its newly introduced EoS. The

revolutionary contribution from Cahn (1961); Cahn and Hilliard (1971) is the extension of the description to unstationary/transitionning configurations. To that effect, the authors have derived an equation to describe the time evolution of the order parameter φ, much like the advection equation used in the FT (Eq. (2.18)), VOF (Eq. (3.3)) and LS (Eq. (3.29a)) methods.
This equation, known as the Cahn-Hilliard equation, together with the free energy description Eq. (4.2), form the two building blocks of most PFM.

The order parameter considered by Cahn and Hilliard in their derivation is the concentration of one fluid for a binary mixture of non-miscible fluids. Their eponymous equation is obtained by following the general guidelines for non-equilibrium thermodynamics prescribed in de Groot and Mazur (1984) (chap. IV, sect. 1) that assumes the concentration flux $\boldsymbol{J}_{\mathrm{CH}}$ to be proportional to the gradient of chemical potential, i.e. that the phenomenological Fick's law applies. Using the generalized chemical potential from Eq. (4.5) the flux writes:

$$\boldsymbol{J}_{\mathrm{CH}} = M_{\mathrm{CH}} \boldsymbol{\nabla} \mu_{\mathrm{PF}} \tag{4.12}$$

In Eq. (4.12), M_{CH} is a coefficient known as the generalized Onsager coefficient or the generalized mobility of the fluid and is analogous to the Fick's coefficient for species diffusion (see Christian (2002), chap. 4, sect. 14). The evolution equation for φ is then obtained by enforcing its local conservation. Thus, the Cahn-Hilliard equation is given by:

$$\frac{\partial \varphi}{\partial t} = \boldsymbol{\nabla} \cdot \boldsymbol{J}_{\mathrm{CH}} = \boldsymbol{\nabla} \cdot (M_{\mathrm{CH}} \boldsymbol{\nabla} \mu_{\mathrm{PF}}) \tag{4.13}$$

$$\frac{\partial \varphi}{\partial t} = \boldsymbol{\nabla} \cdot \left[M_{\mathrm{CH}} \boldsymbol{\nabla} \left(\left(\frac{\partial F_0}{\partial \varphi} \right)_{\boldsymbol{\xi}} - \boldsymbol{\nabla} \cdot (\alpha \boldsymbol{\nabla} \varphi) \right) \right] \tag{4.14}$$

As one can see, the Cahn-Hilliard equation (4.13)/(4.14) is a partial differential equation (p.d.e.) with a fourth order space derivative for φ which is the source of multiple numerical difficulties regarding its solving. Several methods have been tested to perform simulation with this equation: a fully implicit finite difference scheme in Chella and Viñals (1996), an unconditionally gradient stable time marching in Eyre (1998), a fully explicit central difference scheme on a staggered grid in Jacqmin (1999), a fully implicit finite element approach in Barrett et al. (1999), a semi-implicit Fourier spectral method in Liu et al. (2003), a Lattice Boltzmann method in Inamuro et al. (2004), an implicit discontinuous Galerkin method in Kay et al. (2009), a semi-implicit adaptive mesh refinement in Ceniceros et al. (2010) or a semi-implicit finite difference scheme in Lee and Kim (2016).
Explicit methods often lead to very restrictive time steps while implicit methods trade the time step condition for an increased complexity in implementation, in particular when reaching for high order schemes. This explains the recurring resort to semi-implicit schemes.

Numerical results

Fig. 4.3 provides results obtained using the Cahn-Hilliard model with a logarithmic potential comparable to Eq. (4.10). An implicit Euler time stepping combined to a finite element spatial discretization with continuous functions over a triangular mesh have been used in Brassel and Bretin (2011) to simulate the closing of a inside void within a droplet (Fig. 4.3a) and the

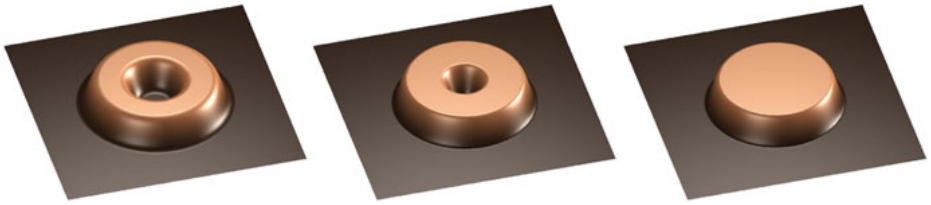

(a) *Closing of an initial inside void*

(b) *Merging of deformed droplets*

Figure 4.3: *Simulation of interface dynamics related configurations using the Cahn-Hilliard equation, taken from Brassel and Bretin (2011)*

coalescence of two initially deformed droplets in (Fig. 4.3b). In Fig. 4.3a, both interior and exterior interfaces are seen to shrink until the inside one closes up the initial void. In Fig. 4.3b, the two droplets start by recovering a near circular shape which causes the outer interfaces to come closer and eventually results in the merging of the two droplets. For both configurations, the intuitive behavior of the interface is properly recovered.
In Kim et al. (2016) a classic case of spinodal decomposition is simulated using the Cahn-Hilliard equation for two different initial conditions. The results are shown in Fig. 4.4 where the Cahn-Hilliard equation with the symmetric potential in Eq. (4.7b) has been solved using a non-linearly stabilized splitting scheme (see Yang et al. (2010)).
A more complex case of binodal decomposition for the Cahn-Hilliard equation is exposed in Fig. 4.5 where an additional convection is forced upon the system. Formally, a velocity field $\mathbf{u}$, satisfying $\boldsymbol{\nabla} \cdot \mathbf{u} = 0$ is introduced in Eq. (4.13) which becomes:

$$\frac{\partial \varphi}{\partial t} + \boldsymbol{\nabla} \cdot (\mathbf{u}\varphi) - \boldsymbol{\nabla} \cdot (M_{\mathrm{CH}} \boldsymbol{\nabla} \mu_{\mathrm{PF}}) = 0 \tag{4.15}$$

To obtain the results in Fig. 4.5, the authors from Kay et al. (2009) have used a stationary circular velocity field. The equation is solved via a discontinuous Galerkin finite element method with an implicit time stepping. Due to the velocity field, the coarsening liquid nuclei quickly organize in concentric rings during the early stage of the spinodal decomposition. Eventually, the rings start to merge, similarly to Fig. 4.3a, to presumably reach a stationary state with a single rotating droplet in the end.

4.1.3.2 The Allen-Cahn equation

Using the notion of gradient flow, further explained in Sec. 4.1.3.5 , the authors in Allen and Cahn (1979) have proposed a new equation, known as the Allen-Cahn equation, to describe

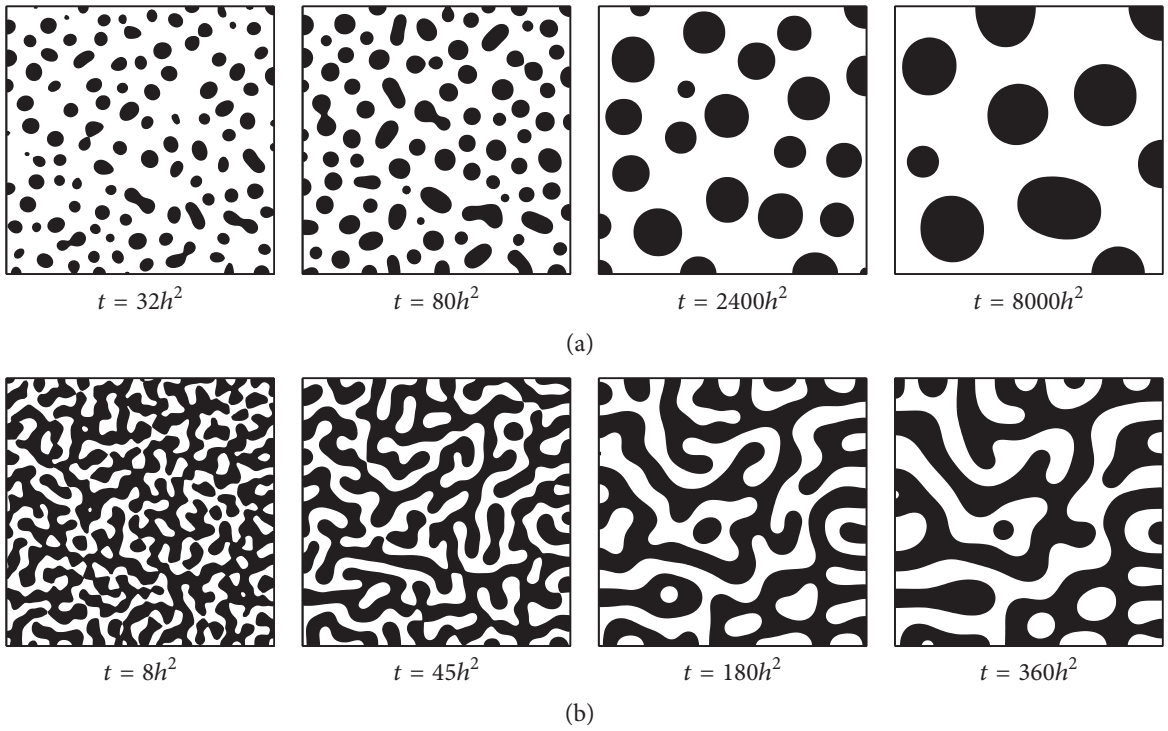

Figure 4.4: *Time evolution of the phase field during a spinodal decomposition and a coarsening simulated with the Cahn-Hilliard equation, taken from Kim et al. (2016)*

the motion of antiphase boundaries while studying the phase change of crystalline solids.

$$\frac{\partial \varphi}{\partial t} = -M_{\mathrm{AC}}\mu_{\mathrm{PF}} = -M_{\mathrm{AC}}\left[\left(\frac{\partial F_0}{\partial \varphi}\right)_{\boldsymbol{\xi}} - \boldsymbol{\nabla}\cdot(\alpha\boldsymbol{\nabla}\varphi)\right] \tag{4.16}$$

Since then, its utilization has been extended to more various problems similar to that addressed with the Cahn-Hilliard equation (see Lee and Kim (2016)), in particular for hydrodynamics studies as in Jeong and Kim (2017).
Just as it was the case for the Cahn-Hilliard equation, different numerical strategies have been tested to solve Eq. (4.16): an unconditionally gradient stable time marching in Choi et al. (2009), a semi-implicit time stepping with moving mesh spectral method in Shen and Yang (2009), a fully explicit local discontinuous Garlerkin in Xia et al. (2009), a semi-implicit residual-based finite element scheme in Vasconcelos et al. (2014) or a semi-implicit finite difference scheme in Lee and Kim (2016).

A well know and potentially detrimental specificity of the Allen-Cahn equation is that it does not inherently conserve the integral of φ. This calls for an additional care when using this equation and it has led to two different strategies regarding the use of the Allen-Cahn model. The first is to limit it to situations where the phase field is effectively not conserved either because it bears no physical meaning or because the associated physical quantity is not conserved (for instance the solid phase concentration in binary alloys). The second is to modify the native phase-field equation, using Lagrange multipliers, to enforce the conservation of φ.

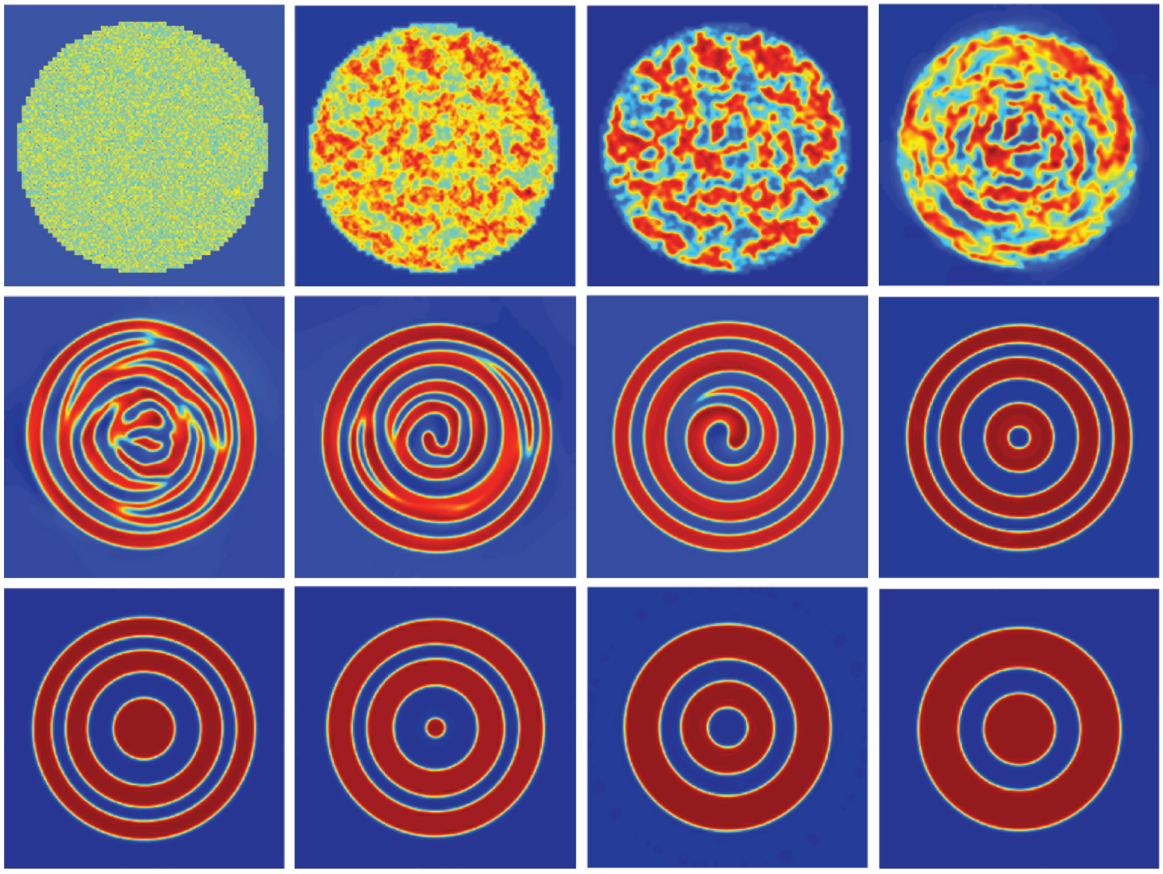

Figure 4.5: *Spinodal decomposition solving Cahn-Hilliard equation with a forced circular convection, taken from Kay et al. (2009)*

This last strategy has first been introduced in Rubinstein and Sternberg (1992) producing the non-local conservative Allen-Cahn equation given by:

$$\frac{\partial \varphi}{\partial t} = -M_{\mathrm{AC}} \left[\left(\frac{\partial F_0}{\partial \varphi} \right)_{\boldsymbol{\xi}} - \boldsymbol{\nabla} \cdot (\alpha \boldsymbol{\nabla} \varphi) - \varsigma(t) \right] \tag{4.17}$$

where ς is the Lagrange multiplier used to enforce conservation, defined by:

$$\varsigma(t) = \int_{\Omega} \left(\frac{\partial F_0}{\partial \varphi} \right)_{\boldsymbol{\xi}} d\mathcal{V} \Bigg/ \int_{\Omega} d\mathcal{V} \tag{4.18}$$

and in Brassel and Bretin (2011) with a semi-local conservative approach which writes:

$$\frac{\partial \varphi}{\partial t} = -M_{\mathrm{AC}} \left[\left(\frac{\partial F_0}{\partial \varphi} \right)_{\boldsymbol{\xi}} - \boldsymbol{\nabla} \cdot (\alpha \boldsymbol{\nabla} \varphi) - \gamma(t) \sqrt{F_0(\boldsymbol{\xi}, \varphi)} \right] \tag{4.19}$$

where γ is also a Lagrangian multiplier defined by:

$$\gamma(t) = \int_{\Omega} \left(\frac{\partial F_0}{\partial \varphi} \right)_{\boldsymbol{\xi}} d\mathcal{V} \Bigg/ \int_{\Omega} \sqrt{F_0(\boldsymbol{\xi}, \varphi)}\, d\mathcal{V} \tag{4.20}$$

Numerical results

Fig. 4.6 shows a comparison between the native equation Eq. (4.16) and the conservative one from Eq. (4.19) with the potential given by Eq. (4.7a). The simulation is performed in Brassel and Bretin (2011) using an implicit Fourier spectral method. For the return to a spherical shape experienced by a torus, the authors observe a 30% mass loss for the native equation. This value descends to 5% when the "conservative" equation is used.

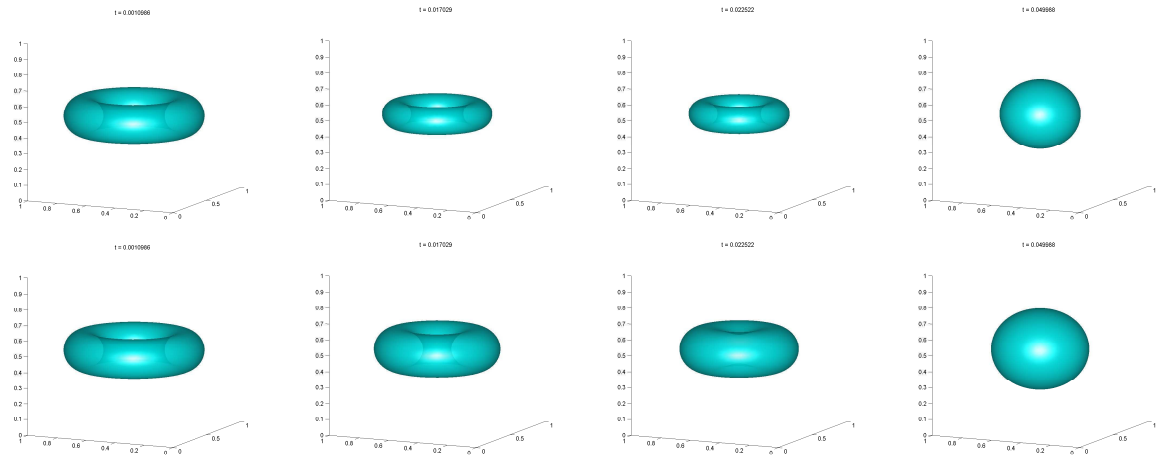

Figure 4.6: *Return to a spherical shape of a liquid torus solving the non-conservative and conservative Allen-Cahn equations, taken from Brassel and Bretin (2011)*

The other conservative Allen-Cahn equation (4.17) is used in Kim and Lee (2017) also with the potential from Eq. (4.7a). More precisely, a multi-species method is presented, for N species, using a phase-field vector $\boldsymbol{\varphi}$ composed of N phase-field functions $\boldsymbol{\varphi} = (\varphi_1, \dots, \varphi_N)$ such as $\varphi_1 + \cdots + \varphi_N = 1$ with the combined potential $F(\boldsymbol{\varphi}) = F(\varphi_1, \dots, \varphi_N) = F_0(\varphi_1) + \cdots + F_0(\varphi_N)$. Formally, $\boldsymbol{\varphi}$ is substituted to φ in (4.17) which is then solved by the authors on a regular cartesian grid using a semi-implicit scheme with flux splitting. The results for spinodal decomposition are show in Fig. 4.7 for different numbers of species. With this numerical method, the authors observe a mass conservation up to computer precision for all species, even for high values of N.

4.1.3.3 Comparison between the Cahn-Hilliard and Allen-Cahn equations

Numerical solving

The first and straightforwardly visible difference between the two equations is that from a mathematical point of view, the Allen-Cahn equation is a only a second order p.d.e. compared to the fourth order Cahn-Hilliard one, which renders the former significantly easier to solve numerically.

Phase field conservation

The conservative formulation in Eq. (4.14) for the Cahn-Hilliard equation ensures the conservation of φ in the domain with the appropriate boundary conditions (non-permeable or

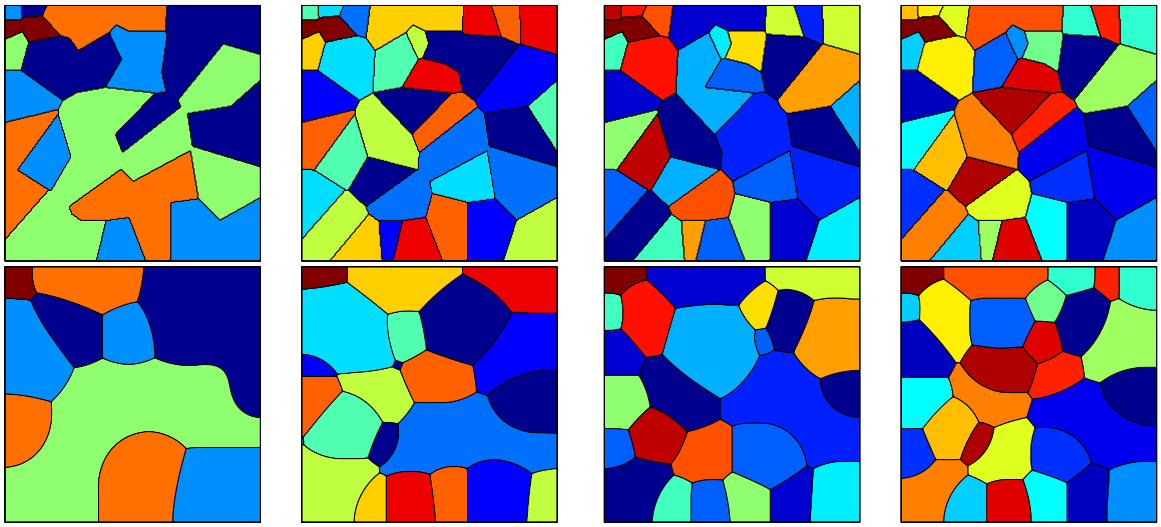

Figure 4.7: *Spinodal decomposition simulated using the conservative Allen-Cahn equations with different numbers of species, taken from Kim and Lee (2017)*

periodic). As discussed in Sec. 4.1.3.2, the Allen-Cahn equation is not conservative by nature and although several strategies have been designed to overcome this difficulty, it should be emphasized that this conservation is only numerically enforced and not physically ensured. In that context, the "conservative" denomination should be understood with this nuance in mind. As such, the denomination can be compared to that of the strategies introduced for the LS methods (see Sec. 3.2.4), also only numerically "conservative".

Energy conservation

The interpretation of PFM equations in the vein of the Cahn-Hilliard equation (4.14) is directly inherited from the work presented by Landau (1937); Ginzburg and Landau (1950) which takes place in a more general setting. As describing gradient flows of the total free energy $\mathcal{F}$, both equations lead to a decreasing energy over time. Indeed, with the hypothesis that α is constant, one has:

$$\begin{aligned}
\frac{d\mathcal{F}}{dt} &= \frac{d}{dt}\int_{\Omega}\left[F_0\left(\boldsymbol{\xi},\varphi\right)+\frac{\alpha}{2}\left(\boldsymbol{\nabla}\varphi\right)^2\right]d\mathcal{V} \\
&= \int_{\Omega}\left[\frac{\partial F_0}{\partial\varphi}\frac{\partial\varphi}{\partial t}-\boldsymbol{\nabla}\cdot\left(\alpha\boldsymbol{\nabla}\varphi\right)\frac{\partial\varphi}{\partial t}\right]d\mathcal{V} \\
\frac{d\mathcal{F}}{dt} &= \int_{\Omega}\left[\frac{\partial F_0}{\partial\varphi}-\boldsymbol{\nabla}\cdot\left(\alpha\boldsymbol{\nabla}\varphi\right)\right]\frac{\partial\varphi}{\partial t}\,d\mathcal{V}
\end{aligned} \tag{4.21}$$

For the Cahn-Hilliard equation, the term $\partial\varphi/\partial t$ can be substituted using Eq. (4.14) to get:

$$\begin{aligned}\left(\frac{d\mathcal{F}}{dt}\right)_{\text{CH}} &= \int_{\Omega}\left[\frac{\partial F_0}{\partial\varphi} - \boldsymbol{\nabla}\cdot(\alpha\boldsymbol{\nabla}\varphi)\right]\boldsymbol{\nabla}\cdot\left[M_{\text{CH}}\boldsymbol{\nabla}\left(\frac{\partial F_0}{\partial\varphi} - \boldsymbol{\nabla}\cdot(\alpha\boldsymbol{\nabla}\varphi)\right)\right]d\mathcal{V} \\ \left(\frac{d\mathcal{F}}{dt}\right)_{\text{CH}} &= -\int_{\Omega} M_{\text{CH}}\left|\boldsymbol{\nabla}\left(\frac{\partial F_0}{\partial\varphi} - \boldsymbol{\nabla}\cdot(\alpha\boldsymbol{\nabla}\varphi)\right)\right|^2 d\mathcal{V} \leqslant 0\end{aligned} \tag{4.22}$$

Likewise, $\partial\varphi/\partial t$ can substituted in Eq. (4.21) using the Allen-Cahn equation (4.16) which leads to:

$$\left(\frac{d\mathcal{F}}{dt}\right)_{\text{AC}} = -\int_{\Omega} M_{\text{AC}}\left[\frac{\partial F_0}{\partial\varphi} - \boldsymbol{\nabla}\cdot(\alpha\boldsymbol{\nabla}\varphi)\right]^2 d\mathcal{V} \leqslant 0 \tag{4.23}$$

Interface dynamics

A comparative study between the conservative approaches for the Allen-Cahn equation in Eqs. (4.17) and (4.19) and the native conservative Cahn-Hilliard in Eq. (4.13) has been performed in Lee and Kim (2016).
The authors noticed that the early evolution of a spinodal decomposition (that is, the creation of new interfaces), for the Allen-Cahn equation, was strongly dependent on the profile of $\partial F_0/\partial\varphi$ and therefore on the form chosen for F_0. Conversely, for the Cahn-Hilliard, this early dynamics was essentially controlled by diffusion. Indeed, a linear analysis of Eq. (4.14) around an equilibrium state (the initial non-perturbed unstable system) shows the equation to reduce to a diffusion equation $\partial F_0/\partial\varphi = D(\varphi)\,\boldsymbol{\Delta}\varphi$ where the coefficient diffusion D depends on φ. In the thermodynamic stable region, $D > 0$ which leads to classic diffusion; in the spinodal region $D < 0$ which results in a backward diffusion; the interface arises from the unbalance between these adverse diffusion processes.
Other significant differences between the models noted by the authors includes:

- their reaction to local hydrodynamics unbalances: for two near droplets of different sizes, the smallest shrinks while the biggest widens using the Allen-Cahn equations where the opposite occurs for the Cahn-Hilliard equation until both droplets reach the same size.
- their behavior for long time simulations: solving the Cahn-Hilliard equation, the values of φ in the bulk phases tend to drift, which is not observed for the conservative Allen-Cahn equations
- the inability of the Cahn-Hilliard equation to preserve the convexity of an initial solution.

In either cases, the relaxation of the order parameter (conserved locally and globally with the Cahn-Hilliard equation (4.14), not conserved in the native Allen-Cahn equation (4.16) and conserved globally/semi-locally with its modified counterparts Eqs. (4.17)-(4.19)) is driven by the local minimization of the free energy subject to phase field conservation (in Lowengrub and Truskinovsky (1998), the authors associate this process to an entropy production) and as a result, the diffusive layers that constitute the interface do not deteriorate dynamically and are preserved in time.

Sharp interface limit

This different behavior can also be observed in the departing sharp interface limits toward which each model converges.

The limit for the Allen-Cahn model is the classic mean curvature flow for which the velocity $\mathbf{v}_\Gamma$ of a point on the interface Γ is directly proportional to the local interface mean curvature κ_Γ as given by Eq. (4.24) and shown in Modica (1987) ($\boldsymbol{n}_\Gamma$ the outer normal to the interface relatively to the values of φ and M is a positive constant).

$$\mathbf{v}_\Gamma = M\kappa_\Gamma \boldsymbol{n}_\Gamma \tag{4.24}$$

For the Cahn-Hilliard model, the sharp interface limit is the Mullins-Sekerka flow (see Mullins and Sekerka (1964)) which has been demonstrated by Pego (1989). The Mullins-Sekerka flow is a particular case of Hele-Shaw flow where the interface velocity is proportional to a state variable gradient jump across said interface. With the superscripts $\cdot^{\text{in}}$ and $\cdot^{\text{out}}$ used in a reference to a quantity taken at the interface just inside or outside of the phase bounded by φ, the complete set of equations writes:

$$\boldsymbol{\Delta}\mu = 0 \tag{4.25a}$$

$$\mathbf{v}_\Gamma = -M\left[\frac{\partial \mu}{\partial \boldsymbol{n}}\right]_\Gamma = -M\left[\frac{\partial \mu}{\partial \boldsymbol{n}}^{\text{out}} - \frac{\partial \mu}{\partial \boldsymbol{n}}^{\text{in}}\right]\boldsymbol{n}_\Gamma \tag{4.25b}$$

Both systems Eq. (4.24) and Eqs. (4.25a)-(4.25b) can be shown to preserve the volume and decrease the surface of an interface delimiting a single fluid region, as it is recalled in Lee and Kim (2016).

Conclusions

To the author's best knowledge and in light of the bibliographic study that has been carried out regarding the Allen-Cahn and Cahn-Hilliard approaches and their variants, there are no clear and definitive argument on whether one model is superior to or more correct than the other. Several questions are to be asked to chose the adequate equation depending on the physical case to be modeled, the numerical methods that are accessible, the nature of the phase-field that is considered and its need for conservation. Besides, this choice may not be unique for a given configuration.

4.1.3.4 On the mobility coefficient

The mobility can be determined experimentally by considering a single component and by correlating the velocity v of an interface in response to a free energy variation $\delta\mathcal{F}$ thanks to the empiric relation (see Christian (2002); Qin and Bhadeshia (2010)):

$$v = M\delta\mathcal{F} \tag{4.26}$$

For simulation purposes however, the mobility is rather treated as a numerical lever to be tuned by a trial and error approach. If chosen too small, it leads to very constraining time steps when used with explicit schemes. On the contrary, when M is to large, it often causes numerical instabilities to appear. Moreover, this coefficient is almost systematically chosen to be constant, often unitary, examples of variable mobility studies include Cahn et al. (1996); Elliott and Garcke (1996); Novick-Cohen (2000); Lee and Kim (2016). If the only goal is to depict the topology, thermodynamic and morphological transformations that occurs in the system, the approach with a constant value for M proves to be useful and sufficient. It however falls short for producing predictive results where a more precise evaluation of M is necessary.

4.1.3.5 Complement on gradient flows

Since its inception, the Cahn-Hilliard equation (4.14) has been noticed to represent a gradient flow of the energy functional in Eq. (4.1).
In a general context, a gradient flow is a scalar dependent vectorial variable $\boldsymbol{\eta}(t)$ which takes entries in $\mathbb{R}^+$ and has values in the metric space Π (with it associated norm $|\cdot|_\Pi$) such as there exists a function $\Psi : \Pi \longrightarrow \mathbb{R}^+$ satisfying:

$$\frac{\partial \boldsymbol{\eta}}{\partial t}(t) = -\boldsymbol{\nabla}_\Pi \Psi(\boldsymbol{\eta}(t)) \tag{4.27}$$

Π can for instance be an Euclidian or a Hilbert space with its canonical norm. The term $\boldsymbol{\nabla}_\Pi$ means that the gradient of the function Ψ is calculated with respect to the metric space $(\Pi, |\cdot|_\Pi)$.
Practically, a gradient flow $\boldsymbol{\eta}(t)$ that satisfies Eq. (4.27) is a flow evolving in the direction of the steepest descent of Ψ. Consequently, the successive values of $\boldsymbol{\eta}(t)$ progressively minimize the value of $\Psi(\boldsymbol{\eta})$. As such, gradient flows are of the utmost interest from theoretical and practical points of view, particularly for minimization problems. They are also prominent in physics as several classic physical equations can be interpreted as describing a gradient flow. For instance, considering the Hilbert space $\mathrm{L}_2(\mathbb{R}^n)$ for $n = 1, 2$ or 3 with its canonical norm, and the functional Ψ defined by:

$$\begin{aligned} \Psi : \mathrm{L}_2(\mathbb{R}^n) &\longmapsto \mathbb{R} \\ \eta &\longrightarrow \frac{1}{2}\int |\boldsymbol{\nabla}\eta|^2 \end{aligned} \tag{4.28}$$

this combination produces a gradient flow problem known as the heat equation which writes:

$$\frac{\partial \eta}{\partial t} = \boldsymbol{\Delta}\eta \tag{4.29}$$

Likewise, several conservative p.d.e. found in hydrodynamics such as the continuity and diffusion equations can be seen as gradient flows related to specific functions Ψ defined with the Wasserstein metric on the distribution space $\mathcal{P}(\mathbb{R}^n)$ (see Dobrushin (1970); Rüschendorf (1985) for the description of the Wasserstein metric and Ambrosio et al. (2004); Santambrogio (2017) for its application to gradient flows)
For the previously mentioned reasons, gradient flows have been the subject of numerous studies, a comprehensive overview of the related results can be found in Ambrosio et al. (2008).

A complete derivation of the Cahn-Hilliard Eq. (4.14) as a gradient flow can be found in Cowan (2005). One of the key idea in this derivation is the choice of the correct metric space $(\Pi; |\cdot|_\Pi)$, which in this case is to be chosen as $H^{-1}(\mathbb{R})$ which is the dual space of the space $H_0^1(\mathbb{R})$ which is the closure in $C^\infty(\mathbb{R})$ of the Sobolev space $H^1(\mathbb{R})$ (see Cowan (2005) for more mathematical details).
To derive the Allen-Cahn equation, the function Ψ used to obtain the corresponding gradient flow is also the free energy Eq. (4.1) as for the Cahn-Hilliard equation. However, the metric space considered is the classic Hilbert space $L^2(\mathbb{R})$ equipped with its canonical norm.

4.1.4 Geometric approach to Phase-Field methods

4.1.4.1 Principles of the geometric approach

In the last two decades, a variant of the PFM has emerged under the impulsion of Karma and Rappel (1998); Beckermann et al. (1999); Folch et al. (1999). This variant departs from the classic and purely variational approaches that drive the derivation of the Allen-Cahn and Cahn-Hilliard equations. At the basis of this new approach is a reflection regarding the pertinence and practicality of Allen-Cahn and Cahn-Hilliard models to deal with specific situations where the interface is undoubtedly thin, in particular when compared to the characteristic length of the system or the physical phenomenon that is considered, however not so thin that the sharp interface limit cannot be applied with absolute certainty. Another interrogation concerns the form taken for the free energy F_0, which in most PFM application is chosen among the canonical forms in Eqs. (4.7a)-(4.7d) but of which physical meaning and validity relatively to the studied cases can reasonably be questioned. In front of these uncertainties, the strategy offered by the authors in Beckermann et al. (1999) is to derive a new system of equations with a specific sharp interface limit used as a target.
This new formulation, much closer in form to the sharp interface capturing (specifically the Level-Set) methods, is usually referred to as the geometric PFM approach.

The starting point to derive the geometric PFM is to consider the classic sharp interface equation Eq. (4.30) where κ is the interface curvature and M a positive constant coefficient.

$$\frac{\partial \varphi}{\partial t} = M\kappa \left|\boldsymbol{\nabla}\varphi\right| \tag{4.30}$$

In the same spirit, to remain consistent with the sharp approach, the definition of the interface normal $\boldsymbol{n}$ and curvature κ are take the same as in the LS method (from Eqs. (3.21a) and (3.21b)):

$$\boldsymbol{n} = \frac{\boldsymbol{\nabla}\varphi}{|\boldsymbol{\nabla}\varphi|} \tag{4.31a}$$

$$\kappa = \boldsymbol{\nabla}\cdot\boldsymbol{n} = \boldsymbol{\nabla}\cdot\left(\frac{\boldsymbol{\nabla}\varphi}{|\boldsymbol{\nabla}\varphi|}\right) \tag{4.31b}$$

By further expanding Eq. (4.31b) one gets:

$$\kappa = \frac{1}{|\boldsymbol{\nabla}\varphi|}\left[\boldsymbol{\Delta}\varphi - \frac{\boldsymbol{\nabla}\varphi\cdot\boldsymbol{\nabla}\left(|\boldsymbol{\nabla}\varphi|\right)}{|\boldsymbol{\nabla}\varphi|}\right] \tag{4.32}$$

In the normal direction to an equilibrium planar interface calculated with either the Allen-Cahn or Cahn-Hilliard approach, the profile φ_0 is given by Eq. (4.8). Using the space variable ξ to refer to this normal direction, one can notice that:

$$\frac{d\varphi_0}{d\xi} = \frac{d}{d\xi}\left[\frac{1}{2}+\frac{1}{2}\tanh\left(\frac{\xi}{2\delta}\right)\right] = \frac{1}{4\delta}\left(1-\tanh\left(\frac{\xi}{2\delta}\right)^2\right) = \frac{1}{\delta}\varphi_0\left(\xi\right)\left(1-\varphi_0\left(\xi\right)\right) \tag{4.33}$$

The modeling assumption made in the geometric approach is to substitute partially the norm of the actual phase-field φ gradient with that of the equilibrium phase-field φ_0 using the

following relations:

$$|\boldsymbol{\nabla}\varphi| \rightarrow |\boldsymbol{\nabla}\varphi_0| = \frac{d\varphi_0}{d\xi} \tag{4.34}$$

$$\boldsymbol{\nabla}\left(|\boldsymbol{\nabla}\varphi|\right) \rightarrow \boldsymbol{\nabla}\left(|\boldsymbol{\nabla}\varphi_0|\right) \tag{4.35}$$

$$\boldsymbol{n} \rightarrow \boldsymbol{n}_0 \tag{4.36}$$

For the equilibrium profile φ_0 in the normal direction it can be noticed that:

$$\frac{d^2\varphi_0}{dx^2} = \boldsymbol{n}_0 \cdot \boldsymbol{\nabla}\left(|\boldsymbol{\nabla}\varphi_0|\right) \tag{4.37}$$

Combining both the substitution relations from Eqs. (4.34)-(4.36) and the results of Eqs. (4.33) and (4.37), a new form can be derived for the second term in the right-hand side of Eq. (4.32) with:

$$\frac{\boldsymbol{\nabla}\varphi \cdot \boldsymbol{\nabla}|\boldsymbol{\nabla}\varphi|}{|\boldsymbol{\nabla}\varphi|} = \boldsymbol{n} \cdot \boldsymbol{\nabla}\left(|\boldsymbol{\nabla}\varphi|\right) \rightarrow \boldsymbol{n}_0 \cdot \boldsymbol{\nabla}\left(|\boldsymbol{\nabla}\varphi_0|\right) = \frac{d^2\varphi_0}{d\xi^2} \tag{4.38}$$

The previous relation can be developed into:

$$\frac{d^2\varphi_0}{d\xi^2} = -\frac{1}{\delta}\frac{d\varphi_0}{dx}\left(1 - 2\varphi_0\left(x\right)\right) = \frac{1}{\delta^2}\varphi_0\left(x\right)\left(1 - \varphi_0\left(x\right)\right)\left(1 - 2\varphi_0\left(x\right)\right) \tag{4.39}$$

Eventually, the native equation in the context of the geometric approach can be obtained and writes:

$$\frac{\partial\varphi}{\partial t} = M\left[\boldsymbol{\Delta}\varphi - \frac{\varphi\left(1-\varphi\right)\left(1-2\varphi\right)}{\delta^2}\right] \tag{4.40}$$

In Eq. (4.40), one can recognize the Allen-Cahn equation Eq. (4.16) with the non-mixing free energy F_0 given by Eq. (4.7a) with the additional assumptions that $M = M_{\mathrm{AC}}$, $\alpha = 1$ and $\Delta F = 1/2$.

The interface behavior as described by Eq. (4.40) is a combination of normal interface movement (to balance the equilibrium profile) and curvature driven motion. In the studies concerned with the use of geometric PFM (see Folch et al. (1999); Sun and Beckermann (2007); Takada et al. (2013)), the curvature driven motion is systematically canceled following a mathematical procedure proposed in Folch et al. (1999). The resulting equation, which is mostly associated to the geometric approach is finally given by:

$$\frac{\partial\varphi}{\partial t} = M\left[\boldsymbol{\Delta}\varphi - \frac{\varphi\left(1-\varphi\right)\left(1-2\varphi\right)}{\delta^2} - |\boldsymbol{\nabla}\varphi|\,\boldsymbol{\nabla}\cdot\left(\frac{\boldsymbol{\nabla}\varphi}{|\boldsymbol{\nabla}\varphi|}\right)\right] \tag{4.41}$$

4.1.4.2 Regarding the geometric approach

In the introduction of Kassner et al. (2001), the authors present an in depth and quiet comprehensive, although concise, discussion regarding the whys and wherefores as well as the pros and cons of the energetic (or variational) and the geometric approaches to the PFM. In this paragraph, a very short and limited summary of said discussion is offered. The main ideas brought up by the authors can be separated into three categories.

Arguments for the energetic approach

Firstly, there are the arguments that make a case for the energetic approach. If the contributions to the free energy are well known and physically justified for a given problem, Gibbs theory predicts that the corresponding model stemming from the variational approach is bound to be right. In such cases, if the sharp interface limit of the model departs from the classic sharp interface models, one can interpret this as a sign that the sharp models lack some profound physics to properly describe the system. The starting argument of this section that this approach can be used to deal with situation where the interface is physically wide of course also applies.

Arguments for the geometric approach

Secondly, one can find arguments that support the geometric approach. As already mentioned, in the case where the interface is small in regards of the system but not physically that small, a situation referred to as the thin interface limit, the energetic approach can become unpractical. It is even shown in Karma and Rappel (1998) that in the thin interface limit, when variational and geometric approaches can both be used to solve the system, the second is usually considerably more practical from a numerical point of view. If a sharp interface model is already well established to describe a system, the only requirement for a PFM to be used as well is to asymptotically converge towards said sharp interface model in the sharp interface limit. Moreover, one strong argument for the energetic approach would be its ability to offer a description of the inner layers of the interface, which is an irrelevant information in the thin interface limit where only the proper macroscopic interface dynamics is targeted. As such, a geometric approach where the free energy is not longer a focal point could be a sounder choice.

Arguments for the PFM

Thirdly, to balance the previous arguments, as one would think that the geometric approach is but a sharp interface method in disguise, the authors recall some arguments championing the PFM altogether. Owing the similarities with the LS methods, geometric PFM shares its main advantages, in particular the simplicity of capturing the interface rather than tracking it without the extra need to reconstruct it as in VOF methods. Besides, the geometric PFM still inherently contains the anti-diffusive properties of the variational PFM which ensure that the interface does not overly diffuse and that its width is maintained without the additional need to solve the LS reinitialization equation. Moreover, depending on the physical system that is treated, sharp interface methods can develop finite-time singularities that render them numerically challenging to solve. These singularities do not appear when PFM, either variational or geometric, are used.

The geometric approach has been successfully be applied in Beckermann et al. (1999) to grain growth and in Boettinger et al. (2002) to dendidric growth. The method has been investigated in more depth from a physical, mathematical and numerical point of view in Folch et al. (1999); Sun and Beckermann (2007); Takada et al. (2013); Chai et al. (2018).

4.1.5 Phase-Field methods with Navier-Stokes equations

Almost from their inception, PFM have been combined with Euler or Navier-Stokes equations to address hydrodynamics problems. The earliest instance of such a combination is referenced in Hohenberg and Halperin (1977) as model H. Since then, variants of model H have been derived, depending on the founding PFM method used (Cahn-Hilliard or Allen-Cahn) and the assumption concerning the flow, particularly regarding its compressibility. It appears that all these derivations essentially follow the same steps and as such, they can be assembled to be described using one unified fashion of which key elements are provided in the following paragraphs. Contrary to the Cahn-Hilliard or Allen-Cahn models which described a motionless evolution of the phase-field φ, these more complete models focus on transformations where the phase-field evolution is accompanied by an inertial fluid motion of which it is the primary cause.

4.1.5.1 Phase-Field methods for compressible flows

If historically, PFM have been first combined with hydrodynamics equation considering incompressible flows through model H, the derivation of such a model can be achieved in a more natural and consistent manner by considering the general case of a compressible flow. A complete derivation of the corresponding model can be found in Truskinovsky (1993). For the resulting model to be applicable to a wide variety of cases, the volumetric free energy F_{PF} is supposed to depend on the fluid temperature T, density ρ, phase-field φ and phase-field gradient $\boldsymbol{\nabla}\varphi$ in the form of Eq. (4.42). (In his paper, Truskinovsky assumes an additional dependency of F_{PF} in the density gradient. This dependency does not modify the nature of the equation and the principle of its derivation. Moreover, in the vast majority of the concerned literature, this dependency seems not to be considered. For these reasons, it is discarded here but the reader can refer to Truskinovsky (1993) for a more complete description.)

$$F_{\mathrm{PF}}\left(T,\rho,\varphi,\boldsymbol{\nabla}\varphi\right)=F_0\left(T,\rho,\varphi\right)+\frac{\alpha}{2}\left(\boldsymbol{\nabla}\varphi\right)^2 \tag{4.42}$$

Then, using a variational approach (also known as the Least Action Principle or Virtual Work Principle) and by compelling the system to satisfy the second law of thermodynamics with increasing entropy, the momentum and, if need be, the energy equations can be derived. A very similar type of derivation is described with more details in Sec. 5.2 (more particularly in C.1 and 5.2.3) for a Korteweg type fluid in the context of the Second Gradient theory. The reader can refer to these sections or to the reference paper Truskinovsky (1993) for further details, only the results are provided in the following.

The first noticeable result is the expression of the pressure P, defined (see Eq. (B.28)) from the specific free energy $F_{\mathrm{PF}}=F_{\mathrm{PF}}/\rho$ by $P\mathrel{\hat{=}}\left(\partial f_{\mathrm{PF}}/\partial\rho\right)_{T,\varphi,\boldsymbol{\nabla}\varphi}$, which is modified compared to the native pressure $P_0\mathrel{\hat{=}}\left(\partial f_0/\partial\rho\right)_{T,\phi}$ without capillary terms to get Eq. (4.43), α being assumed to be independent of the density ρ

$$P=P_0-\frac{\alpha}{2}\left|\boldsymbol{\nabla}\rho\right|^2 \tag{4.43}$$

The second modification is the apparition in the momentum equation (and consequently in the energy equation) of a new non-dissipative tensor $\underline{\underline{\boldsymbol{\tau}}}^{\varphi,*}$ given by:

$$\underline{\underline{\boldsymbol{\tau}}}^{\varphi,*}=\alpha\boldsymbol{\nabla}\varphi\otimes\boldsymbol{\nabla}\varphi \tag{4.44}$$

The third modification is the apparition, in the energy equation, of a peculiar term $\boldsymbol{j}^{\rho e}$ which expression depends on whether the Cahn-Hilliard or the Allen-Cahn equation is chosen as a starting base, the corresponding fluxes are given by Eqs. (4.45) and (4.46) respectively (see Heida et al. (2012b); Heida et al. (2012a)). This term is dubbed peculiar because it does not have its counterpart in the momentum equation, creating a formal asymmetry between the two equations.

$$\boldsymbol{j}^{\rho e}_{\mathrm{CH}} = M_{\mathrm{CH}}\ \mu_{\mathrm{PF}} \boldsymbol{\nabla} \mu_{\mathrm{PF}} \tag{4.45}$$

$$\boldsymbol{j}^{\rho e}_{\mathrm{AC}} = M_{\mathrm{AC}}\ \mu_{\mathrm{PF}} \boldsymbol{\nabla} (\alpha\varphi) \tag{4.46}$$

The final system of equation, written in a partially-conservative form, is given below where $\underline{\underline{\boldsymbol{\tau}}}^{d}$, $\boldsymbol{q}$ and $\boldsymbol{g}$ are the dissipative flux tensor, the thermal flux and the specific body forces and $\underline{\underline{\boldsymbol{\tau}}}^{\varphi}$ is called the capillary stress tensor.

$$\begin{cases} \dfrac{\partial(\rho\mathbf{v})}{\partial t} = -\boldsymbol{\nabla}\cdot[\rho\mathbf{v}] & \text{(4.47a)} \\ \dfrac{\partial\varphi}{\partial t} + \mathbf{v}\cdot\boldsymbol{\nabla}\varphi = \begin{cases} \boldsymbol{\nabla}\cdot[M_{\mathrm{CH}}\boldsymbol{\nabla}(\mu_0 - \boldsymbol{\nabla}\cdot(\alpha\boldsymbol{\nabla}\varphi))] \\ \text{or} \\ -M_{\mathrm{AC}}[\mu_0 - \boldsymbol{\nabla}\cdot(\alpha\boldsymbol{\nabla}\varphi)] \end{cases} & \text{(4.47b)} \\ \dfrac{\partial(\rho\mathbf{v})}{\partial t} = -\boldsymbol{\nabla}\cdot\left[P_0\underline{\underline{\mathbf{I}}} + \rho\mathbf{v}\otimes\mathbf{v} + \underline{\underline{\boldsymbol{\tau}}}^{\varphi} - \underline{\underline{\boldsymbol{\tau}}}^{d}\right] + \rho\boldsymbol{g} & \text{(4.47c)} \\ \dfrac{\partial(\rho e)}{\partial t} = -\boldsymbol{\nabla}\cdot\left[(\rho e + P_0)\,\mathbf{v} + \underline{\underline{\boldsymbol{\tau}}}^{\varphi}\cdot\mathbf{v} + \boldsymbol{j}^{\rho e} - \underline{\underline{\boldsymbol{\tau}}}^{d}\cdot\mathbf{v} + \boldsymbol{q}\right] + \rho\boldsymbol{g}\cdot\mathbf{v} & \text{(4.47d)} \end{cases}$$

$$\begin{cases} \boldsymbol{j}^{\rho e} = \begin{cases} M_{\mathrm{CH}}\ \mu_{\mathrm{PF}}\boldsymbol{\nabla}\mu_{\mathrm{PF}} \\ \text{or} \\ M_{\mathrm{AC}}\ \mu_{\mathrm{PF}}\boldsymbol{\nabla}(\alpha\varphi) \end{cases} & \text{(4.47e)} \\ \underline{\underline{\boldsymbol{\tau}}}^{\varphi} = \alpha\left(\boldsymbol{\nabla}\varphi\otimes\boldsymbol{\nabla}\varphi - \dfrac{1}{2}|\boldsymbol{\nabla}\varphi|^2\,\underline{\underline{\mathbf{I}}}\right) & \text{(4.47f)} \end{cases}$$

Theoretical results

Several papers have been devoted to the study of the aforementioned system, although it should be noticed that the energy equation is usually not considered in such studies. Another important detail is that these papers are focused on the study of the physical and mathematical properties of the equations and to the better of our knowledge, no relevant numerical results have been produced so far involving the full compressible Navier-Stokes (or Euler) equations combined with a PFM approach. Nonetheless, these papers provide an important insight into these new type of complex models and deserve to be mentioned. Only isothermal configurations are considered which means that the energy equation (4.47d) is not taken into account.
In Heida et al. (2012b); Heida et al. (2012a), the authors propose a new fully consistent thermodynamic derivation and generalize to multi-fluid mixtures the Navier-Stokes / PFM model, for the Cahn-Hilliard and Allen-Cahn approaches respectively, based on the founding work of Truskinovsky (1993); Lowengrub and Truskinovsky (1998) and Blesgen (1999).
Regarding the Cahn-Hilliard equation, in Abels and Feireisl (2008) the authors proved the existence of local weak solutions, a result later improved in Kotschote and Zacher (2015)

where the existence and uniqueness of local strong solutions is demonstrated based on the strongly coupled hyperbolic-parabolic nature of the system of equations. More recently, the existence and long time stability of strong solutions have been exposed for one-dimensional configurations in Chen et al. (2018).
For the Allen-Cahn equation, the existence of weak solutions for spherical symmetry has been shown in Witterstein (2008) and that of global in time weak solutions for one dimensional configurations has been proven in Feireisl et al. (2010). In Ding et al. (2013); Chen and Guo (2017), for one dimensional configurations, the authors have demonstrated at once the existence and uniqueness of global classic solutions, the existence of weak solutions and the existence of unique strong solutions.

4.1.5.2 Phase-Field methods for incompressible flows

To obtain the governing equations of the combined Navier-Stokes PFM model for incompressible flows, known as model H (see Hohenberg and Halperin (1977)), one can apply the same methodology as presented in Sec. 4.1.5.1 with the difference that the continuity equation classically reduces to $\boldsymbol{\nabla}\cdot\mathbf{v}=0$ and that the energy equation is no longer considered. This has been done for instance in Gurtin et al. (1996); Liu et al. (2003); Yue et al. (2004) where the subsequent model has been used to study nucleation and flow coarsening, surface tension related effects and droplet coalescence respectively. Practically, the equations can also be formally obtained from the system Eqs. (4.47a) - (4.47f) by discarding the energy equation (with the assumption of an isothermal flow) and by adapting the mass equation to get:

$$\begin{cases} \boldsymbol{\nabla}\cdot\mathbf{v}=0 & \text{(4.48a)}\\ \dfrac{\partial\varphi}{\partial t}+\mathbf{v}\cdot\boldsymbol{\nabla}\varphi=\begin{cases}\boldsymbol{\nabla}\cdot\left[M_{\mathrm{CH}}\boldsymbol{\nabla}\left(\mu_0-\boldsymbol{\nabla}\cdot\left(\alpha\boldsymbol{\nabla}\varphi\right)\right)\right]\\ \text{or}\\ -M_{\mathrm{AC}}\left[\mu_0-\boldsymbol{\nabla}\cdot\left(\alpha\boldsymbol{\nabla}\varphi\right)\right]\end{cases} & \text{(4.48b)}\\ \dfrac{\partial(\rho\mathbf{v})}{\partial t}=-\boldsymbol{\nabla}\cdot\left[P\underline{\underline{\mathbf{I}}}+\mathbf{v}\otimes\mathbf{v}-\underline{\underline{\boldsymbol{\tau}}}^{d}\right]-\boldsymbol{\nabla}\cdot\underline{\underline{\boldsymbol{\tau}}}^{\varphi}+\rho\boldsymbol{g} & \text{(4.48c)}\end{cases}$$

It should be noticed that the system in Eqs. (4.48a)-(4.48c) brings about an additional subtlety relatively to its compressible counterpart. Indeed, in the momentum equation, the classic pressure P_0 has been traded for a general pressure P and the expression of the capillary tensor $\underline{\underline{\boldsymbol{\tau}}}^{\varphi}$ as not been specified. The reasons for these modifications are twofold and related. Firstly, for an isothermal incompressible flow, it is well established that the independent Laplace-like mass equation Eq. (4.48a) decouples the calculation of the velocity field $\mathbf{v}_\Gamma$ from that of the pressure P. Secondly and consequently, the actual value of the P is directly given by the velocity field and the actual analytical expression of P is never used in practice to evaluate it. It results that several expressions have been used in the literature to describe the divergence of the capillary tensor $\boldsymbol{\nabla}\cdot\underline{\underline{\boldsymbol{\tau}}}^{\varphi}$ while the exact expression of the corresponding pressure P is never provided explicitly. In Tab. 4.1 are listed the couples $\left(P,\boldsymbol{\nabla}\cdot\underline{\underline{\boldsymbol{\tau}}}^{\varphi}\right)$ that are commonly encountered with the relevant references. In particular an effort is given to provide the exact expression of the corresponding pressure P relatively to the reference pressure P_0 when possible. Only the last expression of $\boldsymbol{\nabla}\cdot\underline{\underline{\boldsymbol{\tau}}}^{\varphi}$ proposed in Kim (2005) cannot be related to an expression of P arising consistently from P_0.

P	$\boldsymbol{\nabla}\cdot\underline{\underline{\boldsymbol{\tau}}}^{\varphi}$	References
P_0	$\boldsymbol{\nabla}\cdot\left(\alpha\boldsymbol{\nabla}\varphi\otimes\boldsymbol{\nabla}\varphi-\frac{\alpha}{2}\left\|\boldsymbol{\nabla}\varphi\right\|^2\underline{\underline{\mathbf{I}}}\right)$	Starovoitov (1994) Antanovskii (1995) Ding et al. (2013)
$P_0-\frac{1}{2}\left\|\boldsymbol{\nabla}\varphi\right\|^2$	$\boldsymbol{\nabla}\cdot(\alpha\boldsymbol{\nabla}\varphi\otimes\boldsymbol{\nabla}\varphi)$	Lowengrub and Truskinovsky (1998) Liu et al. (2003); Yue et al. (2004) Yang et al. (2006) Guillén-González and Tierra (2014) Shen and Yang (2014) Vasconcelos et al. (2014)
$P_0+\frac{1}{2}\left\|\boldsymbol{\nabla}\varphi\right\|^2$	$\alpha\boldsymbol{\Delta}\varphi\boldsymbol{\nabla}\varphi$	Gurtin et al. (1996)
$P_0+\frac{1}{2}\left\|\boldsymbol{\nabla}\varphi\right\|^2+F_0$	$-\mu\boldsymbol{\nabla}\varphi$	Chella and Viñals (1996) Boyer (2002); Badalassi et al. (2003) Ceniceros et al. (2010) He et al. (2011); Liang et al. (2014) Zhao et al. (2016); Ma et al. (2017)
$P_0+\frac{1}{2}\left\|\boldsymbol{\nabla}\varphi\right\|^2+F_0+\varphi\mu$	$\varphi\boldsymbol{\nabla}\mu$	Jasnow and Vinals (1995) Jacqmin (1999); Jacqmin (2000) Kim et al. (2004) He and Kasagi (2008)
–	$\boldsymbol{\nabla}\cdot\left(\frac{\boldsymbol{\nabla}\varphi}{\left\|\boldsymbol{\nabla}\varphi\right\|}\right)\left\|\boldsymbol{\nabla}\varphi\right\|\boldsymbol{\nabla}\varphi$	Kim (2005); He and Kasagi (2008) Jeong and Kim (2017) Kim and Lee (2017)

Table 4.1: *Pressure and capillary tensor divergence used in the literature for the incompressible Navier-Stokes PFM model.*

A discussion regarding the different expressions for the capillary tensor divergence is proposed in Kim (2005) where the authors justify their new expression as being the sole allowing the direct calculation of the pressure field. However, this argument seems to lack substantial proofs and has not prevented other more classic expressions to still be employed in more recent studies.

Theoretical results

Just as for their compressible counterparts, efforts have been made to characterize the incompressible Navier-Stokes PFM models although studies dedicated to this topic remain very scarce.
For the Cahn-Hilliard equation, Starovoitov (1997) has proven that non-homogeneous stationary solutions are not asymptotically stable in time. In Boyer (1999), the author has proven the existence of global weak solutions in two and three dimensional settings for density matched fluids. Additionally, he has also shown that over a sufficiently long period of time, the solutions are unique and become strong. Still for density matched fluids, the well-posedness of the Navier-Stokes Cahn-Hilliard system has been addressed in Abels (2009b). The authors have proven the existence of weak solutions for the non-stationary system. They also have shown that said solutions continuously converge, for infinite time, towards regular solutions

of the stationary system. The existence of weak solutions has been extended to fluids with different densities in Abels (2009a); Abels et al. (2013a); Abels et al. (2017), to fluids with a degenerate mobility in Abels et al. (2013b) or to problems with solid boundaries and moving contact lines in Gal et al. (2016); Gal et al. (2019).
Regarding the Allen-Cahn equations, the existence and uniqueness of global weak solutions has been established in Du et al. (2007). In Xu et al. (2010), the existence of axisymmetric one-dimensional and three-dimensional solutions has been proved and the authors in Zhao et al. (2011) have shown that in the limit when the viscosity vanishes, the equations consistently degenerate into the combined Euler Allen-Cahn incompressible system. The previously mentioned results have been obtained solely for density matched fluids but more recently, in Li and Huang (2018), the authors have demonstrated the existence and uniqueness of local strong solutions for fluid of different densities in two and three dimensional configurations.
Combined studies have also been performed for the Cahn-Hilliard and Allen-Cahn equations. The well-posedness of the Navier-Stokes Cahn-Hilliard and the volume preserving Navier-Stokes Allen-Cahn system is addressed in Liu et al. (2012). The authors have also studied breakup conditions for both models and in particular, have noticed stricter breakup conditions for the Allen-Cahn equation. For the latter, a local perturbation is usually required in contrast with the Cahn-Hilliard equation for which enough speed and/or shear suffices to initiate the breakup. In Freistühler and Kotschote (2017), the authors have proposed a solution theory for the Korteweg, Cahn-Hilliard and Allen-Cahn models combined with the Navier-Stokes equations. They have again derived systematically all the affiliated equations for non miscible incompressible fluids. Moreover, for fluids with temperature-independent density, the authors have shown that both the Navier-Stokes Cahn-Hilliard and Navier-Stokes Allen-Cahn models reduce to the Navier-Stokes Korteweg model.

Numerical results

Contrary to the compressible system, a substantial list of simulations, using a wide variety of numerical methods, have been performed using either the Cahn-Hilliard or Allen-Cahn equations combined with the incompressible Navier-Stokes system; the few results presented here do not represent a comprehensive description.

Using the Cahn-Hilliard equation, the authors in Jasnow and Vinals (1995) have simulated grain-coarsening under thermocapillary motions, the energy equation is not solved, rather, a temperature dependency is introduced in the capillary coefficient to study the motion under temperature. With the same equation, using a backward fully implicit scheme, authors in Gurtin et al. (1996) have also simulated the grain-coarsening of a binary fluid in two dimensions. Jacqmin (1999) has addressed one and two-dimensional convection and has simulated capillary waves and Rayleigh-Taylor instabilities using second and compact fourth order finite difference schemes. With the same method in, Jacqmin (2000) has also simulated moving contact lines dynamics. Drops falling on a liquid reservoir and Rayleigh-Taylor instabilities for non miscible fluids have been computed in Boyer (2002) using an explicit finite difference scheme with second order anti-diffusion correction. A semi-implicit time-splitting scheme with high order space derivatives (spectral decomposition and finite difference) has been used in Badalassi et al. (2003) to study two and three-dimensional phase separation and pattern formation under shear stress for incompressible binary fluids. The authors in Liu et al. (2003)

have used a Fourier-spectral method with a semi-implicit time discretization in two dimensions to study surface tension effects, bubble relaxation and coalescence.

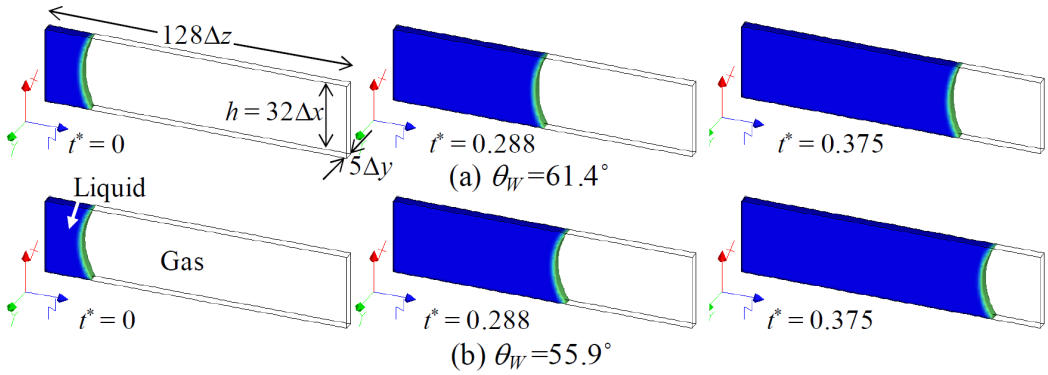

Figure 4.8: *Water penetrating the air-filled gap between parallel plates with hydrophilic properties, taken from Takada et al. (2013)*

A dynamic contact-line problem has been examined in Takada et al. (2013) taking the form of a capillary driven penetration of a liquid phase between two hydrophilic plates with a specified contact angle θ_W. The gap is initially filled with air offering a high density ratio of about 800 (the simulation is also performed with an ethanol-air mixture with a smaller density ratio of 636). Using both a classic central difference scheme and a third-order upwind finite difference scheme on a staggered grid with a second order Runge-Kutta explicit time integration, the authors have obtained the results presented in Fig. 4.8. In particular, they have observed a particularly good agreement of these results with the theory regarding the time evolution of the liquid velocity and length of penetration for both water-air and ethanol-air mixtures. Using multiple-relaxation-time lattice-Boltzman method, the authors in Liang et al. (2014) have simulated Raleigh-Taylor instabilities for different values of Reynolds number. The results, presented in Fig. 4.9, show perfectly the different behavior that occurs for high Reynolds numbers. In particular, the presence of vortices created by the shear layers between the two fluids is strongly visible. The stabilization effect of the higher relative viscosity for low Reynolds numbers prevents these vortices to form and roll-up, the lighter fluid simply rises in the form of macroscopic bubbles.

With the volume preserving Allen-Cahn equation as a basis, solved using a stabilized semi-implicit scheme, the authors in Yang et al. (2006) have simulated jet pinch-off and droplet formation for non miscible fluids, a semi-implicit second-order rotational pressure-correction scheme is used for the Navier-Stokes equation. In Tan et al. (2007), interface dynamics and droplets coalescence of density matched fluids has been studied solving the Navier-Stokes Allen-Cahn system using a semi-implicit finite volume scheme with an adaptive mesh redistribution method. In Vasconcelos et al. (2014), the authors have chosen a residual based finite element scheme with adaptative mesh refinement to study diffusive relaxation, chemical convection, interface dynamics and coalescence by solving the conservative Allen-Cahn equation combined to the incompressible Navier-Stokes equations.
An energy stable and totally decoupled scheme is introduced in Shen and Yang (2014) to simulate the deformation of a liquid crystal immersed into a viscous fluid, as shown in Fig.

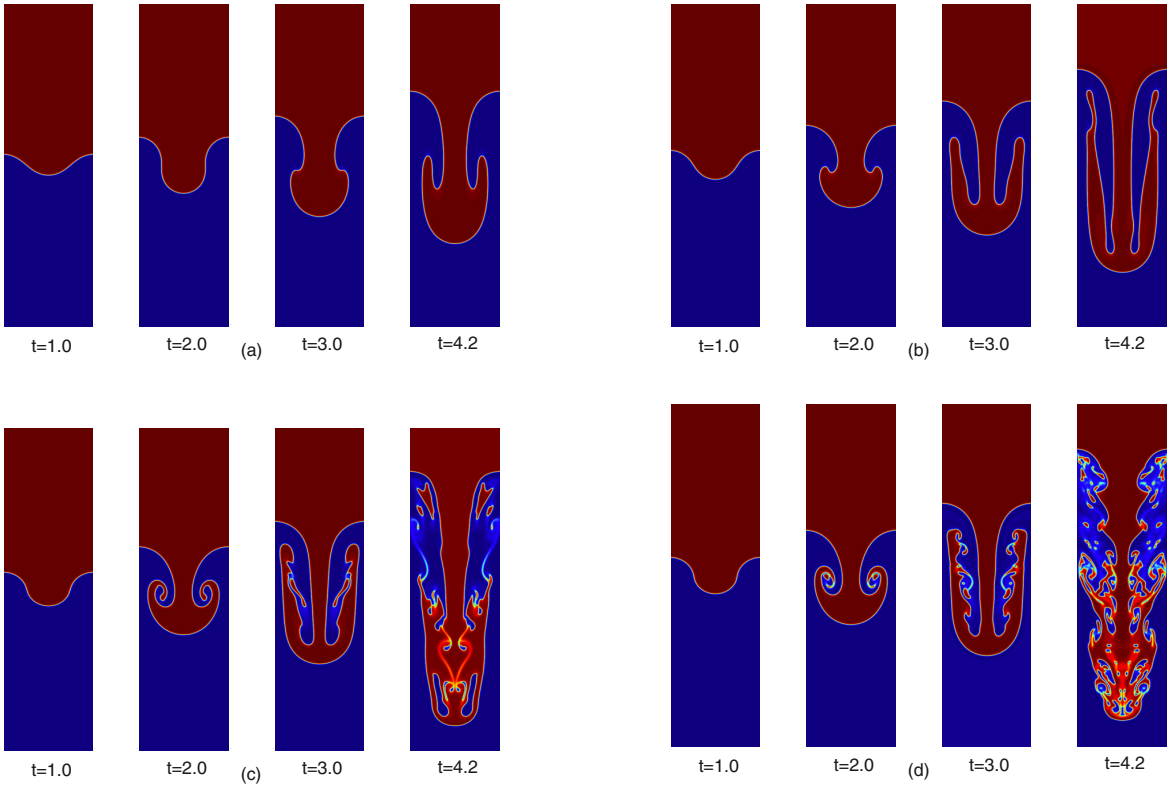

Figure 4.9: *Time evolution of the concentration in a two-dimensional Rayleigh-Taylor instability for different Reynolds numbers ((a) $Re = 30$, (b) $Re = 150$, (c) $Re = 3000$, (d) $Re = 30000$), taken from Liang et al. (2014)*

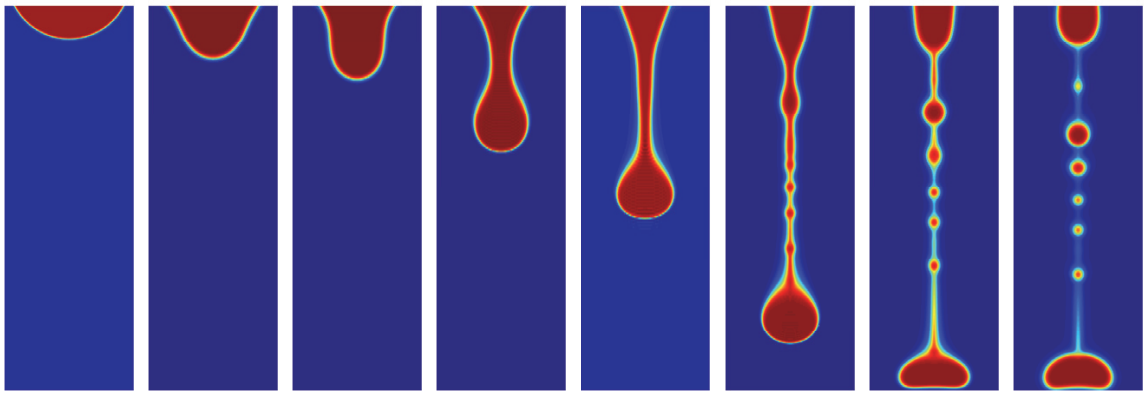

Figure 4.10: *Dynamic deformation of a liquid crystal drop immersed in a viscous fluid, taken from Shen and Yang (2014)*

4.10. A stabilization procedure is used for the classic Allen-Cahn equation while a pressure correction strategy is applied to address the Navier-Stokes equations for fluids with very similar densities (the Boussinesq approximation can be used). The viscosity of the liquid crystal causes a long thread to be created between the leading droplet and the inlet. The elongated thread,

following its narrowing, eventually breaks up into smaller satellite droplets of various sizes. The main droplet also deforms upon impact with the bottom of the reservoir. The authors have concluded with a satisfactory behavior of the system and a good agreement with experimental results. A three-phase model has been developed for the Navier-Stokes Allen-Cahn in Zhao et al. (2017) where two phase fields φ and ψ are used. Likewise, a semi-implicit stabilizing energy stable scheme is used for the phase-field equations while a pressure-correction scheme, reminiscent of the projection method, is used to decouple the computation of the pressure and the velocity. The results in Fig. 4.11 show the gravity-driven rising of a bubble into a layered reservoir with a second and third fluid. The Boussinesq approximation is used to account for the slight differences in the three fluid densities. While crossing the interface between the two layered fluids, the bubble traps a long filament of the lower fluid that eventually breaks and collapses due to gravity. However, due to capillary effects, a small amount of the lower fluid remains glued at the bottom of the bubble which pursues its rising, a behavior consistent with simulations performed using Sharp Interface methods.

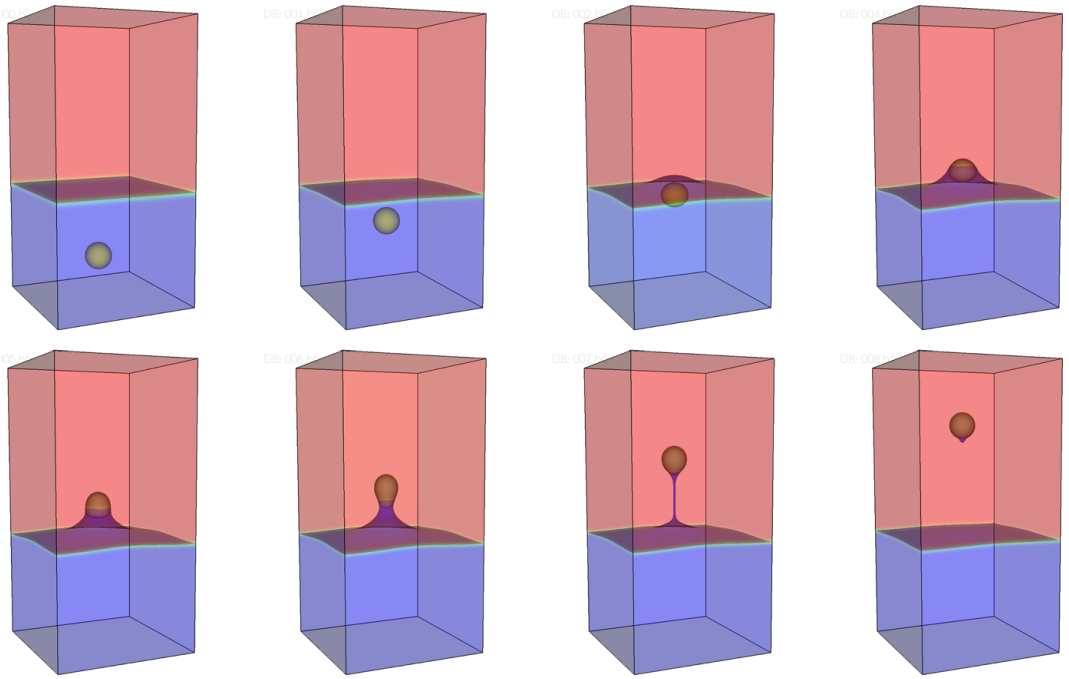

Figure 4.11: *Dynamic time evolution of a bubble rising into two layered non-miscible fluids of different characteristics, taken from Zhao et al. (2017)*

In Chiu and Lin (2011), a semi-implicit dispersion-relation-preserving scheme and a projection method are used to solve the Navier-Stokes equation while a dispersion-relation-preserving dual-compact upwind scheme (see Chiu and Sheu (2009)) is used for the pseudo-conservative geometric phase-field equation. With these methods, the authors have treated the case of a water droplet falling trough air to impact an initially quiescent liquid film. These schemes are paired with a mass-redistribution algorithm to ensure the boundedness of the solution and the perfect mass conservation. The results are presented in Fig. 4.12 where the evolution of the free surface is given: the typical splashing phenomena are qualitatively recovered and permit quantitative comparisons with previous simulations for the same case showing a good

agreement.

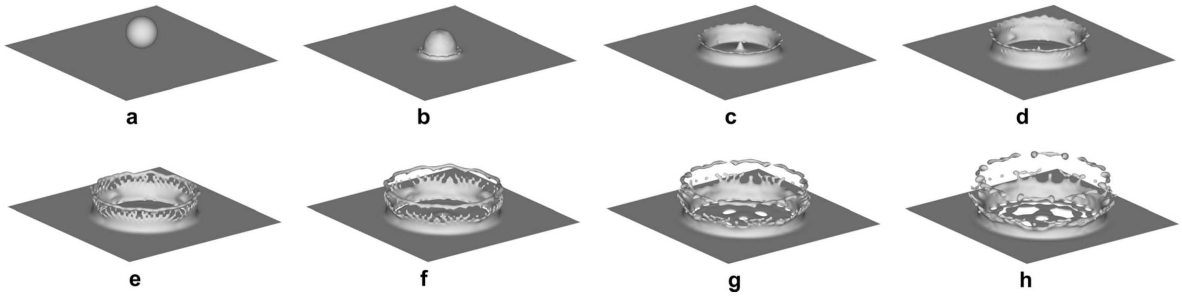

Figure 4.12: *Simulation of a water droplet impacting a quiescent water film using a pseudo-conservative geometric approach for the phase-field equation, take from Chiu and Lin (2011)*

Conclusion and additional remarks

One conclusion of the present bibliographic work is that no results seems to have been produced using either of the Allen-Cahn or Cahn-Hilliard equation combined with hydrodynamics (Euler or Navier-Stokes equation) while actually solving the energy equation. An underlying consequence is that all the numerical results that are presented have been obtained by considering isothermal fluids. It should be emphasized that most of the previously mentioned theoretical work related to this methods actually include the energy equation in their studies, the shortage of results only concerns the numerical simulations.
Two noteworthy exceptions can be found in Antanovskii (1995) and Jasnow and Vinals (1996) where a temperature dependency is introduced, although indirectly and not by solving the energy equation. A temperature gradient is imposed in a single designated direction of the two dimensional computational domain. It then impacts the equations by allowing the coefficient α, i.e. the surface tension in virtue of Eq. (4.6), to vary with the temperature in the form $\alpha(T) = \alpha_0 + \Delta\alpha(T - T_0)$ where T_0 and α_0 are reference values. In Antanovskii (1995), the author has studied the structure of the interfacial layers separating two non-isothermal fluids while said interface is endowed with a constant temperature gradient. Using the same method, the authors in Jasnow and Vinals (1996) have studied the migration of a fluid droplet into an different phase with an imposed temperature gradient.

4.2 Multi-Fluid methods

4.2.1 Historical overview

The foundations of the Multi-Fluid methods have been laid down in the late 1970's and early 1980's by the likes of Drew and Segel (1971); Kuo and Summerfield (1975); Krier and Gokhale (1978); Gough and Zwarts (1979); Butler et al. (1982); Akhatov and Vainshtein (1984). It was initially motivated by the will to simulate highly reactive heterogeneous mixtures such as explosives, solid granulated propellants or heterogeneous reactive gases. The work in Kuo and Summerfield (1975); Gough and Zwarts (1979) proposed some of the first applications of the two-phase flow modeling to highly reactive gases and the studies in Krier and Gokhale (1978); Butler et al. (1982); Akhatov and Vainshtein (1984) have influenced a vast amount of work regarding the deflagration-to-detonation transition in granular two-phase flow materials. Such materials, as well as many others of industrial interest, are characterized by the existence of an interface between their different constituents of which modeling has a strong impact on the other physical phenomena at play such as mass exchange, chemical reactions and shock propagation. As such, it must be handled with a special care.
The thermodynamic basis behind the models used by these various authors had been established in Truesdell and Toupin (1960) where a continuum approach is used to model both fluids. The approach is then completed by expressing the constrained mass, momentum and flux exchanges between the two components. In Drew and Segel (1971); Drew (1983), a different approach is used based on mass,volume or area averaging procedures that encompass the interfacial region. It also leads to a continuous description of the flow with transport equations for the averaged variables.

In Baer and Nunziato (1986), the authors have derived a model, involving seven transport equations, which has established itself as the reference model for the Multi-Fluid methods and has, since then, spawned a wide variety of sub-models. The model of Baer and Nunziato (1986) however, was still strongly oriented towards the modeling of deflagration-to-detonation transition and its formulation was not readily usable in the context of liquid-vapor two-phase flow simulations. An adaptation of the 7-equation model to such configurations has been proposed in Saurel and Abgrall (1999a) after a comparative study of the different available two-phase flow models performed by the same authors in Saurel and Abgrall (1999b). In the latter, the authors emphasized on the practical benefits of having a unified description of the whole flow with an intrinsic handling of the interface when compared to Front-Tracking or Volume-of-Fluid methods. This model has been successfully applied in Saurel et al. (2009) to model air-water shocks and cavitation in one and two dimensions or in Saurel et al. (2003) to study shock-bubble interactions.
The model assumes that the two phases possess their own velocity, pressure, temperature and chemical potential and these variables yearn to balance through local relaxation processes. To better answer different classes of problem, this 7-equation model has then been regularly reworked in ensuing studies by comparing the characteristic times of the different thermodynamic phenomena at play and reducing the number of equations to only account for the slowest one. In Kapila et al. (2001); Allaire et al. (2002) the authors have used two different 5-equation models assuming mechanical and kinematic equilibrium, i.e. equality of the pressure and velocity of both phases. In Saurel et al. (2009), the authors used a 6-equation

model with velocity equality but assumed a stiff relaxation of the pressure, which essentially equated to a 5-equation model. Assuming a stiff relaxation of the temperature, a 4-equation model has been derived in Le Métayer et al. (2005); Saurel et al. (2008) to address cavitation and flashing and in Le Martelot et al. (2014) to incorporate heat transfer and simulate boiling flows. An equivalent 4-equation model has also been used in Gaillard et al. (2016) to perform LES simulations of LO_x/GH_2 flames and in Pelletier (2019) to perform LES simulations of a non-reactive LO_x/GH_2 subcritical jet. By relaxing the chemical potential, a 3-equation model as been obtained in Saurel et al. (2008) and more recently in Morin and Flåtten (2016) and Chiapolino et al. (2017b). It has also been studied in Pelletier (2019). This model ensues from the 4-equation model for which an instantaneous balancing of the chemical potential is assumed, and has provided several successful simulations of evaporating or reactive coaxial jets in subcritical injection conditions, among which Chiapolino et al. (2017b); Matheis and Hickel (2018); Pelletier (2019).

This section focuses on presenting the main models that exist in the literature regarding Multi-Fluid methods and the hypotheses that permit their derivation. A brief overview of important results obtained with these models is proposed.
The Multi-Fluid methods, by construction, offer an Eulerian description of flows involving two phases and possibly multiple components in the sense that the same set of equations is solved in the whole domain without the necessity of special treatment for the regions of interaction between the phases. This feature, shared by the Diffuse Interface Methods, is a strong argument in their favor when compared to Sharp Interface approaches. In the following, the description is limited to the case of a liquid-vapor mixture of the same fluid in a one-dimensional setting.

4.2.2 Out-of-equilibrium model

The founding model set in Saurel and Abgrall (1999a) revolves around seven equations that describe the evolution of the flow. These equations are derived assuming that both the liquid and vapor phases have their own pressure (P_l, P_v), velocity (u_l, u_v), temperature (T_l, T_v) and chemical potential (μ_l, μ_v). The phases can be described by their volume fraction ϕ_l and ϕ_v respectively with the constraint $\phi_l + \phi_v = 1$. Without phase change, the equations are:

$$\frac{\partial \phi_v \rho_v}{\partial t} + \frac{\partial}{\partial x}\left(\phi_v \rho_v u_v\right) = 0 \tag{4.49a}$$

$$\frac{\partial \phi_l \rho_l}{\partial t} + \frac{\partial}{\partial x}\left(\phi_l \rho_l u_l\right) = 0 \tag{4.49b}$$

$$\frac{\partial \phi_v \rho_v u_v}{\partial t} + \frac{\partial}{\partial x}\left[\phi_v\left(\rho_v u_v^2 + P_v\right)\right] = -P_I \frac{\partial \phi_l}{\partial t} - K_u\left(u_v - u_l\right) \tag{4.49c}$$

$$\frac{\partial \phi_l \rho_l u_l}{\partial t} + \frac{\partial}{\partial x}\left[\phi_l\left(\rho_l u_l^2 + P_l\right)\right] = P_I \frac{\partial \phi_l}{\partial t} + K_u\left(u_v - u_l\right) \tag{4.49d}$$

$$\frac{\partial \phi_v \rho_v e_v}{\partial t} + \frac{\partial}{\partial x}\left[\phi_v\left(\rho_v e_v + P_v\right) u_v\right] = -P_I u_I \frac{\partial \phi_l}{\partial t} - K_u u_I\left(u_v - u_l\right) - K_P P_I\left(P_l - P_v\right) \tag{4.49e}$$

$$\frac{\partial \phi_l \rho_l e_l}{\partial t} + \frac{\partial}{\partial x}\left[\phi_l\left(\rho_l e_l + P_l\right) u_l\right] = P_I u_I \frac{\partial \phi_l}{\partial t} + K_u u_I\left(u_v - u_l\right) + K_P P_I\left(P_l - P_v\right) \tag{4.49f}$$

$$\frac{\partial \phi_l}{\partial t} + u_I \frac{\partial \phi_l}{\partial x} = K_p\left(P_l - P_v\right) \tag{4.49g}$$

where K_p and K_u are relaxation coefficients that entice the tendency of the phases to balance their pressure and velocity. This system, apart from the conservative transport terms on the left-hand side, also presents numerous non-conservative source terms on the right-hand side that must be dealt with cautiously.
In the source terms appear the quantities P_I and u_I that represent the interface pressure and velocity, *a priori* different from the pressures and velocities of the phases. The manner in which these interfacial terms are defined has a strong impact on the mathematical properties of the system and should also be carefully done. With the right choices, the system can be proven to be hyperbolic and thus can be treated with standard and powerful dedicated numerical methods. These aspects are discussed in more details in Saurel and Abgrall (1999a); Abgrall and Saurel (2003). This system of equations has the added advantage that the thermodynamic description of each phase, e.i. the relation $e_i = f(\rho_i, T_i)$ for phases $i = l, v$ can be chosen independently, which prove to be convenient for some cases. Moreover, besides the six first equations, which are for the most part the classic Euler equations particularized to each phase, a last equation (4.49g), called the compaction equation, with its peculiar formulation, serves to account for the evolution of the phase volume, in particular when compression or evaporation effects occur.

4.2.3 Mechanical and kinematic equilibrium models

By assuming an infinitely fast relaxation in pressure and velocity, i.e. $K_p \to \infty$ and $K_u \to \infty$, the authors in Kapila et al. (2001) have reduced the degrees of freedom and thus the number of equations. This leads in particular to the relations $P_v = P_l = P_I = P$ and $u_v = u_l = u_I = u$. This simplification is physically motivated by the practical observations which shows these processes to have much lower characteristic times than that of thermal or chemical relaxation. This new model is obtained as an asymptotic limit of the 7-equation model, which has been proven and thoroughly analyzed in Murrone and Guillard (2005). The corresponding equations are:

$$\frac{\partial \phi_v \rho_v}{\partial t} + \frac{\partial \phi_v \rho_v u}{\partial x} = 0 \tag{4.50a}$$

$$\frac{\partial \phi_l \rho_l}{\partial t} + \frac{\partial \phi_l \rho_l u}{\partial x} = 0 \tag{4.50b}$$

$$\frac{\partial \rho u}{\partial t} + \frac{\partial}{\partial x}\left[\left(\rho u^2 + P\right)\right] = 0 \tag{4.50c}$$

$$\frac{\partial \rho e}{\partial t} + \frac{\partial}{\partial x}\left[\left(\rho e + P\right) u\right] = 0 \tag{4.50d}$$

$$\frac{\partial \phi_l}{\partial t} + u\frac{\partial \phi_l}{\partial x} = \phi_l\left(1 - \phi_l\right)\frac{\rho_v c_v^2 - \rho_l c_l^2}{\sum_{i=l,v}\left(1 - \phi_i\right)\rho_i}\frac{\partial u}{\partial x} \tag{4.50e}$$

where the flow density is defined by $\rho = \phi_l \rho_l + \phi_v \rho_v$, the flow volumetric sensible energy is defined by $\rho e_s = \phi_l \rho_l e_{s,l} + \phi_v \rho_v e_{s,v}$ and c_i is the sound speed of the phase $i = l, v$. When the EoSs chosen to describe each phases are convex, the system is shown to remain hyperbolic.

The authors in Allaire et al. (2002) and Saurel et al. (2009) have proposed other methods to achieve a 5-equation model. In the former, the non conservative term in the compaction equation (4.50e) has been removed altogether, which has as a consequence the modification of the characteristic waves of the flow. In the latter, the authors have returned to a 6-equation

model with different pressures, less numerically challenging to solve, but have applied a stiff relaxation on the pressure to regain mechanical equilibrium. Using this approach, they have simulated a shock-bubble interaction and compared it with the experiments, as shown in Fig. 4.13.

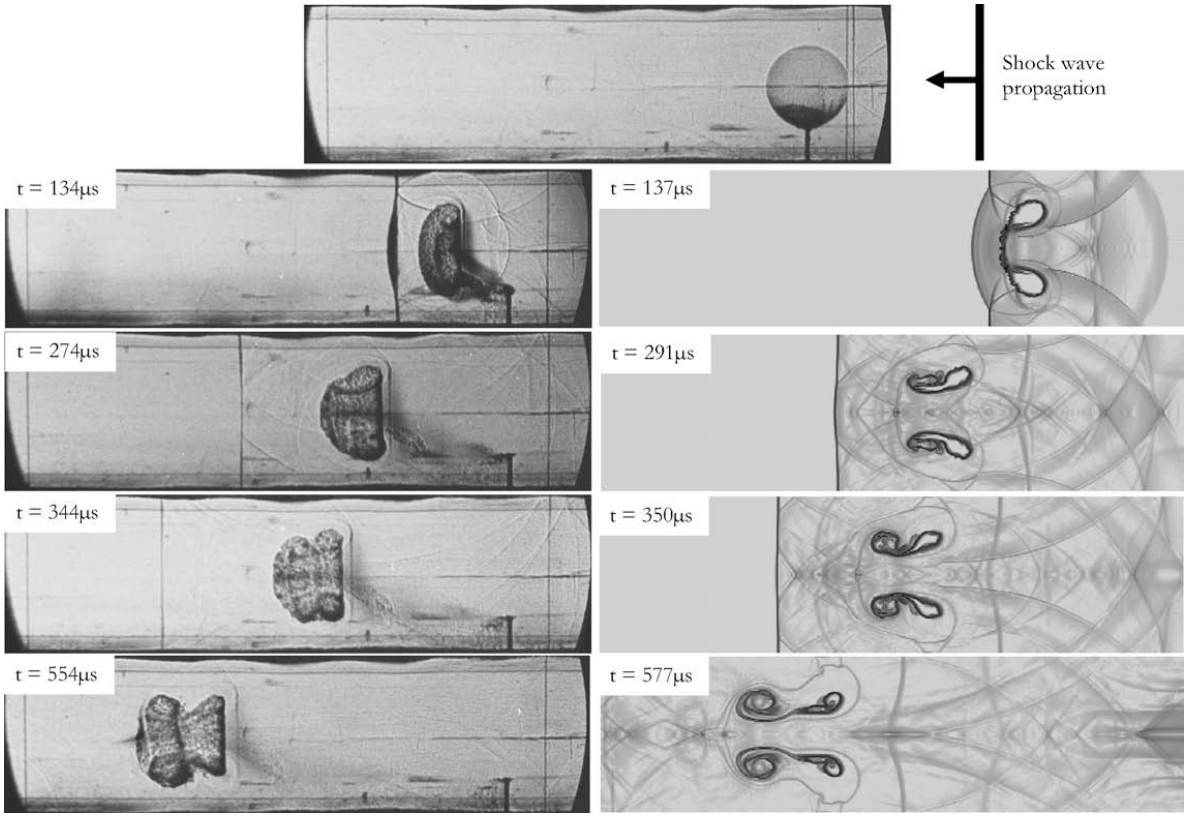

Figure 4.13: *Comparison between experimental results form Layes and Le Métayer (2007) (left images) and simulations using the quick relaxing 6-equation model for a shock-bubble interaction configuration (right images), taken from Saurel et al. (2009)*

4.2.3.1 Thermal and chemical equilibrium models

4.2.3.1.1 Temperature relaxation

Temperature imbalance can be accounted for the in 5-equation model of Kapila et al. (2001) by introducing a relaxation term in the compaction equation in the form $K_T\left(T_v - T_l\right)$, analogous to the pressure or velocity relaxation terms of the 7-equation model in Eqs. (4.49e) - (4.49g). Following the authors in Saurel et al. (2008), the new compaction equation is written:

$$\frac{\partial \phi_l}{\partial t} + u\frac{\partial \phi_l}{\partial x} = \phi_l\left(1-\phi_l\right)\frac{\rho_v c_v^2 - \rho_l c_l^2}{\sum_{i=l,v}\left(1-\phi_i\right)\rho_i}\frac{\partial u}{\partial x} + \frac{\frac{1}{\phi_v \xi_v} + \frac{1}{\phi_l \xi_l}}{\phi_v \rho_v c_v^2 + \phi_l \rho_l c_l^2} K_T\left(T_v - T_l\right) \tag{4.51}$$

With the assumption of an infinitely fast relaxation in temperature, i.e. $K_T \to \infty$ in Eq.

(4.51), the system further reduces into a 4-equation model as follows:

$$\frac{\partial \phi_v \rho_v}{\partial t} + \frac{\partial \phi_v \rho_v u}{\partial x} = 0 \tag{4.52a}$$

$$\frac{\partial \phi_l \rho_l}{\partial t} + \frac{\partial \phi_l \rho_l u}{\partial x} = 0 \tag{4.52b}$$

$$\frac{\partial \rho u}{\partial t} + \frac{\partial}{\partial x}\left[\left(\rho u^2 + P\right)\right] = 0 \tag{4.52c}$$

$$\frac{\partial \rho e}{\partial t} + \frac{\partial}{\partial x}\left[\left(\rho e + P\right) u\right] = 0 \tag{4.52d}$$

Using this type of model, the authors in Hejazialhosseini et al. (2013) have performed an impressive simulation of a three-dimensional shock-bubble interaction in order to study the subsequent vortices. Some of their results are displayed in Fig. 4.14.

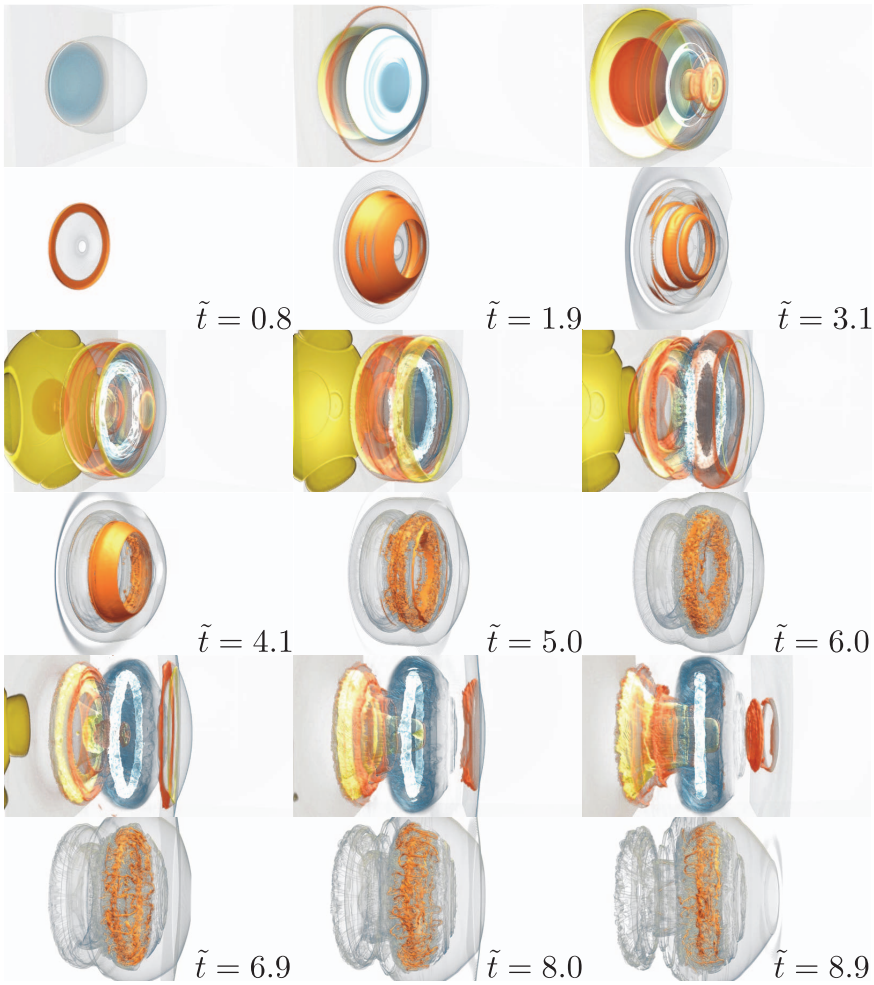

Figure 4.14: *Three dimensional simulation of a shock-bubble interaction with the 4-equation model, taken from Hejazialhosseini et al. (2013)*

The 4-equation model has been extended to multi-species configurations in Gaillard et al. (2016) with which the author has performed a simulation of the bench test Mascotte (see

Habiballah et al. (1996); Vingert et al. (1999); Gicquel et al. (2001)) in subcritical injection conditions with reactive components in a LES framework. Some visualizations for the coaxial LO_x/GH_2 jet simulation are given in Fig. 4.15.

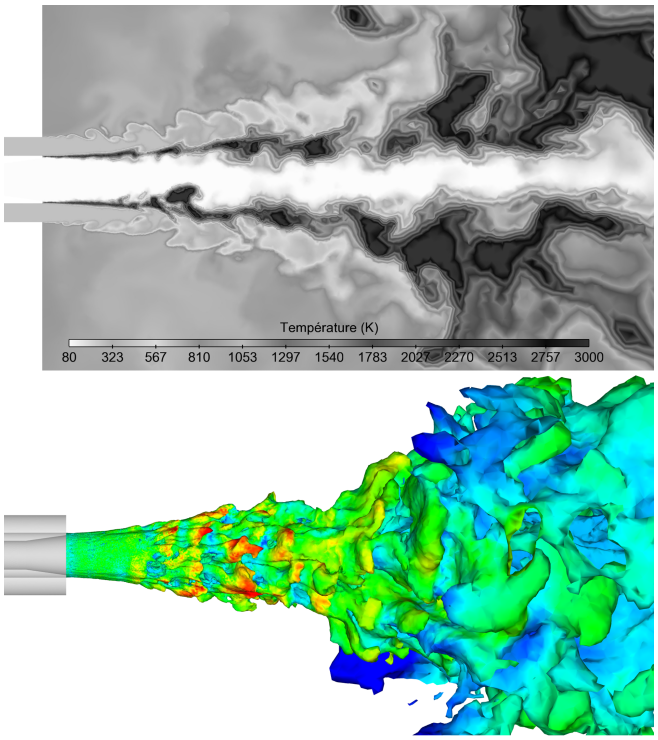

Figure 4.15: *Large Eddy Simulation with the 4-equation model of a reactive LO_x/GH_2 coaxial jet in transcritical injection conditions based in the Mascotte bench (see Habiballah et al. (1996); Vingert et al. (1999); Gicquel et al. (2001)) taken from Gaillard et al. (2016). Instantaneous temperature field in an axial cut plane (upper image) and temperature isosurface at $T = 1500$ K colored by the axial velocity (lower image).*

4.2.3.1.2 Chemical potential relaxation

Finally, the imbalance in the chemical potential of the species can also be accounted for in the 4-equation model as done in Eqs. (4.53a) - (4.53d) where K_μ is also a relaxation coefficient.

$$\frac{\partial \phi_v \rho_v}{\partial t} + \frac{\partial \phi_v \rho_v u}{\partial x} = \rho K_\mu \left(\mu_g - \mu_l\right) \tag{4.53a}$$

$$\frac{\partial \phi_l \rho_l}{\partial t} + \frac{\partial \phi_l \rho_l u}{\partial x} = -\rho K_\mu \left(\mu_g - \mu_l\right) \tag{4.53b}$$

$$\frac{\partial \rho u}{\partial t} + \frac{\partial}{\partial x}\left[\left(\rho u^2 + P\right)\right] = 0 \tag{4.53c}$$

$$\frac{\partial \rho e}{\partial t} + \frac{\partial}{\partial x}\left[\left(\rho e + P\right) u\right] = 0 \tag{4.53d}$$

Directly assuming an infinitely fast relaxation of the chemical potential leads to a 3-equation

model that is formally similar to the Euler equations system and is written:

$$\frac{\partial \rho}{\partial t} + \frac{\partial \rho u}{\partial x} = 0 \tag{4.54a}$$

$$\frac{\partial \rho u}{\partial t} + \frac{\partial}{\partial x}\left[\left(\rho u^2 + P\right)\right] = 0 \tag{4.54b}$$

$$\frac{\partial \phi \rho e}{\partial t} + \frac{\partial}{\partial x}\left[\phi_v \left(\rho e + P\right) u\right] = 0 \tag{4.54c}$$

This model requires the determination of the thermodynamic states of each phase that satisfy the equilibrium conditions:

$$\mu_v \left(\rho_v^{\text{eq}}, e_{s,v}^{\text{eq}}\right) = \mu_l \left(\rho_l^{\text{eq}}, e_{s,l}^{\text{eq}}\right) \tag{4.55a}$$

$$\rho = \phi_v \rho_v^{\text{eq}} + \phi_l \rho_l^{\text{eq}} \tag{4.55b}$$

$$\rho e_s = \phi_v \rho_v^{\text{eq}} e_{s,v}^{\text{eq}} + \phi_l \rho_l^{\text{eq}} e_{s,l}^{\text{eq}} \tag{4.55c}$$

Solving Eqs. (4.55a)-(4.55c) is not trivial, in particular in multi-species configurations, and several methods have been proposed in the literature: an exact multi-species resolution in Pelletier (2019); Pelletier et al. (2020), an exact resolution in simplified conditions in Saurel et al. (2008); Le Martelot et al. (2014), a single-step approximate solver in Chiapolino et al. (2017b); Chiapolino et al. (2017a) or a simplified exact resolution with a single-fluid assumption in Pelletier (2019); Pelletier et al. (2020).

This formulation with the 3-equation model has led to the most conclusive results so far as demonstrated in Figs. 4.16 and 4.17. In 4.16 taken from Chiapolino et al. (2017a), the authors have simulated a non-reactive coaxial LO_x/GH_2 jet with and without evaporation using an approximate one step equilibrium solver and have compared the results in terms of oxygen mass fractions. In Fig. 4.17 taken from Pelletier (2019), a simulation of the bench test Mascotte is presented (see Habiballah et al. (1996); Vingert et al. (1999); Gicquel et al. (2001)) in subcritical injection conditions with reactive components in a LES framework. The different relevant fields subsequent to the LO_x/GH_2 combustion are provided: the dynamics of the reactive jet is well retrieved.

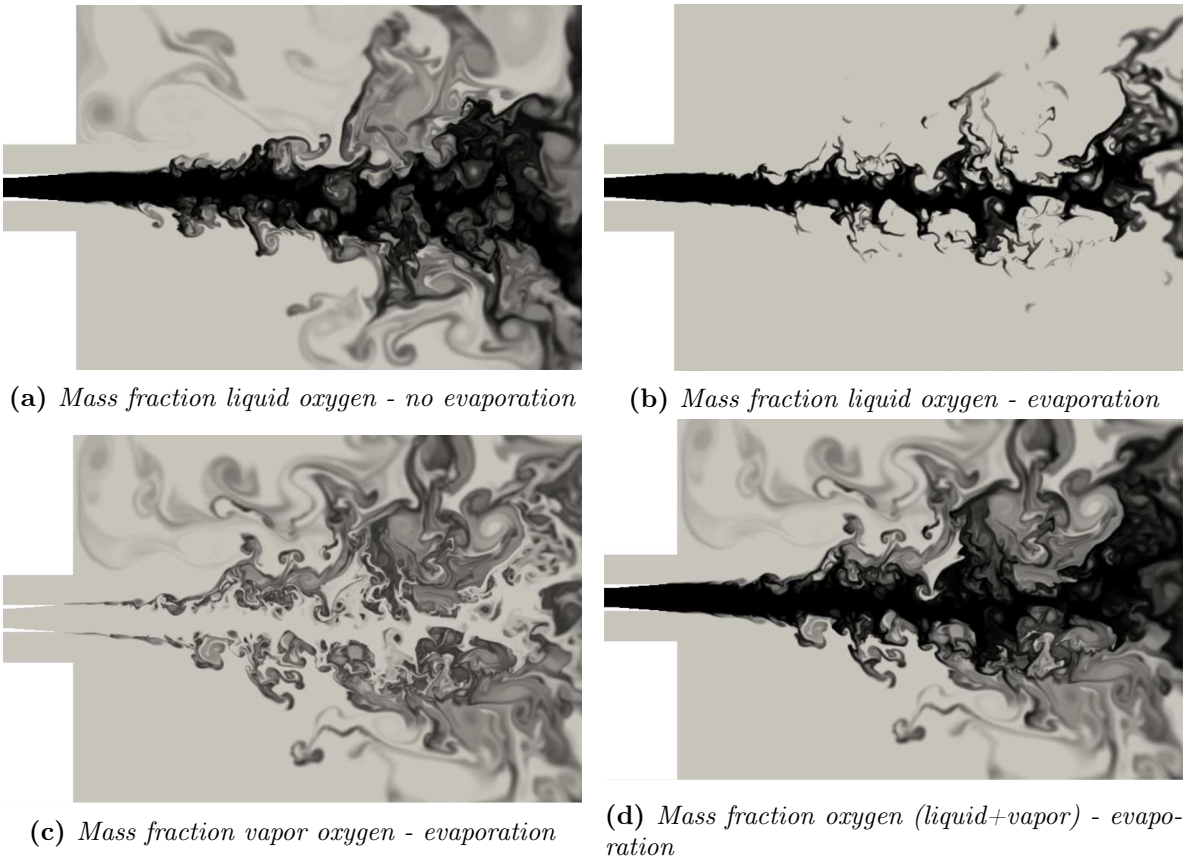

(a) *Mass fraction liquid oxygen - no evaporation*

(b) *Mass fraction liquid oxygen - evaporation*

(c) *Mass fraction vapor oxygen - evaporation*

(d) *Mass fraction oxygen (liquid+vapor) - evaporation*

Figure 4.16: *Simulation of the fragmentation of a liquid oxygen jet by a coaxial gaseous nitrogen co-flow solving the 3-equation model, taken from Chiapolino et al. (2017a).*

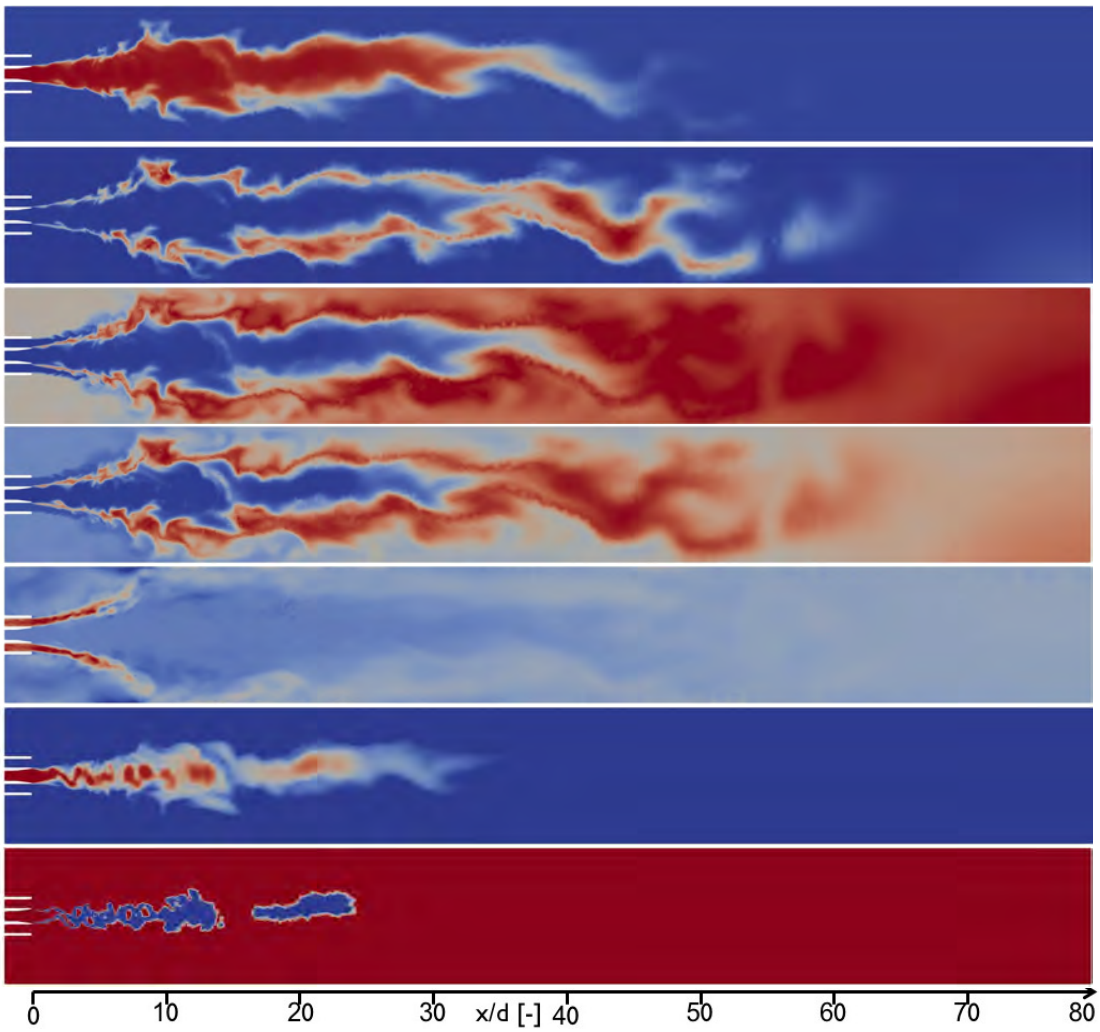

Figure 4.17: *Large Eddy Simulation with the 3-equation model of a reactive LO_x/GH_2 coaxial jet in transcritical injection conditions based in the Mascotte bench (see Habiballah et al. (1996); Vingert et al. (1999); Gicquel et al. (2001)) taken from Pelletier (2019). Instantaneous fields in an axial cut plane, from top to bottom: O_2 mass fraction, OH mass fraction, H_2O mass fraction, temperature, axial velocity, density, stable* ***(red)****/unstable****(blue)*** *thermodynamic state.*

Chapter 5

The Second Gradient theory

The purpose of this chapter is to present the milestones in the derivation of the model known as the Second Gradient theory (SG), also referred to as the Gradient Theory of fluid in the literature. This model allows to faithfully describe the thermodynamics of an interfacial zone between a liquid and a vapor phase. A specific care is given to the justification of the hypotheses used in the derivation to ensure a physical consistency throughout.
This model falls under the Diffuse Interface Methods classification and to some extent, it can be viewed as a more thermodynamically driven Phase-Field model. As such, it offers a description of the internal structure of the interface using the density gradient as an additional thermodynamic independent variable. It is not however limited to a modification of the interfacial thermodynamics. As explained in this chapter, this finer thermodynamic description must go in par with a finer mechanical description of the constraints in the interface to achieve a final model with a complete thermo-mechanical coupling. The origin and necessity of this coupling is developed in Sec. 5.1 where a phenomenological approach is used to set out the fundamental considerations driving the theory. The purpose is therefore to cement the hypotheses that are used to derive the equations of the SG theory. This derivation and the ensuing expressions are presented in Sec. 5.2. This derivation is carefully carried out and rests upon fundamental physical results such as the thermodynamic principles and the Virtual Power Principle.
The description of the interface is then completed in Sec. 5.3 where the variables of the modified thermodynamics are expressed. Finally, in Sec. 5.4, trough a characterization on mono-dimensional planar interfaces, we try to determine the macroscopic values of interest when describing the interface, their link to the microscopic parameters and their interdependency. This will prove useful for in the framework of Chap. 9 where the behavior of the interface will be modified.

All the results presented are to be directly related the work of Germain (1972); Casal and Gouin (1985); Seppecher (1987) and Jamet (1998) to whom the interested reader can turn to for further details. The objective here is to propose a synthetic overview, though comprehensive enough, for the reader to understand the SG theory from its foundations to its more general implications.

5.1 Phenomenological approach to the capillary effects

The objective of this section is to present the different steps that permit to ground the Second Gradient theory both mechanically and thermodynamically. They are characterized by a progressive widening of the point of view used to describe the system, from molecular to macroscopic. To that effect the pressure tensor, referred to as $\underline{\underline{\mathbf{P}}}$, is used as a key thread. First, the molecular point of view of Rocard (1967)is used to demonstrate that the non-kinetic interactions between the molecules of the fluid must be accounted for and how this hypothesis impacts $\underline{\underline{\mathbf{P}}}$. Secondly, using a greater spatial scale, the microscopic point of view of Korteweg (1901) allows to determine how $\underline{\underline{\mathbf{P}}}$ is specifically impacted by the density gradient, with a continuous medium approach. Thirdly, a macroscopic point a view is utilized, through the energetic approach of Cahn and Hilliard (1958) to detail how the thermodynamics of the interface is also impacted by the density gradient.

5.1.1 Molecular description of capillary phenomena

In Rocard (1967), the author expresses the internal forces for a fluid in a high density gradient region using molecular theory. More precisely, he derives an expression for the non-kinetic pressure tensor $\underline{\underline{\mathbf{\Pi}}}$, that is to say the part of the internal pressure tensor not directly due the collisions between the molecules. For an ideal gas, of which thermodynamic equation classically reads $P = \rho r T$ with P the isotropic pressure, r the gas constant, ρ its density and T its temperature, $\underline{\underline{\mathbf{\Pi}}}$ is null. This is due to the founding hypothesis allowing to derive the ideal gas law: molecules do not interact outside of collisions to exchange momentum, kinetic and internal energy, i.e. no remote interactions exist between them. This hypothesis holds as long as molecules are, at a large scale, far away from one another since molecular interactions vanish rapidly with the distance. In dense fluids, this is not the case since the mean distance between molecules strongly reduces. In the van der Waals equation of state , the non-kinetic internal pressure appears clearly in the form of the component $-a\rho^2$ which embeds part of the remote molecular interactions. It is worth noticing that, even though it is no longer null, the non-kinetic internal pressure remains isotropic as $\underline{\underline{\mathbf{\Pi}}} = \Pi \underline{\underline{\mathbf{I}}} = -a\rho^2 \underline{\underline{\mathbf{I}}}$. The presence of an interface makes the matter worse since not only high density values occur but high density gradients are also present, creating a non-trivial repartition of molecular interactions, that must be treated properly. In such cases, not only $\underline{\underline{\mathbf{\Pi}}}$ is not null, but it is no longer isotropic as this will be shown in the following paragraphs.

Classically, the interactions between the molecules of the fluid can be described using a force per volume unit ψ that solely depends on the distance r between the molecules. For a molecule located at the point $O = (0, 0, 0)$, the components of the force $\boldsymbol{f}_0$ applied upon it by the rest of the fluid are given by Eqs. (5.1a)-(5.1c) where $n(x, y, z)$ is the number of molecules in the small volume $dx\,dy\,dz$ centered on the point at (x, y, z).

$$f_{0,x} = \iiint n(x, y, z)\,\psi(r)\,\frac{x}{r}\,dx\,dy\,dz \tag{5.1a}$$

$$f_{0,y} = \iiint n(x, y, z)\,\psi(r)\,\frac{y}{r}\,dx\,dy\,dz \tag{5.1b}$$

$$f_{0,z} = \iiint n(x, y, z)\,\psi(r)\,\frac{z}{r}\,dx\,dy\,dz \tag{5.1c}$$

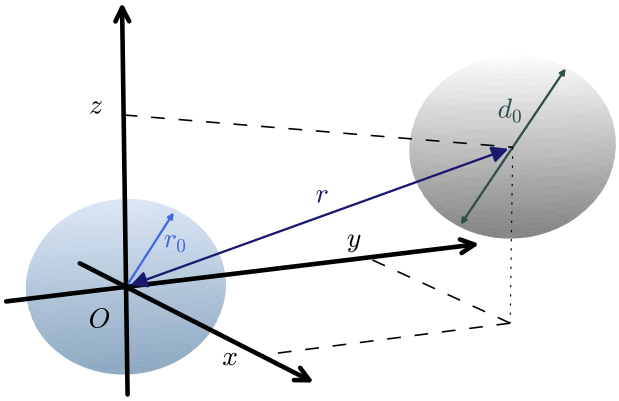

Figure 5.1: *Schematic representation of the molecular interactions between to molecules*

An issue arises when trying to calculate the above integrals because the molecules distribution, represented by n, is not known *a priori*, even in an homogeneous fluid, rendering its determination even harder for a non homogeneous one. Despite this difficulty, the author in Rocard (1967) suggests to make a third order Taylor expansion of n around the point O:

$$\begin{aligned} n(x,y,z) = \; & n_0 + x\left(\frac{\partial n}{\partial x}\right)_0 + y\left(\frac{\partial n}{\partial y}\right)_0 + \cdots + \frac{x^2}{2}\left(\frac{\partial^2 n}{\partial x^2}\right)_0 + \frac{y^2}{2}\left(\frac{\partial^2 n}{\partial y^2}\right)_0 + \cdots \\ & + \frac{x^3}{6}\left(\frac{\partial^3 n}{\partial x^3}\right)_0 + \frac{y^3}{6}\left(\frac{\partial^3 n}{\partial y^3}\right)_0 + \cdots + O\left(r^3\right) \end{aligned} \tag{5.2}$$

The mean force per volume unit $\overline{\boldsymbol{f}}$ is approximately equivalent to $n_0 \boldsymbol{f}_0$. The reciprocity of actions principle grants that ψ is symmetrical for a pure fluid (every two molecules interact with one another in a perfectly symmetrical way). Using this result and the previous Taylor expansion , the components of $\overline{\boldsymbol{f}}$ are expressed in Rocard (1967) by:

$$\bar{f}_x = \frac{A}{M^2}\frac{\partial \rho^2}{\partial x} - \frac{a\zeta {d_0}^2}{5M^2}\rho\frac{\partial \boldsymbol{\Delta}\rho}{\partial x} \tag{5.3a}$$

$$\bar{f}_y = \frac{A}{M^2}\frac{\partial \rho^2}{\partial y} - \frac{a\zeta {d_0}^2}{5M^2}\rho\frac{\partial \boldsymbol{\Delta}\rho}{\partial y} \tag{5.3b}$$

$$\bar{f}_z = \frac{A}{M^2}\frac{\partial \rho^2}{\partial z} - \frac{a\zeta {d_0}^2}{5M^2}\rho\frac{\partial \boldsymbol{\Delta}\rho}{\partial z} \tag{5.3c}$$

where M is the the molar mass of the fluid, d_0 is the penetrability diameter of the molecules (the diameter of the hard sphere molecules or equivalently the smallest distance that can separate two distinct molecules), A and ζ two constants expressed in Eqs. (5.5) and (5.6) depending solely on the interaction force ψ and ρ is the density of the fluid. Using Avogadro's number $\mathcal{N}_A$, these quantities can be expressed by:

$$\rho = n\frac{M}{\mathcal{N}_A} \tag{5.4}$$

$$A = -\frac{{\mathcal{N}_A}^2}{6}\int_{d_0}^{\infty} r\psi\left(r\right)4\pi r^2\,dr \tag{5.5}$$

$$\zeta = -\frac{{\mathcal{N}_A}^2}{6ad_0^2}\int_{r_0}^{\infty} r^3\psi\left(r\right)4\pi r^2\,dr \tag{5.6}$$

The coefficient A is actually the molar internal pressure constant in van der Waals (1873) embodying part of the remote interactions, mostly the long-range attractive terms. It should be noted that the author in Rocard (1967) seems to hint that the previous derivation does not allow, on its own, to account for all the short-range repulsive interactions, even though the reasons why are not elaborated on. This notion seems to have an echo in the literature since for instance, when deriving refined equations of state, the repulsive interactions are mostly accounted for by introducing a term that mathematically impends the density to exceed a certain value. This introduction is somewhat done empirically rather than theoretically. One possible explanation is that at short range, it becomes difficult to separate the kinetic contribution to the pressure from the short range remote interactions as both will result in a tendency of the molecules to part away from one another. Anyhow, this does not limit the reach of the result obtained in Rocard (1967).

The mean force per volume unit $\overline{\boldsymbol{f}}$ is linked to the non-kinetic internal pressure tensor $\underline{\underline{\boldsymbol{\Pi}}}$ (which is symmetrical) trough the relation $\overline{\boldsymbol{f}} = \boldsymbol{\nabla}\cdot\underline{\underline{\boldsymbol{\Pi}}}$. It can then be used to express the components of $\underline{\underline{\boldsymbol{\Pi}}}$ with:

$$\Pi_{xx} = -\frac{A\rho^2}{M^2} - \frac{a\zeta {d_0}^2}{20M^2}\left[\frac{\lambda}{2}\left(\boldsymbol{\nabla}\rho\right)^2 - \left(\frac{\partial\rho}{\partial x}\right)^2 + \rho\boldsymbol{\Delta}\rho\right] \tag{5.7a}$$

$$\Pi_{xy} = \frac{A\zeta {d_0}^2}{20M^2}\frac{\partial\rho}{\partial x}\frac{\partial\rho}{\partial y} \tag{5.7b}$$

$$\Pi_{xz} = \frac{A\zeta {d_0}^2}{20M^2}\frac{\partial\rho}{\partial x}\frac{\partial\rho}{\partial z} \tag{5.7c}$$

$r_0 = d_0/2$ being the penetrability radius. The other components Π_{yx}, Π_{yy}, Π_{yz}, etc... can be obtained in a similar fashion and using the symmetrical nature of the tensor $\underline{\underline{\boldsymbol{\Pi}}}$. Eventually, the result can be condensed into :

$$\underline{\underline{\mathbf{P}}} = P_{\text{kinetic}}\underline{\underline{\mathbf{I}}} + \underline{\underline{\boldsymbol{\Pi}}} = \underbrace{\left(P_{\text{kinetic}} - a\rho^2\right)}_{P_h}\underline{\underline{\mathbf{I}}} + \underline{\underline{\mathbf{P}}}_1\left(\rho, \boldsymbol{\nabla}\rho, \boldsymbol{\Delta}\rho\right) \tag{5.8}$$

where $a = A/M^2$, P_h is the classic isotropic pressure for homogeneous fluid (without interfaces) and $\underline{\underline{\mathbf{P}}}_1$ is an additional tensor depending on the density ρ as well as its first and second derivatives.

The main result from this study is that the internal pressure constraints in the fluid, with a higher order of description, are no longer isotropic. This anisotropy is mostly driven by the

density gradient. To account for the capillary effects due to the presence of an interface, a higher order of modeling is therefore proved to be required.

5.1.2 Microscopic approach : Korteweg's model of capillarity

The previous subsection introduced the impact of non-kinetic, i.e. remote interactions between particles at a molecular level and showed how they were susceptible to impact the macroscopic forces in the fluid. This modification can be further described following the work in Korteweg (1901).

NOTE: *The reader should note that several parts of the development presented here may seem arbitrary. This is mostly due to the lack of justifications in the original study of Korteweg (1901). Efforts have been made to clarify the calculations and to omit seemingly non-necessary and non rigorous parts so as to focus on the articulation of the reasoning. Most of the results in Korteweg (1901) have found validation in later works such as Rocard (1967), Germain (1972) or Casal and Gouin (1985). However, it seemed important for us to present this study where the physical intuition of the phenomena primes over complex mathematical derivations.*

In this subsection, a microscopic point of view is adopted, the fluid is now treated as a continuous medium, however, complex molecular interactions are accounted for in order to derive the equations of motion for a capillary fluid. The starting assumption is that the local and sudden variations of thermodynamic variables, especially the density, should bring about new contributions. The latter are otherwise negligible without the presence of an interface between two phases of a same fluid or two different fluids. It is classic to write the momentum equation of a fluid in the form of Eq. (5.9).

$$\rho \frac{d\mathbf{v}}{dt} = -\boldsymbol{\nabla} \cdot \underline{\underline{\mathbf{T}}} \tag{5.9}$$

The constraints tensor $\underline{\underline{\mathbf{T}}}$ can be separated into different contributions: non-contact internal constraints i.e. internal pressure, contact internal constraints i.e. viscous constraints, external or remote constraints, usually body forces. For a classic viscous compressible fluid, this can be summed up by:

$$\underline{\underline{\mathbf{T}}}_0 = \underline{\underline{\mathbf{P}}}_0 + \underline{\underline{\boldsymbol{\tau}}} + \rho \underline{\underline{\boldsymbol{g}}} \tag{5.10}$$

with $\underline{\underline{\mathbf{P}}}_0 = P_0 \underline{\underline{\mathbf{I}}}$ the isotropic internal pressure, $\underline{\underline{\boldsymbol{\tau}}}$ the viscous tensor and $\underline{\underline{\boldsymbol{g}}}$ the volume body forces. When complex molecular interactions are accounted for, additional internal and remote constraints arise. They are introduced in the momentum equation by modifying the pressure tensor $\underline{\underline{\mathbf{P}}}$ in the following fashion:

$$\underline{\underline{\mathbf{T}}} = \underline{\underline{\mathbf{P}}} + \underline{\underline{\boldsymbol{\tau}}} + \rho \underline{\underline{\boldsymbol{g}}} \tag{5.11}$$

$$\underline{\underline{\mathbf{P}}} = P_0 \underline{\underline{\mathbf{I}}} + \underline{\underline{\boldsymbol{\sigma}}} \tag{5.12}$$

The tensor $\underline{\underline{\boldsymbol{\sigma}}}$ embodies the assembly of all the additional constraints and since $\underline{\underline{\mathbf{T}}}$ can be written as $\underline{\underline{\mathbf{T}}} = \underline{\underline{\mathbf{T}}}_0 + \underline{\underline{\boldsymbol{\sigma}}}$, the calculation to determine the expression of $\underline{\underline{\boldsymbol{\sigma}}}$ will rely on $\underline{\underline{\mathbf{T}}}_0$ as a reference.

To derive the equations of motion for a capillary fluid, a classic strategy, exposed in Fig. 5.2, is to evaluate the momentum variation $d(\rho \mathbf{v})$ for a small volume $d\mathcal{V} = \Delta x \Delta y \Delta z$ centered at $M_0 = (x_0 + \Delta x/2, y_0 + \Delta y/2, z_0 + \Delta z/2)$ over a small time interval dt. Thanks to the impulse-momentum theorem, this momentum variation is equal to the total impulse of all the forces exerted over the volume $d\mathcal{V}$ in the time interval dt, the momentum lost through the particles leaving the volume $d\mathcal{V}$ and the momentum gained thanks to the particles entering the volume $d\mathcal{V}$. Accounting for molecular interactions oblige to further develop this approach.

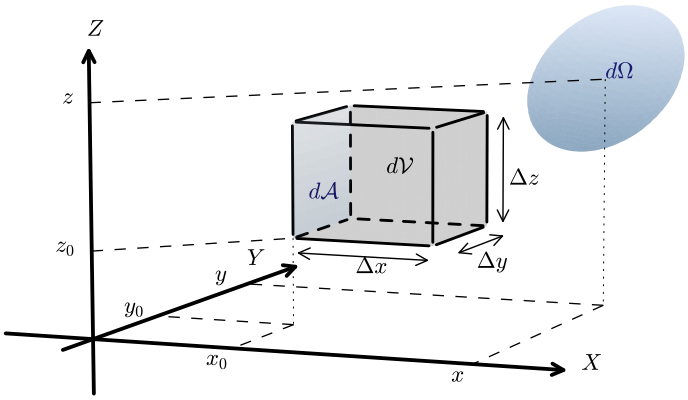

Figure 5.2: *Schematic representation of a control volume $d\mathcal{V}$ and a remote volume $d\Omega$ to evaluate the modified momentum equation for a capillary fluid*

We focus on the surface $d\mathcal{A} = \Delta y \Delta z$ placed at x_0, the impulses received by that surface in the directions x, y and z respectively would be $\mathrm{T}_{0,xx}\, d\mathcal{A}\, dt$, $\mathrm{T}_{0,xy}\, d\mathcal{A}\, dt$ and $\mathrm{T}_{0,xz}\, d\mathcal{A}\, dt$ in the non-capillary case whereas they become $\mathrm{T}_{xx}\, d\mathcal{A}\, dt$, $\mathrm{T}_{xy}\, d\mathcal{A}\, dt$ and $\mathrm{T}_{xz}\, d\mathcal{A}\, dt$ in the general case. The objective is to evaluate the gaps $\mathrm{T}_{xx} - \mathrm{T}_{0,xx}$, $\mathrm{T}_{xy} - \mathrm{T}_{0,xy}$ and $\mathrm{T}_{xz} - \mathrm{T}_{0,xz}$ ensuing from the higher order of modeling used, in particular the introduction of molecular interactions.

Let now $d\Omega$ be a small volume of fluid, distinct of but close to $d\mathcal{V}$ and located at $M = (x, y, z)$. In the absence of strong thermodynamic variations (in our case an interface), these two volumes of fluid would be oblivious to one another. In particular $d\Omega$ would have no effect on the momentum variations in $d\mathcal{V}$, which is not the case anymore with the higher oder of modeling. Due to the non-homogeneities induced by the interface, the density and the temperature in the volume $d\Omega$ are given by $\rho(x, y, z) = \rho_0(x, y, z) + \Delta\rho(x, y, z)$ and $T(x, y, z) = T_0(x, y, z) + \Delta T(x, y, z)$. It should be noticed that the writing $\rho_0(x, y, z)$ and $T_0(x, y, z)$ is used to signify that the homogeneous state without interfaces is not required to be constant. However, the associated variations must be negligible when compared to those created by the presence of interfaces. The same methodology is used to express the velocity components, meaning $u = u_0 + \Delta u$, $v = v_0 + \Delta v$ and $w = w_0 + \Delta w$ in $d\Omega$.
The first hypothesis used by the author in Korteweg (1901) is to consider that the contribution $d(\Delta \mathrm{T}_{xx})$ of $d\Omega$ to $\mathrm{T}_{xx} - \mathrm{T}_{0,xx}$ can formally be written as linearly dependent to the thermodynamic variations as follows:

$$d(\Delta \mathrm{T}_{xx}) = (\alpha_\rho \Delta\rho + \alpha_T \Delta T + \alpha_u \Delta u + \alpha_v \Delta v + \alpha_w \Delta w)\, d\mathcal{V} \tag{5.13}$$

This linear dependency is only formal since the terms α_ρ, α_T, α_u, α_v and α_w actually depend on the density and temperature distribution.

The second hypothesis used is to consider that the density variations dwarf that of the other quantities (temperature and velocity) and that only they should be retained to express $d\left(\Delta \mathrm{T}_{xx}\right)$. Of course, one could argue that this hypothesis greatly reduces the reach of the model, which is most likely true. However, the results obtained even with this simplified version allow significant improvement for the description of capillary phenomena. Accordingly, Eq. (5.13) formally reduces to:

$$d\left(\Delta \mathrm{T}_{xx}\right) = \alpha_\rho\left(\rho, T\right) \Delta\rho \, d\mathcal{V} \tag{5.14}$$

This formulation can be particularized by performing a Taylor expansion of the density around the homogeneous state, it is written:

$$\Delta\rho = \rho - \rho_0 = \sum_{i=1}^{3} \left(x_i - x_{0,i}\right) \frac{\partial \rho}{\partial x_i} + \frac{1}{2} \sum_{i=1}^{3} \sum_{j=1}^{3} \left(x_i - x_{0,i}\right)\left(x_j - x_{0,j}\right) \frac{\partial^2 \rho}{\partial x_i \partial x_j} \tag{5.15}$$

The third hypothesis is used to account for several phenomena at once:

- First, the strong density variations around the volume $d\mathcal{V}$ create a molecular force field that is likely to accelerate/decelerate the molecules going to and coming from the volume $d\mathcal{V}$, modifying the momentum of said molecules. This impacts, for instance, the momentum fluxes through $d\mathcal{A}$.
- Second, the strong density variations around the volume $d\Omega$ also creates a molecular force field that can temper or amplify the impact of $d\Omega$ on the momentum of molecules in $d\mathcal{V}$. It can, for instance, modify the propensity of molecules to agglomerate near the point M.

These two phenomena are indirectly linked to $\Delta \mathrm{T}_{xx}$. They do not directly modify its value but rather the way it is impacted by $d\Omega$. However, this indirect correlation has to be included in the derivation of $d\left(\Delta \mathrm{T}_{xx}\right)$, what is done in Korteweg (1901) through a formal dependency of α_ρ on the density gradient as well.

All the previous hypotheses can be combined by expressing $d\left(\Delta \mathrm{T}_{xx}\right)$ using a formal linear dependency in the different density first order derivatives, $\left(\partial\rho/\partial x_i\right)_{i=1\cdots3}$, their cross products $\left(\left(\partial\rho/\partial x_i\right)\left(\partial\rho/\partial x_j\right)\right)_{i,j=1\cdots3}$, and the second order derivatives $\left(\partial^2\rho/\left(\partial y \partial z\right)\right)_{i,j=1\cdots3}$. Once again, the rigorous mathematical manner in which these terms are introduced is not the focal point in Korteweg (1901). The objective is rather to identify the major phenomena at play and to propose a simple and effective way to introduce them in the equations. The last major step is to integrate the elementary contribution $d\left(\Delta \mathrm{T}_{xx}\right)$ over a region neighboring $d\mathcal{V}$. In a synthetic approach, this will result in the following expression:

$$\mathrm{T}_{xx} - \mathrm{T}_{0,xx} = \sum_{i=1}^{3} \mathfrak{a}_i \frac{\partial \rho}{\partial x_i} + \sum_{i=1}^{3} \sum_{j=1}^{3} \mathfrak{a}_{i,j} \frac{\partial \rho}{\partial x_i} \frac{\partial \rho}{\partial x_j} + \sum_{i=1}^{3} \sum_{j=1}^{3} \mathfrak{a}_{ij} \frac{\partial^2 \rho}{\partial x_i \partial x_j} \tag{5.16}$$

where the coefficients $\mathfrak{a}_*$ depend *a priori* on the density and the temperature. The same expressions can be obtained for $\mathrm{T}_{xy} - \mathrm{T}_{0,xy}$ and $\mathrm{T}_{xz} - \mathrm{T}_{0,xz}$:

$$\mathrm{T}_{xy} - \mathrm{T}_{0,xy} = \sum_{i=1}^{3} \mathfrak{b}_i \frac{\partial \rho}{\partial x_i} + \sum_{i=1}^{3} \sum_{j=1}^{3} \mathfrak{b}_{i,j} \frac{\partial \rho}{\partial x_i} \frac{\partial \rho}{\partial x_j} + \sum_{i=1}^{3} \sum_{j=1}^{3} \mathfrak{b}_{ij} \frac{\partial^2 \rho}{\partial x_i \partial x_j} \tag{5.17}$$

$$\mathrm{T}_{xz} - \mathrm{T}_{0,xz} = \sum_{i=1}^{3} \mathfrak{c}_i \frac{\partial \rho}{\partial x_i} + \sum_{i=1}^{3} \sum_{j=1}^{3} \mathfrak{c}_{i,j} \frac{\partial \rho}{\partial x_i} \frac{\partial \rho}{\partial x_j} + \sum_{i=1}^{3} \sum_{j=1}^{3} \mathfrak{c}_{ij} \frac{\partial^2 \rho}{\partial x_i \partial x_j} \tag{5.18}$$

From Korteweg (1901), additional physical results can be used to simplify the previous expressions. Firstly, Newton's third law of motion applies between subdomains of the fluid and the formulas must not depend on the orientation (i.e. the sign) chosen for the axes. This in turn causes, among others, the internal constraints tensor $\underline{\underline{\mathbf{T}}}$ to be symmetrical. All things considered, it can be shown that Eqs. (5.16), (5.16) and (5.17) turn into:

$$\mathrm{T}_{xx} - \mathrm{T}_{0,xx} = a_x \left(\boldsymbol{\nabla}\rho\right)^2 + b_{xx} \left(\frac{\partial \rho}{\partial x}\right)^2 - c_x \boldsymbol{\Delta}\rho - d_{xx} \frac{\partial^2 \rho}{\partial x^2} \tag{5.19a}$$

$$\mathrm{T}_{xy} - \mathrm{T}_{0,xy} = \mathrm{T}_{yx} = b_{xy} \frac{\partial \rho}{\partial x} \frac{\partial \rho}{\partial y} - d_{xy} \frac{\partial^2 \rho}{\partial x \partial y} \tag{5.19b}$$

$$\mathrm{T}_{xz} - \mathrm{T}_{0,xz} = \mathrm{T}_{zx} = b_{xz} \frac{\partial \rho}{\partial x} \frac{\partial \rho}{\partial z} - d_{xz} \frac{\partial^2 \rho}{\partial x \partial z} \tag{5.19c}$$

where a_x, b_{xx}, b_{xy}, b_{xz}, c_x, d_{xx}, d_{xy} and d_{xz} are coefficients depending *a priori* on the density and the temperature. Finally, given the fact that the quantities $\left(\boldsymbol{\nabla}\rho\right)^2$ and $\boldsymbol{\Delta}\rho$ do not depend on the chosen frame of reference, it comes that $b_{xx} = b_{xy} = b_{xz} = b_x$ and $d_{xx} = d_{xy} = d_{xz} = d_x$. Repeating all the previous developments for the terms $\mathrm{T}_{yy} - \mathrm{T}_{0,yy}$, $\mathrm{T}_{zz} - \mathrm{T}_{0,zz}$ and $\mathrm{T}_{yz} - \mathrm{T}_{0,yz}$ eventually leads to the relations:

$$\mathrm{T}_{ii} - P = a_i \left(\boldsymbol{\nabla}\rho\right)^2 + b_i \left(\frac{\partial \rho}{\partial x_i}\right)^2 - c_i \boldsymbol{\Delta}\rho - d \frac{\partial^2 \rho}{\partial {x_i}^2} \tag{5.20a}$$

$$\mathrm{T}_{ij} - \mathrm{T}_{0,ij} = \mathrm{T}_{ji} - \mathrm{T}_{0,ji} = b_i \frac{\partial \rho}{\partial x_i} \frac{\partial \rho}{\partial x_j} - d_i \frac{\partial^2 \rho}{\partial x_i \partial x_j} \tag{5.20b}$$

By geometrical invariance arguments already used, it comes that $a_x = a_y = a_z = a$, $b_x = b_y = b_z = a$, $c_x = c_y = c_z = a$ and $d_x = d_y = d_z = d$. Coefficients a, b, c, d, may depend on the temperature T and density ρ of the fluid but not on their derivatives. The momentum equation can be written in its final form:

$$\rho \frac{d\mathbf{v}}{dt} = -\boldsymbol{\nabla} P_0 - \boldsymbol{\nabla}\left[a \left(\boldsymbol{\nabla}\rho\right)^2\right] + \boldsymbol{\nabla}\left[c \boldsymbol{\Delta}\rho\right] - \boldsymbol{\nabla}\cdot\left[b \boldsymbol{\nabla}\rho \otimes \boldsymbol{\nabla}\rho\right] + \boldsymbol{\nabla}\cdot\left[d \boldsymbol{\nabla}\boldsymbol{\nabla}\rho\right] - \boldsymbol{\nabla}\cdot\underline{\underline{\boldsymbol{\tau}}} \tag{5.21}$$

From Eq. (5.21), one can extract the capillary tensor $\underline{\underline{\boldsymbol{\sigma}}}$ in Korteweg's theory.

$$\underline{\underline{\boldsymbol{\sigma}}} = \left(a \left(\boldsymbol{\nabla}\rho\right)^2 - c \boldsymbol{\Delta}\rho\right) \underline{\underline{\mathbf{I}}} + b \boldsymbol{\nabla}\rho \otimes \boldsymbol{\nabla}\rho - d \boldsymbol{\nabla}\boldsymbol{\nabla}\rho \tag{5.22}$$

In the case of a mixture, the previous developments should be started back from the beginning accounting for the non-homogeneous interactions between materials of different nature. Although this would be a tedious work, the results would not differ much from that of the pure fluid and Korteweg's work offers an intuitive way to derive the momentum equation for a pure fluid endowed with capillarity. In Sec. 5.2, it is shown that the full development of the Second Gradient theory provides final equations of motion in agreement with those obtained in this short study.

5.1.3 Energetic approach to the Second Gradient model

One aspect missing from the two previous studies, that are mostly oriented on a mechanical description of the interface, is the energetic behavior of the fluid induced by the presence of

said interface. Since van der Walls work in the late 1800's (van der Waals (1893)), the surface tension is known to result from a local accumulation of energy at the interface.
The response from the fluid is a tendency to minimize this additional energy. From the studies presented in Secs. 5.1.1 and 5.1.2, one got that the existence of non-homogeneities due to the presence of an interface requires new terms in the mechanical description of the fluid depending on the density variations trough is derivatives. As expressed by the authors in Cahn and Hilliard (1958), whose considerations will be briefly developed in the following paragraphs, this observation also applies for the energetic description of the fluid. More precisely, the energy of the fluid at the interface should be the addition of the classic energy expected in a homogeneous medium and a "capillary" energy depending on the density (or composition for mixtures) gradient. To that effect, in Cahn and Hilliard (1958), an expression is derived for the free energy $\mathcal{F}$ of a non-homogeneous system. In their founding paper, Cahn and Hilliard considered the mole fraction c of a two-component system $A-B$ and derived an expression for the free energy depending on c and $\boldsymbol{\nabla} c$. Since here we are interested in dealing with an interface between two phases of the same fluid, we will consider the density ρ as our segregation variable (as mentioned in Cahn and Hilliard (1958), any intensive variable other than the pressure P and the temperature T can be considered leaving, the liberty to choose the more suited for the studied case).

Let F the volumetric free energy of a system considered at thermal equilibrium $T = \text{cste}$. F is supposed to be a continuous function of the density and its consecutive derivatives (up to the order 3 at least). An additional hypothesis is that the non-homogeneities (namely, the interface) physically span over a distance greater than the distance of action of the molecular interactions. Given all these hypotheses, one can write the Taylor expansion of F around its value $F_{|0}$ in the homogeneous system:

$$\begin{aligned} F\left(\rho, \rho_{,i}, \rho_{,ij}, \cdots\right) = F_{|0} &+ \left(\rho_{,i} - \rho_{,i_{|0}}\right)\left(\frac{\partial F}{\partial \rho_{,i}}\right)_{|0} + \left(\rho_{,ij} - \rho_{,ij_{|0}}\right)\left(\frac{\partial F}{\partial \rho_{,ij}}\right)_{|0} \\ &+ \frac{1}{2}\left(\rho_{,i} - \rho_{,i_{|0}}\right)\left(\rho_{,j} - \rho_{,j_{|0}}\right)\left(\frac{\partial^2 F}{\partial \rho_{,i}\partial \rho_{,j}}\right)_{|0} \\ &+ \frac{1}{2}\left(\rho_{,i} - \rho_{,i_{|0}}\right)\left(\rho_{,jk} - \rho_{,jk_0}\right)\left(\frac{\partial^2 F}{\partial \rho_{,i}\partial \rho_{,jk}}\right)_{|0} \\ &+ \frac{1}{2}\left(\rho_{,ij} - \rho_{,ij_{|0}}\right)\left(\rho_{,kl} - \rho_{,kl_{|0}}\right)\left(\frac{\partial^2 F}{\partial \rho_{,ij}\partial \rho_{,kl}}\right)_{|0} + \cdots + \mathcal{O}\left({\rho_{,i}}^2, {\rho_{,ij}}^2\right) \end{aligned} \tag{5.23}$$

For $i, j \in [1, 2, 3]$ the following notations are used:

$$\rho_{,i} = \frac{\partial \rho}{\partial x_i} \quad \rho_{,ij} = \frac{\partial^2 \rho}{\partial x_i \partial x_j} \quad \text{etc...}$$

The subscript $|0$ refers to a value taken in the homogeneous system (for a function $\mathtt{f}$ it gives $\mathtt{f}_{|0} = \mathtt{f}\left(\rho, 0, \cdots\right)$), thus for an homogeneous system $\rho_{,i_{|0}} = 0$ and $\rho_{,ij_{|0}} = 0$ which allows to simplify the expression. Moreover, the terms $\left(\partial^2 F/(\partial \rho_{,i}\partial \rho_{,jk})\right)_{|0}$ and $\left(\partial^2 F/(\partial \rho_{,ij}\partial \rho_{,kl})\right)_{|0}$ are considered to be of an order 3 and will ne neglected in regards to the other 1^{st} and 2^{nd} order terms. The previous expression Eq. (5.23) can be further simplified using similar geometrical

arguments as done in Sec. 5.1.2 to simplify Eqs. (5.16)-(5.18). F must also be unchanged by a rotation of the reference frame or by inverting the direction of the axis, resulting in:

$$\left(\frac{\partial F}{\partial \rho_{,i}}\right)_{|0} = 0 \tag{5.24a}$$

$$\left(\frac{\partial F}{\partial \rho_{,ij}}\right)_{|0} = \lambda_1 \quad \text{for } i=j, \qquad \left(\frac{\partial F}{\partial \rho_{,ij}}\right)_{|0} = 0 \quad \text{for } i\neq j \tag{5.24b}$$

$$\left(\frac{\partial^2 F}{\partial \rho_{,i}\partial \rho_{,j}}\right)_{|0} = \lambda_2 \quad \text{for } i=j, \qquad \left(\frac{\partial^2 F}{\partial \rho_{,i}\partial \rho_{,j}}\right)_{|0} = 0 \quad \text{for } i\neq j \tag{5.24c}$$

The simplified expression becomes:

$$F\left(\rho,\rho_i,\rho_{,ij}\right) \approx F_{|0} + \lambda_1 \rho_{,ii} + \frac{1}{2}\lambda_2 {\rho_{,i}}^2 = F_{|0} + \lambda_1 \boldsymbol{\Delta}\rho + \frac{1}{2}\lambda_2 \left(\boldsymbol{\nabla}\rho\right)^2 \tag{5.25}$$

From that expression it comes that:

$$\lambda_1 = \left(\frac{\partial F}{\partial(\boldsymbol{\Delta}\rho)}\right)_{|0} \quad \lambda_2 = 2\left(\frac{\partial^2 F}{\partial\left(\|\boldsymbol{\nabla}\rho\|\right)^2}\right)_{|0} \tag{5.26}$$

To get the free energy over an elementary volume $\partial\mathcal{V}$ of boundary $\partial\mathcal{A}$, one can integrate the previous formula:

$$\partial\mathcal{F} = \int_{\partial\mathcal{V}} F\left(\rho,\rho_{,i},\rho_{,ij}\right) d\mathcal{V} = \int_{\partial\mathcal{V}} \left[F_{|0} + \lambda_1 \boldsymbol{\Delta}\rho + \lambda_2 \left(\boldsymbol{\nabla}\rho\right)^2\right] d\mathcal{V} \tag{5.27}$$

Using Green's theorem, one can write:

$$\int_{\partial\mathcal{V}} \lambda_1 \boldsymbol{\Delta}\rho \, d\mathcal{V} = \int_{\partial\mathcal{V}} \lambda_1 \boldsymbol{\nabla}\cdot\left(\boldsymbol{\nabla}\rho\right) d\mathcal{V} \quad = \int_{\partial\mathcal{V}} \left[\boldsymbol{\nabla}\cdot\left(\lambda_1\boldsymbol{\nabla}\rho\right) - \boldsymbol{\nabla}\lambda_1\cdot\boldsymbol{\nabla}\rho\right] d\mathcal{V} \tag{5.28}$$

$$= \int_{\partial\mathcal{V}} \boldsymbol{\nabla}\cdot\left(\lambda_1\boldsymbol{\nabla}\rho\right) d\mathcal{V} - \int_{\partial\mathcal{V}} \frac{\partial\lambda_1}{\partial\rho}\boldsymbol{\nabla}\rho\cdot\boldsymbol{\nabla}\rho \, d\mathcal{V} \tag{5.29}$$

$$= \int_{\partial\mathcal{A}} \lambda_1 \boldsymbol{\nabla}\rho\cdot\boldsymbol{n} \, d\mathcal{A} - \int_{\partial\mathcal{V}} \frac{\partial\lambda_1}{\partial\rho}\left(\boldsymbol{\nabla}\rho\right)^2 d\mathcal{V} \tag{5.30}$$

where $\boldsymbol{n}$ is the outer normal vector to the surface $\partial\mathcal{A}$. In this particular framework, we are not interested in the effect of the non-homogeneities at the surface boundary and $\partial\mathcal{V}$ can be chosen so as to get $\boldsymbol{\nabla}\rho\cdot\boldsymbol{n} = 0$ over $\partial\mathcal{A}$, leaving only the volume integral over $\partial\mathcal{V}$. This can be injected in the integral Eq. (5.27). Using the notation:

$$\lambda = 2\left[\lambda_2 - \frac{\partial\lambda_1}{\partial\rho}\right] = 2\left[2\left(\frac{\partial^2 F}{\partial\left(\|\boldsymbol{\nabla}\rho\|\right)^2}\right)_{|0} - \left(\frac{\partial^2 F}{\partial(\boldsymbol{\Delta}\rho)\partial\rho}\right)_{|0}\right] \tag{5.31}$$

it comes:

$$\partial\mathcal{F} = \int_{\partial\mathcal{V}} \left[F_{|0}\left(\rho\right) + \frac{\lambda}{2}\left(\boldsymbol{\nabla}\rho\right)^2\right] d\mathcal{V} \tag{5.32}$$

With this recall on the developments by Cahn and Hilliard, later used in Cahn (1959) and Cahn and Hilliard (1959) to treat three dimensional nucleation, we showed that the free energy of a non-homogeneous system can indeed be expressed as the contribution given by the classic free energy of an homogeneous system and the addition of a contribution given by the density gradient. Most of the time, Eq. (5.32) is reinterpreted in a more practical form by giving the expression for the volumetric free energy F:

$$F\left(\rho, \boldsymbol{\nabla}\rho\right) = F_0\left(\rho\right) + \frac{\lambda}{2}\left(\boldsymbol{\nabla}\rho\right)^2 \tag{5.33}$$

5.2 Conservation equations in the Second Gradient theory

The purpose of this section is to derive the momentum and energy equations for a fluid endowed with capillarity in the SG theory. In a first step, the virtual power principle is used with a double objective: firstly as a mean to retrieve the generic form of Cauchy's law for a capillary fluid, secondly as a tools to express the power of the internal forces in a capillary fluid. These results pave the way for the determination of the internal constraints tensor $\underline{\underline{\boldsymbol{\tau}}}$ achieved by the introduction of the first and second principle in a second and a third step. The different results are eventually used to express the system of equations satisfied by the fluid. All along, it is implicitly assumed that the fluid satisfies the continuum mechanics hypotheses and that the local thermodynamic equilibrium is always satisfied, allowing to define the mechanical and state variables for the system and write their differentials. For the sake of clarity, most of the mathematical developments have been omitted when they bore no essential physical meaning. However, the reader can find most of the corresponding calculations in App. C (and if not, in Jamet (1998)), that heavily rely on mathematical and thermodynamic results recalled respectively in App. A.4 and App. B.1. Lastly, when not mentioned otherwise, the fluid is considered to contain a single species.

5.2.1 Virtual power principle

To derive the equations of motion for a fluid in the Second Gradient theory, three main methods can be used. The first one relies on a Hamiltonian approach and has been developed by Casal and Gouin in Casal (1972), Casal and Gouin (1985), Casal and Gouin (1989). The second one, which will be described in the following paragraphs, is based on the virtual power principle (v.p.p.) as demonstrated in Germain (1972), Frémond (2013), Yu (2014) and has been expanded on in Germain (1972), Seppecher (1987) and Jamet (1998). The virtual power principle is used to derive the equations of smooth motions for systems where no shocks occur. It can be shown (Antman (1995)) that describing indirectly the internal forces using their virtual power is equivalent to describing them directly through a momentum equation. This last statement will be further demonstrated in the following. The third method rests on the thermodynamics of irreversible processes introduced around the 1950's by the likes of Haase (1951); Glansdorff and Prigogine (1954); de Groot and Mazur (1954); Meixner et al. (1962) and later refined in Glansdorff and Prigogine (1971); de Groot and Mazur (1984), which has been used by the authors in Jamet (2010) and Gaillard (2015) to derive the equations of motion for a Korteweg-type capillary fluid.

5.2.1.1 The virtual power principle

A domain Ω is considered wherein the fluid is described by the usual thermodynamic variables, i.e. the pressure P, the density ρ, the temperature T, etc. and the variables describing its motion and deformation $\mathbf{v}$, $\boldsymbol{\nabla}\mathbf{v}$, etc. From App. C.1, the v.p.p. states that for a virtual motion characterized by the virtual velocity $\mathbf{v}^*$ in the subdomain $\mathcal{V}$ of Ω, the sum of the virtual powers of the internal forces $\mathcal{P}_{(i)}$ and the virtual power of the external forces $\mathcal{P}_{(e)}$ in $\mathcal{V}$ equals the virtual power of the acceleration forces $\mathcal{P}_{(a)}$ in $\mathcal{V}$, i.e.:

$$\mathbf{v}^* \text{ in } \mathcal{V} \in \Omega \quad \mathcal{P}_{(a)} = \mathcal{P}_{(i)} + \mathcal{P}_{(e)} \tag{5.34}$$

The v.p.p. relies on the axiom of the *virtual power principle for internal forces* which states that for a virtual motion characterized by the virtual velocity $\mathbf{v}^*$ that causes a **rigid body motion** of the fluid in the subdomain $\mathcal{V}$ of Ω, the virtual power of the internal forces $\mathcal{P}_{(i)}$ in $\mathcal{V}$ equals to zero.
The v.p.p is presented in a raw formulation in Eq. (5.34). In the framework of the SG theory, it can be refined by considering a specific subset of virtual motions with corresponding virtual velocity fields $\mathbf{v}^*$ at least two times differentiable. With this additional hypothesis, Germain (1972) and Jamet (1998) derived a more specific set of equations for the fluid. In the next paragraph, such virtual motions are used, the notations remaining unchanged. Additionally, when they exists, $\mathcal{A}$ refers to the surface boundary of $\mathcal{V}$ and $\mathcal{J}$ refers to line boundary of the surface $\mathcal{A}$.

5.2.1.2 Expression of the virtual powers

Let $\mathcal{V}$ a domain of Ω and let $\mathbf{V}^*$ refer to the set of virtual velocities defined over Ω that are at least two times differentiable. The virtual power of the internal forces $\mathcal{P}_{(i)}$ is a continuous linear form over $\mathbf{V}^*$. It comes without difficulty that $\mathbf{V}^*$ is a vector space and that Φ in Eq. (5.35) defines an inner product over $\mathbf{V}^*$.

$$\forall\,(\mathbf{v}^*,\mathbf{u}^*) \in \mathbf{V}^*, \quad \Phi\,(\mathbf{v}^*,\mathbf{u}^*) = \int_{\mathcal{V}} \left[\mathbf{v}^*\cdot\mathbf{u}^* + \boldsymbol{\nabla}\mathbf{v}^* : \boldsymbol{\nabla}^{\mathrm{T}}\mathbf{u}^* + \boldsymbol{\nabla}\boldsymbol{\nabla}\mathbf{v}^* \vdots \widetilde{\boldsymbol{\nabla}\boldsymbol{\nabla}}\mathbf{u}^*\right] d\mathcal{V} \tag{5.35}$$

where $\left(\widetilde{\boldsymbol{\nabla}\boldsymbol{\nabla}}\mathbf{u}^*\right)_{i,j,k} = \partial^2 u_k/(\partial x_j \partial x_i)$.
The Riesz representation theorem allows then to write that it exists $\mathbf{w}^* \in \mathbf{V}^*$ such as:

$$\forall \mathbf{v}^* \in \mathbf{V}^*,\ \mathcal{P}_{(i)}\,(\mathbf{v}^*) = \Phi\,(\mathbf{v}^*,\mathbf{w}^*) \tag{5.36}$$

By defining $\boldsymbol{a} = -\mathbf{w}^*$, $\underline{\underline{\boldsymbol{\varsigma}}} = -\boldsymbol{\nabla}^{\mathrm{T}}\mathbf{w}^*$ and $\underline{\underline{\underline{\mathbf{C}}}} = -\widetilde{\boldsymbol{\nabla}\boldsymbol{\nabla}}\mathbf{w}^*$, it comes:

$$\forall \mathbf{v}^* \in \mathbf{V}^*,\ \mathcal{P}_{(i)}\,(\mathbf{v}^*) = -\int_{\mathcal{V}} \left[\mathbf{v}^*\cdot\boldsymbol{a} + \boldsymbol{\nabla}\mathbf{v}^* : \underline{\underline{\boldsymbol{\varsigma}}} + \boldsymbol{\nabla}\boldsymbol{\nabla}\mathbf{v}^* \vdots \underline{\underline{\underline{\mathbf{C}}}}\right] d\mathcal{V} \tag{5.37}$$

As explained in Seppecher (1987) and Jamet (1998), this expression can be simplified by applying the axiom of the *virtual power principle for internal forces*. By considering successively arbitrary rigid motions of uniform translation and uniform rotation, it can be shown that $\boldsymbol{a} = \mathbf{0}$ and $\underline{\underline{\boldsymbol{\varsigma}}}$ is symmetrical. By enforcing $\underline{\underline{\underline{\mathbf{C}}}}$ to be symmetrical in its two first indexes, the

couple $\left(\underline{\underline{\boldsymbol{\varsigma}}}, \underline{\underline{\underline{\mathbf{C}}}}\right)$ is shown to be unique. Eventually, the virtual power of the internal forces can be written:

$$\forall \mathbf{v}^* \in \mathbf{V}^*,\ \mathcal{P}_{(i)}(\mathbf{v}^*) = -\int_{\mathcal{V}} \left[\boldsymbol{\nabla}\mathbf{v}^* : \underline{\underline{\boldsymbol{\varsigma}}} + \boldsymbol{\nabla}\boldsymbol{\nabla}\mathbf{v}^* \vdots \underline{\underline{\underline{\mathbf{C}}}}\right] d\mathcal{V} \tag{5.38}$$

The previous expression Eq. (5.38) is of the utmost importance and is used extensively in Sec. 5.2.3 and App. C.1 to complete the derivation of the fluxes in the SG framework. In this subsection however, another form is used. Still from Jamet (1998), the previous expression can be further modified using two consecutive integrations by parts allowing to write:

$$\mathcal{P}_{(i)} = \int_{\mathcal{V}} \mathbf{v}^* \cdot \boldsymbol{f}\, d\mathcal{V} + \int_{\mathcal{A}} \left[\mathbf{v}^* \cdot \boldsymbol{s} + (\boldsymbol{\nabla}\mathbf{v}^* \cdot \boldsymbol{n}) \cdot \boldsymbol{m}\right] d\mathcal{A} + \int_{\mathcal{J}} \mathbf{v}^* \cdot \boldsymbol{r}\, dl \tag{5.39}$$

where $\boldsymbol{n}$ is the outer normal to the surface $\mathcal{A}$, $\boldsymbol{f}$, $\boldsymbol{s}$, $\boldsymbol{m}$, $\boldsymbol{r}$ are different vectors introduced during the consecutive integrations by parts to separate the virtual power of the internal forces into volume, surface and line contributions. The virtual power of the external forces $\mathcal{P}_{(e)}$ is then separated in two contributions, $\mathcal{P}_{(d)}$ being from the forces acting remotely on $\mathcal{V}$ and $\mathcal{P}_{(c)}$ being from the contact forces on $\mathcal{A}$ and $\mathcal{J}$. Both these virtual powers can be written in the same fashion as $\mathcal{P}_{(i)}$ in Eq. (5.37). Regarding $\mathcal{P}_{(d)}$, it is supposed that the virtual power of the remote forces related to the simple and double velocity gradients of are negligible. Simultaneously, the same double integration by parts used to get Eq. (5.39) can be applied to $\mathcal{P}_{(c)}$ (noticing that the virtual power of contact forces can not, by definition, stem from body forces, thus the absence of a volume integral in its modified formulation) to get the expressions:

$$\mathcal{P}_{(d)} = \int_{\mathcal{V}} \mathbf{v}^* \cdot \boldsymbol{g}\, d\mathcal{V} \tag{5.40}$$

$$\mathcal{P}_{(c)} = \int_{\mathcal{A}} \left[\mathbf{v}^* \cdot \boldsymbol{t} + (\boldsymbol{\nabla}\mathbf{v}^* \cdot \boldsymbol{n}) \cdot \boldsymbol{\mu}\right] d\mathcal{A} + \int_{\mathcal{J}} \mathbf{v}^* \cdot \boldsymbol{\kappa}\, dl \tag{5.41}$$

where the vectors $\boldsymbol{t}$, $\boldsymbol{\mu}$ and $\boldsymbol{\kappa}$ play the same roles as $\boldsymbol{s}$, $\boldsymbol{m}$, $\boldsymbol{r}$ in Eq. (5.39), of which specific expressions can be found in Jamet (1998).

5.2.1.3 Application of the virtual power principle

Now that the expressions of all the different virtual powers have been obtained, one can write the virtual power principle as enunciated in Eq. (5.34) to get:

$$\begin{aligned}\int_{\mathcal{V}} \rho\mathbf{v}^* \cdot \frac{d\mathbf{v}}{dt}\, d\mathcal{V} = &\int_{\mathcal{V}} \mathbf{v}^* \cdot \boldsymbol{f}\, d\mathcal{V} + \int_{\mathcal{A}} \left[\mathbf{v}^* \cdot \boldsymbol{s} + (\boldsymbol{\nabla}\mathbf{v}^* \cdot \boldsymbol{n}) \cdot \boldsymbol{m}\right] d\mathcal{A} + \int_{\mathcal{J}} \mathbf{v}^* \cdot \boldsymbol{r}\, dl + \\ &\int_{\mathcal{V}} \mathbf{v}^* \cdot \boldsymbol{g}\, d\mathcal{V} + \int_{\mathcal{A}} \left[\mathbf{v}^* \cdot \boldsymbol{t} + (\boldsymbol{\nabla}\mathbf{v}^* \cdot \boldsymbol{n}) \cdot \boldsymbol{\mu}\right] d\mathcal{A} + \int_{\mathcal{J}} \mathbf{v}^* \cdot \boldsymbol{\kappa}\, dl\end{aligned} \tag{5.42}$$

The terms can be rearranged so as to get:

$$\int_{\mathcal{J}} \mathbf{v}^* \cdot [\boldsymbol{r} + \boldsymbol{\kappa}]\, dl + \int_{\mathcal{A}} [\mathbf{v}^* \cdot (\boldsymbol{s} + \boldsymbol{t}) + (\boldsymbol{\nabla}\mathbf{v}^* \cdot \boldsymbol{n}) \cdot (\boldsymbol{m} + \boldsymbol{\mu})]\, d\mathcal{A} - \int_{\mathcal{V}} \mathbf{v}^* \cdot \left[\rho \frac{d\mathbf{v}}{dt} - \boldsymbol{f} - \boldsymbol{g}\right] d\mathcal{V} = 0 \tag{5.43}$$

Given that this equality must hold for any two time differentiable virtual velocity $\mathbf{v}^*$, it is classically possible to chose in succession virtual velocities that are null on $\mathcal{A}$ and $\mathcal{J}$ leading to the momentum equation in Eq. (5.44), then virtual velocities that are null on $\mathcal{J}$ leading the surface boundary conditions in Eqs. (5.45a) - (5.45b) and finally conclude to get the line boundary conditions in Eq. (5.46).

$$\rho \frac{d\mathbf{v}}{dt} = \boldsymbol{f} + \boldsymbol{g} \tag{5.44}$$

$$\boldsymbol{s} = -\boldsymbol{t} \tag{5.45a}$$

$$\boldsymbol{m} = -\boldsymbol{\mu} \tag{5.45b}$$

$$\boldsymbol{r} = -\boldsymbol{\kappa} \tag{5.46}$$

Eq. (5.44) is the Cauchy's law used to describe continuous medium. Its expression still applies in the SG framework as enunciated from Antman (1995) at the beginning of the section. The implications of the boundary conditions Eqs. (5.45a), (5.45b) and (5.46) are further discussed in Seppecher (1987) and Jamet (1998). Mostly, the surface constraint $\boldsymbol{t}$ will no longer solely equals to the normal action of the constraint tensor $\underline{\underline{\boldsymbol{\tau}}}$ but will be modified by an additional contribution arising from the capillary terms, which is not the case when the Second Gradient theory's higher order of modeling is not applied. Overall, the v.p.p. has allowed to derive the momentum equations with the associated boundary conditions in a straightforward and elegant way. In the next subsections, the v.p.p. will be used jointly with the two thermodynamic principles so as to obtain an explicit expression for the internal stress tensor $\underline{\underline{\boldsymbol{\tau}}}$.

5.2.2 First principle of thermodynamics

5.2.2.1 Gibbs relation for a capillary fluid

In the Second Gradient framework, the extensive thermodynamic variables depend on two intensive variables, for instance the temperature T and the density ρ but also on the density gradient $\boldsymbol{\nabla}\rho$. As shown in 5.1.3, a generic yet physically grounded method to introduce this new dependency is to modify the expression of the volumetric free energy F of the fluid like in Eq. (5.33). However in the following, to gain even more generality in the incoming results, the adopted form for F is:

$$F(T, \rho, \boldsymbol{\nabla}\rho) = F_0(T, \rho) + F_1(T, \rho, \boldsymbol{\nabla}\rho) \tag{5.47}$$

where $F_0(T, \rho)$ is the classic volumetric free energy without the Second Gradient considerations and $F_1(T, \rho, \boldsymbol{\nabla}\rho)$ is an additive capillary energy, depending on the density gradient $\boldsymbol{\nabla}\rho$. Additionally, F_1 satisfies:

$$\forall T > 0, \rho > 0, \quad F_1(T, \rho, \mathbf{0}) = 0 \tag{5.48}$$

meaning that this additional energy is null when no non-homogeneities (strong density gradients) are encountered.
In these conditions one can write the differential of the specific internal energy e_s, using the specific entropy s, with:

$$de_s = \left(\frac{\partial e_s}{\partial s}\right)_{\rho,\boldsymbol{\nabla}\rho} ds + \left(\frac{\partial e_s}{\partial \rho}\right)_{s,\boldsymbol{\nabla}\rho} d\rho + \left(\frac{\partial e_s}{\partial \boldsymbol{\nabla}\rho}\right)_{s,\rho} \cdot d\boldsymbol{\nabla}\rho \tag{5.49}$$

The previous equation is a raw writing of the Gibbs relation for a capillary fluid. When $d\boldsymbol{\nabla}\rho = \mathbf{0}$, the description of the capillary fluid must match with that of the classic fluid. This allows to define the thermodynamic temperature T and pressure P for a capillary fluid as:

$$T \hat{=} \left(\frac{\partial e_s}{\partial s}\right)_{\rho,\boldsymbol{\nabla}\rho} \tag{5.50}$$

$$P \hat{=} \rho^2 \left(\frac{\partial e_s}{\partial \rho}\right)_{s,\boldsymbol{\nabla}\rho} \tag{5.51}$$

As done in App. C.2, it can be shown that the final form of the Gibbs relation if therefore:

$$de_s = T\, ds + \frac{P}{\rho^2}\, d\rho + \frac{1}{\rho}\boldsymbol{\mathcal{F}} \cdot d\boldsymbol{\nabla}\rho \tag{5.52}$$

where:

$$\boldsymbol{\mathcal{F}} \hat{=} \left(\frac{\partial F}{\partial \boldsymbol{\nabla}\rho}\right)_{s,\rho} \tag{5.53}$$

$$P = \rho \left(\frac{\partial F}{\partial \rho}\right)_{T,\boldsymbol{\nabla}\rho} - F \tag{5.54}$$

5.2.2.2 Local formulation of the first principle of thermodynamics

The first principle of thermodynamics states that the time variations of the total energy over a domain $\mathcal{V}$ of fluid is equal to the power of the external forces and the energy fluxes through the boundary $\mathcal{A}$ as given by Eq. (5.55). Actually, the energy flux can be interpreted as a surface work associated with microscopic motions ν^* as introduced in Eq. (C.3).

$$\frac{d}{dt}\int_{\mathcal{V}} \rho e\, d\mathcal{V} = \mathcal{P}_{(e)} - \int_{\mathcal{A}} \boldsymbol{q} \cdot \boldsymbol{n}\, d\mathcal{A} \tag{5.55}$$

Here $e = e_s + \mathbf{v}^2/2$ is the specific total energy, $\boldsymbol{q}$ is the surface energy flux, $\boldsymbol{n}$ the outer normal vector to the surface $\mathcal{A}$ and $\mathcal{P}_{(e)}$ is the actual power of the external forces calculated with the real velocity field $\mathbf{v}$ over $\mathcal{V}$. $\mathcal{P}_{(e)}$ is not to be mistaken for the virtual power of the external forces $\mathcal{P}_{(e)}$ used so far and calculated for a virtual velocity field $\mathbf{v}^*$. The same goes for $\mathcal{P}_{(i)}$ and $\mathcal{P}_{(a)}$ that denote the actual powers, respectively of the internal forces and of the acceleration forces, not to be confused with their virtual counterparts $\mathcal{P}_{(i)}$ and $\mathcal{P}_{(a)}$. Applying the v.p.p. to the real velocity field $\mathbf{v}$, one gets:

$$\mathcal{P}_{(a)} = \mathcal{P}_{(i)} + \mathcal{P}_{(e)} \tag{5.56}$$

Noticing that:

$$\mathcal{P}_{(a)} = \int_{\mathcal{V}} \rho \mathbf{v} \cdot \frac{d\mathbf{v}}{dt}\, d\mathcal{V} = \int_{\mathcal{V}} \rho \frac{d}{dt}\left(\frac{\mathbf{v}^2}{2}\right) d\mathcal{V} \tag{5.57}$$

and using Reynolds theorem (see eq:reynolds_formula_integral):

$$\frac{d}{dt}\int_{\mathcal{V}} \rho e\, d\mathcal{V} = \int_{\mathcal{V}} \rho \frac{de}{dt}\, d\mathcal{V} = \int_{\mathcal{V}} \rho \frac{de_s}{dt}\, d\mathcal{V} + \int_{\mathcal{V}} \rho \frac{d}{dt}\left(\frac{\mathbf{v}^2}{2}\right) d\mathcal{V} = \int_{\mathcal{V}} \rho \frac{de_s}{dt}\, d\mathcal{V} + \mathcal{P}_{(a)} \tag{5.58}$$

and finally by applying the Green's theorem (see eq:green_s_theorem) to the energy flux $\boldsymbol{q}$:

$$\int_{\mathcal{A}} \boldsymbol{q} \cdot \boldsymbol{n}\, d\mathcal{A} = \int_{\mathcal{V}} \boldsymbol{\nabla} \cdot \boldsymbol{q}\, d\mathcal{V} \tag{5.59}$$

one can write:

$$\int_{\mathcal{V}} \rho \frac{de_s}{dt}\, d\mathcal{V} + \mathcal{P}_{(i)} + \mathcal{P}_{(e)} = \mathcal{P}_{(e)} - \int_{\mathcal{V}} \boldsymbol{\nabla} \cdot \boldsymbol{q}\, d\mathcal{V} \tag{5.60}$$

what, given the expression for $\mathcal{P}_{(i)}$ found in Eq. (5.38) applied to the real velocity field $\mathbf{v}$ to get $\mathcal{P}_{(i)}$, simplifies in:

$$\int_{\mathcal{V}} \left[\rho \frac{de_s}{dt} - \boldsymbol{\nabla}\mathbf{v} : \underline{\underline{\boldsymbol{\varsigma}}} - \boldsymbol{\nabla}\boldsymbol{\nabla}\mathbf{v} \vdots \underline{\underline{\underline{\mathbf{C}}}} + \boldsymbol{\nabla} \cdot \boldsymbol{q}\right] d\mathcal{V} = 0 \tag{5.61}$$

This equation must hold for any fluid subdomain $\mathcal{V}$ of Ω which implies the local internal energy equation:

$$\rho \frac{de_s}{dt} = \boldsymbol{\nabla}\mathbf{v} : \underline{\underline{\boldsymbol{\varsigma}}} + \boldsymbol{\nabla}\boldsymbol{\nabla}\mathbf{v} \vdots \underline{\underline{\underline{\mathbf{C}}}} - \boldsymbol{\nabla} \cdot \boldsymbol{q} \tag{5.62}$$

and at the same time, from Eq. (5.52) one can derive another expression for the local internal energy equation:

$$\frac{de_s}{dt} = T\frac{ds}{dt} + \frac{P}{\rho^2}\frac{d\rho}{dt} + \frac{1}{\rho}\boldsymbol{\mathcal{F}} \cdot \frac{d\boldsymbol{\nabla}\rho}{dt} \tag{5.63}$$

5.2.3 Second principle of thermodynamics

5.2.3.1 Local formulation of the second principle of thermodynamics

The second principle of thermodynamics states that the time variations of the entropy over a domain $\mathcal{V}$ of fluid is equal to the creation of entropy, always positive, due to a volume source of entropy ϕ_S and the entropy fluxes due to the energy fluxes through the boundary $\mathcal{A}$. Calling s the specific entropy of the fluid, the principle can be written:

$$\frac{d}{dt}\int_{\mathcal{V}} \rho s\, d\mathcal{V} = \int_{\mathcal{V}} \phi_S\, d\mathcal{V} - \int_{\mathcal{A}} \frac{\boldsymbol{q}}{T} \cdot \boldsymbol{n}\, d\mathcal{A} \tag{5.64}$$

As done in Eqs. (5.58) and (5.59), one can use both Reynolds and Green's theorems to end up with the relation:

$$\int_{\mathcal{V}} \left[\rho \frac{ds}{dt} - \phi_S + \boldsymbol{\nabla} \cdot \left(\frac{\boldsymbol{q}}{T}\right)\right] = 0\, d\mathcal{V} \tag{5.65}$$

Once again, this equation must hold for any fluid subdomain $\mathcal{V}$ of Ω which allows to give the local entropy equation:

$$\rho\frac{ds}{dt} = \phi_S - \boldsymbol{\nabla}\cdot\left(\frac{\boldsymbol{q}}{T}\right) \tag{5.66}$$

5.2.3.2 Determination of the stress tensor

In order to express the stress tensor $\underline{\underline{\boldsymbol{\tau}}}$, the hypotheses listed below are made. The validity and implications of said hypotheses are further discussed in Seppecher (1987) and Jamet (1998).

1. the stress tensor $\underline{\underline{\boldsymbol{\tau}}}$ can be separated into dissipative $\underline{\underline{\boldsymbol{\tau}}}^d$ and non-dissipative $\underline{\underline{\boldsymbol{\tau}}}^n$ contributions
2. the dissipative stress tensor $\underline{\underline{\boldsymbol{\tau}}}^d$, due to the viscous constraints, remains the same as in a non-capillary fluid
3. consequently, the second gradient of the velocity does not contribute to the entropy creation

Combining Eqs. (5.62), (5.63) and (5.66), the volume entropy production ϕ_S can be expressed by:

$$T\phi_S = \boldsymbol{\nabla}\mathbf{v} : \underline{\underline{\boldsymbol{\varsigma}}} + \boldsymbol{\nabla}\boldsymbol{\nabla}\mathbf{v}\vdots\underline{\underline{\underline{\mathbf{C}}}} - \frac{P}{\rho}\frac{d\rho}{dt} - \boldsymbol{\mathcal{F}}\cdot\frac{d\boldsymbol{\nabla}\rho}{dt} - \frac{1}{T}\boldsymbol{\nabla}T\cdot\boldsymbol{q} \tag{5.67}$$

Thanks to the mass equation $\partial\rho/\partial t = -\boldsymbol{\nabla}\cdot(\rho\mathbf{v})$, one can write the transport equations for the density and the density gradient :

$$\frac{d\rho}{dt} = -\rho\boldsymbol{\nabla}\cdot\mathbf{v} \tag{5.68}$$

$$\frac{d\boldsymbol{\nabla}\rho}{dt} = \boldsymbol{\nabla}\boldsymbol{\nabla}\rho\cdot\mathbf{v} - \boldsymbol{\nabla}\left(\boldsymbol{\nabla}\cdot\rho\mathbf{v}\right) \tag{5.69}$$

Carring out all the calculations in App. C.3, one eventually gets:

$$T\phi_S = \frac{\partial\mathbf{v}_i}{\partial x_j}\left[\varsigma_{ji} + \frac{\partial\rho}{\partial x_i}\mathcal{F}_j + \left(P + \frac{\partial\rho}{\partial x_k}\mathcal{F}_k\right)\delta_{ij}\right] + \frac{\partial^2\mathbf{v}_i}{\partial x_j\partial x_k}\left[\mathrm{C}_{kji} + \rho\mathcal{F}_k\delta_{ik}\right] - \frac{1}{T}\frac{\partial T}{\partial x_i}q_i \tag{5.70}$$

From hypothesis (3) one has $\mathrm{C}_{kji} + \rho\mathcal{F}_k\delta_{ik} = 0$ and remembering that $\underline{\underline{\underline{\mathbf{C}}}}$ must be symmetrical in its two first indexes, it implies that its components are given by:

$$\mathrm{C}_{ijk} = \frac{1}{2}\rho\left(\delta_{ik}\mathcal{F}_k + \delta_{jk}\mathcal{F}_i\right) \tag{5.71}$$

Besides, in virtue of the relation $\underline{\underline{\boldsymbol{\varsigma}}} = \underline{\underline{\boldsymbol{\tau}}} + \boldsymbol{\nabla}\cdot\underline{\underline{\underline{\boldsymbol{\mathcal{C}}}}}$ with $\mathcal{C}_{ijk} = \mathrm{C}_{kji}$ (from Jamet (1998)), the fact that $\underline{\underline{\boldsymbol{\varsigma}}}$ is symmetrical and hypothesis (1), the volume entropy production is given by:

$$T\phi_S = \frac{\partial\mathbf{v}_i}{\partial x_j}\left[\tau^d_{ij} + \tau^n_{ij} - \frac{1}{2}\frac{\partial(\rho\mathcal{F}_j)}{\partial x_i} + \frac{\partial\rho}{\partial x_i}\mathcal{F}_j + \left(P + \frac{\partial\rho}{\partial x_k}\mathcal{F}_k - \frac{1}{2}\frac{\partial(\rho\mathcal{F}_k)}{\partial x_k}\right)\delta_{ij}\right] - \frac{1}{T}\frac{\partial T}{\partial x_i}q_i \tag{5.72}$$

The mechanical pressure p, of which denomination will be justified in the next paragraphs, is introduced as:

$$p = P - \rho\boldsymbol{\nabla}\cdot\boldsymbol{\mathcal{F}} \tag{5.73}$$

This implies:

$$P + \frac{\partial \rho}{\partial x_k}\mathcal{F}_k = p + \rho\frac{\partial \mathcal{F}_k}{\partial x_k} + \frac{\partial \rho}{\partial x_k} = p + \frac{\partial(\rho\mathcal{F}_k)}{\partial x_k} \tag{5.74}$$

Finally, given hypothesis (2), one can isolate the components of the non-dissipative tensor $\underline{\underline{\boldsymbol{\tau}}}^n$ through:

$$\tau^n_{ji} - \frac{1}{2}\frac{\partial(\rho\mathcal{F}_j)}{\partial x_j} + \frac{\partial \rho}{\partial x_i}\mathcal{F}_j + \left(p + \frac{1}{2}\frac{\partial(\rho\mathcal{F}_k)}{\partial x_k}\right)\delta_{ij} = 0 \tag{5.75}$$

Eventually, the expression of the non dissipative tensor is:

$$\underline{\underline{\boldsymbol{\tau}}}^n = -\left(p + \frac{1}{2}\boldsymbol{\nabla}\cdot(\rho\boldsymbol{\mathcal{F}})\right)\underline{\underline{\mathbf{I}}} - \boldsymbol{\nabla}\rho\otimes\boldsymbol{\mathcal{F}} + \frac{1}{2}\boldsymbol{\nabla}(\rho\boldsymbol{\mathcal{F}})^{\mathrm{T}} \tag{5.76}$$

Regarding the viscous stress tensor $\underline{\underline{\boldsymbol{\tau}}}^d$ and the energy flux $\boldsymbol{q}$, their expressions for a capillary fluid are proposed and discussed in Seppecher (1987), Jamet (1998) and Gaillard (2015). Noticeably, the interface normal direction will be a remarkable direction for these two quantities, leading to a special shear stress in the tangential plan and to an anisotropic heat conduction. For a finer level of modeling, this would allow to challenge the tangential velocity and temperature continuity at the interface. However in this work, the precision granted by a more classic description of these quantities will be satisfactory enough.
Therefore, when considered, the energy flux will correspond to a thermal conductive flux described by the Fourier's law $\boldsymbol{q} = -k_{\mathrm{th}}\boldsymbol{\nabla}T$ and the viscous stress tensor will be that of a classic Newtonian fluid, of which expression is given by $\underline{\underline{\boldsymbol{\tau}}}^d = 2\mu\left(\boldsymbol{\nabla}\mathbf{v} + \boldsymbol{\nabla}\mathbf{v}^{\mathrm{T}}\right) + 2\mu/3\,(\boldsymbol{\nabla}\cdot\mathbf{v})\,\underline{\underline{\mathbf{I}}}$. k_{th} and μ are respectively the thermal diffusion coefficient and the dynamic viscosity of the fluid.

5.2.4 Equations in the Second Gradient theory

5.2.4.1 Equations for a pure fluid motion in the Second Gradient

With the tensors and fluxes expressed, it is possible to derive the different equations that determine the behavior of a capillary fluid.

Mass equation

Of course, capillarity is not a mass inducive/reducive phenomenon, therefore the mass conservation equation is not modified and is written as usual:

$$\frac{\partial \rho}{\partial t} = -\boldsymbol{\nabla}\cdot[\rho\mathbf{v}] \tag{5.77}$$

Momentum equations

The momentum equation, in its base form, is given by $\rho\, d\mathbf{v}/dt = -\boldsymbol{\nabla}\cdot\underline{\underline{\boldsymbol{\tau}}} - \rho\boldsymbol{g}$ and the stress tensor $\underline{\underline{\boldsymbol{\tau}}}$ is given by $\underline{\underline{\boldsymbol{\tau}}}^d + \underline{\underline{\boldsymbol{\tau}}}^n$ where $\underline{\underline{\boldsymbol{\tau}}}^n$ is expressed in Eq. (5.76). This allows to express:

$$\boldsymbol{\nabla}\cdot\underline{\underline{\boldsymbol{\tau}}}^n = -\boldsymbol{\nabla}p - \boldsymbol{\nabla}\cdot(\boldsymbol{\nabla}\rho\otimes\boldsymbol{\mathcal{F}}) \tag{5.78}$$

In Jamet (1998), the author discuses the form of the non dissipative tensor $\underline{\underline{\boldsymbol{\tau}}}^n$ obtained Eq. (5.76) which differs from the tensors obtained by Seppecher (1987) and Gouin (1988).

However, he notices that eventually, this difference has no impact nor on the momentum equation neither on the boundary conditions since the divergence of this tensor is the same for all the formulations. This finally allows to write the momentum equation for the fluid:

$$\rho\frac{d\mathbf{v}}{dt} = -\boldsymbol{\nabla}p - \boldsymbol{\nabla}\cdot(\boldsymbol{\nabla}\rho\otimes\boldsymbol{\mathcal{F}}) + \boldsymbol{\nabla}\cdot\underline{\underline{\boldsymbol{\tau}}}^{d} + \rho\boldsymbol{g} \tag{5.79}$$

The equation can be written in a conservative form, more suited for numerical simulations:

$$\frac{\partial(\rho\mathbf{v})}{\partial t} = -\boldsymbol{\nabla}\cdot\left[p\underline{\underline{\mathbf{I}}} + (\boldsymbol{\nabla}\rho\otimes\boldsymbol{\mathcal{F}}) - \underline{\underline{\boldsymbol{\tau}}}^{d}\right] + \rho\boldsymbol{g} \tag{5.80}$$

The mechanical pressure introduced by the relation in Eq. (5.73) has been named this was because it is the actual isotropic part of the effective non-dissipative stress tensor. For a non-capillary fluid, the actual isotropic non-dissipative mechanical forces are embodied by the thermodynamical pressure tensor $P_0\underline{\underline{\mathbf{I}}}$. For a capillary fluid, this role is fulfilled by p, hence the denomination of mechanical pressure.

Energy equations

To get the equation for the internal energy, one must go back to the relation $\underline{\underline{\boldsymbol{\varsigma}}} = \underline{\underline{\boldsymbol{\tau}}} + \boldsymbol{\nabla}\cdot\underline{\underline{\mathbf{C}}}$ (see Eqs. (C.27) and (C.28)) which allows to write:

$$\underline{\underline{\boldsymbol{\varsigma}}} = -\left[p + \boldsymbol{\nabla}\cdot(\rho\boldsymbol{\mathcal{F}})\right]\underline{\underline{\mathbf{I}}} - \boldsymbol{\nabla}\rho + \underline{\underline{\boldsymbol{\tau}}}^{d} \tag{5.81}$$

This new relation can than be injected in Eq. (5.62) and use jointly with Eq. (5.63) to get:

$$\rho\frac{de_s}{dt} = -\left[p + \boldsymbol{\nabla}\cdot(\rho\boldsymbol{\mathcal{F}})\right](\boldsymbol{\nabla}\cdot\mathbf{v}) - (\boldsymbol{\mathcal{F}}\otimes\boldsymbol{\nabla}\rho) : \boldsymbol{\nabla}\mathbf{v} - \rho\boldsymbol{\mathcal{F}}\cdot\boldsymbol{\nabla}(\boldsymbol{\nabla}\cdot\mathbf{v}) + \underline{\underline{\boldsymbol{\tau}}}^{d} : \boldsymbol{\nabla}\mathbf{v} - \boldsymbol{\nabla}\cdot\boldsymbol{q} \tag{5.82}$$

The equation can be further simplified noticing that:

$$\boldsymbol{\nabla}\cdot(\rho\boldsymbol{\mathcal{F}}\boldsymbol{\nabla}\cdot\mathbf{v}) = (\boldsymbol{\nabla}\cdot\mathbf{v})\,\boldsymbol{\nabla}\cdot(\rho\boldsymbol{\mathcal{F}}) + \rho\boldsymbol{\mathcal{F}}\cdot\boldsymbol{\nabla}(\boldsymbol{\nabla}\cdot\mathbf{v}) \tag{5.83}$$

to finally arrive to:

$$\rho\frac{de_s}{dt} = -p\boldsymbol{\nabla}\cdot\mathbf{v} - (\boldsymbol{\mathcal{F}}\otimes\boldsymbol{\nabla}\rho) : \boldsymbol{\nabla}\mathbf{v} - \boldsymbol{\nabla}\cdot(\rho\boldsymbol{\mathcal{F}}\boldsymbol{\nabla}\cdot\mathbf{v}) + \underline{\underline{\boldsymbol{\tau}}}^{d} : \boldsymbol{\nabla}\mathbf{v} - \boldsymbol{\nabla}\cdot\boldsymbol{q} \tag{5.84}$$

Once again, this equation can be written in a conservative form using the total specific energy $e = e_s + \mathbf{v}^2/2$ by combining Eq. (5.84) and $\mathbf{v}\cdot$ Eq. (5.79) to eventually get:

$$\frac{\partial(\rho e)}{\partial t} = -\boldsymbol{\nabla}\cdot\left[(\rho e + p)\,\mathbf{v} + (\boldsymbol{\mathcal{F}}\otimes\boldsymbol{\nabla}\rho)\cdot\mathbf{v} + \rho\boldsymbol{\mathcal{F}}\boldsymbol{\nabla}\cdot\mathbf{v} - \underline{\underline{\boldsymbol{\tau}}}^{d}\cdot\mathbf{v} + \boldsymbol{q}\right] + \rho\boldsymbol{g}\cdot\mathbf{v} \tag{5.85}$$

Final system of equations

The results obtained at that point can be summarized together with the main hypotheses made along their derivation. We assumed that:

- the virtual power of the remote forces related to the first and second velocity gradients are negligible;
- the viscous constraints ($\underline{\underline{\boldsymbol{\tau}}}^{d}$) remain the same as in a non-capillary fluid;

- the capillary effects do not impact the mass equation and have no dissipative effect;
- the entropy creation is not contributed to by the second gradient of the velocity;
- the viscous stress and energy flux can be written in classic way (Newton/Fourier).

And given all these hypotheses, one obtained the hereunder sets of equations.
These equations can be written in a native, non-conservative way:

$$\begin{cases} \dfrac{\partial \rho}{\partial t} = -\boldsymbol{\nabla} \cdot (\rho \mathbf{v}) & \text{(5.86a)} \\ \rho \dfrac{d\mathbf{v}}{dt} = -\boldsymbol{\nabla} p - \boldsymbol{\nabla} \cdot (\boldsymbol{\nabla}\rho \otimes \boldsymbol{\mathcal{F}}) + \boldsymbol{\nabla} \cdot \underline{\underline{\boldsymbol{\tau}}}^d + \rho \boldsymbol{g} & \text{(5.86b)} \\ \rho \dfrac{de_s}{dt} = -p \boldsymbol{\nabla} \cdot \mathbf{v} - (\boldsymbol{\mathcal{F}} \otimes \boldsymbol{\nabla}\rho) : \boldsymbol{\nabla}\mathbf{v} - \boldsymbol{\nabla} \cdot (\rho \boldsymbol{\mathcal{F}} \boldsymbol{\nabla} \cdot \mathbf{v}) + \underline{\underline{\boldsymbol{\tau}}}^d : \boldsymbol{\nabla}\mathbf{v} - \boldsymbol{\nabla} \cdot \boldsymbol{q} & \text{(5.86c)} \end{cases}$$

or in a numerical-friendly conservative way:

$$\begin{cases} \dfrac{\partial \rho}{\partial t} = -\boldsymbol{\nabla} \cdot (\rho \mathbf{v}) & \text{(5.87a)} \\ \dfrac{\partial (\rho \mathbf{v})}{\partial t} = -\boldsymbol{\nabla} \cdot \left[p \underline{\underline{\mathbf{I}}} + \rho \mathbf{v} \otimes \mathbf{v} + (\boldsymbol{\nabla}\rho \otimes \boldsymbol{\mathcal{F}}) - \underline{\underline{\boldsymbol{\tau}}}^d \right] + \rho \boldsymbol{g} & \text{(5.87b)} \\ \dfrac{\partial (\rho e)}{\partial t} = -\boldsymbol{\nabla} \cdot \left[(\rho e + p)\, \mathbf{v} + (\boldsymbol{\mathcal{F}} \otimes \boldsymbol{\nabla}\rho) \cdot \mathbf{v} + \rho \boldsymbol{\mathcal{F}} \boldsymbol{\nabla} \cdot \mathbf{v} - \underline{\underline{\boldsymbol{\tau}}}^d \cdot \mathbf{v} + \boldsymbol{q} \right] + \rho \boldsymbol{g} \cdot \mathbf{v} & \text{(5.87c)} \end{cases}$$

Finally, to these equations must be added the entropy equation that is ultimately written as:

$$\rho T \frac{ds}{dt} = \underline{\underline{\boldsymbol{\tau}}}^d : \boldsymbol{\nabla}\mathbf{v} - \boldsymbol{\nabla} \cdot \boldsymbol{q} \tag{5.88}$$

5.3 Thermodynamic closure of the Second Gradient model

5.3.1 Thermodynamic variables in the Second Gradient theory

As it has been done for the mechanical equations, one can also derive the different thermodynamic potentials as well as other thermodynamic variables possibly impacted by the Second Gradient modifications. These derivations rely on Eqs. (B.11)-(B.18) and Eqs. (B.22)-(B.29) given in App. B.1.

5.3.1.1 Intensive variables

Throughout the development of the Second Gradient theory, the temperature T and the density ρ have been implicitly supposed to be undifferentiated whether the capillary forces apply or not. The Second Gradient theory changes how the other thermodynamic variables may be calculated from T and ρ but does not, in essence, modify their definitions. However, the pressure as defined by Eq. (B.28) is modified and its expression has already been given by Eq. (5.54) since the two definitions actually match, as shown by:

$$P = \rho^2 \left(\frac{\partial f}{\partial \rho} \right)_{T, \boldsymbol{\nabla}\rho} = \rho^2 \frac{\partial}{\partial \rho} \left(\frac{F}{\rho} \right)_{T, \boldsymbol{\nabla}\rho} = \rho^2 \left(\frac{1}{\rho} \left(\frac{\partial F}{\partial \rho} \right)_{T, \boldsymbol{\nabla}\rho} - \frac{F}{\rho^2} \right) = \rho \left(\frac{\partial F}{\partial \rho} \right)_{T, \boldsymbol{\nabla}\rho} - F \tag{5.89}$$

This allows to get the new expression of the thermodynamic pressure, in particular in regards to the reference pressure P_0 obtained when no capillary forces are considered. As a reminder

of the convention introduced in 5.2.2.1, the subscript $_0$ is used to refer to the expression of a thermodynamic variable when no capillary forces are considered, i.e. as given directly by the equation of state. The new thermodynamic pressure P is thus expressed by:

$$\begin{aligned} P &= \rho\left(\frac{\partial F_0}{\partial \rho}\right)_{T,\boldsymbol{\nabla}\rho} - F_0 + \rho\left(\frac{\partial F_1}{\partial \rho}\right)_{T,\boldsymbol{\nabla}\rho} - F_1 \\ P &= P_0 - F_1 + \rho\left(\frac{\partial F_1}{\partial \rho}\right)_{T,\boldsymbol{\nabla}\rho} \end{aligned} \tag{5.90}$$

5.3.1.2 Specific variables

The specific free energy f is obtained directly by dividing Eq. (5.47) by the density ρ:

$$\begin{aligned} f &= \frac{F}{\rho} = \frac{F_0}{\rho} + \frac{F_1}{\rho} \\ f &= f_0 + \frac{F_1}{\rho} \end{aligned} \tag{5.91}$$

The chemical potential μ (or equivalently the specific free enthalpy g) is calculated with Eq. (B.17):

$$\begin{aligned} \mu &= \left(\frac{\partial F}{\partial \rho}\right)_{T,\boldsymbol{\nabla}\rho} = \left(\frac{\partial F_0}{\partial \rho}\right)_{T,\boldsymbol{\nabla}\rho} + \left(\frac{\partial F_1}{\partial \rho}\right)_{T,\boldsymbol{\nabla}\rho} \\ \mu &= \mu_0 + \left(\frac{\partial F_1}{\partial \rho}\right)_{T,\boldsymbol{\nabla}\rho} \end{aligned} \tag{5.92}$$

The specific entropy s is obtained from Eq. (B.28):

$$\begin{aligned} s &= -\left(\frac{\partial f}{\partial T}\right)_{\rho,\boldsymbol{\nabla}\rho} = -\left(\frac{\partial f_0}{\partial T}\right)_{\rho,\boldsymbol{\nabla}\rho} - \frac{1}{\rho}\left(\frac{\partial F_1}{\partial T}\right)_{\rho,\boldsymbol{\nabla}\rho} \\ s &= s_0 - \frac{1}{\rho}\left(\frac{\partial F_1}{\partial T}\right)_{\rho,\boldsymbol{\nabla}\rho} \end{aligned} \tag{5.93}$$

The specific enthalpy h is then expressed using Eq. (B.23):

$$\begin{aligned} h &= Ts + \mu = Ts_0 - \frac{T}{\rho}\left(\frac{\partial F_1}{\partial T}\right)_{\rho,\boldsymbol{\nabla}\rho} + \mu_0 + \left(\frac{\partial F_1}{\partial \rho}\right)_{T,\boldsymbol{\nabla}\rho} \\ h &= h_0 + \left(\frac{\partial F_1}{\partial \rho}\right)_{T,\boldsymbol{\nabla}\rho} - \frac{T}{\rho}\left(\frac{\partial F_1}{\partial T}\right)_{\rho,\boldsymbol{\nabla}\rho} \end{aligned} \tag{5.94}$$

And finally the specific sensible energy e_s is derived thanks to Eq. (B.22):

$$\begin{aligned} e_s &= h - \frac{P}{\rho} = h_0 + \left(\frac{\partial F_1}{\partial \rho}\right)_{T,\boldsymbol{\nabla}\rho} - \frac{T}{\rho}\left(\frac{\partial F_1}{\partial T}\right)_{\rho,\boldsymbol{\nabla}\rho} - \frac{P_0}{\rho} + \frac{F_1}{\rho} - \left(\frac{\partial F_1}{\partial \rho}\right)_{T,\boldsymbol{\nabla}\rho} \\ e_s &= e_{s0} + \frac{F_1}{\rho} - \frac{T}{\rho}\left(\frac{\partial F_1}{\partial T}\right)_{\rho,\boldsymbol{\nabla}\rho} \end{aligned} \tag{5.95}$$

Essentially, the new expressions of the thermodynamic variables require the expressions of the partial derivatives of the additional volumetric free energy F_1 with respect to T and ρ.

5.3.2 Application to the case $F_1 = \lambda (\boldsymbol{\nabla}\rho)^2 / 2$

So far, the expression of the volumetric free energy has not been specified apart from the formula Eq. (5.47) for the sake of generality. In practice, the common choice made for this expression is the one given by Eq. (5.33) inherited from the work of Cahn and Hilliard (1958) and generalized in Eq. (5.96). To that effect, the capillary coefficient λ is introduced. It depends, a priori, on the temperature of the fluid and as it is shown in later paragraphs, it controls the behavior of the interface by impacting both its width w and its associated surface tension σ.

$$F(T, \rho, \boldsymbol{\nabla}\rho) = F_0(T, \rho) + \frac{\lambda(T)}{2} (\boldsymbol{\nabla}\rho)^2 \tag{5.96}$$

With this definition, the new form of the mechanical equations and the thermodynamic variables can be particularized. From Eqs. (5.53), (5.54) and (5.73), one gets:

$$\boldsymbol{\mathcal{F}} = \left(\frac{\partial F}{\partial \boldsymbol{\nabla}\rho}\right)_{s,\rho} = \left(\frac{\partial F}{\partial \boldsymbol{\nabla}\rho}\right)_{T,\rho} = \lambda \boldsymbol{\nabla}\rho \tag{5.97}$$

$$P = \rho \left(\frac{\partial F}{\partial \rho}\right)_{T,\boldsymbol{\nabla}\rho} - F = \rho \left(\frac{\partial F_0}{\partial \rho}\right)_{T,\rho} - F_0 - \frac{\lambda}{2} (\boldsymbol{\nabla}\rho)^2 = P_0 - \frac{\lambda}{2} (\boldsymbol{\nabla}\rho)^2 \tag{5.98}$$

$$p = P_0 - \frac{\lambda}{2} (\boldsymbol{\nabla}\rho)^2 - \rho \boldsymbol{\nabla} \cdot (\lambda \boldsymbol{\nabla}\rho) \tag{5.99}$$

and with Eqs. (5.76) and (5.78) one also gets:

$$\underline{\underline{\boldsymbol{\tau}}}^n = -\left(p + \frac{1}{2}\boldsymbol{\nabla} \cdot (\lambda\rho \boldsymbol{\nabla}\rho)\right) \underline{\underline{\mathbf{I}}} - \lambda \boldsymbol{\nabla}\rho \otimes \boldsymbol{\nabla}\rho + \frac{1}{2}\boldsymbol{\nabla}(\lambda\rho \boldsymbol{\nabla}\rho)^{\mathrm{T}} \tag{5.100}$$

$$\boldsymbol{\nabla} \cdot \underline{\underline{\boldsymbol{\tau}}}^n = -\boldsymbol{\nabla} p - \boldsymbol{\nabla} \cdot (\lambda \boldsymbol{\nabla}\rho \otimes \boldsymbol{\nabla}\rho) \tag{5.101}$$

The momentum and energy equations can than be written in their two forms:

$$\begin{cases} \rho \dfrac{d\mathbf{v}}{dt} = -\boldsymbol{\nabla} \cdot \left[p \underline{\underline{\mathbf{I}}} + \mathbf{v} \otimes \mathbf{v} + \lambda \boldsymbol{\nabla}\rho \otimes \boldsymbol{\nabla}\rho - \underline{\underline{\boldsymbol{\tau}}}^d\right] + \rho \boldsymbol{g} & \text{(5.102a)} \\ \rho \dfrac{de_s}{dt} = -p \boldsymbol{\nabla} \cdot \mathbf{v} - \lambda (\boldsymbol{\nabla}\rho \otimes \boldsymbol{\nabla}\rho) : \boldsymbol{\nabla}\mathbf{v} - \boldsymbol{\nabla} \cdot (\lambda\rho \boldsymbol{\nabla}\rho \boldsymbol{\nabla} \cdot \mathbf{v}) + \underline{\underline{\boldsymbol{\tau}}}^d : \boldsymbol{\nabla}\mathbf{v} - \boldsymbol{\nabla} \cdot \boldsymbol{q} & \text{(5.102b)} \end{cases}$$

$$\begin{cases} \dfrac{\partial(\rho \mathbf{v})}{\partial t} = -\boldsymbol{\nabla} p - \boldsymbol{\nabla} \cdot \lambda (\boldsymbol{\nabla}\rho \otimes \boldsymbol{\nabla}\rho) + \boldsymbol{\nabla} \cdot \underline{\underline{\boldsymbol{\tau}}}^d + \rho \boldsymbol{g} & \text{(5.103a)} \\ \dfrac{\partial(\rho e)}{\partial t} = -\boldsymbol{\nabla} \cdot \left[(\rho e + p)\mathbf{v} + \lambda (\boldsymbol{\nabla}\rho \otimes \boldsymbol{\nabla}\rho) \cdot \mathbf{v} + \lambda\rho \boldsymbol{\nabla}\rho \boldsymbol{\nabla} \cdot \mathbf{v} - \underline{\underline{\boldsymbol{\tau}}}^d \cdot \mathbf{v} + \boldsymbol{q}\right] + \rho \boldsymbol{g} \cdot \mathbf{v} & \text{(5.103b)} \end{cases}$$

These equations are in a perfect agreement with those obtained by the authors in Korteweg (1901) and Casal and Gouin (1985). Besides, given Eq. (5.99), one can introduce the capillary tensor $\underline{\underline{\boldsymbol{\sigma}}}$ defined by:

$$\underline{\underline{\boldsymbol{\sigma}}} = -\left[\frac{\lambda}{2} (\boldsymbol{\nabla}\rho)^2 + \rho \boldsymbol{\nabla} \cdot (\lambda \boldsymbol{\nabla}\rho)\right] \underline{\underline{\mathbf{I}}} + \lambda \boldsymbol{\nabla}\rho \otimes \boldsymbol{\nabla}\rho \tag{5.104}$$

And the thermodynamic variables can also be expressed:

$$P = P_0 - \frac{\lambda}{2}(\boldsymbol{\nabla}\rho)^2 \tag{5.105}$$

$$e_s = e_{s0} + \frac{1}{2\rho}\left(\lambda - T\frac{d\lambda}{dT}\right)(\boldsymbol{\nabla}\rho)^2 \tag{5.106}$$

$$h_s = h_{s0} - \frac{T}{2\rho}\frac{d\lambda}{dT}(\boldsymbol{\nabla}\rho)^2 \tag{5.107}$$

$$f = f_0 + \frac{\lambda}{2\rho}(\boldsymbol{\nabla}\rho)^2 \tag{5.108}$$

$$\mu = \mu_0 \tag{5.109}$$

$$s = s_0 - \frac{1}{2\rho}\frac{d\lambda}{dT}(\boldsymbol{\nabla}\rho)^2 \tag{5.110}$$

In particular with the additional hypothesis $\frac{d\lambda}{dT} = 0$, one eventually gets:

$$P = P_0 - \frac{\lambda}{2}(\boldsymbol{\nabla}\rho)^2 \tag{5.111}$$

$$e_s = e_{s0} + \frac{\lambda}{2\rho}(\boldsymbol{\nabla}\rho)^2 \tag{5.112}$$

$$h_s = h_{s0} \tag{5.113}$$

$$f = f_0 + \frac{\lambda}{2\rho}(\boldsymbol{\nabla}\rho)^2 \tag{5.114}$$

$$\mu = \mu_0 \tag{5.115}$$

$$s = s_0 \tag{5.116}$$

5.3.3 Words on multi-species cases

5.3.3.1 General formulas

The previous considerations can somewhat be extended to mixtures, what becomes a necessary update when dealing with reactive flows. The starting assumptions are the same, the volumetric free energy F will depend on the temperature T and the densities of the different components $\rho_1, ..., \rho_N$ but also on the densities gradients $\boldsymbol{\nabla}\rho_1, ..., \boldsymbol{\nabla}\rho_N$ as described by:

$$F = F_0(T, \rho_1, ..., \rho_N) + F_1(T, \rho_1, ..., \rho_N, \boldsymbol{\nabla}\rho_1, ..., \boldsymbol{\nabla}\rho_N) \tag{5.117}$$

From this formula, the same developments can be made and both the fluxes in the equations of motion and the thermodynamic variables will be modified. From Gaillard (2015) and Jofre and Urzay (2016) the new Gibbs relation is given by:

$$de_s = T\,ds + \frac{P}{\rho^2}\,d\rho + \frac{1}{\rho}\sum_{i=1}^{N}\mu_i\,dY_i + \frac{1}{\rho}\sum_{i=1}^{N}\boldsymbol{\mathcal{F}}_i \cdot d\boldsymbol{\nabla}\rho_i \tag{5.118}$$

where Y_i is the mass fractions of the i^{th} mixture component, $\boldsymbol{\mathcal{F}}_i = (\partial F_1/\partial\boldsymbol{\nabla}\rho_i)_{T,\rho_j,\boldsymbol{\nabla}\rho_{k\neq i}}$ and the mixture density is given by $\rho = \sum \rho_i Y_i$. Likewise, the mechanical pressure is written:

$$p = P - \sum_{i=1}^{N}\rho_i\boldsymbol{\nabla}\cdot\boldsymbol{\mathcal{F}}_i \tag{5.119}$$

And the new mechanical equations ($\boldsymbol{j}_i$ being the diffusive flux for the species i) written in their conservative form are:

$$\frac{\partial \rho Y_i}{\partial t} = -\boldsymbol{\nabla} \cdot \boldsymbol{j}_i \tag{5.120a}$$

$$\frac{\partial (\rho \mathbf{v})}{\partial t} = -\boldsymbol{\nabla} \cdot \left[p \underline{\underline{\mathbf{I}}} + \rho \mathbf{v} \otimes \mathbf{v} + \sum_{i=1}^{N} (\boldsymbol{\nabla} \rho_i \otimes \boldsymbol{\mathcal{F}}_i) - \underline{\underline{\boldsymbol{\tau}}}^d \right] + \rho \boldsymbol{g} \tag{5.120b}$$

$$\begin{aligned} \frac{\partial (\rho e)}{\partial t} = -\boldsymbol{\nabla} \cdot \Bigg[& (\rho e + p)\, \mathbf{v} + \left(\sum_{i=1}^{N} \boldsymbol{\mathcal{F}}_i \otimes \boldsymbol{\nabla} \rho_i \right) \cdot \mathbf{v} \\ & + \left(\sum_{i=1}^{N} \rho_i \boldsymbol{\mathcal{F}}_i \right) \boldsymbol{\nabla} \cdot \mathbf{v} - \underline{\underline{\boldsymbol{\tau}}}^d \cdot \mathbf{v} + \boldsymbol{q} \Bigg] + \rho \boldsymbol{g} \cdot \mathbf{v} \end{aligned} \tag{5.120c}$$

5.3.3.2 Cahn-Hilliard type volumetric free energy

A classic and general formula for the additional volumetric free energy F_1 is the natural extension of the formula Eq. (5.96) to mixtures, written:

$$F_1 = \frac{1}{2} \sum_{i,j=1}^{N} \lambda_{ij}(T)\, \boldsymbol{\nabla} \rho_i \boldsymbol{\nabla} \rho_j \tag{5.121}$$

where λ_{ij} is the crossed capillary coefficient between the species i and j. The evaluation of such crossed-coefficients is still under investigation. Like the capillary coefficient of a pure fluid λ, they can be obtained using kinetic theory applied in region submitted to species density gradients, see Pismen (2001) and Rowlinson and Widom (1982). However, in spite of its accuracy, this procedure can not be contemplated in the prospect of macroscopic flows simulations.
Given the lack of a proper expression for these coefficients, most studies rely on van der Waals mixing rules which state that $\lambda_{ij} = (1 - k_{ij}) \sqrt{\lambda_i \lambda_j}$ where λ_i, λ_j are the capillary coefficients of the pure species i and j (calculated by the methods given in Sec. 5.4.3) and k_{ij} is an influence parameter, usually set to 0 for the lack of a legitimate method to evaluate it correctly.

Eq. (5.121) can be further simplified by assuming that all the capillary coefficients of the pure species are equal, i.e. $\lambda_1 = ... = \lambda_N = \lambda$. Alternatively, the assumption more commonly made is that only one species will have an overall impact on the interface behavior, usually a species which is the only one that can be found in a liquid phase. For such case, the other species densities and density gradients are not accounted for, meaning $\lambda_1 = \lambda, \lambda_{i \neq 1} = 0$ and in the liquid phase $\rho \approx \rho_1$. Either way, it leads to a simplified set of equations, in particular with the second alternative for which the capillary tensor, the thermodynamic variables and the momentum/energy equations fall back to their expressions given in Eqs. (5.96) to (5.110).
This overall set of equations has been for instance used in Gaillard (2015) to study stretched laminar O_2/H_2 flamelets in subcritical and supercritical conditions, in a low Mach configuration. It also has been used to study the equilibrium and stability limits of pure oxygen interfaces and a liquid oxygen / gaseous oxygen-water binary mixture interface. All these results have then been used to calculate stretched non-premixed LO_x/GH_2 flames in subcritical and supercritical injection conditions.

5.4 Macroscopic characterization of a planar interface

In this last section, the emphasis is put on characterizing the interface, from a macroscopic point of view, both mechanically and thermodynamically. The objective is to grasp the key elements that drive the behavior of the interface which can or should be considered when going toward numerical simulations. A first step is to understand how the different systems of equations and the thermodynamic variables derived in the previous sections of the chapter allow the existence or not of a interface. In that prospect, in the subsection 5.4.1, the different solutions of said systems are investigated. Once the origin of an interface has be established, the macroscopic values of numerical interest, namely the width and the surface tension, are defined in subsection 5.4.2. Eventually, the impact of several parameters of the model on these two values are studied is subsection 5.4.3 so as to provide tools to manipulate them, as it will be required in Chap. 9.

5.4.1 Existence and type of solutions

5.4.1.1 Stable solutions of the equation system

In this subsection, we propose a recall of the developments of Rowlinson and Widom (1982) and Jamet (1998) that allows, in a simple way, to give a physical insight on the different type of profiles predicted by the Second Gradient theory, in particular their conditions of existence and their thermodynamic stability. To that effect, the system considered is that of a closed isothermal one-dimensional fluid domain between $-\frac{h}{2}$ and $\frac{h}{2}$ (the extensive values like the mass m or the volumetric free energy F are implicitly considered to be given by unit of surface to remain consistent). In the framework of the Second Gradient, the stable density profile is the one who minimizes the total free energy $\mathcal{F}$, given i Eq. (5.122), in the domain.

$$\mathcal{F} = \int_{-\frac{h}{2}}^{\frac{h}{2}} F(\rho)\, dx = \int_{-\frac{h}{2}}^{\frac{h}{2}} \left[F_0(\rho) + \frac{\lambda}{2} \left(\frac{d\rho}{dx} \right)^2 \right] dx \tag{5.122}$$

A density profile in the domain implicitly defines a function $\rho'(\rho)$ with:

$$\frac{d\rho}{dx}(x) = \rho'(x) \;\hat{=}\; \rho'(\rho) = \Psi(\rho) \tag{5.123}$$

It has to be noted that Eq. (5.123) does not define a unique profile but a spectrum of different profiles each with defined specificities. For such profiles, a stable phase $\varphi \in (l, v)$ will be characterized by a stable density ρ_φ in the bulk phases, meaning that:

$$\frac{d\rho}{dx}(\rho_\varphi) = 0 \tag{5.124a}$$

$$\frac{d^2\rho}{dx^2}(\rho_\varphi) = 0 \tag{5.124b}$$

As done by in Jamet (1998), we introduce the the function W_{ρ_i} which, for a fixed density ρ_i, is defined as the distance between the curve of $F_0(\rho)$ and its tangent to the point ρ_i. Noticing

that $(\partial F_0/\partial\rho)_T = \mu_0$, its expression is given by Eq. (5.125) and an example of such a function is shown in Fig. 5.3 for $\rho_i = \rho_v$.

$$W_{\rho_i}(\rho) \hat{=} F_0(\rho) - [F_0(\rho_i) + \mu_0(\rho_i)(\rho - \rho_i)] \tag{5.125}$$

It also implies that:

$$\frac{dW_{\rho_i}}{d\rho}(\rho) = \frac{dF}{d\rho}(\rho) - \mu_0(\rho_i) = \mu_0(\rho) - \mu_0(\rho_i) \tag{5.126}$$

With that, the free energy in the domain can be written:

$$\mathcal{F} = \int_{-\frac{h}{2}}^{\frac{h}{2}} \left[W_{\rho_i} + F_0(\rho_i) + \mu_0(\rho_i)(\rho - \rho_i) + \frac{\lambda}{2}\left(\frac{d\rho}{dx}\right)^2 \right] dx \tag{5.127}$$

The system is assumed to be characterized by at least one stable phase φ_1 at $x = x_1$. This phase is associated to an uniform density ρ_1, therefore the profile satisfies:

$$\frac{\partial\rho}{\partial x}(x_1) = 0 \tag{5.128a}$$

$$\frac{\partial^2\rho}{\partial x^2}(x_1) = 0 \tag{5.128b}$$

The system is also characterized by a mean density ρ_m so that the fixed mass m satisfies:

$$m = h\rho_m = \int_{-\frac{h}{2}}^{\frac{h}{2}} \rho\, dx \tag{5.129}$$

Eq. (5.127) can therefore be rewritten by formally choosing $\rho_i = \rho_1$, which lends:

$$\mathcal{F} = \underbrace{h\left[F_0(\rho_1) + \mu_0(\rho_1)(\rho_m - \rho_1)\right]}_{\mathcal{F}_m(\rho_1)} + \int_{-\frac{h}{2}}^{\frac{h}{2}} \left[W_{\rho_1}(\rho) + \frac{\lambda}{2}\left(\frac{d\rho}{dx}\right)^2 \right] dx \tag{5.130}$$

where $\mathcal{F}_m(\rho_1) = h\left[F_0(\rho_1) + \mu_0(\rho_1)(\rho_m - \rho_1)\right]$ is a mean free energy accounting for the hypothesis that the phase φ_1 exists in the domain. It ensues that minimizing the integral in Eq. (5.122) under this assumption amounts to minimizing the integral in Eq. (5.130). This minimization problem can be turned into a differential equation problem thanks to App. A.3, in particular applying the formula of Eq. (A.48) (since the integrand in Eq. (5.122) does not formally depends on the space variable x), the differential problem becomes:

$$W_{\rho_1}(\rho) - \frac{\lambda}{2}\left(\frac{d\rho}{dx}\right)^2 = \text{cste} \tag{5.131}$$

With the conditions satisfied by the stable phase φ_1, in particular Eqs. (5.128a) and (5.128b), one can deduce that the constant in Eq. (5.131) is equal to zero. The problem simplifies in:

$$W_{\rho_1}(\rho) = \frac{\lambda}{2}\left(\frac{d\rho}{dx}\right)^2 \tag{5.132}$$

Besides, by differentiating Eq. (5.132) with respect to x one, also gets the second equation:

$$\begin{aligned}\frac{dW_{\rho_1}}{dx} &= \frac{d}{dx}\left(\frac{\lambda}{2}\left(\frac{d\rho}{dx}\right)^2\right)\\ \frac{d\rho}{dx}\frac{dW_{\rho_1}}{d\rho} &= \lambda\frac{d\rho}{dx}\frac{d^2\rho}{dx^2}\\ \mu_0(\rho) - \mu_0(\rho_1) &= \lambda\frac{d^2\rho}{dx^2}\end{aligned} \tag{5.133}$$

Since for a stable phase φ, both the first and second spatial derivatives of ρ must be null, the stability conditions from Eqs. (5.124a) and (5.124b) can now be expressed as follows:

$$W_{\rho_1}(\rho_\varphi) = 0 \tag{5.134}$$

$$\mu_0(\rho_\varphi) - \mu_0(\rho_1) = 0 \tag{5.135}$$

In a first approach, the condition in Eq. (5.135) is rather classic and states that all the stable phases must have the same chemical potential. This rule is not affected by the capillary contributions. However, when linked to Eq. (5.126), it also implies that the slope of the tangent to W_{ρ_1} is null at ρ_φ. The condition Eq. (5.134) is more abstract but together with Eq. (5.135), they mean that both W_{ρ_1} and its derivative are null at ρ_φ. Using these conditions along with their geometrical interpretations, it is possible to determine the type of density profiles that are admissible in the domain. The nature of the eventual solutions is controlled by the choice of the reference stable phase φ_1.

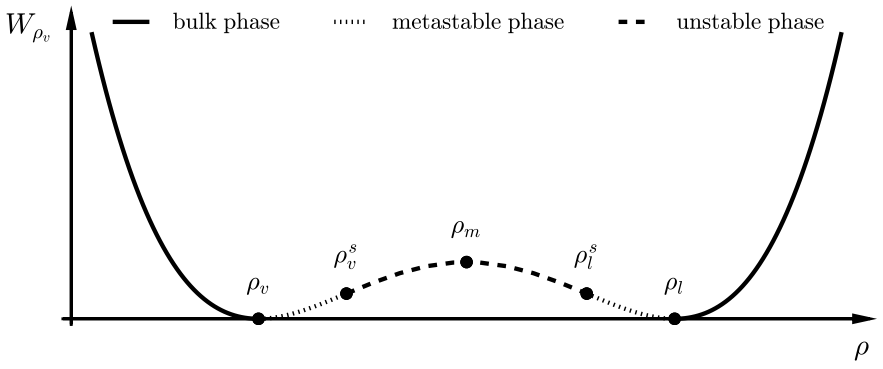

Figure 5.3: *Example of a profile W for $\rho_1 = \rho_v$. The figure shows remarkable densities: the saturation densities ρ_v and ρ_l; the metastable limit densities ρ_v^s and ρ_l^s*

A way to investigate these solutions is to consider the surface $\mathcal{S}$ of equation Eq. (5.136) as done in Jamet (1998):

$$\mathcal{S}(\rho, \rho') = W_{\rho_1}(\rho) - \frac{\lambda}{2}(\rho')^2 \tag{5.136}$$

From Eq. (5.132), the eventual intersections between $\mathcal{S}$ and the plane of equation $\mathcal{P}(\rho, \rho') = 0$ will give the density profiles obtainable in the domain. All the density profiles found in that fashion are not necessarily admissible as they must comply with the following rules:

– A profile must be physically admissible, meaning that a profile can not have simultaneously an increasing density with a negative density gradient and vice-versa.
– A profile must start and end at stable thermodynamic points (one of which is supposed to be φ_1) characterized by the conditions in Eqs. (5.134) and (5.135). Noticeably, such paths remain physically admissible. However, they cannot be spontaneously followed by the system without the action of an external perturbation.

The objective is, starting from different initial phases φ_1 placed differently in Fig. 5.3 to observe whether a second stable phase φ_2 is also be present in the domain. By symmetry of the thermodynamic considerations, only half of the profile W_{ρ_1} ($\rho \leqslant \rho_m$) shown in Fig. 5.3 is investigated explicitly.

5.4.1.2 First type: flat profile

Stable flat profile

If the starting phase φ_1 is in the stable vapor region ($\rho_1 < \rho_v$) or the stable liquid region ($\rho_1 > \rho_l$), Fig. 5.4 shows that the only admissible profile is an isolated point in the phase diagram (ρ, ρ'). Practically, this translates into a constant spatial profile as depicted in Fig. 5.5 at the density $\rho = \rho_1$, a pure bulk phase.

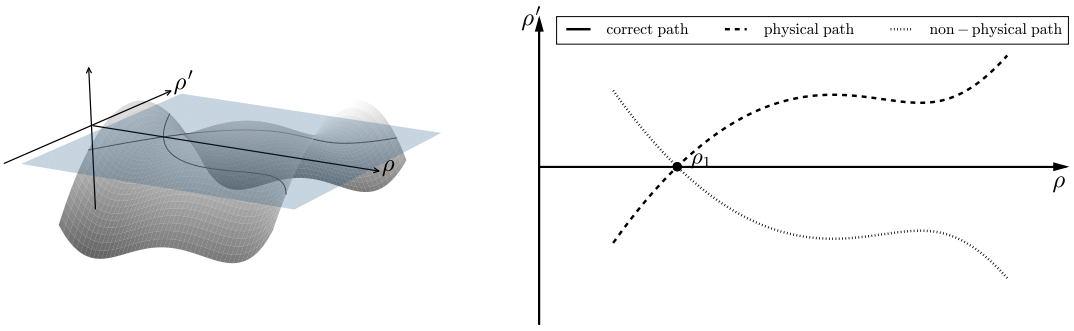

Figure 5.4: *Intersection in 3D (left) and 2D (right) between the surface $\mathcal{S}(\rho, \rho')$ in grey and the plane $\mathcal{P}(\rho, \rho') = 0$ in blue for $\rho_1 < \rho_v$*

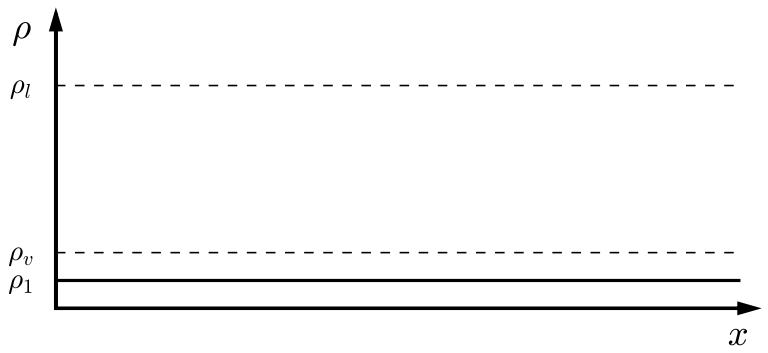

Figure 5.5: *Example of a flat profile in the liquid phase*

Unstable flat profile

Likewise, if the starting phase φ_1 is in the absolute unstable (or spinodal) region ($\rho_v^s \leqslant \rho_1 \leqslant \rho_l^s$), Fig. 5.6 shows that the only admissible profile is also an isolated point in the phase diagram (ρ, ρ'). Practically, this also translates into a constant spatial profile at the density ρ_1, this time a pure unstable phase, as shown in Fig. 5.7. However, oppositely to the previous case where the point φ_1 was on a physically admissible path in Fig. 5.4, here φ_1 is an isolated point not located on any physically admissible path.
This means, for the first case, that a small perturbation will not eventually modify the state of the system because the physically admissible path will lead it back to the stable phase φ_1. The system will return to a pure bulk phase with $\rho = \rho_1$. On the contrary, for this second case, a small perturbation will cause the system to jump to the closest stable phase (the vapor or the liquid depending on how ρ_1 compares to ρ_m and depending on the energetic cost) that is effectively located on physically admissible path and which is therefore much more stable. This allows to explain geometrically and quite simple why this state can indeed be qualified to be unstable.

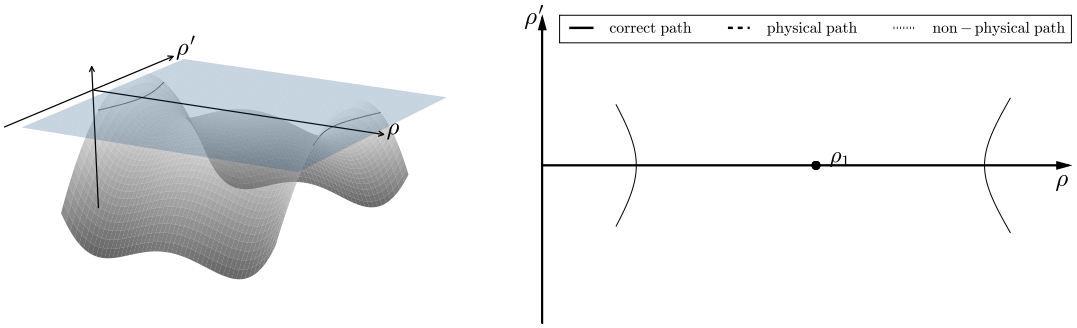

Figure 5.6: *Intersection in 3D (left) and 2D (right) between the surface* $\mathcal{S}(\rho, \rho')$ *in grey and the plane* $\mathcal{P}(\rho, \rho') = 0$ *in blue for* $\rho_v^s < \rho_1 < rho_l^s$

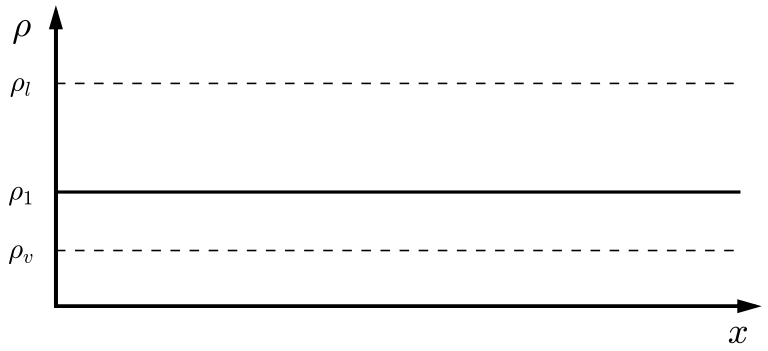

Figure 5.7: *Example of an unstable flat profile in the unstable densities region*

5.4.1.3 Second type: interface

If the starting phase φ_1 is precisely the vapor phase φ_v (or the liquid phase φ_l), meaning that $\rho_1 = \rho_v$ (or ρ_l), then in Fig. 5.8 appears a physically admissible path going from φ_1 to a second stable phase φ_2 with $\rho_1 \neq \rho_2$. By following this path that joins two stable points, one can extract the spatial density profile shown in Fig. 5.9 which corresponds the classic interface. Noticeably, from Fig. 5.3, the only phase φ_2 that can satisfy these conditions, knowing that $\varphi_1 = \varphi_v$, is the liquid phase φ_l at $\rho = \rho_l$ (and vice-versa).

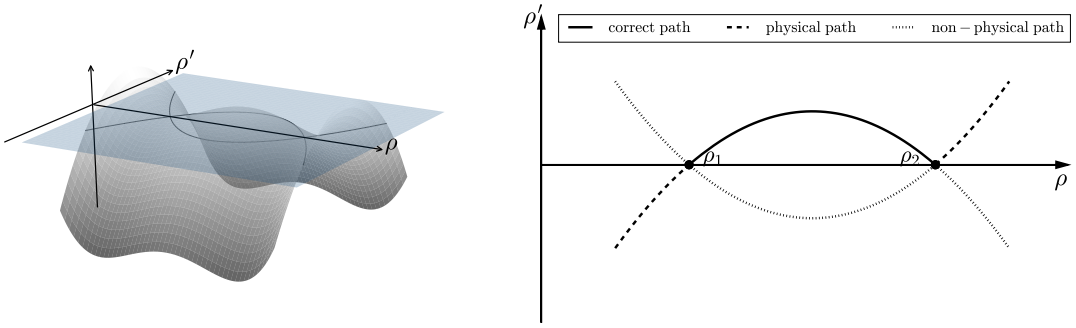

Figure 5.8: *Intersection in 3D (left) and 2D (right) between the surface* $\mathcal{S}(\rho, \rho')$ *in grey and the plane* $\mathcal{P}(\rho, \rho') = 0$ *in blue for* $\rho_1 = \rho_v$

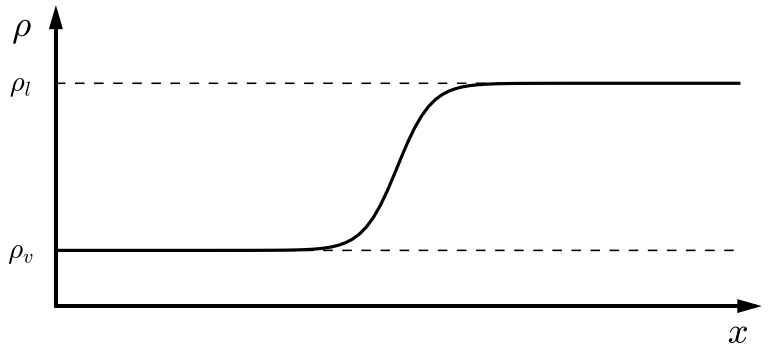

Figure 5.9: *Example of an interface profile between the vapor and liquid densities*

5.4.1.4 Third type: soliton

Lastly, if the starting phase φ_1 is in the metastable vapor region $\rho_v < \rho_1 < \rho_v^s$ (or $\rho_l^s < \rho_1 < \rho_l$), then Fig. 5.10 lets appear a physically admissible path circling back to φ_1 but going through a second phase φ_2 with $\rho'(\rho_2) = 0$. The associated spatial profile is shown in Fig. 5.11 and is referred to as a soliton. One should notice that the phase φ_2 does not satisfies the chemical potentials equality condition Eq. (5.135). It justifies why the path has to circle back to φ_1, impending the formation of an interface.

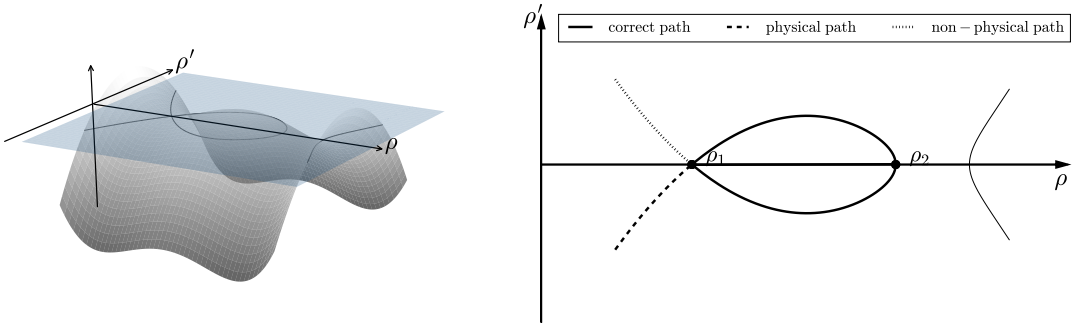

Figure 5.10: *Intersection in 3D (left) and 2D (right) between the surface $\mathcal{S}(\rho, \rho')$ in grey and the plane $\mathcal{P}(\rho, \rho') = 0$ in blue for $\rho_v < \rho_1 < \rho_v^s$*

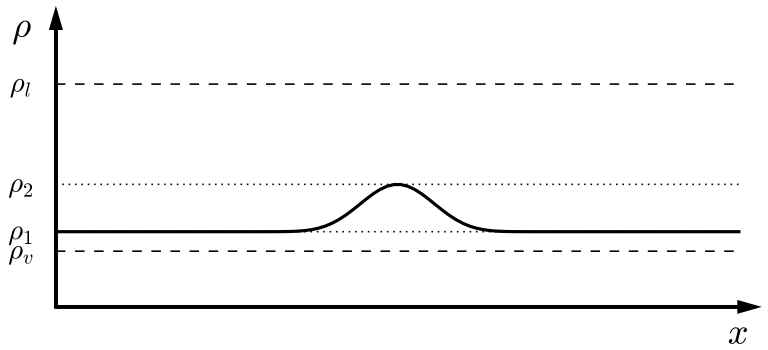

Figure 5.11: *Example of a soliton profile in the metastable densities region*

5.4.1.5 Conclusions on the different types of solution

In his PhD Thesis Jamet (1998), the author showed that in general, the total free energy of an unstable constant profile is more important than that of a vapor-liquid interface but lower than that of a soliton. This explains in part the tendency of subcritical systems to form interfaces and these results will be expended upon in Sec. 5.4.2. Regarding the solitons, although their thermodynamic admissibility has been proven, the conditions for their appearance remains unclear and very peculiar. Moreover, their visible precarious stability probably shortens their time of subsistence, further complicating their study. According to Jamet, solitons should essentially be observed in situations of strong mechanical unbalance, which is the framework within which they are usually studied.

5.4.2 Quantification of interface macroscopic values of interest

One important aspect of the Second Gradient theory is that the surface tension and the interface width are embedded in the model as it will be shown in the following section. These notions are only defined when considering an isothermal interface since they both directly depend on the temperature. To that effect, let us consider a one dimensional-interface at equilibrium shown in Fig. 5.12, at a reference temperature $T^{\mathrm{r}} < T_c$ with a reference capillary coefficient λ^{r}. For such an interface, the system of equations to solve merely reduces to the

momentum equation which simplifies in:

$$\frac{\partial P_0}{\partial x} = \lambda^{\mathrm{r}} \rho \frac{\partial^3 \rho}{\partial x^3} \tag{5.137}$$

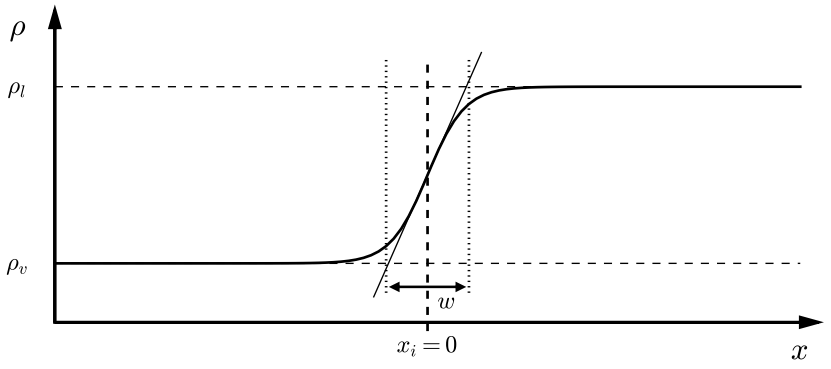

Figure 5.12: *Isothermal interface at equilibrium with the definition of its width w*

The density profile of this reference interface will be referred to by ρ^{r}. Even though this value still has to be defined, let x_i be the position of the interface, for convenience $x_i = 0$. $x_v < x_i$ is the limit position of the vapor phase and $x_l > x_v$ is the limit of the liquid phase, meaning that for $x \leqslant x_v$ one has $\rho^{\mathrm{r}}(x) = \rho_v$ and for $x \geqslant x_l$ one has $\rho^{\mathrm{r}}(x) = \rho_l$). This interface representation will be used as a reference in the ensuing developments.

5.4.2.1 Geometrical properties of the interface

Auto-similarity of the plane interface profiles

The pressure profile of the reference interface is given by the equation of state through ${P_0}^{\mathrm{r}} = P_0(\rho^{\mathrm{r}})$ (the temperature dependency is not mentioned explicitly here fore clarity, since this quantity has been fixed from the beginning). Let ϕ a strictly positive constant, the change of variable $X = x/\phi$ is introduced. Since ρ^{r} satisfies Eq. (5.137) one has:

$$\forall X,\ \frac{\partial {P_0}^{\mathrm{r}}}{\partial x}(X) = \lambda^{\mathrm{r}} \rho^{\mathrm{r}}(X) \frac{\partial^3 \rho^{\mathrm{r}}}{\partial x^3}(X) \tag{5.138}$$

Let ρ^{ϕ} be the density profile defined by:

$$\forall x,\ \rho^{\phi}(x) = \rho^{\mathrm{r}}(X = x/\phi) \tag{5.139}$$

The change of variable with X corresponds to a geometrical dilation if $\phi > 1$, to a compression otherwise. The corresponding pressure profile is given by $P_0^{\phi} = P_0\left(\rho^{\phi}(x)\right) = {P_0}^{\mathrm{r}}(X)$. From these definitions one gets the relations:

$$\frac{\partial P_0^{\phi}}{\partial x}(x) = \frac{1}{\phi} \frac{\partial {P_0}^{\mathrm{r}}}{\partial x}(X) \tag{5.140}$$

$$\frac{\partial^3 \rho^{\phi}}{\partial x^3}(x) = \frac{1}{\phi^3} \frac{\partial^3 \rho^{\mathrm{r}}}{\partial x^3}(X) \tag{5.141}$$

When injected into Eq. (5.138), the previous relations lead to:

$$\frac{\partial P^{\phi}}{\partial x}(x) = \phi^2 \lambda^{\mathrm{r}} \frac{\partial^3 \rho^{\phi}}{\partial x^3}(x) \tag{5.142}$$

The density profile ρ^{ϕ} appears as a solution of the non-linear differential equation Eq. (5.137) where the capillary coefficient has been formally multiplied by a factor ϕ^2. Granted the uniqueness of such a solution (see Benzoni-Gavage et al. (2005), Benzoni-Gavage et al. (2006), Benzoni-Gavage et al. (2007), Haspot (2008)), ρ^{ϕ} is the sole profile to satisfy these conditions. From that, the equivalence between geometrically compressing/dilating an interface and modifying the capillary coefficient is made apparent and is also quantified.

Interface width

The definition of the interface width is not unique. In this study we retain the following formula:

$$w = \frac{(\rho_l - \rho_v)}{\max |\boldsymbol{\nabla}\rho|} \tag{5.143}$$

The visual representation of this width definition is given in Fig. 5.12. This choice bears a practical justification since it relates directly to the resolution of the interface on the computational mesh. With this definition, increasing or decreasing the width directly amounts to changing how well resolved are the stiff gradients on a given mesh. Using this definition and the results from the previous paragraph, one gets:

$$\max \left| \boldsymbol{\nabla}\rho^{\phi} \right| = \frac{1}{\phi} \max |\boldsymbol{\nabla}\rho^{\mathrm{r}}| \tag{5.144}$$

If w^{r} is the width of the reference interface and w^{ϕ} the width of the interface represented by ρ^{ϕ}, Eq. (5.144) gives the result:

$$w^{\phi} = \phi w^{\mathrm{r}} \tag{5.145}$$

Equivalently, Eq. (5.142) and Eq. (5.145) tell that solving Eq. (5.137) while multiplying the capillary coefficient by ϕ^2 corresponds to thickening (or stiffening) the interface with a factor ϕ. Overall, the dependency of the interface width on the capillary coefficient is:

$$w \propto \sqrt{\lambda} \tag{5.146}$$

5.4.2.2 Thermodynamic properties of the interface

Definition of the surface tension

From Carey (2007), one gets the well know result that if no capillary forces are taken into account, a density profile as depicted in Fig. 5.12 is actually unstable. Any point of the profile will instantaneously evolves towards the closest stable thermodynamic state, it being the liquid or vapor phase. The resulting profile is a step with a discontinuity at $x_i = 0$ between the vapor and liquid densities ρ_v and ρ_l. This is the representation of the interface used in the sharp interface methods. This sharp density profile, referred to by $\bar{\rho}$ in the rest of the section, is defined by $\bar{\rho}(x) = \rho_v$ if $x \leqslant x_i$ and $\bar{\rho}(x) = \rho_l$ if $x > x_i$.
The existence of the reference profile Fig. 5.12 is permitted by the energetic unbalance brought by the capillary efforts. In Cahn and Hilliard (1958), the authors expressed a definition of the

surface tension σ based on the notion of excess values (see Edwards et al. (1991) for more details) with a visual example given in Fig. 5.13. This approach is merely a more elegant version of the definition introduced early on in van der Waals (1893) which leads to the same exact results. For any given density profile $\rho(x)$, the excess value $\mathrm{Ex}(\chi)$ of a thermodynamic variable χ is defined by:

$$\begin{aligned}\mathrm{Ex}(\chi)(\rho) &= \int_{x_v}^{x_i} [\chi(\rho) - \chi_0(\rho_v)]\, dx + \int_{x_v}^{x_l} [\chi(\rho) - \chi_0(\rho_l)]\, dx \\ &= \int_{x_v}^{x_l} [\chi(\rho) - \chi_0(\bar{\rho})]\, dx\end{aligned} \tag{5.147}$$

where $\chi(\rho)$ is the profile of χ for the chosen density profile with capillary forces accounted for and $\chi_0(\bar{\rho})$ is the profile of χ for the canonical sharp interface, i.e. as directly given by the native equation of state. In that respect, the position of the interface x_i is chosen so as to get no excess mass, i.e. $\mathrm{Ex}(\rho) = 0$.

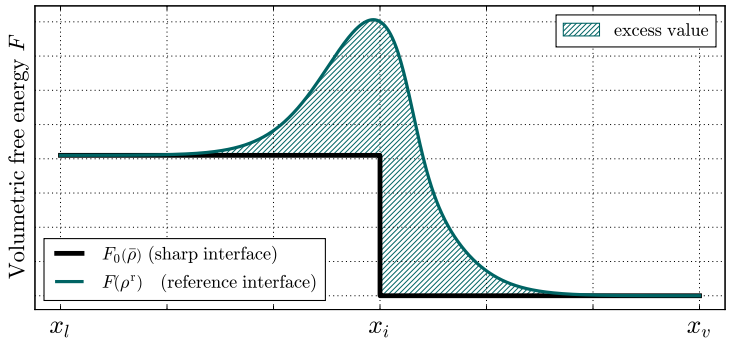

Figure 5.13: *Schematic representation of the excess volumetric free energy for the reference interface profile* ρ^{r}.

The equilibrium density profile is the one that minimizes the total free energy $\mathcal{F}$ in the domain. Since the total free energy $\bar{\mathcal{F}}$ associated to the sharp interface in the domain is a constant, the minimization of $\mathcal{F}$ is equivalent to that of $\mathcal{F} - \bar{\mathcal{F}}$. Using the notation where $\bar{F} = F_0(\bar{\rho})$, one can notice that for a profile $\rho(x)$:

$$\mathcal{F}(\rho) - \bar{\mathcal{F}} = \int_{x_v}^{x_l} \left[F(\rho) - \bar{F}\right] dx = \mathrm{Ex}(F)(\rho) \tag{5.148}$$

From Eq. (5.148), σ is defined as the extra free energy acquired by the interface with the capillary forces compared to the free energy of the discontinuous interface, as shown in Fig. 5.13. The reference density profile ρ^{r} is the one which minimizes $\mathrm{Ex}(F)$ and as such, allows to express the surface tension σ with Eq. (5.149). This definition ensures the uniqueness of the value for σ.

$$\sigma = \min_{\rho} \mathrm{Ex}(F) = \mathrm{Ex}(F)(\rho^{\mathrm{r}}) = \int_{x_v}^{x_l} \left[F^{\mathrm{r}} - \bar{F}\right] dx \tag{5.149}$$

Calculation of the surface tension for $F_1 = \lambda\left(\boldsymbol{\nabla}\rho\right)^2/2$

The integrand I of Eq. (5.148) can be expanded using the expression of F derived from Eq. (5.114):

$$I = F_0\left(\rho\right) + \frac{\lambda^{\mathrm{r}}}{2}\left(\frac{\partial\rho}{\partial x}\right)^2 - \bar{F} \tag{5.150}$$

The evaluation of σ is an integral minimization problem that can be transformed into a differential equation resolution as discussed in App. A.3.1.1 (where the correspondence between the notations is $f = \rho$ and $f' = \partial\rho/\partial x$). Since I has no explicit dependency on x, Eq. (A.48) can be used to get the partial derivative equation:

$$I - \left(\frac{\partial\rho}{\partial x}\right)\left(\frac{\partial I}{\partial\left(\frac{\partial\rho}{\partial x}\right)}\right)_{\rho} = a \tag{5.151}$$

were a is a constant to be determined. Moreover, $\lambda^{\mathrm{r}}/2\left(\partial\rho/\partial x\right)^2$ is the only term in I with a formal dependency on the density gradient $\partial\rho/\partial x$. It further simplifies the problem to give the relation in Eq. (5.152) that is satisfied by the equilibrium profile ρ^{r}.

$$F_0\left(\rho^{\mathrm{r}}\right) - \bar{F} - \frac{\lambda^{\mathrm{r}}}{2}\left(\frac{\partial\rho^{\mathrm{r}}}{\partial x}\right)^2 = a \tag{5.152}$$

In any of the bulk phases, the density gradient is equal to zero and both the canonical sharp profile and the reference equilibrium profile have the same values for the saturation densities. They result in the same values for the volumetric free energy in the bulk phases for both density profiles, ensuring that $a = 0$. This allows to write:

$$F_0\left(\rho^{\mathrm{r}}\right) - \bar{F} = \frac{\lambda^{\mathrm{r}}}{2}\frac{\partial\rho^{\mathrm{r}}{}^2}{\partial x} \tag{5.153}$$

This new relation can then be injected in Eq. (5.149) to finally give the expression of the surface tension:

$$\sigma = \int_{x_v}^{x_l} \lambda^{\mathrm{r}}\left(\frac{\partial\rho^{\mathrm{r}}}{\partial x}\right)^2 dx \tag{5.154}$$

Eq. (5.154) brings about an insightful physical interpretation regarding the capillary forces contribution in the interface. The minimization of the integral of I from Eq. (5.148) results from a balance between two terms to achieve equilibrium. The first term is the integral of $\Delta F_0 = F_0\left(\rho\right) - F_0\left(\bar{\rho}\right)$. It represents the actual energetic cost required to diffuse the interface from a sharp profile where no capillary forces apply. The second term is the integral of $\Delta F^{\mathrm{capi}} = \lambda/2\left(\partial\rho/\partial x\right)^2$. It stands as the energetic cost associated to the capillary forces themselves. To lower ΔF^{capi}, the interface will tend to diffuse itself to reduce its gradient but this will, in turn, increase the energy gap with the sharp profile ΔF_0 and vice versa. The equilibrium is achieved when the two terms are equal.
Additionally, by a variable substitution, Eq. (5.155) can be written in a geometry-independent fashion, which proves to be useful for some developments. The expression hence becomes:

$$\sigma = \int_{\rho_v}^{\rho_l} \lambda^{\mathrm{r}}\frac{\partial\rho^{\mathrm{r}}}{\partial x}\, d\rho \tag{5.155}$$

5.4.2.3 Mechanical, thermodynamic and geometrical points of view

Mechanical and thermodynamic approaches

Following Jamet et al. (1995), the expression in Eq. (5.154) can also be obtained using the momentum equation for a monodimensional planar interface. Indeed, the differential relation $d\mu_0 = -s_0\, dT + dP_0\,/\rho$ which simplifies in $d\mu_0 = dP_0\,/\rho$ for the isothermal case, allows to transform Eq. (5.137) into:

$$\left(\mu_0 - \mu^{\mathrm{sat}}\right)(x) = \lambda^{\mathrm{r}} \frac{\partial^2 \rho}{\partial x^2}(x) \tag{5.156}$$

where μ^{sat} is the value of the non-capillary chemical potential at saturation, this value being the same for the liquid and the vapor phases at equilibrium. Then, using the second differential relation $dF_0 = \mu_0\, d\rho$ which simplifies in $dF_0 = \mu_0\, d\rho$ for the isothermal case, one gets:

$$F_0(\rho) - \bar{F} = \int_{\rho_v}^{\rho_l} \left(\mu_0 - \mu^{\mathrm{sat}}\right)(x)\, d\varrho = \int_{\rho_v}^{\rho_l} \left(\mu_0 - \mu^{\mathrm{sat}}\right) d\varrho = \int_{\rho_v}^{\rho_l} \lambda^{\mathrm{r}} \frac{\partial^2 \varrho}{\partial x^2}\, d\varrho \tag{5.157}$$

The equivalence between Eq. (5.156) and Eq. (5.153) appears as the previous development finally results in Eq. (5.158), which is essentially equivalent to Eq. (5.153).

$$F_0(\rho) - \bar{F} = \int_{\rho_v}^{\rho} \lambda^{\mathrm{r}} \frac{\partial^2 \varrho}{\partial x^2} \frac{\partial \varrho}{\partial x}\, dx = \frac{\lambda^{\mathrm{r}}}{2} \left(\frac{\partial \rho}{\partial x}\right)^2 \tag{5.158}$$

As is has just been demonstrated, the isothermal hypothesis allows to retrieve this result in two different ways, intimately related. From Eq. (5.156) and Eq. (5.153), it results that a unique interface profile achieves thermo-mechanical equilibrium for a chosen temperature and a chosen capillary coefficient. The density profile induced by these two choices, in turn, defines a unique value for the surface tension σ and for the interface width w. These two values are therefore functions uniquely of the temperature at equilibrium (and the capillary coefficient).

Thermodynamics-based definition of σ

This link between Eq. (5.156) and Eq. (5.153) is further developed by the following derivations, first by introducing the variable Υ defined by:

$$\Upsilon(\rho) = 2 \int_{\rho_v}^{\rho} \left(\mu_0 - \mu^{\mathrm{sat}}\right)(\varrho)\, d\varrho \tag{5.159}$$

where ϱ is the density variable used for the integration. Secondly, the development continues by multiplying Eq. (5.156) by $\partial\rho/\partial x$ and integrating it one time to get:

$$2\left(\mu_0 - \mu^{\mathrm{sat}}\right) \frac{\partial \rho}{\partial x} = \lambda^{\mathrm{r}} \frac{\partial}{\partial x} \left(\left(\frac{\partial \rho}{\partial x}\right)^2 \right) \tag{5.160}$$

Using $\varkappa$ as the spatial variable for the integration, one can then write:

$$\int_{x_v}^{x} \frac{\partial}{\partial \varkappa} \left(\lambda^{\mathrm{r}} \left(\frac{\partial \varrho}{\partial \varkappa}\right)^2 \right)(\varkappa)\, d\varkappa = 2 \int_{x_v}^{x} \left(\mu_0 - \mu^{\mathrm{sat}}\right)(\varkappa) \frac{\partial \varrho}{\partial \varkappa}\, d\varkappa \tag{5.161}$$

and by substituting the spatial variable $\varkappa$ with the density variable ϱ, it comes:

$$\int_{x_v}^{x} \left(\mu^{\text{EoS}} - \mu^{\text{sat}}\right)(\varkappa) \frac{\partial \varrho}{\partial \varkappa} d\varkappa = \int_{\rho_v}^{\rho} \left(\mu^{\text{EoS}} - \mu^{\text{sat}}\right)(\varrho) d\varrho \tag{5.162}$$

to eventually get:

$$\lambda^{\text{r}} \left(\frac{\partial \varrho}{\partial \varkappa}\right)^2 (x) = \Upsilon\left(\rho(x)\right) \tag{5.163}$$

The surface tension can therefore be linked to the chemical potential gap with:

$$\sigma = \int_{x_v}^{x_l} \Upsilon(\rho) dx \tag{5.164}$$

The important thing to notice here is that Υ has been expressed as an integral that has formally no dependency on the geometry of the interface. Indeed, the saturation densities ρ_v and ρ_l depend only on the temperature. Formally, Υ depends only on the intrinsic thermodynamic representation of the fluid through the expression of the (thermodynamic) profile $\mu_0(\rho)$. In particular, a purely geometrical modification of the interface that does no modify its thermodynamic description will not impact Υ. However, to access σ, a second integral has to be calculated. The integration variable being x, the results will be impacted by a geometrical deformation of the interface.
From Eq. (5.164), it appears that the value of σ results from two main contributions. The first is the energetic behavior of the interface through its ability to store capillary energy. This contribution is driven purely by the thermodynamics through $\mu^{\text{EoS}} - \mu^{\text{sat}}$. The second is the inherent geometry of the interface which is controlled by the interfacial constraints through, for instance, the value of λ. The impact of these two components will have to carefully be accounted for when trying to modify key aspects of the interface, as it will be done in Part III of this manuscript.

5.4.2.4 Impact of λ on the surface tension and the interface width

The impact of the capillary coefficient on the interface width has already been explored Eq. (5.146). The same analysis can be carried out for the surface tension using the same methodology (multiplying the capillary coefficient λ^{r} by a coefficient ϕ^2). To express the surface tension σ_ϕ associated with the new density profile ρ^ϕ, one can start by transforming Eq. (5.154) (for an arbitrary λ), substituting the variables x and ρ. Similarly to Eq. (5.159), the resulting integral has limits that do not depend on the geometry of the interface.

$$\sigma = \int_{x_v}^{x_l} \lambda \left(\frac{\partial \rho}{\partial x}\right)^2 dx = \int_{x_v}^{x_l} \lambda \frac{\partial \rho}{\partial x} \frac{\partial \rho}{\partial x} dx = \int_{\rho_v}^{\rho_l} \lambda \frac{\partial \rho}{\partial x} d\rho \tag{5.165}$$

With this new expression, the new surface tension σ^ϕ can be compared to the surface tension σ^{r} of the reference profile, it comes that:

$$\sigma^\phi = \int_{\rho_v}^{\rho_l} \lambda_\phi \frac{\partial \rho^\phi}{\partial x} d\rho = \int_{\rho_v}^{\rho_l} \phi^2 \lambda^{\text{r}} \frac{1}{\phi} \frac{\partial \rho^{\text{r}}}{\partial x} d\rho = \phi \int_{\rho_v}^{\rho_l} \lambda^{\text{r}} \frac{\partial \rho^{\text{r}}}{\partial x} = \phi \sigma^{\text{r}} \tag{5.166}$$

Finally, the dependency of σ on λ is similar to that of w and is given by:

$$\sigma \propto \sqrt{\lambda} \tag{5.167}$$

The correlations (5.146) and (5.167) have been retrieved analytically near the critical point by Jamet (1998), numerically observed by Gaillard (2015) and by ourselves as shown in Fig. 5.14.

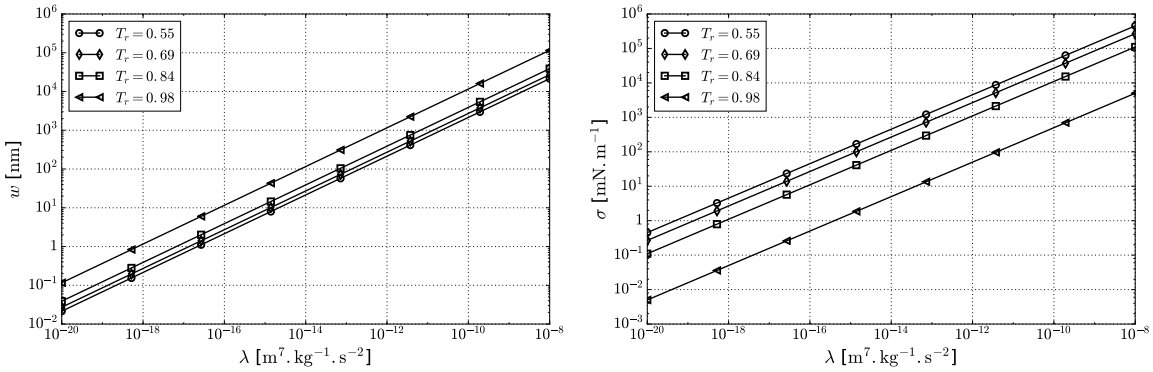

Figure 5.14: *Evolution of the interface thickness w and surface tension σ with the capillary coefficient λ for oxygen O_2 at different reduced temperature T/T_c. Results in logarithmic scale*

5.4.3 Evaluation of the capillary coefficient λ

The impact of the capillary coefficient λ on both the interface width and surface tension has been demonstrated. From a more general point of view, the contribution of λ to the interface behavior is clearly apparent. The ability to properly determine its value is primordial to achieve correct simulations. Granted that σ and w are functions of the temperature (result that is widely confirmed experimentally), λ should, at least at the first order, depend solely on the temperature as well.

5.4.3.1 Evaluation from molecular theory

By relying on the molecular theory, one can obtain a precise expression of the capillary coefficient. For instance, thanks to the developments from Rocard (1967) recalled in Sec. 5.1.1, the expression of λ can be read directly using Eq. (5.7a), it is written:

$$\lambda = \frac{a\zeta r_0^2}{20M^2} \tag{5.168}$$

The molar mass M and the penetrability radius r_0 solely depend on the fluid nature. Coefficients a and ζ given by Eqs. (5.5) and (5.6) depend on the microscopic distribution of the molecular central forces of interaction which, at the first order, depends on the fluid temperature.

Another formula based on molecular theory has been derived in Yang et al. (1976), based on the work from Lovett et al. (1973). It involves the direct correlation function C introduced in Ornstein and Zernike (1914) and is written:

$$\lambda = k_B T \frac{\mathcal{N}_A^2}{6M} \int C(x)\, x^2\, dx \tag{5.169}$$

where k_B is the Boltzmann constant. For very refined chemical computations, formulas as precise as Eqs. (5.168) or (5.169) are required. However, in the context of CFD simulations they are of a limited practical use. Firstly, their different constituents are difficult to access or of a great computational cost. Secondly, the surface tension values predicted by the Second Gradient theory using these formulas tend to significantly differ from experimental data unless extremely precise equations of state are used. Likewise, the computational cost of such equations render their use on great scale simulations hardly conceivable. Despite their theoretical interest, Eqs. (5.168) and (5.169) have not been retained in our study for the previously mentioned reasons.

5.4.3.2 Evaluation from the surface tension

Simpler analytical correlations can be found for λ by exploiting experimental measurements or analytical developments. Indeed, using, Eq. (5.154) backwards at a given temperature, the value of the capillary coefficient can be iterated upon until the surface tension predicted by the Second Gradient theory matches a reference value. This provides the great advantage to dilute the inaccuracies of the equation of state directly into the value of λ.
A dense literature exists around the derivation of such correlations and a non-exhaustive list can be found in Lin et al. (2007). In the same study, the authors propose a more generic correlation which, in particular, achieve better results for strongly polar fluids. They formulated correlations for the Volume Translated Peng-Robinson and the Volume Translated Soave-Redlich-Kwong equations of state. They combined the later equations with precise experimental surface tension data as a reference. For the Volume Translated Soave-Redlich-Kwong equation, the capillary coefficient is given by:

$$\lambda\left(T\right) = a\left(T\right)\left(\frac{bM}{\mathcal{N}_A}\right)^{2/3} \exp\left[k_0 + k_1 \ln\left(1 - T_r\right) - k_2 \left(\ln\left(1 - T_r\right)\right)^2\right] \tag{5.170}$$

where a and b are the specific cohesion pressure and the specific excluded volume from the equation of state and $T_r = T/T_c$ is the reduced temperature. Coefficients k_0, k_1 and k_2 are given by:

$$k_0 = -3.471 + 4.927 Z_c + 13.085 Z_c^2 - 2.067\omega + 1.891\omega^2 - 4.600 \cdot 10^{-6}\vartheta_r^2 \tag{5.171a}$$

$$k_1 = -1.690 + 2.311 Z_c + 5.644 Z_c^2 - 1.027\omega + 1.424\omega^2 - 1.403 \cdot 10^{-6}\vartheta_r^2 \tag{5.171b}$$

$$k_2 = -0.318 + 0.299 Z_c + 1.710 Z_c^2 - 0.174\omega + 0.157\omega^2 + 0.077 \cdot 10^{-6}\vartheta_r^2 \tag{5.171c}$$

where the critical compressibility factor is given by $Z_c = P_c/(\rho_c r T_c)$, ω is the acentric factor and the reduced dipole moment is given by $\vartheta_r = \vartheta/\left(1.01325 T_c^2\right)$ where the dipole moment ϑ is expressed in Debye. This formula has been successfully applied in Dahms (2015) and Gaillard (2015) among others.

In order to simplify even more the formula, we derived a correlation of our own using the analytical formula from Curl and Pitzer (1958) given by Eq. (5.172) to evaluate the surface tension.

$$\sigma\left(T\right) = \sigma_0 \left(1 - T_r\right)^{11/9} \tag{5.172}$$

with:

$$\sigma_0 = T_c^{1/3} P_c^{2/3} \frac{10^{-19/3}\left(1.86 + 1.18\omega\right)}{19.05}\left(\frac{3.75 + 0.91\omega}{0.291 - 0.08\omega}\right)^{2/3} \tag{5.173}$$

We were able to extract a simple correlation also based on the corresponding state principle, producing the formula:

$$\lambda(T) = c_1 (1 - T_r)^{0.55} + c_2 (1 - T_r)^{-0.55} \tag{5.174}$$

where c_1 and c_2 are two constants depending on the considered fluid. It has been validated for a wide range of simple fluids, some values of constants c_1 and c_2 are given in Tab. 5.1. Both Lin's and our correlation are compared Fig. 5.15.

Fluid	c_1 $(\times 10^9)$	c_2 $(\times 10^9)$
H_2	30.434	7.4985
N_2	0.75759	0.69235
O_2	0.52449	0.45867
F_2	0.29025	0.27136
He	1.5538	-0.26531
Ne	0.14707	0.10511
Ar	0.34344	0.27835
Kr	0.15165	0.12305
Xe	0.13297	0.10946
CH_4	4.3025	3.6256
C_2H_6	3.5776	3.8584
C_3H_8	3.3339	4.0523
C_4H_{10}	3.2404	4.3524

Table 5.1: *Coefficients c_1 and c_2 used for the calculation of the capillary coefficient using Eq. (5.174).*

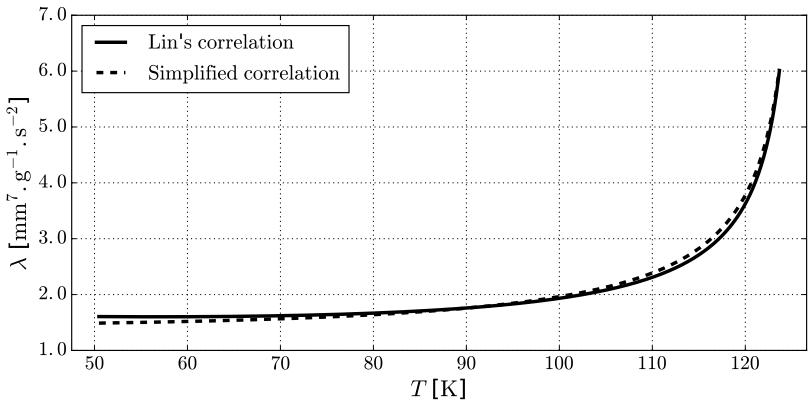

Figure 5.15: *Comparison of Lin's and our simplified correlations for the calculation of the capillary coefficient λ of nitrogen N_2 with the temperature T*

From Fig. 5.15, it appears that both Lin's correlation and our own correlations give the same trend, notwithstanding the difference of equation of state and reference surface tension used to extract them. Over a wide range of temperature, the hypothesis of a constant λ is numerically acceptable. For both correlations, the capillary coefficient diverges in the vicinity

of the critical temperature (126.192 K for nitrogen). For these temperatures, the constant λ hypothesis does not hold anymore. This divergence is a direct consequence of evaluating λ by fitting the surface tension with cubic EoSs.
Indeed, as the temperature increases, the interface widens and thus the density gradient diminished at rate that is more important than the rate at which the surface tension decreases. By virtue of Eq. (5.155), λ has to compensate for this unbalance and thus soars near the critical temperature where it can no longer be considered to be constant. Ans given that the interface eventually becomes infinitely wide once the regime turns to supercritical, the capillary coefficient is "compelled" to diverge.
By reverting to the fundamental definition Eq. (5.168), the use of kinetic theory of gases allows to show that the actual value of λ converges towards a constant as the temperature increases, as shown in McCoy et al. (1981) for the Lennard-Jones potential. Moreover, the energetic considerations made by the authors in Cahn and Hilliard (1958) have no reasons to be discarded above critical conditions meaning that the contributions from λ should still be considered in said conditions despite no actual interface being present. However, as already mentioned in Sec. 5.4.3.1 and as explained in Lin et al. (2007), the surface tension values obtained evaluating λ with expressions from the kinetic theory systematically lead to strong disparities with experimental data.
However, since our primary concern is to ensure that the interface is wide enough to be captured on the simulation mesh, the simplified correlation shown in Fig. 5.15 can still be a useful simplification. The issue caused by the choice of simplified correlation such as Lin's or our own is rather physical than a numerical and as such, of a lesser degree of importance. In particular, when the temperature rises, the interface widens, even for a constant capillary coefficient. In that regards, the hypothesis of a constant capillary coefficient is an acceptable and useful simplification. Moreover, it allows a smooth transition between the subcritical and supercritical regimes without loss of generality. Therefore, if not explicitly mentioned otherwise, λ will be considered as independent of the temperature in the rest of the study.

Conclusions

In this chapter, we have thoroughly described the founding principles behind the Second Gradient theory. Using the Virtual Power Principle, we derived the equations of motion for a capillary fluid. These equations have been particularized using the first and second principles of thermodynamics to express the different new fluxes involved. The mechanical description of the interface has been completed with the derivation of the new thermodynamics associated with the capillary terms.

These sets of equations have been derived under well defined and physically sound hypotheses without loosing the essence behind the impact of capillary phenomena on a fluid behavior in order to achieve a fully consistent model. Additionally, key macroscopic values of the interface, namely the width and the surface tension, have been defined with the same precaution. The impact of the parameters of the model on these two values has been explored and quantified to some extent.

Moreover, apart from dedicated numerical schemes, the system of equations should not require

any special additional treatment and by solving them it is, in principle, possible to perform simulations where multiple phases and interfaces can coexist without the need to treat each of these elements separately. In terms of numerical simulation, the interfaces do not need to be tracked or reconstructed and any interaction between the different phases, in particular mass exchange and phase change, will be intrinsically treated by the physical model.

Chap. 7, the mechanical and thermodynamic equations of the theory are implemented in the real gas solver AVBP presented Chap. 6, to numerically validate the model. As it will be shown in Part III, an additional effort will be required to contemplate real scale simulations as the interface widths predicted by the native model fall way bellow the computational mesh resolutions affordable in practice. To that effect, the behavior of the interface will have to be modified and the design of these alterations will strongly rely on the theoretical developments detailed in this chapter.

Part II

Implementation of the Second Gradient model in the solver AVBP

Chapter 6

Presentation of the AVBP-RG solver

The main purpose of this chapter is to provide an insight on the numerical tools that have been used to produce the numerical results presented in this work. The simulations have been carried out using the compressible AVBP solver developed jointly by CERFACS and IFPEN, in particular the version dedicated to the simulation of real gas flows, AVBP-RG, developed in collaboration with EM2C, CNRS. Taking advantage and building around this already well tested and qualified solver was a key point for this PhD work.
This chapter should allow the reader to better grasp the modifications induced in the code by the Second Gradient and the inherent difficulties associated to said modifications, as detailed in Chap. 7 and Chap. 8 but more importantly by the interface thickening method presented in Chap. 9.

The first section 6.1 provides a broad description of the solver and its main components as well as an insight into the driving philosophies behind its development. In particular, the specifics of the *Cell-Vertex* framework, which is the approach favored in AVBP, and its application to Navier-Stokes equations are specifically explored.

In the second section 6.2, the principal advection and diffusion schemes implemented in AVBP are described. A particular attention is given to the latter diffusion schemes as they present a strategic aspect for the implementation of the Second Gradient model as it is expanded upon in Sec. 7.1.

Eventually, the third section is dedicated to the boundary conditions in AVBP. Their implementation through the characteristics approach is briefly described to better grasp the difficulty of its adaptation to the Second Gradient model as explained in Secs. 7.2.1 and 7.2.2.

6.1 Main features of the AVBP solver

6.1.1 Overwiew of the solver

6.1.1.1 Brief history of AVBP

AVBP is a code created in 1993 and now jointly owned by CERFACS and IFPEN who ensure its development and maintenance. Its main purpose is to solve compressible Navier-Stokes equations and it has been built from the start so as to support unstructured and hybrid meshes ensuring its flexibility and usability for simulations on complex geometries and industrial configurations. Its numerical core has been implemented by Schönfeld and Rudgyard, see Schönfeld and Rudgyard (1999), with a special care taken from the beginning to ensure its ability to run massively parallels simulations on supercomputers, see Gourdain, Gicquel, Montagnac, Vermorel, Gazaix, Staffelbach, Garcia, Boussuge, and Poinsot (2009), Gourdain, Gicquel, Staffelbach, Vermorel, Duchaine, Boussuge, and Poinsot (2009). It also benefits from multiple inputs coming from an ever-growing community in both academic and industrial spheres. Though capable of Direct Numerical Simulations, efforts have been made to increase its Large Eddy Simulation capabilities, see Lamarque (2007). Its thermodynamics have been extended to support simulations with real gas, see Schmitt (2009), and models to deal with two-phase flows have incorporated, see Boileau (2007).

6.1.1.2 Numerical aspects

AVBP functioning relies on multiple key numerical methods of which roles are listed bellow:

1. A numerical scheme to treat the convective part of the Navier-Stoke equations.The different type of numerical methods available in AVBP for the convection will be explored in the following and their interaction with the Second Gradient model will be explored in Chap. 7
2. A numerical scheme to treat the diffusive terms (viscous and thermal fluxes) of the Navier-Stokes equations. This aspect of the code has not been significantly modified during our work and it will not be explored in this document but details can be found in Lamarque (2007)
3. A numerical scheme to treat with source terms, most of the time chemical ones (except, for instance, in two-phase flows) and independent of the thermodynamics. Likewise, this aspect is not treated in this manuscript but is detailed in Lamarque (2007)
4. A proper treatment of the boundary conditions to adequately impose values at the inlets, outlet and walls of the computational domain. Multiple paradigms are available in AVBP but the formulation used is generally based on the Euler/Navier-Stokes characteristic decomposition from Poinsot and Lele (1992). Interactions between the boundary conditions and the Second Gradient will be explored in Chap. 7
5. A proper management of the parallelization to ensure scalability up to thousands of computational cores, not addressed here but explicated in Gourdain, Gicquel, Montagnac, Vermorel, Gazaix, Staffelbach, Garcia, Boussuge, and Poinsot (2009), Gourdain, Gicquel, Staffelbach, Vermorel, Duchaine, Boussuge, and Poinsot (2009)

6.1.1.3 Convective schemes in AVBP

At its core, the spatial discretization of the equations in AVBP is based on a Finite Volume approach which allows to solve the Euler/Navier-Stokes equations through an integration over the cells of the domain. A specific formulation of this integration allows to recover a framework that can be assimilated to Finite Element methods. The accessible types of cells are triangles and quadrilaterals in two dimensions, tetrahedrons, hexahedrons, pyramids and prisms in three dimensions. Different formulations of the Finite Volume approach exits, the main three are listed below and illustrated in Fig. 6.1

1. The *Cell-Centre* approach is the most classic where the nodes of the mesh are used to create the volumes of control trough which the fluxes are calculated using an averaging procedure over the edges of the cells. The variables are stored at the center of the cells and are updated at the same location. The precision of this method strongly depends on the quality of the mesh.
2. The *Vertex-Centre* approach resembles the *Cell-Centre* since the variables are still stored at the center of the cells. However, the volumes of control are created using the center of the cells and the dual mesh, where the variables are updated, instead of the nodes of the mesh. The variables are thus stored and updated at different locations. The fluxes are calculated in the same way as for the *Cell-Centre* approach and this method tends to suffer the same drawbacks.
3. The *Cell-Vertex* approach is in-between the two first formulations. The variables are stored at the mesh nodes but are updated at the center of the cells. The volumes of control are given by the nodal mesh as in the *Cell-Centre* formulation and fluxes are also obtained trough averaging over the cells egdes. This approach is independent of the type of cells used and is robust even for ill-conditioned cells, making it suitable for unstructured and hybrid meshes. This formulation has been selected for AVBP.

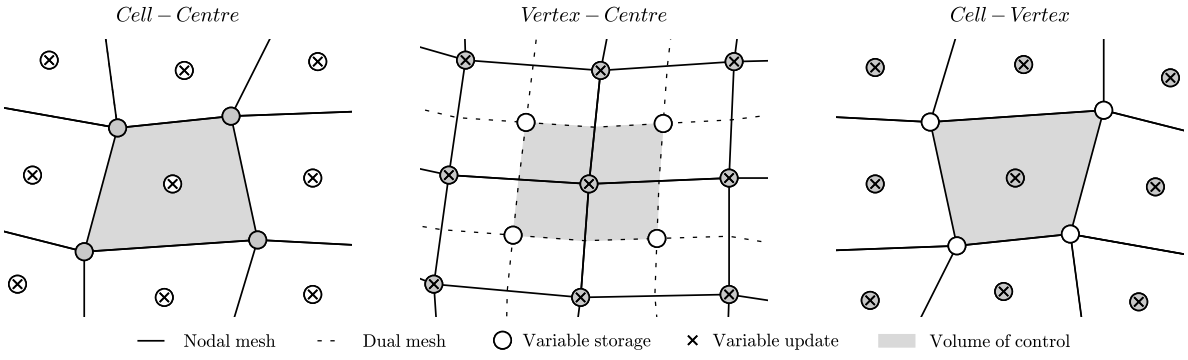

Figure 6.1: *Schematic representation of the meshes used for the three man formulations of Finite Volume methods*

6.1.2 Residual distribution in the *Cell-Vertex* formulation

In the following, the framework of the *Cell-Vertex* is further detailed. As a starting point, the non-reactive Euler/Navier-Stokes equations are considered (without capillary terms) and can

be written in the conservative form:

$$\frac{\partial \mathbf{U}}{\partial t} + \boldsymbol{\nabla} \cdot \underline{\underline{\mathbf{F}}} = 0 \tag{6.1}$$

where $\mathbf{U}$ is the vector of conservatives variables $\mathbf{U} = (\rho, \rho u, \rho v, \rho w, \rho e)^{\mathrm{T}}$ with ρ, u, v, w and e respectively the density, the x, y, z velocity component and the specific total energy . $\underline{\underline{\mathbf{F}}}$ is the associated stress tensor which can be split in two parts as shown in Eq. (6.2). The first part $\underline{\underline{\mathbf{F}}}^c$ is a pure convective tensor depending only on the components of $\boldsymbol{U}$ and the second $\underline{\underline{\mathbf{F}}}^d$ is a diffusive stress tensor depending on $\mathbf{U}$ but also on its spatial derivative $\boldsymbol{\nabla}\mathbf{U}$.

$$\underline{\underline{\mathbf{F}}} = \underline{\underline{\mathbf{F}}}^c(\mathbf{U}) + \underline{\underline{\mathbf{F}}}^d(\mathbf{U}, \boldsymbol{\nabla}\mathbf{U}) \tag{6.2}$$

The convective schemes of AVBP only treat the convective part of the fluxes, i.e. $\underline{\underline{\mathbf{F}}}^c$. As such, only this aspect of the numerical method will be expanded upon here. For more details regarding the treatment of the diffusive part, the reader can refer to the discussion in Sec. 6.2.3 or the more comprehensive description in Lamarque (2007).

Notations

In the rest of the subsection, the following notations will be used.

- The subscript $*_{\mathrm{C}}$ will always refer to a count over a number of cells, in particular N_{C} is the total number of cells in the computational domain Ω
- The subscript $*_{\mathrm{N}}$ will assume the same role for the nodes and N_{N} will be the total number of nodes in the domain
- The indexes e and k will be used exclusively to identify cells (or volumes of control) in the domain Ω. For $e \in \{1, ..., N_{\mathrm{C}}\}$, N^e_{N} is the total number of nodes delimiting the cell Ω_e (idem fo k)
- The indexes i and j will be used exclusively to identify nodes in the domain Ω and for $i \in \{1, ..., N_{\mathrm{N}}\}$, N^i_{C} is the total number of cells to which the node i belongs to (idem for j)
- The index e will be used preferentially to count cells over the whole domain whereas k will used preferentially to count cells affiliated to a given node
- Likewise, the index i will be used preferentially to count nodes over the whole domain whereas j will be used preferentially to counts node affiliated to a given cell

A simplified description of the *Cell-Vertex* procedure is given in Fig. 6.2. The nodes (where variables are stored) are used to evaluate the fluxes residuals in the volumes of control which are the cells of the primal mesh. Once the residuals have been evaluated for all the cells, they are redistributed to all the nodes to update the values of the variables.

More precisely, let Ω_e be a volume of control, represented in Fig. 6.3 as a triangle to simplify the explanations without loss of generality. The averaged residual $\boldsymbol{R}_{\Omega_e}$ of the convective flux over Ω_e is obtained through an integration of its divergence over the domain which can be turned into a surface integral thanks to Green's theorem:

$$\boldsymbol{R}_{\Omega_e} = \frac{1}{V_{\Omega_e}} \int_{\Omega_e} \boldsymbol{\nabla} \cdot \underline{\underline{\mathbf{F}}}^c \, d\mathcal{V} = \frac{1}{V_{\Omega_e}} \int_{\partial\Omega_e} \underline{\underline{\mathbf{F}}}^c \cdot \boldsymbol{n}_e \, d\mathcal{A} \tag{6.3}$$

where V_{Ω_e} is the surface(2D)/volume(3D) of the volume Ω_e, $\partial\Omega_e$ its boundary and $\boldsymbol{n}_e$ the associated normal vector.

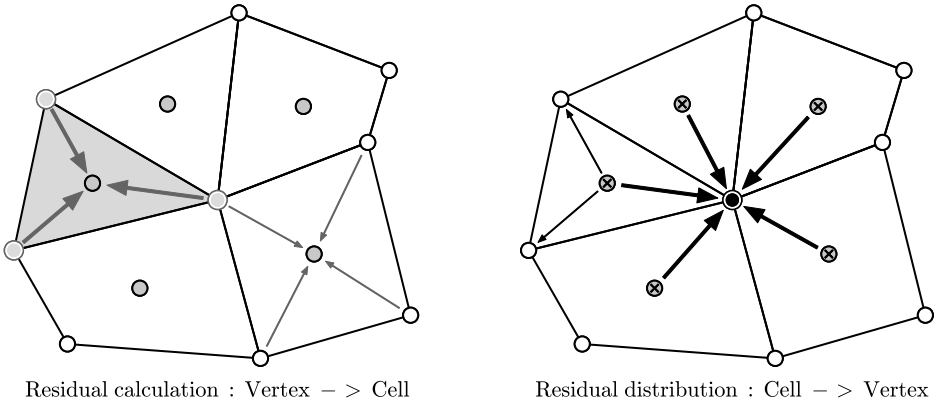

Figure 6.2: *Schematic representation of the Cell-Vertex procedure : the residuals are calculated "at the cells" and are then redistributed to the cells vertices*

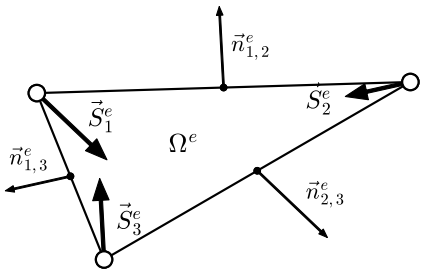

Figure 6.3: *Schematic representation of triangular volume of control (2D) with the faces (edges) normal $\boldsymbol{n}^e_{i,j}$ and the nodes normals $\boldsymbol{S}^e_j$*

To calculate the surface integral Eq. (6.3), the flux is assumed to vary linearly over the edges which gives the numerical residual:

$$\mathbf{R}_{\Omega_e} = \frac{1}{dV_{\Omega_e}} \sum_{j=1}^{N^e_{\mathrm{N}}} \underline{\underline{\mathbf{F}}}^c_j \cdot \boldsymbol{S}^e_j \tag{6.4}$$

d is the number of dimensions that are considered, $\underline{\underline{\mathbf{F}}}^c_j$ is a numerical approximation of the convective flux tensor at the node j and $\boldsymbol{S}^e_j$ the "normal" to the node j. Numerically, $\boldsymbol{S}^e_j$ is defined as the average of the normals to the element faces of Ω_e containing the node j, weighted by their length(2D)/surface(3D). It allows to condense the geometrical information initially contained by the edges of Ω_e to the nodes $m^e_{j\,j\in\{1,\dots,N^e_{\mathrm{N}}\}}$. The procedure of taking the information from the nodes to the cells, as done for the flux residuals, is recurrent in AVBP and referred to as *gather*. The consistency of the method and the linearity of the divergence

are ensured by Eqs. (6.5) and (6.6) respectively:

$$\sum_{j=1}^{N_{\mathrm{N}}^e} \boldsymbol{S}_j^e = \mathbf{0} \tag{6.5}$$

$$\frac{1}{d^2} \sum_{j=1}^{N_{\mathrm{N}}^e} \boldsymbol{x}_j \cdot \boldsymbol{S}_j^e = V_{\Omega_e} \tag{6.6}$$

where $\boldsymbol{x}_j = x_{j_1} \boldsymbol{e}_1 + x_{j_2} \boldsymbol{e}_2$ (in 2D) is the vectorial position of the node j of Ω_e.
In 3D cases, if the surface is a quadrilateral, it is first cut along a diagonal and the integration is made over the two subsequently created triangles. The final flux residual is the average of the residuals over the four triangles obtained by cutting successively along the two diagonals. Again, this is done to ensure the linearity of the calculated flux integral and consequently a satisfying precision even for meshes presenting strong irregularities.

Once the flux residuals have been calculated over all cells, they are distributed to the nodes in order to update the conservative variables vector $\mathbf{U}$. For a node i of the mesh, the spatially discretized scheme is written:

$$\frac{d\mathbf{U}_i}{dt} = -\frac{1}{V_i} \sum_{k=1}^{N_{\mathrm{C}}^i} V_{\Omega_k} \mathbf{D}_{\Omega_k}^i \cdot \mathbf{R}_{\Omega_k} \tag{6.7}$$

This sum is done over all the elements Ω_k containing the node i, $\mathbf{D}_{\Omega_k}^i$ is the distribution matrix of the element Ω_k to the node i and V_i is the volume associated to the node i defined by:

$$V_i = \sum_{k=1}^{N_{\mathrm{C}}^i} \frac{V_{\Omega_k}}{N_{\mathrm{N}}^k} \tag{6.8}$$

The scheme is proven conservative if for all the elements Ω_e:

$$\sum_{j=1}^{N_{\mathrm{N}}^e} \mathbf{D}_{\Omega_e}^j = \mathbf{I} \tag{6.9}$$

The procedure in Eq. (6.7) of distributing the values calculated over the cells to the nodes is also recurrent in AVBP and referred to as *scatter*. The procedures *gather* and *scatter* are central to the calculation paradigm of AVBP and are inherently expensive. As such, a special care has been given to the implementation of these procedures.

6.2 Numerical schemes in AVBP

6.2.1 Advection schemes

The choice of the matrices $\mathbf{D}_{\Omega_e}^j$ will define the different schemes.

6.2.1.1 Central differences

The simplest choice for the distribution matrix is $\forall e \in \{1, ..., N_{\mathrm{C}}\}$ and $\forall j \in \{1, ..., N_{\mathrm{N}}^e\}$:

$$\mathbf{D}_{\Omega_e}^{\mathrm{CV},j} = \frac{1}{N_{\mathrm{N}}^e}\mathbf{I} \tag{6.10}$$

It corresponds to an equal repartition of the cell residual to the surrounding nodes, it matches the second order central finite difference scheme on a 1D regular mesh. As such, this scheme has no dissipation but suffers an important dispersion what makes it highly unstable. It requires an adapted time marching scheme like high order Runge-Kutta time integration and is often used with an additional artificial viscosity.

6.2.1.2 Lax-Wendroff

Multiple schemes in AVBP rely on a Taylor expansion in time of the solution $\mathbf{U}$ and then the replacement of the time derivatives by spatial derivatives, as inspired by the work in Donea (1984). For instance, to derive the *Lax-Wendroff* scheme (see Ni (1981), Hall (1984)), a second order Taylor expansion in time of $\mathbf{U}$ is performed (the superscripts $*^n$, $*^{n+1}$ denotes at which temporal iteration a value is calculated):

$$\mathbf{U}^{n+1} = \mathbf{U}^n + \Delta t \left(\frac{\partial \mathbf{U}}{\partial t}\right)^n + \frac{1}{2}(\Delta t)^2 \left(\frac{\partial^2 \mathbf{U}}{\partial t^2}\right)^n + \mathcal{O}\left((\Delta t)^3\right) \tag{6.11}$$

Time derivatives are then traded for spatial derivatives by reinvesting Eq. (6.1) as follows:

$$\left(\frac{\partial \mathbf{U}}{\partial t}\right)^n = -\left(\boldsymbol{\nabla} \cdot \underline{\underline{\mathbf{F}}}^c\right)^n \tag{6.12}$$

$$\left(\frac{\partial^2 \mathbf{U}}{\partial t^2}\right)^n = -\left(\frac{\partial\left(\boldsymbol{\nabla} \cdot \underline{\underline{\mathbf{F}}}^c\right)}{\partial t}\right)^n \approx -\boldsymbol{\nabla} \cdot \left(\frac{\partial \underline{\underline{\mathbf{F}}}^c}{\partial t}\right)^n \tag{6.13}$$

$$\approx -\boldsymbol{\nabla} \cdot \left(\left(\frac{\partial \underline{\underline{\mathbf{F}}}^c}{\partial \mathbf{U}}\right)^n \cdot \left(\frac{\partial \mathbf{U}}{\partial t}\right)^n\right) \tag{6.14}$$

$$= \boldsymbol{\nabla} \cdot \left(\underline{\underline{\underline{\boldsymbol{\mathcal{F}}}}}^{\mathbf{U}} \cdot \left(\boldsymbol{\nabla} \cdot \underline{\underline{\mathbf{F}}}^c\right)\right)^n \tag{6.15}$$

Injecting the spatial derivatives in Eq. (6.11), the scheme can be written as:

$$\frac{\mathbf{U}^{n+1} - \mathbf{U}^n}{\Delta t} = -\left(\boldsymbol{\nabla} \cdot \underline{\underline{\mathbf{F}}}^c\right)^n + \frac{\Delta t}{2}\boldsymbol{\nabla} \cdot \left(\underline{\underline{\underline{\boldsymbol{\mathcal{F}}}}}^{\mathbf{U}} \cdot \left(\boldsymbol{\nabla} \cdot \underline{\underline{\mathbf{F}}}^c\right)\right)^n + \mathcal{O}\left((\Delta t)^2\right) \tag{6.16}$$

Here, the third order tensor $\underline{\underline{\underline{\boldsymbol{\mathcal{F}}}}}^{\mathbf{U}}$ is the jacobian of the convective flux tensor $\underline{\underline{\mathbf{F}}}^c$ as described in Schmitt (2009) for Euler fluxes when real gas EoS are considered. This tensor is a key element to the *Lax-Wendroff* scheme as well as the other Taylor-Galerkin schemes that are most often used in AVBP. The difficulty to access this tensor in the framework of the Second Gradient theory will be discussed in Sec. 7.2.1. Using Eq. (6.16), one can express the distribution matrix with $\forall e \in \{1, ..., N_{\mathrm{C}}\}$ and $\forall j \{1, ..., N_{\mathrm{N}}^e\}$:

$$\mathbf{D}_{\Omega_e}^{\mathrm{LW},j} = \frac{1}{N_{\mathrm{N}}^e}\mathbf{I} - \frac{(N_{\mathrm{N}}^e)^2}{2d}\frac{\Delta t_{\Omega_e}}{V_{\Omega_e}}\underline{\underline{\underline{\underline{\boldsymbol{\mathcal{F}}}}}}_{\Omega_e}^{\mathbf{U}} \cdot \boldsymbol{S}_j^e \tag{6.17}$$

where Δt_{Ω_e} is the time-step calculated for the element Ω_e, $\boldsymbol{S}_j^e$ is the normal vector of the node j in regard to the element Ω_e and $\underline{\underline{\boldsymbol{\mathcal{F}}}}^{\mathbf{U}}_{\Omega_e}$ is the jacobian tensor calculated a the center of the element Ω_e.
From Eq. (6.17), one gets that this scheme is essentially equivalent to the *Central Difference* scheme with the addition of a dissipative term. This makes the finite volume *Lax-Wendroff* a precise, stable and affordable second order scheme however strongly dissipative.

6.2.1.3 Galerkin finite element discretization

Practically in AVBP, the Taylor time expansion explained for the finite volume *Lax-Wendroff* scheme is often associated with a Galerkin spatial decomposition to generate the so-called Taylor-Galerkin schemes introduced in Donea (1984) and Donea et al. (1987). It has been proven that for centered schemes, the *Cell-Vertex* approach and the Galerkin finite element approach are equivalent.
In this approach, one defines a functional space $\Phi = \{\phi_i,\ i \in \{1, ..., N_{\mathrm{N}}\}$ where ϕ_i is defined such as $\forall\,(i,j) \in \{1, ..., N_{\mathrm{node}}\}$, $\phi_i\,(\boldsymbol{x}_j) = \delta_{ij}$. Classically, ϕ_i is supposed to be a first-degree multivariate polynomial (element P1). The discretized solution $\mathbf{u}$ and convective fluxes $\underline{\underline{\mathbf{f}}}$ are then given by :

$$\mathbf{u}\,(t,\boldsymbol{x}) = \sum_{i=1}^{N_{\mathrm{N}}} \mathbf{U}_i\,(t)\,\phi_i\,(\boldsymbol{x}) \tag{6.18}$$

$$\underline{\underline{\mathbf{f}}}\,(t,\boldsymbol{x}) = \sum_{i=1}^{N_{\mathrm{N}}} \underline{\underline{\mathbf{F}_i}}^{c}\,(t)\,\phi_i\,(\boldsymbol{x}) \tag{6.19}$$

And therefore solving Eq. (6.1) amounts to finding $\mathbf{u}$ such as $\forall i \in \{1, ..., N_{\mathrm{N}}\}$:

$$\left\langle \frac{\partial \mathbf{u}}{\partial t} + \boldsymbol{\nabla} \cdot \underline{\underline{\mathbf{f}}} \,|\, \phi_i \right\rangle = \int_{\Omega} \left(\frac{\partial \mathbf{u}}{\partial t} + \boldsymbol{\nabla} \cdot \underline{\underline{\mathbf{f}}} \right) \phi_i \, d\mathcal{V} = 0 \tag{6.20}$$

Using Eqs. (6.18) and (6.19), one can express Eq. (6.20) as :

$$\forall i \in \{1, ..., N_{\mathrm{N}}\},\ \sum_{e=1}^{N_{\mathrm{C}}} \sum_{j|j\in\Omega_e} \frac{d\mathbf{U}_j}{dt} \int_{\Omega_e} \phi_i \phi_j \, d\mathcal{V} + \sum_{e=1}^{N_{\mathrm{C}}} \sum_{j|j\in\Omega_e} \underline{\underline{\mathbf{F}_i}}^{c} \cdot \int_{\Omega_e} \phi_i \boldsymbol{\nabla} \phi_j \, d\mathcal{V} = 0 \tag{6.21}$$

In particular, the nodal distribution of the cells residuals from Eq. (6.7) can be introduced:

$$\sum_{e=1}^{N_C} \sum_{j|j\in\Omega_e} \underline{\underline{\mathbf{F}_i}}^c \cdot \int_{\Omega_e} \phi_i \boldsymbol{\nabla}\phi_j \, d\mathcal{V} = \sum_{i\in\Omega_k} \sum_{j|j\in\Omega_k} \underline{\underline{\mathbf{F}_i}}^c \cdot \int_{\Omega_k} \phi_i \boldsymbol{\nabla}\phi_j \, d\mathcal{V} \tag{6.22a}$$

$$= \sum_{i\in\Omega_k} \sum_{j|j\in\Omega_k} \underline{\underline{\mathbf{F}_i}}^c \cdot \boldsymbol{\nabla}\phi_j \int_{\Omega_k} \phi_i \, d\mathcal{V} \tag{6.22b}$$

$$= \sum_{i\in\Omega_k} \sum_{j|j\in\Omega_k} \underline{\underline{\mathbf{F}_i}}^c \cdot \boldsymbol{\nabla}\phi_j \frac{V_{\Omega_k}}{N_N^k} \tag{6.22c}$$

$$= \sum_{i\in\Omega_k} \frac{V_{\Omega_k}}{N_N^k} \sum_{j|j\in\Omega_k} \underline{\underline{\mathbf{F}_i}}^c \cdot \boldsymbol{\nabla}\phi_j \tag{6.22d}$$

$$= \sum_{i\in\Omega_k} \frac{V_{\Omega_k}}{N_N^k} \sum_{j|j\in\Omega_k} \underline{\underline{\mathbf{F}_i}}^c \cdot \frac{-1}{dV_{\Omega_k}} \boldsymbol{S}_i \tag{6.22e}$$

$$\sum_{e=1}^{N_C} \sum_{j|j\in\Omega_e} \underline{\underline{\mathbf{F}_i}}^c \cdot \int_{\Omega_e} \phi_i \boldsymbol{\nabla}\phi_j \, d\mathcal{V} = \sum_{i\in\Omega_k} \frac{V_{\Omega_k}}{N_N^k} \mathbf{R}_{\Omega_k} \tag{6.22f}$$

Remark:
Eq. (6.21) is often written in a matrix form :

$$\boldsymbol{\mathcal{M}} \frac{d[\boldsymbol{U}]}{dt} + \underline{\underline{\boldsymbol{\mathcal{K}}}} : \left[\underline{\underline{\mathbf{F}^c}}\right] = 0 \tag{6.23}$$

Where $\boldsymbol{\mathcal{M}}$ is the mass matrix of size $N_C \times N_C$ and $\underline{\underline{\boldsymbol{\mathcal{K}}}}$ is a third order tensor of size $N_C \times d \times N_C$ (granted that $[\boldsymbol{U}]$ is of size $N_C \times N_{cons}$ and $\left[\underline{\underline{\mathbf{F}^c}}\right]$ is of size $N_C \times d \times N_{cons}$, N_{cons} being the number of scalar conservative variables) defined by:

$$\mathcal{M}_{ij} = \int_{\Omega} \phi_i \phi_j \, d\mathcal{V} \tag{6.24}$$

$$\mathcal{K}_{ijk} = \int_{\Omega} \phi_i \boldsymbol{\nabla}\phi_k \, d\mathcal{V} \cdot \boldsymbol{e}_j = \int_{\Omega} \frac{\partial \phi_i}{\partial x_j} \phi_k \, d\mathcal{V} \tag{6.25}$$

The fact that the mass matrix is not *a priori* diagonal makes the time integration of such schemes implicit as $\boldsymbol{\mathcal{M}}$ has to be inverted. The subsequent problems and strategies to overcome them are discussed in Sengupta (2004), Hirsch (2007) and Lamarque (2007). Noticeably, a finite element version of the *Lax-Wendroff* scheme exists in AVBP.

6.2.1.4 Galerkin Runge-Kutta scheme

The finite element *Galerkin Runge-Kutta* scheme of AVBP is also based on a Taylor expansion in time of the equation and a finite element discretization of the equations. It is however allied with a second order Runge-Kutta method for the time integration. By not replacing the time derivatives with spatial derivatives, it avoids the requirement of evaluating the Jacobian tensor of the fluxes. This scheme has a third order in space and has no dissipation, making

it very precise but at the same time very unstable. Although it is slightly more expensive, the overhead cost varying from case to case usually around +20%, the gain in precision and robustness relatively the mesh organization often makes it worth it. For these reasons, and others explored in Chap. 7, this scheme has been preferentially used to carry out simulations with the Second Gradient.

6.2.1.5 Two-step Taylor-Galerkin (TTG) schemes

AVBP also contains a set of Taylor expansion based schemes, of which expressions resemble that of the *Lax-Wendroff* with the exception that the expansion is performed in two steps instead of one. That two-step time expansion is associated with a Galerkin time-space substitution of the derivatives to achieve the final discretization. These schemes have a third order in both time and space for a reasonably affordable cost. More importantly, they are much less dispersive and dissipative than second order schemes which make then suitable for Large Eddy Simulations.

6.2.2 Temporal integration

For the time marching, AVBP uses three explicit methods, that are automatically selected so as to be consistent with the chosen convective scheme (pure finite volume, Lax-Wendroff coupled discretization, Taylor-Galerkin finite element full discretization). Though different in essence, for the sake of modularity they have been expressed and implemented in the code so as to follow the same paradigm, exposed in the following paragraph.
All the time integration methods of AVBP can be written as a m-step low storage Runge-Kutta scheme of which form is given by:

$$\mathbf{U}_i^{n,(0)} = \mathbf{U}_i^n \tag{6.26a}$$

$$\mathbf{U}_i^{n,(1)} = \mathbf{U}_i^n - \alpha_1 \Delta t \mathbf{R}_i^{n,(1)} = \mathbf{U}_i^n - \alpha_1 \Delta t \mathbf{R}_i \left(\mathbf{U}^{n,(0)} \right) \tag{6.26b}$$

$$\vdots$$

$$\mathbf{U}_i^{n,(m-1)} = \mathbf{U}_i^n - \alpha_{m-1} \Delta t \mathbf{R}_i^{n,(m-1)} = \mathbf{U}_i^n - \alpha_{m-1} \Delta t \mathbf{R}_i \left(\mathbf{U}^{n,(m-2)} \right) \tag{6.26c}$$

$$\mathbf{U}_i^{n+1} = \mathbf{U}_i^n - \Delta t \mathbf{R}_i^{n,(m)} = \mathbf{U}_i^n - \Delta t \mathbf{R}_i \left(\mathbf{U}^{n,(m-1)} \right) \tag{6.26d}$$

The coefficients of the method $\alpha_1, ...\alpha_{m-1}$ define its order, precision and stability domain. The low storage appellation refers to the fact that at every substep of the time integration, the only information stored are the reference time solution $\mathbf{U}^n$ and the last substep solution $\mathbf{U}^{n,(j)}$ thus allowing to minimize the memory space required. This is done at the expanse of the method efficiency since most of the time, more substeps are needed to reach the same time accuracy when compared to a classic Runge-Kutta method. For instance, when used with a non Taylor-based scheme, at least three steps are required to achieve 2^{nd} order, four to achieve 3^{rd} order and at least ten for the 4^{th} order. This partially justifies why TTG schemes are much often preferred to perform precise simulations at a reasonable cost.
For our simulations, the time integration methods require both three steps with the following coefficients: $(\alpha_1 = 1/2; \alpha_2 = 1/2)$ for the *Central difference* scheme and $(\alpha_1 = 1/3; \alpha_2 = 1/2)$ for the *Galerkin Runge-Kutta* scheme.

To ensure the overall stability of the schemes, the time step must be chosen with precaution since most of them are submitted to a CFL number (Courant-Friedrichs-Lewy) restriction. An additional care must be taken when diffusion is incorporated to the equations which often leads to an even more restrictive time step. The corresponding expressions can be found in Lamarque (2007).

6.2.3 Diffusive terms

AVBP also possesses numerical schemes specifically dedicated to handle diffusive terms in the NS equations. These terms, modeled by the tensor $\underline{\underline{\mathbf{F}}}^d$, are usually associated with viscosity or thermal diffusion and share the feature of involving spatial derivatives of the state vector $\boldsymbol{\nabla}\mathbf{U}$ in their calculation. Two strategies have been designed in AVBP to handle diffusive terms from the NS equations. Hereunder, the two methods are described and applied to the diffusion of a scalar in order to better grasp their specific behavior.

6.2.3.1 Description of the methods

The 4Δ method

The first one, referred to as 4Δ for reasons that appear clearer once the method is described, methodically follows the *Cell-Vertex* approach defined for the convective fluxes. The initial step consists in evaluating the gradients $\boldsymbol{\nabla}\mathbf{U}$, necessary to calculate the diffusive terms, at the primal mesh nodes where the conservative variables $\mathbf{U}$ are also known. To do so, a *gather*-like procedure is done, as defined in Eq. (6.27) for a cell Ω_e, to evaluate the gradient at the dual mesh nodes:

$$(\boldsymbol{\nabla}\mathbf{U})_{\Omega_e} = -\frac{1}{dV_{\Omega_e}} \sum_{j=1}^{N_{\mathrm{N}}^e} \mathbf{U}_j \boldsymbol{S}_j^e \tag{6.27}$$

It is then followed by a *scatter* procedure to obtain the gradients values at the primal mesh nodes, which, for a node i, is written as:

$$(\boldsymbol{\nabla}\mathbf{U})_i = \frac{1}{V_i} \sum_{k=1}^{N_{\mathrm{C}}^i} \frac{V_{\Omega_k}}{N_{\mathrm{N}}^k} (\boldsymbol{\nabla}\mathbf{U})_{\Omega_k} \tag{6.28}$$

The numerical diffusive fluxes are then evaluated at the primal mesh nodes using the gradients from Eq. (6.28):

$$\underline{\underline{\mathbf{F}}}_i^{\,d} = \underline{\underline{\mathbf{F}}}^d \left(\mathbf{U}_i, (\boldsymbol{\nabla}\mathbf{U})_i\right) \tag{6.29}$$

Eventually, the divergence of the diffusive fluxes is obtain similarly to that of the convective fluxes only that the distribution matrix is chosen from the Central Differences scheme as given by Eq. (6.10). The *gather-scatter* sequence for a cell Ω_e and a node i becomes:

$$\left(\boldsymbol{\nabla} \cdot \underline{\underline{\mathbf{F}}}^d\right)_{\Omega_e} = \frac{1}{dV_{\Omega_e}} \sum_{j=1}^{N_{\mathrm{N}}^e} \underline{\underline{\mathbf{F}}}_j^{\,d} \cdot \boldsymbol{S}_j^e \tag{6.30}$$

$$\left(\boldsymbol{\nabla} \cdot \underline{\underline{\mathbf{F}}}^d\right)_i^{4\Delta} = \frac{1}{V_i} \sum_{k=1}^{N_{\mathrm{C}}^i} \frac{V_{\Omega_k}}{N_{\mathrm{N}}^k} \left(\boldsymbol{\nabla} \cdot \underline{\underline{\mathbf{F}}}^d\right)_{\Omega_k} \tag{6.31}$$

This approach, despite abiding by the *Cell-Vertex* approach, presents multiple shortcomings: it requires two *gather-scatter* sequences which makes it computationally expensive, it is particularly non-dissipative (which in some configurations is arguably a desirable feature but usually not in very sensitive cases), it has a wide stencil since two layers of nodes are necessary to evaluate the divergence which incidentally makes it unable to dissipate perturbations with small characteristic length which are common in our type of simulations.
For those reasons and several other more specific, this approach is often discarded in AVBP (especially for LES simulation, although not a concern for our current study).

The 2Δ method
To alleviate the drawbacks of the 4Δ method, a second approach, dubbed 2Δ, has been designed in AVBP. It departs from the *Cell-Vertex* philosophy to rely on a Galerkin-like approach. Essentially, the main modification consists in evaluating the diffusive fluxes directly at the cell vertices on the dual mesh.
The procedure can be laid down as such: the gradients are still initially calculated in the cell Ω_e as in Eq. (6.27), the diffusive fluxes are then evaluated *in situ* following Eq. (6.32) (it should be noticed that this procedure requires the conservative variable to be gathered to the cell to obtain $\mathbf{U}_{\Omega_e}$)

$$\underline{\underline{\mathbf{F}_{\Omega_e}}}^{d} = \underline{\underline{\mathbf{F}}}^{d}\left(\mathbf{U}_{\Omega_e}, (\boldsymbol{\nabla}\mathbf{U})_{\Omega_e}\right) \tag{6.32}$$

The divergence of the vertex-centered diffusive terms can then be evaluated at the node i with Eq. (6.33):

$$\left(\boldsymbol{\nabla}\cdot\underline{\underline{\mathbf{F}}}^{d}\right)_i^{2\Delta} = \frac{1}{V_i}\sum_{k=1}^{N_{\mathrm{C}}^i}\underline{\underline{\mathbf{F}_{\Omega_k}}}^{d}\boldsymbol{S}_i^k \tag{6.33}$$

With this approach, only one *gather-scatter* sequence is necessary greatly reducing the computational cost, only one layer of nodes is required, a smaller stencil that allows the scheme to dissipate the smallest scales oscillations down to twice the mesh step size.

6.2.3.2 Application to scalar diffusion

To better grasp the differences between the two approaches, a regular one-dimensional setting with a constant mesh size Δx is used to simplify the developments.

Let $\mathcal{F}^d$ be a diffusive flux associated to the scalar field a such as $\mathcal{F}^d = \partial a/\partial x$ for which the numerical divergence $\boldsymbol{\nabla}\cdot\underline{\underline{\mathbf{F}}}^{d}$ has to be evaluated. For the node i the procedure associated with the 4Δ method reads:

$$\left(\frac{\partial a}{\partial x}\right)_i = \frac{a_{i+1}-a_{i-1}}{2\Delta x} \tag{6.34}$$

$$\underline{\underline{\mathbf{F}_i}}^{d} = \underline{\underline{\mathbf{F}}}^{d}\left(a_i, \left(\frac{\partial a}{\partial x}\right)_i\right) = \left(\frac{\partial a}{\partial x}\right)_i \tag{6.35}$$

$$\left(\boldsymbol{\nabla}\cdot\underline{\underline{\mathbf{F}}}^{d}\right)_i^{4\Delta} = \frac{1}{2\Delta x}\left(\left(\frac{\partial a}{\partial x}\right)_{i+1} - \left(\frac{\partial a}{\partial x}\right)_{i-1}\right) = \frac{a_{i+2}-2a_i+u_{i-2}}{(2\Delta x)^2} \tag{6.36}$$

whereas for the 2Δ method it reads:

$$\left(\frac{\partial a}{\partial x}\right)_{i+\frac{1}{2}} = \frac{a_{i+1} - a_i}{\Delta x} \tag{6.37}$$

$$\underline{\underline{\mathbf{F}}}_{i\pm\frac{1}{2}}{}^{d} = \underline{\underline{\mathbf{F}}}^{d}\left(a_{i\pm\frac{1}{2}}, \left(\frac{\partial a}{\partial x}\right)_{i\pm\frac{1}{2}}\right) = \left(\frac{\partial a}{\partial x}\right)_{i\pm\frac{1}{2}} \tag{6.38}$$

$$\left(\boldsymbol{\nabla}\cdot\underline{\underline{\mathbf{F}}}^{d}\right)_{i}^{2\Delta} = \frac{1}{\Delta x}\left(\left(\frac{\partial a}{\partial x}\right)_{i+\frac{1}{2}} - \left(\frac{\partial a}{\partial x}\right)_{i-\frac{1}{2}}\right) = \frac{a_{i+1} - 2a_i + a_{i-1}}{(\Delta x)^2} \tag{6.39}$$

For the constant linear diffusion of a scalar variable, the behavior of both methods appears clearly. In both cases, the divergence of the diffusive flux amounts to the Laplacian of the variable a and both methods actually result in a 2^{nd} order finite difference approximation of said Laplacian. However, where the 2Δ approach leads to a classic approximation with a three-point stencil using all three points $i-1$, i and $i+1$, the 4Δ one lends a five point stencil using only one in two points thus demonstrating its inability to dissipate perturbations with a spatial period smaller than $4\Delta x$, especially point to point $2\Delta x$ oscillations.

6.2.4 Numerical stabilization

There exist two main phenomena that create numerical errors during the simulation and that can possibly lead to a crash: numerical oscillations and local under-resolution. Both phenomena can be encountered separately or simultaneously, so can they be tackled. In the case of real gas simulations, these phenomena are particularly fostered by the non-linearities of the thermodynamics and the strong coupling in the equations.

In the following paragraphs, the main strategies used for our simulations in AVBP are presented. These strategies initially designed for LES settings where the conserved variables, represented by vector $\mathbf{U}$, are supposed to have been filtered by a low-pass spatial filter G so as to obtain a new filtered vector $\bar{\mathbf{U}}$ calculated with $\bar{\mathbf{U}} = G * \mathbf{U}$. The operation in $G * \mathbf{U}$ is to be understood as a convolution, i.e.:

$$\bar{\mathbf{U}}(\boldsymbol{x}) = \int G\left(\boldsymbol{x} - \boldsymbol{x}'\right) \boldsymbol{U}\left(\boldsymbol{x}'\right) d\boldsymbol{x}' \tag{6.40}$$

From the definition of the filtering process in Eq. (6.40), the Favre average $\tilde{\xi}$ of a variable ξ (other then the density) can be defined as:

$$\tilde{\xi} = \frac{\overline{\rho\xi}}{\bar{\rho}} \tag{6.41}$$

For LES applications, the filtering in Eq. (6.40) and the averaging in Eq. (6.41) are never performed in practice. Only, the Euler or Navier-Stokes equations are modified so as to be applied directly to the filtered/averaged variables, with in particular the appearance of new source terms.
For the purpose of the present work however, only DNS applications are targeted. In that prospect, both the filtering in Eq. (6.40) and the averaging in Eq. (6.41) are taken advantage of as they prove particularly efficient to limit the unwanted numerical phenomena previously mentioned. In particular, the filtered and averaged values are explicitly computed to then be used in a fashion further detailed in the next two subsections.

6.2.4.1 Filtering

To limit point-wise oscillations, an explicit spatial filter is used, inspired by the strategy in Mathew et al. (2003) initially designed for LES application as a mean to model sub-grid-scale variables in the filtered equations. To that effect, a low-pass filter G is introduced to be used to perform a convolution of the conservative variable $\mathbf{U}$. An approximate deconvolution Q of G is constructed recursively following the work in Stolz and Adams (1999); Adams and Stolz (2002). Indeed, the exact inverse of G (under additional technical assumptions not expanded upon here) can be expressed as an infinite power series of $1 - G$ as follows:

$$Q_{\text{exact}} = \sum_{k=0}^{\infty} (1 - G)^k \tag{6.42}$$

A N-term approximation Q_N of Q_{exact} can be obtained by truncating the infinite series as done in Eq. (6.43). This truncation provides a very satisfactory approximation even for relatively low values of N ($N \leqslant 1$).

$$Q_N = \sum_{k=0}^{N} (1 - G)^k \tag{6.43}$$

The range of wavelengths covered by Q_N grows with an increasing value of N. A filtered version $\bar{\mathbf{U}}$ of $\mathbf{U}$ can then be obtained by combining G with its approximate deconvolution Q_N to get Eq. (6.44) where $F_N = Q_N * G$.

$$\hat{\mathbf{U}} = Q_N * G * \mathbf{U} = F_N * \mathbf{U} \tag{6.44}$$

The chosen low-pass filter G selected in AVBP is a classic fourth-order bi-Laplacian filter (see Schönfeld and Rudgyard (1999)) Due to the approximate evaluation Q_N of G^{-1}, the ensuing filter F_N acts as a very selective and conservative filter which removes high wavelengths. The filter response function as a function of the wavenumber is given Fig. 6.4 for different values N of G-filter iterations.

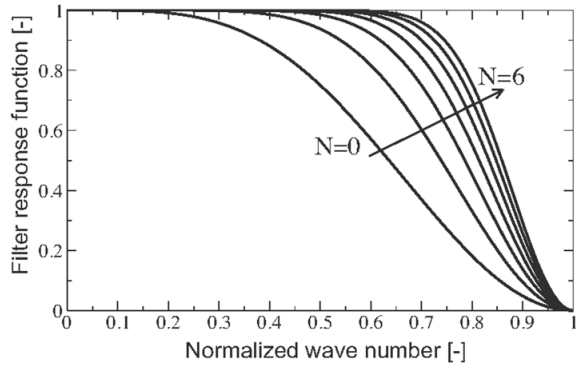

Figure 6.4: *Response of the filter F_N as a function of the normalized wavenumber for different numbers N of G-filter iterations, taken from Schmitt (2020)*

The magnitude of filter G can be controlled with a coefficient which constitutes, together with the number of filter iterations N (usually 1 for Galerkin schemes), parameters that are used to configure the simulation beforehand.

6.2.4.2 Numerical viscosity

For real gas flow, a specific artificial diffusion tool, referred to as LAD viscosity, has been designed and is detailed in Schmitt (2020). A specific sensor S_ρ^0 is used to detect cells with numerical oscillations of under-resolved wavelengths and is written as follows:

$$\mathrm{S}_\rho^0 = \frac{\|\tilde{\boldsymbol{u}} \cdot \boldsymbol{n}_{\boldsymbol{\nabla}\rho}\| \, \Delta t}{\Delta x} \frac{\|\bar{\rho} - \hat{\rho}\|}{0.01\bar{\rho}} \tag{6.45}$$

In practice, a threshold $\mathrm{S}_{\mathrm{thr}}$ can be applied to the sensor to delay its activation, which proves useful quiet frequently. The final expression of the sensor becomes:

$$\mathrm{S}_\rho = \max\left(0; \mathrm{S}_\rho^0 - \mathrm{S}_{\mathrm{thr}}\right) \tag{6.46}$$

where Δt is the time step, Δx the characteristic mesh cell size, $\boldsymbol{n}_{\boldsymbol{\nabla}\rho}$ is the normal to the density gradient, $\bar{\rho}$ the supposedly low-pass filtered density, $\tilde{\boldsymbol{u}}$ is the Favre-averaged velocity and $\hat{\rho}$ is the deconvoluted density calculated following the method in Sec. 6.2.4.1. It means that $\hat{\rho} = Q_M * \bar{\rho}$ where Q_M is M-term approximation G^{-1} with in particular $N \neq M$ in general.

Using this sensor, a laplacian filter is applied to smooth the conservative variables gradient by enforcing an artificial diffusion. The newly artificially diffused ($*^{\mathrm{AD}}$ supercript) conservative variables can be written at a node i as follows (see Sec. 6.1.2 for the notations):

$$\bar{\rho}_i^{\mathrm{AD}} = \bar{\rho}_i + \frac{C_{\mathrm{AD}}}{V_i} \sum_{k=1}^{N_{\mathrm{C}}^i} \frac{V_{\Omega_k}}{N_{\mathrm{N}}^k} \left[\bar{\rho}_i - \bar{\rho}_{\Omega_k}\right] \mathrm{S}_{\rho,\Omega_k} \tag{6.47a}$$

$$(\bar{\rho}\tilde{\boldsymbol{u}})_i^{\mathrm{AD}} = (\bar{\rho}\tilde{\boldsymbol{u}})_i + \frac{C_{\mathrm{AD}}}{V_i} \sum_{k=1}^{N_{\mathrm{C}}^i} \frac{V_{\Omega_k}}{N_{\mathrm{N}}^k} \tilde{\boldsymbol{u}}_{\Omega_k} \left[\bar{\rho}_i - \bar{\rho}_{\Omega_k}\right] \mathrm{S}_{\rho,\Omega_k} \tag{6.47b}$$

$$(\bar{\rho}\tilde{e})_i^{\mathrm{AD}} = (\bar{\rho}\tilde{e})_i + \frac{C_{\mathrm{AD}}}{V_i} \sum_{k=1}^{N_{\mathrm{C}}^i} \frac{V_{\Omega_k}}{N_{\mathrm{N}}^k} \left[(\bar{\rho}\tilde{e}_s)_i - (\bar{\rho}\tilde{e}_s)_{\Omega_k} + \tilde{e}_{c,\Omega_k} \left(\bar{\rho}_i - \bar{\rho}_{\Omega_k}\right)\right] \mathrm{S}_{\rho,\Omega_k} \tag{6.47c}$$

where $\bar{\rho}_{\Omega_k}$, $\tilde{\boldsymbol{u}}_{\Omega_k}$, $(\bar{\rho}\tilde{e_s})_{\Omega_k}$ and $\tilde{e}_{c,\Omega_k}$ are the mean surface weighted values (see Eq. (6.3)) of $\bar{\rho}$, $\tilde{\boldsymbol{u}}$, $\bar{\rho}\tilde{e_s}$ and $\tilde{e_c}$ over the vertices of element Ω_k and C_{AD} is the coefficient chosen for the artificial diffusion. The mean sensor value $\mathrm{S}_{\rho,\Omega_k}$ in the element Ω_k is calculated with:

$$\mathrm{S}_{\rho,\Omega_k} = \frac{1}{N_{\mathrm{N}}^k} \sum_{j=1}^{N_{\mathrm{N}}^k} \mathrm{S}_{\rho,j} \tag{6.48}$$

The summations in Eqs. (6.47a)-(6.47c) and Eq. (6.48) are done over the mesh elements $\Omega_{k\,k=1\cdots N_{\mathrm{C}}^i}$ such as the node i belongs to said elements (see Sec. 6.1.2).
The cell velocity is assumed to be at equilibrium during the diffusion of conservative variables in Eqs. (6.47b) and (6.47c).

The value of the threshold $\mathrm{S}_{\mathrm{thr}}$, along with coefficient C_{AD} and the iteration number M of the sensor filter are also global parameters of the simulation that can be controlled by the user. In practice, the value of M is usually set to 1, that of C_{AD} is set to 1 also and $\mathrm{S}_{\mathrm{thr}}$ is taken to be 0.

6.3 Boundary conditions in AVBP

AVBP provides two methods to enforce Dirichlet boundary conditions (the Neumann conditions are applied by modifying directly the value of the flux at the specified boundary, for instance no mass flux at walls or imposed thermal flux, etc...). The two methods share the principle to modify *a posteriori* the predicted values of the residuals at the boundaries and correct them so that the updated conservative variables match the values prescribed by the boundary condition.

The different examples will be treated considering the mono-dimensional Euler equations for a single species:

$$\frac{\partial \rho}{\partial t} = -\frac{\partial (\rho u)}{\partial x} \tag{6.49a}$$

$$\frac{\partial (\rho u)}{\partial t} = -\frac{\partial}{\partial x}\left[\rho u^2 + P\right] \tag{6.49b}$$

$$\frac{\partial (\rho e)}{\partial t} = -\frac{\partial}{\partial x}\left[(\rho e + P)\, u\right] \tag{6.49c}$$

where ρ, P and u are the density, pressure and velocity of the fluid, $e = e_s + u^2/2$ is the total specific energy of the fluid. The set of conservatives variables is $\mathbf{U} = (\rho, \rho u, \rho e)^{\mathrm{T}}$, the associated set of primitive variables is $\mathbf{V} = (\rho, u, P)^{\mathrm{T}}$, the associated set of characteristic variable is $\mathbf{W} = (W_+, W_-, W_s)^{\mathrm{T}}$ and the associated flux vector is $\mathbf{F}(\mathbf{U}) = \left(\rho u, \rho u^2 + P, (\rho e + P)\, u\right)^{\mathrm{T}}$

The example considered is that of an output with a prescribed target pressure P_t. At the time iteration $n+1$, the numerical scheme predicted a vector of characteristic values residuals $\delta \mathbf{U}_p^n$ so that the predicted conservative variables are $\mathbf{U}_p^{n+1} = \mathbf{U} + \mathbf{U}_p^n$ which might lead to a predicted pressure P_p different from the target; what must be corrected by the boundary condition.

6.3.1 Hard boundary conditions

The first method, label as a HARD boundary condition in the code, is a straightforward modification of the predicted conservatives variables at the boundaries to match the prescribed values. With the given example, the procedure goes in the following order:

- The predicted conservatives variables $\mathbf{U}_p^{n+1}$ and the associated thermodynamic values (P_p, T_p, etc...) are evaluated
- The predicted temperature is considered to be correct, leading to a corrected value of the density $\rho_c = \rho(T_p, P_t)$ using the target pressure P_t (the velocity is not impacted by the boundary condition)
- With the set of corrected values $P_c = P_t, T_c = T_p, \rho_c = \rho(T_p, P_t), u_c = u_p$, the corrected conservatives values are computed: $(\rho u)_c = \rho_c u_c$, $(\rho e)_c = \rho_c \cdot \left(e_s(\rho_c, T_c) + u_c^2\right)$
- Given the corrected conservative variables $\mathbf{U}_c^{n+1}$ the conservative variable residuals are corrected $\delta \mathbf{U}_c^c = \mathbf{U}_c^{n+1} - \mathbf{U}_n$

Though this method eventually lends the correct targeted pressure and thermodynamically consistent values for the conservative variables, it is acoustically completely reflective and the impossibility to evacuate the acoustics out of the domain can be a limitation when carrying out realistic simulations.

6.3.2 Characteristic boundary conditions

The second method is based on the work in Poinsot and Lele (1992) where the idea is to separate the different pieces of information, acoustic and entropic, available at the boundary and treat each of them accordingly to the desired behavior for the boundary condition. This methodology allows to control accurately the acoustic content entering and leaving the domain. The first step to derive the method is to linearize the equation, meaning writing the system Eq. (7.47) as:

$$\frac{\partial \mathbf{U}}{\partial t} = \boldsymbol{A}(\mathbf{U}) \frac{\partial \mathbf{U}}{\partial x} \tag{6.50}$$

where $\boldsymbol{A}(\mathbf{U})$ is the Jacobian matrix of the flux relatively to the conservative variables, i.e. $\boldsymbol{A} = \partial \mathbf{F}(\mathbf{U})/\partial \mathbf{U}$, of which expression is given by:

$$\boldsymbol{A}(\mathbf{U}) = \begin{pmatrix} 0 & 1 & 0 \\ \Lambda\Gamma - u^2 & u(2-\Lambda) & \Lambda \\ u(\Lambda\Gamma - h_t) & h_t - u^2\Lambda & u(1+\Lambda) \end{pmatrix} \quad \text{with} \quad \begin{aligned} h_t &= e + \frac{P}{\rho} = h + \frac{u^2}{2} \\ \Lambda &= \frac{\alpha}{\rho\beta C_v} \\ \Gamma &= \frac{C_p}{\alpha} - h_t + u^2 \end{aligned} \tag{6.51}$$

The possibility to linearize a system in the form in Eq. (6.50) is not readily guaranteed in general cases. In particular, an equation involving the time derivative of each variable of the vector $\mathbf{U}$ must be encountered. It will be shown in Sec. 7.2.1 that this cannot be done for the system of equations used in the SG model.
The matrix has then to be diagonalized into a matrix D so as to write the equation in the form:

$$\frac{\partial \mathbf{W}}{\partial t} = \boldsymbol{D}(\mathbf{U}) \frac{\partial \mathbf{W}}{\partial x} \tag{6.52}$$

defining therefore the characteristic variables $\mathbf{W}$ as the set of variables decomposed over a basis of eigenvectors of the matrix $\boldsymbol{A}(\mathbf{U})$.

One should notice that the dependency of $\mathbf{F}$ in the components of $\mathbf{U}$ and not its derivatives is primordial in order to perform the differentiation $A(\mathbf{U}) = \partial \mathbf{F}/\partial \mathbf{U}$. This key element will also be discussed in the framework of the Second Gradient in Chap. 6. It is well established that the matrix $\boldsymbol{D}(\mathbf{U})$ writes:

$$\boldsymbol{D}(\mathbf{U}) = \begin{pmatrix} u + c_W & 0 & 0 \\ 0 & u - c_W & 0 \\ 0 & 0 & u \end{pmatrix} \tag{6.53}$$

where c_W is the characteristic sound speed of the system. Again, the possibility to diagonalize matrix $\boldsymbol{A}$ into $\boldsymbol{D}$ with only real eigenvalues is not guaranteed in general. This property actually serves as the characterization for a hyperbolic system of equation such as the native Euler's equations system for an hypersonic flow with a convex EoS.

The lasts required elements are the matrices representing the change of basis from the conservative to the characteristic variables, noted $\boldsymbol{L}$ and the other way around, noted $\boldsymbol{R}$. They are

expressed by:

$$\boldsymbol{L} = \begin{pmatrix} -\frac{n_x}{\rho} + \frac{\Lambda\Gamma}{\rho c} & \frac{n_x}{\rho} - \frac{\Lambda u}{\rho c} & \frac{\Lambda}{\rho c} \\ \frac{n_x}{\rho} + \frac{\Lambda\Gamma}{\rho c} & -\frac{n_x}{\rho} - \frac{\Lambda u}{\rho c} & \frac{\Lambda}{\rho c} \\ 1 - \frac{\Lambda\Gamma}{c^2} & \frac{u\Lambda}{c^2} & -\frac{\Lambda}{c^2} \end{pmatrix} \tag{6.54}$$

$$\boldsymbol{R} = \begin{pmatrix} \frac{\rho}{2c} & \frac{\rho}{2c} & 1 \\ \frac{\rho}{2}\left(\frac{u}{c} + n_x\right) & \frac{\rho}{2}\left(\frac{u}{c} - n_x\right) & u \\ \frac{\rho}{2}\left(\frac{c}{\Lambda} - \frac{\Gamma - u^2}{c} + n_x u\right) & \frac{\rho}{2}\left(\frac{c}{\Lambda} - \frac{\Gamma - u^2}{c} - n_x u\right) & -h_t - \frac{C_p}{\alpha} \end{pmatrix} \tag{6.55}$$

where n_x is the direction of the inner normal to the considered boundary. With that, one can express the variations on the conservative/primitive variables relatively to the variations of the characteristic values as done in Eqs. (6.56a) to (6.56e). By convention, W_+ refers to the forward (or entering) acoustic wave propagating at $u + n_x c$, W_- the backward (or exiting) acoustic wave propagating at $u - n_x c$ and W_s is the entropic wave convected at u.

$$\partial\rho = \frac{\rho}{2c}\left(\partial W_+ + \partial W_-\right) + \partial W_s \tag{6.56a}$$

$$\partial(\rho u) = \frac{\rho}{2c}\left(u + n_x c\right)\partial W_+ + \frac{\rho}{2c}\left(u - n_x c\right)\partial W_- + u\partial W_s \tag{6.56b}$$

$$\partial u = \frac{n_x}{2}\left(\partial W_+ - \partial W_-\right) \tag{6.56c}$$

$$\partial P = \frac{\rho c}{2}\left(\partial W_+ + \partial W_-\right) \tag{6.56d}$$

$$dT = \frac{\rho\beta c^2 - 1}{2c\alpha}\left(\partial W_+ + \partial W_-\right) - \frac{1}{\rho\alpha}\partial W_s \tag{6.56e}$$

For the considered outlet, the Characteristic Boundary Conditions procedure goes as follows:

- The predicted conservatives variables $\mathbf{U}_p^{n+1}$ and the associated thermodynamic values (P_p, T_p, $\boldsymbol{L}$, $\boldsymbol{R}$ etc...) are evaluated
- The predicted characteristic variables variations $\delta\mathbf{W}_p^n = \boldsymbol{L}\delta\mathbf{U}_p^n$ are computed
- For an outlet, the entropic wave and the exiting acoustic wave must be left unchanged thus $\partial W_{s_c} = \partial W_{s_p}$ and $\partial W_{+_c} = \partial W_{+_p}$
- Only the entering wave can be modified to enforce the pressure. Thanks to Eq. (6.56d) the modification to apply is $\partial W_{-_c} = -\partial W_{+_p} + 2\left(P_t - P^n\right)/(\rho c)$
- The conservative variables residuals are corrected thanks to the corrected characteristic variables residuals with $\delta\mathbf{U}_c^n = \boldsymbol{R}\delta\mathbf{W}_c^n$

This method allows to control accurately the entering and exiting waves in the domain, in particular it allows to properly derive boundary conditions with time relaxation or completely non-reflective boundary conditions which is impossible with the "hard" approach.

Chapter 7

Numerical implementation of the Second Gradient model

Following the theoretical presentations of the Second Gradient theory in Chap. 5 and the AVBP solver in Chap. 6, this chapter is dedicated to expanding upon the practical implementation of the model into the solver in order to produce preliminary simulations. Indeed, apart from the modifications of the thermodynamics described in Sec. 5.3 that must be integrated into AVBP, the equations derived for the SG model display new terms not typically found in fluid simulations and of which treatment must be addressed.

The first section 7.1 compiles the investigations regarding the discretization of the unconventional high order derivatives that appear in the SG equations. The AVBP solver is not readily designed to handle such terms. As such, a specific treatment has been required to consistently implement them. The different terms that are concerned are systematically listed in Sec. 7.1.1, the different strategies for their discretization are exposed in Sec. 7.1.2 and are then compared numerically in Sec. 7.1.3. It is shown in particular that the choice made for this discretization strongly impacts the stability of the calculations.

The new set of equations also calls for additional precautions that must be taken to ensure a successful simulation, these are discussed in Sec. 7.2. An attempt at characterizing the nature of the equations is made Sec. 7.2.1. It is found to be different from that of the more classic equation systems studied in hydrodynamics. Despite this hurdle, a strategy to treat the boundary conditions for this system, no longer hyperbolic, is proposed in Sec. 7.2.2. Finally, a numerical investigation is also performed in order to extract a time step condition. It is found to be comparable to conditions typical of diffusive equations, a result consistent with the diffusive nature of capillary phenomena.

7.1 Discretization of the Second Gradient equations

7.1.1 Governing equations

As a reminder, the conservative form of the Navier-Stokes equations for the SG model iq:

$$\begin{cases} \dfrac{\partial \rho}{\partial t} = -\boldsymbol{\nabla} \cdot (\rho \mathbf{v}) & \text{(7.1a)} \\ \dfrac{\partial (\rho \mathbf{v})}{\partial t} = -\boldsymbol{\nabla} p - \boldsymbol{\nabla} \cdot \lambda \left(\boldsymbol{\nabla} \rho \otimes \boldsymbol{\nabla} \rho \right) + \boldsymbol{\nabla} \cdot \underline{\underline{\boldsymbol{\tau}}}^{d} + \rho \boldsymbol{g} & \text{(7.1b)} \\ \dfrac{\partial (\rho e)}{\partial t} = -\boldsymbol{\nabla} \cdot \left[(\rho e + p) \mathbf{v} + \lambda \left(\boldsymbol{\nabla} \rho \otimes \boldsymbol{\nabla} \rho \right) \cdot \mathbf{v} + \lambda \rho \boldsymbol{\nabla} \rho \boldsymbol{\nabla} \cdot \mathbf{v} - \underline{\underline{\boldsymbol{\tau}}}^{d} + \boldsymbol{q} \right] - \rho \boldsymbol{g} \cdot \mathbf{v} & \text{(7.1c)} \end{cases}$$

where the mechanical pressure p is given from the EoS pressure P_0 by:

$$p = P_0 - \frac{\lambda}{2} \left(\boldsymbol{\nabla} \rho \right)^2 - \rho \boldsymbol{\nabla} \cdot \left(\lambda \boldsymbol{\nabla} \rho \right) \tag{7.2}$$

Apart from the classic diffusion term (viscous stress, thermal conduction), these equations, in the right hand side fluxes, also contain specific terms which, even without being diffusive per definition, also involve spatial derivatives of the density. These "non-advective" terms, compiled in Tab. 7.1, also require a specific treatment that strongly relies on the two methods already implemented in AVBP and described in Sec. 6.2.3. The interaction between the $2\Delta/4\Delta$ methods and the high order derivative terms in the capillary fluxes is investigated in the following paragraphs.

To simplify the developments, the SG system is considered in one dimension, with neither body forces nor diffusion, together with the mass equation, as follows:

$$\begin{cases} \dfrac{\partial \rho}{\partial t} = -\dfrac{\partial (\rho u)}{\partial x} & \text{(7.3a)} \\ \dfrac{\partial (\rho u)}{\partial t} = -\dfrac{\partial}{\partial x} \left[\rho u^2 + P_0 + \dfrac{\lambda}{2} \left(\dfrac{\partial \rho}{\partial x} \right)^2 - \lambda \rho \dfrac{\partial^2 \rho}{\partial x^2} \right] & \text{(7.3b)} \\ \dfrac{\partial (\rho e)}{\partial t} = -\dfrac{\partial}{\partial x} \left[(\rho e + P_0) u + \dfrac{\lambda}{2} \left(\dfrac{\partial \rho}{\partial x} \right)^2 u + \lambda \rho \dfrac{\partial \rho}{\partial x} \dfrac{\partial u}{\partial x} - \lambda \rho \dfrac{\partial^2 \rho}{\partial x^2} u \right] & \text{(7.3c)} \end{cases}$$

Tab. 7.1 compiles the terms concerned by the following investigation. The derivative term involved in the flux is isolated to recall the symmetry of terms that appear in both the momentum and the energy equations, of which respective flux divergence is provided. The one dimensional versions of said divergence terms are also precised and are used in the analytical developments.
By modifying the formulation of the energy equation as suggested in (7.4), another configuration can be obtained which leads to the appearance of the new terms referred to as C.2/c.2 in Tab. 7.1.

$$\left(\boldsymbol{\nabla} \rho \otimes \boldsymbol{\nabla} \rho \right) \cdot \mathbf{v} + \rho \boldsymbol{\nabla} \rho \boldsymbol{\nabla} \cdot \mathbf{v} = \boldsymbol{\nabla} \rho \boldsymbol{\nabla} \cdot \rho \mathbf{v} \tag{7.4}$$

This modification introduces a formal asymmetry between the momentum and energy equation and the corresponding configuration has also been investigated. However it has shown no effect

whatsoever on the stability of the calculations in itself as the results have been observed to be exactly the same, configuration per configuration, for the two formulations of the energy equation. As such, only the numerical results for the configuration using Eq. (7.4) in the energy Eq. (7.1c), which is the one selected for the application simulations, are presented.

Root term	Flux divergence	1D equivalent	Equation
$(\boldsymbol{\nabla}\rho)^2$ (A)	$\boldsymbol{\nabla}\cdot\left[(\boldsymbol{\nabla}\rho)^2\,\underline{\underline{\mathbf{I}}}\right]$ (A.1)	$\frac{\partial}{\partial x}\left[\left(\frac{\partial\rho}{\partial x}\right)^2\right]$ (a.1)	Momentum
	$\boldsymbol{\nabla}\cdot\left[(\boldsymbol{\nabla}\rho)^2\,\mathbf{v}\right]$ (A.2)	$\frac{\partial}{\partial x}\left[\left(\frac{\partial\rho}{\partial x}\right)^2 u\right]$ (a.2)	Energy
$\boldsymbol{\nabla}\rho\otimes\boldsymbol{\nabla}\rho$ (B)	$\boldsymbol{\nabla}\cdot[\boldsymbol{\nabla}\rho\otimes\boldsymbol{\nabla}\rho]$ (B.1)	$\frac{\partial}{\partial x}\left[\left(\frac{\partial\rho}{\partial x}\right)^2\right]$ (b.1)	Momentum
	$\boldsymbol{\nabla}\cdot[(\boldsymbol{\nabla}\rho\otimes\boldsymbol{\nabla}\rho)\cdot\mathbf{v}]$ (B.2)	$\frac{\partial}{\partial x}\left[\left(\frac{\partial\rho}{\partial x}\right)^2 u\right]$ (b.2)	Energy
$\boldsymbol{\nabla}\rho\boldsymbol{\nabla}\cdot(\rho\mathbf{v})$ (C)	$\boldsymbol{\nabla}\cdot[\rho\boldsymbol{\nabla}\rho\boldsymbol{\nabla}\cdot\mathbf{v}]$ (C.1)	$\frac{\partial}{\partial x}\left[\rho\frac{\partial\rho}{\partial x}\frac{\partial u}{\partial x}\right]$ (c.1)	Energy
	$\boldsymbol{\nabla}\cdot[\boldsymbol{\nabla}\rho\boldsymbol{\nabla}\cdot(\rho\mathbf{v})]$ (C.2)	$\frac{\partial}{\partial x}\left[\frac{\partial\rho}{\partial x}\frac{\partial\rho u}{\partial x}\right]$ (c.2)	Energy
$\boldsymbol{\Delta}\rho$ (D)	$\boldsymbol{\nabla}\cdot\left[\rho\boldsymbol{\Delta}\rho\underline{\underline{\mathbf{I}}}\right]$ (D.1)	$\frac{\partial}{\partial x}\left[\rho\frac{\partial^2\rho}{\partial x^2}\right]$ (d.1)	Momentum
	$\boldsymbol{\nabla}\cdot[(\rho\mathbf{v}\boldsymbol{\Delta}\rho)]$ (D.2)	$\frac{\partial}{\partial x}\left[\rho u\frac{\partial^2\rho}{\partial x^2}\right]$ (d.2)	Energy

Table 7.1: *List of high order derivatives terms in the SG equations*

The next paragraphs show how the methodologies applied in 6.2.3.2 for scalar diffusion can be applied to the previous SG equations. An important detail to notice is that for the first three root terms A, B and C, only first order derivatives are involved which leads to, at most, second order derivatives when their corresponding flux divergence is calculated. This situation is readily analogous to more classic diffusive terms. For the last density Laplacian term D, second order derivatives are already present in the fluxes which leads to third order derivatives once the divergence is calculated. Since AVBP possesses tools to handle second order derivatives and no method readily available to handle third order derivatives, the treatment of the Laplacian related fluxes calls for a different discussion. For that reason, the treatment of A, B and C, gradient related terms and that of D, are addressed separately.

*IMPORTANT: In the following paragraphs, when 2Δ and 4Δ are mentioned, they strictly refer to the corresponding discretization method in Sec. 6.2.3 that is used to evaluate a **second order** derivative involved in the discretization of given terms, independently from the actual stencil that is reached when the complete term is discretized. The actual stencil of the final term will be explicitly designated with its corresponding size. Since the schemes that are used are centered, a 3-point stencil discretization is to be understood as using one point on both sides of the central point where the term is discretized. Likewise, 5-point and 7-point stencils use respectively two and three points on both sides of the central point of discretization.*

7.1.2 Numerical discretization

7.1.2.1 Classic terms

For the sake of completeness, the discretization of the classic terms of the Euler equations are recalled. These terms involve the direct derivation of a conserved variable (ρ, ρu, ρe) or a variable directly calculated from the conserved one without involving any derivation such as ρu^2, P_0 or $(\rho e + P_0)\, u$. Let ξ be any of the previous variable, the objective is to express, at node i the space derivative $\partial\xi/\partial x$. The first step involves expressing ξ at the nodes. The conservative variables are natively stored at the nodes; only the compound variables are concerned by this step which essentially means that these compound variables are expressed at the nodes (and not at the cell centers as done in the 2Δ approach). For instance, one would write:

$$u_i = \frac{(\rho u)_i}{\rho_i} \tag{7.5a}$$

$$\left(\rho u^2\right)_i = (\rho u)_i\, u_i \tag{7.5b}$$

$$P_{0i} = P_0\left(\rho_i, (\rho e)_i\right) \tag{7.5c}$$

$$\left((\rho e + P_0)\, u\right)_i = \left((\rho e)_i + P_{0i}\right) u_i \tag{7.5d}$$

Once the variable ξ has been expressed at the nodes, its "divergence" is given by the classic second order accuracy central difference method which has a 3-point stencil:

$$\left[\frac{\partial \xi}{\partial x}\right]_i = \frac{\xi_{i+1} - \xi_{i-1}}{2\Delta x} \tag{7.6}$$

7.1.2.2 Gradient related terms

As already mentioned regarding the capillary terms, a first class can be discriminated from the root terms A, B and C as they directly involve gradients of conservative variables. The divergence of this terms causes the apparition of second order derivatives for which the methods in Sec. 6.2.3.2 can be directly applied. In the one dimensional formulation, four terms are to be considered: a.1 (which is equivalent to b.1), a.2 (which is equivalent to b.2), c.1 and c.2.

In higher dimensions, the terms A.1 and B.1 (or A.2 and B.2) do not lead to the same formulation and must be discretized in a different way, which as been done in the actual implementation of the SG equations in AVBP. This aspect is not treated here to simplify the message, which is not modified in its core by this subtlety.

2Δ approach

The discretization of the terms a.1 and c.2 follows the same procedure since these terms include a product of two gradients. The focus is put on c.2 for which the discretization is given by:

$$\left[\frac{\partial}{\partial x}\left(\frac{\partial \rho}{\partial x}\frac{\partial \rho u}{\partial x}\right)\right]_i^{2\Delta} = \frac{1}{\Delta x}\left(\left[\frac{\partial \rho}{\partial x}\right]_{i+\frac{1}{2}}^{2\Delta}\left[\frac{\partial \rho u}{\partial x}\right]_{i+\frac{1}{2}}^{2\Delta} - \left[\frac{\partial \rho}{\partial x}\right]_{i-\frac{1}{2}}^{2\Delta}\left[\frac{\partial \rho u}{\partial x}\right]_{i-\frac{1}{2}}^{2\Delta}\right) \tag{7.7a}$$

$$= \frac{1}{\Delta x}\left(\frac{\rho_{i+1}-\rho_i}{\Delta x}\frac{(\rho u)_{i+1}-(\rho u)_i}{\Delta x} - \frac{\rho_i-\rho_{i-1}}{\Delta x}\frac{(\rho u)_i-(\rho u)_{i-1}}{\Delta x}\right) \tag{7.7b}$$

The expression for a.1 simplifies greatly and is obtained by formally replacing ρu by ρ which provides:

$$\left[\frac{\partial}{\partial x}\left(\left(\frac{\partial \rho}{\partial x}\right)^2\right)\right]_i^{2\Delta} = \frac{1}{\Delta x}\left(\left(\frac{\rho_{i+1}-\rho_i}{\Delta x}\right)^2 - \left(\frac{\rho_i-\rho_{i-1}}{\Delta x}\right)^2\right) \tag{7.8}$$

Terms a.2 and c.1 involve an additional product with a non-gradient variable. Term a.2 is easier to handle since it involves only gradient of a conservative variable. Its discretization is:

$$\left[\frac{\partial}{\partial x}\left(\left(\frac{\partial \rho}{\partial x}\right)^2 u\right)\right]_i^{2\Delta} = \frac{1}{\Delta x}\left(\left(\left[\frac{\partial \rho}{\partial x}\right]_{i+\frac{1}{2}}^{2\Delta}\right)^2 u_{i+\frac{1}{2}} - \left(\left[\frac{\partial \rho}{\partial x}\right]_{i-\frac{1}{2}}^{2\Delta}\right)^2 u_{i-\frac{1}{2}}\right) \tag{7.9a}$$

$$= \frac{1}{\Delta x}\left(\left(\frac{\rho_{i+1}-\rho_i}{\Delta x}\right)^2 \frac{(\rho u)_{i+\frac{1}{2}}}{\rho_{i+\frac{1}{2}}} - \left(\frac{\rho_i-\rho_{i-1}}{2\Delta x}\right)^2 \frac{(\rho u)_{i+\frac{1}{2}}}{\rho_{i-\frac{1}{2}}}\right) \tag{7.9b}$$

Given that for a conservative variable a, the value at a cell vertex $i+1/2$ is given by:

$$a_{i+\frac{1}{2}} = \frac{a_{i+1}+a_i}{2} \tag{7.10}$$

the final expression for term a.2 is:

$$\left[\frac{\partial}{\partial x}\left(\left(\frac{\partial \rho}{\partial x}\right)^2 u\right)\right]_i^{2\Delta} = \frac{1}{\Delta x}\left(\left(\frac{\rho_{i+1}-\rho_i}{\Delta x}\right)^2 \frac{(\rho u)_{i+1}+(\rho u)_i}{\rho_{i+1}+\rho_i} - \left(\frac{\rho_i-\rho_{i-1}}{2\Delta x}\right)^2 \frac{(\rho u)_i+(\rho u)_{i-1}}{\rho_i+\rho_{i-1}}\right) \tag{7.11}$$

Starting with the same approach, the discretization of term c.1 becomes:

$$\left[\frac{\partial}{\partial x}\left(\rho\frac{\partial \rho}{\partial x}\frac{\partial u}{\partial x}\right)\right]_i^{2\Delta} = \frac{1}{\Delta x}\left(\rho_{i+\frac{1}{2}}\left[\frac{\partial \rho}{\partial x}\right]_{i+\frac{1}{2}}^{2\Delta}\left[\frac{\partial u}{\partial x}\right]_{i+\frac{1}{2}}^{2\Delta} - \rho_{i-\frac{1}{2}}\left[\frac{\partial \rho}{\partial x}\right]_{i-\frac{1}{2}}^{2\Delta}\left[\frac{\partial u}{\partial x}\right]_{i-\frac{1}{2}}^{2\Delta}\right) \tag{7.12}$$

However, since u is not a conservative variable, the calculation of its gradient at the cell vertices $i \mp 1/2$ is not straightforward but actually given by:

$$\left[\frac{\partial u}{\partial x}\right]_{i+\frac{1}{2}}^{2\Delta} = \frac{1}{\rho_{i+\frac{1}{2}}}\left(\left[\frac{\partial \rho u}{\partial x}\right]_{i+\frac{1}{2}}^{2\Delta} - u_{i+\frac{1}{2}}\left[\frac{\partial \rho}{\partial x}\right]_{i+\frac{1}{2}}^{2\Delta}\right) \tag{7.13a}$$

$$= \frac{2}{\rho_{i+1}+\rho_i}\left(\frac{(\rho u)_{i+1}-(\rho u)_i}{\Delta x} - \frac{(\rho u)_{i+1}+(\rho u)_i}{\rho_{i+1}+\rho_i}\frac{\rho_{i+1}-\rho_i}{\Delta x}\right) \tag{7.13b}$$

Eventually, the full discretized expression of c.1 can be obtained:

$$\begin{aligned}\left[\frac{\partial}{\partial x}\left(\rho\frac{\partial \rho}{\partial x}\frac{\partial u}{\partial x}\right)\right]_i^{2\Delta} =& \frac{1}{\Delta x}\left(\frac{(\rho u)_{i+1}-(\rho u)_i}{\Delta x}\frac{\rho_{i+1}-\rho_i}{\Delta x} - \frac{(\rho u)_{i+1}+(\rho u)_i}{\rho_{i+1}+\rho_i}\left(\frac{\rho_{i+1}-\rho_i}{\Delta x}\right)^2\right.\\ &\left. - \frac{(\rho u)_i-(\rho u)_{i-1}}{\Delta x}\frac{\rho_i-\rho_{i-1}}{\Delta x} + \frac{(\rho u)_i+(\rho u)_{i-1}}{\rho_i+\rho_{i-1}}\left(\frac{\rho_i-\rho_{i-1}}{\Delta x}\right)^2\right)\end{aligned} \tag{7.14}$$

It clearly shows that the divergence of the gradient related terms with the 2Δ approach finally leads to a 3-point stencil.

4Δ *approach*

For term c.2, the 4Δ discretization is given by:

$$\left[\frac{\partial}{\partial x}\left(\frac{\partial \rho}{\partial x}\frac{\partial \rho u}{\partial x}\right)\right]_i^{4\Delta} = \frac{1}{2\Delta x}\left(\left[\frac{\partial \rho}{\partial x}\right]_{i+1}^{4\Delta}\left[\frac{\partial \rho u}{\partial x}\right]_{i+1}^{4\Delta} - \left[\frac{\partial \rho}{\partial x}\right]_{i-1}^{4\Delta}\left[\frac{\partial \rho u}{\partial x}\right]_{i-1}^{4\Delta}\right) \tag{7.15a}$$

$$= \frac{1}{2\Delta x}\left(\frac{\rho_{i+2}-\rho_i}{2\Delta x}\frac{(\rho u)_{i+2}-(\rho u)_i}{2\Delta x} - \frac{\rho_i-\rho_{i-2}}{2\Delta x}\frac{(\rho u)_i-(\rho u)_{i-2}}{2\Delta x}\right) \tag{7.15b}$$

and similarly to the 2Δ approach, the discretization of term a.1 can be inferred from Eq. (7.15b) to get:

$$\left[\frac{\partial}{\partial x}\left(\left(\frac{\partial \rho}{\partial x}\right)^2\right)\right]_i^{4\Delta} = \frac{1}{2\Delta x}\left(\left(\frac{\rho_{i+2}-\rho_i}{2\Delta x}\right)^2 - \left(\frac{\rho_i-\rho_{i-2}}{2\Delta x}\right)^2\right) \tag{7.16}$$

The term a.2 is easier to obtain for the 4Δ approach because the non-conservative variable u is expressed directly at the nodes. Its discretization becomes:

$$\left[\frac{\partial}{\partial x}\left(\left(\frac{\partial \rho}{\partial x}\right)^2 u\right)\right]_i^{4\Delta} = \frac{1}{2\Delta x}\left(\left[\left(\frac{\partial \rho}{\partial x}\right)^2\right]_{i+1}^{4\Delta} u_{i+1} - \left[\left(\frac{\partial \rho}{\partial x}\right)^2\right]_{i-1}^{4\Delta} u_{i-1}\right) \tag{7.17a}$$

$$= \frac{1}{2\Delta x}\left(\left(\frac{\rho_{i+2}-\rho_i}{2\Delta x}\right)^2\frac{(\rho u)_{i+1}}{\rho_{i+1}} - \left(\frac{\rho_i-\rho_{i-2}}{2\Delta x}\right)^2\frac{(\rho u)_{i-1}}{\rho_{i-1}}\right) \tag{7.17b}$$

The discretization of term c.1 requires to evaluate the derivative of u even for the 4Δ approach. The formulation is similar to that of the 2Δ approach given in Eqs. (7.13a)-(7.13b) but is somewhat simpler since the values are evaluated at the nodes rather than the cells center, according to Eqs. (7.18a)-(7.18b).

$$\left[\frac{\partial u}{\partial x}\right]_i^{4\Delta} = \frac{1}{\rho_i}\left(\left[\frac{\partial \rho u}{\partial x}\right]_i^{4\Delta} - u_{i+\frac{1}{2}}\left[\frac{\partial \rho}{\partial x}\right]_i^{4\Delta}\right) \tag{7.18a}$$

$$= \frac{1}{\rho_i}\left(\frac{(\rho u)_{i+1} - (\rho u)_{i-1}}{2\Delta x} - \frac{(\rho u)_i}{\rho_i}\frac{\rho_{i+1} - \rho_{i-1}}{2\Delta x}\right) \tag{7.18b}$$

The discretized expression of term c.1 can thus be written:

$$\begin{aligned}\left[\frac{\partial}{\partial x}\left(\rho\frac{\partial \rho}{\partial x}\frac{\partial u}{\partial x}\right)\right]_i^{4\Delta} = \frac{1}{2\Delta x}\Bigg(&\frac{(\rho u)_{i+2} - (\rho u)_i}{2\Delta x}\frac{\rho_{i+2} - \rho_i}{2\Delta x} - \frac{(\rho u)_{i+1}}{\rho_{i+1}}\left(\frac{\rho_{i+1} - \rho_i}{2\Delta x}\right)^2 \\ &- \frac{(\rho u)_i - (\rho u)_{i-2}}{2\Delta x}\frac{\rho_i - \rho_{i-2}}{2\Delta x} + \frac{(\rho u)_{i-1}}{\rho_{i-1}}\left(\frac{\rho_i - \rho_{i-2}}{2\Delta x}\right)^2\Bigg)\end{aligned} \tag{7.19}$$

Conversely, with the 4Δ approach, the divergence of the gradient related terms eventually leads to a 5-point stencil.

7.1.2.3 Laplacian related terms

The Laplacian related terms already involve a second order derivative term in the corresponding fluxes prior to the evaluation of its divergence. This difficulty is a magnified version of what occurs for the gradients in the fluxes : evaluating numerically the spatial derivatives requires a larger stencil on more points associated with potentially more *gather-scatter* sequences and therefore a bigger computational cost. Besides, an ill-handled stencil, such it is the case with the 4Δ approach can lead to the wrong treatment of short length perturbations.
Given that the Laplacian is a second order derivative, it can only be calculated at the nodes (in opposition to the cell centers) and requires at least a 3-point stencil. This means that evaluating the corresponding divergence afterwards leads to at least a 5-point stencil, the "compressive" strategy of the 2Δ approach in Sec. 6.2.3 cannot be adapted to evaluate at once the divergence of the Laplacian related terms. The calculation of the density Laplacian and the calculation of the divergence in terms d.1 (D.1 in general) and d.2 (D.2 in general) must be treated sequentially.

Evaluation of the density Laplacian

Mathematically, the Laplacian of a variable a is nothing but the divergence of its gradient, i.e $\boldsymbol{\Delta} a = \boldsymbol{\nabla} \cdot (\boldsymbol{\nabla} a)$. As such, to evaluate the density Laplacian at the mesh nodes, the 2Δ and 4Δ approaches can be used as demonstrated in Sec. 6.2.3.2. The corresponding expressions are:

$$\left[\frac{\partial^2\rho}{\partial x^2}\right]_i^{2\Delta} = \frac{\rho_{i+1} - 2\rho_i + \rho_{i-1}}{(\Delta x)^2} \tag{7.20}$$

$$\left[\frac{\partial^2\rho}{\partial x^2}\right]_i^{4\Delta} = \frac{\rho_{i+2} - 2\rho_i + \rho_{i-2}}{(2\Delta x)^2} \tag{7.21}$$

Evaluation of the flux divergence

Knowing the Laplacian at the nodes, the discretization of terms d.1 and d.2 is written following the conventional *Cell-Vertex* methodology, applied for the classic terms, as described in Eq. (7.6).
If the density Laplacian is calculated with the 2Δ approach, the discretization of term d.1 becomes:

$$\left[\frac{\partial}{\partial x}\left(\rho\frac{\partial^2\rho}{\partial x^2}\right)\right]_i^{2\Delta} = \frac{1}{2\Delta x}\left(\rho_{i+1}\left[\frac{\partial^2\rho}{\partial x^2}\right]_{i+1}^{2\Delta} - \rho_{i-1}\left[\frac{\partial^2\rho}{\partial x^2}\right]_{i-1}^{2\Delta}\right) \tag{7.22a}$$

$$= \frac{1}{2\Delta x}\left(\rho_{i+1}\frac{\rho_{i+2} - 2\rho_{i+1} + \rho_i}{(\Delta x)^2} - \rho_{i-1}\frac{\rho_i - 2\rho_{i-1} + \rho_{i-2}}{(\Delta x)^2}\right) \tag{7.22b}$$

and the discretized expression of term d.2 is obtained by replacing the factors ρ_{i+1} and ρ_{i-1} by $(\rho u)_{i+1}$ and $(\rho u)_{i-1}$ to get:

$$\left[\frac{\partial}{\partial x}\left(\rho u\frac{\partial^2\rho}{\partial x^2}\right)\right]_i^{2\Delta} = \frac{1}{2\Delta x}\left((\rho u)_{i+1}\frac{\rho_{i+2} - 2\rho_{i+1} + \rho_i}{(\Delta x)^2} - (\rho u)_{i-1}\frac{\rho_i - 2\rho_{i-1} + \rho_{i-2}}{(\Delta x)^2}\right) \tag{7.23}$$

The final discretization of terms d.1 and d.2 when a 2Δ approach is used to calculate the density Laplacian clearly leads to a 5-point stencil.

If the density Laplacian is calculated with the 4Δ approach, the discretization of term d.1 now becomes:

$$\left[\frac{\partial}{\partial x}\left(\rho\frac{\partial^2\rho}{\partial x^2}\right)\right]_i^{4\Delta} = \frac{1}{2\Delta x}\left(\rho_{i+1}\left[\frac{\partial^2\rho}{\partial x^2}\right]_{i+1}^{2\Delta} - \rho_{i-1}\left[\frac{\partial^2\rho}{\partial x^2}\right]_{i-1}^{2\Delta}\right) \tag{7.24a}$$

$$= \frac{1}{2\Delta x}\left(\rho_{i+1}\frac{\rho_{i+3} - 2\rho_{i+1} + \rho_{i-1}}{(2\Delta x)^2} - \rho_{i-1}\frac{\rho_{i+1} - 2\rho_{i-1} + \rho_{i-3}}{(2\Delta x)^2}\right) \tag{7.24b}$$

and the discretized expression for term d.2 is:

$$\left[\frac{\partial}{\partial x}\left(\rho u\frac{\partial^2\rho}{\partial x^2}\right)\right]_i^{4\Delta} = \frac{1}{2\Delta x}\left((\rho u)_{i+1}\frac{\rho_{i+3} - 2\rho_{i+1} + \rho_{i-1}}{(2\Delta x)^2} - (\rho u)_{i-1}\frac{\rho_{i+1} - 2\rho_{i-1} + \rho_{i-3}}{(2\Delta x)^2}\right) \tag{7.25}$$

7.1.3 Comparisons between the 2Δ and 4Δ discretizations

The multiple strategies for the discretization of the high order capillary terms are compared on one-dimensional and two-dimensional cases where a liquid droplet is convected at a constant speed into its own vapor in isothermal and non-isothermal settings.
Depending on whether the 2Δ or the 4Δ approach is used to calculate the divergence of the non-conventional capillary terms, eight different configurations, summarized in Tab. 7.2, are created. For the sake of consistency, terms appearing in both the momentum and energy equations are discretized using the same approach. The distinction between the two possible ways to write the energy equation, already addressed with Eq. (7.4) and in Tab. 7.1 (term C) has been made in the simulations. To that effect, all configurations in Tab. 7.2 have been tested twofold, a first time using the discretization of $\boldsymbol{\nabla}\cdot[\rho\boldsymbol{\nabla}\rho\boldsymbol{\nabla}\cdot\mathbf{v}]$ (term c.1 in Tab. 7.1) and a second time using the discretization of $\boldsymbol{\nabla}\cdot[\boldsymbol{\nabla}\rho\boldsymbol{\nabla}\cdot(\rho\mathbf{v})]$ (term c.2 in Tab. 7.1), as recalled by the use of "OR" in the leftmost cell in the last row of Tab. 7.2.
Depending on the formulation used (c.1 or c.2), the eight configurations (a) to (h) have been added the index '.1' or '.2' accordingly. It led to a total of sixteen configurations. One should notice that the previous distinction does not apply for isothermal settings where the energy equation is not solved. It is also important to mention that these two possible choices for the energy equation have not led to any substantial difference in the one dimensional simulations, all other settings remaining equal.

Configuration	$(a.1)$ or $(a.2)$	$(b.1)$ or $(b.2)$	$(c.1)$ or $(c.2)$	$(d.1)$ or $(d.2)$	$(e.1)$ or $(e.2)$	$(f.1)$ or $(f.2)$	$(g.1)$ or $(g.2)$	$(h.1)$ or $(h.2)$
$\boldsymbol{\nabla}\cdot\left[(\boldsymbol{\nabla}\rho)^2\,\underline{\underline{\mathbf{I}}}\right]$ and $\boldsymbol{\nabla}\cdot\left[\mathbf{v}\,(\boldsymbol{\nabla}\rho)^2\right]$	4Δ	2Δ	4Δ	4Δ	2Δ	2Δ	4Δ	2Δ
$\boldsymbol{\nabla}\cdot[\boldsymbol{\nabla}\rho\otimes\boldsymbol{\nabla}\rho]$ and $\boldsymbol{\nabla}\cdot[(\boldsymbol{\nabla}\rho\otimes\boldsymbol{\nabla}\rho)\cdot\mathbf{v}]$	4Δ	4Δ	2Δ	4Δ	2Δ	4Δ	2Δ	2Δ
$\boldsymbol{\nabla}\cdot[\rho\boldsymbol{\nabla}\rho\boldsymbol{\nabla}\cdot\mathbf{v}]$ OR $\boldsymbol{\nabla}\cdot[\boldsymbol{\nabla}\rho\boldsymbol{\nabla}\cdot(\rho\mathbf{v})]$	4Δ	4Δ	4Δ	2Δ	4Δ	2Δ	2Δ	2Δ

Table 7.2: *List of tested configurations depending on the discretization of the capillary terms*

The relevant parameters for the different simulations can be found in Tab. 7.3. The initially isothermal nitrogen droplet, in diameter, is about ten times wider than the interface and the domain is three times the size of the droplet. A purposely high number of points has been used for the mesh so as to mitigate possible numerical errors due to the precision of the numerical scheme and focus the discussion only on the discretization strategy. For the same reason, no filtering nor artificial viscosity has been used. When possible, the simulation is performed so as to allow the droplet to perform one complete crossing of the domain. When the crossing has been completed by the droplet, the progression is by convention set to 100%.

T	113.57 K	λ	$1.0 \cdot 10^{-10}$ m$^7 \cdot$ kg$^{-1} \cdot$ s^{-2}	σ	3.26 N $\cdot$ m
P^{sat}	18.15 bar	points in int.	≈ 30	w	4.42 μm
ρ_l	542.1 kg $\cdot$ m^{-3}	equations	mass + mom. + ener.	u	10 m $\cdot$ s^{-1}
ρ_v	80.3 kg $\cdot$ m^{-3}	diffusion	Chung	CFL	0.95

Table 7.3: *Simulation parameters used with N_2 for one and two dimensional comparisons for the implementation of the SG model in the solver AVBP*

7.1.3.1 One-dimensional cases

Isothermal case

Fig. 7.1 shows the resulting density, pressure, temperature and velocity profiles after one attempted crossing of the domain with a fixed temperature. All configurations have led to a successful simulation with very limited numerical errors merely noticeable on the velocity profiles. In particular, configurations $(a.1)$ and $(d.1)$ display very clean profiles with an error on the velocity three order of magnitude lower compared to the other configurations. This case isothermal does not permit to discriminate between the different discretization strategies.

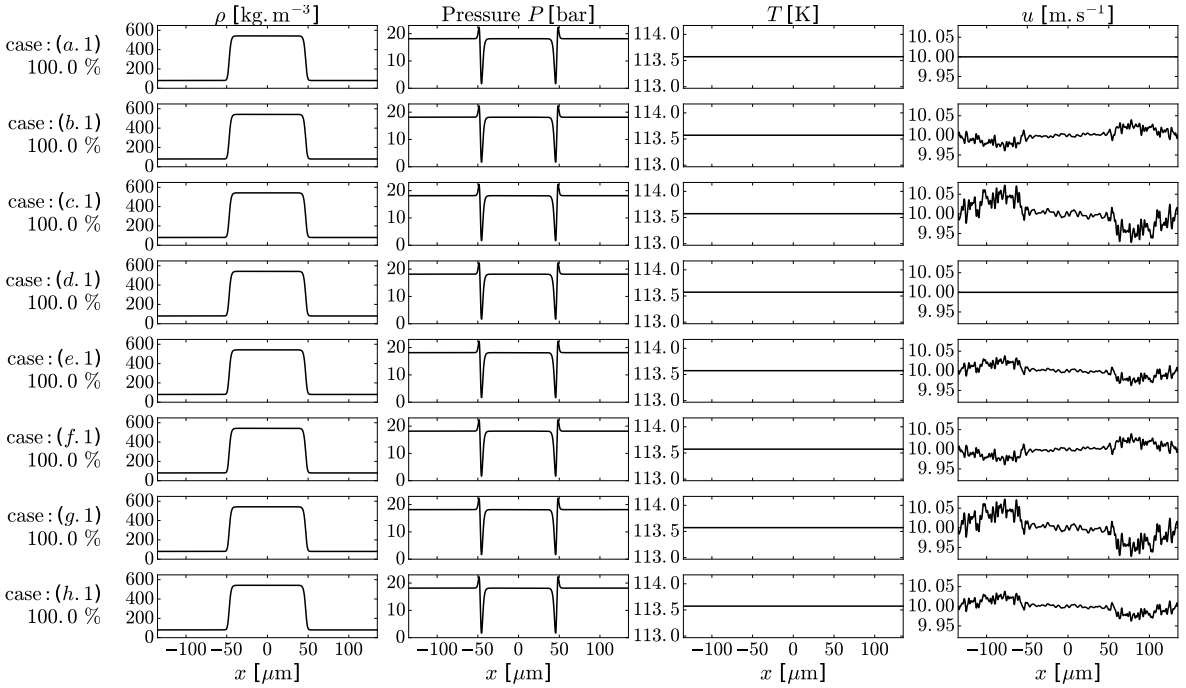

Figure 7.1: *Final density, pressure, temperature and velocity profiles of one dimensional isothermal nitrogen droplets after one crossing of the periodic domain to compare different discretizations of capillary fluxes terms*

Non-isothermal case

Equivalent results are presented in Fig. 7.2 but in a non-isothermal setting for which the different configurations have led to a wide variety of outcomes.

Firstly, configurations $(c.1)$, $(e.1)$ and $(f.1)$ (it is too be understood that configurations $(c.2)$, $(e.2)$ and $(f.2)$ have led to the same outcome) have crashed in the early instants of the simulation with very large undershoots and overshoots visible in the pressure, temperature and velocity profiles. Secondly, configurations $(b.1)$, $(g.1)$ and $(h.1)$ (likewise configurations $(b.2)$, $(g.2)$ and $(h.2)$) have led to successful simulations with small errors on the velocity profile comparable to that in the isothermal setting, accompanied however with slight undershoots and overshoots in the temperature. Finally, configurations $(a.1)$ and $(d.1)$ (likewise configurations $(a.2)$ and $(d.2)$) have also led to successful simulations. Very minor undershoots and overshoots can be noticed in the temperature profiles but the velocity profiles are mostly as precise as they were in the isothermal setting. At that point, configurations $(c.1)/(c.2)$, $(e.1)/(e.1)$ and $(f.1)/(f.2)$ can be discarded as they already fail for one dimensional simulations.

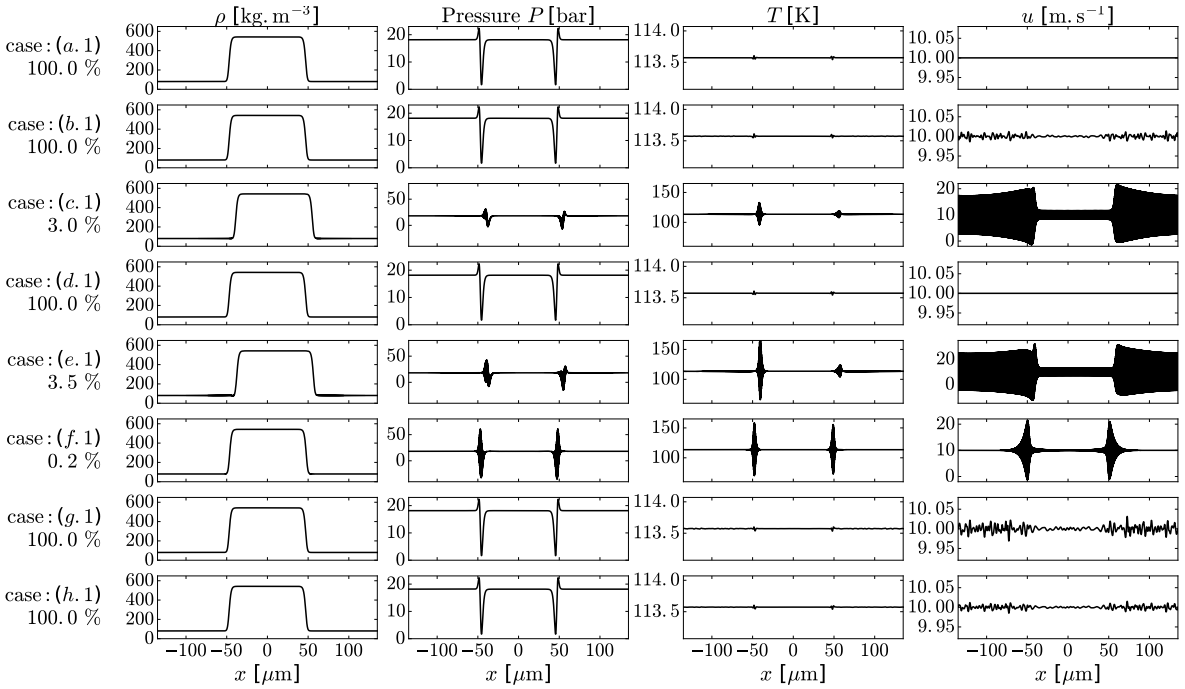

Figure 7.2: *Final density, pressure, temperature and velocity profiles of one dimensional non-isothermal nitrogen droplets after one crossing of the periodic domain to compare different discretizations of capillary fluxes terms*

7.1.3.2 Two-dimensional cases

To further the analysis, two dimensional cases are also presented using the same configurations and methodology. Only the configurations that have already come out successful in one dimension are considered. It is also important to notice that for two dimensional cases, differences in the results appear among paired configurations. For instance, configurations $(a.1)$ and $(a.2)$ no longer lend the same results, and likewise for the other pairs. In that respect, the more relevant results from the other configurations in the pairs are also presented.

Isothermal case

Figs. 7.3 and 7.4 show the density and pressure profiles respectively when an isothermal setting is used. These results allow to discard more configurations, namely $(b.1)$, $(g.1)$, $(g.2)$ and $(h.1)$ (configurations $(b.2)$ and $(h.2)$, not shown here, have led to results similar to that of configurations $(b.1)$ and $(h.1)$ respectively).

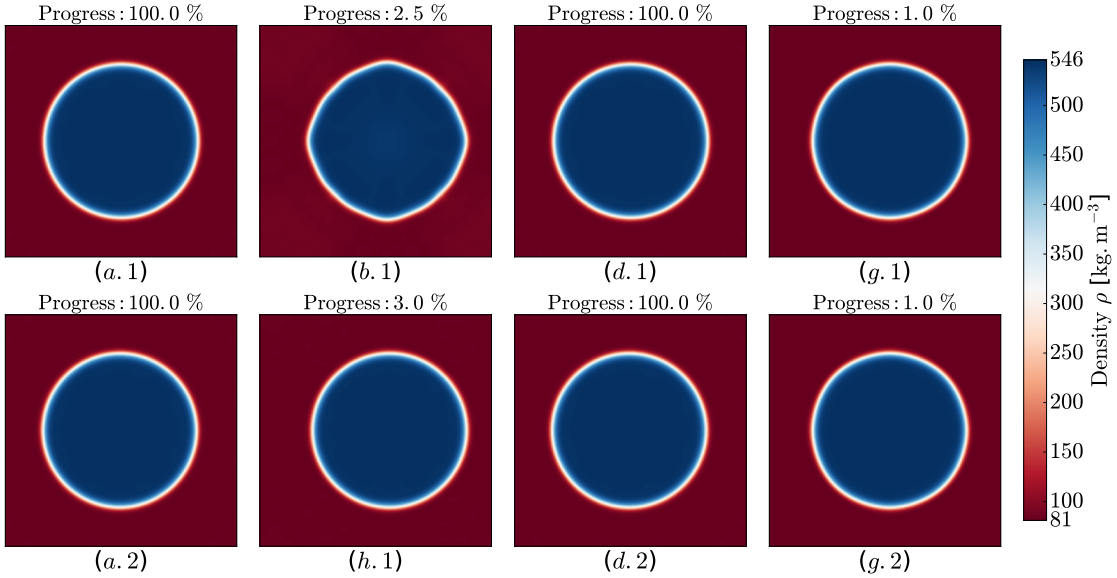

Figure 7.3: *Density profiles of two dimensional isothermal nitrogen droplets after one crossing of the periodic domain to compare different discretizations of capillary fluxes terms*

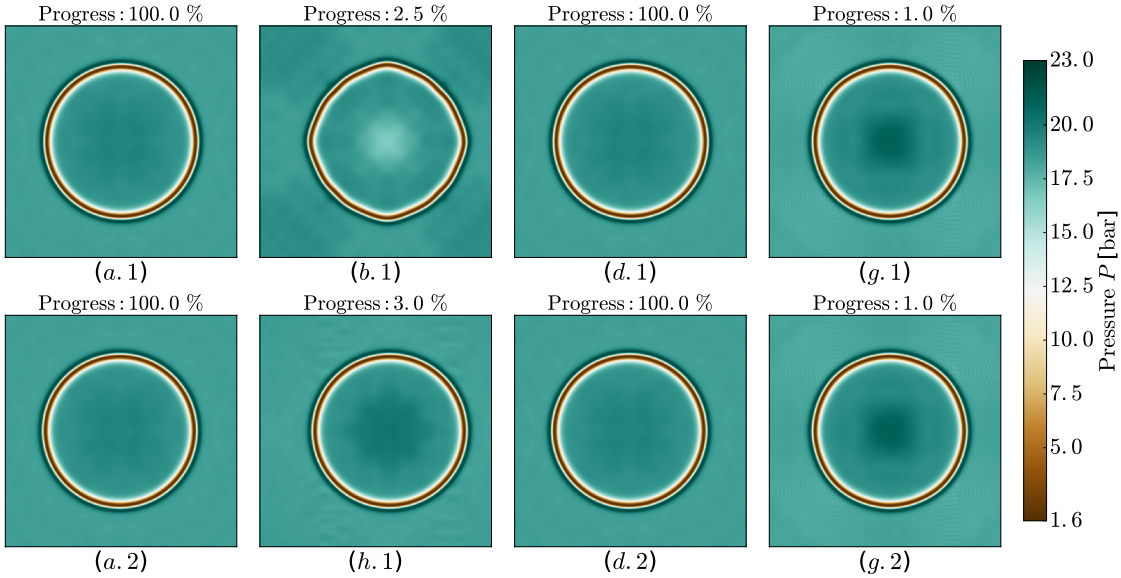

Figure 7.4: *Pressure profiles of two dimensional isothermal nitrogen droplets after one crossing of the periodic domain to compare different discretizations of capillary fluxes terms*

Non-isothermal case

Confronting the four remaining configurations in a non-isothermal setting allows to confirm this hint. The results given in Fig. 7.5 show the success of configurations (a.1) and (a.2) and the crash of configurations (d.1) and (d.2) in the very early moments of the simulation. From Tab. 7.2, the pairs (a) and (d) differs in their discretization of the last capillary term C in Tab. 7.1: a 4Δ approach for pair (a) and a 2Δ for pair (d). This means that this study advocates for a full consistency in the discretization of the three capillary terms since configurations (a.1) and (a.2) use a 4Δ approach for all three terms.

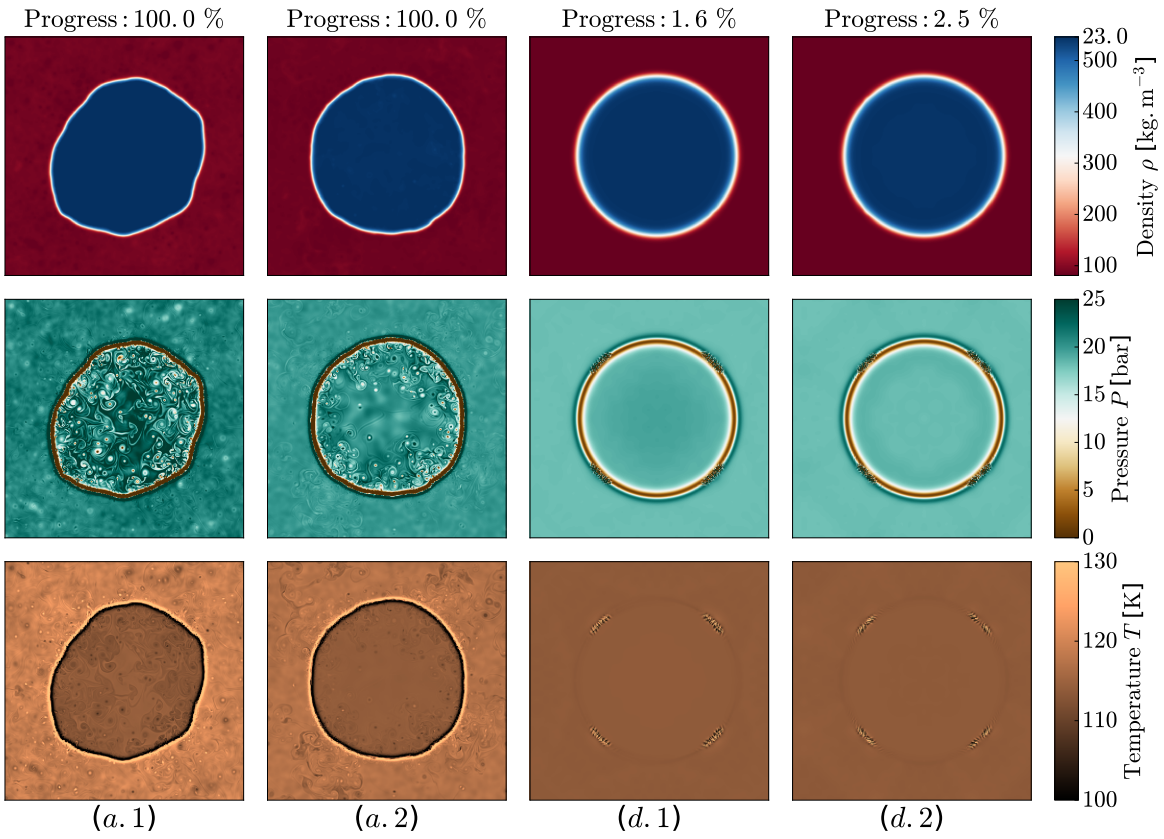

Figure 7.5: *Density, pressure and temperature profiles of two dimensional non-isothermal nitrogen droplets after one crossing of the periodic domain to compare different discretizations of capillary fluxes terms*

Although the result could lead to favor configuration (a.2) over configuration (a.1), the quality of the result actually depends on the physical case to be simulated and is never substantial enough to discriminate one configuration as the best. Thus, to retain the partial symmetry in the momentum and energy equations, configuration (a.1) has been used by default even if this choice is, to a large extent, arbitrary.

7.1.3.3 Impact of the Laplacian discretization

Finally, the impact of the method used to discretize the density Laplacian has also been tested. To better capture this impact, a lesser resolution of 10 points in the interface has been used.

Moreover, the impact on the numerical stability is such that it can be observed in a static setting. As such, the results in Fig. 7.6 are given for a droplet set still with no initial velocity.

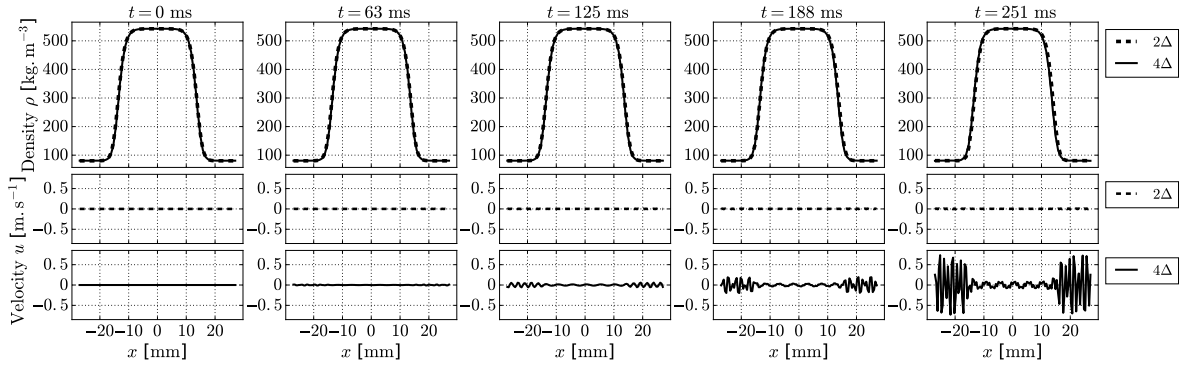

Figure 7.6: *Time evolution of density and velocity profiles for a one dimensional isothermal oxygen droplet using* 2Δ *and* 4Δ *configurations for the calculation of the Laplacian terms*

After simulation, the droplet is expected to remain immobile, what indeed happens during the early instants of the simulation. However, as time progresses, the perturbations created at the beginning start to amplify in the 4Δ configuration what eventually leads to the crash of the simulation. The same perturbations in the 2Δ configuration are simply stabilized and longer simulations (up to ten times the duration reached with the 4Δ configuration) showed no further amplification of the perturbations.
It should be noted that the results in Fig. 7.6 have been obtained using the $(a.1)$ configuration that has been previously determined to be the best. However, the $2\Delta/4\Delta$ discretization of the Laplacian term has also been tested with other configurations and has only confirmed the initial observations. In particular, no configuration has led to better results when the 4Δ discretization has been used for the Laplacian term. This is the reason why all the results shown in Figs. 7.1, 7.2, 7.3, 7.4, 7.5 have been obtained using the 2Δ discretization for the Laplacian term.

7.1.3.4 Conclusion on the discretization strategies

One clear outcome of the previous comparisons is the necessity to discretized the Laplacian using the 2Δ-like approach prior to calculating the divergence of the different fluxes which eventually leads to a 5-point stencil. This applies independently of the strategies used to discretize the divergence for the rest of the capillary fluxes.

The one and two-dimensional comparisons seem to point out that terms A.1 and A.2 involving the squared density gradient and terms B.1 and B.2 involving the self-tensor product of the density gradient must be discretized using the same strategy, which is a sound result given the formal proximity between these two terms. More precisely, the configurations that performed the poorest are specifically those using a $2\Delta/4\Delta$ mix for terms A.1-A.2 and B.1-B.2, i.e. (b), (c), (f) and (g), especially (c) and (g) for which the 2Δ approach is used to discretize the squared density gradient. Between the four remaining, only configurations (a) and (d) provided stable calculations, despite configurations (e) and (h) having somewhat better results than the totally falling configurations previously described. This is concordant with the fact

that using a 2Δ approach leads to the poorest results, even among the already poor ones. This carried over to the better cases as configurations (e) and (h) uses a 2Δ approach for terms A.1-A.2 and B.1-B.2. Only the configurations (a) and (d) where a 4Δ approach is used, for all terms A.1, A.2, B.1 and B.2, have proven to be stable in two-dimensional isothermal settings. Removing the isothermal hypothesis has allowed to observe the impact of the discretization of the third class of terms C.1, C.2 as configuration (d), which uses a 2Δ approach, has led to unsuccessful simulations. Finally, only the configurations where a 4Δ approach is used to discretize all three first order capillary terms.

These results, at first glance, can seem contradictory with the theoretical motivations behind the introduction of the 2Δ approach. However, when considering the divergence of the fluxes involving the density Laplacian (terms D.1, D.2), of which discretization is necessarily done on a 5-point stencil, the fact that the 4Δ approach has to be used for the divergence of the gradient related fluxes (terms A.1, A.2, B.1 and B.2), which also leads to a 5-point stencil, eventually appears as a matter of numerical consistency.
As already mentioned, it should be noted that the discretization strategy used for the flux divergence relative to the root term C does not seem to have an impact on the stability of the calculation. This is the case whatever form of this term is used between C.1 and C.2. This observation, for which no satisfactory explanation has been found, further cements the peculiar nature of this term beyond the fact that it only appears, in an asymmetric fashion, in the energy equation. With no additional information, the formulation with term C.2, easier to implement, has been selected and the choice has been made, preserving consistency, to discretize it using a 4Δ approach.

For the remainder of the document, the strategy used to discretize the divergence of the capillary terms is the following. The density Laplacian is calculated at the mesh nodes using the 2Δ-like method presented previously. Its divergence is obtained following the conventional transport method of Central Difference. The divergence of the terms with density gradient, including the peculiar term unique to the energy equation, is obtained with a 4Δ approach. Moreover, when not mentioned otherwise, the 3^{rd} order Galerkin-Runge-Kutta (GRK) AVBP scheme is used for the convective fluxes.

7.2 Characterization of the Second Gradient equations

Besides providing insight on the proper way to discretized them, a systematic analysis of the equations can also permit to unveil elements indispensable to a successful simulation such as their well-posedness, the actual existence of solutions, the best suited numerical schemes to solve them, the proper method to enforce boundary conditions if needed and the presence of eventual stability criteria.

A substantial amount of studies regarding the well posedness of the Korteweg model and the existence of affiliated solutions have been proposed in the last twenty years. In Gavrilyuk and Gouin (1998), the existence of a symmetric form of the equation has been proven in the one-dimensional inviscid barotropic case. For the isothermal inviscid case, the authors in

Benzoni-Gavage et al. (2006) have shown that the system becomes Hamiltonian and admits traveling solutions. Moreover, starting from equilibrium profiles, the well-posedness has been proven for small enough perturbations in one dimension. The result has been extended to multidimentional cases, still for isothermal flows, in Benzoni-Gavage et al. (2007). The stability of steady states, steady waves and traveling waves has also been studied in Benzoni-Gavage et al. (2007). The existence of global weak solutions in one and two dimensional cases for isothermal has been proven in Haspot (2008). In Charve and Haspot (2013), the authors have proven the existence of global strong solutions to the Navier-Stokes Kortewegg system for isothermal flows in one dimension. More importantly, for the specific expression of the pressure $P = a\rho^\gamma$ where ρ is the density, a and γ are strictly positive constant with $\gamma > 1$, in the limit of a vanishing viscosity and capillarity, they have proven that the system consistently degenerates into the classic compressible Euler system. For one and two dimensional settings, the existence and uniqueness of global and stable solutions near equilibrium has been proven in Kotschote (2014) even for non-isothermal flows. Other associated results can be found in Bresch et al. (2008); Audiard (2010); Benzoni-Gavage (2010); Höwing (2011); Freistühler and Kotschote (2017); Paddick (2017)
Despite their fundamental importance in the understanding of the capillary model of Korteweg, these studies which are usually addressing the isothermal and thus limited system, do not provide practical tools that can be used to when trying to numerically solve the associated equations.

The question of the numerical scheme has not been addressed beyond the study presented in Sec. 7.1. In that prospect, the starting choice for this doctoral study to take advantage of the highly qualified solver AVBP also came with the drawback of limiting the options regarding the numerical schemes. The Central Difference and the Galerkin Runge-Kutta schemes have been used preferentially.

In Sec. 7.2.1, the system is studied to determine its nature and eventually extract its characteristics. Classically, this information proves useful to answer interrogations regarding boundary conditions and stability criteria, in particular for hyperbolic systems where these information can readily be inferred from the system characteristics. The limited success of this attempt has led to the development of a more practical strategy to treat the boundary conditions in a characteristic fashion which is presented in Sec. 7.2.2. A time step condition is also extracted in Sec. 7.2.3 using a series of numerical experiments in front of the lack of theoretical results.

7.2.1 Nature of the equations

7.2.1.1 Methodology for the studies of PDEs

In Hirsch (2007), the author lays down a methodology to determine the nature of a system of partial differential equations. The purpose of the next paragraphs is to apply this methodology to the equation system described by the SG model. To that effect, the key steps of the methodology are firstly recalled. A few examples are then provided for simple classic equations to better demonstrate the application of said methodology.

General methodology

If one considers a system of K equations with L variables $(v_1, \cdots, v_L)$ that depends on M independent variables $(x_1, \cdots, x_M)$, the corresponding system of partial differential equations, of order at most n, can be written:

$$f_k\left(x_1, \cdots, x_M, v_1, \cdots v_n, \frac{\partial v_1}{\partial x_1}, \cdots, \frac{\partial v_i}{\partial x_j}, \cdots, \frac{\partial v_L}{\partial x_M}, \cdots, \frac{\partial^2 v_1}{\partial x_1 x_2}, \cdots, \frac{\partial^t v_j}{\partial x_1^{n_1} x_M^{n_M}}\right) = 0 \tag{7.26}$$

where $n_1 + \cdots + n_M = t$ with $t = 1, \cdots, n$ and where $(f_k)_{k=1,\cdots,K}$ are arbitrary functions. If all $(f_k)_{k=1,\cdots,K}$ are linear, the system of PDEs is said to be linear as well, but this condition is not systematically satisfied in practice.

The first step of Hirsch's methodology consists in transforming the very generic formulation of the system in Eq. (7.26) into a system of quasi-linear differential equations. To that effect, a vector set of N variables $\mathbf{U} = (u_1, \cdots, u_N)^{\mathrm{T}}$ must be selected to arrive to the new formulation:

$$\sum_{i=1}^{M} \boldsymbol{A}_i(\mathbf{U}) \frac{\partial \mathbf{U}}{\partial x_i} = \mathbf{Q}(\mathbf{U}) \tag{7.27}$$

where $(\boldsymbol{A}_i)_{i=1,\cdots,M}$ are $N \times N$ matrices and $\mathbf{Q}$ is a N-sized vector. the important features of the system in Eq. (7.27) are that only first order derivatives of the vector variables $\mathbf{U}$ are involved and that matrices $(\boldsymbol{A}_i)_{i=1,\cdots,M}$ and vector $\mathbf{Q}$ only depend on $\mathbf{U}$ and not its derivatives. As shown in the later examples, the obtaining of Eq. (7.27) often calls for a regularization procedure when higher than first order derivatives of variables in $(v_1, \cdots, v_L)$ are involved. The regularization implies to use partial derivatives of $(v_l)_{l=1,\cdots,L}$ as elements of $\mathbf{U}$, for instance $\partial v_1/\partial x_1$ or $\partial^2 v_2/(\partial x_2 \partial x_4)$.

The second step of Hirsch's methodology consists in determining the eigenvalues of the homogeneous system where the right-hand side member $\mathbf{Q}(\mathbf{U})$ is discarded. The objective is thus to find the vectors $\mathbf{L} = (l_1, \cdots, l_M)^{\mathrm{T}}$ such as:

$$\det\left(\sum_{i=1}^{M} l_i \boldsymbol{A}_i\right) = 0 \tag{7.28}$$

The solutions $\mathbf{L}$ must be linearly independent to be considered as distinct.

A solution vector $\mathbf{L}$ of which components are all real is associated to an hyperbolic characteristic, i.e. a system of advection equations can be extracted from the system. A solution vector $\mathbf{L}$ of which components are complex with a non-zero imaginary part is associated to an elliptic characteristic, i.e. a system of diffusion equations can be extracted from the system.
Depending on the outcome of the second step, the conclusions on the system are different. If N characteristics are found and all of them are associated to hyperbolic characteristics, the system is said to be hyperbolic.
If N characteristics are found and all of them are associated to elliptic characteristics, the system is said to be elliptic.

If N characteristic are found and are related to both hyperbolic and elliptic characteristic, the system is said to be hybrid and must be treated on a case to case basis.
In some cases, less than N characteristics are found, the system in thus said to be parabolic. This case often occurs when one of the solving variables v_i lacks a partial derivative relatively to one describing variable x_j, in which case the regularization usually leads to a loss of one or more characteristics.

Preliminary examples

To offer a better insight into the mechanics of the methodology, the latter is applied to classic PDEs.

Wave equation

The one dimensional wave equation is given by Eq. (7.29) where c is a constant. It is a second order PDE in both time t and space x.

$$\frac{\partial^2 v}{\partial t^2} = c^2 \frac{\partial^2 v}{\partial x^2} \tag{7.29}$$

Firstly, the equation must be transformed into a first order system of PDEs. A regularization is needed since derivatives higher than the first order are involved. To that effect, the variable vector $\mathbf{U}$ is introduced as follows:

$$\mathbf{U} = \left(\frac{\partial v}{\partial t}, \frac{\partial v}{\partial x} \right)^{\mathrm{T}} \tag{7.30}$$

Using these new notations, Eq. (7.29) can be written in the new form:

$$\frac{\partial U_1}{\partial t} - c^2 \frac{\partial U_2}{\partial x} = 0 \tag{7.31}$$

Schwarz's theorem, which states that $\partial^2 v/(\partial t \partial x) = \partial^2 v/(\partial x \partial t)$, allows to write:

$$\frac{\partial U_1}{\partial x} - \frac{\partial U_2}{\partial t} = 0 \tag{7.32}$$

Eventually the system becomes:

$$\begin{pmatrix} 1 & 0 \\ 0 & 1 \end{pmatrix} \frac{\partial}{\partial t} \begin{pmatrix} U_1 \\ U_2 \end{pmatrix} + \begin{pmatrix} 0 & -c^2 \\ -1 & 0 \end{pmatrix} \frac{\partial}{\partial x} \begin{pmatrix} U_1 \\ U_2 \end{pmatrix} = 0 \tag{7.33}$$

The problem to solve is then to find the couples (l_1, l_2) such as:

$$\det \left(l_1 \begin{pmatrix} 1 & 0 \\ 0 & 1 \end{pmatrix} + l_2 \begin{pmatrix} 0 & -c^2 \\ -1 & 0 \end{pmatrix} \right) = \begin{vmatrix} l_1 & -l_2 c^2 \\ -l_2 & l1 \end{vmatrix} = l_1^2 - l_2^2 c^2 = 0 \tag{7.34}$$

The solutions are given by $l_1 = \pm c l_2$, i.e. the solutions vectors $(c, 1)$ and $(-c, 1)$. Both solutions are real, the system is hyperbolic and displays two characteristic waves traveling upwards

and backwards at velocity c.

Laplace's equation

The two dimensional Laplace equation is given by:

$$\frac{\partial^2 v}{\partial x^2} + \frac{\partial^2 v}{\partial y^2} = 0 \tag{7.35}$$

It is also a second order PDE, which means a regularization is also needed to transform it into a first order system. The variable vector used to that effect is:

$$\mathbf{U} = \left(\frac{\partial v}{\partial x}, \frac{\partial v}{\partial y} \right)^{\mathrm{T}} \tag{7.36}$$

The new notations and Schwarz's theorem allow to write the system:

$$\frac{\partial U_1}{\partial x} + \frac{\partial U_2}{\partial y} = 0 \tag{7.37}$$

$$\frac{\partial U_1}{\partial y} - \frac{\partial U_2}{\partial x} = 0 \tag{7.38}$$

The problem to solve is then to find the couples (l_1, l_2) such as:

$$\det \left(l_1 \begin{pmatrix} 1 & 0 \\ 0 & 1 \end{pmatrix} + l_2 \begin{pmatrix} 0 & 1 \\ -1 & 0 \end{pmatrix} \right) = \begin{vmatrix} l_1 & l_2 \\ -l_2 & l1 \end{vmatrix} = l_1^2 + l_2^2 = 0 \tag{7.39}$$

The solutions are given by $l_1 = \pm i l_2$ with $i^2 = -1$, i.e. the solutions vectors $(1, i)$ and $(1, -i)$. Both solutions have non-real component, the system is elliptic. The absence of intrinsic propagating waves makes the elliptic equations better suited to describe static or steady-state systems.

Heat equation

The one dimensional heat equation is given by Eq. (7.40) where k is a strictly positive constant.

$$\frac{\partial v}{\partial t} = k \frac{\partial^2 v}{\partial x^2} \tag{7.40}$$

It is a PDE of the first order in time t but of the second order in space x. This asymmetry between the variables t and x is most often the cause for the loss of one or more characteristics. Indeed, a regularization is required to handle the second order space derivative, the variable vector $\mathbf{U}$ thus must be:

$$\mathbf{U} = \left(v, \frac{\partial v}{\partial x} \right)^{\mathrm{T}} \tag{7.41}$$

which leads Eq. (7.40) to be written:

$$\frac{\partial U_1}{\partial t} - k \frac{\partial U_2}{\partial x} = 0 \tag{7.42}$$

Another equation is required to complete the system. The differential relation between U_1 and U_2 is trivially given by:

$$\frac{\partial U_1}{\partial x} = U_2 \tag{7.43}$$

This equation does not involve the time derivative of U_2 leading to a formal asymmetry. If one wishes to introduce the time derivative of U_2, the following relation can be used:

$$\frac{\partial U_2}{\partial t} = \frac{\partial}{\partial t}\left(\frac{\partial v}{\partial x}\right) = \frac{\partial^2 u}{\partial t x} = \frac{\partial}{\partial x}\left(\frac{\partial v}{\partial t}\right) = k\frac{\partial}{\partial x}\left(k\frac{\partial^2 v}{\partial t x}\right) = k\frac{\partial^3 v}{\partial x^3} \tag{7.44}$$

However, this new relation leads to the appearance of a third order spatial derivative of v which would require a new regularization with the introduction a new variable $U_3 = \partial^2 v/\partial x^2$ that would also require a new equation for its time derivative, and so on. A vicious circle thus appears if one tries to overcome the initial asymmetry in that fashion. The only solution is to settle with the initial Eq. (7.43) to get to the system:

$$\begin{pmatrix} 1 & 0 \\ 0 & 0 \end{pmatrix} \frac{\partial}{\partial t}\begin{pmatrix} U_1 \\ U_2 \end{pmatrix} + \begin{pmatrix} 0 & -k \\ 1 & 0 \end{pmatrix} \frac{\partial}{\partial x}\begin{pmatrix} U_1 \\ U_2 \end{pmatrix} = \begin{pmatrix} 0 \\ U_2 \end{pmatrix} \tag{7.45}$$

The problem from the homogeneous system is then:

$$\det\left(l_1\begin{pmatrix} 1 & 0 \\ 0 & 0 \end{pmatrix} + l_2\begin{pmatrix} 0 & -k \\ 1 & 0 \end{pmatrix}\right) = \begin{vmatrix} l_1 & -l_2 k \\ -l_2 & 0 \end{vmatrix} = -k l_2^2 = 0 \tag{7.46}$$

The system, of size 2, is of rank 1 since $(0, 0)$ is a valid solution. The system is parabolic. Additionally, the other solution is of the form $(a, 0)$ with a a non-zero real. In general, parabolic equations are harder to handle when compared to the hyperbolic and elliptic ones. In particular, they often tend to be not well-posed and the existence and unicity of their solution is difficult to assess.

Euler equations

To complete the example, the case of the one-dimensional Euler equations, given in Eqs. (7.47a)-(7.47c), is also investigated.

$$\frac{\partial \rho}{\partial t} = -\frac{\partial(\rho u)}{\partial x} \tag{7.47a}$$

$$\frac{\partial(\rho u)}{\partial t} = -\frac{\partial}{\partial x}\left[\rho u^2 + P\right] \tag{7.47b}$$

$$\frac{\partial(\rho e)}{\partial t} = -\frac{\partial}{\partial x}\left[(\rho e + P)\, u\right] \tag{7.47c}$$

It is shown in Sec. 6.3.2 that the previous system can be written in the pseudo-linear form of Eq. (7.48) with the variable vector $\mathbf{U} = (\rho, \rho u, \rho e)^{\mathrm{T}}$ and matrix $\boldsymbol{A}$ expressed in Eq. (6.51).

$$\frac{\partial \mathbf{U}}{\partial t} = \boldsymbol{A}(\mathbf{U})\frac{\partial \mathbf{U}}{\partial x} \tag{7.48}$$

Eq. (7.48) is particular form of Eq. (7.27), that simplifies here into

$$\boldsymbol{A}_t\left(\mathbf{U}\right)\frac{\partial \mathbf{U}}{\partial t}+\boldsymbol{A}_x\left(\mathbf{U}\right)\frac{\partial \mathbf{U}}{\partial x}=0 \tag{7.49}$$

where $\boldsymbol{A}_t=\boldsymbol{I}_3$ is the identity matrix and $\boldsymbol{A}_x=-\boldsymbol{A}$.
The problem in Eq. (7.28) becomes.

$$\det\left(l_1\boldsymbol{I}_3-l_2\boldsymbol{A}\right)=0 \tag{7.50}$$

Provided that $l_2\neq 0$, the variable $\alpha=l_1/l_2$ can be introduced and the problem finally writes:

$$\det\left(A-\alpha\boldsymbol{I}_3\right)=0 \tag{7.51}$$

From Eq. (7.51), it appears clearly that for the Euler equations in one dimension, applying Hirsh's methodology is equivalent to finding the eigenvalues of matrix $\boldsymbol{A}$ and its eigenvectors, which is done in details in Sec. 6.3.2 to derive the characteristic boundary conditions.

7.2.1.2 Application to the Second Gradient equations

To simplify the developments, a one-dimensional setting is used and the diffusion effects (viscosity, conduction) are omitted. The equations to solve are given by Eqs. (7.52a)-(7.52c) and form a third order non-linear PDE system.

$$\begin{cases}\dfrac{\partial \rho}{\partial t}=-\dfrac{\partial}{\partial x}\left[\rho u\right] & \text{(7.52a)}\\[2ex] \dfrac{\partial \rho u}{\partial t}=-\dfrac{\partial}{\partial x}\left[\rho u^2+P_0+\dfrac{\lambda}{2}\left(\dfrac{\partial \rho}{\partial x}\right)^2-\lambda\rho\dfrac{\partial^2\rho}{\partial x^2}\right] & \text{(7.52b)}\\[2ex] \dfrac{\partial \rho e}{\partial t}=-\dfrac{\partial}{\partial x}\left[\left(\rho e+P_0\right)u+\lambda\dfrac{\partial \rho}{\partial x}\dfrac{\partial \rho u}{\partial x}-\dfrac{\lambda}{2}\left(\dfrac{\partial \rho}{\partial x}\right)^2 u-\lambda\dfrac{\partial^2\rho}{\partial x^2}\rho u\right] & \text{(7.52c)}\end{cases}$$

To pseudo-linearize the system, a regularization must be performed beforehand since first and second order derivatives already appear in the fluxes. The chosen variables vector $\mathbf{U}$ is given by:

$$\mathbf{U}=\left(\rho,\rho u,\rho e,\frac{\partial \rho}{\partial x},\frac{\partial \rho u}{\partial x},\frac{\partial^2\rho}{\partial x^2}\right)^{\mathrm{T}} \tag{7.53}$$

Using these new variables, the new system becomes Eqs. (7.54a)-(7.54f). A classic consequence of the regularization is that the new system no longer represents a set of conservative laws,

meaning that the system is not guaranteed to be hyperbolic.

$$\begin{cases} \dfrac{\partial U_1}{\partial t} + \dfrac{\partial U_2}{\partial x} & = 0 \quad (7.54a) \\ \dfrac{\partial U_2}{\partial t} + \dfrac{\partial}{\partial x}\left(\dfrac{U_2^2}{U_1} + P_0 + \dfrac{\lambda}{2}U_4^2 - \lambda U_1 U_6\right) & = 0 \quad (7.54b) \\ \dfrac{\partial U_3}{\partial t} + \dfrac{\partial}{\partial x}\left(\dfrac{U_2\left(U_3+P_0\right)}{U_1} + \lambda U_4 U_5 - \dfrac{\lambda}{2}\dfrac{U_2}{U_1}U_4^2 - \lambda U_2 U_6\right) & = 0 \quad (7.54c) \\ \dfrac{\partial U_4}{\partial t} + \dfrac{\partial U_5}{\partial x} & = 0 \quad (7.54d) \\ \dfrac{\partial U_2}{\partial x} & = U_5 \quad (7.54e) \\ \dfrac{\partial U_4}{\partial x} & = U_6 \quad (7.54f) \end{cases}$$

The second step for the pseudo-linearization is to make matrices $\boldsymbol{A}_t$, $\boldsymbol{A}_x$ and vector $\mathbf{Q}$ emerge such as the system can be written in the form:

$$\boldsymbol{A}_t\left(\mathbf{U}\right)\frac{\partial \mathbf{U}}{\partial t} + \mathbf{A}_x\left(\mathbf{U}\right)\frac{\partial \mathbf{U}}{\partial x} = \mathbf{Q}\left(\mathbf{U}\right) \tag{7.55}$$

To do so, it is necessary to express the differential of the classic pressure P_0 relatively to the other variables in $\mathbf{U}$, just as done in Sec. 6.3.2. Using the definition in Sec. 6.3.2 for Λ and Γ and using the subscript $*_0$ to refer to a variable as given directly by the equation of state, the differential is given by:

$$dP_0 = \frac{\alpha_0}{\rho\beta_0 C_{v0}}\left[d\left(\rho e\right) - u\,d\left(\rho u\right) + \left(\frac{C_{p0}}{\alpha_0} - h_{s0} + \frac{1}{2}u^2\right)d\rho - \lambda\frac{d\rho}{dx}\,d\left(\frac{d\rho}{dx}\right)\right] \tag{7.56}$$

$$= \Gamma\left[d\left(\rho e\right) - u\,d\left(\rho u\right) + \Lambda\,d\rho - \lambda\frac{d\rho}{dx}\,d\left(\frac{d\rho}{dx}\right)\right] \tag{7.57}$$

The pseudo-linearization of the system lends the following expressions for $\boldsymbol{A}_t$, $\boldsymbol{A}_x$ and $\mathbf{Q}$:

$$\boldsymbol{A}_t = \begin{pmatrix} 1 & 0 & 0 & 0 & 0 & 0 \\ 0 & 1 & 0 & 0 & 0 & 0 \\ 0 & 0 & 1 & 0 & 0 & 0 \\ 0 & 0 & 0 & 1 & 0 & 0 \\ 0 & 0 & 0 & 0 & 0 & 0 \\ 0 & 0 & 0 & 0 & 0 & 0 \end{pmatrix} \quad \boldsymbol{A}_x = \begin{pmatrix} 0 & 1 & 0 & 0 & 0 & 0 \\ a_{21} & a_{22} & a_{23} & a_{24} & 0 & a_{26} \\ a_{31} & a_{32} & a_{33} & a_{34} & a_{35} & a_{36} \\ 0 & 0 & 0 & 0 & 1 & 0 \\ 0 & 1 & 0 & 0 & 0 & 0 \\ 0 & 0 & 0 & 1 & 0 & 0 \end{pmatrix} \quad \mathbf{Q} = \begin{pmatrix} 0 \\ 0 \\ 0 \\ 0 \\ U_5 \\ U_6 \end{pmatrix} \tag{7.58}$$

where:

$$a_{21} = \Gamma\Lambda - u^2 - \lambda\frac{\partial^2\rho}{\partial x^2},\ a_{22} = u\left(2-\Gamma\right),\ a_{23} = 2\lambda\frac{\partial\rho}{\partial x}\left(2-\Gamma\right),\ a_{24} = \Gamma,\ a_{26} = -\lambda\rho$$

$$a_{31} = u\left(\Gamma\Lambda - h_{s0} - \frac{1}{2}u^2\right),\ a_{32} = h_{s0} + u^2\left(\frac{1}{2} - \Gamma\right) - \lambda\frac{\partial^2\rho}{\partial x^2},\ a_{33} = u\left(1+\Gamma\right)$$

$$a_{34} = \lambda\left(\frac{\partial(\rho u)}{\partial x} - u\left(1+\Gamma\right)\frac{\partial\rho}{\partial x}\right),\ a_{35} = \frac{\lambda}{2}\frac{\partial\rho}{\partial x},\ a_{36} = -\lambda\rho u$$

The third step is to find the couples (l_t, l_x) such as $\det(l_t \boldsymbol{A}_t + l_x \boldsymbol{A}_x) = 0$, which leads to the equation:

$$\det(l_t \boldsymbol{A}_t + l_x \boldsymbol{A}_x) = \begin{vmatrix} l_t & 1 & 0 & 0 & 0 & 0 \\ l_x a_{21} & l_t + l_x a_{22} & l_x a_{23} & l_x a_{24} & 0 & l_x a_{26} \\ l_x a_{31} & l_x a_{32} & l_t + l_x a_{33} & l_x a_{34} & l_x a_{35} & l_x a_{36} \\ 0 & 0 & 0 & l_t & l_x & 0 \\ 0 & l_x & 0 & 0 & 0 & 0 \\ 0 & 0 & 0 & l_x & 0 & 0 \end{vmatrix} = 0 \tag{7.59}$$

After multiple simplifications, essentially due to the regularization of the equation with $\mathbf{U}$ that makes lines of zeros appear in $\boldsymbol{A}_t$, the equation simplifies in:

$$l_t l_x^4 \left[l_x \left(a_{23} a_{36} - a_{26} a_{33} \right) - a_{26} l_t \right] = 0 \tag{7.60}$$

Which, after substitution, becomes:

$$\det(l_t \boldsymbol{A}_t + l_x \boldsymbol{A}_x) = \lambda \rho l_t l_x^4 \left(u l_x + l_t \right) = 0 \tag{7.61}$$

Given the previous results, the conditions to find characteristics becomes:

$$\det(l_t A_t + l_x A_x) = 0 \qquad \Longleftrightarrow \qquad l_t = -u l_x,\ l_t = 0,\ l_x = 0 \tag{7.62}$$

The system only has 3 solutions (all real) for a six-component state vector :

- couples of the form $(-um, m)$ are solutions of multiplicity one
- couples of the form $(0, m)$ are solution of multiplicity one
- couples of the form $(m, 0)$ are solution of multiplicity four

where m is a non-zero real number. The system is simultaneously weakly hyperbolic and parabolic, in particular, only the characteristic with the wave velocity u has been unveiled. As such, this investigation does not permit to further qualify the equations, neither derive adequate boundary conditions nor to infer some stability condition.

7.2.2 Boundary conditions

Although it could have been anticipated that the characteristic boundary conditions of AVBP described in Sec. 6.3.2 could not be used with the equations, the lack of properly defined characteristics for the capillary system even prevents *a priori* to derive new adequate ones. To avoid possible detrimental interactions at the boundaries, the consensus used for our applications has been to settle with no interfaces entering or exiting the domain. Nonetheless, the presence of strong acoustic noise in several cases has led to the design of a practical strategy, hereunder presented, in order handle the interaction between said noise and the boundaries.

The ad-hoc method that has been implemented relies on the two following observations. Firstly, for the SG model, the conservatives variables remain $(\rho, \rho\mathbf{v}, \rho e)$ which are formally the same as for the classic Euler equations except that the specific sensible energy e_s included within the total specific energy e is formed by the addition of the classic sensible energy e_{s0} and the capillary energy $\lambda(\boldsymbol{\nabla}\rho)/\rho$. Secondly, when no interface is present, i.e. when no

macroscopic density gradient in the binodal region is present, the contribution of the capillary energy to the total volumetric energy, $\lambda\left(\boldsymbol{\nabla}\rho\right)^2$, is negligible.
These two observations have led to the following strategy, applied at each temporal step (or substep for multi-step time integration schemes):

1. The density gradient at the boundaries $\left(\boldsymbol{\nabla}\rho^n\right)^{\text{bound}}$ is stored before the time step begins.
2. The SG conservative variables are updated in the whole domain using the full set of capillary equations to get the predicted values $\left(\rho^{n+1,*}, \rho u^{n+1,*}, \rho e^{n+1,*}\right)_{SG}^{\text{bound}}$ at the boundaries.
3. At the boundaries, the predicted SG conservative variables $\left(\rho^{n+1,*}, \rho\mathbf{v}^{n+1,*}, \rho e^{n+1,*}\right)_{SG}^{\text{bound}}$ are transformed into the Euler conservative variables $\left(\rho^{n+1,*}, \rho\mathbf{v}^{n+1,*}, \rho e^{n+1,*}\right)_{Euler}^{\text{bound}}$. This is done by removing the capillary energy from the full energy using the previously stored density gradient:
$$\rho e_{Euler}^{n+1,*} = \rho e_{SG}^{n+1,*} - \frac{\lambda}{2}\left(\boldsymbol{\nabla}\rho^n\right)^2 \tag{7.63}$$
4. Using the Euler conservative variables, the native characteristic boundary conditions in Sec. 6.3.2 are applied to get the final Euler variables $\left(\rho^{n+1}, \rho\mathbf{v}^{n+1}, \rho e^{n+1}\right)_{Euler}^{\text{bound}}$
5. The updated SG conservative variables $\left(\rho^{n+1}, \rho\mathbf{v}^{n+1}, \rho e^{n+1}\right)_{SG}^{\text{bound}}$ are recovered from the updated Euler conservative variables by injecting back the previously removed capillary energy into the total energy:
$$\rho e_{SG}^{n+1} = \rho e_{Euler}^{n+1} + \frac{\lambda}{2}\left(\boldsymbol{\nabla}\rho^n\right)^2 \tag{7.64}$$

There exist *a priori* two configurations in which this approach should hold. The first and most straightforward one is when the density gradient is negligible at the boundaries and can be discarded from the equations altogether. The second one is more peculiar and may occur when the local variation, at the boundaries, in total energy is not actually due to a change in the density gradient, should the latter be nonetheless not negligible. This configuration most likely applies when acoustic waves propagates in the bulk phases and interact with the boundaries. The viability of this strategy has been assessed on several canonical cases, some of which are presented hereunder.

T_{init}	110.0 K	equations	mass + mom + ener.
P_{init}	134 bar	scheme	GRK
ρ_{init}	700 kg · m^{-3}	diffusion	Chung

Table 7.4: *Simulation parameters used for the one dimensional N_2 uniform system to test the characteristic boundary conditions.*

Fig. 7.7 presents the case of a forward acoustic wave placed in static and uniform liquid N_2. The capillary Navier-Stokes equations are solved and the main parameters for the simulation are compiled in Tab. 7.4.

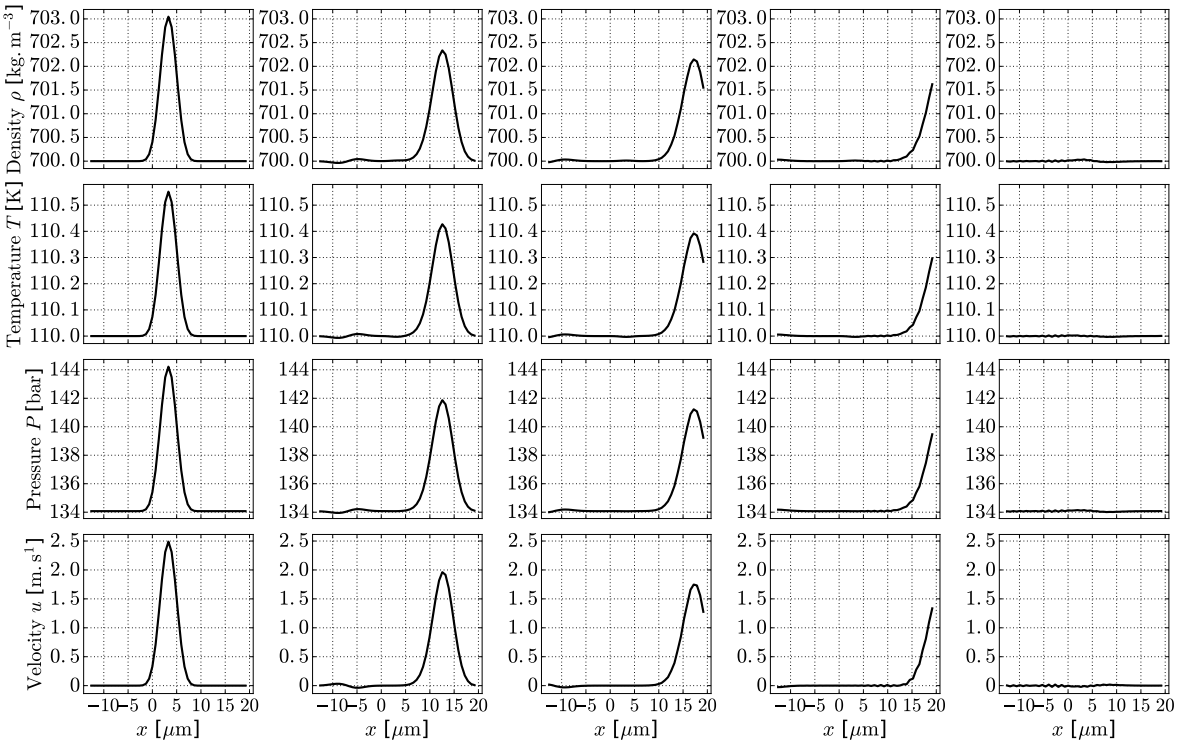

Figure 7.7: *Evacuation of an acoustic wave in the SG system, non reflecting boundary conditions are used on both the left and right sides*

.

Non reflecting boundary conditions have been placed on both the left and right sides. It should be noticed that the absence of characteristics for the capillary system also prevents the creation of proper characteristic waves, either acoustic or entropic. For this case and the case presented in Fig. 7.8, said waves have been generated using the non capillary system and the total energy has then been corrected with the density gradient to account for the capillary energy. This practical creation of characteristic waves must be accounted for when analyzing the outcome of the simulations. In Fig. 7.7, the wave is damped by the physical diffusion of the Navier-Stokes equations. It is nonetheless properly advected and adequately evacuated of the domain with an extremely negligible noise being reflected back into the computational domain. The amplitude of the residual noise is comparable to that of classic non-capillary real gas simulations caused by the non-linearity of the EoS.

In Fig. 7.8, an entropic wave is placed into the same N_2 system described with the parameters in Tab. 7.4, endowed with a constant velocity of 50 m $\cdot$ s^{-1}. The wave is also damped by the diffusion and the tail of the wave experiences a dispersion phenomenon, characteristic of non-isothermal advection for capillary system, which is further discussed in Sec. 8.1.3. The phenomenon essentially impacts the pressure and causes a minor acoustic noise to be created and/or reflected at the boundary, with an amplitude however still mostly negligible.
Finally, the practical strategy that has been implemented effectively allows to evacuate characteristic waves granted that the conditions of applicability previously enunciated are respected.

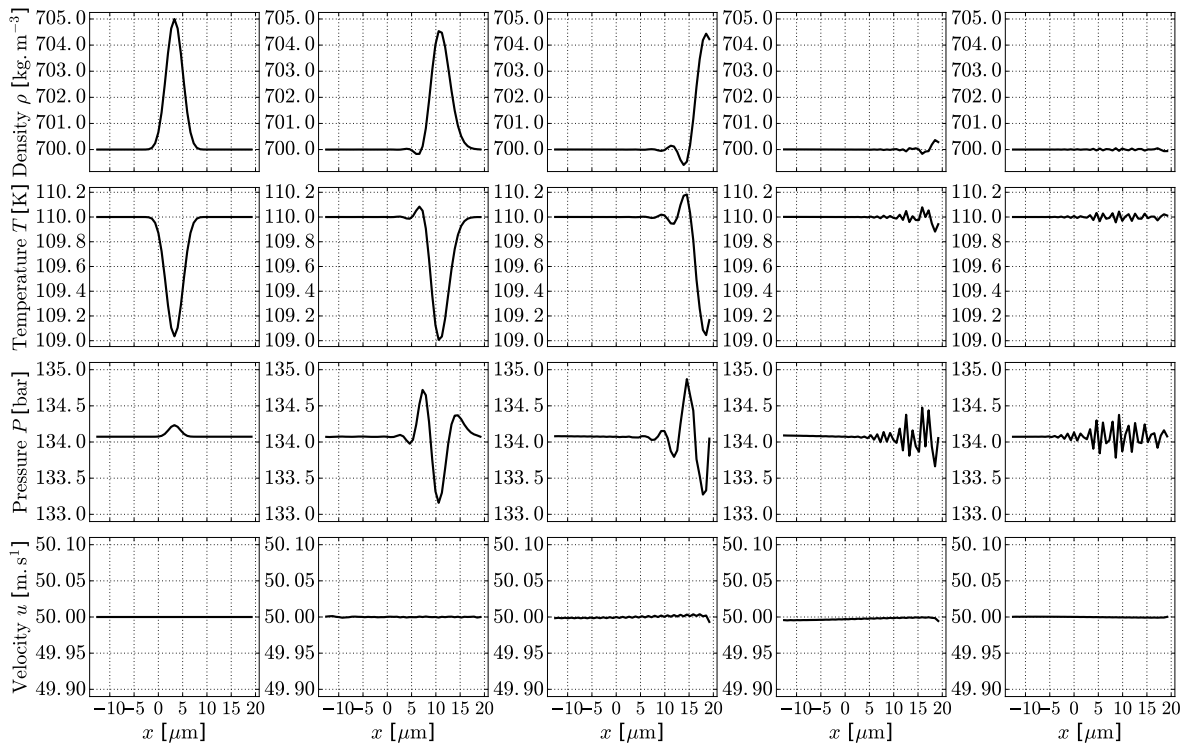

Figure 7.8: *Evacuation of an entropic wave in the SG system, non reflecting boundary conditions are used on both the left and right sides*

.

A question that naturally arises concerns the reaction of the boundary if one tries to evacuate an interface. Such a case is presented in Fig. 7.9, for a N_2 interface, using the parameters compiled in Tab. 7.5.

T	113.57 K	λ	$1.0 \cdot 10^{-10}$ m$^7 \cdot$ kg$^{-1} \cdot$ s^{-2}	σ	3.26 N $\cdot$ m
P^{sat}	18.15 bar	points in int.	≈ 6	w	4.42 μm
ρ_l	542.1 kg $\cdot$ m^{-3}	equations	mass + mom. + ener.	u	50 $m \cdot s^{-1}$
ρ_v	80.3 kg $\cdot$ m^{-3}	diffusion	Chung	CFL	0.95

Table 7.5: *Simulation parameters used for the one dimensional N_2 uniform system to test the characteristic boundary conditions in presence of an interface.*

One can observe that strong temperature, velocity and particularly pressure oscillations appear at the boundary when the interface starts to cross it. These oscillations peak in amplitude when the "liquid side" of the interface is evacuated (the tail of the interface in that case). The interface is nonetheless completely evacuated. However, a slight drift is then observed in the uniform velocity and an important noise propagates downwards and is associated to strong pressure oscillations. Eventually, this noise is evacuated by the left-side non-reflecting boundary and the system eventually reaches an uniform equilibrium state, however with a slightly

decreased velocity (48.5 $m \cdot s^{-1}$ instead of 50.0 $m \cdot s^{-1}$), a slightly increased temperature (114.11 K instead of 113.57 K) and a noticeably increased pressure (21.82 bar instead of 18.15 bar). This discrepancy between the expected and computed final values entails that, in spite of the interface being ultimately evacuated trough the boundary, doing so can nonetheless lead to a propagation of numerical errors in the domain which could in turn jeopardize the integrity of the simulations.

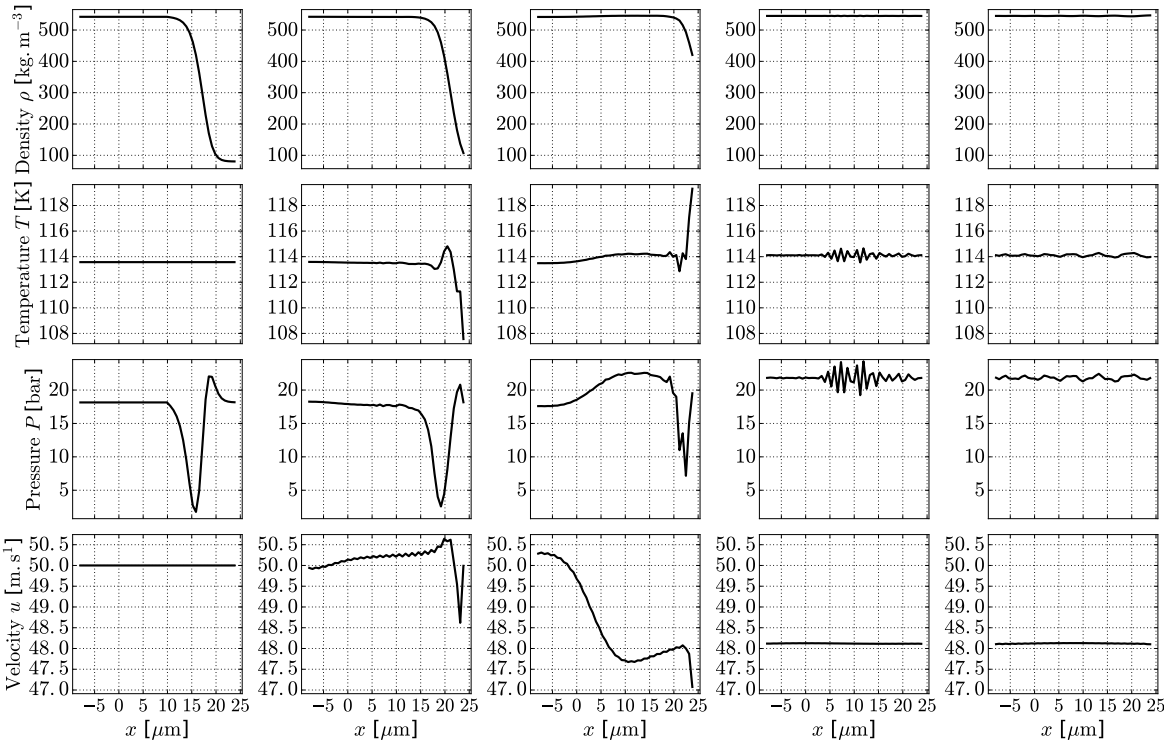

Figure 7.9: *Evacuation of an interface in the SG system, non reflecting boundary conditions are used on both the left and right sides*

.

In light of the previous results, for the remaining numerical applications presented in this document, a special care is taken to ensure that no interface is ever evacuated through a characteristic boundary.

7.2.3 Determination of a time step condition

As already mentioned, the absence of proper characteristics for the system of equations also renders more complicated the extraction of possible time step conditions.
More precisely, for the case at hands, the difficulty is twofold: the classic CFL condition requires the evaluation of the sound speed which is not properly defined in the capillary regions where the classic definition can lead to negative values, and the capillary terms, with the corresponding high order derivatives, are most likely to call for additional time step conditions, just as it is the case with the Fourier number when physical diffusion is introduced in the Navier-Stokes equations.

To partially overcome this hurdle, a practical approach as been used in order to infer the time condition associated with the SG equation system. To that effect, a one dimensional setting similar to the one presented in 7.1.3.1 has been used: an isothermal liquid droplet is inserted into a periodic domain of twice its diameter and is convected at constant speed. During each simulation, a specific time step is enforced and, expectedly, too high values lead to a crash whereas smaller values ensure a stable calculation. By fine tuning the value of this time step, it is possible to find the limit around which the stability of the simulation switches. To automatize the process, an arbitrary choice has been made to consider the simulation stable once the droplet is able to perform ten sweeps of the domain.
By associating value 1 to a successful simulation and value -1 to a failed one and by using a root-finding algorithm, it is possible to extract the value of the limit time step.

All the procedures described herein after have been performed using different fluids O_2, N_2 and H_2 to maximize the generality of the findings. The presentation is however focused on the results obtained for N_2. They can be adapted to the other fluids without loss of generality nor accuracy.

7.2.3.1 Impact of the mesh size and capillary coefficient

The first series of tests consists in evaluating both the impact of the mesh size Δx and the capillary coefficient λ on the time step Δt. To do so, a reduced temperature $T_r = 0.90$ is fixed (which correspond to an effective temperature of $T = 139.12$ K for N_2).

As shown in Fig. 7.10, two correlations are extracted. For different fixed values of capillary coefficient λ, the mesh size is used as a parameter to get the results on the left graph. Conversely, with fixed values of mesh size Δx, the capillary coefficient is in turn used as the entry parameter to get the results on the right graph.

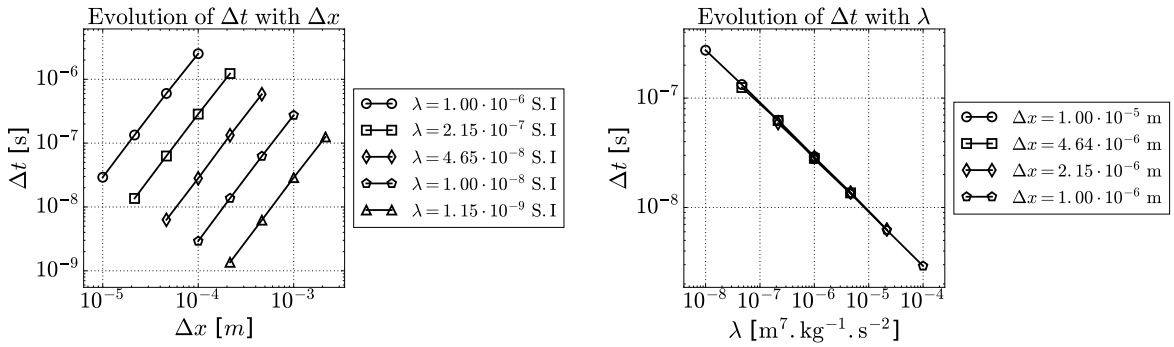

Figure 7.10: *Evolution, in log scale, of the limit time step: with respect to the mesh size for different capillary coefficients (left), with respect to the capillary coefficient for different mesh sizes (right).*

The logarithmic scale used in Fig. 7.10 allows to unequivocally evaluate the impact of both Δx and λ. The slopes of the obtained straight lines can be interpolated, the results are given in Tabs. 7.6 and 7.7.

λ [S.I]	$1.00 \cdot 10^{-6}$	$2.15 \cdot 10^{-7}$	$4.65 \cdot 10^{-8}$	$1.00 \cdot 10^{-8}$	$1.15 \cdot 10^{-9}$
slope of Δt	1.9377	1.958	1.974	1.973	1.97

Table 7.6: *Slope of Δt with respect to Δx in logarithmic scale for different values of λ*

Δx [m]	$1.00 \cdot 10^{-5}$	$4.64 \cdot 10^{-6}$	$2.15 \cdot 10^{-6}$	$1.00 \cdot 10^{-6}$
slope of Δt	-0.486	-0.485	-0.486	-0.489

Table 7.7: *Slope of Δt with respect to λ in logarithmic scale for different values of Δx*

From Tab. 7.7 it comes that $\Delta t \propto 1/\sqrt{\lambda}$ which can come across as partially counterintuitive since the interface width w follows the trend $w \propto \sqrt{\lambda}$ and a thinner interface can be assumed to cause a bigger strain on the numerical methods due to greater values of gradients. However, a smaller value of λ actually causes the interface to have a stiffer behavior and be less sensitive to external perturbations. This can be observed on 2D simulations involving droplets/bubbles. When too high of a value is used for the capillary coefficient, the interfaces start to deform more easily, capillary waves form with greatest amplitude and overall, interfaces showcase a more "malleable" aspect.

From Tab. 7.6 it the comes that $\Delta t \propto (\Delta x)^2$ which is reminiscent of the condition involving the Fourier number and is characteristic to diffusion fluxes, a result consistent with the microscopic phenomena occurring near and inside the interfacial region which are essentially diffusive. This result could be somewhat expected given the abundance of capillary terms in the fluxes involving first order spatial derivatives.
An empirical rule commonly observed in fluid dynamics states that n^{th} derivative in the fluxes calls for at least a n^{th} order dependency on the mesh size for the time step. For instance a first order convection equation leads to first order dependency of the limit time step on the mesh size via the CFL number. Likewise, a second order diffusive equation is met with a second order dependency of the limit time step on the mesh size via the Fourier number. Following this empirical rule, the presence of the density Laplacian in the flux that leads to third order spatial derivative of the density should cause a $(\Delta x)^3$ dependency to appear, which is not observed. The importance of this non-occurrence must be mitigated and can be explained by the empirical nature of this rule. Another possible explanation could be that the third order dependency is actually true but that it requires smaller mesh sizes to be unveiled numerically just as for big mesh size, the CFL condition can easily supplant that of the Fourier number.

In the later case, the 3^{rd} order dependency can be dismissed since our simulations will most likely rarely involve mesh sizes smaller than those that have been used during these numerical experiments. However, if this should be the case, an extra care should be given when choosing the time step condition since the current correlations could prove to be insufficient.

7.2.3.2 Impact of the temperature

Although the previous results have been replicated for different fluids and at different reduced temperatures (T_r = 0.85, 0.90 and 0.95) with consistency. These results are however not enough in the prospect of non-isothermal simulations since they fail to provide the actual

impact of the temperature on the time step. To that effect, the same solving process has been used to determine the limit time step with fixed mesh size and capillary coefficient, taking the reduced temperature as a parameter.
The main difficulty of this approach comes from the fact that along with the reduced temperature, numerous variables that were otherwise fixed, such as the saturation densities, are now also changing and variables that had know variations with respect to λ, such as the interface width w, the density gradient $\boldsymbol{\nabla}\rho$ or the surface tension σ, are varying in an uncontrolled fashion. Therefore, it seemed necessary to assess not only the impact of the reduced temperature but also the impact of other main variables that vary with it. For N_2, the results of such an inquiry can be found in Tab. 7.8 for a mesh size of $\Delta x = 4.64 \cdot 10^{-5}$ m.

T_r	Δt	T	ρ_v	ρ_l	w	$\max \lvert\boldsymbol{\nabla}\rho\rvert$	σ
[-]	[ns]	K	$[\mathrm{kg \cdot m^{-3}}]$	$[\mathrm{kg \cdot m^{-3}}]$	[mm]	$[\mathrm{kg \cdot mm^{-3}/mm}]$	[N.m]
0.90	31.47	113.5	80.3	542.1	0.442	202.1	1.69
0.91	31.93	114.8	87.4	527.5	0.467	177.8	1.48
0.92	32.42	116.1	95.3	512.0	0.497	153.9	1.28
0.93	32.96	117.4	104.1	495.5	0.533	130.6	1.09
0.94	33.57	118.6	113.9	477.9	0.578	107.9	0.90
0.95	34.26	119.9	125.2	458.9	0.635	86.0	0.72
0.96	35.06	121.1	138.2	438.0	0.711	65.1	0.55
0.97	36.03	122.4	153.8	414.5	0.824	45.3	0.38
0.98	36.64	123.7	179.3	384.4	1.011	27.1	0.23

Table 7.8: *Impact of the reduced temperature T_r on the time step Δt and several other main variables, with $\Delta x = 4.64 \cdot 10^{-5}$ m*

Additional variables such as $\bar{\rho} = (\rho_v + \rho_l)/2$, $\Delta\rho = \rho_l - \rho_v$, σ and $\max \lvert\boldsymbol{\nabla}\rho\rvert / w$ have also been considered as possible candidates to extract a correlation. Examples of graphs are provided for N_2 in Fig. 7.11.

Among all the studied variables, the liquid and vapor densities ρ_l and ρ_v and the density gap $\Delta\rho$ have provided a notable correlation. This result could have been partially hinted by dimensional analysis since, from the previously known correlation $\Delta t = A\,(\Delta x)^2 / \sqrt{(\lambda)}$ it comes that the dimension of A is analogous to $1/\sqrt{(\mathrm{kg \cdot m^{-3}})}$. Although the results in Fig. 7.11 has allowed to discard $\bar{\rho}$ beforehand, the dimensional analysis on its own has not discarded ρ_l, ρ_v or $\Delta\rho$ for which further comparisons between fluids have been necessary.

Figs. 7.12 to 7.14 show, for nitrogen, oxygen and hydrogen, the impact on the limit time step of the density gap $\Delta\rho$, the vapor density ρ_v and the liquid density ρ_l respectively. The mesh sizes are $\Delta x_{N_2} = 33.3\ \mu m$, $\Delta x_{O_2} = 33.3\ \mu m$ and $\Delta x_{H_2} = 92.8$ nm for nitrogen, oxygen and hydrogen respectively. In particular, these figures clearly demonstrate that only the liquid density ρ_l has a log-linear and repeatable relation with the limit time step, further confirmed by the red-dotted lines in 7.14 that show the corresponding correlation of which slopes are given in 7.9 with the associated mesh size used for the simulations.

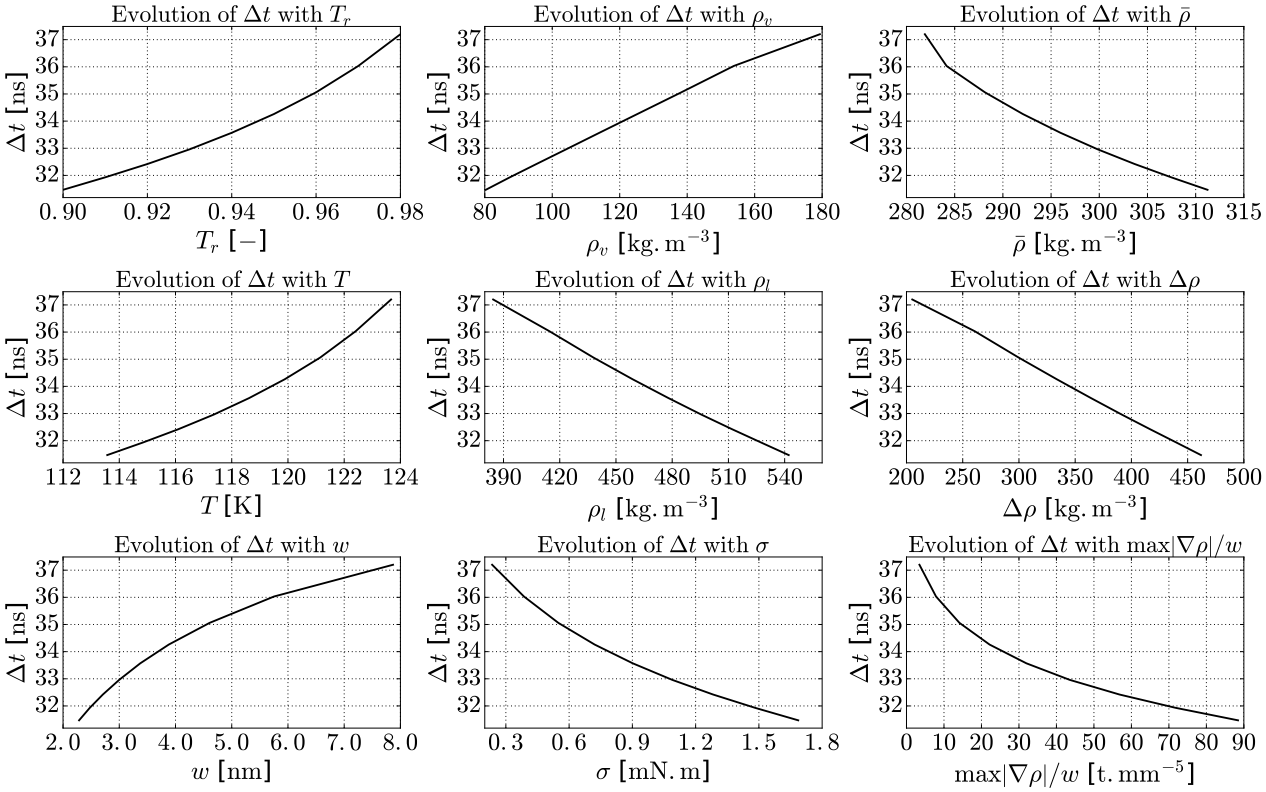

Figure 7.11: *Evolution of the limit time step with respect to different variables impacted by the varying reduced temperature.*

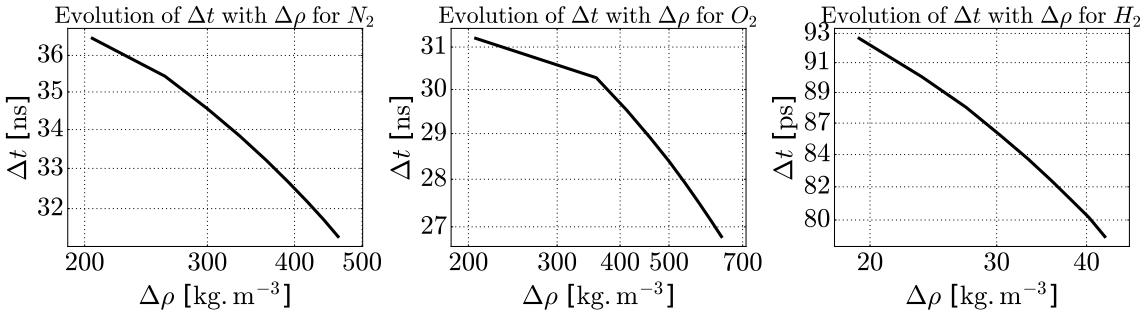

Figure 7.12: *Evolution, in log scale, of the limit time step with respect to the density gap $\Delta\rho$: for N_2 (left), O_2 (center) and H_2 (right)*

We mention here that to double proof these results, a second series of simulation has been done for all fluids in the same conditions, only varying the mesh size, taken three times greater. However, for these cases, the analysis of the result has later showed that the time step was actually controlled by the CFL condition. For this reason, the corresponding results have been omitted here.

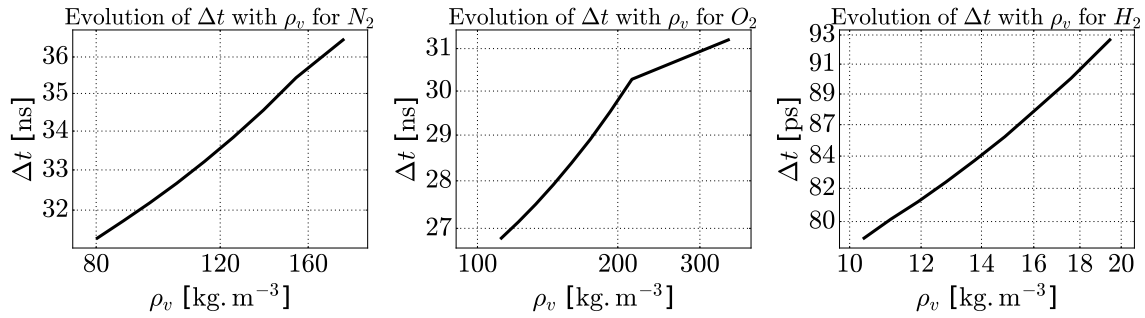

Figure 7.13: *Evolution, in log scale, of the limit time step with respect to the vapor density ρ_v: for N_2 (left), O_2 (center) and H_2 (right)*

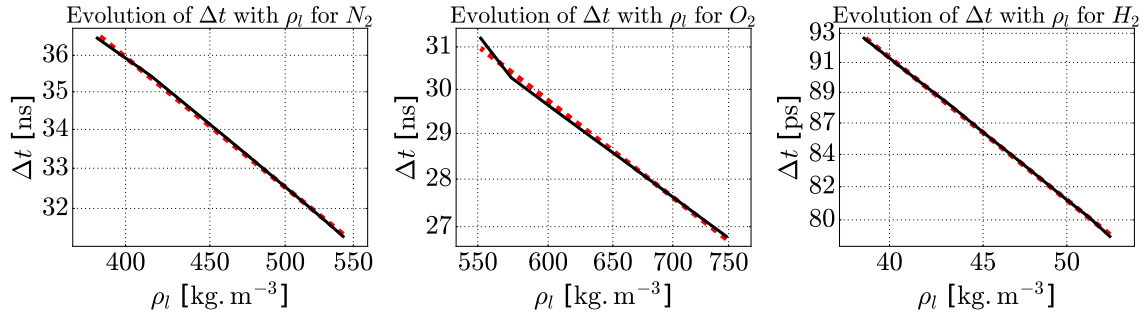

Figure 7.14: *Evolution, in log scale, of the limit time step with respect to the liquid density ρ_l: for N_2 (left), O_2 (center) and H_2 (right). Red dotted lines for the log-linear regression.*

Element	N_2	O_2	H_2
Slope	-0.491	-0.528	-0.532

Table 7.9: *Slope of Δt with respect to ρ_l in logarithmic scale for different elements*

Using the values in Tab. 7.9, it is possible to infer the partial expression for the limit time step which given in Eq. (7.65).

$$\Delta t_{\max} = C\frac{(\Delta x)^2}{\sqrt{\lambda \rho_l}} \tag{7.65}$$

To achieve the formula, constant C must be determined, which can be done by evaluating $\Delta t_{\max}/\left(\frac{(\Delta x)^2}{\sqrt{\lambda \rho_l}}\right)$ for the different configurations, which is done for N_2, O_2 and H_2 in Fig. 7.15. Again, a trend clearly appears as the results concentrate around the value $2/3$ with a very small overall deviation. The final expression is obtained by noticing that during a non isothermal simulation, the local density may probably exceed its liquid saturation value, therefore the ρ_l must be treaded for $\rho_{\max}$. Eventually the limit time step is given by Eq. (7.66) and this expression has been used for the rest of our simulations.

$$\Delta t_{\max} = \frac{2}{3}\min_{\text{Mesh}}\left(\frac{(\Delta x)^2}{\sqrt{\lambda \rho}}\right) \tag{7.66}$$

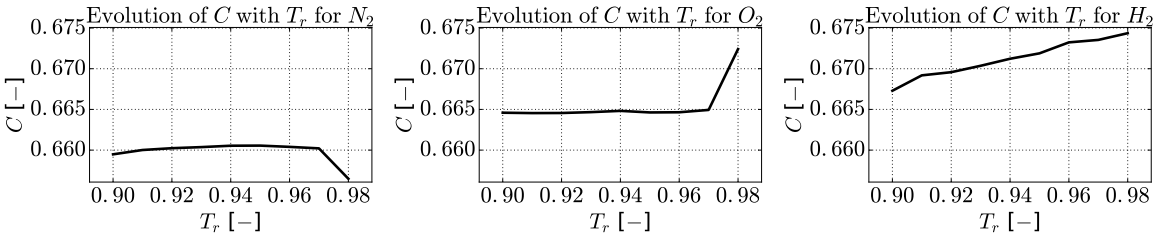

Figure 7.15: *Evolution of the limit time step constant coefficient with respect to the reduced temperature.*

Comparison with the literature

In Brackbill et al. (1992) the authors derive a different time step condition, based on the velocity of capillary waves (see Sect. 6.3 in Elmore and Heald (1985)), which is written:

$$\Delta t^{\mathrm{Br}}_{\mathrm{max}} = \min_{\mathrm{Mesh}} \left(\sqrt{\frac{\rho_l + \rho_v}{4\pi\sigma}} \left(\Delta x\right)^{1.5} \right) \tag{7.67}$$

The question arises about the reasons why this condition has not been recovered by the present investigation. Firstly, the exponent 1.5 on the mesh size Δx in Eq. (7.67) compared to the exponent 2.0 in Eq. (7.66) makes the former condition *a priori* less restrictive, which is confirmed by the comparative curves in Fig. 7.16.
This observation does not however explain the existence of the condition Eq. (7.66) in the first place. For this, one needs to remember that the capillarity model proposed by Brackbill is essentially geometrical as the capillary flux is given by $\sigma\kappa\boldsymbol{n}$ where κ is the interface curvature and $\boldsymbol{n}$ is the interface normal vector. This formulation is intrinsically multi-dimensional, as well as the notion of capillary waves which propagate on the interface and not through it. The time step condition in Eq. (7.66) has been obtained studying one dimensional cases since the notion of capillarity, in the SG model, still makes sense in one dimension. Indeed, the capillary terms from the SG model possess intrinsic diffusive characteristics which ensure the stability of the interface in one dimension and that, consequently, ensures that the interface has an intrinsic width. The time step condition Eq. (7.66), analogous to diffusive time step conditions in virtue of the exponent 2.0, is presumably associated to stabilization processes of the interface. As such, it becomes clear why such a condition has no relevance for models such as Brackbill's. Conversely, the condition in Eq. (7.67) still needs to be compelled in multi-dimensional SG simulations where the notion of capillary waves also applies.

As it is usual during a numerical simulation, a margin is taken relatively to the limit time step. To that effect we introduce a "Second Gradient" Fourier number Fo^{SG} and practically $\Delta t = Fo^{\mathrm{SG}}\Delta t_{\mathrm{max}}$ with the constraint that $0 < Fo^{\mathrm{SG}} < 1$ (the value $Fo^{\mathrm{SG}} = 0.75$ has been used by default).

It also should be noticed that the limit diffusion time step imposed by the diffusion fluxes changes by a factor 1/2 when going from one-dimensional to two-dimensional configurations. Given the diffusion-like expression found for the SG limit time step, the same precaution has been taken during our two-dimensional simulations.

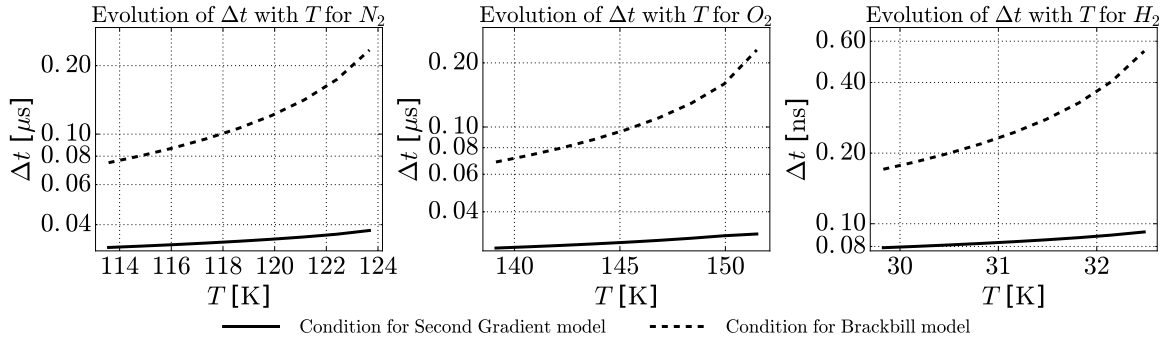

Figure 7.16: *Comparative evolution, in semi-log scale, of the limit time steps for the Second Gradient (full line) and Brackbill (dashed line) models with respect to the temperature T: for N_2 (left), O_2 (center) and H_2 (right)*

Conclusion on the implementation of the SG model into the AVBP solver

In this chapter, key aspects regarding the implementation of the SG model into the AVBP solver have been discussed.

The high order spatial derivatives introduced by the capillary terms require a special treatment that did not appear clear at first sight in the context of the AVBP numerical framework, a matter that has been thoroughly investigated.
Attempts have been made to analytically qualify the nature of the SG equations system but have been meet with limited success due to their peculiar and complex form.
The lack of theoretical information regarding the treatment of boundary conditions, the choice of the numerical scheme and the associated time step has been circumvented by the analysis of practical simulations that provided insightful information and practical correlations. With the proposed strategy to handle boundary conditions and the time step condition numerically derived, qualitative and quantitative simulations can now be performed.

Chapter 8

Numerical validation of the Second Gradient model

This chapter provides the numerical validation of the implementation of the Second Gradient model on canonical cases.
Firstly, one-dimensional simulations are performed in Sec. 8.1. A stationary solver is used as a springboard towards dynamic cases. Solving the SG equations in a stationary setting as done in Sec. 8.1.1 serves a dual purpose: firstly, it allows to verify the thermodynamic behavior of the model and its ability to properly retrieve the saturation variables, secondly it permits to generate the adequate initial solutions that can be used in other one or two-dimensional configurations. The ensuing one-dimensional simulations in Sec. 8.1.2 performed using AVBP are mostly conducted under isothermal conditions, preferential to qualify the implementation. Non-isothermal cases are also discussed in Sec. 8.1.3.
In Sec. 8.2, all the gathered information is used to perform two-dimensional simulations. Two cases are investigated: in Sec. 8.2.1 the oscillations of a planar interfaces initially perturbed are simulated and the oscillations of an initially squeezed droplet are studied in Sec. 8.2.2. For both cases, different sets of equations are solved, Euler or Navier-Stokes, in isothermal and non-isothermal formulations, to allow for an in depth investigation of the model behavior.
These cases allow comparisons with theoretical results regarding the periods and damping of the oscillations observed and therefore also serve as an additional validation of the implementation.

The purposes of this chapter are twofold and intimately linked.
Firstly, it serves as a validation of the implementation of the model in the AVBP solver and the pertinence of the discretization strategies presented in Chap. 7. Following that line of thoughts, the main objective is to determine the operating conditions, from a numerical point of view, that permit to achieve successful simulations with exploitable results. This task is mostly addressed through mesh convergence investigations and studies involving the resolution of different sets of equations, Euler or Navier-Stokes, in different settings, isothermal or non-isothermal. Some simulations have required the use of the stabilization strategies presented in Sec. 6.2.4, mostly the selective high order filter and more occasionally the artificial viscosity, in order to address more sensitive cases.
Secondly, provided that the numerical operating conditions have been established and cali-

brated, the other main objective is to qualify the intrinsic thermodynamic behavior of the model in and out of equilibrium, which is done by performing qualitative and, when possible, quantitative comparisons with theoretical results on canonical cases. For these cases, the use of a sufficient mesh resolution has been favored to the use of excessive stabilization strategies, in particular the artificial viscosity, in order to limit its impact on the results and thus focus on the thermodynamic behavior of the SG model. It is recalled that the artifical viscosity used in this work has not been initially designed to interact with capillary-like terms in the equations and as such, it may have an unexpected interaction with the SG model.
Although these two objectives cannot be addressed separately in virtue of their direct dependency, an effort has however been made to emphasize on one or the other by varying the conditions of the simulations and adapting the ensuing analysis.

8.1 Validation cases in one dimension

8.1.1 Stationary cases

8.1.1.1 On the need for a stationary solver

When considering the path towards simulating complex configurations involving interfaces while using the Second Gradient model, the ability to generate accurate 1D canonical isothermal interfaces proves extremely useful, if not necessary, as it serves multiple roles.
Firstly, it can be used to assess the correct thermodynamic behavior of the model, i.e. its ability for a given temperature to retrieve the saturation values of the fluid such as the liquid and vapor densities or the saturation pressure.
Secondly, it provides the means to properly determine or confirm the different correlations mentioned when characterizing the behavior of the model, such as the evolution of the capillary coefficient λ with the temperature given in Eq. (5.174), Tab. 5.1 and Fig. 5.15 or the impact of λ on the interface width and surface tension theoretically assessed in Eqs. (5.146) and (5.167).
Thirdly, it allows to generate initial configurations for one or two-dimensional simulations in a mostly consistent fashion rather than by guessing the value of the different variables and letting the system relax on its own during a non-stationary simulation.
This last consideration is partially crucial when dealing with out-of-equilibrium situations such as oscillating droplets or planar interfaces where non-idealities in the initial solution can create numerical noise that can possibility temper with the physical effect one would want to study.
For all these reasons, efforts have been made to implement a robust strategy for solving the equilibrium equation for a one-dimensional isothermal planar interface, given by Eq. (8.1) where P_0 is the pressure from the EoS, lending solutions such as displayed in Fig. 5.12.

$$\frac{\partial P_0}{\partial x} = \lambda \rho \frac{\partial^3 \rho}{\partial x^3} \tag{8.1}$$

It should be emphasized that these stationary calculations have been performed on a in house solver and not AVBP.

8.1.1.2 Root-finding algorithm

In the prospect of solving Eq. (5.137), the only real unknown of the system is the density profile $\rho(x)$ since no velocity is considered and the fixed temperature allows to evaluate all the other thermodynamic variables. The density profile is considered here as a vector $\mathrm{P} = [\rho_1, \rho_2, \cdots, \rho_{n-1}, \rho_n]^{\mathrm{T}}$ where n is the number of points. With these notations, Eq. (5.137) can be written in the vectorial form of Eq. (8.2) where $\mathbf{G}$ is a non linear function of vector P.

$$\mathbf{G}(\mathrm{P}) = 0 \tag{8.2}$$

A wide variety of methods exist to solve Eq. (8.2). Given the strongly non linear behavior of function $\mathbf{G}$ and the sensitivity of the system, we opted for the global affine invariant Newton's scheme devised in Deuflhard (1991). This method builds upon the classic Netwon's scheme which updates the value of the guessed solution at each step by following the direction of the gradient as enunciated by Eq. (8.3) where P^k, P^{k+1} are the guessed values for the solution at iterations k and $k+1$ and $J^k_{\mathbf{G}}$ is the Jacobian matrix of function $\mathbf{G}$ evaluated at P^k.

$$\mathrm{P}^{k+1} = \mathrm{P}^k - {J^k_{\mathbf{G}}}^{-1} \cdot \mathrm{P}^{k+1} \tag{8.3}$$

Newton's scheme is notorious for providing a quadratic convergence once close enough to the solution. This is however not the case when far from the solution where strictly following the full update imposed by the gradient can lead to steps too large that fail to decrease the values of $\mathbf{G}\left(\mathrm{P}^k\right)$ at each iterations. The idea behind Deuflhard's approach is to temper *a posteriori* the size of the step by a factor μ if the initial Newton's step has failed to reduced the value of function $\mathbf{G}$. In that case, a new guessed solution $\tilde{\mathrm{P}}^{k+1}$ is calculated as expressed by:

$$\tilde{\mathrm{P}}^{k+1} = \mathrm{P}^k - \mu {J^k_{\mathbf{G}}}^{-1} \cdot \mathrm{P}^{k+1} \tag{8.4}$$

More precisely, the introduction of the tempering factor μ, a process known as backtracking, is not due to Deuflhard. Rather, he proposed a method to optimize the choice for the value of μ involving only the know value of $\mathbf{G}\left(\mathrm{P}^{k-1}\right)$ and those of $\mathbf{G}\left(\mathrm{P}^k\right)$ and $J^k_{\mathbf{G}}$ known when the classic Newton's step has been tested. Thus, applying this method optimizes the update step when far from the solution (which is often the case during the first iterations in our problem) and achieves the quadratic convergence of the classic Newton's scheme when backtracking is no longer needed. A practical implementation of the scheme can be found in Sect. 9.7 of Teukolsky et al. (1992) and has been used in this work.

8.1.1.3 Application to interface equilibrium calculations

For our practical implementation, the variable $X = \ln(\mathrm{P})$ is used to ensure that no negative density values are encountered during the calculation. This tweak proves absolutely necessary when solving for low temperatures when the vapor densities reach low values.
As an initial guess, an arctan-like shape is used with arbitrary but purposefully exaggerated values of liquid and vapor densities. Regarding the initial width, only a trial-and-error approach can be used to start the process, usually starting at high temperatures for which the system is less sensitive. However, once a good initial guess for the width has been found, a step-by-step continuation approach can be used to progressively reduce the temperature, using the result from the last higher temperature as an initial guess for the next lower one.

The results presented in the following paragraph focus on the assessment of the purely thermodynamic behavior of the SG model. Fig. 8.1 shows graphs comparing the saturation densities as calculated using the argument of thermodynamic equilibrium (equality of the chemical potential of the two phases) and the values obtained using the SG model solving Eq. (8.2). The comparison is done for several values of temperature and the relative errors between the equilibrium and SG approach are also provided.

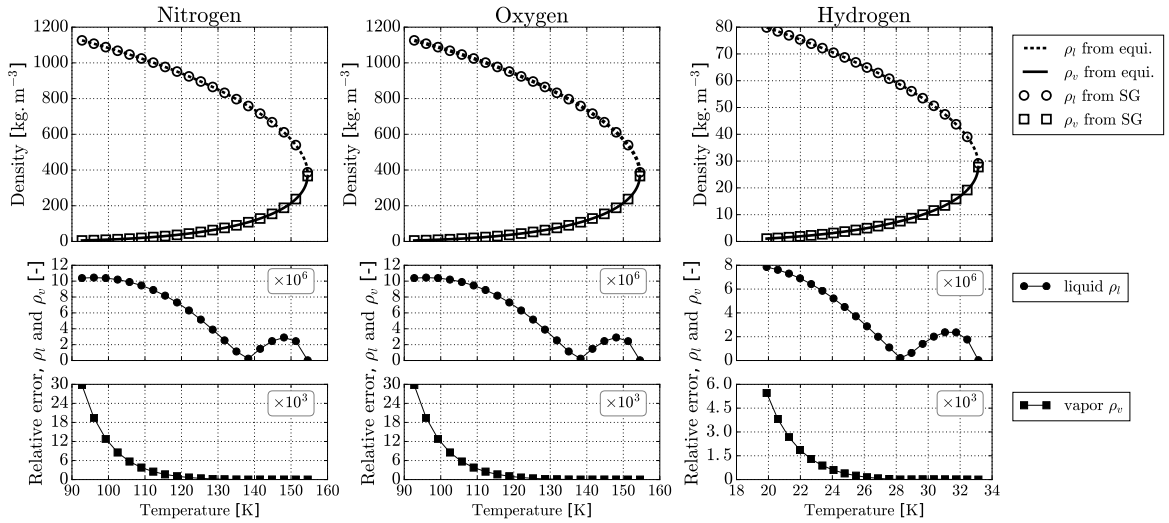

Figure 8.1: *Comparison between the saturation densities calculated with the equilibrium criterion and predicted by the Second Gradient model for several single species. The relative errors for ρ_l and ρ_v are magnified.*

The results show a very good agreement, even for low reduced temperatures leading to very low vapor densities, what further validates the behavior of the SG model from a purely thermodynamic point of view.

8.1.2 Isothermal 1D simulations

Using solutions from the stationary solver, unsteady one-dimensional simulations involving moving and deformed interfaces have been performed using AVBP. The initial setting for the four cases presented hereafter is mostly the same, a single isothermal interface of N_2 is placed in an open domain. The general parameters used for these simulations are recalled in Tab. 8.1 and the set of equations solved is given by Eqs. (8.5a) - (8.5b)

$$\begin{cases} \dfrac{\partial \rho}{\partial t} = -\dfrac{\partial (\rho u)}{\partial x} & \text{(8.5a)} \\ \dfrac{\partial (\rho u)}{\partial t} = -\dfrac{\partial}{\partial x}\left[\rho u^2 + P_0 + \dfrac{\lambda}{2}\left(\dfrac{\partial \rho}{\partial x}\right)^2 - \lambda \rho \dfrac{\partial^2 \rho}{\partial x^2}\right] & \text{(8.5b)} \end{cases}$$

Since only the thermodynamic behavior of the interface is being studied, to avoid possible numerical difficulties that might perturb the calculations, a relatively high number of geometric points (361 point) is used for these simulations. For static cases (no initial velocity for the

interface), pressure outlets are used on both boundaries of the domain, whereas for convected cases, a velocity-temperature inlet is used on the left boundary and a pressure outlet is used on the right boundary. In either cases, the boundaries are non-reflective. These conditions are enforced following the strategy described in Sec. 7.2.2.

T	113.57 K	λ	$1.0 \cdot 10^{-10}$ m$^7 \cdot$ kg$^{-1} \cdot$ s^{-2}	σ	3.26 N $\cdot$ m
P^{sat}	18.15 bar	points in int.	≈ 30	w	4.42 μm
ρ_l	542.1 kg $\cdot$ m^{-3}	equations	mass + mom.	scheme	GRK
ρ_v	80.3 kg $\cdot$ m^{-3}	time step	automatic (CFL+SG)	CFL	0.95

Table 8.1: *Simulation parameters used for the one dimensional N_2 planar interface in isothermal configurations solving Euler SG equations*

The first case demonstrates the ability to convect the interface and allows to partially assess the behavior of the boundary conditions. As shown in Fig. 8.2 where an initial constant speed $u = 10\text{m} \cdot \text{s}^{-1}$ is applied, the interface shape is perfectly preserved during the convection and no perturbation coming from the boundaries are observed as long as the interface is not in contact with one of them.

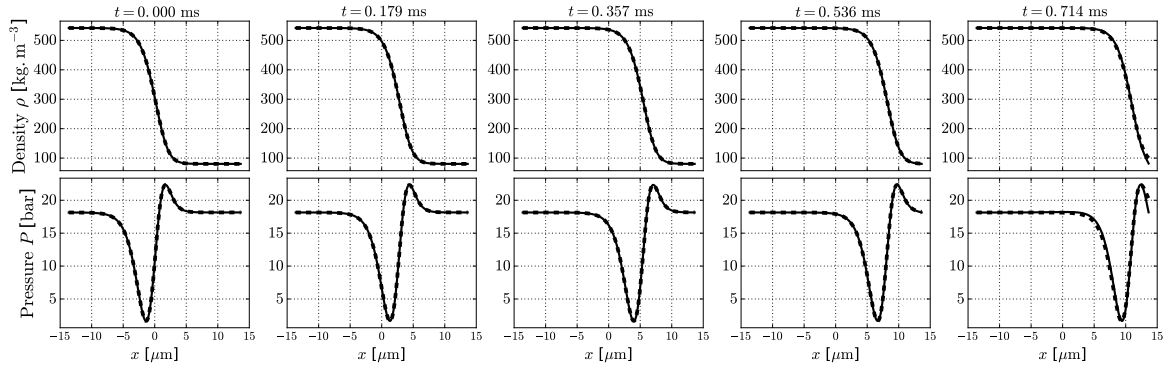

Figure 8.2: *Density and pressure profiles of an isothermal N_2 interface convected at constant speed $u = 10\text{m}\cdot\text{s}^{-1}$. The plain lines show the calculation results and the dashed lines show the theoretical/ideal position of the interface. Non-reflecting velocity-temperature inlet (left) and pressure outlet (right) used.*

The second and third cases, shown respectively in Figs. 8.3 and 8.4, demonstrate the ability of the model to handle mechanical perturbations applied to the interface. To that effect, the interface has been artificially either stretched (Fig. 8.3) or compressed (Fig. 8.4).
In each case, the interface is able to return to its equilibrium shape. The important acoustic waves created by the reshaping of the interface, particularly in the case of Fig. 8.4, are properly evacuated at the boundaries, further validating their ability to handle interface-free flows.
The fourth case combines advection and mechanical deformation as the interface, again convected at an initial constant speed $u = 10\text{m} \cdot \text{s}^{-1}$, has also been stretched. The simulation goes as expected, the interface properly returns to its equilibrium profile while being convected.

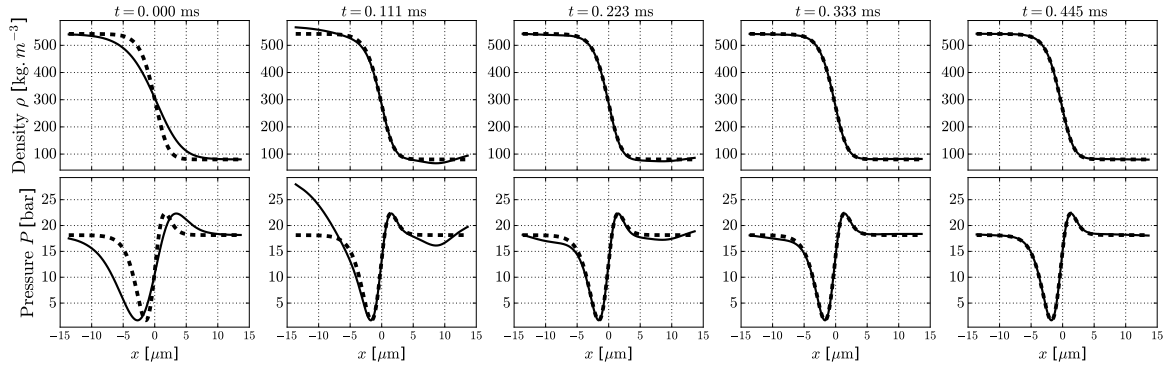

Figure 8.3: *Density and pressure profiles of a static isothermal N_2 interface initially stretched by a factor 2. The plain lines show the calculation results and the dashed lines show the theoretical/ideal position of the interface. Non-reflecting pressure outlets (left and right) used.*

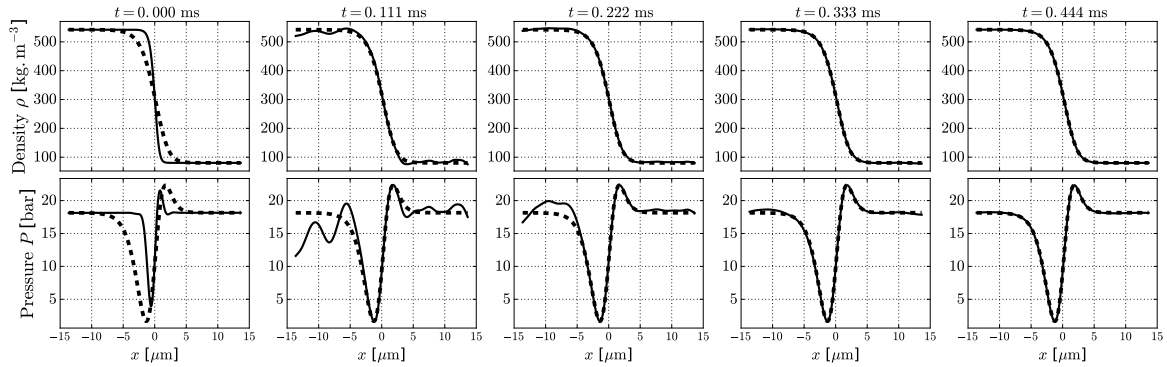

Figure 8.4: *Density and pressure profiles of a static isothermal N_2 interface initially compressed by a factor 3. The plain lines show the calculation results and the dashed lines show the theoretical/ideal position of the interface. Non-reflecting pressure outlets (left and right) used.*

Overall, the model responds properly to the various configurations imposed upon the interface and behaves as expected for these canonical one-dimensional cases.

8.1.3 Non isothermal 1D simulations

In this section, non-isothermal simulations are performed although starting from the same isothermal initial solution. The configuration used in Sect. 8.1.3.1-8.1.3.2 is similar to that described in Tab. 8.1 with the major difference that all three Euler SG equations (mass, momentum and energy), as recalled in Eqs. (8.6a) - (8.6c), are solved instead of only the first two for the previous isothermal cases.
Moreover, to achieve reasonable time steps when the Navier-Stokes equations are solved with diffusive terms, pertaining to the Fourier condition, the mesh resolution as been reduced to about 8 points in the interface, without loss of generality in the results. The details of the configuration are recalled in Tab. 8.2. To study the case of a vanishing interface, a similar

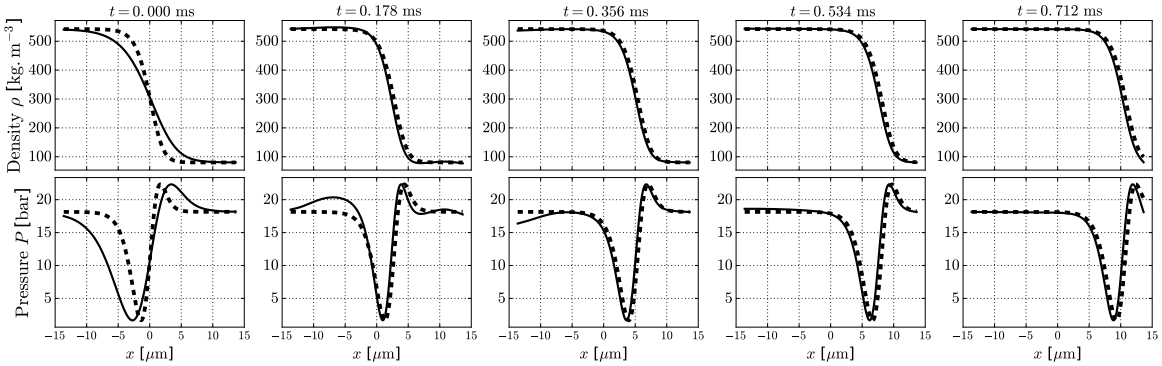

Figure 8.5: *Density and pressure profiles of an isothermal N_2 interface initially stretched by a factor 2 and convected at constant speed $u = 10\text{m} \cdot \text{s}^{-1}$. The plain lines show the calculation results and the dashed lines show the theoretical/ideal position of the interface. Non-reflecting velocity-temperature inlet (left) and pressure outlet (right) used.*

but slightly more realistic configuration is considered in 8.1.3.3 where oxygen O_2 is used.

$$\begin{cases} \dfrac{\partial \rho}{\partial t} = -\dfrac{\partial (\rho u)}{\partial x} & \text{(8.6a)} \\ \dfrac{\partial (\rho u)}{\partial t} = -\dfrac{\partial}{\partial x}\left[\rho u^2 + P_0 + \dfrac{\lambda}{2}\left(\dfrac{\partial \rho}{\partial x}\right)^2 - \lambda\rho\dfrac{\partial^2 \rho}{\partial x^2}\right] & \text{(8.6b)} \\ \dfrac{\partial (\rho e)}{\partial t} = -\dfrac{\partial}{\partial x}\left[(\rho e + P_0)\, u + \dfrac{\lambda}{2}\left(\dfrac{\partial \rho}{\partial x}\right)^2 u + \lambda\rho\dfrac{\partial \rho}{\partial x}\dfrac{\partial u}{\partial x} - \lambda\rho\dfrac{\partial^2 \rho}{\partial x^2}u\right] & \text{(8.6c)} \end{cases}$$

T	113.57 K	λ	$1.0 \cdot 10^{-10}$ m$^7 \cdot$ kg$^{-1} \cdot$ s^{-2}	σ	3.26 N $\cdot$ m
P^{sat}	18.15 bar	points in int.	≈ 8	w	4.42 μm
ρ_l	542.1 kg $\cdot$ m^{-3}	equations	mass + mom. + ener.	scheme	GRK
ρ_v	80.3 kg $\cdot$ m^{-3}	time step	automatic (CFL+SG)	CFL	0.95

Table 8.2: *Simulation parameters used for the one dimensional N_2 planar interface in non-isothermal configurations solving Euler/Navier-Stokes SG equations*

8.1.3.1 Deformed static interfaces

To compute the case of a stretched interface, the initial solution must be generated consistently. All three conservative variables (density ρ, momentum ρu, total volumetric energy ρe) must be stretched in a similar fashion and the position of the interface must be adjusted to ensure that the initial total energy in the domain is equal to that of the theoretical final solution. The initial pressure and temperature are then calculated from the density and energy profiles. This leads to the peculiar and non isothermal initial solution visible in Fig. 8.6.

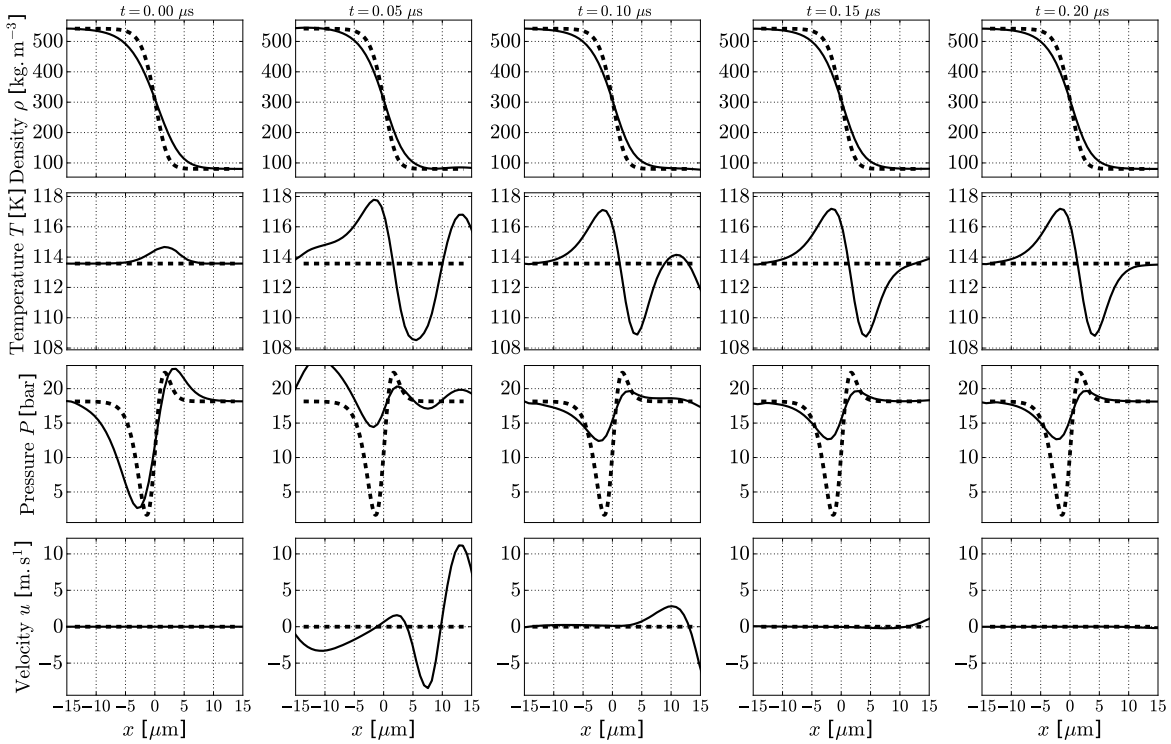

Figure 8.6: *Density, temperature, pressure and velocity profiles of a non isothermal N_2 interface interface initially stretched by a factor 2. The plain lines show the calculation results and the dashed lines show the theoretical/ideal position of the interface. Non-isothermal Euler SG equations (mass, momentum, energy) are solved. Non-reflecting pressure outlets (left and right) used.*

Although this case can be computed without additional difficulties, it appears in the profiles of Fig. 8.6, that the interface does not return to its equilibrium profile. Instead, a different non constant temperature profile is created and the pressure profile also retains a peculiar aspect. This case has been prolonged up to a hundred times the return-to-equilibrium time of the isothermal case in Fig. 8.3 with the interface not showing any sign of returning to its original isothermal profile. A mesh convergence study up to extremely resolved cases has shown this result not to be directly caused by an insufficient mesh resolution.

The same case, for which results are given in Fig. 8.7, has been computed solving the Navier-Stokes equations. The diffusion coefficients (dynamic viscosity and thermal conduction coefficient) have been calculated according to Chung et al. (1988) method presented in Sec. 1.2.4. It clearly appears that due to the thermal conduction coercing the interface into having a constant temperature profile, the interface returns to its equilibrium profile in terms of density and energy with a zero final velocity. The interface simulated solving only the non-isothermal Euler equations, in contrast, remains in the peculiar state reached after 20 μs in Fig. 8.6 even after the long time simulation of 7.5 ms, which represents a factor of 375.

No definitive explanation has been found for the behavior observed in Fig. 8.6. The evolution of the total entropy of the system, expected to be constant, has also been analyzed for different

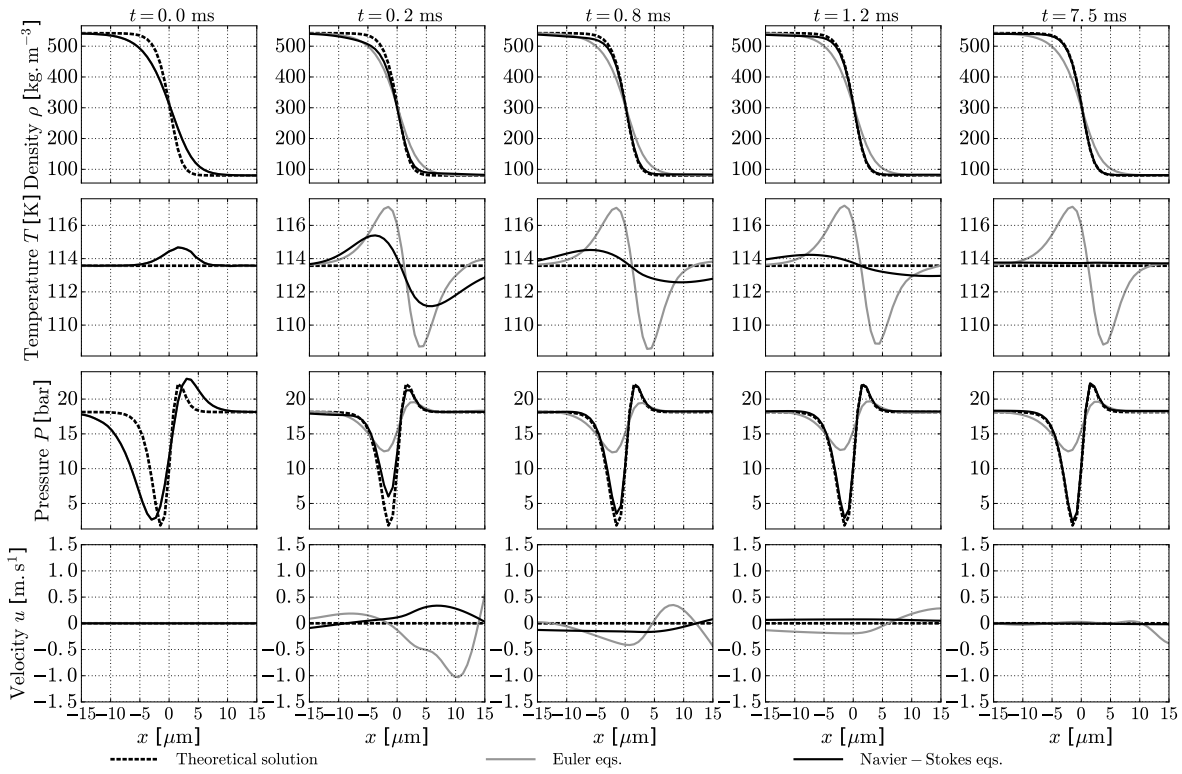

Figure 8.7: *Density, temperature, pressure and velocity profiles of a non isothermal N_2 interface interface initially stretched by a factor 2. Euler and Navier-Stokes SG equations (mass, momentum, energy) are solved. Non-reflecting pressure outlets (left and right) used.*

mesh resolutions. It must be emphasized that the numerical scheme used in our simulations does not satisfy the second thermodynamic principle by nature at the discretized level. However, the curves have shown to converge towards a constant entropy evolution as the mesh resolution was increased, further enticing that this peculiar behavior is actually valid from a thermodynamic point of view, and thus remains unexplained.
However, the reach of this result must be moderated since the initial configuration used for the simulation can hardly be compared to a realistic physical case. In two or three dimensions, situations leading to the deformation of the interface would be accompanied with a non null velocity and therefore a convection, of sort, of the interface. Moreover, for the interface to be compressed and/or stretched in the first place, it requires an upset in the thermodynamic balance that cannot be achieved, to the best of our knowledge, at an initially constant temperature for a single species fluid, especially for a constant, let alone null, velocity field.

8.1.3.2 Convected interfaces

To study interface convection without interference from the boundary conditions, a one dimensional periodic setting is used as done in Sec. 7.1.3.1 retaining the same parameters as given in Tab. 8.2 and the convection speed is 10 m.s^{-1}.
The results in Fig. 8.8 have been obtained with a mesh resolution resulting in 8 points in the interface. Whereas the density and velocity profiles have been mostly well convected, strong

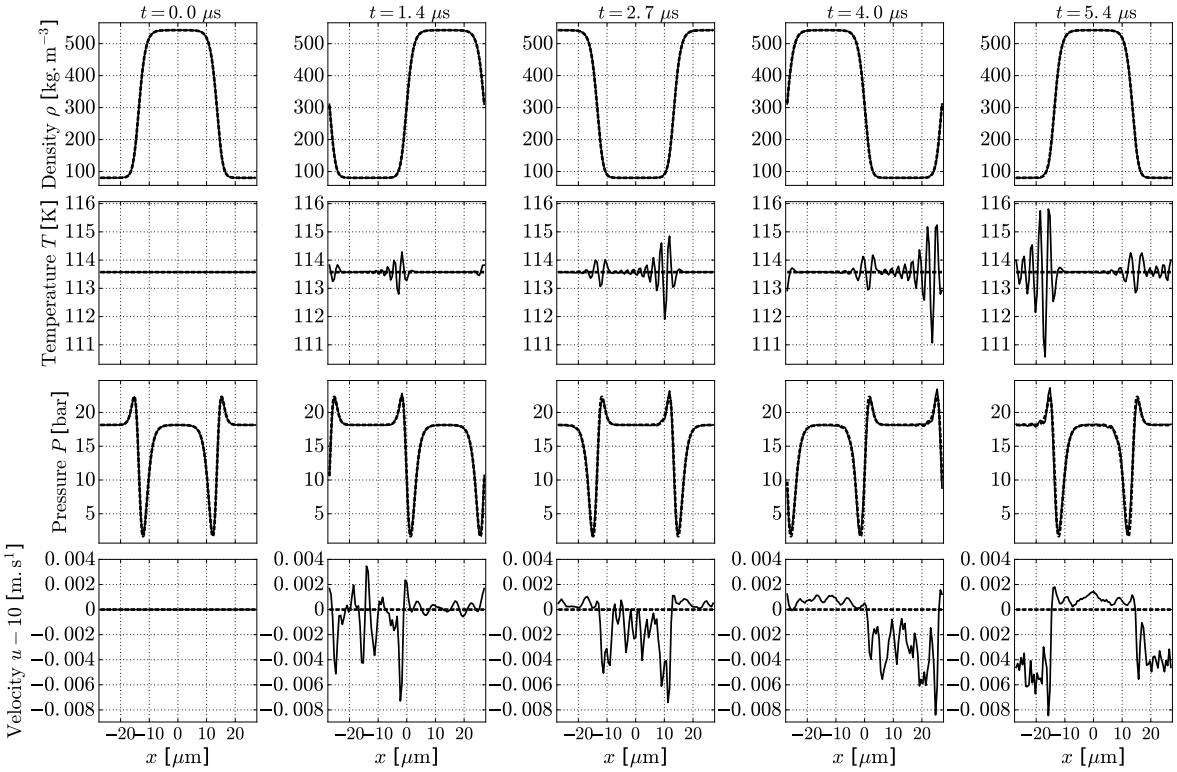

Figure 8.8: *Density, temperature, pressure and velocity profiles of a N_2 droplet convected at constant speed $u = 10\ \mathrm{m \cdot s^{-1}}$. The plain lines show the calculation results and the dashed lines show the theoretical/ideal position of the interface. Periodic boundary conditions (left and right) used. Non isothermal SG Euler equations are solved, 8 points in the interface*

undershoots and overshoots that can be observed on the temperature profiles and have also lead to strong discrepancies in the convected pressure profiles. These errors grow steadily and quite rapidly with time.

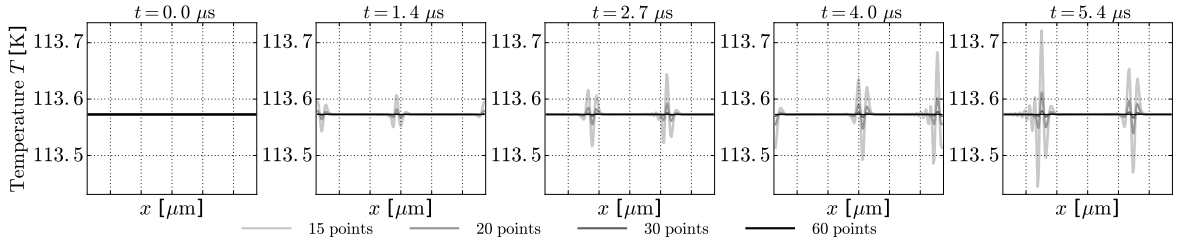

Figure 8.9: *Temperature profiles of a N_2 droplet convected at constant speed $u = 10\mathrm{m \cdot s^{-1}}$. The plain lines show the calculation results and the dashed lines show the theoretical/ideal position of the interface. Periodic boundary conditions (left and right) used. Non isothermal SG Euler equations are solved for multiple higher mesh resolutions.*

One can observe in Fig. 8.10 that the amplitude of the discrepancies in the temperature and pressure profiles are strongly dependent on the mesh resolution while the density and velocity

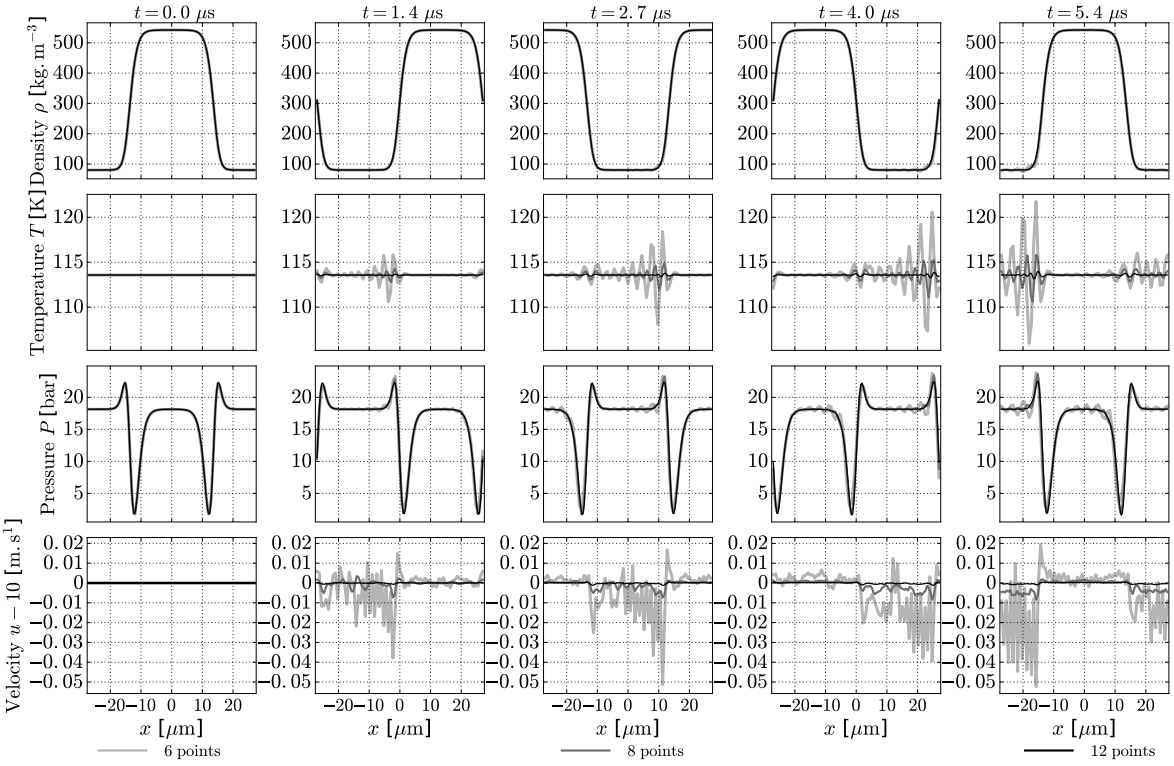

Figure 8.10: *Density, temperature, pressure and velocity profiles of a N_2 droplet convected at constant speed $u = 10\text{m} \cdot \text{s}^{-1}$. Periodic boundary conditions (left and right) used. Non isothermal SG Euler equations are solved for multiple lower mesh resolutions*

profiles tend to maintain a reasonable accuracy even for lower resolutions. However, even with twelve points in the interface, the errors in the temperature remain important, more than 0.5 K after only one crossing of the domain.
The problem is still visible for very high resolutions as exposed in Fig. 8.9 where only the evolution of the temperature profiles is provided. Since the GRK scheme, that has been used to carry out these simulations, is centered and completely non-dissipative, such characteristic oscillating numerical errors could have been expected. However, the still relatively important amplitude of these oscillations, even for very high mesh resolutions, remains puzzling and probably cannot be only justified by this shortcoming of the GRK scheme.

This aspect is evoked again in the next paragraph where the impact of artificial viscosity is discussed. This discussion is all the more motivated by the fact that the addition of physical diffusion, presented in Fig. 8.11, seems to have only a limited impact on the results (which however could be explained by the design used for this specific case). Indeed, while the point-to-point errors are slightly damped, the curves show a significant improvement only at sufficient mesh resolutions, typically with at least eight points in the interface.
Nonetheless, the dissipation provided by viscosity and thermal diffusion, that could be deemed more physical than the eponymous artificial viscosity of AVBP, still provides the ideal approach to foster the stability of the calculations when possible. This important aspect is further elaborated upon in Sec. 8.2 where two-dimensional cases are addressed.

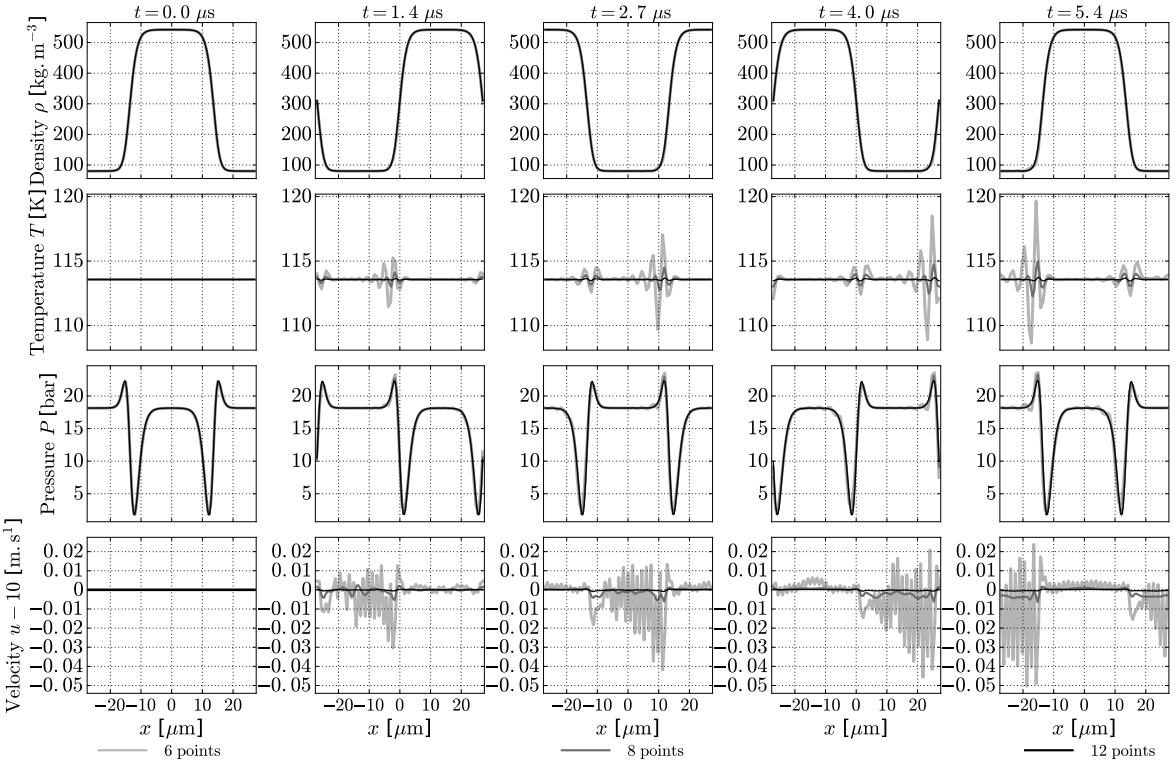

Figure 8.11: *Density, temperature, pressure and velocity profiles of a N_2 droplet convected at constant speed $u = 10\text{m} \cdot \text{s}^{-1}$. Periodic boundary conditions (left and right) used. Non isothermal SG Navier-Stokes equations are solved with Chung's diffusion model, for multiple lower mesh resolutions*

Impact the artificial viscosity:

An additional set of simulations, fostered by the minimal impact of the physical diffusion, has been performed trading Chung's diffusion model for the artificial viscosity implemented in the AVBP solver and presented in Sec. 6.2.4.2. As evidenced by the curves in Fig. 8.12, the impact of this approach on the lower mesh resolutions is much more significative, as the 3-point and 4-points cases are solved to completion. The poor accuracy of these meshes, in particular their inability to properly capture the density gradient and more importantly the characteristic pressure variation when crossing the saturation curve, prevents the corresponding results to be accurate and leads to important numerical errors. Nonetheless, the fact that the native artificial viscosity has permitted these cases to be simulated led us to believe that the numerical difficulties observed for the non-isothermal cases and particularly visible in the temperature fields, are typical numerical issues associated with centered schemes such the as GRK scheme used in these simulations. High-order centered schemes are notorious for being strongly oscillatory, even more so when their formulation is totally non-dissipative as it is the case for the GRK scheme.

These numerical difficulties are recurrent in compressible real gas simulations where the strong coupling of the momentum and energy equations leads to strong numerical oscillations when

simulations are performed with this class of schemes. The artificial viscosity in AVBP has first and foremost been developed in order to address these difficulties and offer a tool to temper these oscillations. The strong positive effect of said artificial viscosity on the lower mesh resolutions configurations could be interpreted as an indication that the same issue is being encountered in our case of interest. These difficulties can moreover be amplified by the inherent stiff nature of the equations when enriched with the high-order derivatives of the capillary terms. A last hint in that direction is the observation that the errors in the temperature field are indeed oscillations over several mesh step sizes rather than point-to-point oscillations, what can be noticed by comparing the temperature and velocity fields in Fig. 8.11.

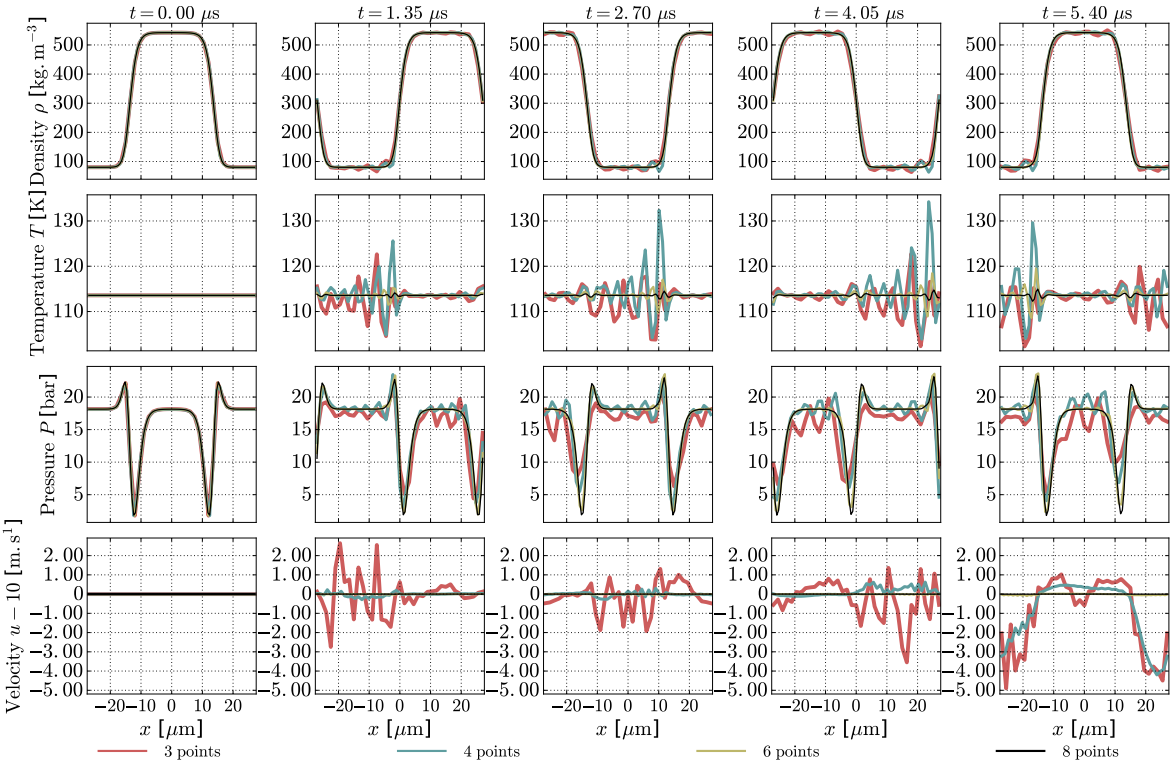

Figure 8.12: *Density, temperature, pressure and velocity profiles of a N_2 droplet convected at constant speed $u = 10\text{m} \cdot \text{s}^{-1}$. Periodic boundary conditions (left and right) used. Non isothermal SG Navier-Stokes equations are solved with native AVBP artificial viscosity.*

Beyond this potential direction, this issue had not been with met satisfactory explanations but we firmly believe that it is the manifestation of a deep-rooted issue that should be a priority point of investigation for future work regarding the SG model.

8.1.3.3 Interfaces with thermal conduction

In this last section, the interaction between the SG model and thermal conduction is addressed more intimately. To that effect, a different configuration has been used, with oxygen, and of which relevant parameters are compiled in Tab. 8.3. Navier-Stokes equations (8.7a)-(8.7c) are solved where the diffusion coefficients (viscosity and thermal conduction coefficients) have been calculated according to Chung et al. (1988) method presented in Sec. 1.2.4. A constant temperature is imposed on the left and right walls and a temperature temporal relaxation condition is used on both boundaries.

$$\begin{cases} \dfrac{\partial \rho}{\partial t} = -\dfrac{\partial (\rho u)}{\partial x} & \text{(8.7a)} \\ \dfrac{\partial (\rho u)}{\partial t} = -\dfrac{\partial}{\partial x}\left[\rho u^2 + P_0 + \dfrac{\lambda}{2}\left(\dfrac{\partial \rho}{\partial x}\right)^2 - \lambda\rho\dfrac{\partial^2 \rho}{\partial x^2} - \dfrac{4}{3}\mu\dfrac{\partial u}{\partial x}\right] & \text{(8.7b)} \\ \dfrac{\partial (\rho e)}{\partial t} = -\dfrac{\partial}{\partial x}\left[(\rho e + P_0)\, u + \dfrac{\lambda}{2}\left(\dfrac{\partial \rho}{\partial x}\right)^2 u + \lambda\rho\dfrac{\partial \rho}{\partial x}\dfrac{\partial u}{\partial x} - \lambda\rho\dfrac{\partial^2 \rho}{\partial x^2}u - \dfrac{4}{3}\mu u\dfrac{\partial u}{\partial x} - k_{\text{th}}\dfrac{\partial T}{\partial x}\right] & \text{(8.7c)} \end{cases}$$

T_{init}	110 K	λ	$1.173 \cdot 10^{-17}$ m$^7 \cdot$ kg$^{-1} \cdot$ s^{-2}
P^{sat}	5.45 bar	points in int.	≈ 8
ρ_l	1017.7 kg $\cdot$ m^{-3}	σ	8.37 mN $\cdot$ m^{-1}
ρ_v	21.4 kg $\cdot$ m^{-3}	w	0.97 nm
scheme	GRK	equations	mass + mom. + ener.
CFL	0.95	time step	(CFL+SG+Fourier)

Table 8.3: *Simulation parameters used for the one dimensional O_2 planar interface in non-isothermal configurations solving SG Navier-Stokes equations*

Evaporation in a closed domain

The first case addresses the evaporation of an interface caused by the elevation of its temperature from a subcritical (110 K) to a transcritical (170 K) temperature (the critical temperature of oxygen being $T_{cO_2} = 154.6$ K). This evaporation is performed in two steps to validate both subcritical-subcritical and subcritical-supercritical transitions: in the first step, the temperature is elevated from 110 K to 140 K, it is then further elevated to reach 170 K.

The results in Fig. 8.13 show that as the temperature stabilizes at 140 K and the velocity returns to 0, the density and the pressure profiles properly adopt their equilibrium shapes at that temperature. The same satisfactory results are obtained in Fig. 8.14 where the density gradient, and thus the interface, slowly smooths out and eventually vanished once the critical temperature is passed. This observation also applies to the pressure profile which no longer displays the subcritical shape typical of the binodal region. All the mechanical and thermodynamic variables become uniform at the right values by the end of the simulation.

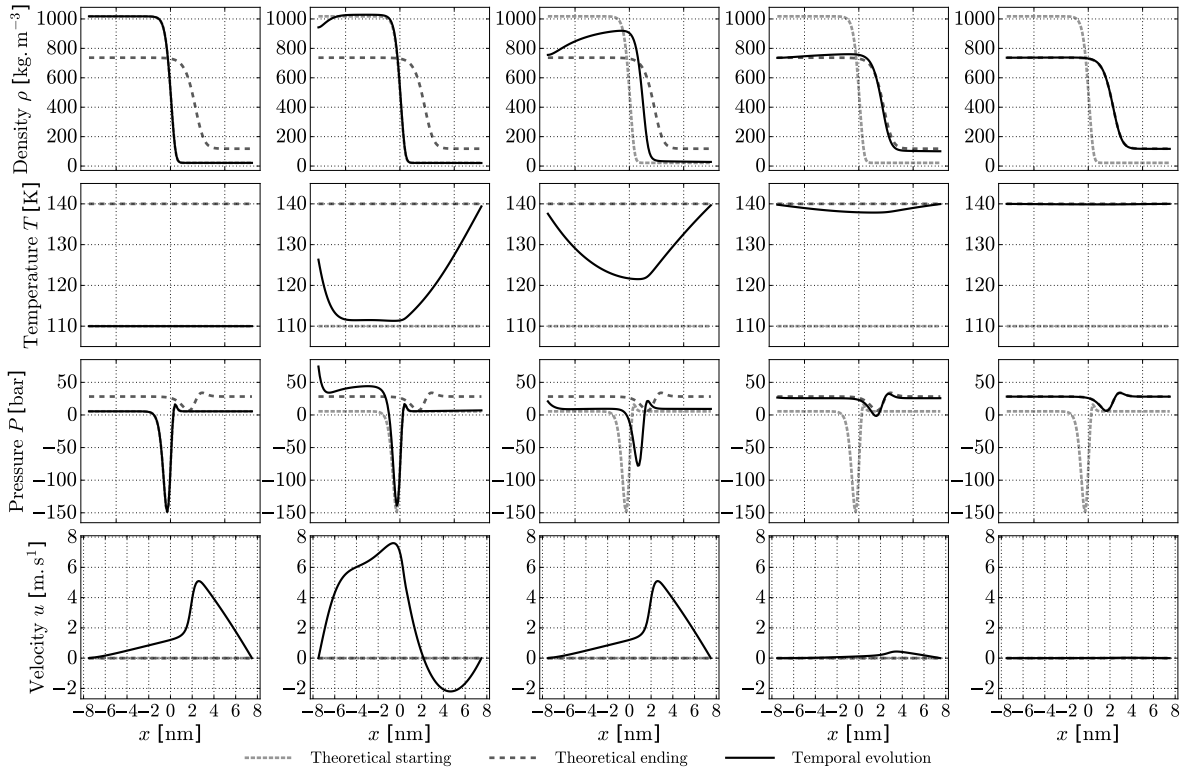

Figure 8.13: *Density, temperature, pressure and profiles of a heated O_2 droplet with viscosity and thermal conduction. The dashed lines show the theoretical isothermal profiles at 110K and 140K, the plain lines show the calculation results. Isothermal boundary conditions at 140K are used on both sides. SG Navier-Stokes equations are solved, Chung model is used for the diffusive fluxes.*

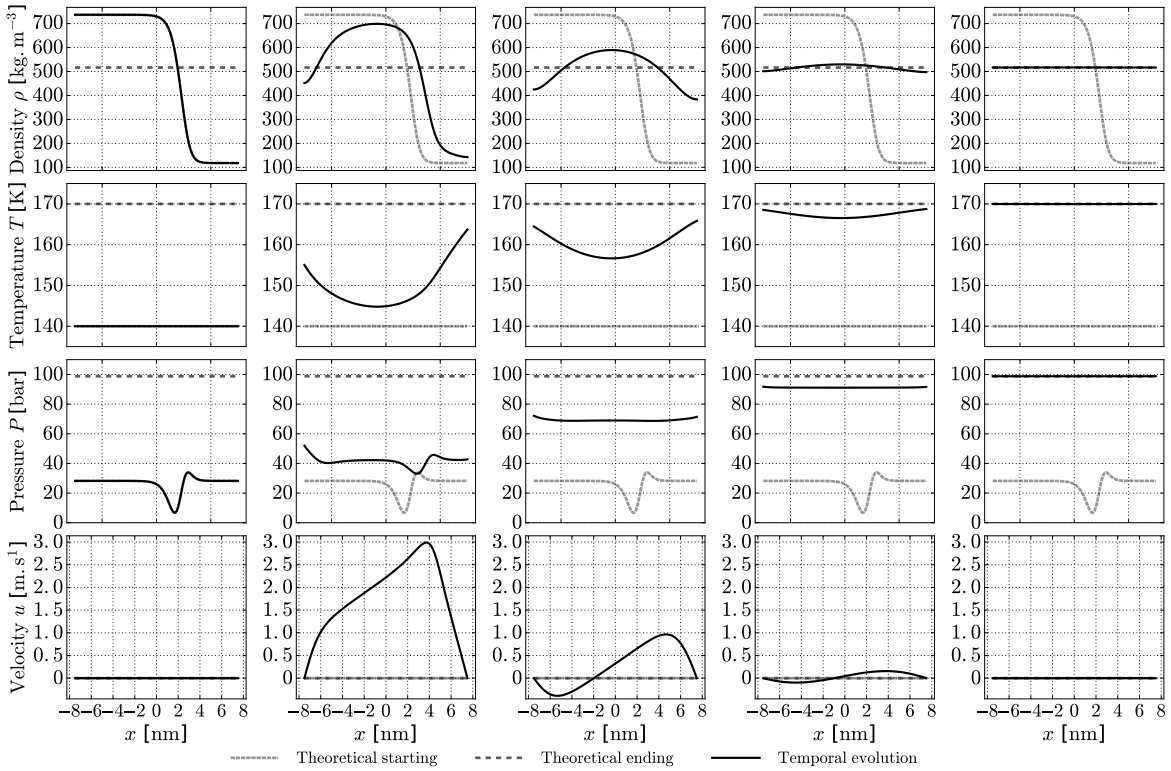

Figure 8.14: *Density, temperature, pressure and profiles of a vanishing heated O_2 droplet with viscosity and thermal conduction (continuation of Fig. 8.13). The dashed lines show the theoretical isothermal profiles at 140K and 170K, the plain lines show the calculation results. Isothermal boundary conditions at 170K are used on both sides. SG Navier-Stokes equations are solved, Chung model is used for the diffusive fluxes.*

Condensation in a closed domain

The inverse process has been applied to simulate the condensation of said interface. The initial profile are taken from the final form in Fig. 8.14, all variables are uniform with no velocity at 170 K. The value of the uniform density profile ensures that the simulation is performed with the same mass of nitrogen. Similarly to the evaporating case, a two step approach has been used to validate both subcritical-supercritical and subcritical-subcritical transitions: in the first step, the temperature is lowered from 170 K to 140 K, it is then further lowered to reach 110 K.

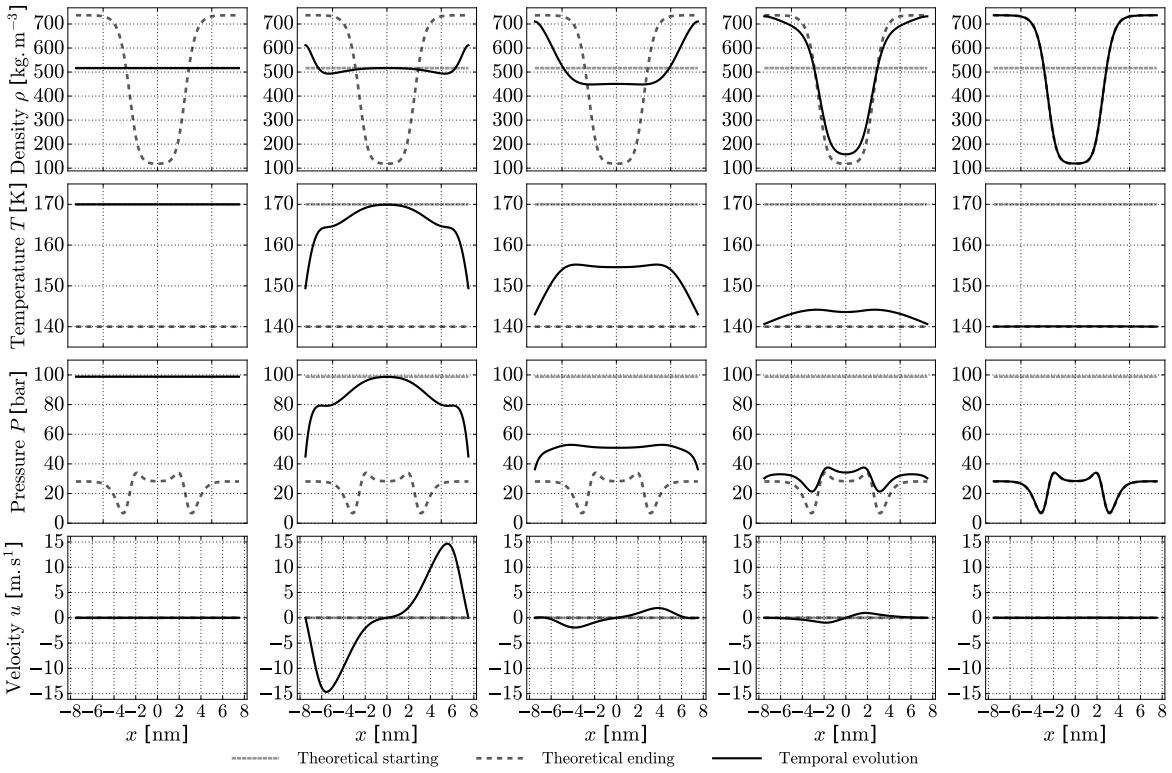

Figure 8.15: *Density, temperature, pressure and profiles of the creation of O_2 droplet with viscosity and thermal conduction. The dashed lines show the theoretical isothermal profiles at 170K and 140K, the plain lines show the calculation results. Isothermal boundary conditions at 140K are used on both sides. SG Navier-Stokes equations are solved, Chung model is used for the diffusive fluxes.*

One noticeable difference is that instead of the single interface profile used as the initial solution for the evaporating case, a double interface profile is adopted by the system when the critical temperature level is crossed, as shown in Fig. 8.15. Notwithstanding this difference, the correct profiles are reached at 140 K with no velocity and the typical subcritical pressure evolution in the binodal region. When the temperature is further lowered in Fig. 8.16, the correct final states are also reached with no additional difficulties.

Although no definitive argument has been found to justify whether the single ou double interface should be preferred by the system, an *a posteriori* analysis on has shown that the double interface (droplet) configuration at 110 K presents the highest final entropy and requires the least energy exchange, which is consistent with a more stable thermodynamic final state starting from the flat supercritical configuration at 170 K.

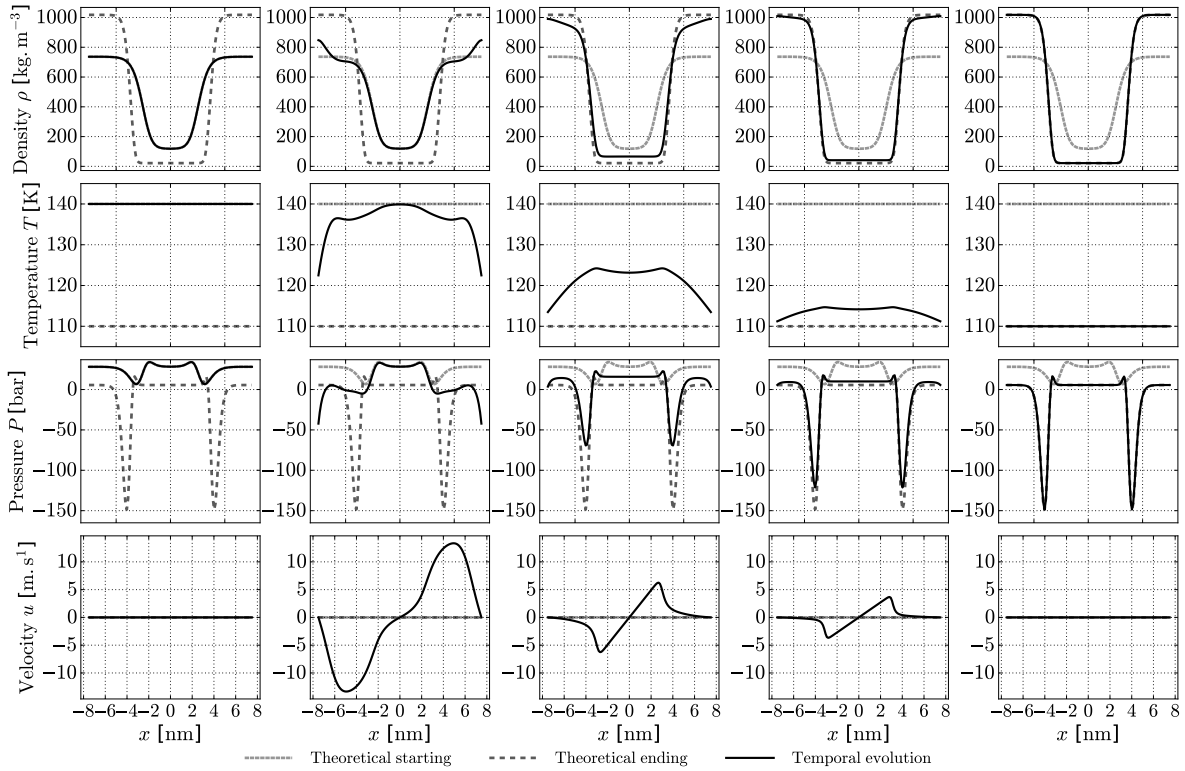

Figure 8.16: *Density, temperature, pressure and profiles of a cooled O_2 droplet with viscosity and thermal conduction (continuation of Fig. 8.15). The dashed lines show the theoretical isothermal profiles at 140K and 110K, the plain lines show the calculation results. Isothermal boundary conditions at 140K are used on both sides. SG Navier-Stokes equations are solved, Chung model is used for the diffusive fluxes.*

Configuration	$E\ \left[\mathrm{nJ}\cdot\mathrm{m}^{-2}\right]$	$S\ \left[\mathrm{nJ}\cdot.\mathrm{K}^{-1}\cdot\mathrm{m}^{-2}\right]$	$\underset{170\ K\to 110\ K}{\Delta E}\ \left[\mathrm{nJ}\cdot\mathrm{m}^{-2}\right]$
Single interface 110 K	−8.65	0.308	10.60
Double interface 110 K	−8.21	0.311	10.16
"Flat" interface 170 K	1.95	0.385	-

Table 8.4: *Integrated energy E and entropy S balance for different interface configurations*

Evaporation in a semi-infinite domain

Finally, a last case of evaporation has also been addressed. The oxygen interface is simulated with the same parameters as in Tab. 8.3, in a larger domain with different boundary conditions. The interface is initially at equilibrium at 110 K the left boundary is set to be an isothermal wall at 140 K where a temperature relaxation occurs. Oppositely, the right boundary is a classic non-reflecting pressure outlet. As shown in Fig. 8.17 and as expected, the interface moves towards the right boundary as the liquid progressively evaporate into gas.

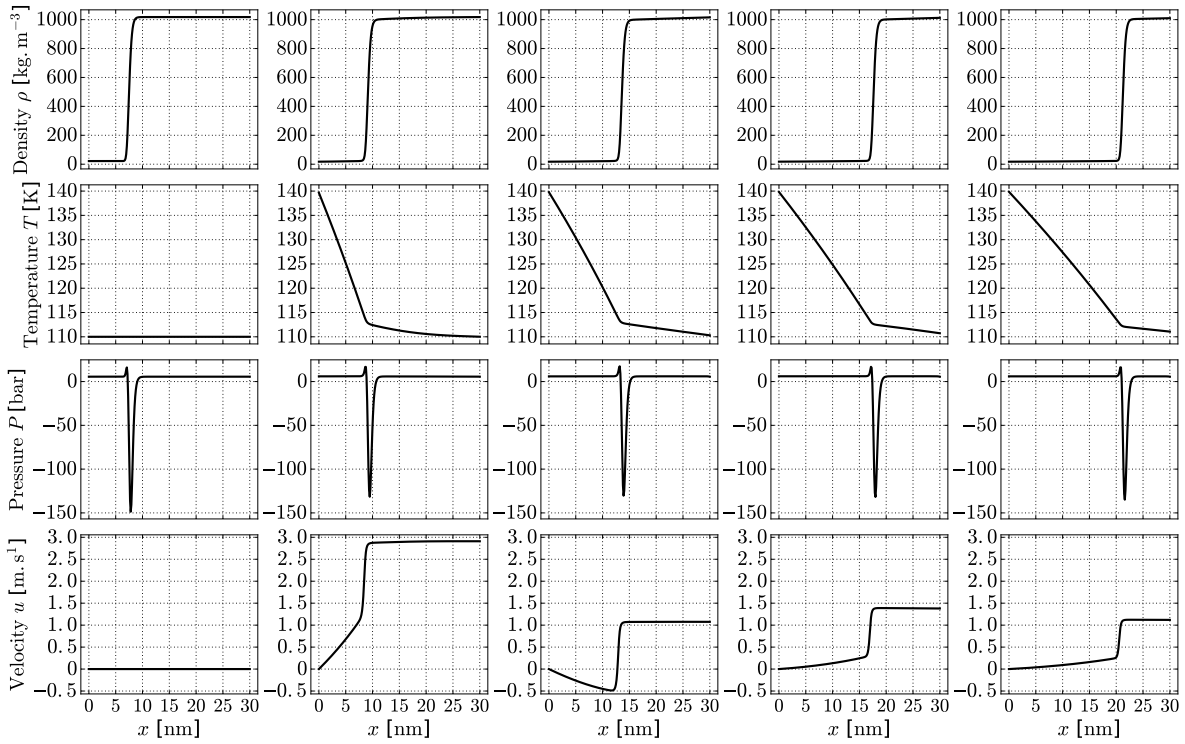

Figure 8.17: *Density, temperature, pressure and profiles of an evaporating O_2 interface with viscosity and thermal conduction. An isothermal wall at 140K is used on the left side with a temperature relaxation condition while an non-reflecting outlet is used on the right boundary. SG Navier-Stokes equations are solved, Chung model is used for the diffusive fluxes.*

8.1.4 Convergence orders

An additional key point that can be evaluated to asses de validity of our implementation is the convergence order of the numerical method. The GRK spatial scheme used for our simulation has a theoretical 4^{th} order super-convergence for linear advection and a 3^{rd} order convergence for Euler equations. To estimate said convergence order, the simulation case used is that of the one-dimensional convected nitrogen droplet from Fig. 8.8.
A varying the number of points has been used to discretize the interfacial zone thus defining the different mesh resolutions used for the study. This number has been taken among the following values $[4, 6, 8, 10, 12, 15, 20, 24, 30, 40, 60]$. Three sets of equations have been considered in relation with the SG model: the isothermal Euler equations, the non-isothermal Euler equations and the (non-isothermal) Navier-Stokes equations with the diffusion model described by Chung et al. (1988).

Since only the spatial order of the scheme has been studied, a common time step (imposed by the most restrictive simulation mesh resolution of 60 points "in the interface"), has been used for the simulations with all the other mesh resolutions. The classic L_2 norm has been used as a metric to evaluate the convection errors for the conserved variables $(\rho, \rho u, \rho e)$ as well as the thermodynamic variables (T, P) directly involved in the simulations. For the isothermal case, the errors for ρe and T have been discarded as being non-relevant. The results observed after a half-crossing of the domain are compiled in Fig. 8.18 and after a complete crossing of the domain in Fig. 8.19.

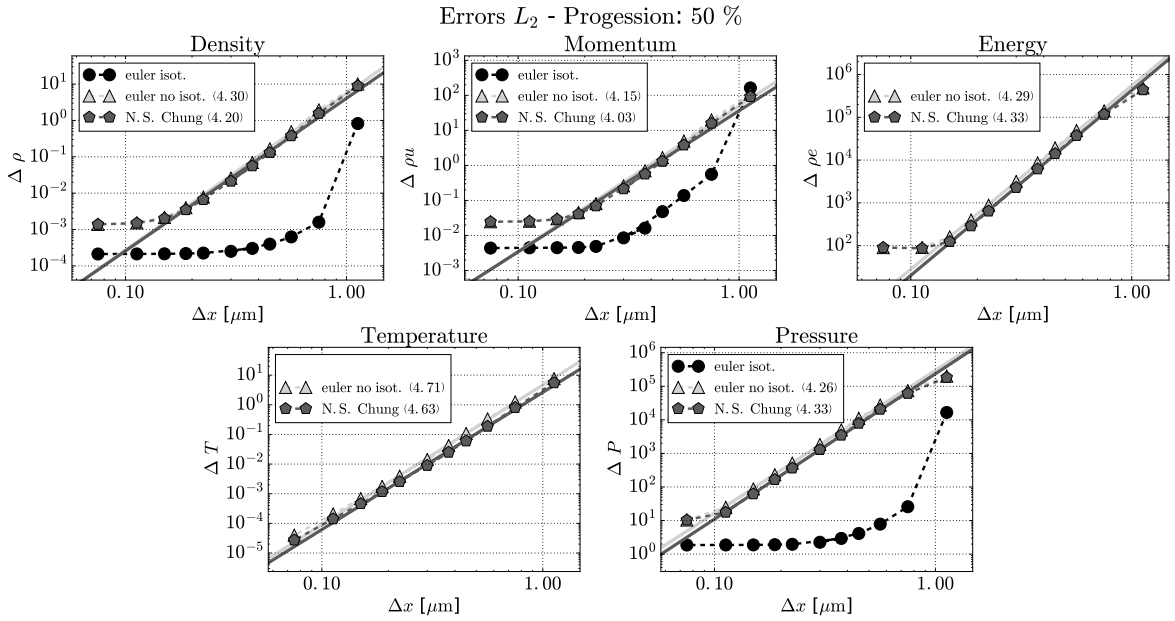

Figure 8.18: *Convergence orders of AVBP's GRK numerical scheme with the SG model implementation in 1D solving Euler isothermal, Euler non isothermal and Navier-Stokes (Chung model) equation. Results after after half a crossing of the domain. Logarithmic scale used for both axis. Interpolation slopes in legend.*

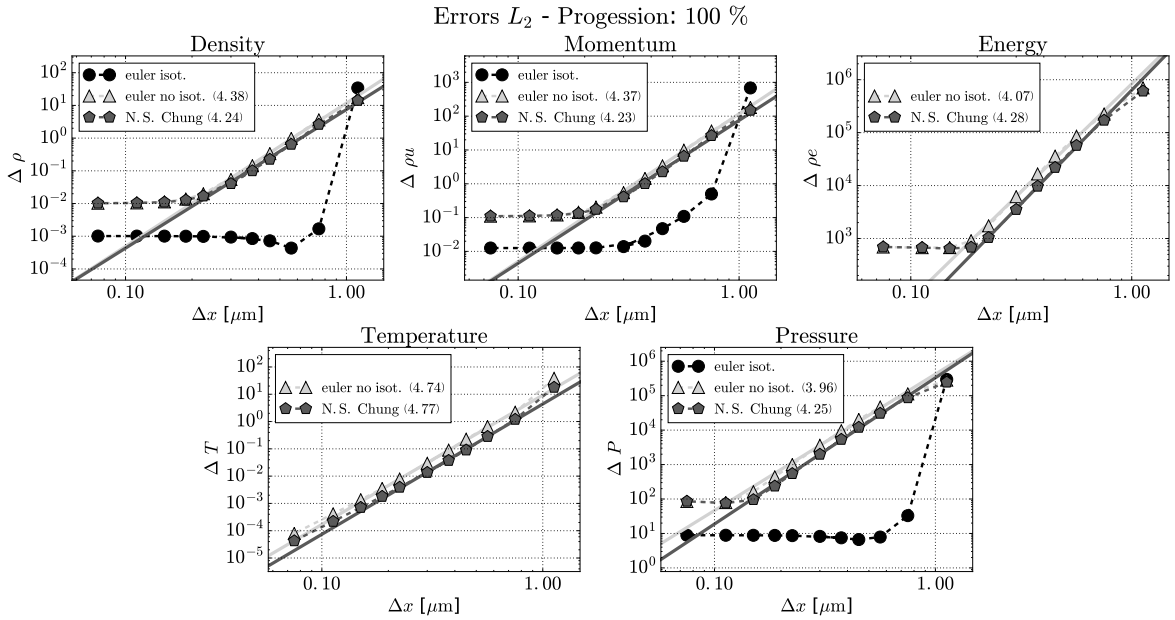

Figure 8.19: *Convergence orders of AVBP's GRK numerical scheme with the SG model implementation in 1D solving Euler isothermal, Euler non isothermal and Navier-Stokes (Chung model) equation. Results after after one crossing of the domain. Logarithmic scale used for both axis. Interpolation slopes in legend.*

The results after a half-crossing and after a complete crossing of the domain are essentially the same. Only an earlier plateau effect can be observed for the 100 % progression with the highest resolution at higher values for the errors. This is consistent with the fact that errors tend to accumulate with time and become harder to mitigate despite using high mesh resolutions.
The set of equations that is solved has a strong impact on the results. More precisely, the system of isothermal Euler equations seems to represent an outlier as it leads to errors on the density, momentum and pressure that drop steeply for the very first resolutions to then remain at values substantially lower than that of the other (and non-isothermal) sets of equations. As such, no order can be established for this set of equations, which is consequently discarded for the rest of the discussion.

For all the variables, the orders of convergence are observed to be above 4 which represents a surprising value on multiple accounts.
Firstly, these orders are above the theoretical 4^{th} order linear super-convergence (see Sengupta (2004)) and the 3^{rd} order Euler convergence (see Lamarque (2007)) of the GRK scheme.
Secondly, it has been established in Sec. 7.1.2 that the discretization of the high-order derivative capillary terms, in particular the Laplacian, leads theoretically to a 2^{nd} order convergence in space.
Thirdly, this last remark is doubly valid when the Navier-Stokes equations are solved and the 2^{nd} order diffusive scheme of AVBP is used to discretize the viscous and conductive terms.
However, the solving of this set of equations has not led to degraded orders but rather to slightly lower values for the errors.

Although all corresponding figures are not presented here for the sake of conciseness, these simulations have been replicated by modifying multiple variables: other values of the capillary coefficient λ (for the same fluid and temperature), other values of temperature (for the same fluid), other metrics (L_1 and L_∞) to evaluate the errors. This full study has also been carried out using oxygen, acting on the same different variables in a similar fashion. For each scenario, the above fourth orders have been observed with regularity for the non-isothermal Euler and Navier-Stokes equations and the extremely fast convergence for the isothermal Euler equations has also been noticed.
The relative contributions of the capillary terms to the momentum and energy balance have also been estimated and confirmed to be homogeneous and of the same magnitude as that of the pressure, momentum transport and energy transport terms. This observation increases the perplexing aspect of the convergence orders that have been extracted. It implies that the discretization of the capillary terms, of order two at most and which should have a significant impact on the overall orders of convergence, does not act so in practice.

No satisfactory answer has been found for this above linear super-convergence for the GRK scheme. It is further proof that the investigation of the mathematical behavior of the SG model from a theoretical and numerical point of view is of the utmost relevance for further studies on that matter. Be that as it may, these unexpectedly good results, although unexplained, cast a rather positive light on our implementation of the SG model in the AVBP solver.

8.2 Validation cases in two dimensions

8.2.1 Oscillating planar interfaces

8.2.1.1 Configuration

To validate the method in two dimensional configurations, the first case chosen is an oscillating isothermal planar interface initially deformed by a harmonic longitudinal perturbation as illustrated in Fig. 8.20. The wavelength of the perturbation is reduced to one period in the domain so that the local curvature radius of the interface remains substantially higher than the interface thickness. Moreover, the amplitude A of the perturbation has been kept low in order to remain in the linear deformation regime. With this setting, the interface is expected to oscillate almost indefinitely since no dissipation, apart from the numerical diffusion, is integrated in the equations.
The relevant parameters used for this calculation are compiled in Tab. 10.2, the fluid used is nitrogen. The GRK scheme of AVBP is used and a selective filter (see Sec. 6.2.4.1) has also been applied to the mass, momentum and energy equations during the simulation with a factor $1.0 \cdot 10^{-2}$ in order to limit point-to-point oscillations typical of high order centered schemes. No slippery walls boundary conditions are used a the top and bottom of the domain which is horizontally periodic.
From a macroscopic point of view, the expected oscillations of the interface are well retrieved as demonstrated by monitoring the time evolution of the density at the center of the domain in Fig. 8.21 and by the series of time snapshots in Fig. 8.22.

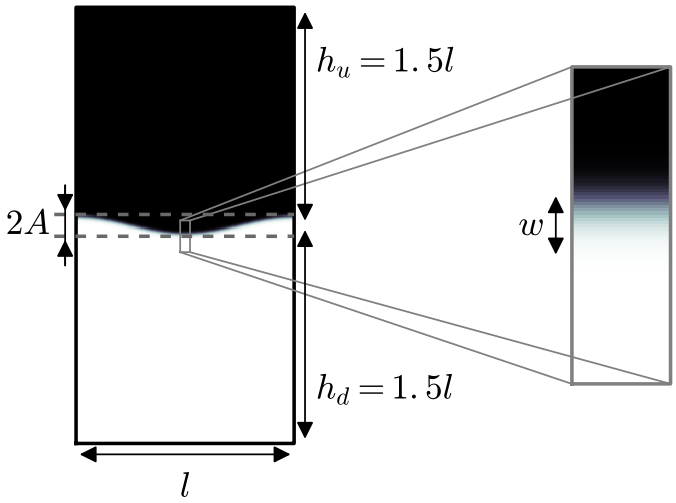

Figure 8.20: *Schematic representation of the computational setting for the oscillating planar interface*

T	119.88 K	λ	$1.0 \cdot 10^{-16}$ m$^7 \cdot$ kg$^{-1} \cdot$ s^{-2}	$L_x = l$	150 nm
P^{sat}	25.20 bar	w	6.34 nm	$L_y = 3l$	450 nm
ρ_l	458.94 kg $\cdot$ m^{-3}	σ	1.18 mN $\cdot$ m^{-1}	N_x	250
ρ_v	125.22 kg $\cdot$ m^{-3}	points in int.	≈ 10	N_y	750

Table 8.5: *Simulation parameters used for the first test case of an oscillating two dimensional N_2 planar interface*

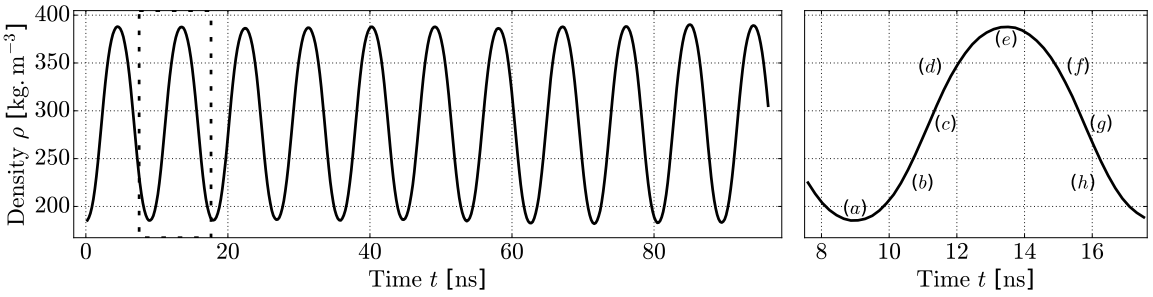

Figure 8.21: *Time evolution of the density at the center of the domain for the oscillation of an initially harmonically perturbed plane nitrogen N_2 interface*

8.2.1.2 Period calculation

From Fyfe et al. (1988) one gets that the expected pulsation of the oscillations ω obeys Eq. (8.8) where ρ_{u} (resp. ρ_{d}) and h_{u} (resp. h_{d}) are the density and width of the upper (res. lower) fluid, σ the surface tension of the interface, g the gravity acceleration and k the wavenumber of the deformation. Noticeably, it does not depend on the amplitude of the initial deformation

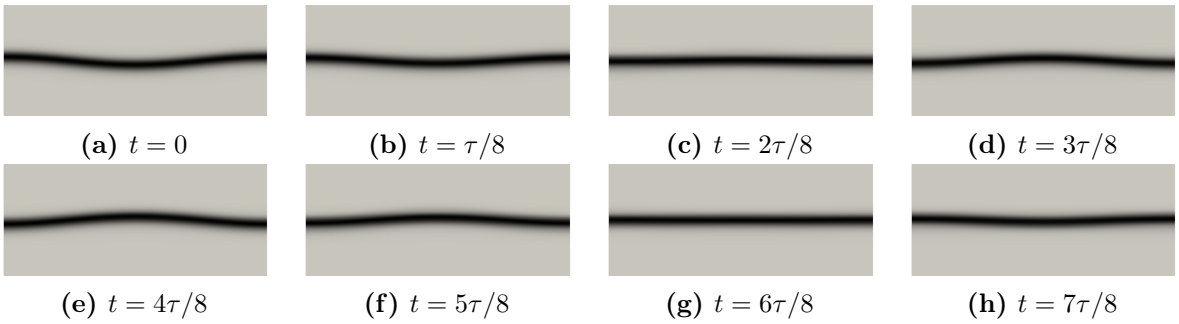

(a) $t = 0$ **(b)** $t = \tau/8$ **(c)** $t = 2\tau/8$ **(d)** $t = 3\tau/8$

(e) $t = 4\tau/8$ **(f)** $t = 5\tau/8$ **(g)** $t = 6\tau/8$ **(h)** $t = 7\tau/8$

Figure 8.22: *Zoom on the normalized density gradient profiles at different instants for the oscillation of an initially harmonically perturbed plane N_2 interface*

(in linear regime).

$$\omega^2 = \frac{(\rho_\mathrm{d} - \rho_\mathrm{u})\, gk + \sigma k^3}{\rho_\mathrm{d} \coth kh_\mathrm{d} + \rho_\mathrm{u} \coth kh_\mathrm{u}} \tag{8.8}$$

In our configuration, no gravity is considered, the upper and lower densities are the saturation densities ρ_v and ρ_l, only one period of a sine is used for the deformation therefore $k = 2\pi/l$ where l is the domain width i.e. the length of the interface when no perturbation is applied and the upper and lower widths h_u, h_d have been chosen so that $h_\mathrm{u} = h_\mathrm{d} = 1.5l$. It comes that $\coth kh_\mathrm{d} = \coth kh_\mathrm{u} = \coth(3\pi) \approx 1.0 + 1.3 \cdot 10^{-8} \approx 1.0$. The simplified and classic expression of the pulsation in then given by:

$$\omega^2 = \frac{\sigma k^3}{\rho_l + \rho_v} \tag{8.9}$$

The ensuing simplified expression for the period τ (with $\tau = 2\pi/\omega$) is now given by Eq. (8.10).

$$\tau = \frac{l^{3/2}}{\sigma^{1/2}} \sqrt{\frac{(\rho_l + \rho_v)}{2\pi}} \tag{8.10}$$

Applying Eq. (8.10), the expected period is $\tau_\mathrm{th} = 17.14$ ns while the period given by the simulation is $\tau_\mathrm{sim} = 17.89$ ns which represents a very satisfactory error below 5%.

Mesh convergence studies

The very encouraging results from Sec. 8.2.1.1 have fostered a more in depth study to further qualify the behavior of the model for this canonical two-dimensional configuration. To that effect, a slight modification has been applied to the parameters used for the simulation, in particular the temperature that has been significantly reduced from about 120 K ($T_r \approx 0.95$) to 100 K ($T_r \approx 0.80$) to be more challenging. The absolute dimensions of the domain have been modified to accommodate for this new temperature, the length-to-height ratio of 3.0 has however been conserved as presented in Fig. 8.20. The amplitude of the initial deformation is $A = 0.015l$. The new relevant parameters for the nitrogen based calculations are compiled in Tab. 8.6. The GRK scheme is still used with the contribution of AVBP selective filter (see Sec. 6.2.4.1) using a factor $1.0 \cdot 10^{-2}$. Different mesh resolutions, detailed in Tab. 8.7, have been used to perform a rudimentary convergence study.

T	100 K	λ	$1.0 \cdot 10^{-16}$ m$^7 \cdot$ kg$^{-1} \cdot$ s^{-2}
P^{sat}	7.85 bar	w	2.97 nm
ρ_l	667.14 kg $\cdot$ m^{-3}	σ	9.32 mN $\cdot$ m^{-1}
ρ_v	31.6 kg $\cdot$ m^{-3}	$L_x = L_y/3 = l$	80 nm

Table 8.6: *Simulation parameters used for the additional tests of an oscillating two dimensional N_2 planar interface*

Points in interface ($\approx$)	4	6	8	10
$N_x (= N_y/3)$	110	165	218	245

Table 8.7: *Interface and mesh resolutions used for the convergence study of an oscillating nitrogen interface initially at 100 K*

Isothermal simulations with no viscosity

The first series of simulations have been performed in an isothermal setting solving Euler equations (mass and momentum only) and the results for the central density time evolution are given in Fig. 8.23. Although the sustained oscillations can mostly be observed as in Fig. 8.21, the mesh resolution is seen to have a strong impact. The uppermost resolutions of eight and ten points in the interface provide clean results that display a relative convergence. The quality of the oscillations is reduced for the lower 6-points resolution in the interface. Finally, when only four points are used in the interface, the oscillations are progressively perturbed to eventually become completely disrupted.

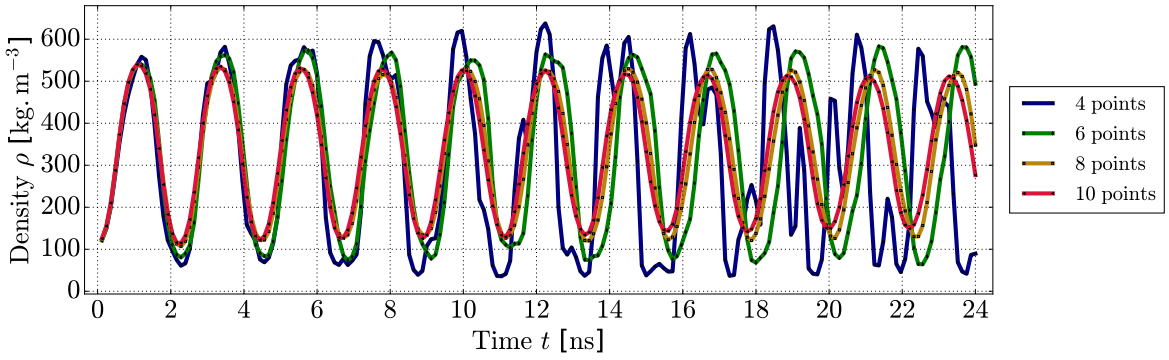

Figure 8.23: *Comparison of the central density time evolution of a two-dimensional planar oscillating interface for different mesh resolutions. Isothermal Euler equations are solved using a selective numerical filter (coeff $1.0 \cdot 10^{-2}$).*

A closer look at the time snapshots of the interface, provided in the comparative images of Fig. 8.24, shows that for the lowest 4-point interface resolution, the interface is completely perturbed. A possible explanation is that the numerical errors, of a too high magnitude at this resolution, eventually excite other modes of oscillation of the interface that superimpose on each other to completely and unevenly deform the interface. The 6-point resolution case

seems to be at the limit: the oscillations are not severely impacted but showcase a starting tendency to amplification that could lead to a similar disrupted behavior given enough time.

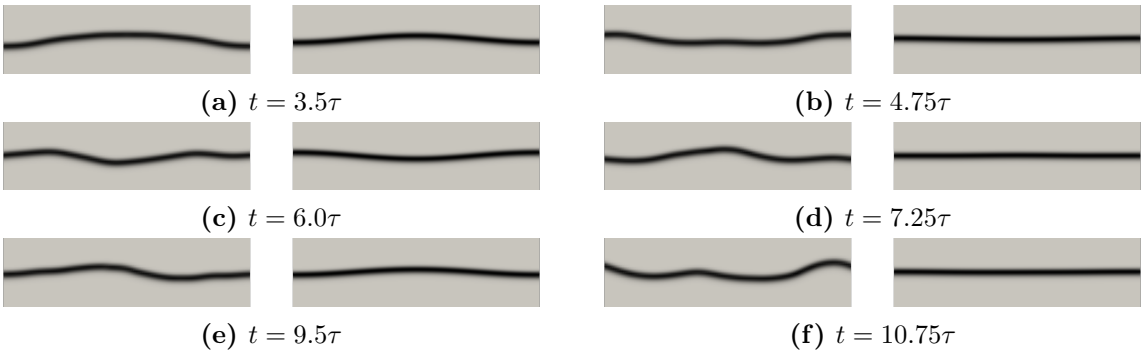

(a) $t = 3.5\tau$ **(b)** $t = 4.75\tau$

(c) $t = 6.0\tau$ **(d)** $t = 7.25\tau$

(e) $t = 9.5\tau$ **(f)** $t = 10.75\tau$

Figure 8.24: *Zoom on the normalized density gradient profiles at different instants for the oscillation of an isothermal N_2 interface. Comparison between a 4-point (leftmost) and a 8-point (rightmost) interface resolutions.*

For the sufficiently resolved cases, the mean oscillating period that can be extracted is $\tau_{\text{sim}} = 2.25$ ns which represents a reasonable 7.5% error when compared to the theoretical value $\tau_{\text{th}} = 2.42$ ns.
A very slight damping of the oscillations can be observed but has not been met with a satisfactory explanation, in particular given the fact that wall and periodic boundary conditions are used and that the GRK numerical advection scheme is strictly non-dissipative. This effect was invisible in the results from Fig. 8.21 performed at a higher temperature (120 K instead of 100 K), which represents an easier physical configuration to compute. A possible source for the dissipation can be the implementation of the high order derivatives capillary terms into the AVBP solver which is not guaranteed to be dissipation free, contrary to the GRK scheme used for the purely advective terms.

Isothermal simulations with viscosity

The second series of simulations have been performed trading Euler equations for Navier-Stokes equations: the isothermal constraint is still imposed and physical viscosity is introduced (no thermal diffusion is considered so far). For all simulations, the dynamic viscosity coefficient μ has been taken constant in the whole domain, several values of said viscosity have however been used in the following set: $\left[10^{-8}, 10^{-7}, 10^{-6}, 10^{-5}, 10^{-4}\right]$ (in $\text{kg} \cdot \text{m}^{-1} \cdot \text{s}^{-1}$). Given the proximity of the 8-point and 10-point resolution results in Fig. 8.23, only the 4-point, 6-point and 8-point resolution cases have been simulated. For the sake of clarity, only noticeable results for $\mu = 10^{-4},\ 10^{-6},\ 10^{-8}$ $\text{kg} \cdot \text{m}^{-1} \cdot \text{s}^{-1}$ are presented in Fig. 8.25 where the central density time evolution is plotted. The corresponding Laplace La numbers are also provided. This number compares the surface tension constraints to the diffusive inertial process and is evaluated with Eq. (8.11) where σ is the surface tension, μ the viscosity of interest, ρ the density of interest and L_c the characteristic length of the problem.

$$La = \frac{\sigma L_c \rho}{\mu^2} \tag{8.11}$$

For this case, the liquid density ρ_l has been chosen for ρ and the domain width l has been chosen for L_c.

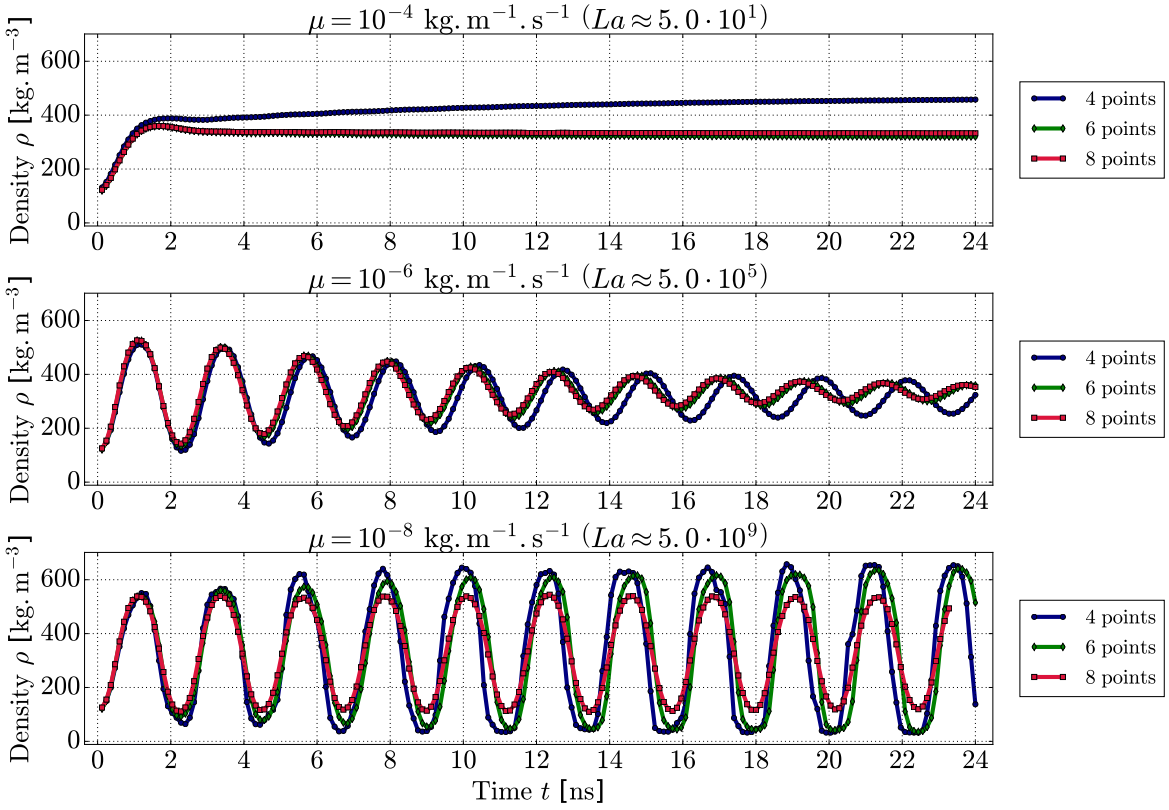

Figure 8.25: *Comparison of the central density time evolution of a two-dimensional planar oscillating nitrogen interface for different mesh resolutions. Isothermal Navier-Stokes equations are solved with constant dynamic viscosity and no thermal conduction. A selective numerical filter (coeff* $1.0 \cdot 10^{-2}$*) is used.*

As expected, the oscillations present a damping depending on the viscosity magnitude: the stronger the viscosity, the more important the damping. Another impact of the viscosity is the modification of the oscillation periods. These two observations are actually predicted by the theory, in particular in Prosperetti (1976); Prosperetti (1981) where the author predicts an decreasing pulsation, i.e. an increasing period with respect to an increasing viscosity, which can be observed in Fig. 8.25. The damping of the oscillations is addressed more thoroughly in a Sec. 8.2.1.3, the oscillating periods and characteristic damping times extracted from the simulations are however provided in Tab. 8.8 for the most precise 8-point interface resolution. The characteristic damping time could no be evaluated with enough precision for the cases with $\mu = 1.0 \cdot 10^{-8}$ and $\mu = 1.0 \cdot 10^{-4}$: the damping was to weak for the former and occurred two rapidly for the second with merely any oscillations visible. For that same reason, no oscillating period has been extracted when $\mu = 1.0 \cdot 10^{-4}$.

Non-isothermal simulations with viscosity

The previous investigation has been performed with the same mesh resolutions and dynamic

μ $\left[\mathrm{kg}\cdot\mathrm{m}^{-1}\cdot\mathrm{s}^{-1}\right]$	0	$1.0\cdot10^{-8}$	$1.0\cdot10^{-7}$	$1.0\cdot10^{-6}$	$1.0\cdot10^{-5}$
$\tau_{\mu,\mathrm{sim}}$ [ns]	2.25	2.25	2.25	2.26	2.46
$\delta_{\mu,\mathrm{sim}}$ [ns]	-	*	119	11.0	3.62

Table 8.8: *Oscillating periods and characteristic damping times extracted from the simulations, for an oscillating nitrogen interface at 100 K (eight points in the interface) for different values of dynamic viscosity solving isothermal Navier-Stokes equations*

viscosity values and the same initial deformation relative amplitude $A = 0.015l$, however in a non-isothermal setting. The initial solution remains unchanged, i.e. isothermal, however, the non-isothermal Navier-Stokes equations are solved, still with no thermal conduction. The results are provided for a handful of dynamic viscosity values in Fig. 8.26 and present a trend somewhat similar to that of the isothermal cases: the higher the viscosity, the greater the damping on the oscillations. A noticeable difference however is that an important damping remains even for the smallest value of the viscosity $\mu = 1.0\cdot10^{-8}$ kg $\cdot$ m$^{-1}\cdot$ s^{-1}, and for all the mesh resolutions.

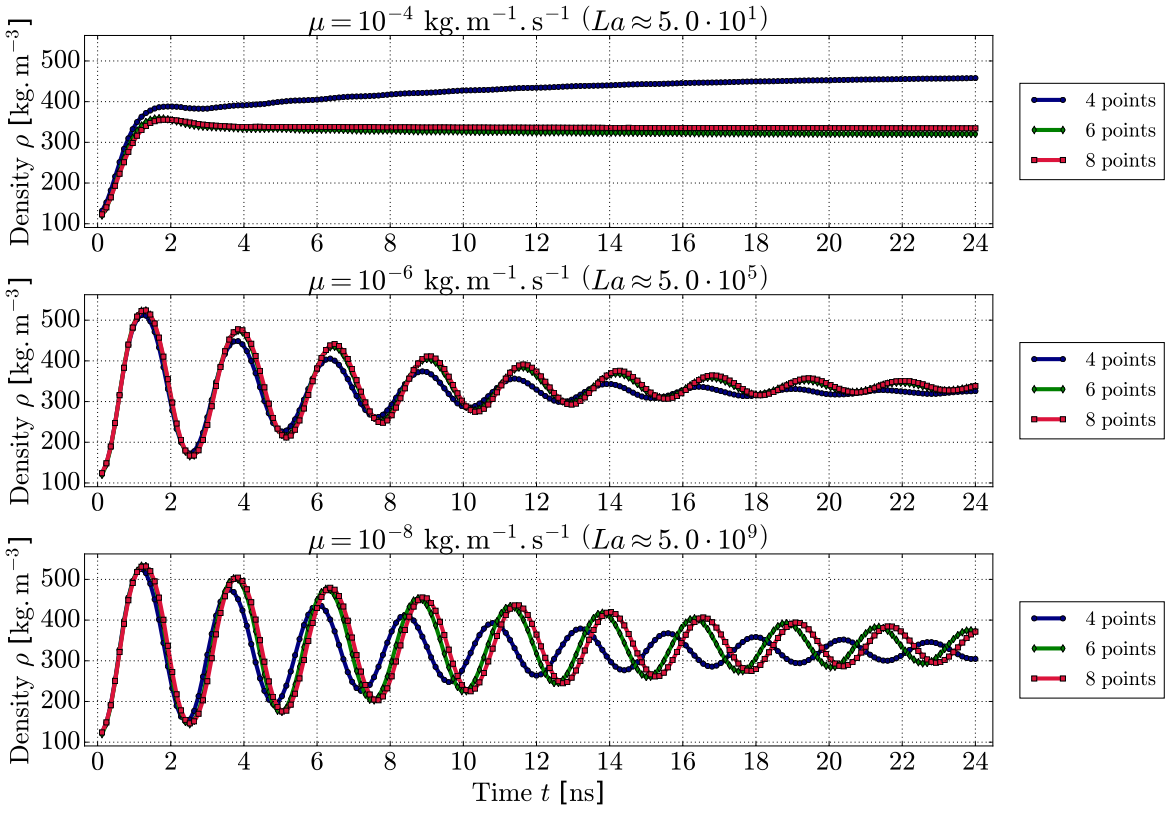

Figure 8.26: *Comparison of the central density time evolution of a two-dimensional planar oscillating nitrogen interface for different mesh resolutions. Non-isothermal Navier-Stokes equations are solved with constant dynamic viscosity and no thermal conduction. A selective numerical filter (coeff* $1.0\cdot10^{-2}$*) is used.*

A second observation is that the values of the oscillating periods and characteristic damping

times are substantially different when switching between the isothermal and non-isothermal settings, all other things remaining equal. The values for the isothermal and non-isothermal settings (with the 8-point interface resolution) are given in Tab. 8.9 where the results for the non-isothermal non-viscous Euler equations case are also provided (column $\mu = 0$). In order to simulate this case solving non-isothermal equations, even with the 8-point resolution, the selective filter coefficient had to be increased from $1.0 \cdot 10^{-2}$ to $1.0 \cdot 10^{-1}$ to achieve stability in the computations.

μ $\left[\mathrm{kg \cdot m^{-1} \cdot s^{-1}}\right]$	0	$1.0 \cdot 10^{-8}$	$1.0 \cdot 10^{-7}$	$1.0 \cdot 10^{-6}$	$1.0 \cdot 10^{-5}$
$\tau_{\mu,\text{no isot}}$ [ns]	2.70	2.55	2.55	2.60	2.70
$\tau_{\mu,\text{isot}}$ [ns]	2.25	2.25	2.25	2.26	2.46
$\delta_{\mu,\text{no isot}}$ [ns]	14.8	13.9	11.7	7.91	3.03
$\delta_{\mu,\text{isot}}$ [ns]	-	*	119	11.0	3.62

Table 8.9: *Oscillating periods and characteristic damping times from the simulation of an oscillating nitrogen interface initially at 100 K (eight points in the interface) solving non-isothermal and isothermal Navier-Stokes equations for different values of dynamic viscosity*

Even in with no viscosity, a damping of the oscillations is observed. The value of the characteristic damping time actually seems to converge as the viscosity diminishes. Both mass and total energy conservation has been verified in the domain for all mesh resolutions.

An attempt has been made to perform an entropy analysis but it has faced the limitation that the numerical scheme currently used does not verify, at the discretized level, the second law of thermodynamics. However, the curves describing the time evolution of the entropy has been observed to converge with the increase of the mesh resolution toward a quasi constant entropy evolution, consistent with the boundaries used (periodic on the left and right sides, adiabatic wall on the upper and lower sides).
Another analysis has consisted in monitoring the evolution of the acoustic energy in the domain: since the total energy is conserved and the oscillations, i.e. the kinetic energy dissipates, this energy must be transferred through an isentropic process. Only acoustics seemed to satisfy the previous conditions. Nonetheless, the evolution of said acoustic energy has shown no correlation whatsoever with the damping of the oscillations.
Beyond these investigations, no satisfactory explanation has been found for this phenomenon.

Comparison between isothermal and non-isothermal simulations

The figure in Fig. 8.27 allows to compare the behavior of the interface depending on the viscosity but mostly on the isothermal or non-isothermal setting used for the simulations. The increase of the oscillating periods caused by the non-isothermal setting clearly appears as well as the fact that the oscillations are still damped for the lowest viscosity value.
The impact of the dynamic viscosity on the interface oscillations seems to be fairly similar, this can be visualized on the graph in Fig. 8.28. Since no theoretical ground have been found to explain the persistent damping effect of the non-isothermal setting (keeping in mind that the domain is initially at a constant temperature) and compare to the values in Tab. 8.9, this

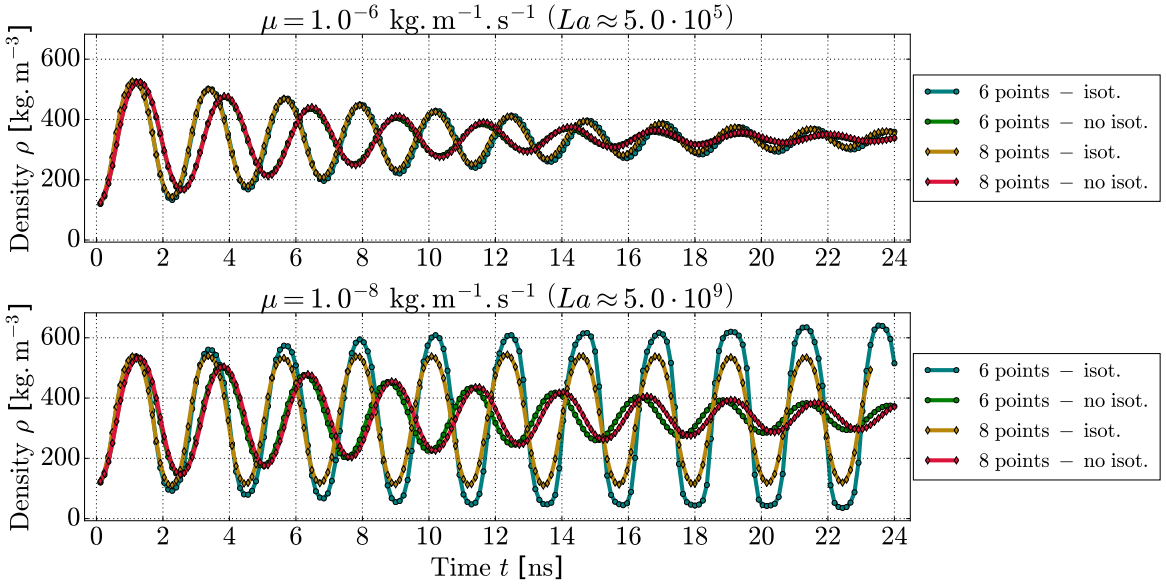

Figure 8.27: *Comparison of the central density time evolution of a two-dimensional planar oscillating nitrogen interface for different mesh resolutions. Isothermal and non-isothermal Navier-Stokes equations are solved with constant viscosity and no thermal conduction, for different mesh resolutions. A selective numerical filter (coeff* $1.0 \cdot 10^{-2}$*) is used.*

observation cannot be confirmed numerically.

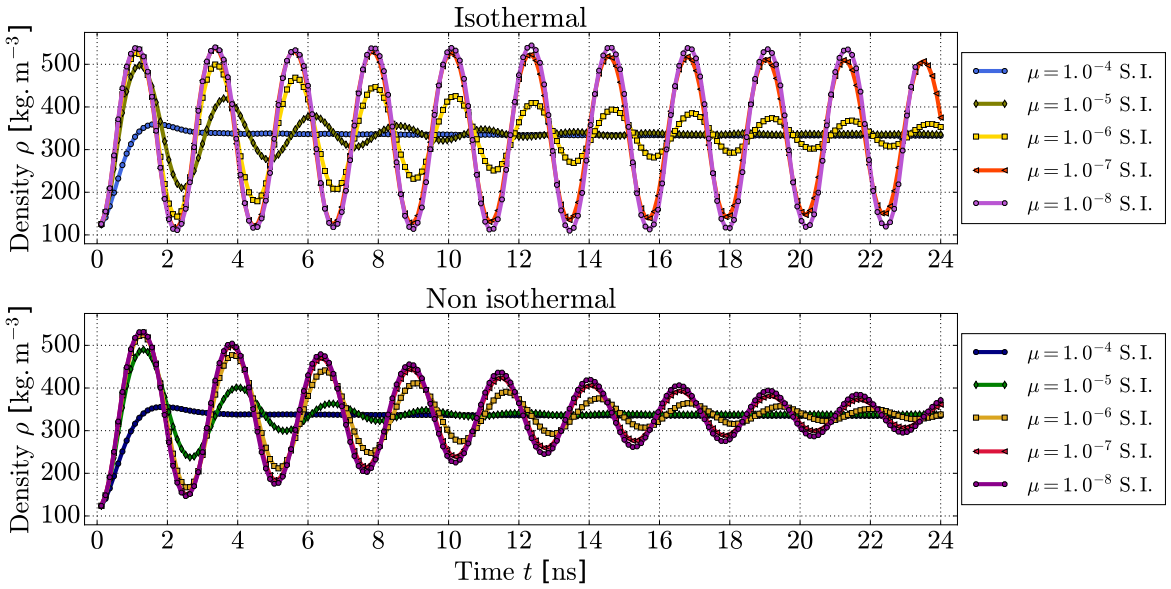

Figure 8.28: *Comparison of the central density time evolution of a two-dimensional planar oscillating interface for different values of dynamic viscosity. Navier-Stokes equations are solved with constant viscosity and no thermal conduction in isothermal and non-isothermal settings. A selective numerical filter (coeff* $1.0 \cdot 10^{-2}$*) is used on the 8-point resolution mesh.*

Overall impact of the equation system

A last series of simulations has been carried out to evaluate and summarize the impact of the system of equations solved while simulating the oscillating interface case. Aside from the non-viscous Euler equations solved in isothermal and non-isothermal settings, the non-isothermal Navier-Stokes equations have been solved using Chung et al. (1988) model for the diffusion. More precisely, three settings have been considered with Chung's model: a first one where only the thermal conduction is activated, a second one where only the viscosity is activated and a third complete one where both diffusive processes are activated. All simulations have been performed with the 8-point interface resolution, the selective filter with coefficient $1.0 \cdot 10^{-2}$ has been used for all cases except for the non-isothermal Euler equations where the coefficient has been increased to $1.0 \cdot 10^{-1}$ and the full Navier-Stokes equations with viscosity and thermal conduction where no filter has been used.

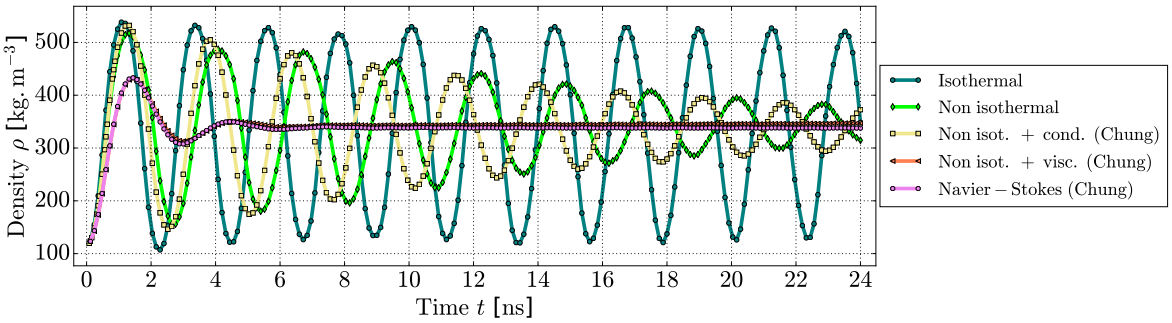

Figure 8.29: *Comparison of the central density time evolution of a two-dimensional planar oscillating nitrogen interface for different sets of equations. Euler and Navier-Stokes equations are solved in isothermal and non-isothermal settings on the 8-point interface resolution mesh with different diffusive processes.*

The results in Fig. 8.29 are consistent. Asides from the curves for the non-isothermal and the isothermal Euler equations, already covered, the Navier-Stokes equations impact the oscillations is as expected. When only the thermal conduction is introduced, the curve presents the exact same characteristic damping time as that obtained for the non-isothermal Euler equations. A verification of the density-pressure scatter plots confirms that throughout the simulation, the initial temperature is perfectly maintained for the conductive-only Navier-Stokes equations and sensibly maintained for the non-isothermal Euler equations (which is not automatically guaranteed, see Sec. 8.1.3.2, in particular Fig. 8.9). These observations discard the hypothesis that the damping associated with solving non-viscous non-isothermal equations could be caused by the loss of the isothermal nature of the interface. The fact that the interface remains isothermal in this case causes however the oscillating period to sit between those extracted for the isothermal and non-isothermal Euler equations.
When only the viscosity is activated, the oscillations are rapidly damped which, given that the kinematic viscosity of the liquid in this case is about $\mu = 6.0 \cdot 10^{-5}$ kg $\cdot$ m$^{-1} \cdot$ s^{-1}, almost halfway between $1.0 \cdot 10^{-5}$ kg $\cdot$ m$^{-1} \cdot$ s^{-1} and $1.0 \cdot 10^{-4}$ kg $\cdot$ m$^{-1} \cdot$ s^{-1} is to be expected when comparing to the two corresponding curves in Tab. 8.28.
Finally, the addition of the thermal conduction to the viscosity has negligible effects apart from preventing a light density drift slightly noticeable with the case introducing solely viscosity.

8.2.1.3 Quantitative impact of the viscosity

Theory

The evolution of capillary waves in presence of viscosity has been studied in the literature, in particular in Prosperetti (1976); Prosperetti (1981) where the case of interface between two different viscous fluids is addressed. In most cases, no analytical solution exists to describe the time evolution of the interface displacement in such configurations unless additional hypotheses are met to simplify the developments. The first hypothesis is met if one of the two fluid has a negligible inertial contribution, which in the case of the a liquid-vapor interface would mean $\rho_l \geqslant \rho_v$ and $\mu_l \geqslant \mu_v$. The second hypothesis is verified if the two fluids have the same kinematic viscosity, i.e $\nu_l = \nu_v$ where $\nu = \mu/\rho$. Each hypothesis leads to a different expression of the time evolution of the interface displacement.
It clearly appears that neither of these two hypotheses is respected in the cases that have been presented, independently of the type of equations that have been solved, since both phases have been set with the same dynamic viscosity μ instead of the kinematic viscosity and the ratio between the liquid and vapor densities is not important enough to discard the vapor phase altogether. For the values in Tabs. 8.8-8.9, a comparison with theoretical results is thus compromised.

Whatever the hypothesis that is retained, a global kinematic viscosity ν can be defined (that of the single phase retained or the value common to both phases) and in Prosperetti (1981) the author provides means to approximate the new oscillating period τ_μ and characteristic damping time δ_μ assuming a damping in the form $e^{-t/\delta}$ for the interface displacement amplitude. These two approximations are given by Eqs. (8.12)-(8.13) where $k = 2\pi/l$ is the spatial period of the initial deformation and ω_0, the non-viscous pulsation, is given by Eq. (8.9).

$$\omega_\nu^2 = \omega_0^2 - 4\nu^2 k^4 \tag{8.12}$$

$$\delta_\nu = \frac{1}{2\nu k^2} \tag{8.13}$$

Constant kinematic viscosity

To comply with the previously mentioned conditions, a new series of simulations has been performed solving the isothermal Navier-Stokes equations with only viscosity, still considering the nitrogen interface, however with constant values of kinematic viscosity rather than dynamic viscosity, in order to accommodate for the theoretical hypothesis needed to ensure quantitative comparisons. For the three values of ν that have been considered ($1.5 \cdot 10^{-9}$, $5.0 \cdot 10^{-9}$, $1.5 \cdot 10^{-8}$ $\mathrm{m^2.s^{-1}}$), the central density time evolution is given in Fig. 8.30. The comparison between the values of oscillating periods and characteristic damping times, from the simulations and the theory using Eqs. (8.12)-(8.13), are given in Tab. 8.10.
As it has already been observed in the previous cases, in particular with a constant dynamic viscosity, the periods are well retrieved with a very satisfactory error of roughly 8%. Regarding the characteristic damping times, the errors have been strongly reduced with factors between the theory and the simulation lower than two but still representing about a 40% error. Several factors could explained these differences, however two of them seem more likely: firstly

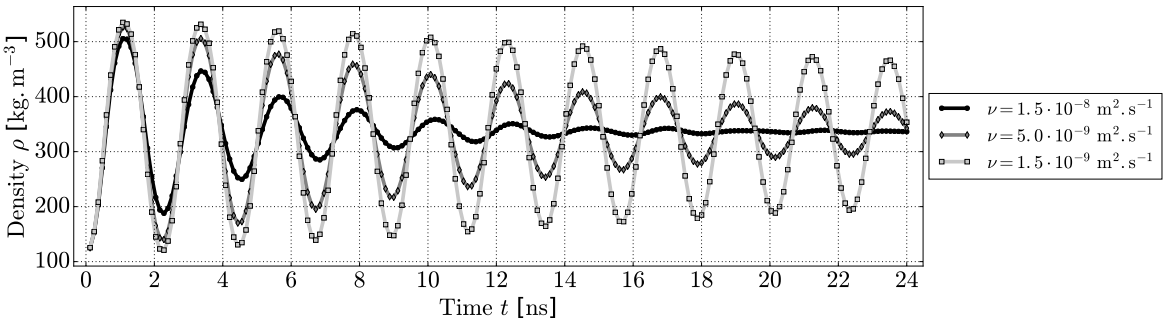

Figure 8.30: *Comparison of the central density time evolution of a two-dimensional planar oscillating nitrogen interface at 100 K for different values of kinematic viscosity. Isothermal Navier-Stokes equations are solved with no thermal conduction. A selective numerical filter (coeff* $1.0 \cdot 10^{-2}$*) is used.*

ν [m^2.s^{-1}]	$1.5 \cdot 10^{-9}$	$5.0 \cdot 10^{-9}$	$1.5 \cdot 10^{-8}$
$\tau_{\nu,\text{th}}$ [ns]	2.42	2.44	2.46
$\tau_{\nu,\text{sim}}$ [ns]	2.24	2.24	2.28
error$_\tau$ [%]	8.2	8.3	7.0
$\delta_{\nu,\text{th}}$ [ns]	56.5	17.6	6.26
$\delta_{\nu,\text{sim}}$ [ns]	41.1	12.2	4.24
error$_\delta$ [%]	37.3	44.1	47.6

Table 8.10: *Oscillating periods and characteristic damping times, from theory and simulations, for an oscillating isothermal nitrogen interface at 100 K (eight points in the interface) for different values of kinematic viscosity*

the ratio between the interface width and the domain width, which is not negligible, when considering that Eqs. (8.12)-(8.13) have been derived under the assumption of an infinitely thin interface; secondly the relative magnitude between the liquid and vapor densities which, despite the constant kinematic viscosity constraint, needs to be as high as possible in order for the approximations of Eqs. (8.12)-(8.13) to become more precise.

This last assumption has been tested by trading the previous case for a new one with more realistic features in terms of thermodynamics. To that effect, an isothermal oxygen interface at 110 K ($T_r \approx 0.7$) has been considered with the theoretical value of the capillary coefficient predicted at that temperature (ensuring that the interface width is at its correct theoretical value). The geometrical setting remains similar the one described in Fig. 8.20, however the exact dimensions have been proportionally modified to ensure the same domain-to-interface width ratio. The exact parameters are compiled in Tab. 8.11, and one can notice that the ratio between the liquid and vapor densities has increased from five to fifty. The central density time evolution for the three values of ν that have been considered ($1.0 \cdot 10^{-9}$, $3.3 \cdot 10^{-9}$, $1.0 \cdot 10^{-8}$ in m^2.s^{-1}) is given in Fig. 8.31 and the comparisons between the values of oscillating periods and characteristic damping times, from the simulations and the theory using Eqs. (8.12)-(8.13) are given in 8.12.

T	110 K	λ	$1.173 \cdot 10^{-17}$ m$^7 \cdot$ kg$^{-1} \cdot$ s^{-2}
P^{sat}	5.45 bar	w	0.97 nm
ρ_l	1017.7 kg $\cdot$ m^{-3}	σ	8.37 mN $\cdot$ m^{-1}
ρ_v	21.4 kg $\cdot$ m^{-3}	$L_x = L_y/3 = l$	26 nm
points in int.	≈ 8	N_x	218

Table 8.11: *Simulation parameters used for the additional tests of an oscillating two dimensional O_2 planar interface with viscosity*

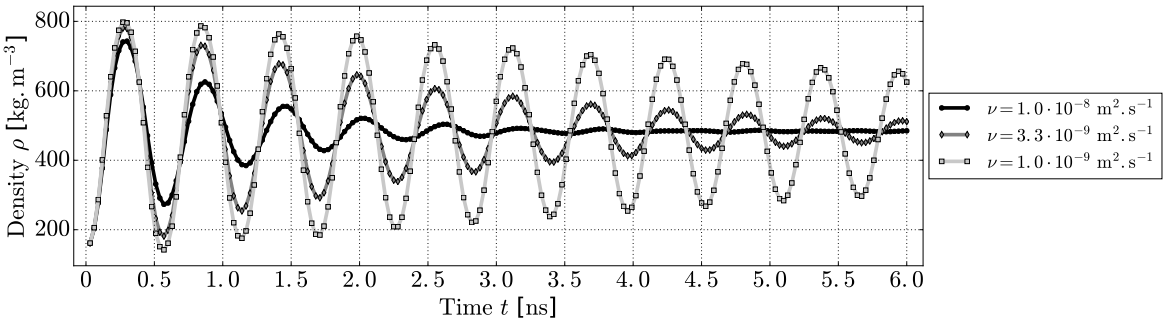

Figure 8.31: *Comparison of the central density time evolution of a two-dimensional planar oscillating oxygen interface at 110 K for different values of kinematic viscosity. Isothermal Navier-Stokes equations are solved with no thermal conduction. A selective numerical filter (coeff $1.0 \cdot 10^{-2}$) is used.*

The comparisons in Tab. 8.12 show a great improvement from the results obtained with the nitrogen interfaces. The relative error on the periods has been reduced to around 4% and below but more importantly, values for the characteristic damping time have become significantly better with a error around 12% and as low as 3% for the case $\nu = 1.0 \cdot 10^{-9}$ m^2; s^{-1}. These last results seem to confirm that the approximation Eq. (8.13) is representative and predictive enough only when the liquid-to-vapor density ratio is very important.
To go a step further, the author in Prosperetti (1981) derives the actual analytical expression of the time evolution of the normalized interface displacement when the constant kinematic viscosity hypothesis is respected. Fig. 8.32 presents the time evolution of said normalized interface displacement, comparing the theory and the simulations. As expected from the errors in Tab. 8.12, the results are very satisfying and represent a strong argument in favor of the Second Gradient theory regarding its ability to describe the behavior of dynamic isothermal interfaces.

ν $[\mathrm{m}^2;\mathrm{s}^{-1}]$	$1.0 \cdot 10^{-9}$	$3.3 \cdot 10^{-9}$	$1.0 \cdot 10^{-8}$
$\tau_{\nu,\mathrm{th}}$ [ns]	0.589	0.591	0.599
$\tau_{\nu,\mathrm{sim}}$ [ns]	0.566	0.568	0.586
error_τ [%]	4.1	4.0	2.6
$\delta_{\nu,\mathrm{th}}$ [ns]	9.04	2.87	1.03
$\delta_{\nu,\mathrm{sim}}$ [ns]	8.73	2.54	0.916
error_δ [%]	3.5	13.0	12.7

Table 8.12: *Oscillating periods and characteristic damping times, from theory and simulations, for an oscillating isothermal oxygen interface at 110 K (eight points in the interface) for different values of kinematic viscosity*

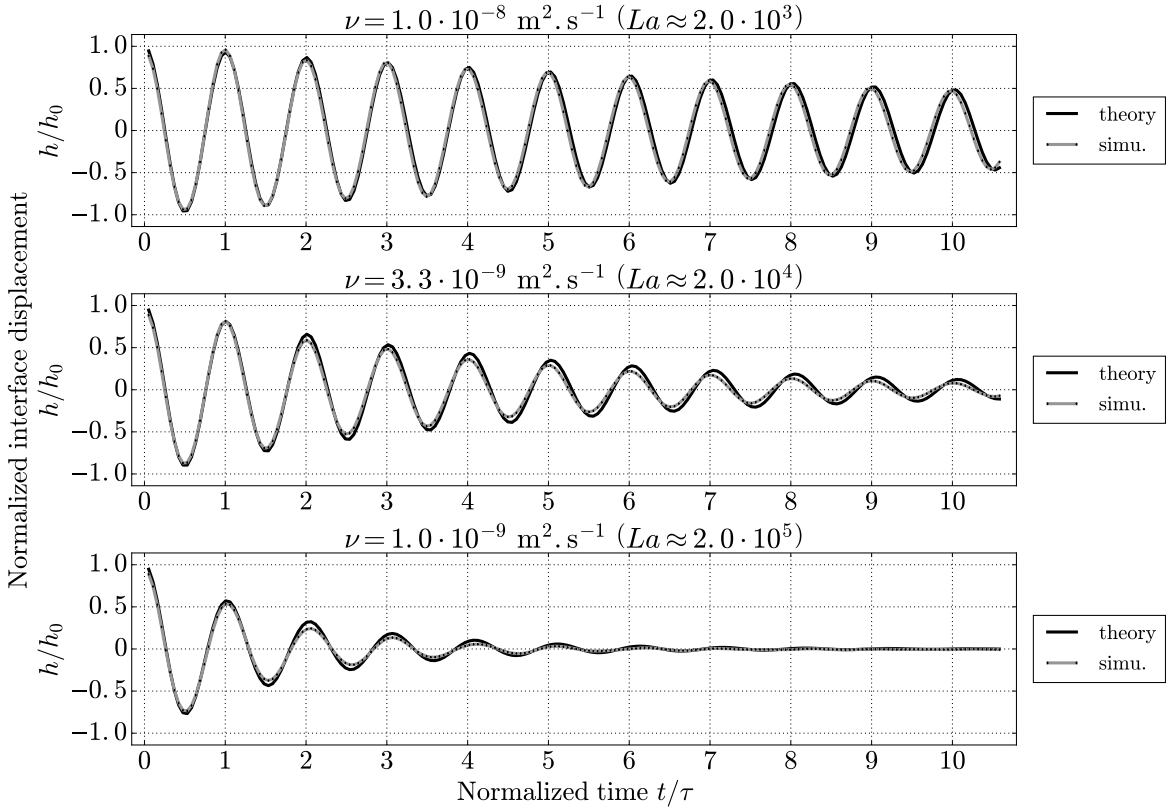

Figure 8.32: *Comparison between the theory and simulation results for the normalized displacement of a two-dimensional isothermal planar oscillating oxygen interface at 110 K for different values of kinematic viscosity. Isothermal Navier-Stokes equations are solved with no thermal conduction. A selective numerical filter (coeff* $1.0 \cdot 10^{-2}$*) is used.*

8.2.2 Oscillating droplets

8.2.2.1 Configuration

The second test case consists in a classic oscillating droplet as schematically described in Fig. 8.33. The circular droplet, of radius R, is squeezed so as to create an elliptic shape of radii r_1 and r_2. To remain in a linear regime, the relation $r_1 = 1.5r_2$ is chosen, leading to $r_1 = R\sqrt{1.5}$ and $r_2 = R/\sqrt{1.5}$. A tilt angle of 22.5° is also applied so as to mitigate possible numerical effects from the Cartesian mesh used for the simulations.

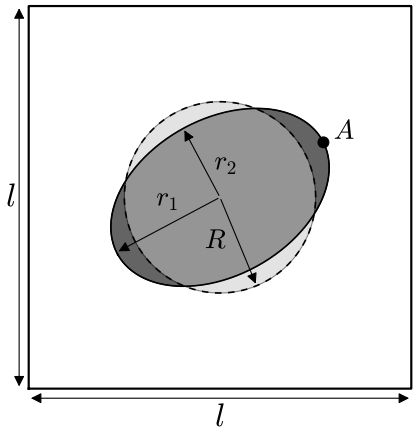

Figure 8.33: *Schematic representation of the computational setting for the oscillating droplet. Not to scale*

To further investigate the capabilities of the SG model, a more physically representative description of the droplet has been chosen, based on the oxygen configuration in Tab. 8.11 used for the last validation cases on the oscillating interfaces. In particular, a smaller reduced temperature has been used and the exact value of the capillary coefficient λ at that temperature, leading to the correct value of surface tension σ, has been selected.
The value of the radius R has been selected to ensure a reasonable radius-to-interface width ratio of about 10. The relevant parameters used for this calculation are compiled in Tab. 8.13. The GRK scheme of AVBP is used and a selective filter (see Sec. 6.2.4.1) is still applied to the mass, momentum and energy equation with a coefficient $1.0 \cdot 10^{-2}$ to ensure numerical stability. Periodic boundary conditions have been used. The droplet is expected to oscillate between two extreme elliptic shapes while progressively returning to its circular form.

T_{init}	110.0 K	λ	$1.17 \cdot 10^{-17}$ m$^7 \cdot$ kg$^{-1} \cdot$ s^{-2}	l	90 nm
P^{sat}	5.45 bar	w	0.97 nm	N	748
ρ_l	1017.7 kg $\cdot$ m^{-3}	σ	8.37 mN $\cdot$ m^{-1}	R	10 nm
ρ_v	21.4 kg $\cdot$ m^{-3}	points in int.	≈ 8	μ	$1.0 \cdot 10^{-5}$ Pa.s

Table 8.13: *Simulation parameters used for the two dimensional* 0_2 *oscillating droplet*

8.2.2.2 Non-viscous simulations

To first validate the configuration and the model, a series of non-viscous simulations, without artificial stabilization, has been carried out but has been face with important numerical difficulties that have led to mixed results.

Non-viscous isothermal simulations

When the isothermal Euler equations are solved, the oscillatory behavior expected from the droplet is properly retrieved as exposed in Fig. 8.34 where the time evolution of the density field is provided (the figure zoom on the droplet, only the center part of the domain is depicted).

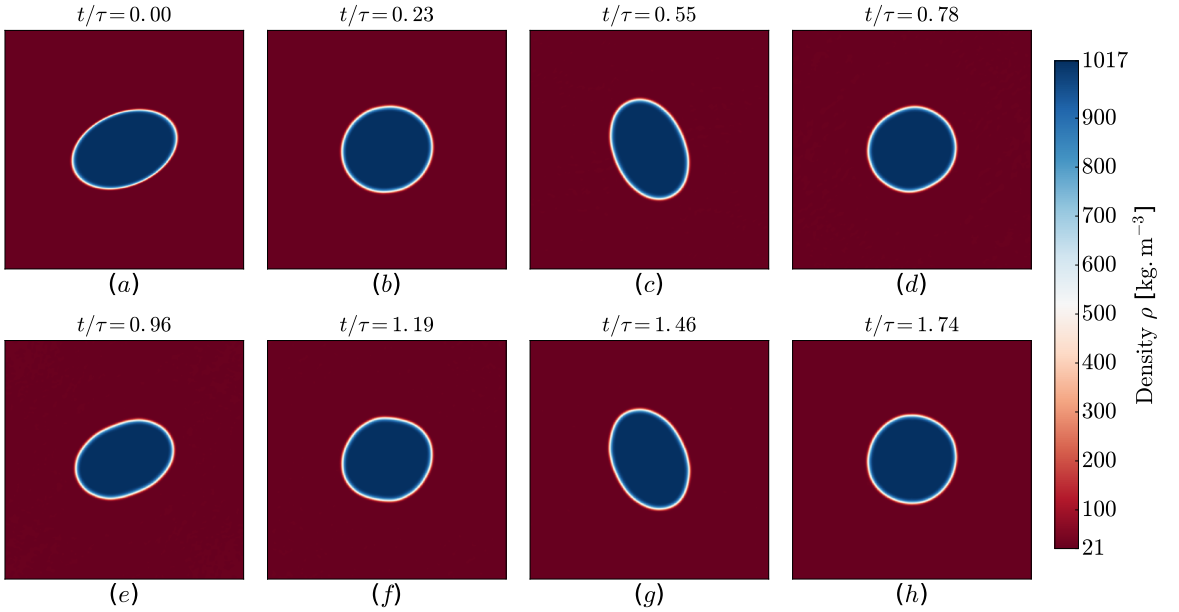

Figure 8.34: *Snapshots of the temporal evolution of the density for a non-viscous initially deformed O_2 droplet in an isothermal setting.*

The theoretical period of these oscillations can be evaluated using Eq. (8.14) from Art. 273 in Lamb (1975) that expresses the pulsation ω from which the period is extracted with $\tau = 2\pi/\omega$.

$$\omega = \sqrt{\frac{6\sigma}{(\rho_l + \rho_v)\, R^3}} \tag{8.14}$$

To extract the period from the simulation results, the time evolution of the total kinetic energy can be tracked as shown in Fig. 8.35. A very important observation from this curve is that this total energy, although oscillating in time, keeps on increasing with a quasi linear slope after an initial violent increase. The constant increase of kinetic energy that is observed is attributed to a continuous generation of parasitic noise and acoustic waves that cannot exit the periodic computational domain. A spectral analysis of the curve in Fig. 8.35 allows nonetheless to extract the oscillatingg period. The final value is $\tau_{\text{sim}} = 0.874$ ns while using the simulation parameters in Tab. 8.13, the expected period is $\tau_{\text{th}} = 0.905$ ns, which represents merely a 3.5% error. This comparison entices that the intrinsic oscillatory behavior of the interface is

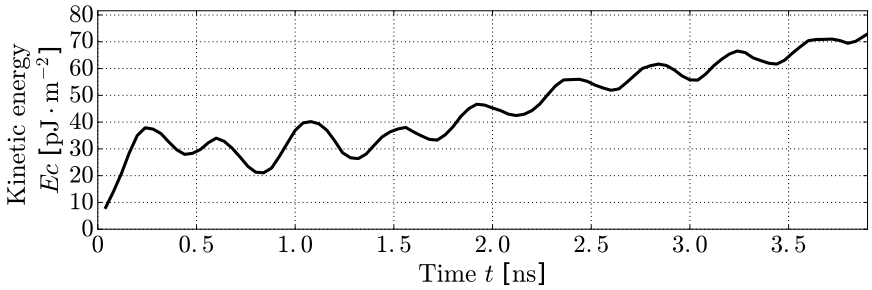

Figure 8.35: *Temporal evolution of the total kinetic energy of a non-viscous oscillating O_2 droplet in an isothermal setting*

marginally affected by the velocity perturbations which participate to the continuous kinetic energy increase.

Non-viscous non-isothermal simulations

Attempts have been made to replicate this previous simulation in a non-isothermal setting but they all turned unsuccessful with crashes early on in the computation, no matter the mesh resolution (up to 15 points in the interface) and the value of the selective filter coefficient in a range from $1.0 \cdot 10^{-5}$ to $1.0 \cdot 10^{-1}$. Without dissipation, point-to-point numerical errors appear rapidly in the simulation leading to crashes, as depicted in Fig. 8.36. These results were to be expected given the difficulties already encountered in Sec. 8.1.3 when trying to simulate unsteady one-dimensional interfaces solving non-isothermal Euler equations without the inclusion of diffusive processes.

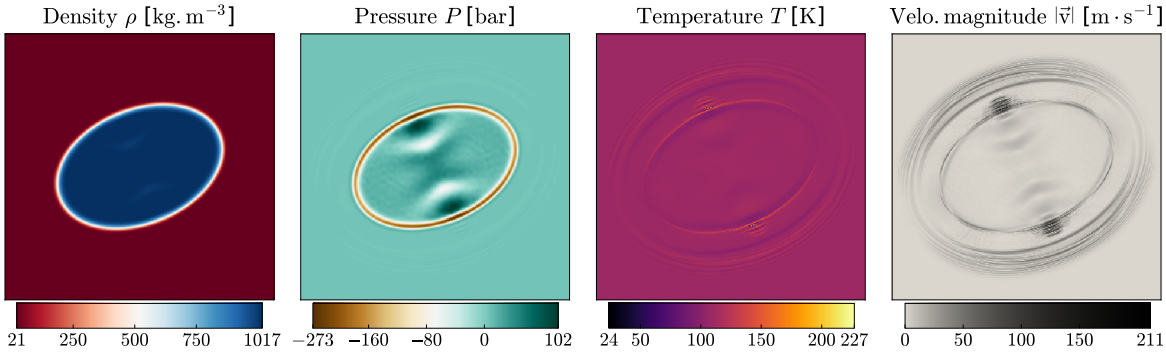

Figure 8.36: *Snapshots of the density, pressure, temperature and velocity magnitude field for an non-viscous initially deformed O_2 droplet in a non-isothermal setting before crash iteration.*

These difficulties are not without explanations: the non-dissipative nature of the GRK scheme and its tendency to generate oscillatory errors, the propensity of the oscillating droplet configuration to be faced with the issue of spurious currents, the design of the initial solution leading to a very a strong initial acoustic dynamics and the periodic domain that prevents the evacuation of this acoustic energy could be some of the causes behind the very noisy results encountered when solving isothermal equations or the unsuccessful simulations when solving non-isothermal equation. These difficulties can be compared to those already observed in a one-dimensional setting, in particular regarding the non-viscous non-isothermal simulations.

8.2.2.3 Viscous simulations

The puzzling time evolution of the total kinetic energy in the non-viscous isothermal setting and the apparent impossibility to achieve a successful non-viscous non-isothermal simulation has motivated the exploration of cases where viscous dissipation is taken into account. To that effect, Euler equations have been traded for the Navier-Stokes equations, however considering only viscosity and discarding thermal conduction. A constant dynamic viscosity of $\mu = 1.0 \cdot 10^{-5}$ Pa.s has been used. All the other parameters of the case have been left unchanged, in particular the selective filter still being applied with a coefficient $1.0 \cdot 10^{-2}$.

Viscous isothermal simulations

When the isothermal condition is enforced, very satisfactory results are obtained, as it can been seen with the time evolution of the density, pressure and velocity magnitude fields presented in Figs. 8.37 - 8.38. The oscillatory nature of the movement is still present and the damping of the oscillations can be guessed from the evolution of the droplet deformation of which magnitude visibly decreases with time in the different snapshots. Moreover, the velocity field no longer displays overshoots and is more characteristic of typical droplet oscillations.

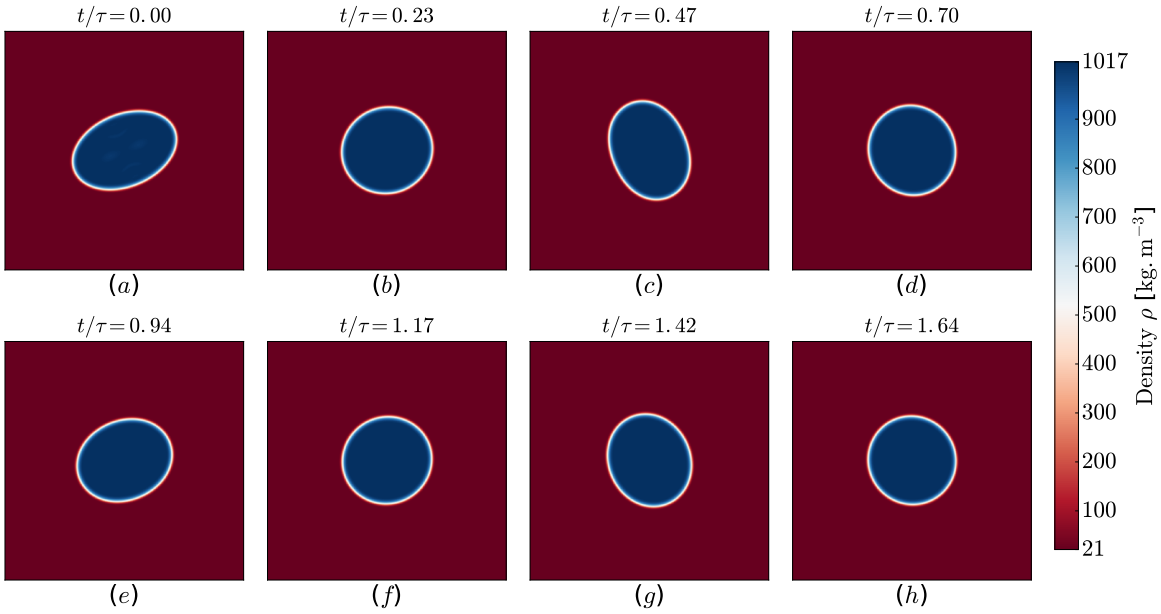

Figure 8.37: *Snapshots of the temporal evolution of the density for a viscous and initially deformed O_2 droplet. Isothermal Navier-Stokes equations are solved with a constant dynamic viscosity $\mu = 1.0 \cdot 10^{-5}$ Pa.s and no thermal conduction.*

This improvement of the result also manifests itself in the time evolution of the total kinetic energy provided in Fig. 8.40. The damping, expected of the viscous dissipation, is retrieved while the oscillations are perfectly maintained. The same spectral analysis allows to extract the period of said oscillations and find a value of $\tau_{\text{sim}} = 0.926$ ns which still represents a very satisfactory 2.3% error compared to the theoretical value $\tau_{\text{th}} = 0.905$ ns.

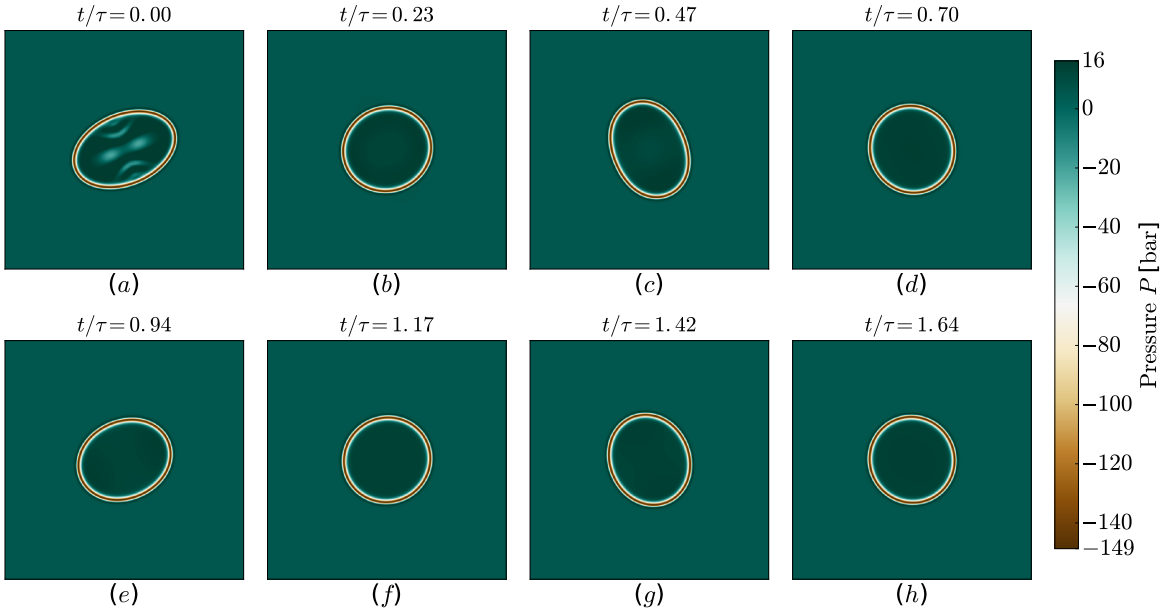

Figure 8.38: *Snapshots of the temporal evolution of the pressure for a viscous and initially deformed O_2 droplet. Isothermal Navier-Stokes equations are solved with a constant dynamic viscosity $\mu = 1.0 \cdot 10^{-5}$ Pa.s and no thermal conduction.*

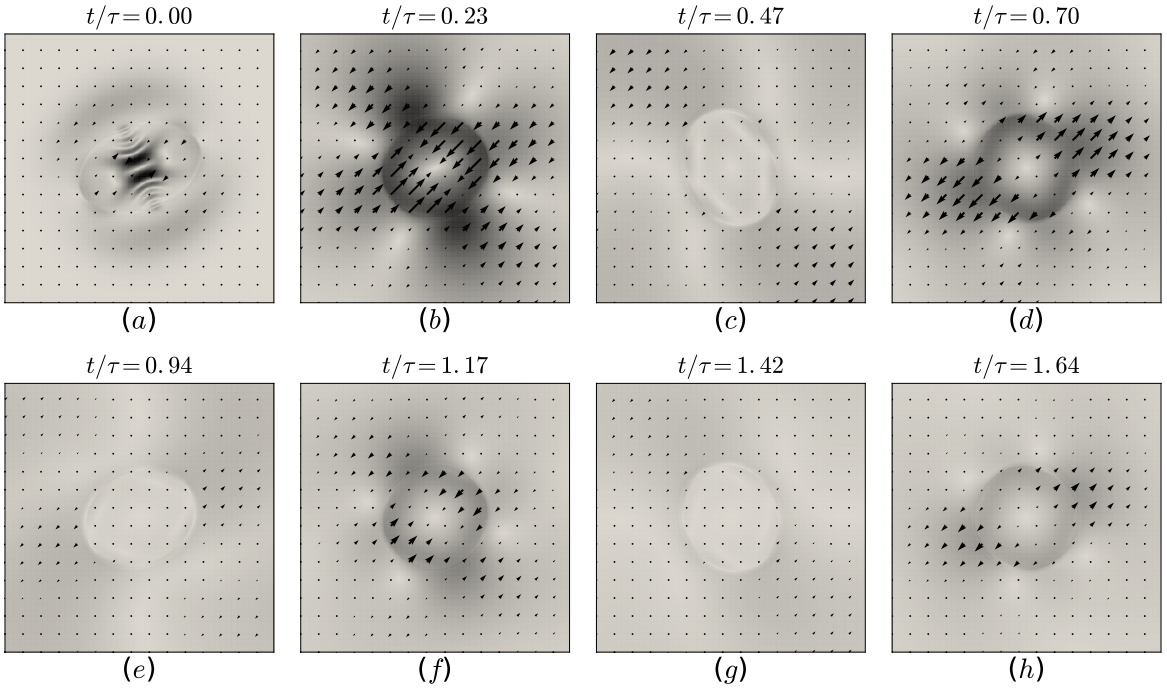

Figure 8.39: *Snapshots of the temporal evolution of the velocity field for a viscous and initially deformed O_2 droplet. Isothermal Navier-Stokes equations are solved with a constant dynamic viscosity $\mu = 1.0 \cdot 10^{-5}$ Pa.s and no thermal conduction. Velocity vectors (arrows) are superimposed over the normalized velocity amplitude in gray scale.*

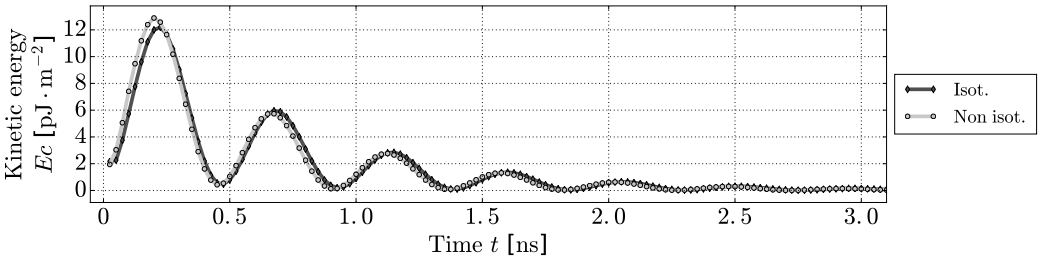

Figure 8.40: *Comparison of the temporal evolution of the total kinetic energy of a viscous ($\mu = 1.0 \cdot 10^{-5}$ Pa.s) oscillating O_2 droplet in isothermal and non-isothermal setting*

Viscous non-isothermal simulations

As done in the non-viscous case, the same simulation has been performed, only removing the isothermal setting so as to include the viscous energy equation in the computation, all other parameters remaining equal. As demonstrated by Fig. 8.40, the results for the kinetic energy decay is virtually the same and lead to very close values of oscillating period ($\tau_{\text{isot}} = 0.926$ ns / $\tau_{\text{nisot}} = 0.917$ ns) and characteristic damping time ($\delta_{\text{isot}} = 0.580$ ns / $\delta_{\text{nisot}} = 0.652$ ns).

Impact of the viscosity

Although several authors such as Lamb (1916); Chandrasekhar (1959); Prosperetti (1980) have derived an expression to evaluate the characteristic damping time δ of an oscillating viscous droplet, this expression is limited to three dimensional droplets oscillations around an equilibrium globe shape. To the best of our knowledge, no such analytical results have been produced regarding the damping of viscous droplets in two-dimensional configurations. The expressions derived in Prosperetti (1980) for δ rely on three main hypotheses: the behavior of the fluid is mostly dominated by one fluid, the initial deformation of the droplet is moderate (typically $r_1/r_2 \leqslant 1.5r$) and the viscosity is small enough. The first hypothesis is essentially verified here since $\rho_l \approx 50\rho_v$ and by imposing a constant kinematic viscosity it also comes that $\mu_l \approx 50\mu_v$ where μ is the dynamic viscosity. The second and third hypotheses are more intricate to be confirmed beforehand as they may vary from case to case depending on the geometry dimensions and fluid thermodynamic description.
Nonetheless, the final expression of δ, the damping coefficient of the interface normal velocity, builds upon the introduction of a capillary Reynolds number Re_α which is given here by Eq. (8.15) where ρ_l, μ_l are the liquid density and dynamic viscosity, ν is the kinematic viscosity, R is the equilibrium droplet diameter and σ is the capillary coefficient.

$$Re_\alpha = \frac{\sqrt{\rho_l R\sigma}}{\mu_l} = \frac{\sqrt{R\sigma}}{\rho_l \nu} \tag{8.15}$$

The damping is then defined with Eq. (8.16) where ω_0 is the oscillating pulsation with no viscous perturbations given by Eq. (8.14).

$$\delta = \frac{Re_\alpha}{5\sqrt{\omega_0^2/6}} \tag{8.16}$$

To assess this formula, a series of simulations has been performed solving isothermal Navier-Stokes equations with no thermal conduction and a selective filter with a coefficient of $1.0 \cdot$

ν $\left[\mathrm{m^2.s^{-1}}\right]$	$1.8 \cdot 10^{-9}$	$3.3 \cdot 10^{-9}$	$5.8 \cdot 10^{-9}$	$1.0 \cdot 10^{-8}$	$1.8 \cdot 10^{-8}$	$3.3 \cdot 10^{-8}$
$\tau_{\nu,\mathrm{sim}}$ [ns]	0.843	0.844	0.848	0.859	0.879	0.908
$\delta_{\nu,\mathrm{sim}}$ [ns]	8.27	4.31	2.71	1.76	1.16	0.78
$\delta_{\nu,\mathrm{th}}$ [ns]	11.1	6.06	3.45	2.00	1.11	0.61
$\mathrm{error}_{\tau}^{\mathrm{th}}$ [%]	34.4	40.4	27.5	14.0	4.0	28.9

Table 8.14: *Oscillation periods and characteristic damping times, from the simulation, the three-dimensional theory and the simplified two-dimensional correlation, for an oscillating isothermal oxygen droplet at 110 K (eight points in the interface) for different values of kinematic viscosity*

10^{-2}. For each simulation, a constant value of kinematic viscosity ν has been used in the list $\left[1.8 \cdot 10^{-9},\ 3.3 \cdot 10^{-9},\ 5.8 \cdot 10^{-9},\ 1.0 \cdot 10^{-8},\ 1.8 \cdot 10^{-8},\ 3.3 \cdot 10^{-8}\right]$ (in $\mathrm{m^2.s^{-1}}$). In each instance, the normal velocity of the droplet at point A (see Fig. 8.33) has been tracked, following the displacement of said point with the droplet oscillations and the resulting curves are compiled in Fig. 8.41.

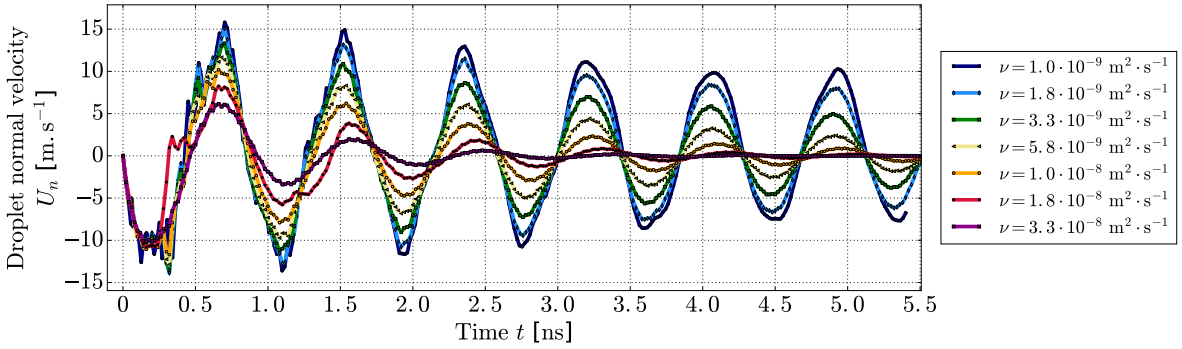

Figure 8.41: *Comparison of the normal velocity at the maximal deformation point A in Fig. 8.33 following its movement in an oscillating isothermal oxygen droplet configuration for different values of kinematic viscosity. Isothermal Navier-Stokes equations are solved with no thermal conduction and a selective numerical filter (coeff* $1.0 \cdot 10^{-2}$*) is used.*

The characteristic damping time extracted from the curves in Fig. 8.41 can be compared with the three-dimensional theoretical values predicted by Eq. (8.16). It should be mentioned that the initial instants of the simulations have been discarded when extracting the characteristic damping times given the strong perturbations observed in the curves during this period. The comparison values, compiled in Tab. 8.14, show an overall correct agreement between the theory and the simulations with a mean error of 25%, which can be put into perspective but remains nonetheless encouraging given the already mentioned limitations of this approach. The inviscid oscillating periods can still be compared and the value $\tau_{\mathrm{sim}} = 0.84$ ns from the simulation with the lowest kinematic viscosity only presents a 7% error with the value $\tau_{\mathrm{th}} = 0.90$ ns from the theory which is another comparison furthering the pertinence of the SG model to simulate such configurations.

8.2.2.4 Mesh convergence studies

To conclude the section dedicated the oscillating droplet, a brief mesh study convergence has been carried out in three different physical settings to evaluate the impact of the mesh resolution on the quality of the results. The different resolutions that have been used are referred to according the number of mesh points in the interface they permit. The corresponding numbers of mesh points in the domain are compiled in Tab. 8.15.

Points in interface ($\approx$)	4	5	6	7	8
Points in diameter ($\approx$)	41	52	62	72	83
$N_x = N_y$	373	466	559	652	748

Table 8.15: *Interface, droplet and mesh resolutions used for the convergence study of an oscillating O_2 droplet*

The impact of the spatial resolution on the total kinetic energy decay, considering viscous droplets, is given in Fig. 8.42 for simulations performed solving isothermal Navier-Stokes equations. Two different values of dynamic viscosity have been used and the results display consistency in regard of the mesh resolution. For the two values of dynamic viscosity that have been considered, $\mu = 1.0 \cdot 10^{-5}$ Pa.s and $\mu = 1.0 \cdot 10^{-6}$ Pa.s, the simulations have been carried out successfully for all interface resolutions. For the higher value $\mu = 1.0 \cdot 10^{-5}$ Pa.s, which is approximately the physical value of the dynamic viscosity in the oxygen vapor at 110K, the curves, for all mesh resolutions, almost perfectly superimpose. Reducing the value of the dynamic viscosity by a factor 10 to reach $\mu = 1.0 \cdot 10^{-6}$ Pa.s leads to slightly more perturbed simulations. The 4-point, and to a lesser extent the 5-point, interface resolutions curves display a minor deviation from the higher resolutions for which the curves once again perfectly superimpose.
These results seem to confirm that the behavior observed in Fig. 8.35 is a conjunction of numerical error and lack of dissipation. Adding only viscosity is a first path to address this issue but, as shown by the 3-point resolution for $\mu = 1.0 \cdot 10^{-6}$ Pa.s, it is not enough, numerical errors are still present and a decent mesh resolution is required for precise results. When the viscosity is further increased, cases with low mesh resolution start the behave more properly but it should not mask the fact that strong numerical errors exist in the first place when the mesh resolution is insufficient.

For the isothermal setting, the simulations have successfully advanced for most resolutions and asides from the 3-point interface resolution, have led to quasi indistinguishable time evolution of the total kinetic energy, a mesh convergence far superior to that observed for the oscillating interface. For the non-isothermal setting, the 3-point resolution case has crashed in the early instants of the simulation and the 4-point resolution case has merely passed the first oscillation before crashing. Asides from these two cases, the resulting curves for the total kinetic energy decay perfectly superimpose on each other. Even up to the crash, the curve for the 4-point resolution coincide with those of the other resolutions. Added with the result in Fig. 8.40, it appears that for the oscillating droplet case, once the minimal mesh resolution is reached to ensure correct simulation in the viscous case, neither further mesh refinement nor switch between the isothermal and non-isothermal settings, has a substantial impact on

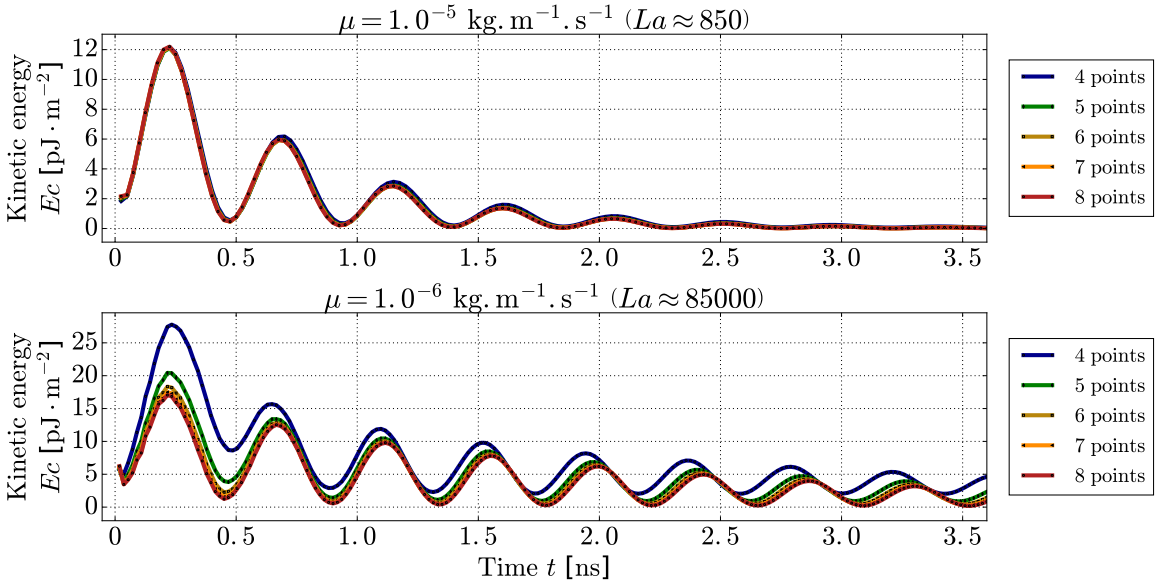

Figure 8.42: *Impact of the spatial resolution on the temporal decay of the total kinetic energy of an oscillating O_2 droplet. Isothermal Navier-Stokes equations are solved with a constant dynamic viscosity and no thermal conduction. A selective numerical filter (coeff $1.0 \cdot 10^{-2}$) is used.*

the droplet oscillating behavior. This observation is in radical contrast with the one made for the oscillating planar interface for which switching from the isothermal to the non-isothermal equations has had a radical impact on both the oscillating period and characteristic damping time.

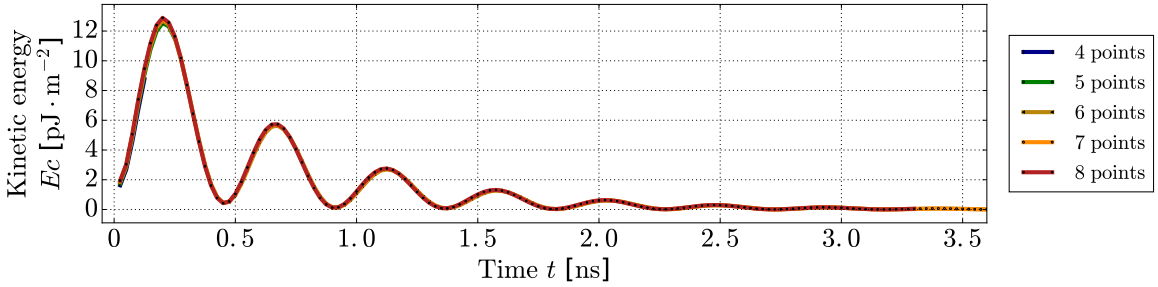

Figure 8.43: *Impact of the spatial resolution on the temporal decay of the total kinetic energy of an oscillating O_2 droplet. Non-isothermal Navier-Stokes equations are solved with a constant dynamic viscosity ($\mu = 1.0 \cdot 10^{-5}$ Pa.s, $La \approx 850$) and no thermal conduction. A selective numerical filter (coeff $1.0 \cdot 10^{-2}$) is used.*

Finally, an attempt has been made to carry out the simulations solving Navier-Stokes equations with the full Chung et al. (1988) model to account for physical dissipation. Since the straightforward application of Chung's model leads to instantly damped oscillations, the values of the diffusion coefficients, namely the dynamic viscosity μ and thermal conduction coefficient k_{th}, have been multiplied simultaneously by different reducing factors.
The results in Fig. 8.44 present a behavior similar to the previous configuration with only viscosity. Actually, the results could have been inferred, to some extent, directly from Figs.

8.35 and 8.43. As already mentioned, when a factor 1 is applied, the outcome is uneventful and limits the analysis to be drawn. It should be mentioned that the 3-point resolution case has crashed in the early instants of the simulation, meaning that even with canonical thermal conduction, the behavior when solving strictly isothermal equations cannot be completely replicated. When a factor 1/10 is applied, the preservation of the initial isothermal behavior becomes more tedious but all the curves still display a very reasonable behavior. This situation is mostly similar the one in Fig. 8.43 except that the thermal conduction has allowed to simulate the 4-point resolution case to its completion. For both factors 1 and 1/10, all curves superimpose with no visible impact of the mesh resolution. When the factor is further reduced to 1/100, both the thermal conduction and the viscosity start to become inefficient at tempering the numerical errors for the lower mesh resolutions (4-point and 5-point) which either become unstable or feature a drift in the time evolution of the total kinetic energy as observed in Fig. 8.35. However, despite the low physical dissipation applied in the case of a factor 1/100 and reminding the fact that no additional viscosity has been used for any of the droplet cases presented in this section, the period and characteristic damping time are qualitatively well retrieved, even for the lower 5-point interface resolution.

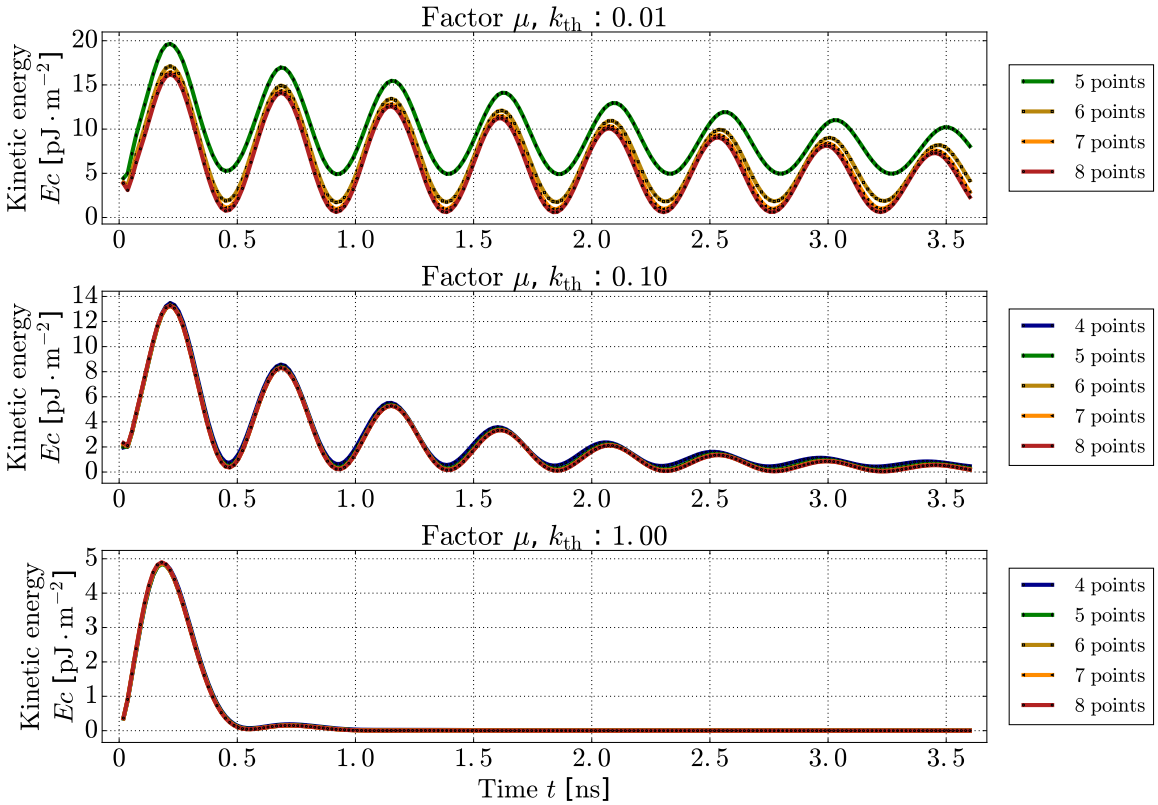

Figure 8.44: *Impact of the spatial resolution on the temporal decay of the total kinetic energy of an oscillating O_2 droplet. Non-isothermal simulations with the SG model solving Navier-Stokes equations, viscosity and thermal conduction coefficient calculated with Chung's method with a reduced factor applied to the diffusion coefficients μ and k_{th}*

Conclusions on the validation

A wide variety of steady and unsteady canonical cases in one and two dimensions have been addressed using the Second Gradient model with the main objective of validating its implementation in the AVBP solver and confirm the ability of the model to allow unsteady compressible simulations. Both one-dimensional cases (stationary interfaces, advected and/or deformed interfaces, conductive interfaces with evaporation and liquefaction) and two-dimensional cases (oscillating planar interfaces, oscillating deformed droplets) have led to draw the same overall conclusions regarding the behavior of said model in its current formulation and implementation.

In isothermal conditions, solving either Euler equations or Navier-Stokes equations, the model responds as expected and this satisfactory behavior has been confirmed with comparisons to the theory for the two-dimensional cases. The clearly defined value of the surface tension under isothermal conditions was in ideal setting to validate the intrinsic capillary behavior of the interface in unsteady cases. The corresponding one-dimensional simulations have been very stable and in perfect agreement with the expected behavior of the interface when submitted to deformation or advection. The two-dimensional cases have also led to very satisfactory results, noticeably without the necessity to add artificial viscosity to stabilize the calculations. The comparisons with the theory have shown very good results for both the oscillating interfaces and droplets, in terms of periods and damping times.
When non-isothermal equations are solved, great difficulties appear if no dissipation is introduced. The temperature often showcased a pathological behavior that was correlated or led to oscillatory numerical errors which propagated to the over variables through a coupling mechanism. For the most part, we believe this issue to be a manifestation of the typical oscillatory behavior of non-dissipative centered numerical schemes although this intuition does not suffice to explain the magnitude of these errors. Adding physical dissipation, mostly viscosity and to a lesser extent thermal conduction, permits to carry out the simulations and has led to good results regarding oscillating interfaces and droplets.

Throughout the cases, we have resolved to use actual physical dissipation when needed rather than artificial viscosity as the manner in which the latter has been developed in AVBP does not ensure a consistent interaction with the added capillary terms from the SG model and their peculiar nature. Accessing this interaction in further details could be the focus of a different study that was beyond the scope of this work. Multiple tests have however shown that adding artificial viscosity, which leads to a limitation of the numerical oscillations, allows to carry out the simulations. The accuracy of the results from said simulations needs nonetheless to be cautiously assessed. The more classic point-to-point errors have been suppressed for most cases using the native high order selective filter of AVBP without any noticeable difficulties.

We are convinced that the difficulty faced with the temperature may rather be caused by numerical issues and the practical implementation in the solver, which is strongly dependent on the numerical schemes available in AVBP that are not inherently suited to handle the SG equations, as already mentioned. The focus point of this chapter should however remain that the different tests that it has been submitted to, and the qualitative and quantitative results that have been obtained, have shown the ability of the Second Gradient model to properly

recover unsteady dynamics typical of two-phase flows. Even if the addition of dissipation is generally needed to ensure stability, the implementation of the model seems to be properly done in AVBP and allows to now contemplate more complicated configurations as the ones presented in the last part of this document.

Part III

The Thickened Interface Method for the Second Gradient theory

Chapter 9

Thickening strategies for the Second Gradient theory

The purpose of this chapter is to present a new method, called Thickened Interface Method (TIM), devised to thicken an interface up to widths numerically acceptable for our targeted applications i.e. adapted to typical Direct Numerical Simulation meshes.
The motivations behind the design of the TIM are explained in Sec. 9.1 where the limitations of the native SG model in terms of computational cost are exposed. In particular in Sec. 9.1.1, a prompt investigation of pertinent experimental and numerical results regarding transcritical flows allows to compare the relevant physical length scales to the widths predicted by the SG model and to point-out their incompatibility. This issue has already been observed in Jamet (1998) where the author proposed two different methods to addressed it. These methods are recaled in Sec. 9.1.2 and Sec. 9.1.3 respectively along with the justification behind their dismissal for our simulations.
Legitimate questions can be raised regarding the other class of PFMs described in Sec. 4.1, in particular when considering Eq. (4.8) that provides an actual expression for the interface equilibrium profile and even more so considering Eq. (4.9) which expresses analytically the interface width. Such methods can, theoretically, allow to accommodate any physical case by selecting an interface width δ that is relevant for the simulated configuration. However, Eqs. (4.8) and (4.9) are only permitted by the use of specific forms of the volumetric free energy F such as given by Eqs. (4.7a) or (4.7d). This aspect prevents the use of these specific PFMs because these latter expressions for F cannot be related to any EoS whatsoever, much less so to an actual real gas EoS that is required for our targeted applications. Even the temperature dependent expressions for F in Eqs. (4.10), (4.11a) and (4.11b) cannot be linked to a proper EoS that would permit their use in the context of this study. To some extent, the different strategies presented in this chapter try to replicate or to adapt, as much as possible, the convenient properties of these phase driven PFMs to the density driven SG model.
In that prospect, Sec. 9.2 is then dedicated to the presentation of the TIM, in particular its derivation. Just as it has been done in 5 for the SG model, both a thermodynamic and a mechanical descriptions have to be introduced by the method to preserve the complete thermo-mechanical coupling already granted by the SG model. A specific care is given to the clarity and rigor of the calculations, in particular the physical hypotheses used to derive the expres-

sions. The complete modified thermodynamics associated to the TIM is thus laid down along with the modified Navier-Stokes equations to be solved. The results are linked and compared to that of the previous methods created by Jamet, in particular the impact of the TIM on the macroscopic variables of interest is analyzed. The main objective of these methods is being able to modify (usually increase) the interface width while maintaining the value of the surface tension which drives most of the relevant macroscopic phenomena we are interested in.

In 9.1.2 and 9.1.3 and 9.2, the different methods are always devised starting by considering the case of an isothermal planar interface as done in Sec. 5.4, depicted in Fig. 5.9 and described in Sec. 5.4.2. The eventual extension of the method to non-isothermal cases is specifically mentioned when addressed.

9.1 The need for thickening strategies

9.1.1 Adaptation of the Second Gradient theory to DNS meshes

The test cases of Chap. 8 and in particular Sec. 8.2 showcased the ability of the native Second Gradient model to adequately represent interfaces in canonical configurations. In particular, together with the theoretical developments in Chap. 5, they prove that the SG model can properly describe the thermodynamic and mechanical behavior of a simple interface. The model clearly defines an equilibrium profile with a correct value of surface tension and a fixed value for the interface width. Noticeably, any deformation applied to the interface will trigger a tempering response: the interface will try to return to its equilibrium profile and reach back its initial width. As such, it is our personal conviction that the SG model is particularly suited for in depth studies of canonical interfaces while additional efforts are needed to make it applicable to more ambitious configurations.

The major point holding the model back is the unreasonable computational price required to simulate industrial cases. This price is induced by the mesh sizes one would need to use to properly resolve the interface. Even if the authors in Moin and Mahesh (1998) showed that precise enough numerical schemes (such as the ones available in the AVBP solver) alleviate the mesh size from the requirement to match the Kolmogorov length scales, the difference between the smallest eddies in typical rocket engines and the interface widths predicted is of such a magnitude that it cannot be overlooked. To better illustrate these discrepancies, examples of the evolution of the interface width with the temperature are provided in Fig. 9.1 for species commonly used in cryogenic rocket engines. The values range from fewer than a nanometer to a few micrometers at best, depending on the species.
In parallel, a brief review of experimental studies and numerical simulations performed on rocket engines can provide some notions of the typical length scales to be expected.
In Branam and Mayer (2002), an injection of liquid nitrogen into gaseous nitrogen was conducted at supercritical pressures using an axi-symmetrical cylindrical injector. The observed Kolmogorov scales ranged between 1 μm and 10 μm, depending on the injection velocity and the distance to the injector, for an injection diameter of 2.2 mm.
A fairly similar experiment was proposed in Ivancic and Mayer (2002) involving liquid oxygen injected into gaseous hydrogen. The same methodology yielded Kolmogorov scales between 2 μm and 60 μm for an injection diameter of 6.5 mm. In both these studies, the experimental

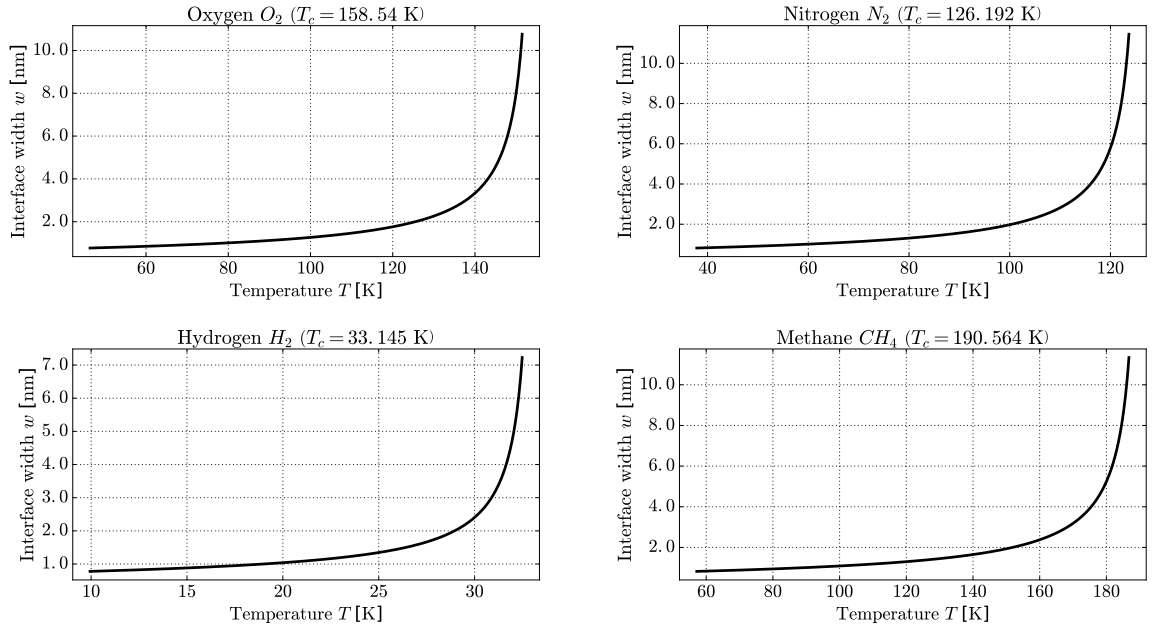

Figure 9.1: *Evolution of the interface width w with respect to the temperature T as predicted by the Second Gradient theory for pure oxygen, nitrogen, hydrogen and methane*

measurements were satisfactorily confronted to numerical simulations.
In Ruiz (2012), the author considered the configuration already studied in Oefelein (2005) to perform a DNS calculation. He evaluated the mean Kolmogorov scale around 160 μm.
More recently, a benchmark configuration has been established in Ruiz et al. (2015), still an axi-symmetrical injection of dense oxygen into gaseous hydrogen, to compare CFD codes with different numerical setups and strategies. A mesh convergence study showed that a mesh resolution of 1 μm (for an injection diameter of 0.5 mm) was enough to properly reach mesh insensitivity in the results and a quick calculation with a purposely overestimated Reynolds number landed a smallest Kolmogorov scale of 0.2 μm.
In Wang and Yang (2016), the authors considered a liquid-oxygen/kerosene bi-swirl injector to investigate mixing and combustion. A mesh convergence study provided a conservative value of 1 μm for the Kolmogorov scale.

When comparing the values for the interface width and the estimated Kolmogorov scales, the difference in magnitude is glaring. The scaling factor between the smallest turbulent scales and the interface widths is at least of 100 but can easily reach values greater than 1000. It is flagrant that the interface need to be thickened somehow if one is to perform the calculations presented in the previously mentioned studies, even for DNS purposes.
Of course, this thickening process must be carried out cautiously so as to preserve the macroscopic behavior of the interface which is already faithfully transcribed by the native SG model. For instance, the intuitive idea to increase the capillary coefficient λ in virtue of the relation $w \propto \sqrt{\lambda}$ in Eq. (5.146) is immediately dismissed by the relation $\sigma \propto \sqrt{\lambda}$ in Eq. (5.167) which shows that the effective augmentation of the interface width goes hand in hand with an augmentation of the surface tension which is the primary value driving the macroscopic behavior

of the interface. To avoid this major drawback along with other possible inconveniences, we present in Sec. 9.2 a new method in order to properly thicken an interface up to typical DNS mesh sizes.

9.1.2 Thickening near the critical point

In his PhD thesis Jamet (1998), Jamet notices that the problem of characterizing an isothermal planar interface at equilibrium is significantly simplified when the temperature is selected in the vicinity of the critical temperature since, to some extent, the problem becomes analytically solvable. Indeed, such an interface satisfies the differential equation Eq. (9.1) which, using thermodynamic arguments, can be modified into Eq. (9.2) where P_0 and μ_0 are the thermodynamic pressure and chemical potential given directly by the EoS.

$$\frac{\partial P_0}{\partial x} = \lambda \rho \frac{\partial^3 \rho}{\partial x^3} \tag{9.1}$$

$$\left(\mu_0 - \mu^{\text{sat}}\right)(x) = \lambda \frac{\partial^2 \rho}{\partial x^2}(x) \tag{9.2}$$

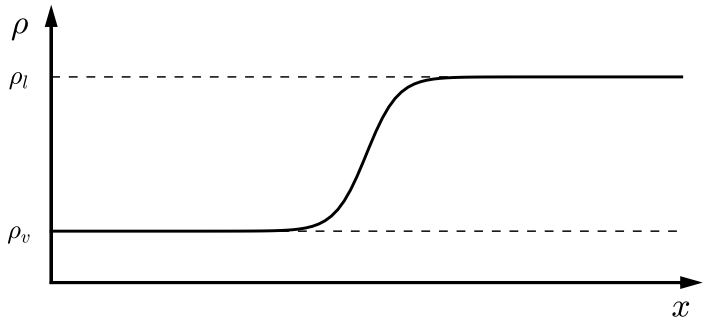

Figure 9.2: *Example of an interface profile between the vapor and liquid densities*

From Fig. 9.2, it is clear that in the liquid and vapor phases, i.e. when $\rho = \rho_l$ or $\rho = \rho_v$, the first and second spatial derivatives of $\rho(x)$ are null :

$$\frac{\partial \rho}{\partial x}(x_{\rho=\rho_l}) = \frac{\partial \rho}{\partial x}(x_{\rho=\rho_v}) = 0 \tag{9.3a}$$

$$\frac{\partial^2 \rho}{\partial x^2}(x_{\rho=\rho_l}) = \frac{\partial^2 \rho}{\partial x^2}(x_{\rho=\rho_v}) = 0 \tag{9.3b}$$

Given Eq. (9.2), it comes trivially that $\mu(\rho_l) = \mu(\rho_v) = 0$ but moreover, by multiplying both sides of Eq. (9.2) by $\dfrac{\partial \rho}{\partial x}$ and performing an integration between $x_{\rho=\rho_l}$ (limit of the pure liquid phase) and $x_{\rho=\rho_v}$ (limit of the pure vapor phase) it comes:

$$\int_{x_{\rho=\rho_v}}^{x_{\rho=\rho_l}} \left(\mu_0 - \mu^{\text{sat}}\right)(x) \frac{\partial \varrho}{\partial x} dx = \int_{x_{\rho=\rho_v}}^{x_{\rho=\rho_l}} \lambda \frac{\partial^2 \varrho}{\partial x^2}(x) \frac{\partial \varrho}{\partial x}(x) dx \tag{9.4a}$$

$$\int_{\rho_v}^{\rho_l} \left(\mu_0 - \mu^{\text{sat}}\right)(\varrho) d\varrho = \left[\frac{\lambda}{2}\left(\frac{\partial \rho}{\partial x}\right)^2(x)\right]_{x_{\rho=\rho_v}}^{x_{\rho=\rho_l}} = 0 \tag{9.4b}$$

Thus, as a function of the density, for such an interface, $\mu_0 - \mu^{\text{sat}}$ must satisfy the conditions:

$$\begin{cases} \left(\mu_0 - \mu^{\text{sat}}\right)(\rho_l) = \left(\mu_0 - \mu^{\text{sat}}\right)(\rho_v) = 0 & \text{(9.5a)} \\ \displaystyle\int_{\rho_v}^{\rho_l} \left(\mu_0 - \mu^{\text{sat}}\right)(\varrho)\, d\varrho = 0 & \text{(9.5b)} \end{cases}$$

In the vicinity of the critical temperature, the simplest non-trivial function to satisfy Eqs. (9.5a)-(9.5b) is a third order polynomial zeroing at $\rho = \rho_v$, $\rho = \rho_l$ and at a third value ρ_m in-between. The additional symmetry of the equations of state near the critical point in subcritical regions allows to identify $\rho_m = (\rho_l + \rho_v)$. The ensuing profile is given in Fig. 9.3 which also corresponds to the profile of $P_0 - P^{\text{sat}}$ since this function respects conditions formally identical to that of Eqs. (9.5a)-(9.5b).

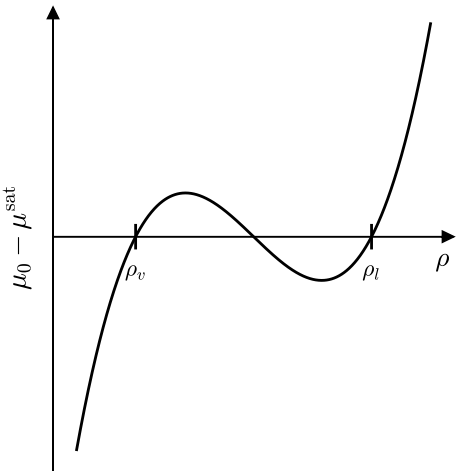

Figure 9.3: *Profile of the function $\mu_0 - \mu^{\text{sat}}$ relatively to the density in the vicinity of the critical point.*

It comes that Eq. (9.2) can thus be transformed into:

$$\lambda \frac{\partial^2 \rho}{\partial x^2}(x) = 2A\left(\rho(x) - \rho_v\right)\left(\rho(x) - \rho_v\right)\left(\rho(x) - \frac{\rho_v + \rho_l}{2}\right) \tag{9.6}$$

where A is a constant whose physical meaning is detailed later. Eq. (9.6) can be integrated two times to get the solution:

$$\rho(x) = \frac{(\rho_l + \rho_v)}{2} + \frac{(\rho_l - \rho_v)}{2} \tanh\left(\frac{\rho_l - \rho_v}{2}\sqrt{\frac{\lambda}{A}}x\right) \tag{9.7}$$

With the definitions of the interface width and the surface tension introduced in Eqs. (5.143) and (5.155), these two variables can be fully expressed:

$$w = \frac{4}{\rho_l - \rho_v}\sqrt{\frac{\lambda}{A}} \tag{9.8}$$

$$\sigma = \frac{(\rho_l - \rho_v)^3}{6}\sqrt{\lambda A} \tag{9.9}$$

These two relations provide two major and insightful results.
Firstly, the dependencies of w and σ on λ found in Eq. (5.146) and Eq. (5.167) respectively are formally retrieved in this special case.
Secondly, the dependencies of w and σ on λ are the same ($\propto \lambda$) whereas they are inverted for A ($w \propto 1/\sqrt{A}$ and $\sigma \propto \sqrt{A}$), which means that by adjusting both the values of A and λ, it is theoretically possible to specify designated values for w and σ (for a fixed temperature where ρ_l and ρ_v are fixed).
In particular, the objective to widen the interface while maintaining its surface tension is achievable. This solution presents several advantages: it is analytical, relatively simple and easy to implement and it allows not only to increase w but to actually choose a specific value (and even if of a smaller interest, the value of σ can also be specified). To a degree, a parallel can be drawn between the thickening mechanism of this method and the ability to chose the interface width through the adjustment of factor ϵ in some PF methods.

Despite the previous encouraging points, the first method introduced by Jamet falls short on multiple points with different degrees of criticality, further developed hereunder.
A prerequisite to apply the method is to access the values of the saturation densities ρ_v and ρ_l. Although this does not represent an insurmountable task, it nonetheless requires an additional treatment that needs to be efficiently implemented not to impede the calculations.
A second hurdle appears when trying to modify the value of constant A. From Eqs. (5.156) and (9.6), A directly impacts the slope of μ(as a function of ρ) near the saturation densities as given by Eq. (9.10).

$$\frac{\partial(\mu_0 - \mu^{\text{sat}})}{\partial\rho}(\rho_l) = \frac{\partial(\mu_0 - \mu^{\text{sat}})}{\partial\rho}(\rho_v) = A(\rho_l - \rho_v)^2 \tag{9.10}$$

Using the differential relation $d\mu_0 = -s_0\, dT + dP_0/\rho$ which simplifies in $d\mu_0 = dP_0/\rho$ for the isothermal case, A can directly be linked to the isothermal compressibility coefficient β at saturation with:

$$A = \frac{1}{\rho_l(\rho_l - \rho_v)^2}\frac{\partial P_0}{\partial\rho}(\rho_l) \qquad \left(= \frac{1}{\rho_v(\rho_l - \rho_v)^2}\frac{\partial P_0}{\partial\rho}(\rho_v)\right) \tag{9.11}$$

$$A = \frac{1}{\rho_l^2(\rho_l - \rho_v)^2\beta_l} \qquad \left(= \frac{1}{\rho_v^2(\rho_l - \rho_v)^2\beta_v}\right) \tag{9.12}$$

The relations in Eqs. (9.11)-(9.12) show that a modification of A produces a modification of the isothermal compressibility coefficients at saturation what can have unexpected and detrimental repercussions. In particular, such a modification may impact the sound speed and the heat capacities. In Jamet (1998), the author also details the impact of said modification on curved interfaces: the Laplace relation in itself is not modified (meaning that the relative difference between the inner and outer pressures is unchanged) but the lack of second order continuity for $P_0(\rho)$ introduces an error in the absolute values of the inner and outer pressures. Jamet however also shows that this error decreases rapidly with the inclusion radius (the error is inversely proportional to the third power of the radius) thus still making this method usable, in principle, for a wide variety of configurations. It has for instance been successfully applied to study nucleate boiling in Fouillet (2003).
The third and most significant obstacle to this method is its apparent range of application which is extremely narrow around the critical conditions. Indeed, strong hypotheses have been

made regarding the behavior of classic EoS near the critical point to extract the expression in Eq. (9.6) (which is essentially a physically driven Taylor expansion). During our practical tests, the method seemed to fail for reduced temperatures below $T_r = 0.99$ thus dramatically reducing it range of application and therefore making it irremediable not suitable for our targeted industrial applications in its current formulation.

9.1.3 Thermodynamically consistent thickening

Subsequent to the shortcomings of the first approach, Jamet proposed a second thickening strategy, both more thorough and intricate.

The key point that limits the reach of the first method is the simplified profile introduced for $\left(\mu_0 - \mu^{\text{sat}}\right)(\rho)$ which satisfies only part of the conditions one would like to apply.
In this new strategy, Jamet makes use of the function Ψ introduced in Eq. (5.123) as $\Psi(\rho) \hat{=} \rho'(x)$ which establishes an implicit link between the density profile ρ and its first spatial derivative $d\rho/dx(x) = \rho'$. The solution density profile must compel with the conditions enunciated in Eqs. (9.3a), (9.3b) and (9.5b). In order to maintain the isothermal compressibility coefficients at saturation, the differential relation $d\mu_0 = dP_0/\rho$ also adds the conditions in Eqs. (9.13a) and (9.13b). Finally, if one is to prescribe specific values for the interface width w and surface tension σ, the density profile must also satisfy the relations Eqs. (5.143) and (5.155).

$$\begin{cases} \dfrac{\partial(\mu_0 - \mu^{\text{sat}})}{\partial\rho}(\rho_v) = \dfrac{\partial P_0}{\partial\rho}(\rho_v) & \text{(9.13a)} \\ \dfrac{\partial(\mu_0 - \mu^{\text{sat}})}{\partial\rho}(\rho_l) = \dfrac{\partial P_0}{\partial\rho}(\rho_l) & \text{(9.13b)} \end{cases}$$

All these conditions can be reformulated in terms of Ψ to get the system, assuming ρ_v, ρ_l, $dP_0/d\rho(\rho_v)$, $dP_0/d\rho(\rho_l)$, w and σ are known:

$$\Psi(\rho_v) = 0 \tag{9.14a}$$
$$\Psi(\rho_l) = 0 \tag{9.14b}$$
$$\left(\frac{d\Psi}{d\rho}(\rho_v)\right)^2 = \frac{1}{\lambda}\frac{1}{\rho_v}\frac{\partial P_0}{\partial\rho}(\rho_v) \tag{9.14c}$$
$$\left(\frac{d\Psi}{d\rho}(\rho_l)\right)^2 = \frac{1}{\lambda}\frac{1}{\rho_l}\frac{\partial P_0}{\partial\rho}(\rho_l) \tag{9.14d}$$
$$\max\Psi = \frac{\rho_l - \rho_v}{w} \tag{9.14e}$$
$$\lambda\int_{\rho_v}^{\rho_l}\Psi(\rho)\,d\rho = \sigma \tag{9.14f}$$

The system can be further simplified by nondimensionalizing it, introducing the reduced quantities r and ψ as follows:

$$\begin{cases} r = \dfrac{\rho - \rho_v}{\rho_l - \rho_v} & \text{(9.15a)} \\ \psi(r) = \dfrac{w}{\rho_l - \rho_v}\Psi(\rho) & \text{(9.15b)} \end{cases}$$

Besides, λ is not an input of the system but rather an unknown to be evaluated to achieved the desired thickening, therefore Eqs. (9.14c) and Eqs. (9.14c) must be rearranged accordingly. All things considered, the new system is given by:

$$\psi(0) = 0 \tag{9.16a}$$

$$\psi(1) = 0 \tag{9.16b}$$

$$\left(\frac{d\psi/dr(0)}{d\psi/dr(1)}\right)^2 = \frac{\rho_l \, \partial P_0/\partial\rho(\rho_v)}{\rho_v \, \partial P_0/\partial\rho(\rho_l)} \tag{9.16c}$$

$$\max\psi = 1 \tag{9.16d}$$

$$\frac{1}{(d\psi/dr(0))^2}\int_0^1 \psi(r)\,dr = \frac{\rho_v}{(\rho_l-\rho_v)^2 \, \partial P_0/\partial\rho(\rho_v)}\frac{\sigma}{w} \tag{9.16e}$$

$$\lambda = \frac{w^2}{\rho_v \, (d\psi/dr(0))^2}\frac{\partial P_0}{\partial\rho}(\rho_v) \tag{9.16f}$$

Further investigations allowed Jamet to identify the form in Eq. (9.17) as a suitable candidate for a solution. Coefficient α is chosen *a priori* whereas coefficients a, b and c have to be determined using a Newton-like solver to satisfy the complete system (9.16).

$$\phi(r) = \left[4(1+a)\,r(1-r) + (br+c)^2\right]^\alpha - [br+c]^{2\alpha} \tag{9.17}$$

The author shows that this method ensures the thermodynamic consistency of the system, in particular a second order continuity of the proper thermodynamic variables at saturation. The determination of ψ and therefore Ψ is done *a priori* for a fixed temperature, meaning that it implicitly defines a function $\Psi(\rho, T)$. This function of both the density ρ and the temperature T can be used to define the complete modified thermodynamics, of which the expression of the modified variables (with the subscrip $^{\text{mod}}$) are given hereunder.

$$P^{\text{mod}}(\rho,T) = P^{\text{sat}}(T) + \lambda\Psi(\rho,T)\left[\rho\left(\frac{\partial\Psi}{\partial\rho}\right)_T(\rho,T) - \frac{1}{2}\Psi(\rho,T)\right] \tag{9.18a}$$

$$e_s{}^{\text{mod}}(\rho,T) = \frac{\lambda}{\rho}\Psi(\rho,T)\left[\frac{1}{2}\Psi(\rho,T) - T\left(\frac{\partial\Psi}{\partial T}\right)_\rho(\rho,T)\right] + \Pi(e_s)(\rho,T) \tag{9.18b}$$

$$h_s{}^{\text{mod}}(\rho,T) = \lambda\Psi(\rho,T)\left[\left(\frac{\partial\Psi}{\partial\rho}\right)_T(\rho,T) - \frac{T}{\rho}\left(\frac{\partial\Psi}{\partial T}\right)_\rho(\rho,T)\right] + \Pi(h_s)(\rho,T) \tag{9.18c}$$

$$s^{\text{mod}}(\rho,T) = -\frac{\lambda}{\rho}\Psi(\rho,T)\left(\frac{\partial\Psi}{\partial T}\right)_\rho(\rho,T) + \Pi(s)(\rho,T) \tag{9.18d}$$

$$\mu^{\text{mod}}(\rho,T) = \mu^{\text{sat}}(T) + \lambda\Psi(\rho,T)\left(\frac{\partial\Psi}{\partial\rho}\right)_T(\rho,T) \tag{9.18e}$$

where for a variable χ, the quantity $\Pi(\chi)$ is defined as :

$$\Pi(\chi)(\rho,T) = \frac{\rho_v(\rho_l-\rho)}{\rho(\rho_l-\rho_v)}\chi_v(T) + \frac{\rho_l(\rho-\rho_v)}{\rho(\rho_l-\rho_v)}\chi_l(T) \tag{9.19}$$

The modified specific heat capacities are obtained using respectively $C_v = (\partial e_s/\partial T)_\rho$ and $C_p = C_v + (T/\rho^2)\left((\partial P/\partial T)^2_\rho/(\partial P/\partial \rho)_T\right)$. It is possible to show that Eqs. (9.18a)-(9.18e) with the relations for C_v and C_p ensure the desired level of regularity for the thermodynamics when crossing the binodal curve : the volumetric free energy F is of class $\mathcal{C}^2$, P, e_s, h_s, μ and s are of class $\mathcal{C}^1$, C_v and C_p are continuous at saturation.

This second thickening method is both powerful and consistent and the authors in Jamet, Lebaigue, Coutris, and Delhaye (2001) successfully applied it to several typical capillary phenomena such as the disappearance or the coalescence of bubbles and the dynamical hysteresis in the contact angle of a bubble with a wall.

Notwithstanding all its benefits, we identified three crucial impediments when contemplating the application of this method to our targeted simulations.
The first one stems from the necessity to geometrically locate the interface as the method consists in not only a thermodynamic modification but also an actual geometrical deformation of the interface as testified by the definition of Ψ linking the density profile to its spatial derivative. In contrast, Jamet's first method only requires to evaluate the saturation densities relatively to the local temperature.
A possible second hurdle manifests itself by the Newton-like solving procedure that is required multiple times to evaluate the coefficients in Eq. (9.17) and of which numerical implementation has come with substantial difficulties and has not been met with success so far. Although not a definitive issue by itself, since other Newton-like solving procedures are already used in real gas simulations, the fact that this additional one, with its relative sensitivity, would have to be replicated multiple times for one single time step could render it numerically costly and unpractical.
Finally, the last obstacle is apparent when looking at Eqs. (9.18a) to (9.18e). Indeed, multiple variables that are actually to be used to conduct simulations require the differentiation of Ψ relatively to the temperature when this dependency is only know implicitly.
This means additional instances of solving Eq. (9.17) are required solely to evaluate these thermodynamic variables, further increasing the complexity and consequently the numerical cost of this method. Arguably, computational time could be saved by pre-tabulating parts of the useful results but such a tabulation would be mixture-dependent for multi-species cases and would certainly constitute a definitive drawback regarding the extension of the method to such more complex simulations.

9.2 The Thickened Interface Method

In light of the thickening required for our targeted applications and the several shortcomings of the two previous Jamet's thickening strategies rendering them inadequate for our usage, we present here the method devised during the course this PhD to better suit our requirements.
Referred to as the Thickened Interface Method (TIM), this approach substantially borrows from and builds upon Jamet's methods and essentially aim for stricking a balance between their respective advantages and drawbacks.
Ideally, the approach should limit the additional computations required (for instance by having a fully analytical description), grant a complete thermo-mechanical consistency, allow the

choice of a specific value for the interface width and possibly the surface tension, restrain the modifications to the binodal region (keep the bulk phases unchanged) and be easily implemented into a solver already capable of native SG model simulations. Certainly, achieving all these perks at once seems ambitious but selecting the more important and relevant attributes makes the task, if not doable, a lot easier.

9.2.1 Modification of the thermodynamics

9.2.1.1 Fundamental modification

For all its relative simplicity, Jamet's first method shows that despite the fact, known from Eqs. (5.146) and (5.167), that changing the value of λ to thicken the interface cannot be done without augmenting the surface tension, the addition of a second parameter is a sound strategy in order to control simultaneously w and σ and should be capitalized on.
Conversely, behind the complex mechanics of Jamet's second method transpires the necessity to damp the variation of key thermodynamic variables around their saturation values, more specifically μ_0 and/or P_0.
Finally, any modification done in the limited case of an isothermal interface should be designed so as to easily carry over to a non-isothermal paradigm.

Using these observations, the purpose is therefore to derive a method by introducing two coefficients ϕ_λ and ϕ_σ, reminiscent of Jamet's first strategy. Coefficient ϕ_λ is to be directly applied to the capillary coefficient λ thus modifying w and σ in the same fashion. On the opposite, ϕ_σ should impact the thermodynamics so as to get $\sigma \propto \sqrt{\phi_\sigma}$ whereas $w \propto 1/\sqrt{\phi_\sigma}$ thus allowing to mitigate the effect of modifying λ.

Combining all mentioned considerations, the starting point of the TIM derivation is studying the impact of some constant η onto the thermodynamics granted that this study is, in a first time, limited to the non-capillary thermodynamics (i.e. the variables are extracted directly from the equation of state) and that η is used to damp the specific free enthalpy μ^{EoS} as described in Eq. (9.20) which will act as the founding relation of our method. The actual link between η and ϕ_σ is clarified after the impact of the former is properly established.

$$\mu^{\eta}(\rho, T) = \mu^{\mathrm{sat}}(T) + \frac{\mu^{\mathrm{EoS}}(\rho, T) - \mu^{\mathrm{sat}}(T)}{\eta} \tag{9.20}$$

NOTE: In the next paragraphs, we use notation conventions presented in App. B.4 so as to distinguish the different instances of similar thermodynamic variables. Mainly, the superscripts $*^{\mathrm{EoS}}$, $*^{\mathrm{sat}}$ and $*^{\eta}$ are use respectively to designate a non-capillary variable as directly given by the equation of state, as defined at saturation and as defined by the η-modification. The superscript $*^{\mathrm{TIM}}$ is later used to refer to a fully capillary variable as modified by the complete TIM modeling. We also emphasize here that the notation $\bar{\chi}(T)$, which designates the saturation value of a thermodynamic variable χ^{EoS} calculated indifferently in the liquid or the vapor phase for the temperature T, does not implies that the two corresponding values are equal (like it is the case for the pressure or the specific free enthalpy). It however means that for the calculation of a quantity where this notation appears, any of the two saturation values can be chosen as long as this choice remains the same to calculate all the "bar-variables" required to evaluate said quantity.

9.2.1.2 Extension to other thermodynamic variables

The modification introduced in Eq. (9.20) has to be consistently expanded to the other thermodynamic variables. This requires in particular the ability to evaluate the temperature derivatives of the saturation values of several thermodynamic variables. For the sake of clarity, the associated development for these calculations are left in App. B.4.1, here we focus on the derivation of the actual "η-modified" variables and even so, only the major steps are presented, a comprehensive derivation can also be found in App. B.4.1.

Firstly, the "η-modified" volumetric free energy F^η can be determined using the differential relation Eq. (B.17) which becomes $\mu = (\partial F/\partial \rho)_T$ in an isothermal setting. By reformulating Eq. (9.20) into $\mu^\eta(\rho, T) = \mu^{\text{EoS}}(\rho, T)/\eta + (1 - 1/\eta)\,\mu^{\text{sat}}(T)$, the integration leads to:

$$F^\eta(\rho, T) = \frac{1}{\eta} F^{\text{EoS}}(\rho, T) + \left(1 - \frac{1}{\eta}\right) \mu^{\text{sat}}(T)\rho + C(T) \tag{9.21}$$

where $C(T)$ is function of solely the temperature. To compel to the condition of leaving the bulk phases unchanged, we can impose the condition $F^\eta(\rho_v(T), T) = F^{\text{EoS}}(\rho_v(T), T)$ which leads to $C(T) = -(1 - 1/\eta)\,P^{\text{sat}}(T)$ and eventually:

$$F^\eta(\rho, T) = F_*^{\text{sat}}(\rho, T) + \frac{F^{\text{EoS}}(\rho, T) - F_*^{\text{sat}}(\rho, T)}{\eta} \tag{9.22}$$

where $F_*^{\text{sat}}(\rho, T) = \rho\mu^{\text{sat}}(T) - P^{\text{sat}}(T)$.
Noticeably, due to the fact that $\mu^{\text{EoS}}(\rho_v(T), T) = \mu^{\text{EoS}}(\rho_l(T), T)$ and $P^{\text{EoS}}(\rho_v(T), T) = P^{\text{EoS}}(\rho_l(T), T)$, the same expression is obtained enforcing $F^\eta(\rho_v(T), T) = F^{\text{EoS}}(\rho_v(T), T)$ instead, further cementing its consistency.

From Eq. (B.13) that defines the volumetric free energy with $F = -P + \mu\rho$, it comes that the new pressure must respect ${P_0}^\eta = \rho\mu^\eta - F^\eta$ which, using Eqs. (9.20) and (9.22), leads to:

$${P_0}^\eta(\rho, T) = P^{\text{sat}}(T) + \frac{P^{\text{EoS}}(\rho, T) - P^{\text{sat}}(T)}{\eta} \tag{9.23}$$

Differentiating the new volumetric free energy following Eq. (B.17) which becomes $s^\eta = -(1/\rho)(\partial F^\eta/\partial T)_\rho$, the modified specific entropy can be written:

$$s^\eta(\rho, T) = \bar{s}(T) + \frac{s^{\text{EoS}}(\rho, T) - \bar{s}(T)}{\eta} + \left(1 - \frac{1}{\eta}\right)\left(\frac{1}{\rho} - \frac{1}{\bar{\rho}(T)}\right)\frac{dP^{\text{sat}}}{dT}(T) \tag{9.24}$$

To draw further attention to the notation $\bar{\chi}(T)$ which appears two times in Eq. (9.24) with $\bar{s}(T)$, $\bar{\rho}(T)$, it means that to evaluate s^η for a couple (ρ, T) one is required to evaluate the entropy and the density at saturation. However, these two values differ between the liquid and the vapor phases and therefore a choice has to be made, apparently arbitrarily, between one of the two phase to consider. This is where the notation $\bar{\chi}(T)$ comes into play and states that any of the two phases can be used and both choices lead to the same value of $s^\eta(\rho, T)$ as long as the same phase is used to evaluate $\bar{s}(T)$ and $\bar{\rho}(T)$. Formally, this means that Eq.

(9.24) can, indifferently, be developed into:

$$s^{\eta}(\rho,T)\begin{cases} = s_l^{\text{sat}} + \dfrac{s^{\text{EoS}}(\rho,T) - s_l^{\text{sat}}}{\eta} + \left(1-\dfrac{1}{\eta}\right)\left(\dfrac{1}{\rho}-\dfrac{1}{\rho_l}\right)\dfrac{dP^{\text{sat}}}{dT}(T) \\ \text{or} \\ = s_v^{\text{sat}} + \dfrac{s^{\text{EoS}}(\rho,T) - s_v^{\text{sat}}}{\eta} + \left(1-\dfrac{1}{\eta}\right)\left(\dfrac{1}{\rho}-\dfrac{1}{\rho_v}\right)\dfrac{dP^{\text{sat}}}{dT}(T) \end{cases} \tag{9.25}$$

The specific internal energy ${e_s}^{\eta}$ is obtained straightforwardly by applying the definition in Eq. (B.22) stating that $e_s = Ts - \frac{P}{\rho} + \mu$ where P, μ and s are now known to get:

$$\begin{aligned} {e_s}^{\eta}(\rho,T) = \bar{e_s}(T) &+ \frac{{e_s}^{\text{EoS}}(\rho,T) - \bar{e_s}(T)}{\eta} \\ &+ \left(1-\frac{1}{\eta}\right)\left(\frac{1}{\rho}-\frac{1}{\bar{\rho}(T)}\right)\left(T\frac{dP^{\text{sat}}}{dT}(T) - P^{\text{sat}}(T)\right) \end{aligned} \tag{9.26}$$

The specific isochoric heat capacity ${C_v}^{\eta}$ can be expressed by using either its definition ${C_v}^{\eta} = \left(\partial {e_s}^{\eta}/\partial T\right)_{\rho}$ or the relation ${C_v}^{\eta} = T\left(\partial {s}^{\eta}/\partial T\right)_{\rho}$ (providing a mean to verify the calculations) which results in:

$$\begin{aligned} {C_v}^{\eta}(\rho,T) = \bar{C_v}(T) &+ \frac{{C_v}^{\text{EoS}}(\rho,T) - \bar{C_v}(T)}{\eta} \\ &+ T\left(1-\frac{1}{\eta}\right)\left[\frac{\bar{\alpha}^2}{\bar{\rho}\bar{\beta}} + \Xi(\rho,T)\frac{\underset{sat}{\Delta}(C_P)}{T} + -2\zeta\left(\frac{\alpha}{\rho}\right)\frac{dP^{\text{sat}}}{dT} + \zeta\left(\frac{\beta}{\rho}\right)\left(\frac{dP^{\text{sat}}}{dT}\right)^2\right] \end{aligned} \tag{9.27}$$

where

$$\Xi(\rho,T) = \frac{\dfrac{1}{\rho} - \dfrac{1}{\bar{\rho}(T)}}{\dfrac{1}{\rho_l} - \dfrac{1}{\rho_v}} \tag{9.28}$$

and for a thermodynamic variable χ, the quantity $\zeta(\chi)$ is defined by:

$$\zeta(\chi)(\rho,T) = \bar{\chi}(T) + \Xi(\rho,T)\underset{sat}{\Delta}(\chi)(T) \tag{9.29}$$

The specific isobaric heat capacity ${C_p}^{\eta}$ is obtained via the classic relation Eq. (B.67), i.e. $C_p = C_v + \left(T\alpha^2\right)/(\rho\beta)$, noticing however that the isothermal compressibility and thermal expansion coefficients must be modified beforehand accordingly with their respective definitions in Eqs. (1.39) - (1.40) leading to the expressions:

$${C_p}^{\eta} = {C_v}^{\eta} + \frac{T{\alpha^{\eta}}^2}{\rho\beta^{\eta}} \tag{9.30}$$

$$\alpha^{\eta}(\rho,T) = \alpha^{\text{EoS}}(\rho,T) + (\eta-1)\,\beta^{\text{EoS}}(\rho,T)\frac{dP^{\text{sat}}}{dT}(T) \tag{9.31}$$

$$\beta^{\eta}(\rho,T) = \eta\beta^{\text{EoS}}(\rho,T) \tag{9.32}$$

The profiles of several modified thermodynamic variables are given in Figs. 9.4 and 9.5 for different values of η. In particular, the damping effect of η in the binodal region can easily be observed for P^{η} and μ^{η}.

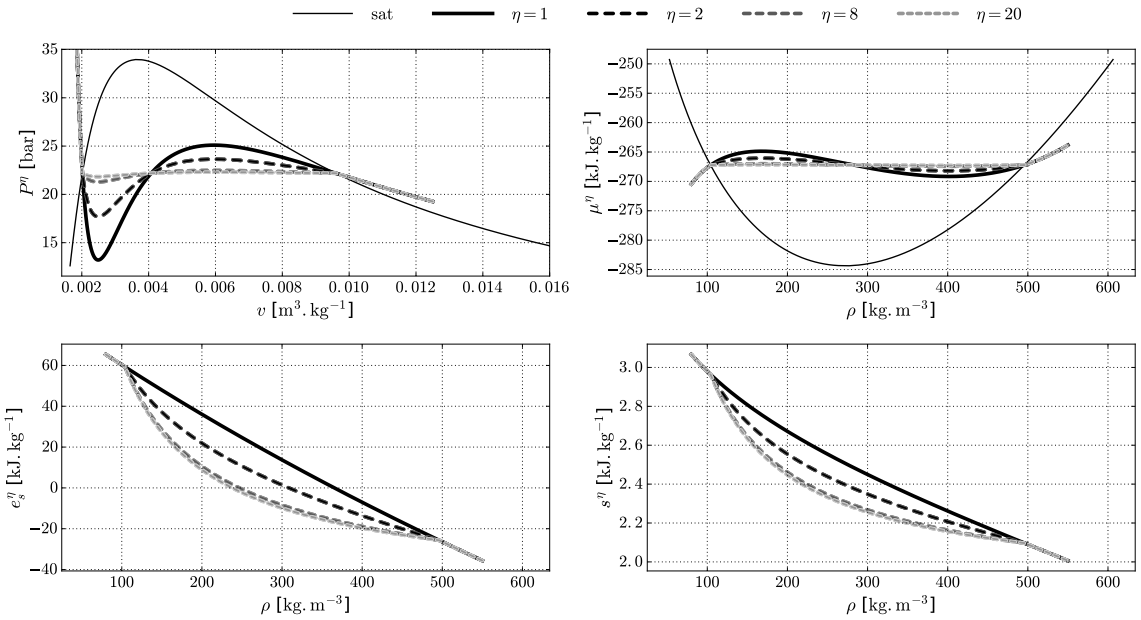

Figure 9.4: *Pressure, specific free enthalpy, specific internal energy and specific entropy of nitrogen N_2 at $T = 117$ K as modified by Eqs. (9.23), (9.20), (9.26) and (9.24) for different values of η*

9.2.1.3 Additional remarks

One result implied by the derivation is that during a computation, the criterion used to choose in which phase $\bar{\chi}$ is evaluated can differ from one point to the other in the computational domain and can change from one iteration to the other as long as, for one evaluation of a quantity, this choice is fixed.
Moreover, this choice can also differ between two different quantities, even when evaluated at the same time on the same point, once again, as long as the internal consistency of the phase choice is kept for each quantity.
Conveniently, this leads to the useful following results (where $\rho_k = \rho_l$ or ρ_v) ensuring the continuity of the thermodynamics when crossing the binodal curve, independently of η:

$$\begin{cases} \lim\limits_{\rho\to\rho_k} {e_s}^\eta(\rho,T) = {e_s}^{\text{EoS}}(\rho_k(T),T) & \text{(9.33a)} \\ \lim\limits_{\rho\to\rho_k} {h_s}^\eta(\rho,T) = {h_s}^{\text{EoS}}(\rho_k(T),T) & \text{(9.33b)} \\ \lim\limits_{\rho\to\rho_k} s^\eta(\rho,T) = s^{\text{EoS}}(\rho_k(T),T) & \text{(9.33c)} \\ \lim\limits_{\rho\to\rho_k} {C_v}^\eta(\rho,T) \neq {C_v}^{\text{EoS}}(\rho_k(T),T) & \text{(9.33d)} \end{cases}$$

9.2.1.4 Impact on the isothermal interface

The previous developments essentially represent a modification of the equation of state since no aspect of the capillary description of the fluid has been modified yet. However, the behavior of the interface is actually already impacted by the introduction of the factor η into the

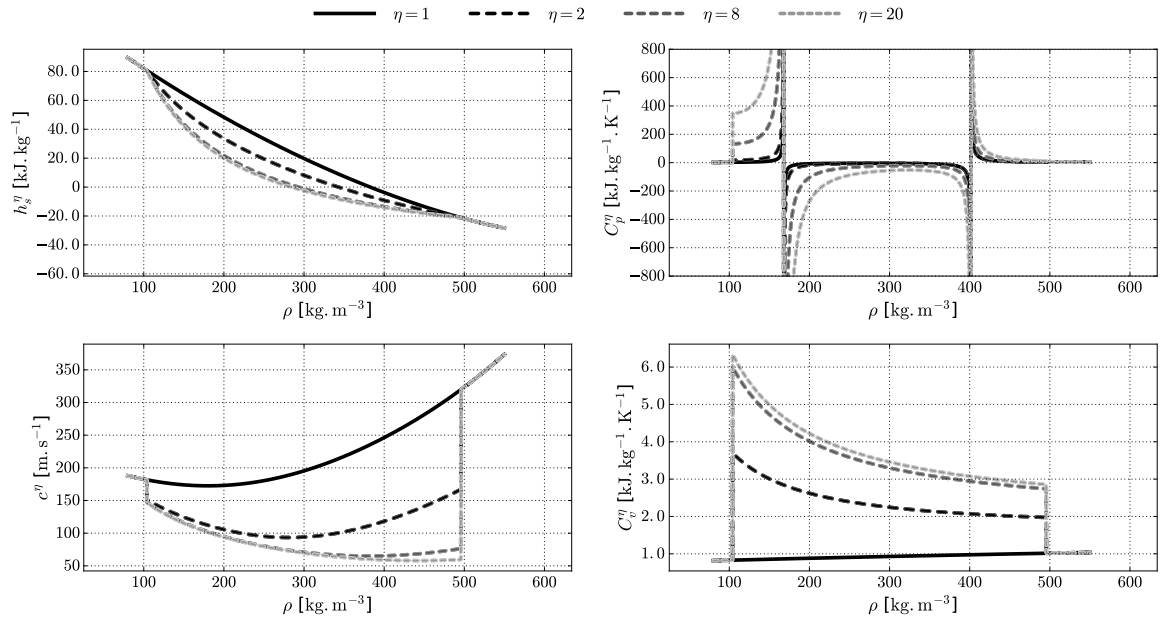

Figure 9.5: *Specific enthalpy, specific isobaric capacity, sound speed and isochoric heat capacity of nitrogen N_2 at $T = 117$ K as modified by Eqs. (9.27), (9.30), (9.31) and (9.32) for different values of η*

thermodynamics. This next paragraph is dedicated to a more in depth analysis to this new, non-capillary related, thermodynamic behavior of the interface. Using a reference capillary coefficient λ_0, the momentum equation for an isothermal interface at equilibrium, given Eq. (5.137), can be written:

$$\frac{\partial P^\eta}{\partial x} = \lambda_0 \rho^\eta \frac{\partial^3 \rho^\eta}{\partial x^3} \tag{9.34}$$

The notation ρ^η is purposefully used to account for the fact that the solution density profile is affected by the modified equation of state and does not, *a priori*, coincide with that of the native solution of Eq. (5.137).
Discarding $P^{\text{sat}}(T)$ in Eq. (9.23) which is constant for an isothermal interface, the equation transforms into Eq. (9.35) where one can recognize the native momentum equation Eq. (5.137) however written for a capillary coefficient $\eta\lambda_0$.
Thanks to the study in Sec. 5.4.2.1, we now know that the solution of Eq. (9.35) is the density profile solution of Eq. (5.137) with a capillary coefficient λ_0 only thickened by a factor $\sqrt{\eta}$, i.e. $w^\eta = \sqrt{\eta} w_0$ where w^η is the new interface width and w_0 is the interface width with the native EoS.

$$\frac{\partial P^{\text{EoS}}(\rho^\eta)}{\partial x} = \eta \lambda_0 \rho^\eta \frac{\partial^3 \rho^\eta}{\partial x^3} \tag{9.35}$$

This means in particular that the variable change $X = x/\sqrt{\eta}$ allows to write $\rho^\eta(X) = \rho(x)$ and subsequently, from Eqs. (5.159) and (9.20) it comes that $\Upsilon(\rho^\eta) = \Upsilon\left(\rho^0\right)/\eta$. Using Eq. (5.164), the new value of the surface tension resulting from the modified equation of state can

thus be obtained:

$$\sigma_\eta = \int_{X_l}^{X_v} \Upsilon\left(\rho^\eta\right) dX = \int_{x_l}^{x_v} \frac{\Upsilon\left(\rho^0\left(X\right)\right)}{\sqrt{\eta}}\, dx = \frac{\sigma^0}{\sqrt{\eta}} \tag{9.36}$$

where σ^0 is the surface tension obtained with the native equation of state. With this consistently modified EoS, the impact of η onto w and σ is clearly established and can be compared to the targeted effect of coefficient ϕ_σ which was $\sigma \propto \sqrt{\phi_\sigma}$ and $w \propto 1/\sqrt{\phi_\sigma}$. This easily allows to identify ϕ_σ with $1/\eta$ and for the remainder of the document, the notation χ^η is dismissed in favor of χ^{ϕ_σ} which will designate a variable χ for a modified EoS where η is formally replaced by $1/\phi_\sigma$. Such a modified thermodynamics corresponds to a specific free enthalpy given by Eq. (9.37) and with the modifications consistently expanded to the other thermodynamic variables as done hereinabove.

$$\mu^{\phi_\sigma}\left(\rho, T\right) = \mu^{\text{sat}}\left(T\right) + \phi_\sigma\left(\mu^{\text{EoS}}\left(\rho, T\right) - \mu^{\text{sat}}\left(T\right)\right) \tag{9.37}$$

9.2.2 Thermo-mechanical equation of the TIM

With coefficient ϕ_σ properly introduced, we know that simply modifying the EoS is not sufficient to achieve the global effects we desire for the TIM, in particular the role of ϕ_λ needs to be clarified. Conveniently, by using the latter directly as a multiplicative factor applied to the capillary coefficient, one obtains the dependencies $h \propto \sqrt{\phi_\lambda}$ and $\sigma \propto \sqrt{\phi_\lambda}$ which, combined together with the modifications induced by ϕ_σ, leads to the final dependencies Eqs. 9.38 which were targeted from the inception of the method. In particular, this proves that a combined action of ϕ_σ and ϕ_σ should allow to act independently on either w or σ.

$$\begin{cases} w \propto \sqrt{\phi_\lambda/\phi_\sigma} & \text{(9.38a)} \\ \sigma \propto \sqrt{\phi_\lambda \phi_\sigma} & \text{(9.38b)} \end{cases}$$

9.2.2.1 Thermodynamic variables in the TIM

One of the requirements for the method was to leave the bulk phases unchanged but, as expressed in Eqs. (9.20) - (9.32), the modifications of the EoS are applied to the whole subcritical domain (as long as saturation density values are defined), which is unsatisfactory. In its final form, the TIM must restrain the thermodynamic and mechanical modifications to the binodal region only. In particular here, the EoS modifications should only take place in that said region. Even in that cases, the continuity of the thermodynamic variables is ensured by the results Eqs. (9.33). In that respect, their final expressions (referred to with the exponent $^{\text{TIM}}$) can be detailed, starting with the variables (represented with χ_λ) not impacted by the capillary contributions of the native SG model, namely μ, P_0, h_s, s and C_v, which only undergo the modifications from the EoS:

$$\chi_\lambda{}^{\text{TIM}} = \begin{cases} \chi_\lambda{}^{\phi_\sigma} & \text{in the binodal region} \\ \chi_\lambda{}^{\text{EoS}} & \text{otherwise} \end{cases} \tag{9.39}$$

As previously mentioned, coefficient ϕ_λ is applied to the capillary coefficient λ leading to the

new expression in the TIM framework:

$$\lambda^{\mathrm{TIM}} = \begin{cases} \phi_\lambda \lambda_0 & \text{in the binodal region} \\ \lambda_0 & \text{otherwise} \end{cases} \tag{9.40}$$

This allows to express the thermodynamic variables that were already impacted by the native SG model, namely p and e_s (f and F should also be included but are of limited interest in the prospect of numerical simulation and are omitted here for more clarity), which now endure modifications from both λ^{TIM} and the transformed EoS:

$$p^{\mathrm{TIM}} = \begin{cases} P^{\phi_\sigma} - \dfrac{\phi_\lambda \lambda_0}{2}\left[(\boldsymbol{\nabla}\rho)^2 + 2\rho\boldsymbol{\Delta}\rho\right] & \text{in the binodal reg.} \\ P^{\mathrm{EoS}} - \dfrac{\lambda_0}{2}\left[(\boldsymbol{\nabla}\rho)^2 + 2\rho\boldsymbol{\Delta}\rho\right] & \text{otherwise} \end{cases} \tag{9.41}$$

$$e_s{}^{\mathrm{TIM}} = \begin{cases} e_s{}^{\phi_\sigma} + \dfrac{\phi_\lambda \lambda_0}{2\rho}(\boldsymbol{\nabla}\rho)^2 & \text{in the binodal reg.} \\ e_s{}^{\mathrm{EoS}} + \dfrac{\lambda_0}{2\rho}(\boldsymbol{\nabla}\rho)^2 & \text{otherwise} \end{cases} \tag{9.42}$$

Essentially, all the previous formulas can be summed-up by saying that the thermodynamic variables and the capillary coefficient are untouched in the bulk phases and switch to their ϕ_σ-modified (eventually also ϕ_λ-modified) counterparts within the binodal region.

9.2.2.2 Navier-Stokes equations in the TIM

To preserve the consistency, the mechanical description must not be forgotten as the capillary coefficient also appears within the Euler/Navier Stokes equations. Thanks to the preserved consistency of the ϕ_σ-modified thermodynamics and the known impact of ϕ_λ onto the capillary coefficient, one gets that no profound modification is applied to the system Eqs. (5.87), only the global thermodynamic modifications of the TIM that have to be included in order to obtain the new system. This update is achieved by substituting p, λ^0 and E with p^{TIM}, λ^{TIM} and $e^{\mathrm{TIM}} = e_s{}^{\mathrm{TIM}} + \mathbf{v}^2/2$, to get the following equations:

$$\begin{cases} \dfrac{\partial \rho}{\partial t} = -\boldsymbol{\nabla}\cdot[\rho\mathbf{v}] & \text{(9.43a)} \\ \dfrac{\partial \rho\mathbf{v}}{\partial t} = -\boldsymbol{\nabla}\cdot\left[\rho\mathbf{v}\otimes\mathbf{v} + p^{\mathrm{TIM}}\underline{\underline{\mathbf{I}}} + \lambda^{\mathrm{TIM}}\boldsymbol{\nabla}\rho\otimes\boldsymbol{\nabla}\rho - \underline{\underline{\boldsymbol{\tau}}}^d\right] & \text{(9.43b)} \\ \dfrac{\partial \rho e^{\mathrm{TIM}}}{\partial t} = -\boldsymbol{\nabla}\cdot\left[\left(\rho e^{\mathrm{TIM}} + p^{\mathrm{TIM}}\right)\mathbf{v} + \lambda^{\mathrm{TIM}}(\boldsymbol{\nabla}\rho\otimes\boldsymbol{\nabla}\rho)\cdot\mathbf{v} \right. \\ \qquad\qquad \left. + \lambda^{\mathrm{TIM}}\rho\boldsymbol{\nabla}\rho(\boldsymbol{\nabla}\cdot\mathbf{v}) - \underline{\underline{\boldsymbol{\tau}}}^d : \mathbf{v} + \boldsymbol{q}\right] & \text{(9.43c)} \end{cases}$$

In practice, the common objective of the TIM will be to apply a defined thickening factor F to the interface width while maintaining the value of the surface tension. The dependencies in Eqs. (9.38) thus become $\sqrt{\phi_\lambda\phi_\sigma} = 1$ and $\sqrt{\phi_\lambda/\phi_\sigma} = \mathrm{F}$ which leads to the following expressions for ϕ_λ and ϕ_σ.

$$\phi_\lambda = 1/\phi_\sigma = \sqrt{\mathrm{F}} \tag{9.44}$$

When not mentioned otherwise, the relations Eq. (9.44) are definitively adopted for the rest of the discussion involving the TIM.

9.2.2.3 Additional remarks regarding the TIM

To conclude this theoretical presentation of the Thickened Interface Method, it seemed important to us to draw a critical portrait of our method similarly to those we granted to both Jamet's methods.

Firstly and similarly to both Jamet's methods, the TIM requires the calculation of saturation values (pressure and density) jointly with the ability to discriminate the stable or unstable nature of a given thermodynamic state so as to apply the modifications only when needed. This is done using a thermodynamic equilibrium solver: the saturation values are retrieved by equalizing the chemical potential of the liquid and vapor states at a given temperature. Such a calculation is already partly performed in real gas solvers as it is required when trying to calculate the density corresponding to a couple (T, P), only the saturation values are new quantities to be extracted.

As in Jamet's first method, the entirety of the modification only involves the introduction of two coefficients and moreover, no definitive profile is imposed to the specific free enthalpy, a philosophy closer to the broader profile preferred in Jamet's second method.
Besides, the form of system (9.43) implies that only the thermodynamic routines of a solver have to be modified to transit from the native Second Gradient to the TIM-modified system, thus greatly reducing the implementation difficulties and efforts. This tendency is further supported by the fact that all the modified variables can be accessed analytically, contrary to Jamet's second and most complete method, albeit using fairly intricate formulas for some of them.

However, for all these satisfactory points, the method is far from being free of defaults.

The first flaw that can be noticed is the inability of the method to straightforwardly attribute a desired width to the interface. Indeed, the TIM only allows to apply a multiplicative coefficient to the latter. As such, the initial value of the interface width need to be known *a priori* in order to properly choose the thickening factor F to fit a targeted width.

The lack of high order regularity for the new thermodynamic variables cannot be overlooked, especially since it was one of the starting motivation behind the design of Jamet's second method. With the modification from the TIM, the new variables are mostly only continuous, of order $\mathcal{C}^1$ at best for some, which is not sufficient and can lead to unwanted and unexpected difficulties.
However, given the specific cases presented by Jamet to demonstrate these difficulties, given the range within which such irregularities can be omitted without a dramatic loss of precision (still according to Jamet) and furthermore given the very convincing application of Jamet's first method in Fouillet (2003) despite it suffering the same problem, we opted to pursue with the current formulation of the TIM.
This choice was further motivated by the apparently elevated numerical price to be paid (along with the implementation difficulties) to access a higher order of regularity, which, for us, ground this approach to very academical cases as those performed in Jamet et al. (2001).

As explained in Jamet (1998); Fouillet (2003), in some cases, modifying the behavior of the thermodynamics inside the binodal curve is not without adverse consequences. In the prospect of simulating bubble-driven phenomena, boiling flows or configurations where gravity plays an active role, it can generate conflicts with the very modifications that ensue from the philosophy of the TIM and other thickening methods. Indeed, a modified compressibility of the fluid in the binodal region leads to a modified metastability limit for the bulk phases (by a factor equal to that of the thickening), which is felt predominantly in the liquid. When heated, the latter tends to first reach an overheated metastable state before starting to evaporate and creating an interface. A reduced metastable limit results in a spontaneous creation of interfaces, a behavior not observed in reality.
This difficulty can be overcome by formally modifying the law $P^{\text{sat}}(T)$, but this, in turn, modifies the latent heat of evaporation. This second difficultly can also so be overcome, as done in Fouillet (2003), by modifying the definition of the temperature in the EoS, which leads to a new description $\tilde{P}\left(\rho, \tilde{T}\right)$ that permits to handle boiling flows with bubbles creation.
However, if gravity is included, it forces upon the system an intrinsic scale for the pressure variations, via Pascal's law, that is no longer respected by the new description $\tilde{P}\left(\rho, \tilde{T}\right)$. For instance, Rayleigh-Taylor instabilities cannot be simulated in such a framework.
These additional information serve as reminder that the application of the TIM must be met with caution and cannot be used straightforwardly in all circumstances. In our cases of interest, i.e. liquid rocket engines, gravity and bubble production are negligible phenomena and the use of the TIM is expected to be pertinent

Regarding the extension of the TIM to multi-species cases, the method can be applied straightforwardly if the full-equilibrium hypothesis is made since, in such a case, the fluid is still described using single pressure, energy, entropy, etc... functions. It would also be necessary for the capillary coefficient λ to be unique, a hypothesis already put forth when discussing the extension of the SG model to multi-species cases in Sec. 5.3.3. This implementation would thus require the use of a thermodynamic equilibrium solver, a non trivial task, discussed for instance in Pelletier (2019).
One should however notice that such a direct implementation is only possible because the TIM exclusively allows to widen or straighten the interface and not to choose its actual width. Doing so would require to know beforehand the initial interface width for all the possible simulation conditions, a task already tedious for a single fluid but virtually impossible for cases with numerous species.

Evidently, a gray area still surround the impact of the thickening process on the diffusive fluxes (for all three methods as it so happens). To us, inferring that the thermal conductivity k_{th} and the dynamic viscosity μ coefficients are not modified by the new modeling seems a hasty conclusion if drawn without additional investigation.

Regarding the thermal conductivity, the different tests we carried out seem to lean toward an application of the multiplicative factor F. Indeed, the thickening of the density profile leads to a smaller temperature gradient throughout the interface which, in order to maintain a specific heat flux across the interface, must be balanced by augmenting the thermal conductivity. The choice to maintain the heat flux is justified by the fact that the latent heat of vaporisation

$\mathcal{L} = {h_{s,v}}^{\text{sat}} - {h_{s,l}}^{\text{sat}}$ is conserved by the TIM and therefore to ensure the same mass rate of vaporization, the heat flux should not be modified as well. In practice, conductive cases involving the TIM have to be simulated by applying the same thickening coefficient F to the thermal conduction coefficient, i.e. by substituting k_{th} by ${k_{\text{th}}}^{\text{TIM}} = \text{F}k_{\text{th}}$ in the expression of the Fourier's law used to express the thermal flux $\boldsymbol{q}$ in the energy equation.
Concerning the viscosity, its usage has been essentially dismissed in this work as its initial interaction with the SG model is already an unanswered questions beyond the scope of our study. Besides, we faced difficulties when trying to design cases balancing the contributions of both the surface tension and the viscosity while applying a thickening so as to gather relevant information. It is our personal belief that these questions are of the utmost importance in the path of developing and strengthening the TIM for future and ever more complex applications.

Chapter 10

Numerical validation of the Thickened Interface Method

This chapter is dedicated to the numerical validation of the Thickened Interface Method (TIM). To that effect, the study performed in Chap. 8 on the native Second Gradient model has been reinvested and articulated around similar cases, in a more concise fashion. This approach allows to draw direct comparisons between the non-thickened and the thickened configurations while simultaneously assessing the correct behavior of the TIM-thickened SG model and its proper implementation in the AVBP solver.
As such, in the first section 10.1, the one dimensional cases of Sec. 8.1 are revisited and serve as a preliminary validation of both the implementation and the behavior of the TIM. Unsteady isothermal and non-isothermal cases are simulated to test the ability to transport interfaces in and out of equilibrium. These simulations reveal the necessity to introduce artificial viscosity, in particular when higher values of thickening coefficients are used.
In a second time, in Sec. 10.2, the TIM is tested on canonical two-dimensional cases. The emphasis is put on the oscillating planar interfaces from Sec. 8.2.1 for which the two-dimensional theoretical results are well established and for which comparisons between the simulations and the theory have led to very good results for non-thickened cases. The oscillating deformed droplets from Sec. 8.2.2 have also been simulated for practical validation. However, due to the lack of theoretical results in two-dimensions for this configuration, apart from the oscillating period, the conclusions drawn from these simulations are more marginal but nonetheless positive. Besides, more sophisticated cases involving three-dimensional droplets are presented in Chap. 11.

10.1 Validation of the method in 1D configurations

10.1.1 Isothermal 1D simulations with the TIM

10.1.1.1 Configuration

To validate the TIM in one-dimensional configurations, the single nitrogen interfaces of Sec. 8.1.2 are replicated using various thickening coefficients from 10 to 10000. The general parameters used for these simulations are recalled in Tab. 10.1, w_0 being the native width

of the interface when no thickening is applied. The choice is maintained to perform these simulations with an important number of points in the interface in order to minimize the possible interference from the numerical scheme and focus on the thermodynamic behavior of the TIM-thickened model. For the sake of conciseness, only relevant results are presented and if not mentioned otherwise, it is to be understood that these results have been duplicated successfully with different values of thickening coefficient.

T	113.57 K	λ	$1.0 \cdot 10^{-10}$ m$^7 \cdot$ kg$^{-1} \cdot$ s^{-2}	σ	3.26 N $\cdot$ m
P^{sat}	18.15 bar	points in int.	≈ 30	w_0	4.42 μm
ρ_l	542.1 kg $\cdot$ m^{-3}	equations	mass + mom.	scheme	GRK
ρ_v	80.3 kg $\cdot$ m^{-3}	time step	automatic (CFL+SG)	CFL	0.95

Table 10.1: *Simulation parameters used for the one dimensional N_2 planar interface in isothermal configurations solving Euler SG equations modified by the TIM. w_0 is the interface thickness prior to the application of the thickening method.*

The results in Figs. 10.1 (F=10) and 10.2 (F=1000) show that isothermal interfaces are still properly convected when the TIM is applied.

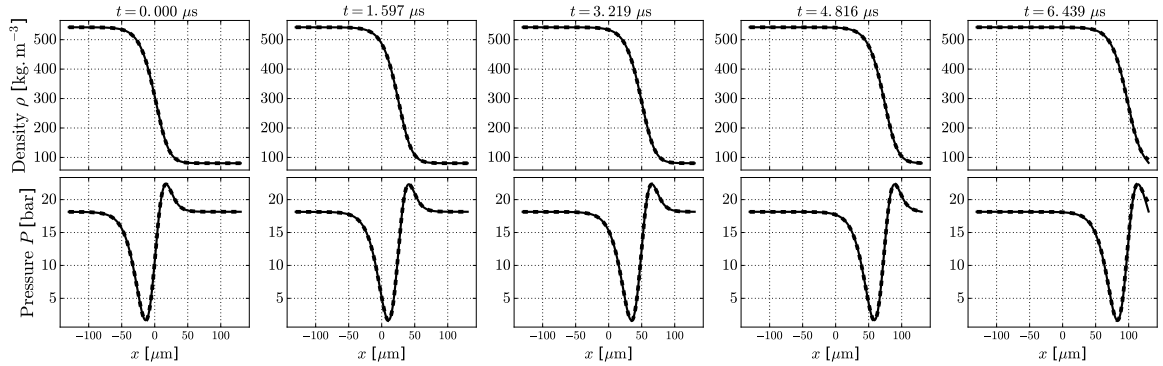

Figure 10.1: *Density and pressure profiles of an isothermal N_2 interface convected at constant speed $u = 15\text{m}\cdot\text{s}^{-1}$. The plain lines show the calculation results and the dashed lines show the theoretical/ideal position of the interface. The interface has been thickened by a factor* F = 10 *using the TIM.*

Figs. 10.3 and 10.4 show the response of the interface to a mechanically forced stretching for different TIM factors. In each case, the interface is able to return to its equilibrium shape. The behavior is similar to that of the non TIM-thickened case in Fig. 8.3: important acoustic waves are created by the reshaping of the interface and are appropriately evacuated at the boundaries.

Similar conclusive results are obtained with a mechanically compressed interface, as show in Fig. 10.5.
Eventually, both convection and mechanical deformation are combined in Figs. 10.6 and 10.7 where the interface is initially artificially stretched. The simulations go as expected, the interface properly returns to its equilibrium profile while being convected. However, instead of more classic acoustic waves perceptible in Figs. 10.3 and 10.4, a different type of perturbations,

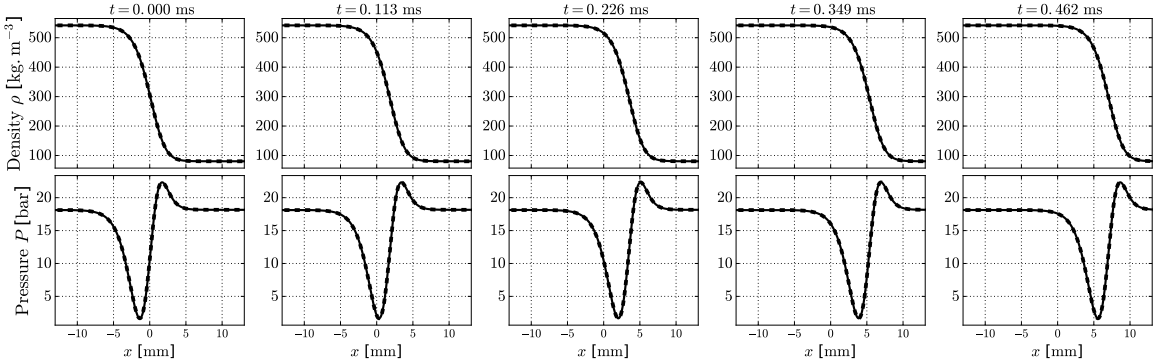

Figure 10.2: *Density and pressure profiles of an isothermal N_2 interface convected at constant speed $u = 15\text{m}\cdot\text{s}^{-1}$. The plain lines show the calculation results and the dashed lines show the theoretical/ideal position of the interface. Non-reflecting velocity-temperature inlet (left) and pressure outlet (right) used. The interface has been thickened by a factor* $\text{F} = 1000$ *using the TIM.*

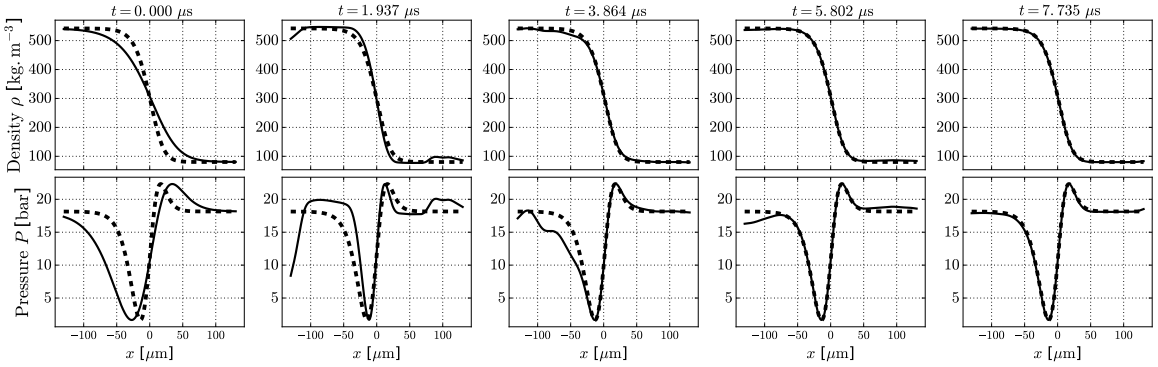

Figure 10.3: *Density and pressure profiles of a static isothermal N_2 interface initially stretched by a factor 2. The plain lines show the calculation results and the dashed lines show the theoretical/ideal position of the interface. Non-reflecting velocity-temperature inlet (left) and pressure outlet (right) used. The interface has been thickened by a factor* $\text{F} = 10$ *using the TIM.*

not present in the non-thickened cases, are generated during the return to equilibrium. One can notice that the increasing size of the domain relatively to the invariant velocity of the perturbations causes the latter to linger on in the images for a relatively longer time as the thickening factor F gets bigger. Another noticeable and positive fact is that these perturbations seem to be handled without difficulties by the boundary conditions. This velocity could not be matched with that of acoustic waves in these thermodynamic conditions. These perturbations can be noticed for $\text{F} = 100$ but are clearly visible for $\text{F} = 1000$. They also have been observed in two-dimensional simulations and are believed to be caused by a slowed dynamic response of the interface when the latter is thickened using the TIM. This slowed response could authorize the persistence of unstable thermodynamic points in the domain that lay in the binodal region, for a much longer time than what would occur without thickening. The existence of these unstable points could also be fostered by the isothermal conditions that prevents the interface to adjust the temperature in order to avoid their appearance. Further analysis are however necessary to assess the validity of these hypotheses as they should be an important point of

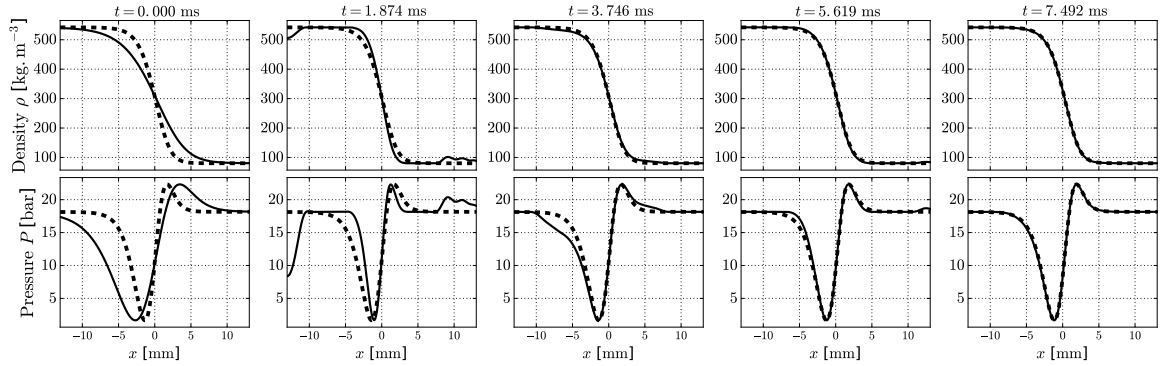

Figure 10.4: *Density and pressure profiles of a static isothermal N_2 interface initially stretched by a factor 2. The plain lines show the calculation results and the dashed lines show the theoretical/ideal position of the interface. Non-reflecting pressure outlets (left and right) used. The interface has been thickened by a factor* $\mathrm{F} = 1000$ *using the TIM.*

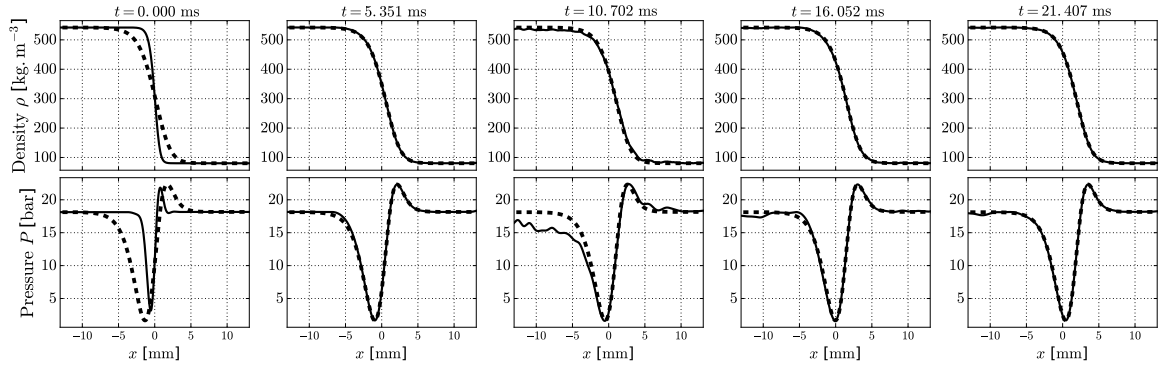

Figure 10.5: *Density and pressure profiles of a static isothermal N_2 interface initially compressed by a factor 3. The plain lines show the calculation results and the dashed lines show the theoretical/ideal position of the interface. Non-reflecting pressure outlets (left and right) used. The interface has been thickened by a factor* $\mathrm{F} = 1000$ *using the TIM.*

focus for future studies regarding the SG model and the TIM.

10.1.2 Non-isothermal 1D simulations with the TIM

When the non-isothermal equations are solved, the SG model with the application of the TIM also displays a behavior similar to the one observed without thickening. As such, it suffers the same shortcomings when the non-isothermal Euler equations are solved without any diffusion: deformed interfaces do not return to their equilibrium isothermal shape, convected interfaces present very important oscillatory numerical errors. Conversely, the conjunction of the SG model and the TIM also reacts positively to the introduction of diffusion, mostly viscosity and, to a lesser degree, thermal diffusion, of which characteristic time of action is often far greater than that of the viscous processes in our cases. The high order selective filter, already used in some cases for the non-thickened model, is used most of the time, even in one-dimensional cases, once large values of thickening are used with the TIM. For these cases, the configuration with nitrogen described in Tab. 10.1 is used with different values of thickening coefficient.

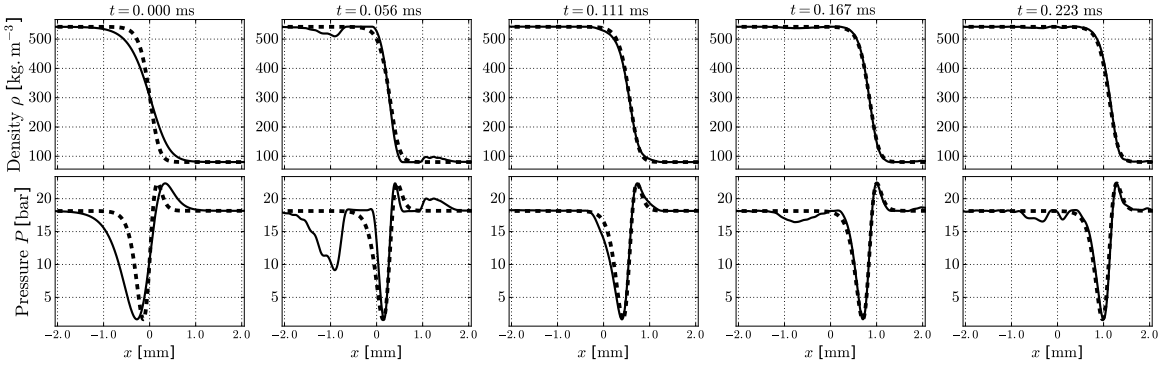

Figure 10.6: *Density and pressure profiles of an isothermal N_2 interface initially stretched by a factor 2 and convected at constant speed $u = 5\mathrm{m} \cdot \mathrm{s}^{-1}$. The plain lines show the calculation results and the dashed lines show the theoretical/ideal position of the interface. Non-reflecting velocity-temperature inlet (left) and pressure outlet (right) used. The interface has been thickened by a factor* $\mathrm{F} = 100$ *using the TIM.*

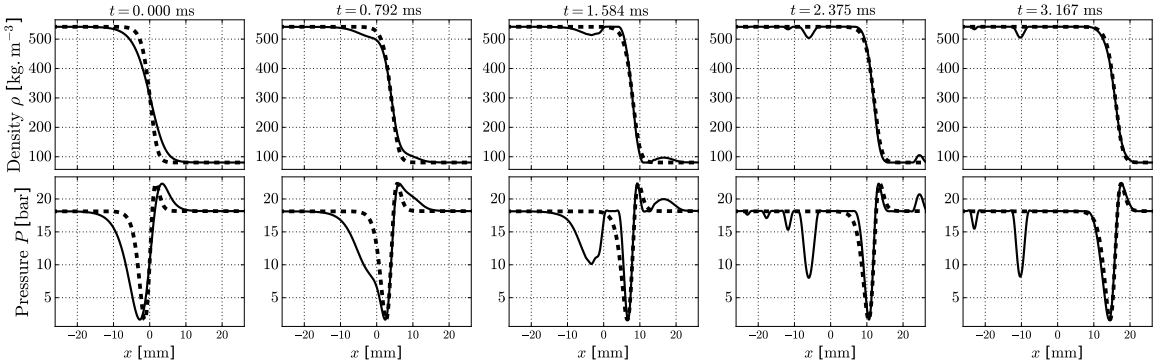

Figure 10.7: *Density and pressure profiles of an isothermal N_2 interface initially stretched by a factor 2 and convected at constant speed $u = 5\mathrm{m} \cdot \mathrm{s}^{-1}$. The plain lines show the calculation results and the dashed lines show the theoretical/ideal position of the interface. Non-reflecting velocity-temperature inlet (left) and pressure outlet (right) used. The interface has been thickened by a factor* $\mathrm{F} = 1000$ *using the TIM.*

10.1.2.1 Deformed static interfaces

The case of an initially expanded interface, computed without additional difficulties while solving non-isothermal Euler equations with application of the TIM, has led to a non constant temperature profile and a damped pressure profile at equilibrium, as already observed in Fig. 8.6 with no thickening, despite no initial velocity being imposed to the interface. It seems however that the discrepancy in the temperature profile (and consequently in the pressure profile) has a lesser magnitude in the case of the thickened interface. This could be explained by the much lower temperature gradient that exists once the TIM is applied, a hypothesis that needs further investigation to be confirmed.
However, just like in Fig. 8.7 for the non-thickened case, with the addition of thermal conduction that constrains the temperature to return to a constant profile, the thickened interface also returns to its equilibrium profile with no adverse impact of the TIM.

10.1.2.2 Convected interfaces

Likewise, as shown in Fig. 10.8 for a thickening factor F = 100, trying to convect an interface solving non-isothermal Euler equations without any source of diffusion leads to strong oscillations in the temperature even for fairly decent mesh resolutions, a phenomenon already observed in Fig. 8.10 for the non-thickened case. However, one has to mention that the amplitude of the errors in the temperature for this convected cases seems to have a much lower amplitude than that of its non-thickened counterpart in Fig. 8.8 (just as the amplitude of the temperature discrepancy for the deformed interface seems to be lower when a greater thickening coefficient is used). The same hypothesis, to be verified, of gradients damped by the TIM can be assumed to explain this observation.

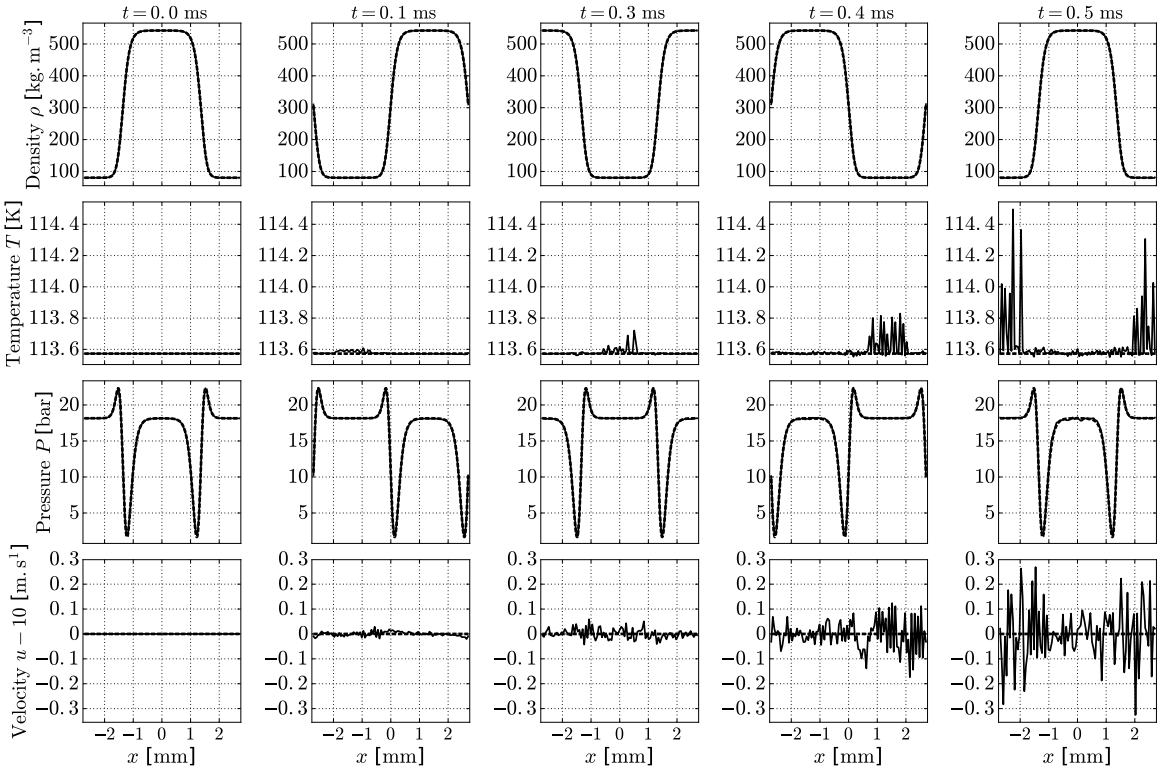

Figure 10.8: *Density, temperature, pressure and velocity profiles of a N_2 droplet convected at constant speed $u = 10\ \mathrm{m \cdot s^{-1}}$. The plain lines show the calculation results and the dashed lines show the theoretical position of the interface. Periodic boundary conditions (left and right) used. Non-isothermal SG+TIM Euler equations are solved with a eight-point interface resolution. The interface has been thickened by a factor* F = 100 *using the TIM. The high-order selective filter is used (coeff.* $1.0 \cdot 10^{-4}$*).*

Similarly to the non-thickened case, the switch from the non-isothermal Euler equations to the non-isothermal Navier-Stokes equations with diffusion provides a fair gain in the quality of the results and a substantial gain in the stability of the calculation,s as shown for F = 100 in Fig. 10.9. It must be mentioned that these calculations have required the addition of artificial viscosity to limit the oscillations around the density gradient when higher thickening coefficients have been used, typically above a few hundreds (this threshold value being probably case-dependent). An example of such calculations is given in Fig. 10.10 for F = 10000 where

the different profiles are mostly well advected, even though numerical oscillations remain visible on the velocity field for the coarser meshes.

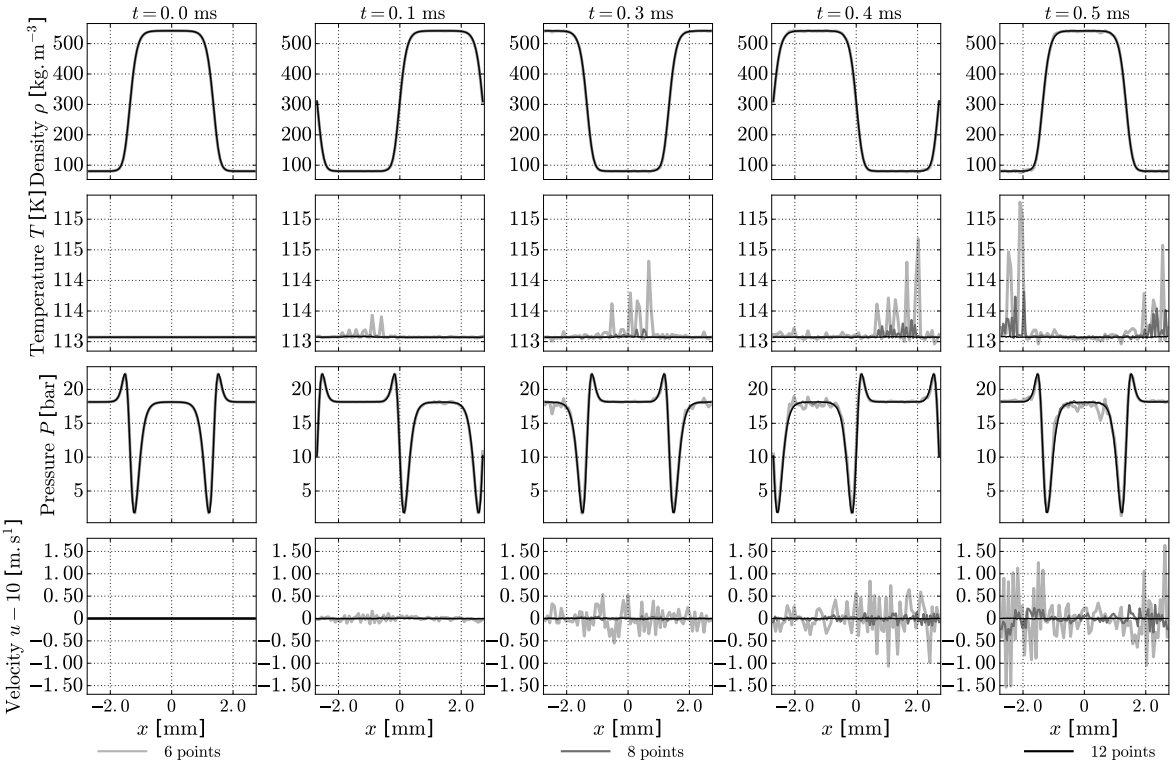

Figure 10.9: *Density, temperature, pressure and velocity profiles of a N_2 droplet convected at constant speed $u = 10\text{m} \cdot \text{s}^{-1}$. Periodic boundary conditions (left and right) used. Non isothermal SG+TIM Navier-Stokes equations are solved with Chung's diffusion model, for multiple lower mesh resolutions. The interface has been thickened by a factor* $\text{F} = 100$ *using the TIM. The high-order selective filter is used (coeff.* $1.0 \cdot 10^{-4}$*).*

10.1.3 Convergence orders

Finally, the impact of the TIM on the convergence order of the method has been evaluated. All the calculations have been performed using the methodology presented in Sec. 8.1.4 with the initially isothermal droplet that has been thickened by factors $\text{F} = 100$ and $\text{F} = 10000$ using the TIM. The results after a half-crossing of the domain are presented in Figs. 10.11 and 10.12 respectively. The results for both thickening factors are very similar and can be compared to those obtained with no thickening in Fig. 8.18.

The first observation is that the peculiar behavior of the isothermal Euler cases is non-longer present, which allows to properly define a convergence order. Moreover, both the error level and the convergence order of the isothermal Euler cases are worse than that of the non-isothermal Euler and Navier-Stokes cases. The second observation is that for some variables, the order is strongly degraded, from above 4 with no thickening to more expected values between 2 and 3, which is particularly true for the pressure and the momentum. For the density, energy and temperature, the diminishing of the convergence order is still visible but to a much lower

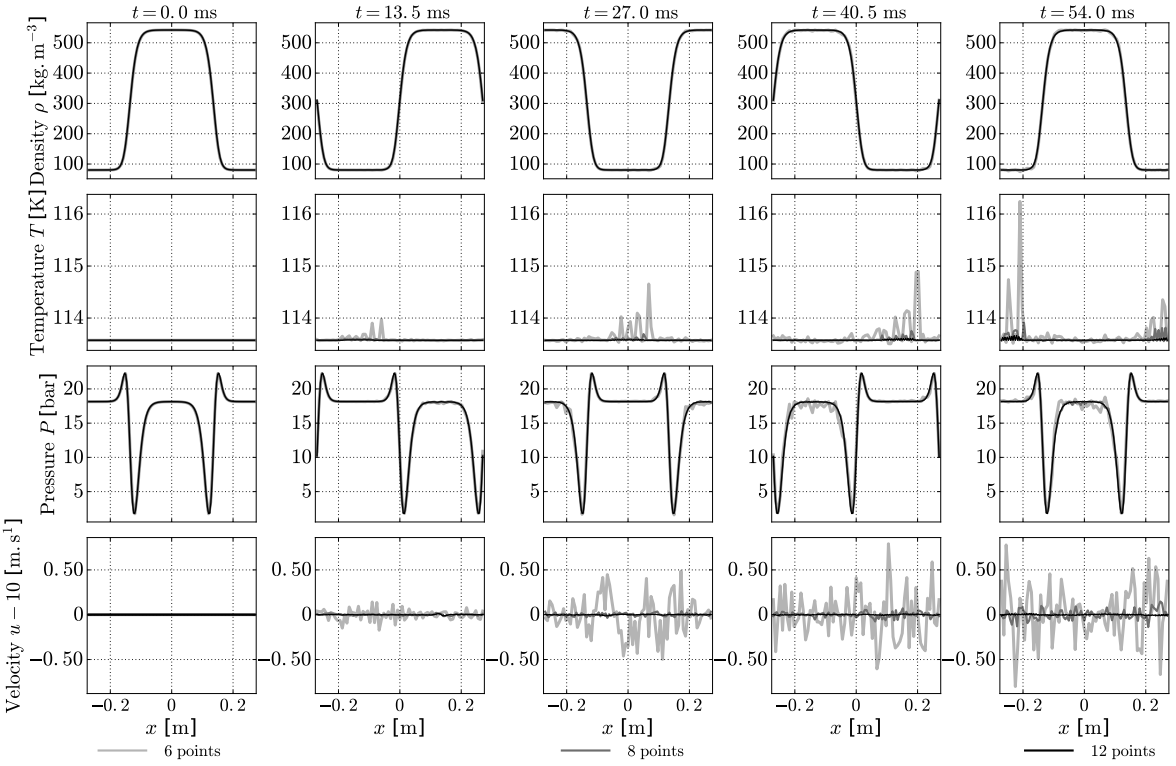

Figure 10.10: *Density, temperature, pressure and velocity profiles of a N_2 droplet convected at constant speed $u = 10\text{m}\cdot\text{s}^{-1}$. Periodic boundary conditions (left and right) used. Non isothermal SG+TIM Navier-Stokes equations are solved with Chung's diffusion model, for multiple lower mesh resolutions. The interface has been thickened by a factor $\text{F} = 10000$ using the TIM. AVBP's artificial viscosity is used. The high-order selective filter is used (coeff. $1.0 \cdot 10^{-4}$).*

extent. In particular, the final orders remain above the theoretical order of the method of at most three.

These puzzling results, either for the super-convergence still observed for some variables or for the drastic drop of the order for some others, have not been met with a satisfactory answer. Together with the ones obtained in the non-thickened cases, these results demonstrate the need to further investigate the intricacies and subtleties of the numerical behavior of the SG model and even more so once the TIM is applied.

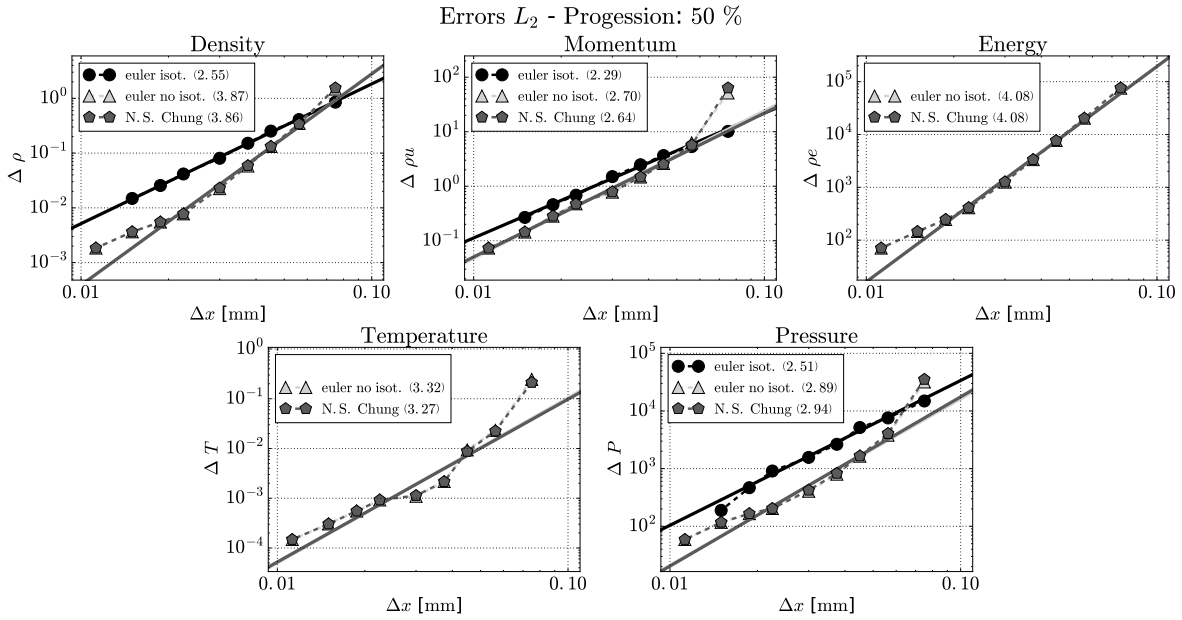

Figure 10.11: *Convergence orders of AVBP's GRK numerical scheme with the SG model implementation in 1D isothermal and non-isothermal cases using the TIM with a thickening coefficient* $\mathrm{F} = 100$. *Logarithmic scale used for both axis. Interpolation slopes in legend.*

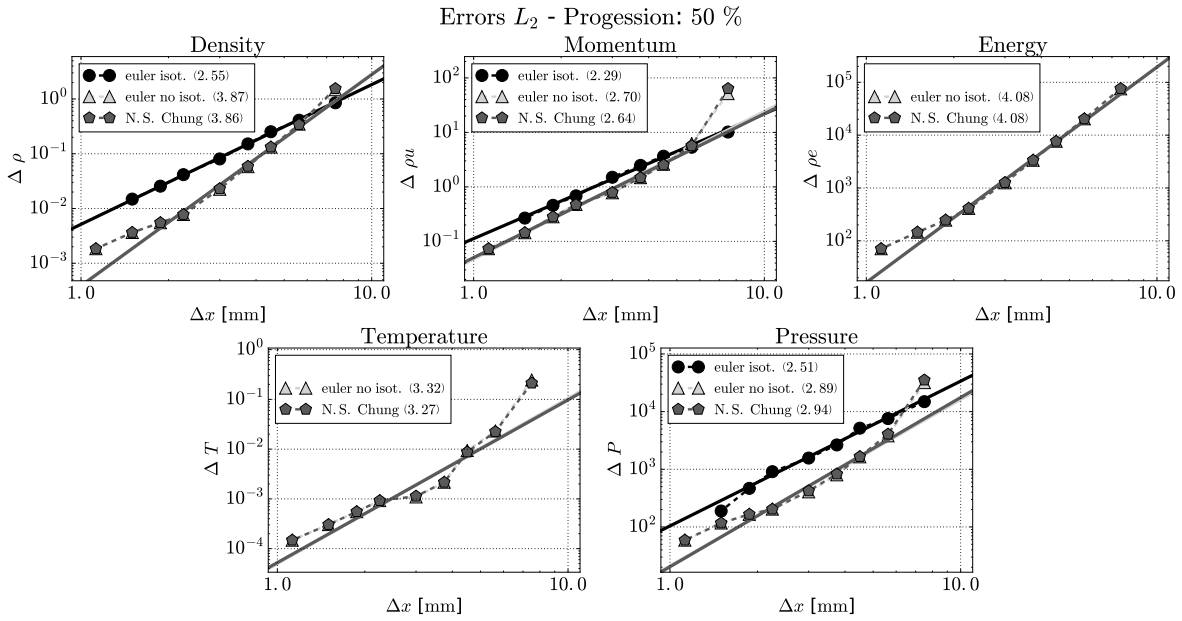

Figure 10.12: *Convergence orders of AVBP's GRK numerical scheme with the SG model implementation in 1D isothermal and non-isothermal cases using the TIM with a thickening coefficient* $\mathrm{F} = 10000$. *Artificial viscosity from AVBP used for the calculations. Logarithmic scale used for both axis. Interpolation slopes in legend.*

10.2 Validation of the method in 2D configurations

10.2.1 Planar oscillating interface

10.2.1.1 Case design

The first two-dimensional validation case for the TIM consists in the oscillating planar interface presented in Fig. 8.20 and studied in Sec. 8.2.1. The main parameters used for the simulation are compiled in Tab. 10.2. Euler equations are solved and the high order selective filter is used with a coefficient 10^{-4}, no artificial diffusion is required to stabilize this case.

T	119.88 K	λ	$1.0 \cdot 10^{-16}$ m$^7 \cdot$ kg$^{-1} \cdot$ s^{-2}
P^{sat}	25.20 bar	w_0	6.34 nm
ρ_l	458.94 kg $\cdot$ m^{-3}	σ	1.18 mN $\cdot$ m^{-1}
ρ_v	125.22 kg $\cdot$ m^{-3}	points in int.	≈ 10

Table 10.2: *Simulation parameters used for the two dimensional N_2 planar interface with the TIM*

Using Eq. (8.10), its is possible to asses whether the TIM preserves the surface tension while the interface is thickened. To perform this study, multiple approaches can be used, provided that the relative amplitude of the imposed deformation (5%) should remain unchanged.
The most intuitive approach is to use the same geometry for all cases and progressively thicken the interface while maintaining its initial wavy shape, as exposed in Fig. 10.13. However, this approach has two correlated shortcomings. Firstly, one needs to ensure that for the biggest thickening coefficients, the interface width is still very small relatively to the size of the domain and, more importantly, relatively to the radius of curvature at the strongest deformation. To do so, either reasonable values of said biggest thickening coefficients must be used or the initial thickness of the interface without thickening must be chosen very small. This leads to the second shortcoming. For the simulations, one must use a mesh for which the interface is well resolved (at least five points in the gradient region). While this can be achieved fairly simply for the widest interface, the mesh size can rapidly shrinks for the thinnest interface leading the very costly simulations. Finally, for this approach, one has to choose between very costly simulations in order to test a wide range of thickening coefficients or very limited values of thickening coefficients that can however be computed at an affordable cost.

A second strategy can be used, as exposed in Fig. 10.14 where an expansion $\delta = \text{F}$ is applied to the whole geometry while simultaneously thickening the interface by a factor F.
With this approach, all the cases are ensured to be homothetic (in particular the ratio between the interface width and the radius of curvature or the interface width and the domain size are preserved). As such, all the cases are expected to mimic the reference case. Additionally, the same expansion $\delta = \text{F}$ can be applied simultaneously to the mesh size thus ensuring that the nominal computational cost for one temporal iteration is constant throughout all cases.
Contrary to the design in Fig. 10.13, this homothetic transformation is expected to alter the oscillation period since the interface becomes longer. However, the expected period can be evaluated for all cases using Eq. (8.10) where the modified length l can be accounted for.
For the aforementioned reasons, this strategy is adopted to validate the TIM on this oscillating

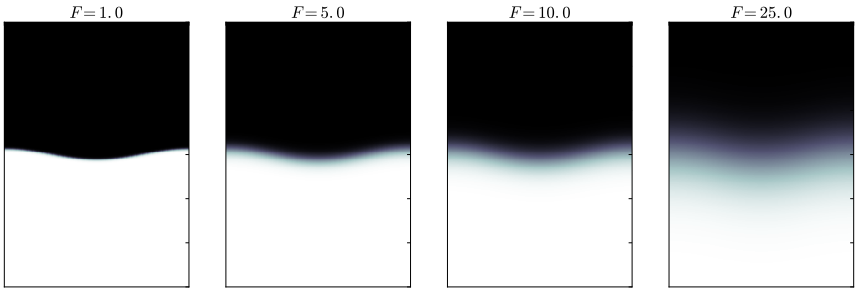

Figure 10.13: *Evolution of the initial density profiles for interfaces with different thickening factors, a fixed relative interface perturbation and a fixed geometry*

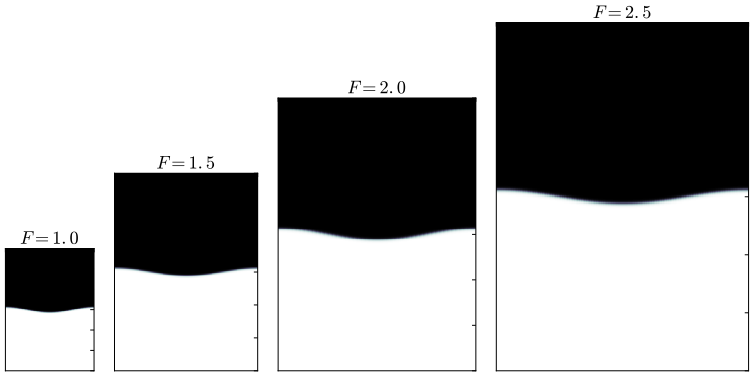

Figure 10.14: *Evolution of the initial density profiles for interfaces with different thickening factors, a fixed relative interface perturbation and a proportionally expanded geometry*

planar interface. For the sake of clarity, the relative scales of the different configurations in Fig. 10.14 are respected and thus represented for small factors only. However, for the results presented hereafter, the methodology is used for factors up to $\mathrm{F} = 10^4$.

10.2.1.2 Validation for isothermal interfaces

The simulations have been performed for different values of the thickening factor F ranging from 1 to 10^4. For each value of F, the thickening has been enforced in two different ways. The first one, referred to as inconsistent, is done by only modifying the capillary coefficient λ, i.e. using only the factor ϕ_λ from Eq. (9.40) (with $\phi_\lambda = \mathrm{F}^2$). The second one is by applying the TIM with the combined actions of ϕ_σ and ϕ_λ. In either case, the oscillations of the central density value are tracked, similarly to Fig. 8.21 and the oscillation period of the interface is extracted. The evolution of the period relatively to the thickening coefficient is presented in Fig. 10.15.

From Eq. (5.167) one knows that thickening the interface by a factor F using only the coefficient ϕ_λ should result in the same factor being applied to the surface tension. Therefore, from Eq. (8.10) it can be concluded that the period should behaves as shown by Eq. (10.1),

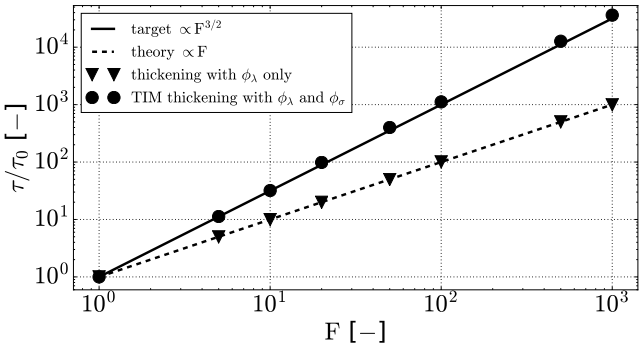

Figure 10.15: *Evolution of the interface oscillation period (normalized by $T_{F=1}$) with the thickening coefficient* F *(in log-log scale) for consistent and inconsistent thickening strategies, comparison between theoretical and numerical results using the inconsistent and TIM methods*

i.e proportionally to F. This expected result is symbolized by the dashed line in Fig. 10.15.

$$\frac{\tau^{\phi_\lambda}}{\tau_0} = \frac{(\mathrm{F}l_0)^{3/2}}{(\mathrm{F}\sigma_0)^{1/2}} \frac{{\sigma_0}^{1/2}}{{l_0}^{3/2}} = \mathrm{F} \tag{10.1}$$

The same *a priori* estimation of the period evolution can be done with Eq. (8.10) for the TIM, supposed to thicken the interface by a factor F without modifying its surface tension. The expected trend is given by Eq. (10.2) with a period increasing proportionally to $\mathrm{F}^{3/2}$. (Practically, this last result entails that actual simulation time for the cases using this thickening strategy increases by a factor $\mathrm{F}^{1/2}$.) This expected behavior is symbolized with a solid line in Fig. 10.15.

$$\frac{\tau^{\mathrm{TIM}}}{\tau_0} = \frac{(\mathrm{F}l_0)^{3/2}}{{\sigma_0}^{1/2}} \frac{{\sigma_0}^{1/2}}{{l_0}^{3/2}} = \mathrm{F}^{3/2} \tag{10.2}$$

The two theoretical behaviors obtained with Eqs. (10.1) and (10.2) are accurately retrieved in the simulations. The results for the "inconsistent" thickening method using only ϕ_λ further demonstrate the predictive capabilities of the native Second Gradient model and its proper implementation in the code AVBP. Likewise, the results obtained with the TIM offer an additional validation for its mechanical consistency, in a two-dimensional setting. The error between the theoretical and numerical periods, already below 5% in the non-thickened case, remains in that range for all the thickening coefficients that have been considered.

10.2.1.3 Validation for non-isothermal interfaces

The previous results cement the ability of the TIM to treat isothermal cases but at its core, the method has been derived to work in non-isothermal settings and should be tested accordingly. To that effect, the previous cases have also been simulated solving the non-isothermal Euler equations (only the TIM thickening strategy is considered). The central density oscillation curves are given Fig. 10.16 for thickening coefficients from $\mathrm{F} = 1$ to $\mathrm{F} = 1000$. The time scale has been normalized by a factor $\mathrm{F}^{3/2}$.

It has already been observed for the non-thickened cases in Sec. 8.2.1, with Figs. 8.25, 8.26 and 8.27, that the switch from the isothermal to the non-isothermal setting causes the oscillations

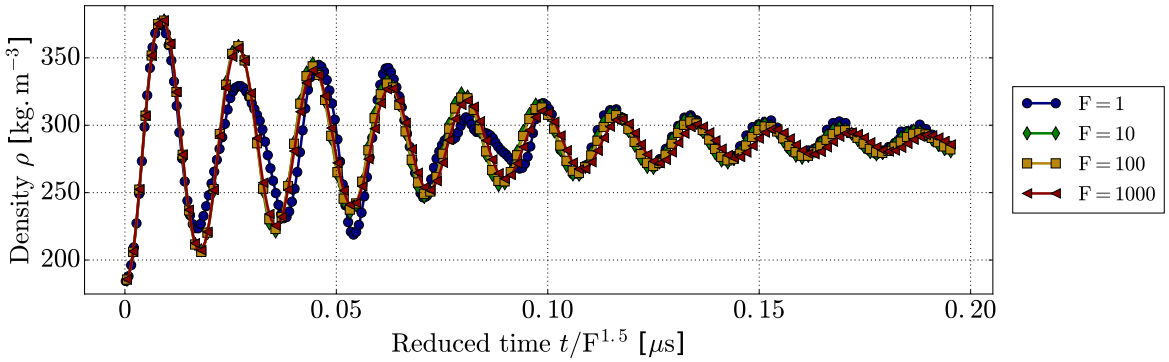

Figure 10.16: *Comparison of the central density time evolution of a two-dimensional, initially isothermal, planar oscillating nitrogen interface for different thickening factors. Non-isothermal Euler equations are solved applying the TIM. A selective numerical filter (coeff* $1.0 \cdot 10^{-2}$*) is used but no artificial viscosity.*

to become damped in this configuration. This unexplained phenomenon also occurs for the TIM-thickened cases.
However, an important result is that this damping is consistent as in the normalized time scale $t/\mathrm{F}^{3/2}$, all the curves properly superimpose except for the case F = 1 which is perturbed by acoustic noise in the early instants of the simulation.
Fig. 10.16 also shows that the correlation in Eq. (10.2) is also respected in a non-isothermal setting, despite being derived with the assumption of an isothermal interface and despite the damping of the oscillations.

To validate the model and the method further still, simulations with non-isothermal initial solutions have been carried out. The case design is still the one presented in Fig. 8.2.1 and shown in Fig. 8.20 while the parameters are compiled in Tab. 10.3.

T_i	110 K	λ	$1.0 \cdot 10^{-12}$ m$^7 \cdot$ kg$^{-1} \cdot$ s^{-2}
P^{sat}	14.84 bar	w_0	0.39 μm
ρ_l	580.1 kg $\cdot$ m^{-3}	σ	0.469 mN $\cdot$ m^{-1}
ρ_v	63.3 kg $\cdot$ m^{-3}	l	8.0 μm

Table 10.3: *Simulation parameters used for the two dimensional* N_2 *planar interface using the TIM with a non-isothermal initial solution*

The expansion strategy proposed in Fig. 10.14 and the TIM are still applied. The only modifications are applied to the reference one-dimensional profiles used to create the initial planar interface solution, which so far was isothermal even outside the interfacial region. For these last cases, the temperature outside the interface is modified linearly, the vapor is superheated and the liquid is supercooled, which creates formal bulk phases far from the binodal region, as shown in Fig. 10.17. While the temperature is modified, the pressure outside the interface remains constant, equal to the saturation pressure associated to the interface temperature, to prevent acoustics driven movements. As a result, the density in the

liquid and the vapor phases is also no longer constant.

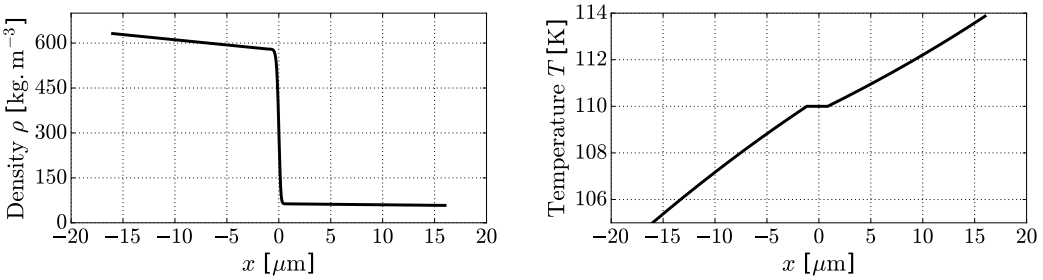

Figure 10.17: *1D density (left) and temperature (right) profiles for an isobaric nitrogen N_2 interface at a reference temperature of 110 K*

The central density oscillation curves for this configuration are given in Fig. 10.18. The same behavior of a damped oscillatory motion is observed and remains unexplained.

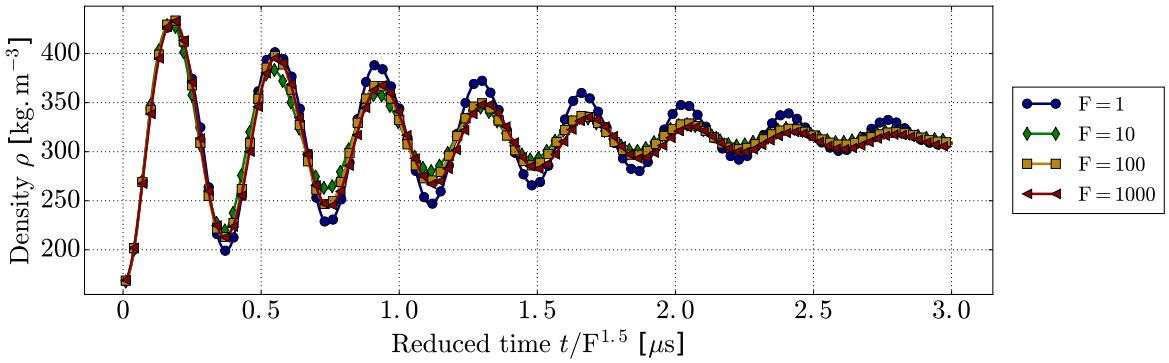

Figure 10.18: *Comparison of the central density time evolution of a two-dimensional, initially non-isothermal, planar oscillating nitrogen interface for different thickening factors. Non-isothermal Euler equations are solved applying the TIM. A selective numerical filter (coeff $1.0 \cdot 10^{-2}$) is used but no artificial viscosity.*

A slight acoustic noise can be noticed for the case F = 1 and the curves do not superimpose perfectly compared to configurations with an isothermal initial solution. This difference is suspected to be caused by the differences in density and temperature gradients on either side of the interface which are strongly different from one thickening coefficient to the other since the initial solutions are homothetic. The density and the temperature, outside the interface, vary between the same extremal values but over strongly different distances. This means in particular that as the thickening coefficient increases, the initial solution becomes relatively more isothermal seen from the interface, explaining the proximity of the central density curves for F = 100 and F = 1000 in Fig. 10.18.
Nonetheless, the period of oscillation is found to follow the theoretical trend $\tau \propto \mathrm{F}^{1.5}$. Additionally, for this configuration, using Eq. (8.10) and the values in Tab. 10.3, the expected oscillation period without thickening is 0.35 μs and the period extracted from the simulation is 0.37 μs which represents once again a very satisfactory agreement with only a 6% error.

The previous results are compiled in Fig. 10.19 where the nondimensionalized periods have been extracted for different thickening factors for the three studied configurations, using either an isothermal or an non-isothermal initial solution and solving either the isothermal or the non-isothermal Euler equations.
For all the configurations, the theoretical trend $\tau \propto \mathrm{F}^{1.5}$ is retrieved, further validating the correct behavior of the TIM even for non-isothermal simulations.

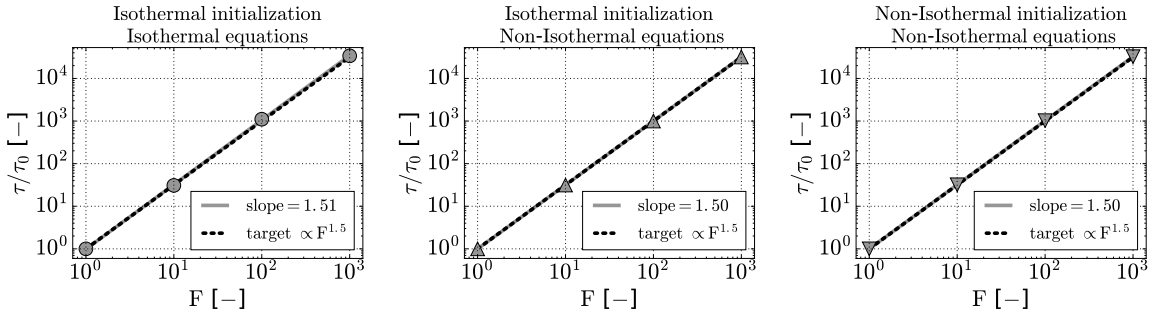

Figure 10.19: *Evolution of the normalized interface oscillation period, with the thickening coefficient* F *(in log-log scale) for different types of initialization and equations solving*

10.2.1.4 Impact of the viscosity

To anticipate the final numerical configurations that are used to perform the applicative cases of the TIM in Chap. 11, several series of simulations have been performed trading the Euler equations for the Navier-Stokes equations to also validate the interaction between the TIM and the diffusion, more particularly the viscosity, which has been shown in Fig. 8.29 to have the greater impact on the interface behavior when compared to the thermal conduction.
It has been explained in Sec. 8.2.1.3 that to perform a quantitative comparison with the literature, the case of the oscillating interface with damping needed to be cautiously designed to satisfy a specific set of conditions: an isothermal setting, an important liquid-to-vapor density ratio and a constant value of kinematic viscosity $\nu = \mu/\rho$ rather than dynamic viscosity μ. To that effect, the configuration that has led to satisfactory results in Sec. 8.2.1.3, with an oxygen interface, is reinvested with the parameters recalled in Tab. 10.4 where w_0 and l_0 are the interface and domain width when no thickening is applied.

T	110 K	λ	$1.173 \cdot 10^{-17}$ m$^7 \cdot$ kg$^{-1} \cdot$ s^{-2}
P^{sat}	5.45 bar	w_0	0.97 nm
ρ_l	1017.7 kg $\cdot$ m^{-3}	σ	8.37 mN $\cdot$ m^{-1}
ρ_v	21.4 kg $\cdot$ m^{-3}	$L_{x,0} = L_{y,0}/3 = l_0$	26 nm
points in int.	≈ 8	N_x	218

Table 10.4: *Simulation parameters used for the additional tests of an oscillating two dimensional oxygen planar interface thickened with the TIM*

With this configuration, two series of simulations have been performed using two values of thickening coefficient F = 100 and F = 10000, applying the TIM to thicken the interface while simultaneously increasing the dimensions of the domain following the principle exposed in Fig. 10.14. The isothermal Navier-Stokes equations are solved with a constant kinematic viscosity. The selective numerical filter is used with a coefficient $1.0 \cdot 10^{-2}$ but no artificial viscosity has been needed for these cases, even for the thickening factor F = 10000. For both thickening factors, three values of kinematic viscosity, compiled in Tab. 10.5, have been chosen to obtain the same Laplace numbers La than the ones used for the non-thickened simulations.

La	$2.0 \cdot 10^5$	$2.0 \cdot 10^4$	$2.0 \cdot 10^3$
$\nu_{\mathrm{F}=1}$ $\left[\mathrm{m}^2 \cdot \mathrm{s}^{-1}\right]$	$1.0 \cdot 10^{-9}$	$3.3 \cdot 10^{-9}$	$1.0 \cdot 10^{-8}$
$\nu_{\mathrm{F}=100}$ $\left[\mathrm{m}^2 \cdot \mathrm{s}^{-1}\right]$	$1.0 \cdot 10^{-8}$	$3.3 \cdot 10^{-8}$	$1.0 \cdot 10^{-7}$
$\nu_{\mathrm{F}=10000}$ $\left[\mathrm{m}^2 \cdot \mathrm{s}^{-1}\right]$	$1.0 \cdot 10^{-7}$	$3.3 \cdot 10^{-7}$	$1.0 \cdot 10^{-6}$

Table 10.5: *Laplace numbers and corresponding values of kinematic viscosity to perform simulation-theory comparisons for an oscillating isothermal oxygen interface at 110 K using different thickening factors in the TIM*

The time evolution of the central density for the thickening factors F = 1, F = 100 and F = 10000 is shown in Fig. 10.20 for all three Laplace numbers. The curves for the three thickening factors are combined on the same graph using the reduced time $t/\mathrm{F}^{1.5}$ to adjust the abscissa. As such, a first encouraging observation is that for the three factors, the curves are virtually indistinguishable from one another, regardless of the Laplace number, which is particularly auspicious given the good comparative results that have been obtained without thickening.
This suspicion is confirmed once the values of the oscillation period τ and characteristic damping time δ are extracted by following the interface during its movement, i.e. the time evolution of the position for the central point of the interface. We recall that as a simplified approximation, these two variables can be obtained with the expressions in Eq. (10.4) (knowing that $\tau = 2\pi/\omega$) and Eq. (10.5) respectively where $k = 2\pi/l$ is the spatial period of the oscillations and ω_0 is the fundamental pulsation without viscosity.

$$\omega_0^2 = \frac{\sigma k^3}{\rho_l + \rho_v} \tag{10.3}$$

$$\omega_\nu^2 = \omega_0^2 - 4\nu^2 k^4 \tag{10.4}$$

$$\delta_\nu = \frac{1}{2\nu k^2} \tag{10.5}$$

The simulation and theoretical values for the period τ and characteristic damping time δ are compiled and compared in Tab. 10.6 for thickening factor F = 100 and in Tab. 10.7 for thickening factor F = 10000. The comparisons are very satisfactory overall, in particular for the oscillation periods, which lend a maximal error lower than 5% for all thickening factors (F = 1 included). For the characteristic damping time, the errors place around 20% in average which still constitutes a very satisfactory result. Moreover, as done in the non-thickened case, the correlation from Prosperetti (1981) allows to extract the exact theoretical time evolution of the interface displacement without resorting to the approximations in Eqs. (10.4) and (10.5). These theoretical curves have been calculated and compared with the simulations in Figs. 10.21 and 10.22 for thickening factors F = 100 and F = 10000 respectively.

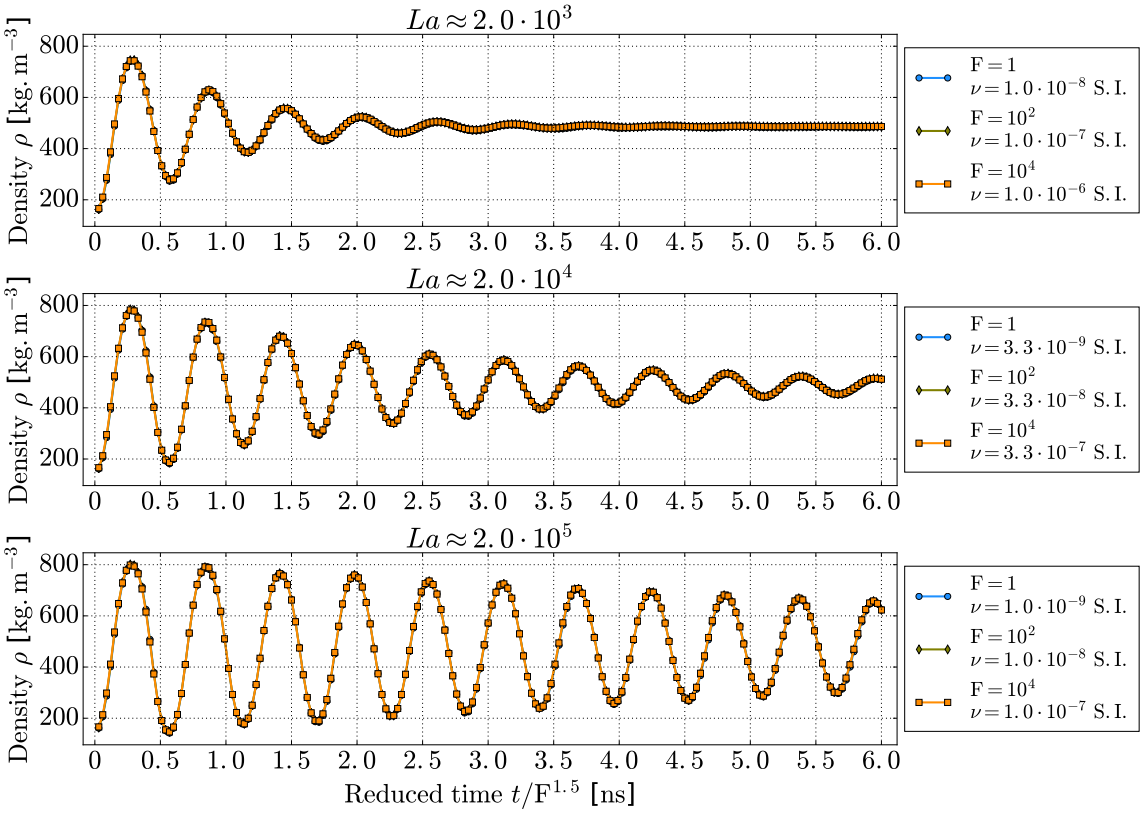

Figure 10.20: *Comparison of the central density time evolution of a two-dimensional planar oscillating oxygen interface for different values of kinematic viscosity. Isothermal Navier-Stokes equations are solved with constant kinematic viscosity and no thermal conduction. Different thickening factors* F = 1, F = 100 *and* F = 10000 *are applied following the TIM. A selective numerical filter (coeff* $1.0 \cdot 10^{-2}$*) is used.*

The results for both thickening factors perfectly follows the tendency initiated by the non-thickened case in Fig. 8.32 with a very strong agreement between the theory and the simulation for all three Laplace numbers. This represents a strong argument in favor of the pertinence and consistency of the TIM.

ν $[\mathrm{m}^2 \cdot \mathrm{s}^{-1}]$	$1.0 \cdot 10^{-8}$	$3.3 \cdot 10^{-8}$	$1.0 \cdot 10^{-7}$
$\tau_{\nu,\mathrm{th}}$ $[\mu\mathrm{s}]$	0.589	0.591	0.599
$\tau_{\nu,\mathrm{sim}}$ $[\mu\mathrm{s}]$	0.566	0.568	0.585
error_τ [%]	4.1	4.0	2.5
$\delta_{\nu,\mathrm{th}}$ $[\mu\mathrm{s}]$	9.04	2.87	1.03
$\delta_{\nu,\mathrm{sim}}$ $[\mu\mathrm{s}]$	7.62	2.30	0.868
error_δ [%]	18.6	25.1	18.9

Table 10.6: *Oscillation periods and characteristic damping times, from theory and simulations, for an oscillating isothermal oxygen interface at 110 K (eight points in the interface) for different values of kinematic viscosity. Results obtained with a thickening factor* $\mathrm{F} = 100$ *applied following the TIM.*

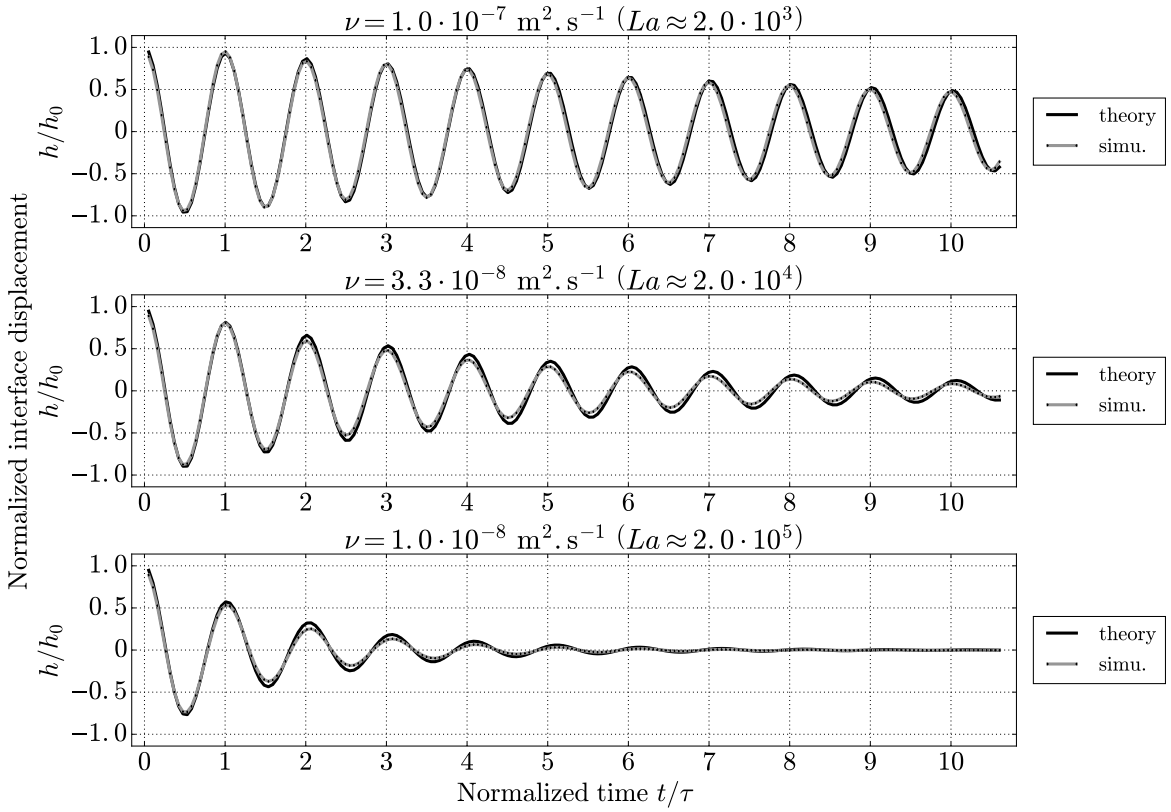

Figure 10.21: *Comparison between the theory and simulation results for the normalized displacement of a two-dimensional isothermal planar oscillating oxygen interface at 110 K for different values of kinematic viscosity. Isothermal Navier-Stokes equations are solved with no thermal conduction. A thickening factor* $\mathrm{F} = 100$ *is applied following the TIM. A selective numerical filter (coeff* $1.0 \cdot 10^{-2}$*) is used.*

ν $[\mathrm{m}^2 \cdot \mathrm{s}^{-1}]$	$1.0 \cdot 10^{-7}$	$3.3 \cdot 10^{-7}$	$1.0 \cdot 10^{-6}$
$\tau_{\nu,\mathrm{th}}$ [s]	0.589	0.591	0.599
$\tau_{\nu,\mathrm{sim}}$ [s]	0.567	0.568	0.585
error_τ [%]	4.1	4.0	2.4
$\delta_{\nu,\mathrm{th}}$ [s]	9.04	2.87	1.03
$\delta_{\nu,\mathrm{sim}}$ [s]	7.73	2.31	0.874
error_δ [%]	16.9	24.3	17.9

Table 10.7: *Oscillation periods and characteristic damping times, from theory and simulations, for an oscillating isothermal oxygen interface at 110 K (eight points in the interface) for different values of kinematic viscosity. Results obtained with a thickening factor* $\mathrm{F} = 10000$ *applied following the TIM*

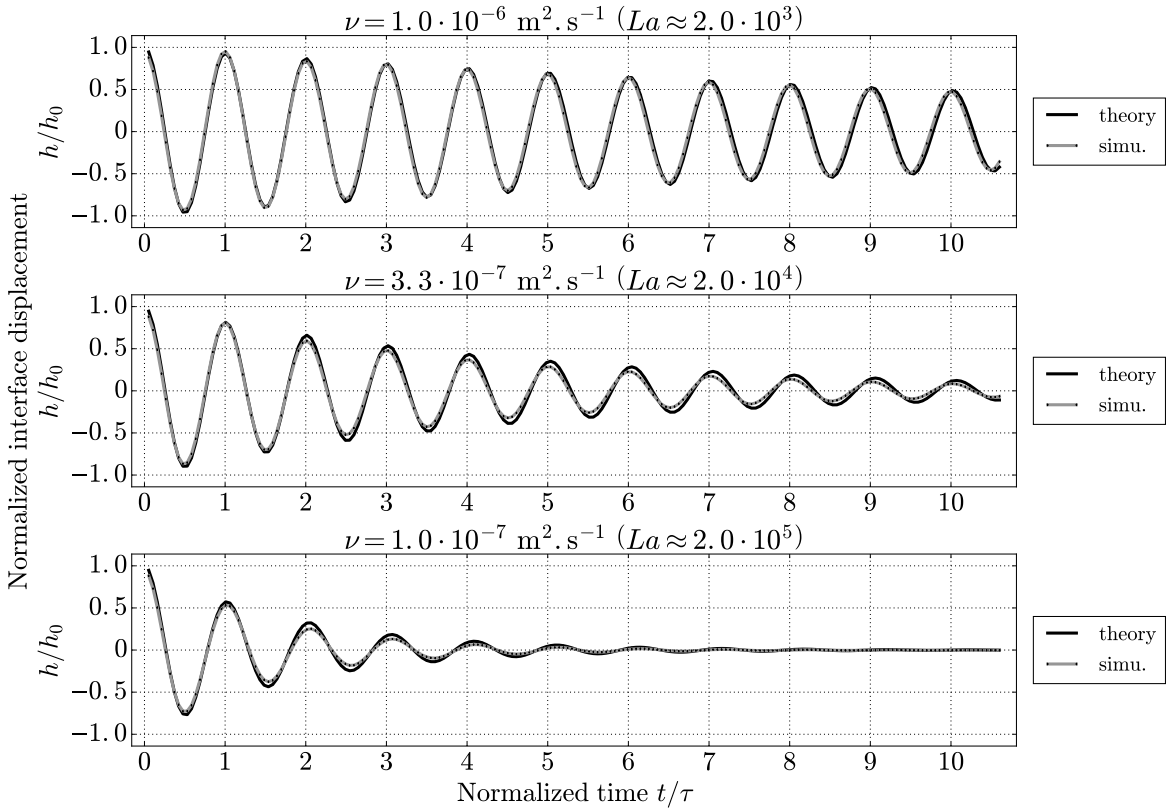

Figure 10.22: *Comparison between the theory and simulation results for the normalized displacement of a two-dimensional isothermal planar oscillating oxygen interface at 110 K for different values of kinematic viscosity. Isothermal Navier-Stokes equations are solved with no thermal conduction. A thickening factor* $\mathrm{F} = 10000$ *is applied following the TIM. A selective numerical filter (coeff* $1.0 \cdot 10^{-2}$*) is used.*

10.2.2 Oscillating droplets

A final validation of the TIM in two dimensions, more qualitative, has been carried out using the scenario of an oscillating deformed droplet, already simulated with no thickening in Sec. 8.2.2, and of which configuration is recalled in Fig. 10.23. Given the limited opportunities to perform comparisons with the theory, a fact already mentioned in Sec. 8.2.2, the purpose of this case is essentially to validate the ability of the TIM to handle a different type of configuration.

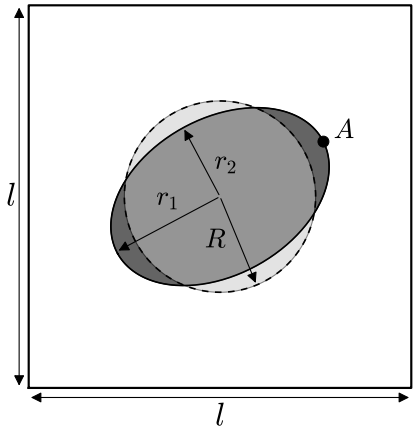

Figure 10.23: *Schematic representation of the computational setting for the oscillating droplet. Not to scale*

The simulations have been performed for two thickening coefficients F = 100 and F = 10000, the relevant parameters are compiled in Tab. 10.8 where w_0, l_0 and R_0 are the interface width, domain length and droplet radius respectively when no thickening is applied. When a thickening factor has been applied to the interface, the domain length and droplet diameter have been increased by the same factor.

T_{init}	110.0 K	λ	$1.173 \cdot 10^{-17}$ m$^7 \cdot$ kg$^{-1} \cdot$ s^{-2}
P^{sat}	5.45 bar	σ	8.37 mN $\cdot$ m^{-1}
ρ_l	1017.7 kg $\cdot$ m^{-3}	w_0	0.97 nm
ρ_v	21.4 kg $\cdot$ m^{-3}	R_0	10 nm
N	748	l_0	90 nm

Table 10.8: *Simulation parameters used for the two dimensional isothermal oscillating oxygen droplets using the TIM*

The isothermal Navier-Stokes equations are solved with a constant value of kinematic viscosity. The high order selective filter is also used with a coefficient 10^{-2}. Several values of kinetic viscosity have been considered, they have been adjusted to each thickening factor in order to obtain the same Laplace numbers La as the ones used in the non-thickened case of Fig.

8.41, the corresponding values are given in Tab. 10.9. For both thickening coefficients, the simulations have been carried out to completion but have suffered from important acoustic perturbations, regularly generated during the simulation regardless of the viscosity level, of which origin is still under investigation.

La	82440	25500	7570	2450	825	255	76
$\nu_{\mathrm{F}=1}\ \left[\mathrm{m}^2\cdot\mathrm{s}^{-1}\right]$	$1.0\cdot10^{-9}$	$1.8\cdot10^{-9}$	$3.3\cdot10^{-9}$	$5.8\cdot10^{-9}$	$1.0\cdot10^{-8}$	$1.8\cdot10^{-8}$	$3.3\cdot10^{-8}$
$\nu_{\mathrm{F}=100}\ \left[\mathrm{m}^2\cdot\mathrm{s}^{-1}\right]$	$1.0\cdot10^{-8}$	$1.8\cdot10^{-8}$	$3.3\cdot10^{-8}$	$5.8\cdot10^{-8}$	$1.0\cdot10^{-7}$	$1.8\cdot10^{-7}$	$3.3\cdot10^{-7}$
$\nu_{\mathrm{F}=10000}\ \left[\mathrm{m}^2\cdot\mathrm{s}^{-1}\right]$	$1.0\cdot10^{-7}$	$1.8\cdot10^{-7}$	$3.3\cdot10^{-7}$	$5.8\cdot10^{-7}$	$1.0\cdot10^{-6}$	$1.8\cdot10^{-6}$	$3.3\cdot10^{-6}$

Table 10.9: *Values of Laplace number and kinematic viscosity used for the two dimensional isothermal oscillating oxygen droplets using the TIM with thickening coefficients* $\mathrm{F}=100$ *and* $\mathrm{F}=10000$

In Figs. 10.24 and 10.25 are presented snapshots of the density and velocity fields respectively for the case with thickening factor $\mathrm{F}=10000$ and kinematic viscosity $\nu=1.0\cdot10^{-6}\ \mathrm{m}^2\cdot\mathrm{s}^{-1}$. Theses images show that the dynamics of the viscous droplet is satisfactorily described by the thickened model.

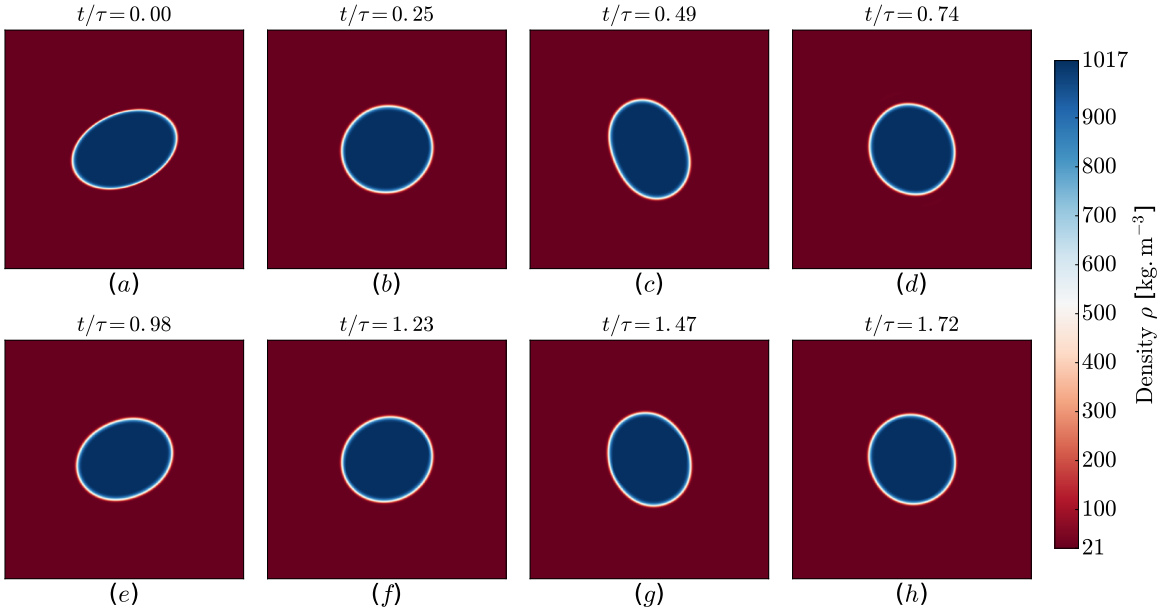

Figure 10.24: *Snapshots of the temporal evolution of the density field for a viscous and initially deformed* O_2 *droplet. Isothermal Navier-Stokes equations are solved with a constant kinematic viscosity* $\nu=1.0\cdot10^{-6}\ \mathrm{m}^2\cdot\mathrm{s}^{-1}$ *and no thermal conduction. A thickening factor* $\mathrm{F}=10000$ *is applied following the TIM. A selective numerical filter (coeff* $1.0\cdot10^{-2}$*) is used.*

The time evolution of the total kinetic energy for the different values of kinematic viscosity are presented in Fig. 10.26 for thickening factor $\mathrm{F}=100$ and Fig. 10.27 for thickening factor $\mathrm{F}=100$. This energy is expected to decay while oscillating, which is respected for most cases and the increasing impact of higher values of viscosity is also well retrieved. Acoustic perturbations, visible in the velocity field Fig. 10.25, can also be observed and are more important for lower values of kinetic viscosity and more prominent for the larger thickening

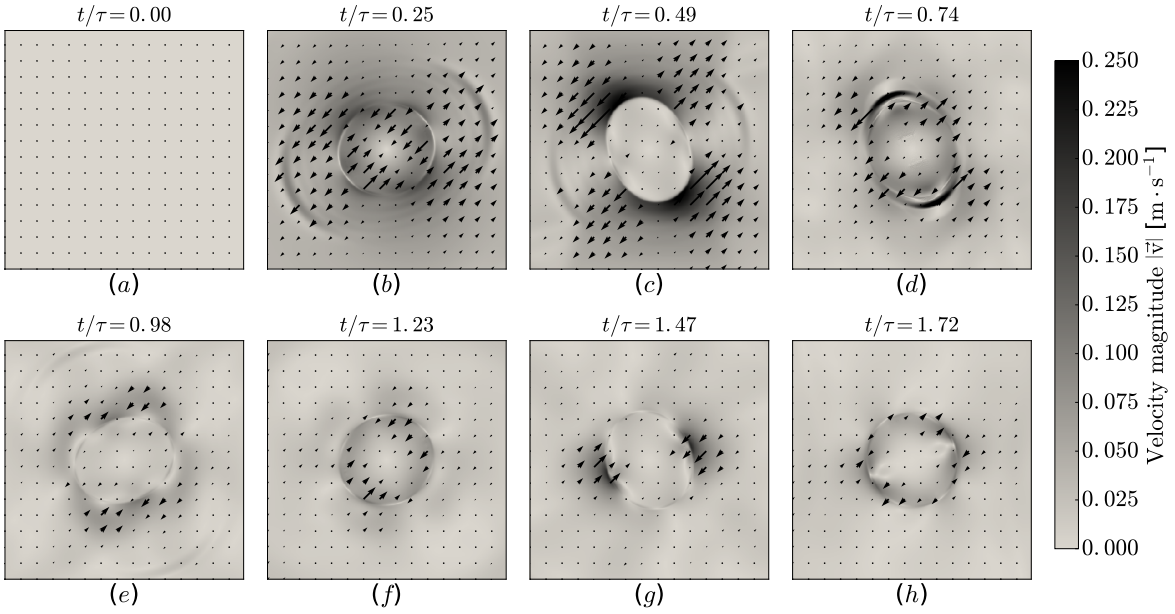

Figure 10.25: *Snapshots of the temporal evolution of the velocity field for a viscous and initially deformed O_2 droplet. Isothermal Navier-Stokes equations are solved with a constant kinematic viscosity $\nu = 1.0 \cdot 10^{-6}$ m^2·s^{-1} and no thermal conduction.A thickening factor* F = 10000 *is applied following the TIM. A selective numerical filter (coeff* $1.0 \cdot 10^{-2}$*) is used. Velocity vectors (arrows) are superimposed over the normalized velocity amplitude in gray scale.*

factor F = 10000. Nonetheless, the oscillations period for simulations with the lowest kinematic viscosity can be extracted for the two thickening factors thanks to a spectral analysis. The results, $\tau_{\text{sim,F=100}} = 0.85$ μs and $\tau_{\text{sim,F=10000}} = 0.84$ ms for the thickening factors F = 100 and F = 10000 respectively can then be compared to the theoretical values for inviscid oscillations obtained with Eq. (10.6), $\tau_{\text{th,F=100}} = 0.90$ μs and $\tau_{\text{th,F=10000}} = 0.90$ ms respectively. The small errors of 7% and 6% respectively are still very satisfactory and further advocate for the pertinence of the TIM methodology to consistently thicken the interface and perform unsteady simulations.

$$\tau = 2\pi\sqrt{\frac{(\rho_l + \rho_v)\, R^3}{6\sigma}} \tag{10.6}$$

Conclusions on the validation

The Thickened Interface Method (TIM) has been tested on a large variety of one and two-dimensional unsteady configurations. The objective was to confirm that the correct numerical and thermodynamic behavior observed in Chap. 8 for the native Second Gradient model was not impacted by the thickening methodology and that the results of the simulations remained consistent from a physical stand point.
In one-dimensional cases, both isothermal and non-isothermal simulations have led to satisfactory results. Additional artificial viscosity has been necessary to stabilize the calculations which was not the case with the non-thickened model. This difficulty is believed to be related to a reduced stiffness of the capillary terms in the equations due to smaller gradients present

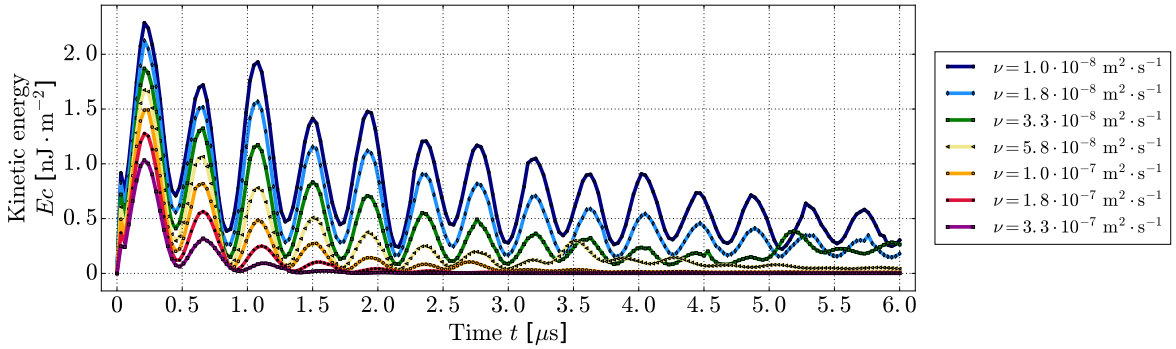

Figure 10.26: *Comparison of the temporal evolution of the total kinetic energy for an oscillating oxygen droplet with different values of kinematic viscosity. Isothermal Navier-Stokes equations are solved with no thermal conduction and the addition of artificial viscosity. A thickening factor* $\mathrm{F} = 100$ *is applied following the TIM. A selective numerical filter (coeff* $1.0 \cdot 10^{-2}$*) is used.*

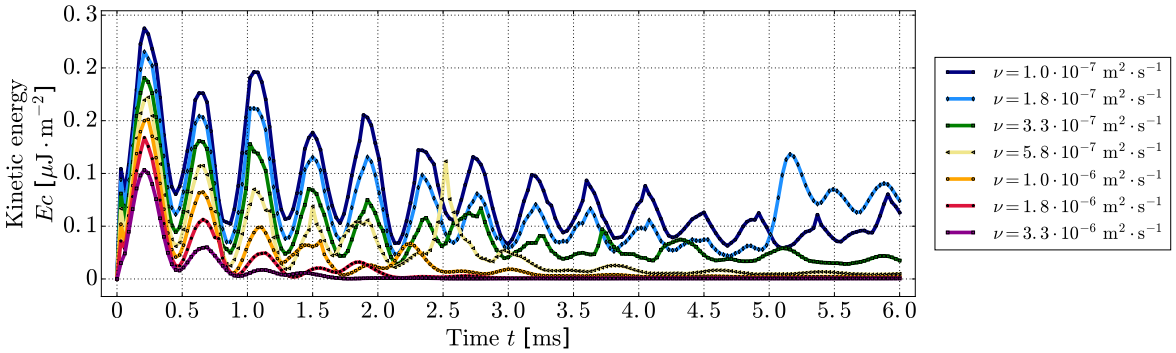

Figure 10.27: *Comparison of the temporal evolution of the total kinetic energy for an oscillating oxygen droplet with different values of kinematic viscosity. Isothermal Navier-Stokes equations are solved with no thermal conduction and the addition of artificial viscosity. A thickening factor* $\mathrm{F} = 10000$ *is applied following the TIM. A selective numerical filter (coeff* $1.0 \cdot 10^{-2}$*) is used.*

after the thickening. This loss of stiffness could have resulted in an interface with a greater characteristic response time and thus a lowered ability to resist to exterior perturbations, for instance acoustic noise, very present in non-isothermal simulations. This hypothesis would require additional studies to further assess its validity.

In two dimensions, the simulations of oscillating planar interfaces have also led to good results for which the macroscopic behavior of the interface was preserved throughout the thickening. The comparison between the simulations and the theory regarding the oscillations period and characteristic damping time has proven to be very good, a tendency already observed in Chap. 8 without thickening. Finally, the TIM has also permitted to simulate oscillating deformed droplets. These last cases, more challenging from a physical point of view, have suffered from an acoustic perturbation, properly resolved, that has been generated regularly during the simulations. This perturbation, of which origin is still unknown at the moment, has locally perturbed the interface. Despite these difficulties, for all cases, the droplets have displayed the correct expected macroscopic behavior.

The good results presented in this chapter have given confidence in the consistency of the TIM and its ability to preserve the correct thermodynamic behavior already observed for the native SG model. Consequently, they have motivated the use of the TIM to address more complicated cases that are presented in Chap. 11.

Chapter 11

Application of the Thickened Interface Method

This last chapter is dedicated to the application of the Thickened Interface method to concrete cases. Firstly, the TIM in used to study the impact of two colliding oxygen droplets in three dimensions. Secondly, the TIM is applied to simulate the two-dimensional breakup of liquid nitrogen jets. All these cases are compared with theoretical and experimental results to qualify the strengths and weaknesses of the TIM.

11.1 Colliding droplets

11.1.1 General results for colliding droplets

The fist applicative case for the TIM presented in this work is that of three-dimensional colliding droplets of which general setting is presented in Fig. 11.1.

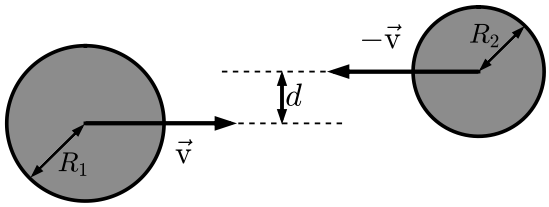

Figure 11.1: *Schematic representation of the configuration used to study the collision of two droplets*

Among the important characteristics of a spray, the mechanisms controlling the droplets creation and the droplets size distribution are of a particular interest. This is more so true when it comes to modeling a fuel injection given that the spray has a direct impact on the combustion efficiency and thus on the power output and the fuel consumption.
After the primary breakup that creates long liquid sheets, ligaments and big droplets, smaller droplets can be created either by shear stresses due to the velocity differential with the ambient gas or the collisions between the bigger liquid structures. This is one justification for

the attention given to the configuration of Fig. 11.1 in this work as well as in many other studies. Moreover, it also represents another partially canonical case to further validate the numerical and thermodynamic behavior of the TIM-thickened SG model, conveniently in three dimensions.

In Fig. 11.3 are given snapshots capturing the time evolution of droplets collisions obtained experimentally by Jiang et al. (1992) for different flow conditions using hydrocarbons. Thanks to these results and several other experimental studies such as Ashgriz and Poo (1990); Brenn et al. (1997); Qian and Law (1997); Estrade et al. (1999); Rabe et al. (2010), a series of recurring regimes, all of them illustrated in Fig. 11.3, have been identified, described and analyzed.
When two droplets collide, they share mass, momentum and energy upon contact. In absence of notable body forces and combustion, the energy that can be traded by the droplets has two principal origins: the kinetic energy from their respective velocity and the surface energy generated by the surface tension. During the impact, part of the energy will be dissipated through viscous tress, the remaining being distributed between the whole mass of liquid (if one assumes that the role of the ambient gas is negligible).
Intuitively, depending on the initial velocity of the droplets (i.e. their kinetic energy) and their surface tension, the collision can result in either a coalescence or a merging sometimes followed by a separation. Moreover, it is to be expected that the droplets absolute and relative sizes, as well as the liquid viscosity coefficient, also play an important role in the outcome of the collision.

The authors in multiple studies (see Adam et al. (1968); Park (1970); Podvysotsky and Shraiber (1984); Ashgriz and Poo (1990); Jiang et al. (1992)) have shown that for a fixed size ratio $\Delta = R_1/R_2$ between the droplets, the different regimes can be agglomerated into a We - δ graph where $We = \rho_l D_2 \left(2\mathbf{v}\right)^2 / \sigma$ is the Weber number associated with the bigger droplet of diameter $D_2 = 2R_2$, $\mathbf{v}$ is the norm of the velocity of both droplets and $\delta = d/(R_1 + R_2)$ is called the impact parameter.
The typical graphs that are obtained are given in Fig. 11.2 and the regimes are to be identified to that of the snapshots in Fig. 11.3. Four main regimes can be identified.

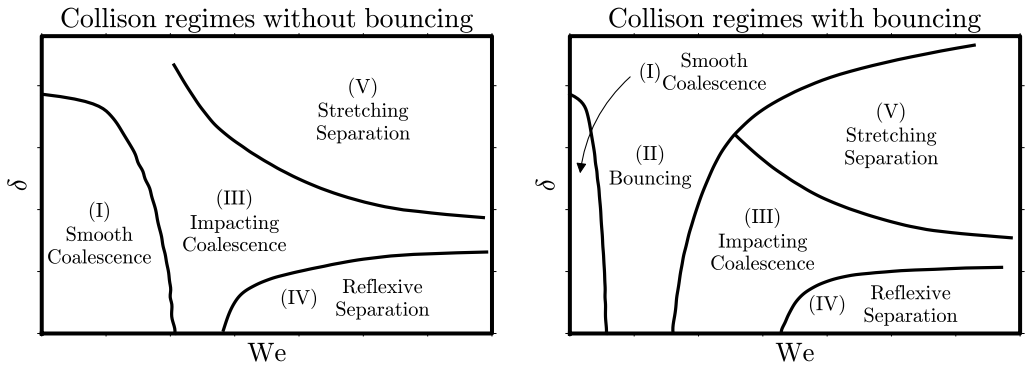

Figure 11.2: *Typical collision regimes observed in experiments depending on the Weber number and the impact parameter*

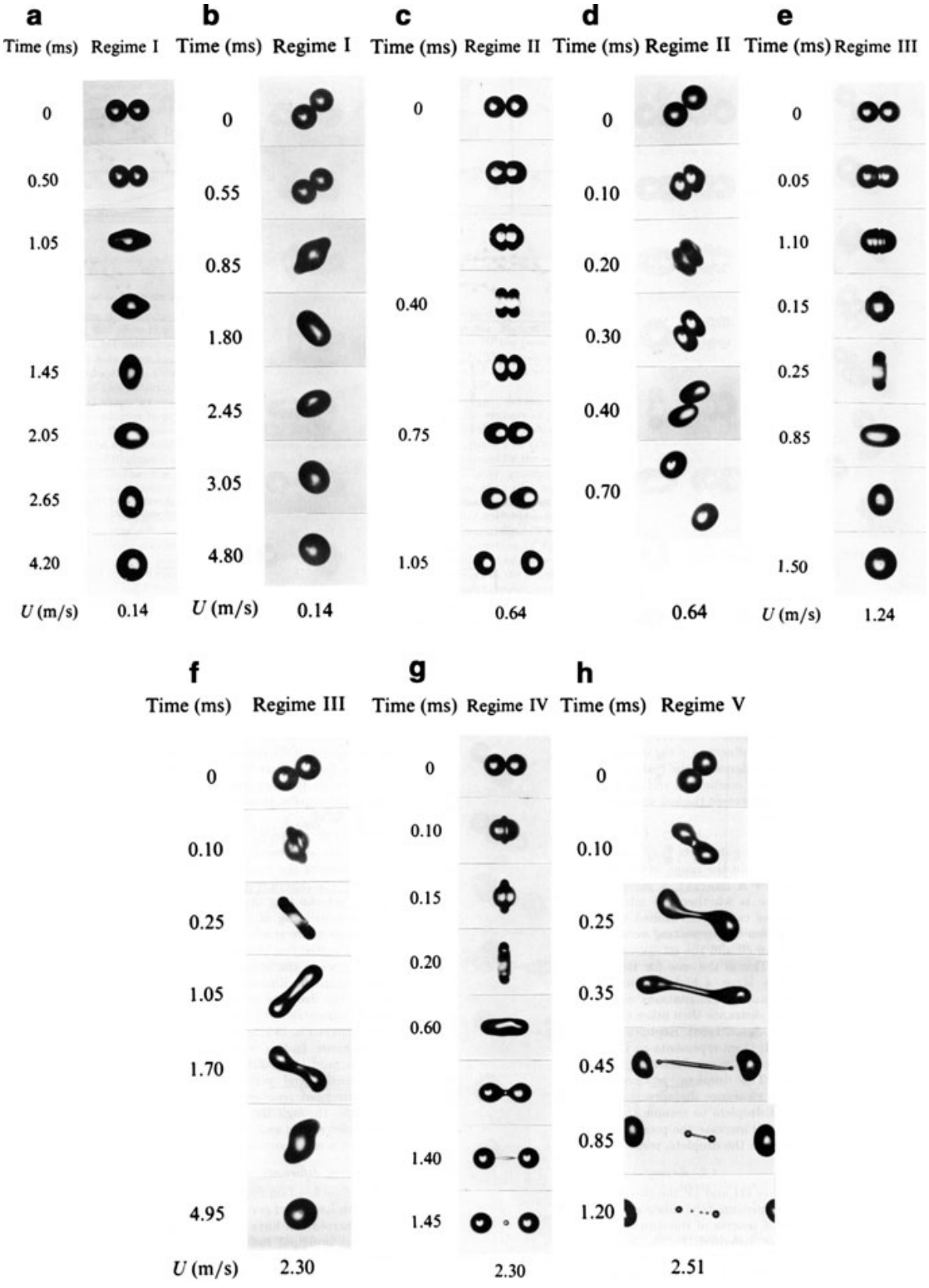

Figure 11.3: *Example of liquid droplet collision regimes for different configurations, taken from Brenn (2011) adapted from Jiang et al. (1992)*

For low Weber numbers, the droplets will tend to coalesce. This coalescence can happen smoothly where the droplets suffer minor deformations as exposed in cases (a) and (b) of Fig. 11.3 or more violently where the liquid torus, typical of droplets impact, can be observed as in cases (e) and (f) of Fig. 11.3. These two types coalescence define two regimes referred to as (I) Smooth Coalescence and (III) Impacting Coalescence.

If the Weber number increases too much or if the collision is sufficiently off-centered, the droplets will merge upon impact and then separate according to two possible modes.
For near head-on collisions, after the creation of an initial liquid torus, the liquid mass takes the form of a cylinder that elongates and eventually separates, trough impingement, on one point or more. This mode of separation constitutes the regime (IV) Reflexive Separation.
For off-centered collisions, a thin liquid filament is created between the two droplets which begins to stretch as the droplets continue on their separating path until the ligament shatters into smaller droplets. This mode of separation constitutes the regime (V) Stretching Separation.

For some fluids, which have not been precisely characterized so far, a third mode can exist where the droplets effectively collide but never actually come into contact as their kinetic energy and their viscosity are just sufficient enough to trap a thin layer of gas between them that prevents the merging of the two liquid masses.

11.1.2 Numerical simulations

11.1.2.1 Numerical setting

For the rest of the study, we only consider head-on collisions ($\delta = 0$) between two liquid oxygen droplets of the same size $D_1 = 2R_1 = 2R_2 = D2$ initially at constant temperature 110 K. The corresponding three dimensional initial solution (density isosurface at $\rho = 500\ \mathrm{kg \cdot m^{-3}}$) with the relevant two-dimensional fields of reference (density, pressure, normalized velocity) are given in Fig. 11.4. The full set of non-isothermal Navier-Stokes equations, modified by the TIM, are solved for all cases without the use of artificial viscosity except for the most extreme case (($We = 192$) described later.
For such a configuration, several experimental results are available. However, the fluid considered is often water or occasionally some type of hydrocarbon. The extent to which the simulation results using oxygen can be compared to these results is not know *a priori*.
When using water or hydrocarbons, a precise We - δ regime graph has been produced, using water droplets, by Ashgriz and Poo (1990) and is shown in Fig. 11.5. Experimentally, the authors found the transition between regime (III) of coalescence and regime (IV) of separation to occur at $We = 19$ for head-on collisions. The authors still observed coalescence at $We = 23$ for a slightly off-centered collision (see Fig. 11.8).

The generic parameters used for the simulations are compiled in Tab. 11.1, periodic boundary conditions are used in the direction parallel to the droplets movement and partially relaxing inlets are used on the two other sides, perpendicularly the droplets movement.
To access different collision regimes exposed in Fig. 11.2, several droplets velocities have been used, all the other characteristics of the configuration remaining equal. These velocities have led to different values of liquid Weber number $We = \rho_l \left(2\mathbf{v}\right)^2 D/\sigma$ and Reynolds number

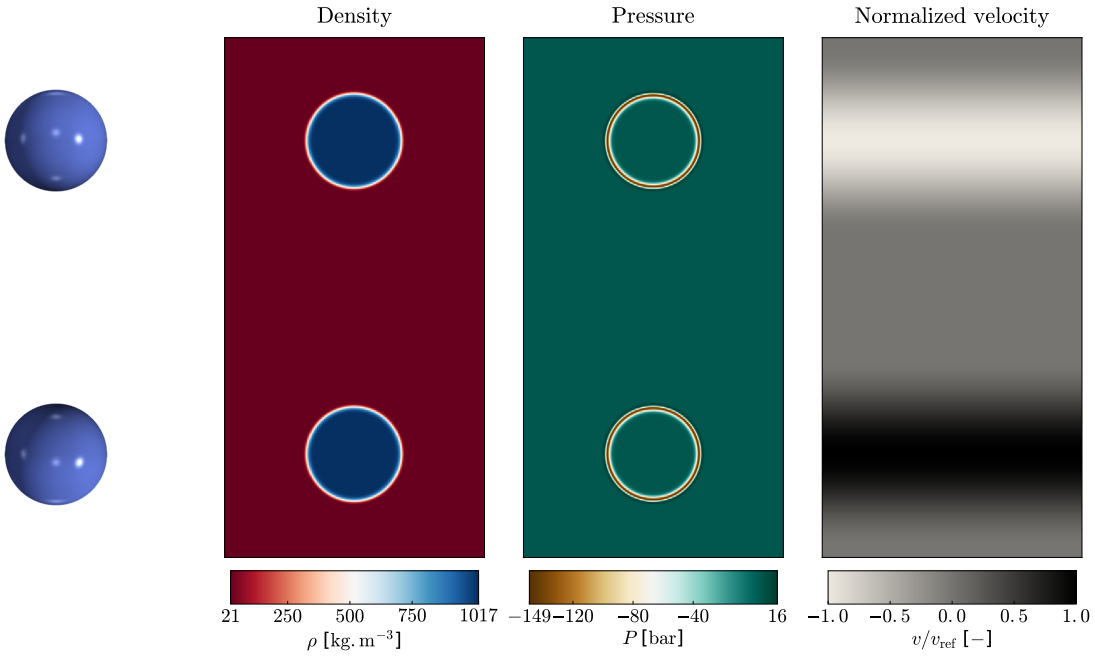

Figure 11.4: *Initial solution used to study the collision of same sized initially isothermal oxygen droplets in their own vapor. The three-dimensional $\rho = 500$ kg $\cdot$ m^{-3} isosurface and the reference two dimensional density, pressure and normalize density fields are provided.*

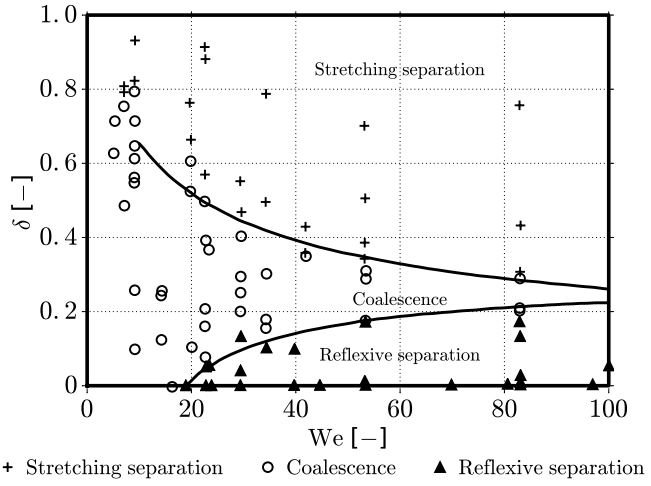

Figure 11.5: *Collision regimes in the parameter space $\delta -$ We extracted for same size droplets of water into air, taken from Ashgriz and Poo (1990)*

$Re = \rho_l \mathbf{v} D/\mu_l$. The Laplace number $La = \rho_l \sigma D/\mu_l$, which is not impacted by the changes in velocity, remains constant. All these characteristics values are compiled in Tab. 11.3.

For all cases except the most extreme ($We = 192$), for which the size of the domain has been increased, no additional stabilization tool has been needed. For this latter case, the artificial

T_i	110.0 K	λ_0	$1.173 \cdot 10^{-17}$ m$^7 \cdot$kg$^{-1} \cdot$s^{-2}	$\Delta_x = \Delta_y = \Delta_z$	0.184 μm
P^{sat}	5.45 bar	w	0.97 μm	points in int.	≈ 5
ρ_l	1017.7 kg $\cdot$ m^{-3}	F	1000	$L_y = L_x/2$	55.0 μm
ρ_v	21.4 kg $\cdot$ m^{-3}	μ_l	$1.05 \cdot 10^{-4}$ Pa.s	$N_y = Nz = (N_x + 1)/2$	300
σ	8.37 mN $\cdot$ m^{-1}	D	20 μm	points in diam.	≈ 110

Table 11.1: *Parameters used for the three dimensional simulations of colliding O_2 droplets*

v $[\text{m} \cdot \text{s}^{-1}]$	1.43	2.03	2.18	2.87	4.44
We	20	40	46	80	192
Re	556	790	840	1100	1720
La	$1.545 \cdot 10^6$	$1.545 \cdot 10^6$	$1.545 \cdot 10^6$	$1.545 \cdot 10^6$	$1.545 \cdot 10^6$
figure	Fig. 11.6	Fig. 11.8	Fig. 11.7	Fig. 11.9	Fig. 11.11

Table 11.2: *Values of the Weber We, Reynolds Re and Laplace La numbers of the collisions depending on the initial velocity of the droplets, with the corresponding figures*

viscosity of AVBP has been used and modified: an sensor based on the temperature has been introduced in supplement of the native density-based sensor. Indeed, the temperature experiences a strong overshoots, not understood at this point, at the contact zone between the droplets during the early instants of the impact. To some extent, the system acts as if the gas between the droplets was being heated. It should be noticed however that apart from this specific instant, the artificial viscosity is never actually triggered in the simulation.

As a reference, one simulation for this configuration requires a computational time of 24 hours on 2240 cores i.e. about 54 000 CPU-hours for more or less 90 μs of physical time in the simulation. This important cost can be explained by several reasons.
Firstly, it is due to the very large size of the domain that needs to be discretized compared to the size of the interface, provided that the radius of the droplets needs to be sufficiently great when compared to the interface thickness. Secondly, the explicit numerical scheme used for the simulation leads to very restrictive time steps given that the system is strongly compressible, the physical diffusion is activated and thus the stability conditions on the CFL and Fourier numbers must be respected.
This explains the small number of simulation cases that are exposed in the present document.

11.1.2.2 Results analysis

Preliminary results

The two first simulations have been done using Weber numbers of $We = 20$ (v = 1.43 m.s^{-1}) and $We = 46$ (v = 2.18 m.s^{-1}). The results, in the form of snapshots, are given in Figs. 11.6 and 11.7 respectively.

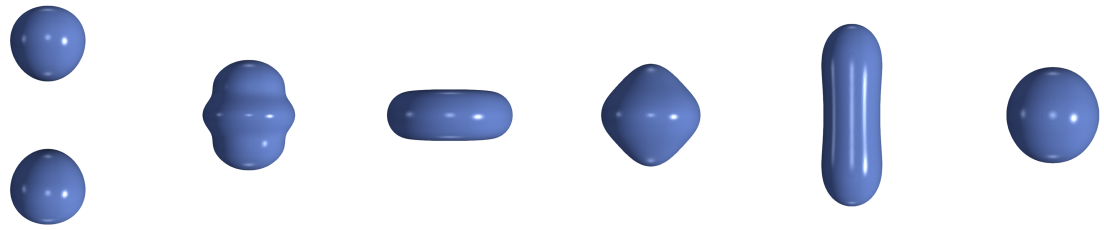

Figure 11.6: *Head-on collision of liquid droplets, simulation results with oxygen droplets at* $We = 20$ *(*$Re_l = 556$*) using the TIM*

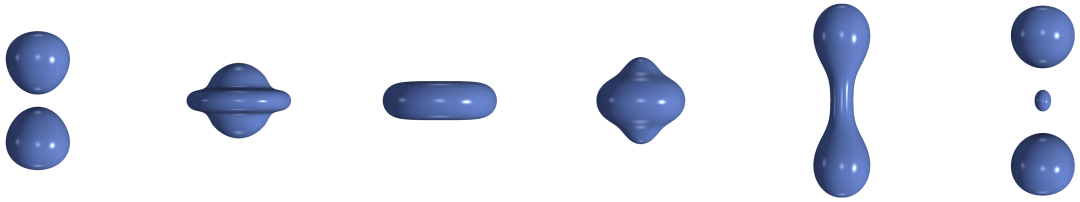

Figure 11.7: *Head-on collision of liquid droplets, simulation results with oxygen droplets at* $We = 46$ *(*$Re_l = 840$*) using the TIM*

For each case, a behavior typical of one of the regimes presented in Figs. 11.3 and 11.2 can be recognized. The impact torus, elongated cylinder and final droplet of the Impacting Coalescence can be observed for $We = 20$. The torus still appears for $We = 46$, however the cylinder display a much more pronounced impingement that ultimately results in a Reflexive Separation with the creation of an additional small droplet at the center.

In an effort to emulate the case from Ashgriz and Poo (1990) at $We = 23$ and $\delta = 0.05$ where a reflexive separation occurs without the creation of a satellite droplet, another simulation, for which results are shown in Fig. 11.8, has been performed at Weber number $We = 40$ ($\mathrm{v} = 2.03$ m.s^{-1}).
Firstly, it can be observed that the scenario of the collisions is very similar for the two cases $We = 46$ and $We = 40$. The scenario is also very comparable to that of the experiment with $We = 23$ taken from Ashgriz and Poo (1990). The only noticeable differences are the impingement of the liquid cylinder that is more accentuated when the Weber number increases and the size of the satellite droplet which decreases in accordance with the decreasing Weber number. An additional simulation, not presented here, has shown that this satellite droplet is still present even for $We = 36$.
The question of obtaining a Reflexive Separation without satellite droplets seems not to be directly addressed in the literature. Such outcomes have been observed experimentally for water in air in Ashgriz and Poo (1990) and numerically, still for water, using either LS methods in Tanguy and Berlemont (2005); Pan and Suga (2005) or VOF methods in Rieber and Frohn (1997). Most other results involving different fluids, either experimentally or numerically, showcase reflexive separations with creation of at least a very small droplet in the center.
In Ashgriz and Poo (1990), the authors observed the same satellite-free reflexive separation over the range $19 \leqslant We \leqslant 23$.

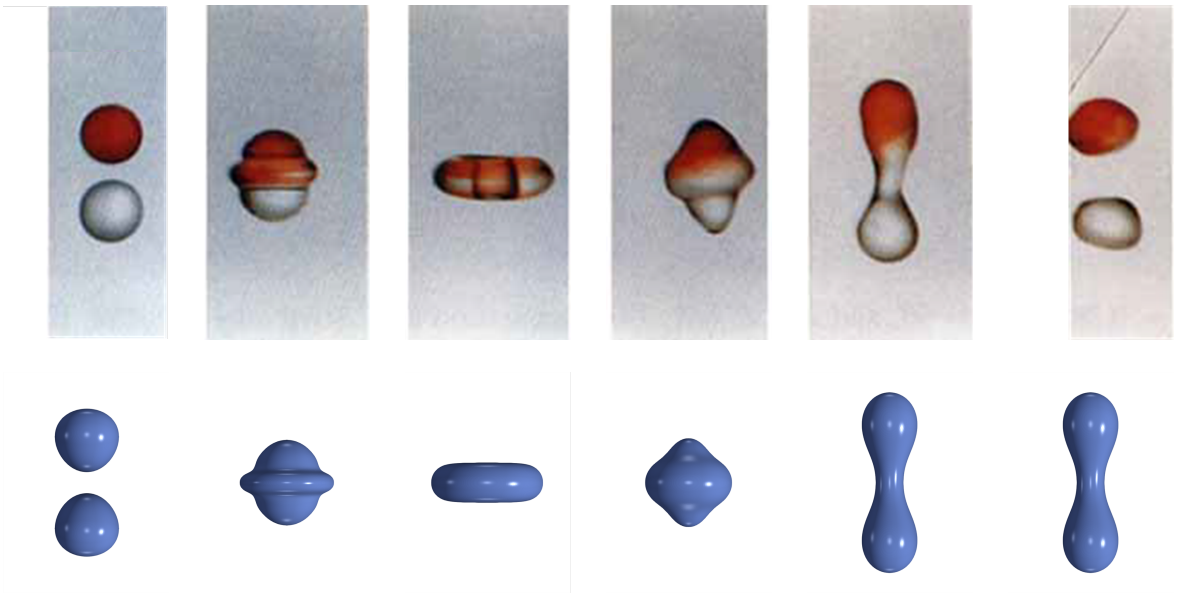

Figure 11.8: *Head-on collision of liquid droplets, comparison between experiments with water droplets at $We = 23$ from Ashgriz and Poo (1990) and simulation results with oxygen droplets at $We = 40$ ($Re_l = 790$) using the TIM*

Additional results

To obtain a clearly defined single satellite drop, reminiscent of the head-on collision at $We = 40$ from Ashgriz and Poo (1990), a simulation at $We = 80$ (v = 2.87 m.s^{-1}) is performed, the comparative results are shown Fig. 11.9.
As it was the case in Fig. 11.8, a very strong agreement is obtained, in terms of behavior, between the simulation and the experiment. The relative sizes of the two departing and the one stagnant satellite droplets are also well predicted. However, the Weber number required in the simulation seems to be twice the one used the experiments to obtain the same regime.

11.1.3 Critical Weber identification

11.1.3.1 Experimental results

The question of identifying the critical Weber We_c at which the transition between regimes (III) and (IV) occurs has been addressed by the authors in Ashgriz and Poo (1990); Jiang et al. (1992) who found this number to be linearly dependent with the ratio μ/σ in the form:

$$We_c = k\,(\mu/\sigma) + l \tag{11.1}$$

This trend can be seen in Fig. 11.10 where the line separating the regimes (III) Impacting Coalescence and (IV) Reflexive Coalescence is apparent. Additionally, the authors in Jiang et al. (1992) provide the limit lines between regimes (II) Bouncing and (III) Impacting Coalescence and also between regimes (I) Smooth Coalescence and (II) Bouncing. In particular, one can see that these two lines converge as their have slopes of opposite signs (the (I) Smooth Coalescence / (II) Bouncing limit is actually decreasing with μ/σ).

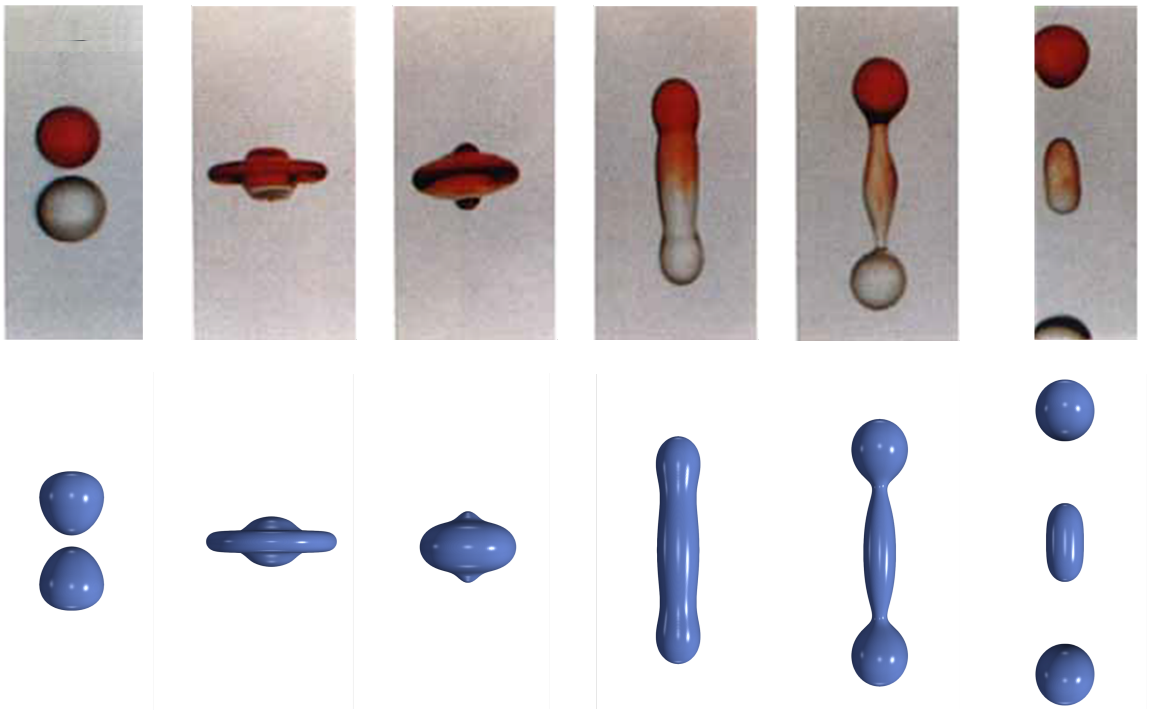

Figure 11.9: *Head-on collision of liquid droplets, comparison between experiments with water droplets at $We = 40$ from Ashgriz and Poo (1990) and simulation results with oxygen droplets at $We = 80$ ($Re_l = 1100$) using the TIM*

The principal result from this observation is that fluids with a too small ratio μ/σ will not experience the (II) Bouncing regime. For instance, this value was too small for the water used in Ashgriz and Poo (1990), explaining why this bouncing regime was not observed.

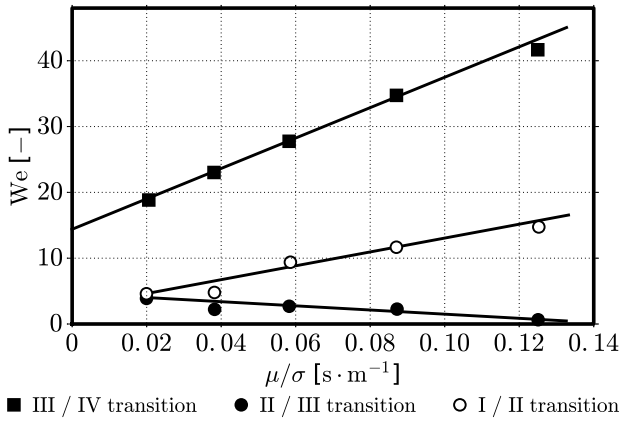

Figure 11.10: *Critical Weber numbers separating different collision regimes for hydrocarbons droplets in air, taken from Jiang et al. (1992)*

The result from Eq. (11.1) has been improved by the authors in Qian and Law (1997) who showed that We_c actually varies linearly with the Ohnesorge number $Oh = \mu_l/\sqrt{\rho_l \sigma D}$. The

correlation is:

$$We_c = 679 \cdot Oh + 16 \tag{11.2}$$

With the values compiled in Tab. 11.1, the constant Ohnesorge number used in our simulation is $8.04 \cdot 10^{-4}$ and the corresponding critical Weber number is $We_c^{\text{th}} = 16.5$. Our different simulations have shown our critical Weber number to lay somewhere between 28 and 36, which could, once again, lead to a factor two between the experimental and simulation Weber numbers to access the same regimes.

11.1.3.2 Qualitative discussion

Several factors could potentially explain the difference between the Weber numbers in our simulation and the experiments of Ashgriz and Poo (1990) that allowed to lend a similar behavior for the droplets consequently to the collisions:
- Firstly, the liquid oxygen used for the simulations has thermo-chemical properties (except the density) that are substantially further away from water than that of the hydrocarbons, which have been used to obtain the trends in Fig. 11.10 and Eqs. (11.1) and (11.2), are. These trends could be limited to a certain range of fluids.
- Secondly, the size of the droplets used for the simulations is substantially smaller than that used in the various experiments with at least one order of magnitude between them. Additionally, even if the radius of the droplets in the simulation has been calibrated to be much greater than the interface width, this value may not been sufficiently larger to ensure that wrongly induced curvature effects do not compromise the representative value of the results.
- Thirdly, all the experiments have been performed in air or nitrogen at ambient pressure and temperature, which offer exterior conditions substantially different to that of the cold oxygen vapor at almost 5 bar used in our simulations. This represents more than a factor twenty in terms of density and a factor one half in terms of viscosity. The recipient gas is suspected to have a strong impact on the collision outcome but this idea has not been actively investigated nor quantitatively characterized so far. For these reasons, the previous trends may not hold with such different gaseous conditions.
Of course, these previous possible explanations do not discard the possibility of a divergence between the theoretical, experimental and simulation results caused by a limitation in the paradigm of the TIM.

The last simulation, presented in Fig. 11.11, is set at a substantially high Weber number $We = 192$ ($\text{v} = 4.44$ m.s^{-1}) to test the model and the method in more severe conditions.
A strong Reflexive Separation occurs and one can observe the creation of two main satellite droplets. Each of these satellite is itself at the limit of breaking into two smaller droplets. Due to the increased velocity, the two initial colliding droplets impact the inlet boundaries on their way back after the reflexion, despite having increased the length and width of the computational domain by 25%. Given that the same mesh size, and thus the same interface resolution, have been used, it caused the simulation computational time to double. Additionally, an almost negligible satellite droplet is also created at the center of the domain.
The only approaching case, with which only qualitative comparisons can be made, was obtained in Ashgriz and Poo (1990) for a Weber number $We = 96$ where three clear satellite droplets have been created.

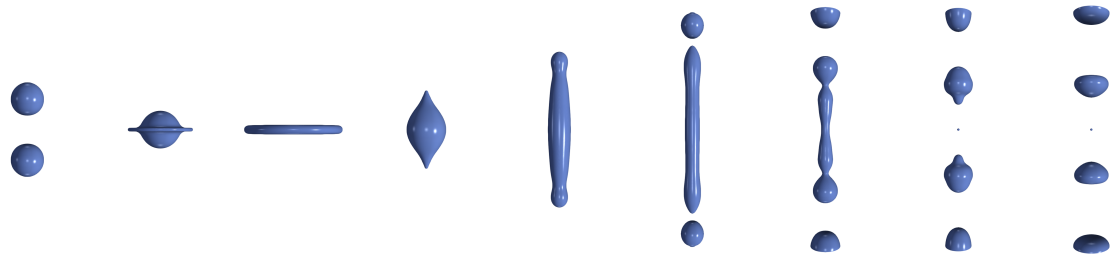

Figure 11.11: *Head-on collision of liquid droplets, simulation results with oxygen droplets at* $We = 192$ *(*$Re_l = 1720$*) using the TIM*

The question can be asked as to whether the initial colliding droplets have been constrained by the boundaries of the domain during the elongation phase of the central cylinder, which prevented the creation of four satellite droplets instead of the only two actually observed. Only a simulation with a bigger domain but also a much more important computational cost can help in settling this question.

11.1.3.3 Quantitative discussion

In Ko and Ryou (2005), the authors developed a model, based on the work in Ashgriz and Poo (1990), to predict the number of satellite droplets that are created after the collision, depending on the impact conditions. This model is briefly presented hereunder for the head-on collision of equally-sized droplets.
For that purpose, the authors in Ashgriz and Poo (1990) introduced the total kinetic energy KE and surface energy SE of a single droplet, defined in Eqs. (11.3) and (11.4) respectively.

$$KE = \frac{1}{2}\rho\left(\frac{1}{6}\pi D^3\right)\mathrm{v}^2 \tag{11.3}$$

$$SE = \sigma\pi D^2 \tag{11.4}$$

They also introduced the effective reflexive energy KE_{er}, given by Eq. (11.5), which consists of the sum of the kinetic energy of counteractive flows KE_{co} of the droplets pulling away and the excess surface energy SE_{es} induced by the stretching liquid cylinder between the droplets, defined in Eqs. (11.6) and (11.7) respectively.

$$KE_{er} = KE_{co} + SE_{es} \tag{11.5}$$

$$KE_{co} = \rho\left(\frac{1}{6}\pi D^3\right)\mathrm{v}^2 = 2KE \tag{11.6}$$

$$SE_{es} = \sigma\pi D^2 \tag{11.7}$$

A critical surface energy SE_c for reflexive separation is obtained experimentally by observing systematic separation when $KE_{er} \geqslant SE_c$. It is expressed by:

$$SE_c = \frac{3}{4}\sigma\pi\left(2D^3\right)^{\frac{2}{3}} \tag{11.8}$$

Using KE_{er} and SE_c, the authors in Ko and Ryou (2005) defined a separation volume coefficient C as follows:

$$C = \frac{KE_{er} - SE_c}{KE_{er} + SE_c} \tag{11.9}$$

This coefficient allows to evaluate the size of the colliding droplets after separation, which is $D_a = (1 - C)^{1/3} D$. A ratio of kinetic energy dissipation α is also used and allows the evaluate the velocity of the colliding droplets after impact with $\mathrm{v}_a = (1 - \alpha)^{1/2} \mathrm{v}$. In Ashgriz and Poo (1990), alpha is experimentally evaluated at 0.55 for water but the legitimacy of this value for other fluids has not been addressed and should be met with caution.
Eventually, the total kinetic energy KE_a and the surface energy SE_a of the colliding droplets after impact can be expressed by adapting Eqs. (11.3) and (11.4) with the known definitions of D_a and v_a, they are given by:

$$KE_a = \frac{1}{2}\rho\left(\frac{1}{6}\pi D_a^3\right)\mathrm{v}_a^2 = KE\,(1 - C)\,(1 - \alpha) \tag{11.10}$$

$$SE_a = \sigma\pi D_a^2 = SE\,(1 - C)^{\frac{2}{3}} \tag{11.11}$$

As the dissipated kinetic energy is, by hypothesis, proportional to the total kinetic energy of the two colliding droplets by factor α, an energy balance can be written for the whole process, neglecting the possible energetic contributions coming from the ambient gas. The energy conservation is thus written:

$$2KE + 2SE = 2KE_a + 2SE_a + \alpha KE + SE_s \tag{11.12}$$

where SE_s is the total surface energy remaining available after the separation of the two main droplets, of which value controls how many satellite droplets can be created and whether any is created in the first place.

Using Eqs. (11.3), (11.4), 11.10 and 11.11, SE_s can be isolated in Eq. (11.12) to get:

$$SE_s = 2KE\,[1 - \alpha - (1 - \alpha)\,(1 - C)] + 2SE\left[1 - (1 - C)^{\frac{2}{3}}\right] \tag{11.13}$$

Finally, the number of satellite droplets N_a is given by:

$$N_a = \left(\frac{SE_s}{\sigma\pi}\right)^3 \frac{1}{4C^2D^6} \tag{11.14}$$

The results for several values of coefficients alpha have been compiled in Tab. 11.3.
One can see that for values of factor α around 0.55 prescribed in Ashgriz and Poo (1990), the model from Eq. (11.14) is strongly over predictive for our high Weber numbers. For all values of alpha, the absence of satellite droplet for $We = 20$ is retrieved. Overall, the predicted values of N_a are very sensitive to α. Values around $\alpha = 0.85$ seem to provide an acceptable correlation. One must challenge this result as α is, by definition, the ratio of kinetic energy lost by the droplets during the impact through viscous dissipation. The observed trend of a lower value of N_a for higher values of α is physically sound. A value of 0.85 seems very large but is nonetheless consistent with the simulations where very high values of Weber number are required to create visible satellite droplets, which could be the sign that a great amount of energy is lost by the liquid masses during these collisions. The physical accuracy of this last intuition needs however to be studied more thoroughly.

α	$N_{a,We=20}$	$N_{a,We=36}$	$N_{a,We=40}$	$N_{a,We=46}$	$N_{a,We=80}$	$N_{a,We=192}$
0.5	0.003	0.06	0.08	1.08	4	33
0.55	0.028	0.51	0.68	0.96	3.5	27
0.60	0.026	0.46	0.60	0.84	2.9	21
0.7	0.024	0.36	0.47	0.64	2.0	12
0.8	0.19	0.28	0.36	0.47	1.3	6
0.85	0.017	0.25	0.31	0.40	1.02	4.2
0.90	0.016	0.21	0.26	0.33	0.78	2.6
Simu.	0	≈ 0	≈ 0	$\ll 1$	1	2

Table 11.3: *Number of satellite droplets created by colliding O_2 droplets as predicted by the model from Ko and Ryou (2005) in Eq.* (11.14)

Conclusions on the three-dimensional colliding droplets

The TIM has allowed to perform stable and coherent simulations of colliding oxygen droplets at multiple velocities using a reasonable interface resolution solving the full set of non-isothermal, compressible et physically diffusive Navier-Stokes equations, mostly without requiring the addition of artificial viscosity.
Quantitative comparisons with literature is rendered difficult by the scarcity of experiments or numerical results directly involving cryogenic fluids, most of them being carried out with water or hydrocarbons in air. However, the qualitative comparisons with the results in Ashgriz and Poo (1990) have shown that the different head-on collision regimes can be retrieved. Moreover, by applying a factor two from the experimental to the simulation Weber numbers, the exact same outcomes can be obtained, although the origin of this factor remains unexplained.

11.2 Periodic liquid jets

11.2.1 Numerical setup

11.2.1.1 Case design

For this second applicative case, more complexity is introduced by considering a symmetrical mixing layer that takes the aspect of a liquid jet in its own vapor.
The interface is initially set at $T_i = 100$ K and the initial solution is isobaric at $P^{\text{sat}} = 7.85$ bar. The surrounding vapor is initially at rest whereas the liquid has a constant descending vertical velocity $\mathbf{v}_l$. The simulations are performed on a regular cartesian mesh. The domain, as depicted in Fig. 11.12, is periodic vertically. Periodic boundary conditions are also used on the lateral sides to avoid crashes susceptible to be caused by small droplets impacting the outlet boundaries. The useful parameters used for the simulations are recalled in Tab. 11.4 where D is the jet diameter and w is the interface width. The full capillary Navier-Stokes equations are solved using Chung et al. (1988) model for the diffusion. In the following, the magnitude of the viscosity is increased by a factor 5 in order to adjust the Reynolds number to the grid resolution (see Sec. 11.2.1.2 for details). A high order selective filter with a coefficient 10^{-2} is used to suppress point-to-point oscillations.

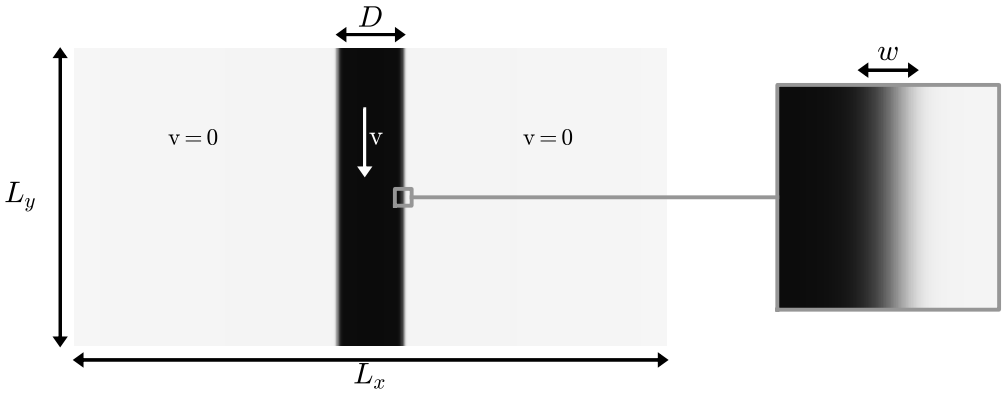

Figure 11.12: *Schematic representation of the density field for the simulation configuration of a periodic liquid jet in its vapor*

T_i	100.0 K	$\lambda_{F=1}$	$1.96 \cdot 10^{-17}$ m$^7 \cdot$ kg$^{-1} \cdot$ s^{-2}	w	1.31 μm
P^{sat}	7.85 bar	σ	4.134 mN $\cdot$ m^{-1}	D	20 μm
ρ_l	667.14 kg $\cdot$ m^{-3}	F_0	1000	$N_{y0} = N_{x0}/2$	675
ρ_v	31.6 kg $\cdot$ m^{-3}	$L_y = L_x/2$	90.0 μm	$\Delta_{x0} = \Delta_{y0}$	0.133 μm

Table 11.4: *Simulation parameters used for the two dimensional N_2 jets (reference mesh resolution and interface thickening leading to about nine points in the interface)*

While the initial density, pressure and temperature fields have remained unchanged for all cases, four different values of liquid velocity, compiled in Tab. 11.5, have been used so as to get four different liquid Weber numbers $We = \rho_l v^2 D/\sigma$ typical of different atomization regimes.

v [m $\cdot$ s^{-1}]	11.3	17.9	25.4	35.9
Re	460	730	1040	1470
We	412	1030	2080	4150
Oh	$4.38 \cdot 10^{-2}$	$4.38 \cdot 10^{-2}$	$4.38 \cdot 10^{-2}$	$4.38 \cdot 10^{-2}$

Table 11.5: *Simulation velocities and corresponding liquid Reynolds, Weber and Ohnesorge numbers used for the simulations of two dimensional N_2 jets with a liquid viscosity $\mu_l = 3.25 \cdot 10^{-4}$ kg $\cdot$ m$^{-1} \cdot$ s^{-1}*

The results, for which numerous examples are provided in the next paragraphs, can be compared to the chart in Shimasaki and Taniguchi (2011) (Fig. 11.13), inspired from Reitz (1978), which provides insight on the jet behavior relatively to the injection conditions, in particular the liquid Reynolds $Re = \rho_l v D/\mu_l$ and Ohnesorge $Oh = \mu_l/\sqrt{\rho_l \sigma D}$ numbers. With the physical parameters from the simulations, the resulting (constant) Oh number is $4.38 \cdot 10^{-2}$. The regime for the case with the lower Re number (460) should correspond to the first wind induced regime while the case at $Re = 1470$ should be laying in the second wind-induced regime region.

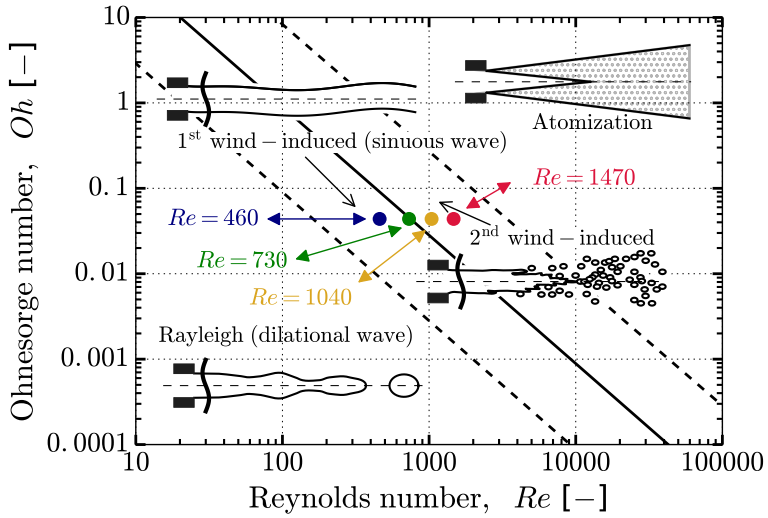

Figure 11.13: *Breakup regimes for liquid round jets in the parameter space* $\mathrm{Re}_l - \mathrm{Oh}$ *extracted for a hydrocarbons-air configuration, taken from Shimasaki and Taniguchi (2011)*

11.2.1.2 Direct Numerical Simulation conditions

Given that the main objective of this study is to present a framework in which the Second Gradient can permit Direct Numerical Simulation (DNS) involving interfaces, a specific care has been taken to ensure that the mesh resolution was fine enough to accommodate the smallest scales of turbulence. However, rather than choosing directly a mesh fitted to the Kolmogorov turbulent scale, the fluid viscosity has been scaled to ensure that the Kolmogorov scale was apportioned to the mesh resolution fixed by the interface resolution, set to eight points in the reference case. This approach is justified by the fact that in most cases, the interface width is much smaller than the smallest turbulent scales and thus is the limiting factor in terms of mesh resolution prior to applying an interface thickening methodology. By artificially changing the viscosity of the fluid, we ensure that the case remains numerically affordable and the numerical errors from the potentially unresolved turbulent scales have a minimal impact on the interface behavior, which is the main aspect these simulations aim at qualifying.

Three-dimensional turbulence

Classically, when considering three-dimensional turbulence, the hierarchy and the relations between the different turbulent scales are determined using the assumption that the average rate of dissipation of turbulent energy ε is preserved from one scale to the over. This rate is apportioned to the ratio between the typical scale of kinetic energy $[e_c]$ and the considered characteristic time $[\tau]$, as exposed in Eq. (11.15) where $[l]$ is the considered characteristic length scale and $[u]$ is the characteristic velocity at that scale.

$$\varepsilon \sim \frac{[e_c]}{[\tau]} \sim \frac{[u]^2}{[u]/[l]} \sim \frac{[u]^3}{[l]} \tag{11.15}$$

The largest scale of the turbulence with characteristic length l and velocity u are characterized by a liquid Reynolds number $Re_l^* = \rho_l u l/\mu_l = ul/\nu_l$. This Reynolds number is not to be mistaken with the Reynolds number of the jet $Re_l = vD/\nu_l$ evaluated using the jet diameter

and velocity. At the Kolmogorov length scale l_k, the turbulent energy is dissipated only through viscous interactions, which leads to writing:

$$\varepsilon \sim \nu_l \frac{du}{dx}^2 \sim \frac{[u]^2}{[l]^2} \sim \nu_l \frac{v_k^2}{l_k^2} \tag{11.16}$$

Combining Eqs. (11.15) and (11.16), it comes that:

$$l_k \sim \left(\frac{\nu_l^3}{\varepsilon}\right)^{\frac{1}{4}} \tag{11.17}$$

Finally, the relation between the largest and smallest length scales l and l_k can be established using the relation $Re_l^* = \rho_l u l/\mu_l = ul/\nu_l$ and Eqs. (11.15) and (11.17):

$$l_k \sim \left(\frac{\nu_l^3}{\varepsilon}\right)^{\frac{1}{4}} \sim \left(\frac{\nu_l^3}{u^3/l}\right)^{\frac{1}{4}} \sim \left(l^4 \frac{\nu_l^3}{u^3 l^3}\right)^{\frac{1}{4}} \sim \left(\frac{l^4}{Re_l^{*3}}\right)^{\frac{1}{4}} \sim l Re_l^{*-\frac{3}{4}} \tag{11.18}$$

Given that the greater l_k, the better the scale is resolved, Eq. (11.18) leads to the condition:

$$Re_l^* < \left(\frac{l}{l_k}\right)^{\frac{4}{3}} \iff \frac{\rho_l u l}{\mu_l} < \left(\frac{l}{l_k}\right)^{\frac{4}{3}} \iff \mu_l > \rho_l u l \left(\frac{l_k}{l}\right)^{\frac{4}{3}} \iff \boxed{\mu_l > \rho_l u \left(\frac{l_k^4}{l}\right)^{\frac{1}{3}}} \tag{11.19}$$

To obtain quantitative values for our case, the length scale l and the corresponding velocity u must be evaluated. Typical values for such type of jets are $l = 0.3D$ and $u = 0.3v$ where D and v are the diameter and velocity of the liquid jet. The velocity that is considered here is that of the most critical case $We = 4150$, i.e. $v = 35.9\ \mathrm{m \cdot s^{-1}}$. The mesh size is selected to achieve a 9-point resolution in the interface which leads to the value $\Delta_x = 0.133\ \mu$m. A satisfactory DNS can be achieved if the Kolmogorov scale is comparable to the mesh size, which leads to the choice $l_k = \Delta_x = 0.133\ \mu$m. All the corresponding values are compiled in Tab. 11.6 where the macroscopic, large turbulent and Kolmogorov scales are described with their associated velocities and Reynolds numbers. The resulting maximal value for the turbulent scale Reynolds number is $Re^*_{l\,\mathrm{max}} = 157$ and the corresponding minimal value for the liquid dynamic viscosity is $\mu_{l_{\mathrm{min}}} = 2.72 \cdot 10^{-5}\ \mathrm{kg \cdot m^{-1} \cdot s^{-1}}$, to be compared with the native value of $\mu_{l_{\mathrm{th}}} = 6.5 \cdot 10^{-5}\ \mathrm{kg \cdot m^{-1} \cdot s^{-1}}$ predicted using the model from Chung et al. (1988).

D	20 μm	l	6 μm	l_k	0.133 μm
v	35.9 m $\cdot$ s^{-1}	u	10.77 m $\cdot$ s^{-1}	u_k	3.04 m $\cdot$ s^{-1}
$Re_{l\mathrm{max}}$	1755	$Re^*_{l\,\mathrm{max}}$	157	Re_l^k	1

Table 11.6: *Characteristic lengths, velocities and Reynolds numbers for the relevant scale to determine the critical conditions for the DNS (3D) of a liquid nitrogen jet at 100 K in its own vapor.*

Two-dimensional turbulence

To be rigorous, one can only apply the previous discussion to three-dimensional turbulence for which the concept of Kolmogorov's cascade applies. A different theory must be used in two dimensions. In such cases, the hypothesis of the conservation of the average rate of dissipation of turbulent energy ε is not satisfied at all scales but only from the largest scales down a cut-off scale (l', u'). Below this cut-off scale, a new quantity is conserved, namely the average rate of dissipation of turbulent enstrophy ξ which, similarly to the relation in Eq. (11.15), can be apportioned to the characteristic length scale $[l]$ and velocity $[u]$ as done in Eq. (11.20). Further details on the theory behind two-dimensional turbulence can be found in Kraichnan (1967); Leith (1968); Batchelor (1969); Kraichnan (1971); Frisch and Kolmogorov (1995).

$$\xi \sim \frac{[u]^3}{[l]^3} \tag{11.20}$$

When trying to apply this theory, one is faced with the major issue of determining the cut-off scale at which the transition between energy and enstrophy occurs. In particular, for the two dimensional jets considered in these simulations, no correlation have been extracted in the literature, the corresponding experiments being intrinsically performed in three dimensions.
If one assumes that the transition occurs before the length scale l with velocity u, the derivation performed in Eq. (11.18) can be adapted. Firstly, it can be shown that Eq. (11.17) expressed with ε becomes Eq. (11.21) when expressed with ξ.

$$l_k \sim \left(\frac{\nu_l^3}{\xi}\right)^{\frac{1}{6}} \tag{11.21}$$

It then follows that:

$$l_k \sim \left(\frac{\nu_l^3}{\xi}\right)^{\frac{1}{6}} \sim \left(\frac{\nu_l^3}{u^3/l^3}\right)^{\frac{1}{6}} \sim \left(l^6\frac{\nu_l^3}{u^3 l^3}\right)^{\frac{1}{6}} \left(\frac{l^6}{Re_l^{*3}}\right)^{\frac{1}{6}} \sim l Re_l^{*-\frac{1}{2}} \tag{11.22}$$

Finally, the condition on the viscosity can also be expressed

$$Re_l^* < \left(\frac{l}{l_k}\right)^2 \iff \frac{\rho_l u l}{\mu_l} < \left(\frac{l}{l_k}\right)^2 \iff \mu_l > \rho_l u l \left(\frac{l_k}{l}\right)^2 \boxed{\mu_l > \rho_l u \frac{l_k^2}{l}} \tag{11.23}$$

With the same considerations used for the three-dimensional turbulence, the remarkable values can be evaluated, they are compiled in Tab. 11.7. The new resulting maximal value for turbulent scale Reynolds number is $Re^*_{l\,\max} = 1985$ and the corresponding minimal value for the liquid dynamic viscosity is $\mu_{l_{\min}} = 2.15 \cdot 10^{-5}$ kg $\cdot$ m^{-1} $\cdot$ s^{-1} to be compared with the value of $\mu_{l_{\text{th}}} = 6.5 \cdot 10^{-5}$ kg $\cdot$ m^{-1} $\cdot$ s^{-1} predicted by Chung's model for liquid nitrogen at that temperature.

Final choices regarding the turbulence

As evidenced by Tabs. 11.6 and 11.7, the two-dimensional turbulence paradigm is *a priori* much more permissive than its three-dimensional counterpart. Moreover, the uncertainty regarding the choice of the cut-off scale leads to treating the results in Tab. 11.7 with caution. It seems reasonable to assume that the actual cut-off scale lies between the typical macroscopic scale (l, u) and the Kolmogorov scale (l_k, v_k) and should lead to critical values between those

D	20 μm	l	6 μm	l_k	0.133 μm
v	35.9 $\mathrm{m \cdot s^{-1}}$	u	10.77 $\mathrm{m \cdot s^{-1}}$	u_k	0.24 $\mathrm{m \cdot s^{-1}}$
$Re_{l\max}$	22055	$Re^*_{l\,\max}$	1985	Re^k_l	1

Table 11.7: *Characteristic lengths, velocities and Reynolds number for the relevant scale to determine the critical conditions for the DNS (2D) of a liquid nitrogen jet at 100 K in its own vapor.*

obtained for the extreme cases in Tabs. 11.6 and 11.7. To verify this idea, an analysis has been performed assuming the cut-off scale to be the so called Taylor micro-scale, of characteristic length l_T and velocity v_T It is defined as the intermediary scale with the velocity of the largest vortex $v_T = u$ and the viscous dissipation rate equal to ε which leads to $l_T = v_T\sqrt{\nu_l/\varepsilon}$. This choice of cut-off scale actually leads to the same conditions as that of the pure three-dimensional turbulence.
Given the previous information and results, the final choice has been made to accommodate the stricter conditions imposed by the three-dimensional turbulence approach and thus, a factor five has been applied to the values of the dynamic viscosity predicted by Chung's diffusion model, which leads to a reference liquid viscosity of $\mu_l = 3.25 \cdot 10^{-4}$ $\mathrm{kg \cdot m^{-1} \cdot s^{-1}}$ and a Kolmogorov length scale of 0.153 μm, slightly greater than the mesh resolution $\Delta_x = 0.133$ μm. The final values for the Reynolds numbers are compiled in Tab. 11.5.

11.2.1.3 Mesh and interface resolution

For this jet configuration, apart from the Weber (and subsequently the Reynolds) number that is varied to study its impact on the jet topology and compare it to the diagram in Fig. 11.13, the resolution of the interface is also modified to assess its impact on the quality of the results. Two different approaches have been used to modify the resolution of the interface: directly by modifying the mesh resolution and diminishing the number of points in the domain, indirectly by maintaining the same mesh but reducing the thickening factor F used in the TIM to enlarge the interface. Both processes have been applied to achieve roughly the same number of points in the interface. As such, a one half and a one third resolutions have been considered additionally to the reference resolution described in Tab. 11.4. The complete set of mesh and interface resolutions used are compiled in Tab. 11.8.

N_y	675	338	224	675	675
F	1000	1000	1000	500	333
Δ_x	0.133 μm	0.267 μm	0.404 μm	0.133 μm	0.133 μm
points in int.	≈ 9	≈ 5	≈ 3	≈ 5	≈ 3

Table 11.8: *Mesh resolutions and thickening factors used to study the impact of the interface resolution on the simulation results for a two-dimensional nitrogen jet in its own vapor*

11.2.2 Impact of the jet velocity

The first aspect addressed with these simulations is the impact of the jet velocity on its topology and behavior. A time evolution of the two-dimensional density fields for all Reynolds numbers is presented in Fig. 11.15 for the reference spatial resolution. For $Re = 460$ $(We = 412)$ the jet faces a mild macroscopic deformation with no clear breakup, in accordance with the first wind-induced regime in Fig. 11.13. For $Re = 730$ $(We = 1030)$, the deformation gets stronger and macroscopic ligaments start to form. For $Re = 1040$ $(We = 2080)$, theses macroscopic structures also form and eventually start separating and coalescing. Both results are consistent with regimes in-between the first and second wind induced regimes in Fig. 11.13. For $Re = 730$, a small number of big droplets are generated whereas for $Re = 1040$, only very large filaments are created and can be expected to quickly recombine without formation of smaller droplets. With the case $Re = 1470$ $(We = 4150)$, a great modification occurs in the jet topology. Long macroscopic ligaments form and quickly break-up to create droplets, among which the biggest ones also tend to experience a secondary break-up, thus giving birth to smaller droplets. This result properly follows the behavior of a fully installed second wind-induced regime, as predicted by Fig. 11.13.

Upon closer observation, one can notice a very subtle yet observable interface diffusion in the density fields for the case $Re = 1470$ $(W = 4015)$ in the snapshots in Fig. 11.15. This excessive diffusion manifests itself by the creation of small dimmed whitened regions in the vapor phase. This marginal observation is briefly addressed in Secs. 11.2.3 and 11.2.4 but it does not impedes the advancement of the simulations and the quality of the results. Overall, the four test cases qualitatively display the expected behavior in agreement with experimental studies. In particular, the transition from the sinus-like macroscopic undulations to the microscopic, droplet creating, atomization regimes that is observed in the simulations concurs adequately with the correlations in Fig. 11.13.
The temperature and (thermodynamic) pressure fields for the same cases are also provided in Figs. 11.16 and 11.17 respectively. The temperature experiences mild undershoots and strong overshoots, fostered for higher initial velocities. These temperature variations however do not jeopardize the simulations for the values that have been used. They appear to be timely restrained to the period where the jet first faces the creation of macroscopic vertices that pull liquid matter out the core stream. They then seem to be progressively damped as the simulations advance. These observations are to be related with those already faced when simulating more simple cases, for instance the one dimensional configurations presented in Sec. 8.1.3.2. The conclusion drawn for these simple cases applies here: combined with the high-order selective filter, the taking into account of the physical diffusive fluxes are enough to ensure the stability of the computations, as expected for direct numerical simulations, even on such demanding cases. The thickening of the interface tends to alleviate the gradients of all the thermodynamic variables, temperature included.

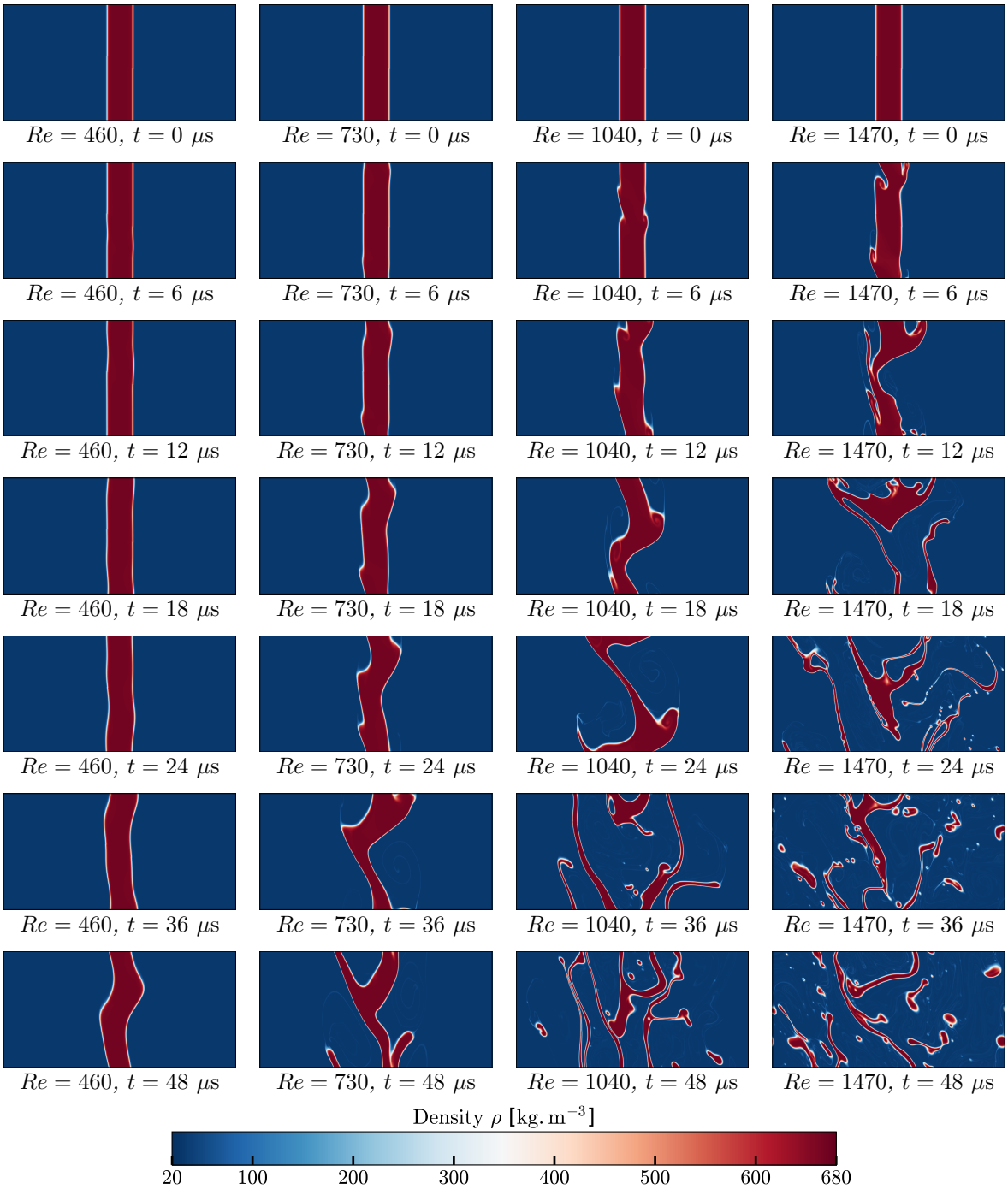

Figure 11.15: *Evolution in time of the density profiles for two-dimensional periodic Nitrogen liquid jets in their vapor. Four cases have been carried out with the reference spatial resolution and thickening factor* F = 1000 *for different Reynolds numbers, from left to right:* $Re = 460$ (412), $Re = 730$ (1030), $Re = 1040$ (2080) *and* $Re = 1470$ (4150)

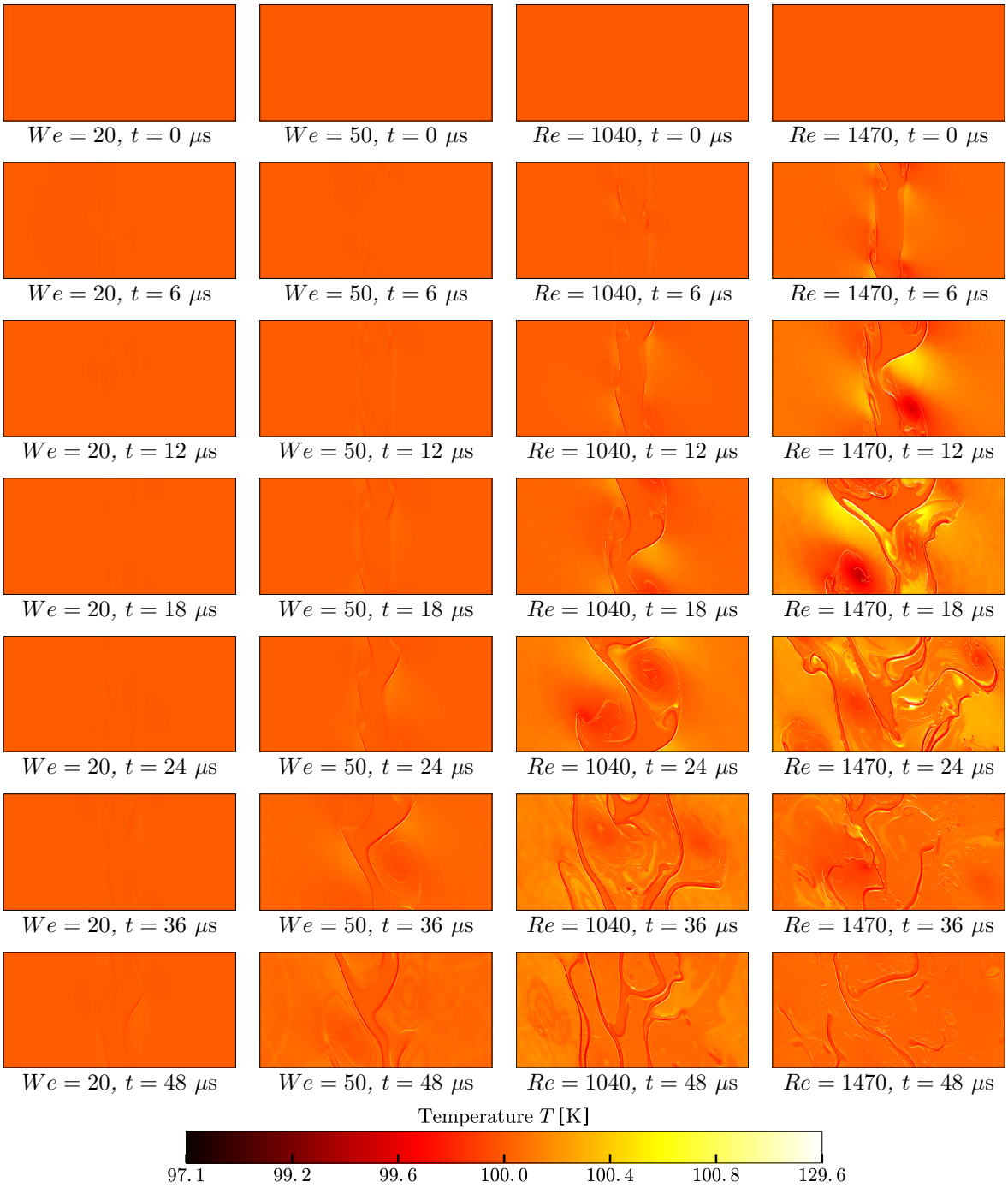

Figure 11.16: *Evolution in time of the temperature profiles for two-dimensional periodic Nitrogen liquid jets in their vapor. Four cases have been carried out with the reference spatial resolution and thickening factor* $\mathrm{F} = 1000$ *for different Reynolds numbers, from left to right:* $Re = 460$ (412), $Re = 730$ (1030), $Re = 1040$ (2080) *and* $Re = 1470$ (4150)

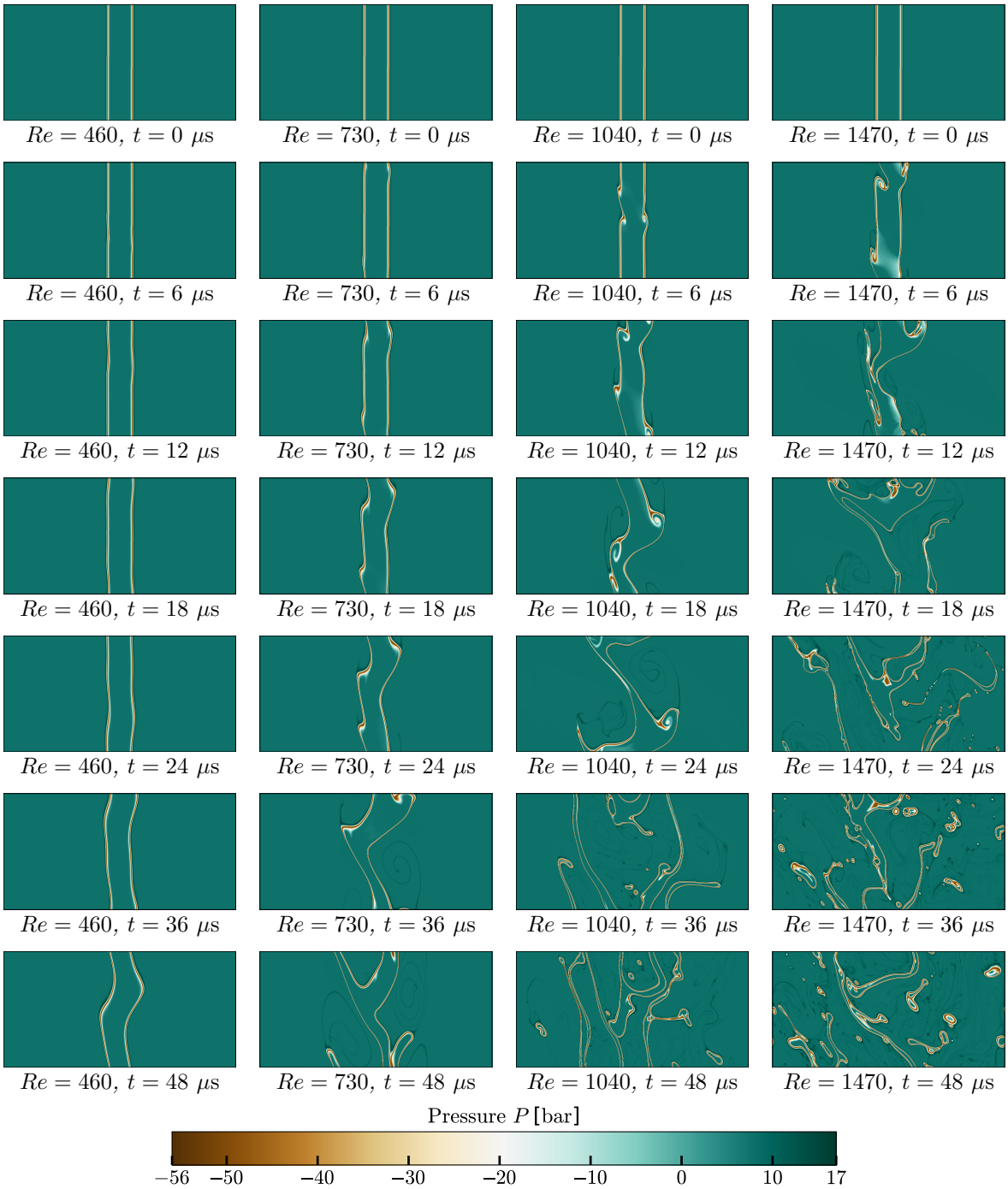

Figure 11.17: *Evolution in time of the pressure profiles for two-dimensional periodic Nitrogen liquid jets in their vapor. Four cases have been carried out with the reference spatial resolution and thickening factor* F = 1000 *for different Reynolds numbers, from left to right:* $Re = 460$ (412), $Re = 730$ (1030), $Re = 1040$ (2080) *and* $Re = 1470$ (4150)

11.2.3 Impact of the spatial resolution

To further test the behavior of the model, a second series of simulations has been done for all four values of the jet velocity (i.e. Reynolds and Weber numbers) using degraded meshes, with a lower, following the prescriptions in Tab. 11.8. The time evolution of the density fields is provided in Figs. 11.18 and 11.19, for the three mesh resolutions and for the Reynolds numbers $Re = 1470$ $(We = 4150)$ and $Re = 730$ $(We = 1030)$ respectively.

The two immediate observations are that for the case $Re = 730$ $(We = 1030)$, the mesh resolution has little to no impact and that in the more dynamic case $Re = 1470$ $(We = 4150)$, the interface diffusion, that was merely noticeable with the reference mesh, is largely amplified by the use of a coarser mesh resolution. It goes to the point where a substantial part of the liquid has essentially disappeared from the domain by the end of the simulation for the coarser mesh. Even if the SG model introduces some new terms in the flow equations that can be interpreted as diffusive, its actual expected action is to diffuse the interface when it is submitted to mechanical thinning, but conversely, to become anti-diffusive if the interface is mechanically stretched. From the point of view of the SG model, a diffusion as intense as seen in Fig. 11.18 should only apply if actual thermal diffusion and/or a temperature increase justified the interface to actually become wider. Besides, not only the interface becomes wider but the liquid eventually vanishes while the total mass of fluid is conserved.

A closer attention is given to the temperature time evolution, an example of which is given in Fig. 11.20 for all spatial resolutions at $Re = 1470$ $(We = 4150)$. In the early instants of the simulation and as observed previously for the finest grid, strong temperature oscillations occur for all spatial resolutions close to the interface. A poorer resolution causes the thickness of the region where the temperature increase occurs to be wider. Acoustic noise, *a priori* generated at the interface, is also becoming apparent on the temperature field.

Temperature-density diagrams are plotted in Fig. 11.21. If for the most part, the points remain close to the isothermal straight line at $T_i = 100$ K, the temperature undershoots and overshoots, already noticed in Figs. 11.16 and 11.20, are clearly visible in the diagram and actually occur both uniquely on the vapor side of the interface. A closer analysis has shown that the overshoots occur in the bulk vapor phase whereas the undershoots occurs in the binodal region near low density values. Additional observations can be made from Fig. 11.22 where the relative distribution is given in the temperature-density diagram.
Firstly, contrary to what could have hinted Fig. 11.21, most of the points tend to, not only experience just a very limited temperature increase but even more predominantly, experience a temperature decrease. This could actually have been expected since only the points at the vapor limit of the interface were concerned by the temperature increase.
Secondly, the points in the liquid essentially vanish whereas an important portion of the points migrates towards the inside of the binodal region on the vapor side, this size of said portion increasing with a coarser mesh resolution.

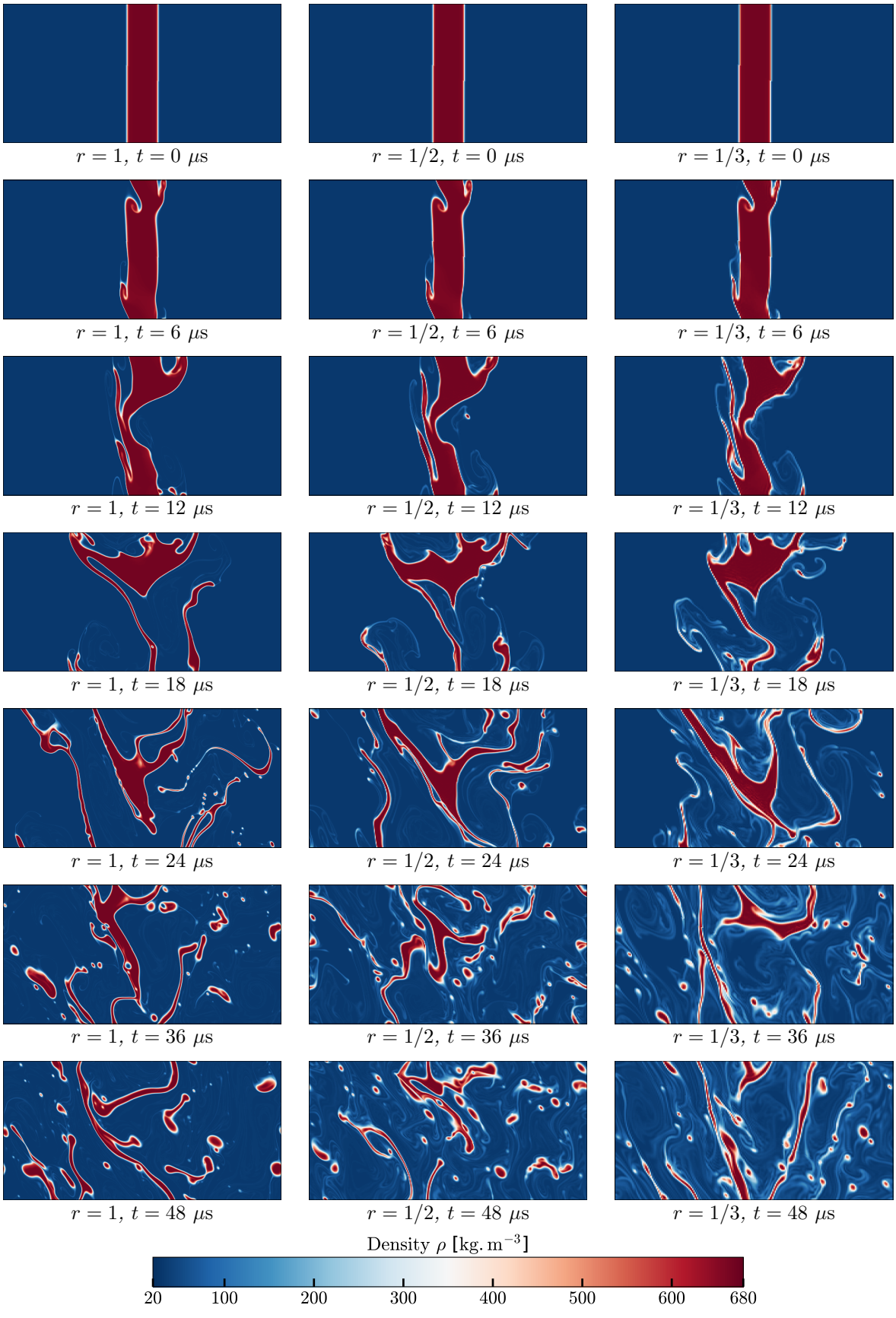

Figure 11.18: *Evolution in time of the density profiles for two-dimensional periodic Nitrogen liquid jets in their vapor. Three cases have been carried out for* $Re = 1470$ $(We = 4150)$ *with the reference thickening factor* $\mathrm{F} = 1000$ *and three different spatial resolutions (left: reference* $r = 1$*, center: coarse* $r = 1/2$*, right: very coarse* $r = 1/3$*).*

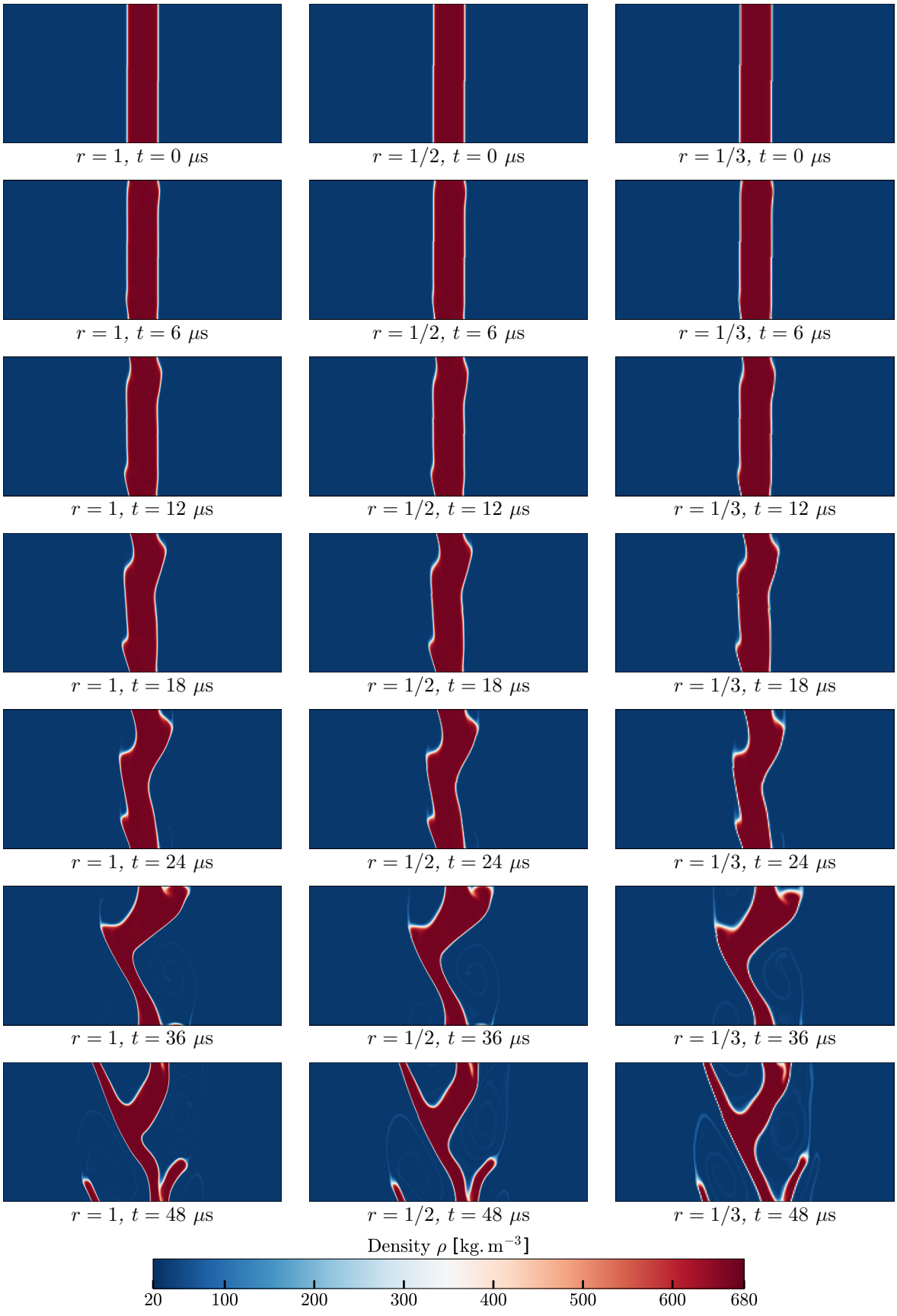

Figure 11.19: *Evolution in time of the density profiles for two-dimensional periodic Nitrogen liquid jets in their vapor. Three cases have been carried out at* $Re = 730$ $(We = 1030)$ *with the reference thickening factor* $\mathrm{F} = 1000$ *and three different spatial resolutions (left: reference* $r = 1$*, center: coarse* $r = 1/2$*, right: very coarse* $r = 1/3$*)*

Figure 11.20: *Evolution in time of the temperature profiles for two-dimensional periodic Nitrogen liquid jets in their vapor. Three cases have been carried out for* $Re = 1470$ $(We = 4150)$ *with the reference thickening factor* $\mathrm{F} = 1000$ *and three different spatial resolutions (left: reference* $r = 1$*, center: coarse* $r = 1/2$*, right: very coarse* $r = 1/3$*)*

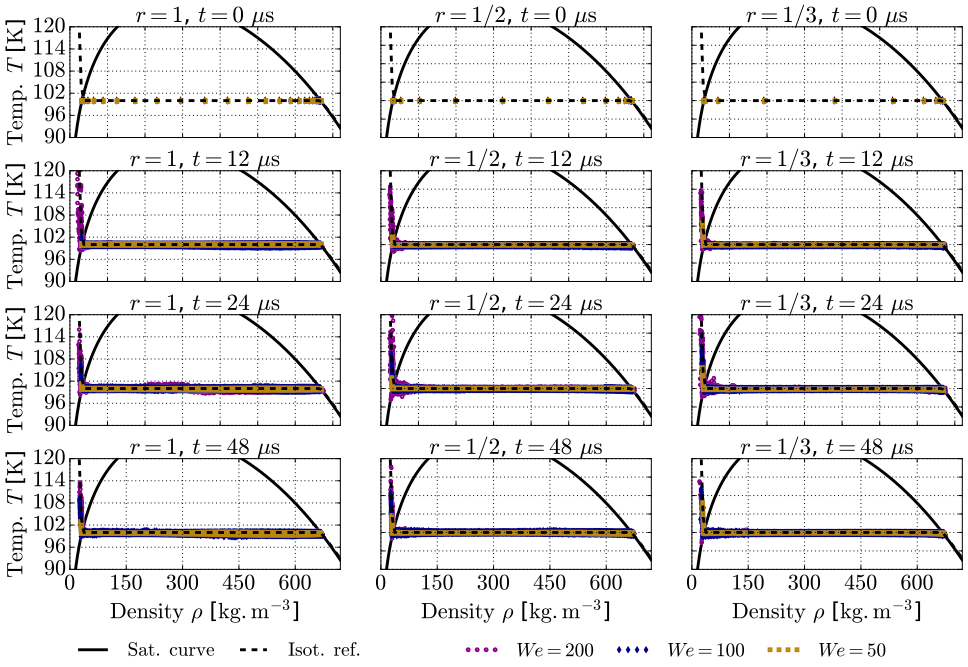

Figure 11.21: *Time evolution of liquid nitrogen jets thermodynamic regime in a temperature-density diagram for different Reynolds numbers using three different spatial resolutions (left: reference $r = 1$, center: coarse $r = 1/2$, right: very coarse $r = 1/3$)*

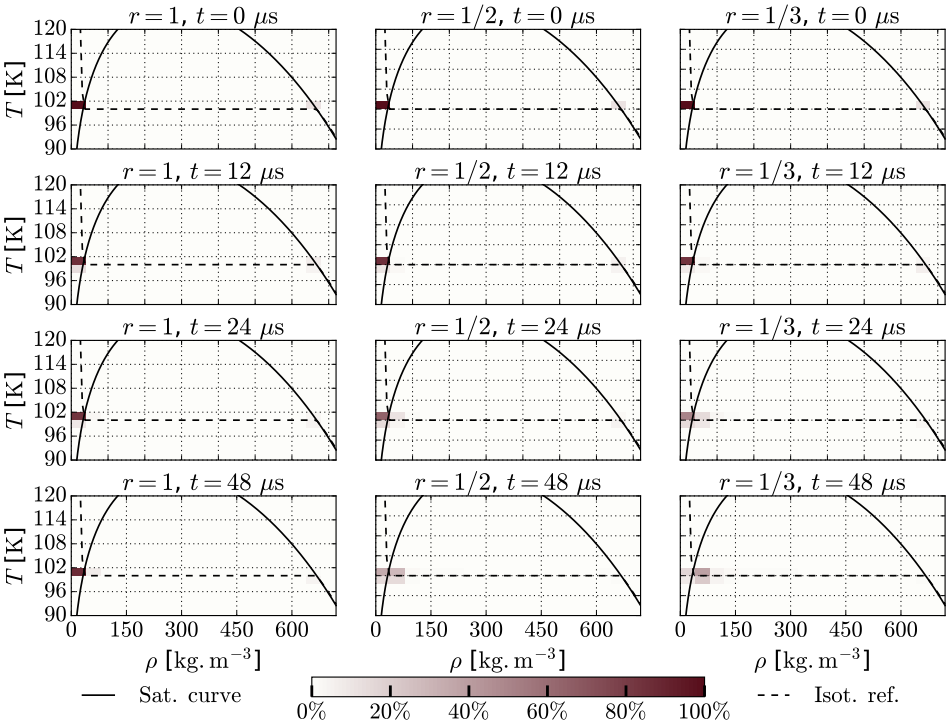

Figure 11.22: *Time evolution of liquid nitrogen jets thermodynamic regime in temperature-density diagram for $Re = 1470$ ($We = 4150$) using three different spatial resolutions (left: reference $r = 1$, center: coarse $r = 1/2$, right: very coarse $r = 1/3$)*

11.2.4 Impact of the thickening coefficient

To complete the tests regarding the behavior of the model, a third series of simulations has been performed for all four values of the jet velocity (i.e. Reynolds and Weber numbers) using the reference mesh resolution and reduced values of thickening coefficients F, following the prescriptions in Tab. 11.8. The time evolution of the density is provided in Fig. 11.24 for the three thickening coefficients, for Reynolds number $Re = 1470$ $(We = 4150)$.

The first observation that can be made is that, comparatively to the result with degraded a mesh resolution shown in Fig. 11.18 for the same Reynolds number, the visual quality of the results is essentially unchanged by the modification of the thickening factor. In particular, the very strong interface diffusion observed for the coarser mesh $r = 1/3$ in Fig. 11.18 is not present in its counterpart case with F = 333 in Fig. 11.24, despite the two approaches leading to the same interface resolution of about three points.
This observation entices that the cause behind the loss of interface spatial resolution is important to consider when evaluating the errors that can occur during the simulation. Indeed, when the overall mesh resolution is lowered, not only the mesh resolution is reduced, leading to more difficulties in the discretization of the capillary terms, but the precision of the numerical scheme jeopardizes altogether the handling of classic diffusion or advection : the system becomes more prone to numerical errors. Conversely, when only the thickening factor is reduced on a maintained mesh resolution, all the classic terms in the Navier-Stokes equations are handled with the same precision and only the discretization of the capillary terms is rendered more tedious by the loss of interface resolution. As clearly showed by Figs. 11.18 and 11.24, the latter is more less detrimental to the quality of the simulation results. The stable quality of the results for different thickening factors can be seen in the temperature and pressure fields, provided in Figs. 11.26 and 11.28 for Reynolds number $Re = 1470$ $(We = 4150)$.

The second observation that can be made is that although the thickening factor has a limited impact on the results visual quality, it has conversely a greater impact on the jet topology than the overall mesh resolution had. Despite the strong interface diffusion, the results in Fig. 11.18 showcase a very visible similarity from one mesh to the other. Essentially, the results for the lower mesh resolutions are "simply diffused" versions of the results on the reference mesh. This similarity seems to not apply anymore for the varying thickening factor. Although the regime of the jet is properly retrieved, as demonstrated in Fig. 11.30 where are presented the density fields for all the Reynolds numbers using the smallest thickening factor F = 333, the aspect of the jet, from one factor to the other, can be seen to strongly vary.
From Fig. 11.24 for $Re = 1470$ $(We = 4150)$, it appears that the lower the thickening factor is, i.e. the thinner the interface is, the smaller are the structures that are created during the atomization. This could be explained by the fact that the sizes of said structures apportion to the interface thickness and cannot appear spontaneously and/or cannot be sustained by the system, thus leading to bigger droplets and thicker filaments for F = 1000. This hypothesis would however require further analysis to be assessed.
Finally, the previous observation can be made at once thanks to Fig. 11.32 where the density fields at $Re = 1470$ $(We = 4150)$ are presented for the two strategies used to lower the interface resolution: a mesh resolution or a thickening factor divided by a factor two to obtain a 5-point interface resolution (results in the leftmost images) and a mesh resolution or a

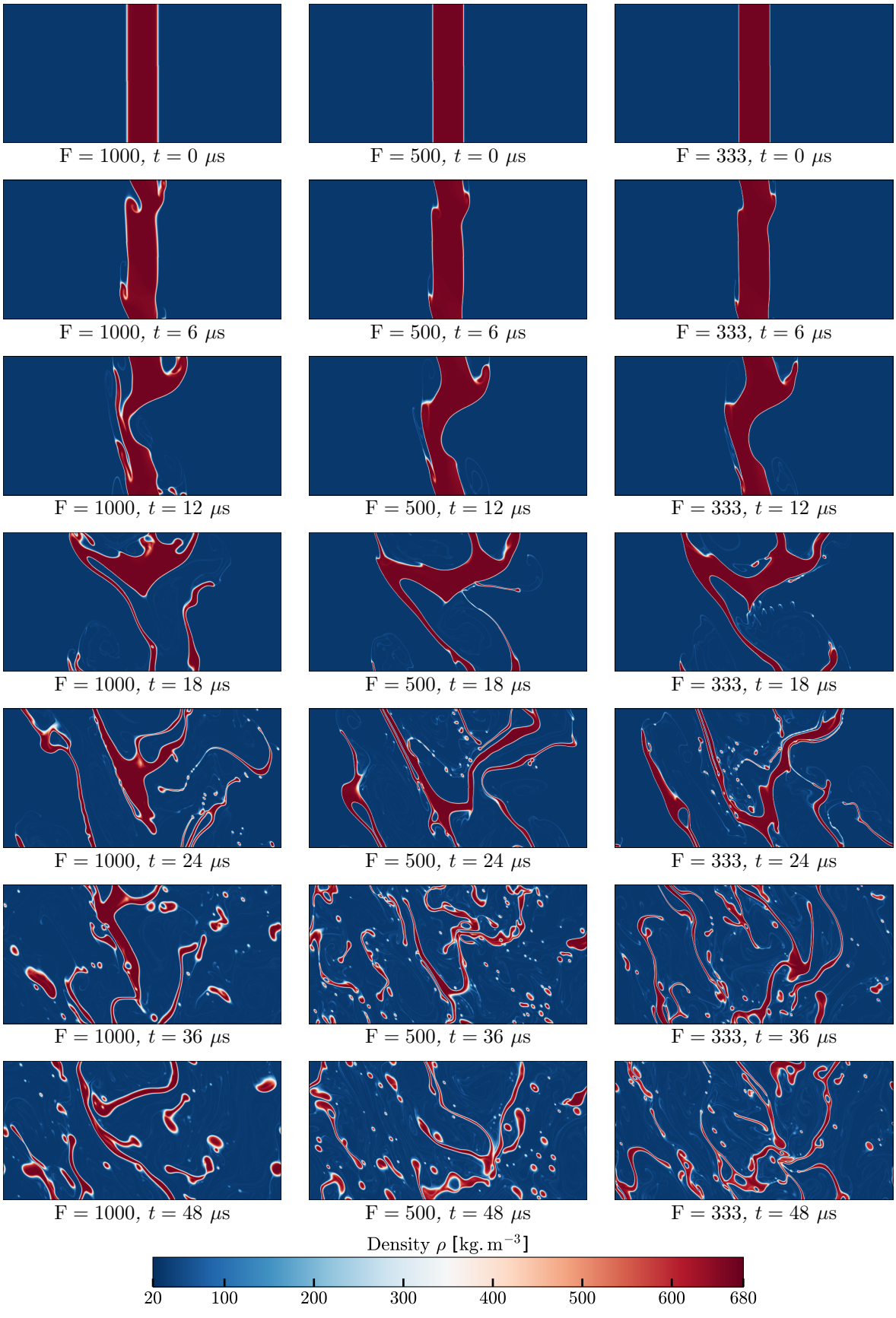

Figure 11.24: *Evolution in time of the density profiles for two-dimensional periodic Nitrogen liquid jets in their vapor. Three cases have been carried out at* $Re = 1470$ *(4150) with the reference spatial resolution and three different thickening factors (left: large* $\mathrm{F} = 1000$*, center: medium* $\mathrm{F} = 500$*, right: low* $\mathrm{F} = 333$*)*

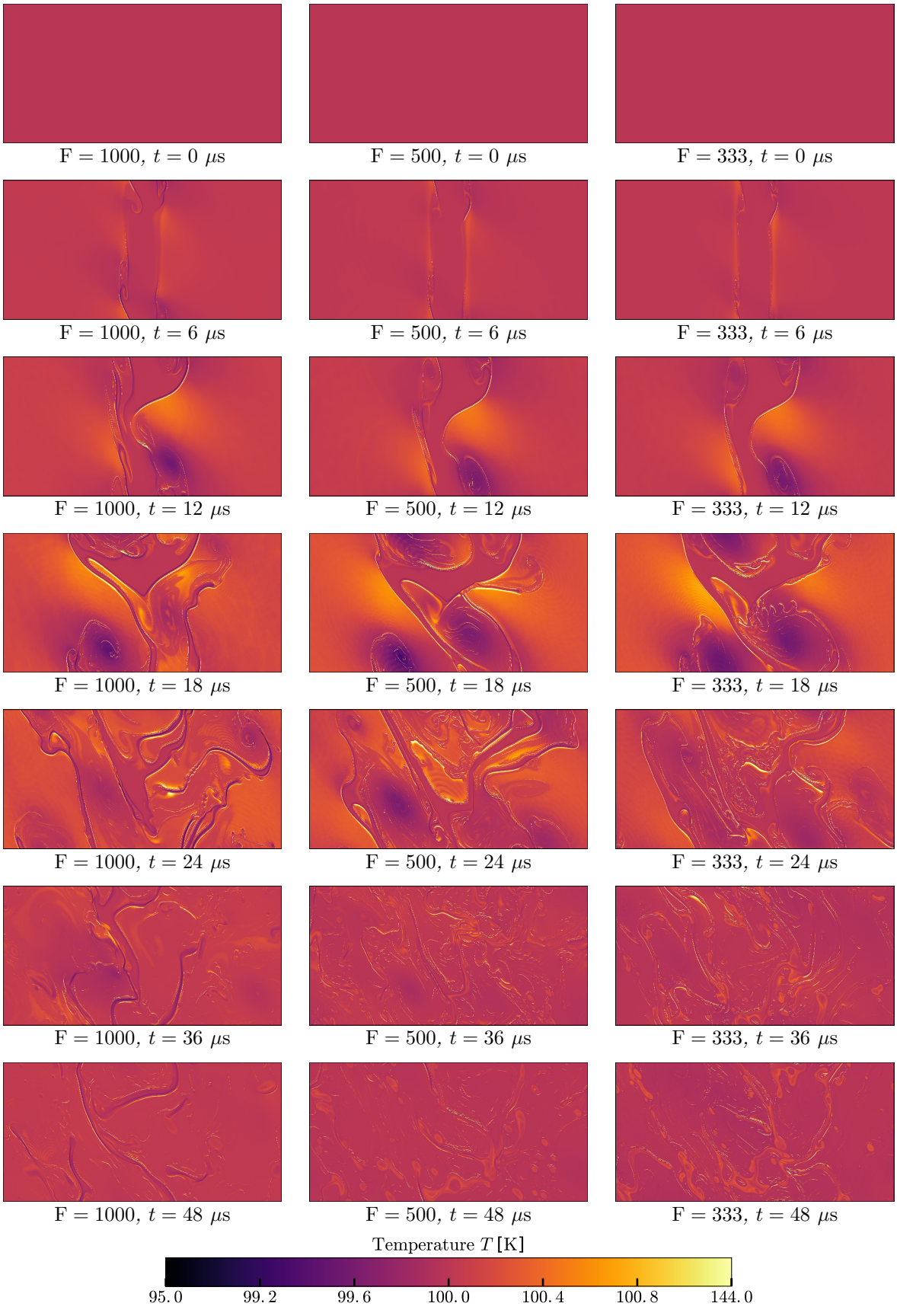

Figure 11.26: *Evolution in time of the temperature profiles for two-dimensional periodic Nitrogen liquid jets in their vapor. Three cases have been carried out at* $Re = 1470$ (4150) *with the reference spatial resolution and three different thickening factors (left: large* $\mathrm{F} = 1000$*, center: medium* $\mathrm{F} = 500$*, right: low* $\mathrm{F} = 333$*)*

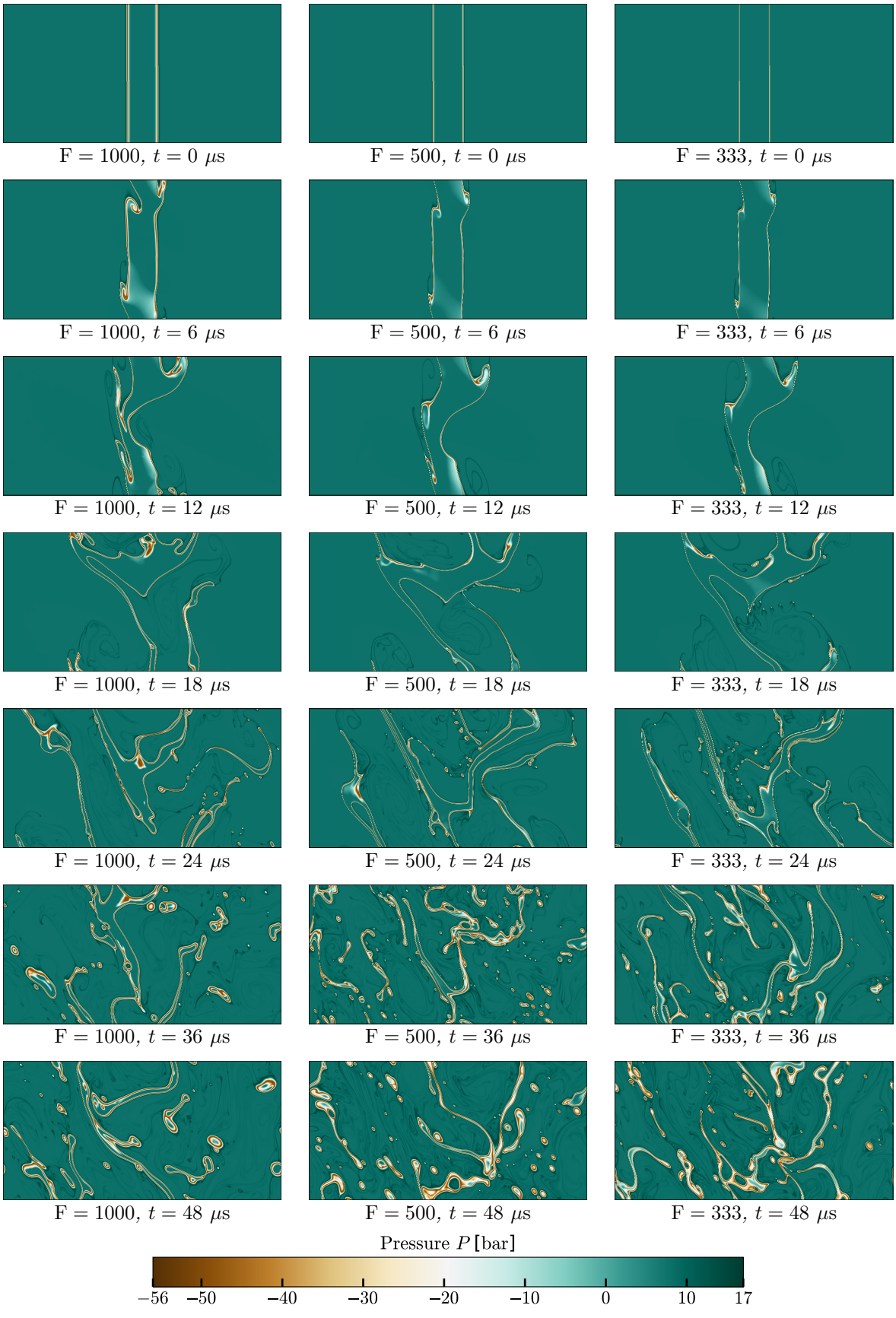

Figure 11.28: *Evolution in time of the pressure profiles for two-dimensional periodic Nitrogen liquid jets in their vapor. Three cases have been carried out at* $Re = 1470$ *(4150) with the reference spatial resolution and three different thickening factors (left: large* $\mathrm{F} = 1000$*, center: medium* $\mathrm{F} = 500$*, right: low* $\mathrm{F} = 333$*)*

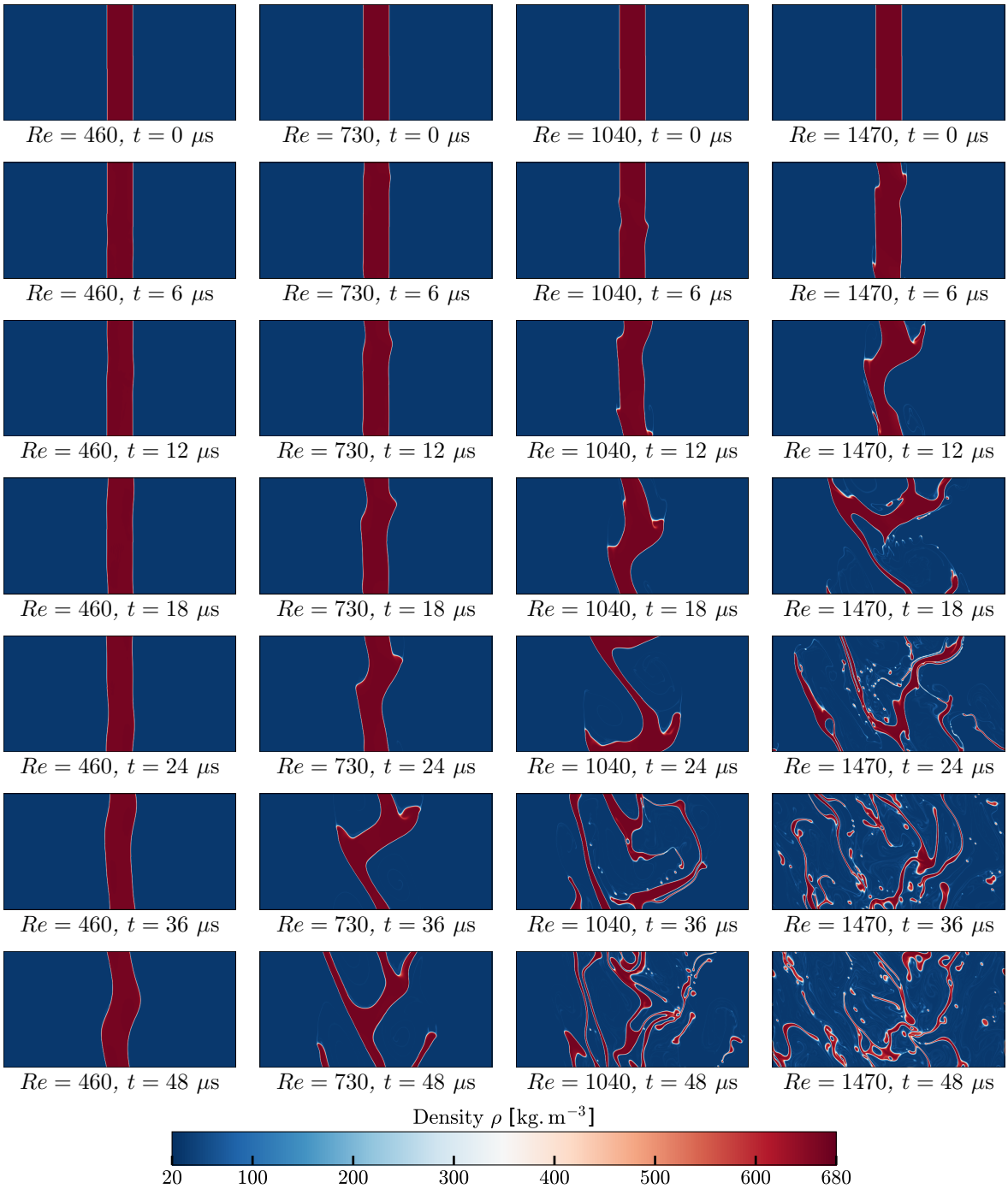

Figure 11.30: *Evolution in time of the density profiles for two-dimensional periodic Nitrogen liquid jets in their vapor. Four cases have been carried out with the reference spatial resolution and a reduced thickening factor* F = 333*, for different Reynolds numbers, from left to right:* $Re = 460$ $(We = 412)$*,* $Re = 730$ $(We = 1030)$*,* $Re = 1040$ $(Re = 46080)$ *and* $Re = 1470$ $(We = 4150)$

thickening factor divided by a factor three to obtain a 3-point interface resolution (results in the rightmost images).

Conclusions on the two-dimensional liquid jets

The simulations performed using different Reynolds numbers have led to results which present a satisfactory qualitative agreement with the experimental observations from Reitz (1978) compiled in Fig. 11.13. The expected undulating to atomization regimes are properly retrieved, the interface separation and recombination is correctly handled and lead to the creation and coalescence of multiple droplets for the concerned regimes.

A convergence analysis, led on two fronts, has shown that the results are very sensitive to the interface resolution. When the interface resolution is reduced due to an overall reduction of the mesh resolution, an excessive diffusion is observed for the lower resolutions at the higher Reynolds numbers while the liquid portion of the fluid completely vanishes. Using thermodynamic diagrams, these two peculiar and presumably erroneous phenomena have been characterized in more details although they remain not fully understood at the time. On the opposite, when the reduced interface resolution is due to a reduced thickening factor used on the same native mesh resolution, the diffusion issue is far less noticeable and from a purely visual criterion, the thickening factor has no definitive impact on the quality of the results. However, where the density fields for different mesh resolutions (with a fixed thickening coefficient) were very similar notwithstanding the diffusion, the same fields showcase more noticeable differences in topology when the thickening factor is changed, all being at a fixed Reynolds number.

Following the theory behind the SG model, points in the binodal region should only exist inside interfaces or subsist for a very short time during out of equilibrium phenomena such as interface stretching or evaporation.
This principle is clearly not respected in these simulations as the majority of the points in the computational domain resides in the binodal region by the end of the simulations. This can be the sign of a limitation of the SG model, but more likely, of an unwanted effect of the TIM. Indeed, the thickening of the interface is also accompanied by an increase of its characteristic thermal and mechanical times of relaxation.
The apparition of points in the binodal region is, to our belief, not incorrect by nature as the case simulated is strongly out of equilibrium. We however suspect the increased relaxation times to allow these points to persist in time where they would normally quickly return to bulk values in more conventional conditions, i.e. with no thickening applied. Unfortunately, testing this hypothesis would require to perform the same simulations without interface thickening, which would not be computationally affordable.

Moreover, it is well known that these two-dimensional simulations can be affected by computational difficulties that do not exist in three dimensions. This is particularly true when surface tension in involved, of which action, strongly related to the interface curvature, has a strongly different effect in three dimensions for such configurations. A three-dimensional simulation could help to provide more insight on the origins of these problematic behaviors if they are still visible at that point. The stable behavior of the jets when the mesh resolution

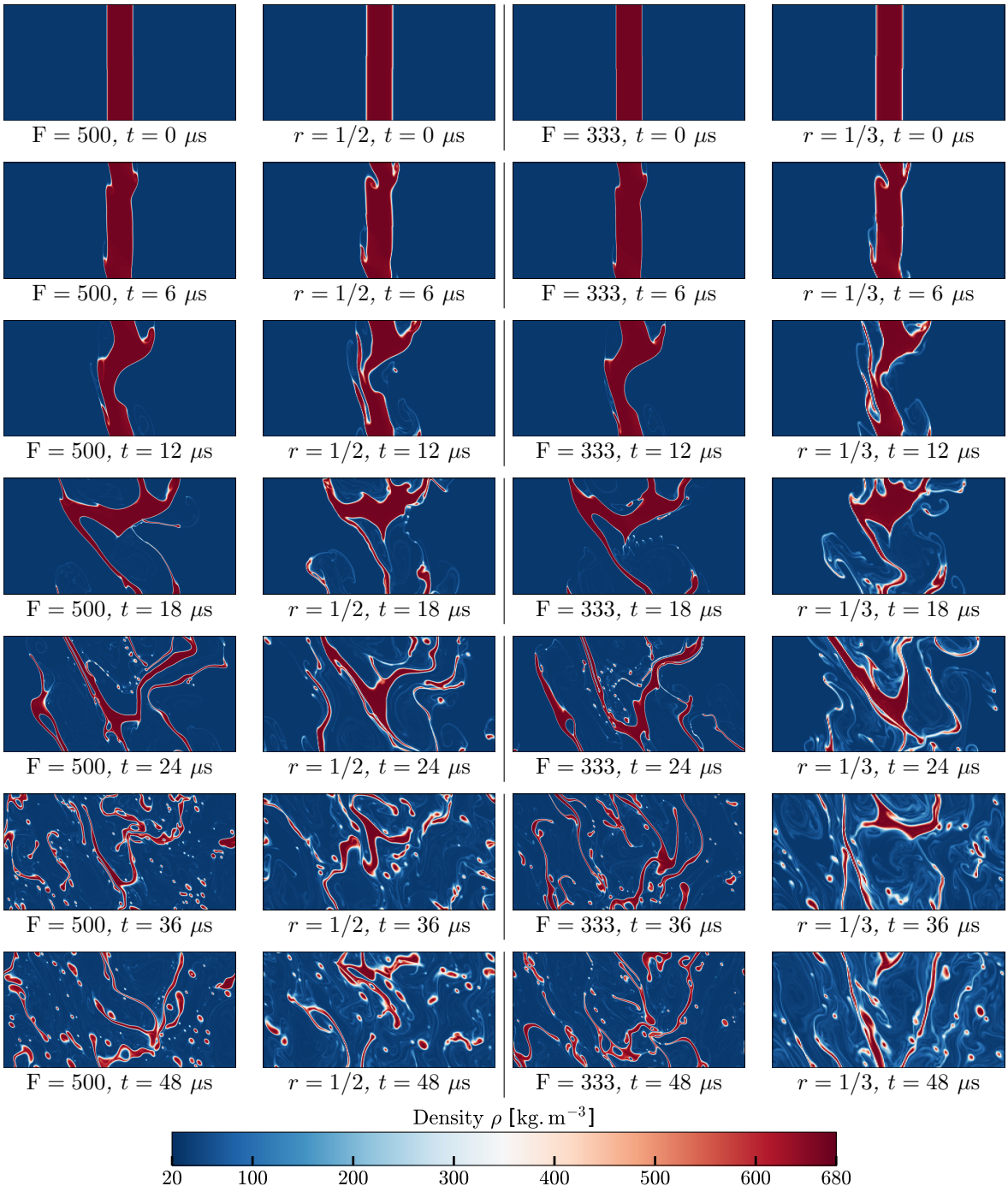

Figure 11.32: *Evolution in time of the density profiles for two-dimensional periodic Nitrogen liquid jets in their vapor at* $Re = 1470$ $(We = 4150)$. *Two thickening factors and two mesh resolutions are used to get the same interface resolutions of five points* (F = 500 / $r = 1/2$, *left images) and three points* (F = 333 / $r = 1/3$, *right images)*

is maintained and the thickening factor is reduced is however as strong argument for both the ability of the TIM to allow access to DNS scale simulations and doing so consistently but moreover, on the ability of the Second Gradient theory to address numerically complex capillary configurations when the spatial resolution is sufficient.

Conclusion

General conclusions

The main objective of this thesis was to assess the ability of the Second Gradient theory to allow two-phase flow simulations with real-gas fluids. The main questioning revolved around the pertinence of this coupled thermodynamical-mechanical model, dedicated to the study of capillary phenomena, in the context of non-reactive single-species Direct Numerical Simulation in an HPC unstructured solver. To achieve this goal and answer the ensuing questions, several actions have been undertaken.

In a first time, the thermodynamics of real-gas flows has been thoroughly studied to better model the non-linear molecular interactions that occur at high pressure and/or high temperature, conditions reminiscent of cryogenic rocket engines. Using cubic equations of state, in particular the Soave-Redlich-Kwong equation, that have been proven to provide precise results at a reasonable complexity level and computational cost, the full thermodynamics for a single species has been derived.

In a second time, the theoretical foundations behind the Second Gradient theory has been fleshed out and consistently justified. An emphasis has been put on linking the multiple results that have contributed to shape the current formulation of the model. The intrinsic connection between the thermodynamic description of van der Waals, the mechanical approach of Korteweg and the unstationary modeling of Cahn & Hilliard has been highlighted. Additionally, the same investigation and bibliographical work has been done for several more classic two-phase flow modeling methods in order to provide grounds for theoretical comparison with the Second Gradient model and a better insight into the mechanics of these methods.

By combining the real gas modeling from the cubic equation of state and the thermodynamical-mechanical description of capillary phenomena offered by the Second Gradient model, the full set of Navier-Stokes equations have been obtained. The complete model and equations have been successfully implemented into the solver AVBP. New high order derivative terms have appeared in the different fluxes and have proven to be challenging to handle, from theoretical and numerical points of view. Classic theoretical tools for numerical analysis failed to provide a complete characterization of the new set of equations which impended the access to precious practical information to safely conduct the simulations such as the formulation of the boundary conditions and the time step conditions for explicit advection schemes. In parallel, the consistent discretization of these terms has required smart reinvestment of the schemes in AVBP as the solver was not readily equipped to handle such high order derivatives.

The implementation of the model has been validated thermodynamically on static configurations, qualitatively on simplified mono-dimensional cases and quantitatively on canonical two-dimensional configurations. A systematic numerical investigation has permitted to unveil key parameters needed to ensure the stability of the simulations, such as the time step condition or the minimal spatial resolution needed for the interfaces. The model has been shown to be very sensitive to numerical noise which was often the cause of temperature under/overshoots and simulation crashes.
Simulations solving solely the Euler equations are notoriously tedious to stabilize and often rely on the intrinsic dissipation embedded in the numerical schemes that are used to provide the required stabilization. To ensure the precision of the calculations, more so given the particularly stiff terms related to the capillary stresses, and to compel with the available schemes in AVBP, a Galerkin Runge-Kutta discretization has been used. This high order scheme is totally non-dissipative and centered, a combination that renders it very pron to oscillatory numerical errors, which have been observed in our simulations. Thus, we firmly believe that these errors, particularly visible in the temperature field, are more so a matter of numerical implementation that thermodynamic behavior of the model. This intuition has been reinforced by the substantial gain in stability that has been granted by the addition of dissipation, in the form of viscosity or thermal diffusion, that has come with the switch to Navier-Stokes equations.
Classic point-to-point errors have been dealt with using the high order filter of AVBP. The artificial viscosity, already regularly used in AVBP, has been occasionally required but limited to the most demanding cases with violent interface dynamics or when very high values of thickening coefficient have been used. For these latter cases, we suspect that the thickening might adversely impact the stiffness of the interface, due to reduced gradients, and in the same time, reduce its propensity to resist physical or numerical noise which, in turn, could diminish its stability. Nonetheless, the taking into account of all these possibilities and limitations has permitted to successfully simulate two-dimensional oscillating planar interfaces and deformed droplets solving the full set of compressible Navier-Stokes equations, which had never been done using this model so far, to the best of our knowledge. The comparison with the available theory, when possible, has led to remarkable results.

As expected beforehand, the SG model in its native formulation predicted interface widths of multiple orders of magnitude lower than the typical mesh sizes used for practical applications, even in DNS configurations. Part of the motivation behind this work was also to provide a mean to address this hurdle that rendered the SG model unusable even for academic studies. To that effect, the Thickened Interface Method (TIM) has been derived to thicken an interface in a thermodynamically consistent manner while maintaining its surface tension and therefore its macroscopic behavior.
The TIM has been submitted to the same systematic testing applied to the native SG model and invariably responded with the expected behavior on simplified cases. Furthermore, quantitative comparisons have allowed to confirm that the method indeed preserves the surface tension and the macroscopic behavior of the interface. Finally, the method has been used to simulate more practical configurations, two dimensional periodic jets and three-dimensional colliding droplets. The results for different Weber number showed a good agreement with experimental results.

The previously mentioned results have laid ground, that we trust to be solid, for further studies involving the Second Gradient theory and have established one of the first path towards the realization of fully compressible, non-isothermal, turbulent simulations with real gas in sub-critical conditions accounting for capillary phenomena. With these encouraging results have also arisen several issues that confirm the substantial amount of work that remains ahead for this model to become a conceivable industrial tool for real gas two-phase flow simulations.

Regarding the native SG model, for some configurations, in particular the oscillating planar interfaces, the switch from an isothermal to a non-isothermal setting caused a strong modification of the interface behavior. More specifically for the planar interfaces, the oscillations that were sustained in the isothermal cases, were unequivocally damped in the non-isothermal cases, all other things being equal.

The simulations using the TIM also led to some questioning.
When simulating two-dimensional nitrogen liquid jets, a strong diffusion of the interface has been observed with an abundant number of points in the computational domain falling into the binodal region. Although amplified by a poorer spatial resolution, this phenomenon is still prominent for well resolved interfaces, hinting a more profound issue with the TIM.

Perspectives

Overall, the SG model and the TIM have showcased an undeniable ability to properly describe the thermodynamic and mechanical behavior of an interface and the ability to consistently thicken said interface. Together, they have permitted to conduct multiple qualitative and quantitative simulations with very promising success for DNS. However, there is still plenty of room for improvement in this regard.

The brief theoretical characterization of the native SG equations initiated in Chap. 8 could be completed to gain better understanding on the model behavior and assess the well-posedness of the associated mathematical problem. This will prove useful to devise adapted numerical methods as well as properly derived boundary conditions. In particular, the sometimes unexpected behavior showcased by the model in some simulations leads us to believe that the unconventional high order derivative terms that appear in the expression of the new fluxes should be discretized with specifically designed schemes to ensure a full discrete consistency. We believe these questions to be pivotal for future work with this model.

The minimal number of points needed in the interface to properly retrieve the macroscopic fluid behavior is theoretically four but has been observed, in our simulations, to rather be positioned between five or six in practice. Despite being very encouraging, this number is still vastly superior to the two to three points used in more classic methods like the Level- Set or the Volume-of-Fluid. Efforts should be made to further reduce this number if the SG model pretends to become competitive in the future. The most likely explanation for this required resolution is that the steep density and pressure profiles complicate the evaluation of their derivatives even when using high order schemes.

We also noticed that, even for single-species configurations, the TIM still needs further development. The excessive interface diffusion observed for the two-dimensional jets could be permitted by a unwanted modification of the characteristic time needed by the interface to return to its equilibrium profile, which could have been caused by the TIM. Besides, the impact of the TIM on the diffusion coefficients (for that matter, the impact of the native SG model also), i.e. the viscosity and the thermal conduction coefficient, has been discarded in this study but is an important issue that need to be addressed.

Finally, the investigations of both the SG model and the TIM should also be broaden to multi-species configurations so as to simulate reactive cases in the future. The work done in Gaillard (2015) showed that the extension to such cases is possible but not trivial and requires additional modeling efforts. The formulation of the TIM should allow a theoretical adaptation to multi-species flows easier than with the thickening methods previously developed in Jamet (1998) that rely on an *a priori* shape for the chemical potential profile in the interface. In particular, its application can be made independent to the fluid composition. However the consistency of this extension does not seem to be ensured straightforwardly.

Appendix A

Usefull mathematical results

A.1 Results for linear and tensorial algebra

A.1.1 Definitions

Let $\mathcal{B}(\boldsymbol{e}_i)_{i=1,3}$ a direct orthonormal basis of $\mathbb{R}^3$. Here, $\mathbb{R}^3$ and its dual space will not be differentiated. By definition, a tensor $\mathbf{T}$ of order $n > 1$ is a linear application which, to any vector $\boldsymbol{x}$ of $\mathbb{R}^3$, associates a tensor of order $n-1$ noted $\mathbf{T}(\boldsymbol{x})$ or $\mathbf{T} \cdot \boldsymbol{x}$:

$$\mathbf{T} \longrightarrow \mathbf{T}(\boldsymbol{x}) = \mathbf{T} \cdot \boldsymbol{x} \tag{A.1}$$

By convention, a tensor of order 0 is a scalar. A tensor of order 1 is a vector and a tensor of order 2 is a matrix as they are classically defined. The order of the tensor gives the number of indexes required to describe its components.

A.1.2 Operations

A.1.2.1 Addition

Tensor can be added if they are of the same order. Let $\mathbf{A}$ and $\mathbf{B}$ two tensors of order n, the addition of $\mathbf{A}$ and $\mathbf{B}$ is a tensor $\mathbf{C}$ noted $\mathbf{A} + \mathbf{B}$ of order n such as:

$$\mathbf{C} = \mathbf{A} + \mathbf{B} \quad \text{with} \quad \mathrm{C}_{i_1 i_2 \cdots i_k \cdots i_n} = \mathrm{A}_{i_1 i_2 \cdots i_k \cdots i_n} + \mathrm{B}_{i_1 i_2 \cdots i_k \cdots i_n} \tag{A.2}$$

A.1.2.2 Outer product $\otimes$

Let $\mathbf{A}$ and $\mathbf{B}$ two tensors respectively of order $n > 0$ and $m > 0$, the outer product of $\mathbf{A}$ and $\mathbf{B}$ is a tensor $\mathbf{C}$ of order $n + m$ noted $\mathbf{A} \otimes \mathbf{B}$ such as:

$$\mathbf{C} = \mathbf{A} \otimes \mathbf{B} \quad \text{with} \quad \mathrm{C}_{i_1 i_2 \cdots i_n j_1 j_2 \cdots j_m} = \mathrm{A}_{i_1 i_2 \cdots i_n} \mathrm{B}_{j_1 j_2 \cdots j_m} \tag{A.3}$$

For instance, the outer product of two vectors $\boldsymbol{a}$, $\boldsymbol{b}$ will be a matrix $\boldsymbol{C}$ such as

$$C_{ij} = (\boldsymbol{a} \otimes \boldsymbol{b})_{ij} = a_i b_j$$

The outer product of a matrix $\boldsymbol{A}$ and a vector $\boldsymbol{b}$ will be a tensor of order 3 $\underline{\underline{\underline{\mathbf{C}}}}$ such as

$$\mathrm{C}_{ijk} = (\boldsymbol{A} \otimes \boldsymbol{b})_{ijk} = \mathrm{A}_{ij} b_k$$

The outer product of a vector $\boldsymbol{a}$ and a matrix $\boldsymbol{B}$ will be a tensor of order 3 $\underline{\underline{\underline{\mathbf{C}}}}$ such as

$$\mathrm{C}_{ijk} = (\boldsymbol{a} \otimes \boldsymbol{B})_{ijk} = a_i B_{jk}$$

The outer product of two matrices $\boldsymbol{A}$ and $\boldsymbol{B}$ will be a tensor of order 4 $\underline{\underline{\underline{\underline{\mathbf{C}}}}}$ such as

$$\mathrm{C}_{ijkl} = (\boldsymbol{A} \otimes \boldsymbol{B})_{ijkl} = A_{ij} B_{kl}$$

A.1.2.3 Inner products ·

Let $\mathbf{A}$ and $\mathbf{B}$ two tensors respectively of order $n > 0$ and $m > 0$, the inner product of $\mathbf{A}$ and $\mathbf{B}$ is a tensor $\mathbf{C}$ of order $n + m - 2$ noted $\mathbf{A} \cdot \mathbf{B}$ such as:

$$\mathbf{C} = \mathbf{A} \cdot \mathbf{B} \quad \text{with} \quad \mathrm{C}_{i_1 i_2 \cdots i_{n-1} j_2 \cdots j_m} = \sum_k \mathrm{A}_{i_1 i_2 \cdots i_{n-1} k} \mathrm{B}_{k j_2 \cdots j_m} \tag{A.4}$$

For instance, the inner product of two vectors $\boldsymbol{a}$, $\boldsymbol{b}$ will be a scalar c such as:

$$c = \boldsymbol{a} \cdot \boldsymbol{b} = a_i b_i$$

It is the usual scalar product between two vectors.
The inner product of a matrix $\boldsymbol{A}$ and a vector $\boldsymbol{b}$ will be a vector $\boldsymbol{c}$ such as:

$$\boldsymbol{c}_i = (\boldsymbol{A} \cdot \boldsymbol{b})_i = A_i j b_j$$

It is the classic matrix-vector multiplication.
The inner product of two matrices $\boldsymbol{A}$ and $\boldsymbol{B}$ will be a matrix $\mathbf{C}$ such as:

$$\mathrm{C}_{ij} = (\boldsymbol{A} \cdot \boldsymbol{B})_{ij} = A_{ik} B_{kj}$$

It is the classic inner product for two matrices.
Let $\mathbf{A}$ and $\mathbf{B}$ two tensors respectively of order $n > 1$ and $m > 1$, the double inner product of $\mathbf{A}$ and $\mathbf{B}$ is a tensor $\mathbf{C}$ of order $n + m - 4$ noted $\mathbf{A} : \mathbf{B}$ such as:

$$\mathbf{C} = \mathbf{A} : \mathbf{B} \quad \text{with} \quad \mathrm{C}_{i_1 i_2 \cdots i_{n-2} j_3 \cdots j_m} = \sum_k \sum_l \mathrm{A}_{i_1 i_2 \cdots i_{n-2} k l} \mathrm{B}_{l k j_3 \cdots j_m} \tag{A.5}$$

In a more general way, it is possible to define a inner product of certain order r between two tensor $\mathbf{A}$ and $\mathbf{B}$ of order at least r, the result will be a tensor of order $n + m - 2r$ (where n and m are the order of $\mathbf{A}$ and $\mathbf{B}$) noted $\mathbf{A} \left(\cdot\right)^r \mathbf{B}$ such as:

$$\mathbf{C} = \mathbf{A} \left(\cdot\right)^r \mathbf{B} \quad \text{with} \quad \mathrm{C}_{i_1 i_2 \cdots i_{n-r} j_{r+1} \cdots j_m} = \sum_{k_r} \cdots \sum_{k_1} \mathrm{A}_{i_1 i_2 \cdots i_{n-k} k_r k_{r_1} \cdots k_1} \mathrm{B}_{k_1 \cdots k_{r_1} k_r j_3 \cdots j_m} \tag{A.6}$$

For instance the, double inner product between two matrices $\boldsymbol{A}$ and $\boldsymbol{B}$ is a scalar c such as:

$$c = \boldsymbol{A} : \boldsymbol{B} = A_{ij} B_{ji}$$

As a matter of fact, $\boldsymbol{A} : \boldsymbol{B} = \mathrm{tr}\left((\boldsymbol{A} \cdot \boldsymbol{B})\right)$ in that case. The triple inner product between a third order tensor $\underline{\underline{\underline{\mathbf{A}}}}$ and a fourth order tensor $\underline{\underline{\underline{\underline{\mathbf{B}}}}}$ is a vector $\boldsymbol{c}$ such as:

$$c_i = \left(\underline{\underline{\underline{\mathbf{A}}}} \vdots \underline{\underline{\underline{\underline{\mathbf{B}}}}}\right)_i = \sum_l \sum_k \sum_j \mathrm{A}_{lkj} \mathrm{B}_{jkli}$$

A.1.2.4 Cross product $\times$

Let $\boldsymbol{a}$ and $\boldsymbol{b}$ be two vectors of $\mathbb{R}^3$, the cross product (or vector product) of $\boldsymbol{a}$ and $\boldsymbol{b}$ is a vector $\boldsymbol{c}$ such as:

$$\boldsymbol{c} = \boldsymbol{a} \times \boldsymbol{b} = (a_2 b_3 - a_3 b_2)\, \boldsymbol{e}_1 + (a_3 b_1 - a_1 b_3)\, \boldsymbol{e}_2 + (a_1 b_2 - a_2 b_1)\, \boldsymbol{e}_3 \tag{A.7}$$

A.2 Result for differential calculus

A.2.1 Differential operators

In the following, the formal "nabla" differential operator will be noted using a bold font $\boldsymbol{\nabla}$ and is not to be confused with the "nabla vector" noted $\vec{\nabla}$ and defined by:

$$\vec{\nabla} = \frac{\partial}{\partial x_1}\boldsymbol{e}_1 + \frac{\partial}{\partial x_2}\boldsymbol{e}_2 + \frac{\partial}{\partial x_3}\boldsymbol{e}_3 = \left(\frac{\partial}{\partial x_1}, \frac{\partial}{\partial x_2}, \frac{\partial}{\partial x_3}\right)^{\mathrm{T}} \tag{A.8}$$

A.2.1.1 Gradient

The gradient of a tensor $\mathbf{T}$ of order n is a tensor of order $n+1$ noted $\boldsymbol{\nabla}\mathbf{T}$ of which coordinates are the covariant derivatives of the coordinates of the tensor $\mathbf{T}$. Practically, in the basis $\mathcal{B}\left(\boldsymbol{e}_i\right)_{i=1,3}$ it is given by:

$$\left(\boldsymbol{\nabla}\mathbf{T}\right)_{i_1 \cdot i_n j} = \frac{\partial \mathrm{T}_{i_1 \cdot i_n}}{\partial x_j} \tag{A.9}$$

Using the vector $\vec{\nabla}$, the gradient can be defined as $\boldsymbol{\nabla}\mathbf{T} = \mathbf{T} \otimes \vec{\nabla}$.

For instance the gradient of a scalar a is a vector $\boldsymbol{\nabla} a$ such as $\left(\boldsymbol{\nabla} a\right)_i = \dfrac{\partial a}{\partial x_i}$.

The gradient of a vector $\boldsymbol{u}$ is a matrix $\boldsymbol{\nabla}\boldsymbol{u}$ such as $\left(\boldsymbol{\nabla}\boldsymbol{u}\right)_{ij} = \dfrac{\partial u_i}{\partial x_j}$. This is the jacobian matrix of the associated vectorial application.

The gradient of a matrix $\boldsymbol{M}$ will be a third order tensor such as $\left(\boldsymbol{\nabla}\boldsymbol{M}\right)_{ijk} = \dfrac{\partial M_{ij}}{\partial x_k}$, and so forth...

A.2.1.2 Divergence

The divergence of a tensor $\mathbf{T}$ of order $n > 0$ is a tensor of order $n-1$ noted $\boldsymbol{\nabla} \cdot \mathbf{T}$ of which coordinates are the covariant derivatives of the coordinates of $\mathbf{T}$ relatively to its last contravariant index. Practically, in the basis $\mathcal{B}\left(\boldsymbol{e}_i\right)_{i=1,3}$ it is given by:

$$\left(\boldsymbol{\nabla} \cdot \mathbf{T}\right)_{i_1 \cdots i_{n-1}} = \sum_k \frac{\partial \mathrm{T}_{i_1 \cdots i_{n-1} k}}{\partial x_k} \tag{A.10}$$

Using the vector $\vec{\nabla}$, the divergence can be defined as $\boldsymbol{\nabla} \cdot \mathbf{T} = \mathbf{T} \cdot \vec{\nabla}$.

The divergence of a vector $\boldsymbol{u}$ is a scalar given by $\boldsymbol{\nabla} \cdot \boldsymbol{u} = \dfrac{\partial u_1}{\partial x_1} + \dfrac{\partial u_2}{\partial x_2} + \dfrac{\partial u_3}{\partial x_3}$. One can notice that $\boldsymbol{\nabla} \cdot \boldsymbol{u} = \mathrm{tr}\left(\boldsymbol{\nabla}\boldsymbol{u}\right)$

The divergence of a matrix $\boldsymbol{M}$ is a vector given by $\left(\boldsymbol{\nabla} \cdot \boldsymbol{M}\right)_i = \dfrac{\partial M_{ij}}{\partial x_j}$

A.2.1.3 Rotational

The rotational of a vector $\boldsymbol{u}$ is a vector noted $\boldsymbol{\nabla} \times \boldsymbol{u}$ of which coordinates are given by:

$$(\boldsymbol{\nabla} \times \boldsymbol{u})_1 = \frac{\partial u_3}{\partial x_2} - \frac{\partial u_2}{\partial x_3} \tag{A.11}$$

$$(\boldsymbol{\nabla} \times \boldsymbol{u})_2 = \frac{\partial u_1}{\partial x_3} - \frac{\partial u_3}{\partial x_1} \tag{A.12}$$

$$(\boldsymbol{\nabla} \times \boldsymbol{u})_3 = \frac{\partial u_2}{\partial x_1} - \frac{\partial u_1}{\partial x_2} \tag{A.13}$$

Using the vector $\vec{\nabla}$, the divergence can be defined as $\boldsymbol{\nabla} \times \boldsymbol{u} = \vec{\nabla} \times \boldsymbol{u}$.

A.2.1.4 Laplacian

The laplacian of a tensor $\mathbf{T}$ is a tensor noted $\boldsymbol{\Delta}\mathbf{T}$ of the same order given by:

$$\boldsymbol{\Delta}\mathbf{T} = \boldsymbol{\nabla} \cdot (\boldsymbol{\nabla}\mathbf{T}) \tag{A.14}$$

The laplacian is a second order differential operator

A.2.2 Transport theorems

A.2.2.1 Transport theorem in 1D (Leibniz integral rule)

Let f be a function depending on both time and space, defined over the domain $\mathbb{R}_+ \times I$ where I is an interval of $\mathbb{R}$. One wants to evaluate the time variations of the integral of $f(t,x)$ over the segment $s(t) = [r(t), l(t)]$. By definition:

$$\frac{d}{dt} \int_{l(t)}^{r(t)} f(t,x)\, dx = \lim_{\Delta t \to 0} \frac{1}{\Delta t} \left[\int_{l(t+\Delta t)}^{r(t+\Delta t)} f(t+\Delta t, x)\, dx - \int_{l(t)}^{r(t)} f(t,x)\, dx \right] \tag{A.15}$$

Under the assumption that function f is regular enough from an analytical point of view (to use the Taylor-Lagrange inequality and to use the limit under the integral sign), one can derive the mono-dimensional transport theorem, also known as the Leibniz integral rule, that states:

$$\frac{d}{dt} \int_{l(t)}^{r(t)} f(t,x)\, dx = \int_{l(t)}^{r(t)} \frac{\partial f}{\partial t}(t,x)\, dx + \frac{db}{dt}(t)\, f(t, b(t)) - \frac{da}{dt}(t)\, f(t, a(t)) \tag{A.16}$$

A.2.2.2 Transport theorem in higher dimensions

The Leibniz integral rule can be extended to two or three dimensions, although its proof becomes technical and will not be given here. This rule is often reformulated when used in three dimensions to study fluid dynamics and is referred to as the Reynolds transport theorem. Let $f(t, \boldsymbol{x})$ be a scalar field depending on both time and space, defined over the $\mathcal{V}$ and let $\mathcal{V}_A(t)$ be an arbitrary region of $\mathcal{V}$. This region, supposed to have a boundary surface $\mathcal{A}_A(t)$,

may be moving/deforming with time, $\boldsymbol{w}_A(t)$ and $\boldsymbol{n}_A(t)$ being respectively the velocity of and the outer the normal to the surface $\mathcal{A}_A(t)$. The transport theorem is:

$$\frac{d}{dt}\int\limits_{\mathcal{V}_A(t)} f(t,\boldsymbol{x})\,d\mathcal{V} = \int\limits_{\mathcal{V}_A(t)} \frac{\partial f}{\partial t}(t,\boldsymbol{x})\,d\mathcal{V} + \int\limits_{\mathcal{A}_A(t)} f(t,\boldsymbol{x})\,\boldsymbol{w}_A(t)\cdot\boldsymbol{n}_A(t)\,d\mathcal{A} \tag{A.17}$$

Using Green's theorem in Eq. (A.72a) it becomes:

$$\frac{d}{dt}\int\limits_{\mathcal{V}_A(t)} f(t,\boldsymbol{x})\,d\mathcal{V} = \int\limits_{\mathcal{V}_A(t)} \left[\frac{\partial f}{\partial t}(t,\boldsymbol{x}) + \boldsymbol{\nabla}\cdot(f\boldsymbol{w}_A)\right] d\mathcal{V} \tag{A.18}$$

When applied to a fixed region $\mathcal{V}_A$ ($\boldsymbol{w}_A(t)=\mathbf{0}$), it becomes:

$$\frac{d}{dt}\int\limits_{\mathcal{V}_A} f(t,\boldsymbol{x})\,d\mathcal{V} = \int\limits_{\mathcal{V}_A} \frac{\partial f}{\partial t}(t,\boldsymbol{x})\,d\mathcal{V} \tag{A.19}$$

When applied to a material region of the fluid $\mathcal{V}_M(t,\boldsymbol{x})$ of which boundary surface velocity matches the velocity of the fluid $\mathbf{v}$, it becomes

$$\frac{d}{dt}\int\limits_{\mathcal{V}_M(t)} f(t,\boldsymbol{x})\,d\mathcal{V} = \int\limits_{\mathcal{V}_M(t)} \frac{\partial f}{\partial t}(t,\boldsymbol{x})\,d\mathcal{V} + \int\limits_{\mathcal{A}_M(t)} f(t,\boldsymbol{x})\,\mathbf{v}(t)\cdot\boldsymbol{n}(t)\,d\mathcal{A} \tag{A.20}$$

$$\frac{d}{dt}\int\limits_{\mathcal{V}_M(t)} f(t,\boldsymbol{x})\,d\mathcal{V} = \int\limits_{\mathcal{V}_M(t)} \left[\frac{\partial f}{\partial t}(t,\boldsymbol{x}) + \boldsymbol{\nabla}\cdot(f\mathbf{v})\right] d\mathcal{V} \tag{A.21}$$

For a material region $\mathcal{V}_M(t,\boldsymbol{x})$ and an arbitrary region $\mathcal{V}_A(t,\boldsymbol{x})$ that coincide at instant t, it becomes:

$$\frac{d}{dt}\int\limits_{\mathcal{V}_M(t)} f(t,\boldsymbol{x})\,d\mathcal{V} = \frac{d}{dt}\int\limits_{\mathcal{V}_A(t)} f(t,\boldsymbol{x})\,d\mathcal{V} + \int\limits_{\mathcal{A}_A(t)} f(t,\boldsymbol{x})\,(\mathbf{v}-\boldsymbol{w}_A)(t)\cdot\boldsymbol{n}(t)\,d\mathcal{A} \tag{A.22}$$

A.2.3 Differential relationships

A.2.3.1 Partial derivatives

Let three functions x, y and z (for instance P, T and ρ) such as:
$x = x(y,z)$, $y = y(x,z)$ and $z = z(x,y)$

One has: $\quad dx = \left(\frac{\partial x}{\partial y}\right)_z dy + \left(\frac{\partial x}{\partial z}\right)_y dz \quad$ **and** $\quad dy = \left(\frac{\partial y}{\partial x}\right)_z dx + \left(\frac{\partial y}{\partial z}\right)_x dz$

Thus: $\quad dx = \left(\frac{\partial x}{\partial y}\right)_z \left(\frac{\partial y}{\partial x}\right)_z dx + \left(\frac{\partial x}{\partial y}\right)_z \left(\frac{\partial y}{\partial z}\right)_x dz + \left(\frac{\partial x}{\partial z}\right)_y dz$

$$dx\left(1 - \left(\frac{\partial x}{\partial y}\right)_z \left(\frac{\partial y}{\partial x}\right)_z\right) = dz\left(\left(\frac{\partial x}{\partial y}\right)_z \left(\frac{\partial y}{\partial z}\right)_x + \left(\frac{\partial x}{\partial z}\right)_y\right) \tag{A.23}$$

what is verified for whatever independent variations dx and dz .

For $dx \neq 0$ and $dz = 0$: $\quad 1 - \left(\frac{\partial x}{\partial y}\right)_z \left(\frac{\partial y}{\partial x}\right)_z = 0$

$$\boxed{\left(\frac{\partial x}{\partial y}\right)_z \left(\frac{\partial y}{\partial x}\right)_z = 1} \tag{A.24}$$

For $dx = 0$ and $dz \neq 0$: $\quad \left(\frac{\partial x}{\partial y}\right)_z \left(\frac{\partial y}{\partial z}\right)_x + \left(\frac{\partial x}{\partial z}\right)_y = 0 \;\Rightarrow\; \left(\frac{\partial x}{\partial y}\right)_z \left(\frac{\partial y}{\partial z}\right)_x = -\left(\frac{\partial x}{\partial z}\right)_y$

Thus: $\quad \boxed{\left(\frac{\partial x}{\partial y}\right)_z \left(\frac{\partial y}{\partial z}\right)_x \left(\frac{\partial z}{\partial x}\right)_y = -1}$ (A.25)

Besides, for a function as $A = A(x, y)$,
then $A = A(x(y, z), y(x, z)) = A(x, z) = A(y, z)$ and:

$$\left(\frac{\partial A}{\partial x}\right)_y = \left(\frac{\partial A}{\partial x}\right)_z + \left(\frac{\partial A}{\partial z}\right)_x \left(\frac{\partial z}{\partial x}\right)_y \tag{A.26}$$

$$dA = \left(\frac{\partial A}{\partial x}\right)_y dx + \left(\frac{\partial A}{\partial y}\right)_x dy = \left(\frac{\partial A}{\partial x}\right)_z dx + \left(\frac{\partial A}{\partial z}\right)_x dz \tag{A.27}$$

Given that $dz = \left(\frac{\partial z}{\partial x}\right)_y dx + \left(\frac{\partial z}{\partial y}\right)_x dy$ it gives:

$$dA = \left(\frac{\partial A}{\partial x}\right)_z dx + \left(\frac{\partial A}{\partial z}\right)_y \left(\left(\frac{\partial z}{\partial x}\right)_y dx + \left(\frac{\partial z}{\partial y}\right)_x dy\right) \tag{A.28}$$

$$= \left(\left(\frac{\partial A}{\partial x}\right)_z + \left(\frac{\partial A}{\partial z}\right)_y \left(\frac{\partial z}{\partial x}\right)_y\right) dx + \left(\frac{\partial A}{\partial z}\right)_y \left(\frac{\partial z}{\partial y}\right)_x dy \tag{A.29}$$

Thus: $\quad \boxed{\left(\frac{\partial A}{\partial x}\right)_y = \left(\frac{\partial A}{\partial x}\right)_z + \left(\frac{\partial A}{\partial z}\right)_x \left(\frac{\partial z}{\partial x}\right)_y}$ (A.30)

A.3 Additional results

A.3.1 Minimization of parametric integrals

A.3.1.1 Single independent variable, single dependent variable

The objective is to find a function f of the variable x, supposed two times differentiable, for which the integral Eq. (A.31) reach a stationary value, ideally an extremum:

$$J(f) = \int_{x_1}^{x_2} I\left(x, f, f'\right) dx \tag{A.31}$$

Here, the limits x_1 and x_2 are fixed as well as the values taken by f at those points. The notation f' formally stands for the variable df/dx and I is formally a function of the variables x, a, b supposed independent from its point of view. For a function g satisfying the stated hypothesis for f, one can define:

$$I_g : x \longmapsto I\left(x, g(x), \frac{dg}{dx}(x)\right) = I\left(x, g, g'\right) \tag{A.32}$$

With these notations, x is called a dependent variable because in I_g, from the point of view of I, its value does not depend on any other variable. In return, g (or f) is called a dependent variable because in I_g, from the point of view of I, the value of this variable depends of the value of an other variable (here x). In other words, changing the function f will not change the values of the independent variable x whereas changing the values of x will change the values of the dependent variable $f = f(x)$. The differential of I is written:

$$dI = \frac{\partial I}{\partial x} dx + \frac{\partial I}{\partial y} dy + \frac{\partial I}{\partial z} dz \tag{A.33}$$

Therefore the derivative of I_f takes the form:

$$dI_f\, x = \frac{\partial I}{\partial x} + \frac{\partial I}{\partial y}\frac{df}{dx} + \frac{\partial I}{\partial z}\frac{d^2 f}{dx^2} = \frac{\partial I}{\partial x} + f'\frac{\partial I}{\partial y} + f_{xx}\frac{\partial I}{\partial z} \tag{A.34}$$

Let F an admissible function for the calculation of Eq. (A.31), meaning that F is two times differentiable and that $F(x_1) = f(x_1)$ and $F(x_2) = f(x_2)$. For any f-dependent variable h, we note $\delta_F h$ the variation between the values of h when calculating using the path given by F and the path given by f. This gives in particular:

$$\delta_F f(x) = F(x) - f(x) \tag{A.35}$$

$$\delta_F I_f(x) = I(x, F(x), F_x(x)) - I\left(x, f(x), f'(x)\right) \tag{A.36}$$

$$\begin{aligned} \delta_F J = J(F) - J(f) &= \int_{x_1}^{x_2} \left(I(x, F(x), F_x(x)) - I\left(x, f(x), f'(x)\right)\right) dx \\ &= \int_{x_1}^{x_2} \delta_F I_f(x)\, dx \end{aligned} \tag{A.37}$$

From this definition of δ we have $\delta x = 0$ and when applied to f' it lends:

$$\delta_F f' = F' - f' = \frac{dF}{dx} - \frac{df}{dx} = \frac{d\left(F - f\right)}{d} = \frac{d}{dx}\left(\delta_F f\right) \tag{A.38}$$

With the extra assumption that F and f differ with a small amplitude, one can also write a 1^{st} Taylor expansion of I_f to lend:

$$\begin{aligned}
\delta_F I_f\left(x\right) &= I\left(x, F\left(x\right), F'\left(x\right)\right) - I\left(x, f\left(x\right), f'\left(x\right)\right) && \text{(A.39)}\\
&\approx \left(F\left(x\right) - f\left(x\right)\right)\frac{\partial I}{\partial y} + \left(F'\left(x\right) - f'\left(x\right)\right)\frac{\partial I}{\partial z} && \text{(A.40)}\\
&= \delta_F f\left(x\right)\frac{\partial I}{\partial y} + \delta_F f'\left(x\right)\frac{\partial I}{\partial z} && \text{(A.41)}
\end{aligned}$$

A necessary condition for $J\left(f\right)$ to be a stationary value is that for any admissible function F infinitely close to f, the variation $\delta_F J$ should tend to zero, i.e.:

$$\int_{x_1}^{x_2} \delta_F I_f\left(x\right) dx = 0 \tag{A.42}$$

The relations in Eqs. (A.38) and (A.41) can then be used to write:

$$\int_{x_1}^{x_2} \left(\delta_F \frac{\partial I}{\partial y} + \frac{d}{dx}\left(\delta_F f\right)\frac{\partial I}{\partial z}\right) dx = 0 \tag{A.43}$$

What can be simplified using an integration by parts:

$$\int_{x_1}^{x_2} \left(\delta_F f \frac{\partial I}{\partial y} + \frac{d}{dx}\left(\delta_F f\right)\frac{\partial I}{\partial z}\right) dx = 0 \tag{A.44a}$$

$$\int_{x_1}^{x_2} \delta_F f \frac{\partial I}{\partial y}\, dx + \cancel{\left[\delta_F f \frac{\partial I}{\partial z}\right]_{x_1}^{x_2}} - \int_{x_1}^{x_2} \delta_F f \frac{d}{dx}\left(\frac{\partial I}{\partial z}\right) dx = 0 \tag{A.44b}$$

$$\int_{x_1}^{x_2} \delta_F f \left[\frac{\partial I}{\partial y} - \frac{d}{dx}\left(\frac{\partial I}{\partial z}\right)\right] dx = 0 \tag{A.44c}$$

The bracketed quantity is equal to zero thanks to the admissibility of F which gives $\delta_F f\left(x_1\right) = \delta_F f\left(x_2\right) = 0$. Given this equality or any admissible function F infinitely close to f, it leads to the nullity of the integrand, lending:

$$\frac{\partial I}{\partial y} - \frac{d}{dx}\left(\frac{\partial I}{\partial z}\right) = 0 \quad \text{or} \quad \boxed{\frac{\partial I}{\partial f} - \frac{d}{dx}\left(\frac{\partial I}{\partial f'}\right) = 0} \tag{A.45}$$

Multiplying Eq. (A.45) by f' and using Eq. (A.34), the previous result can be written in a more classic form:

$$\frac{df}{dx}\left[\frac{\partial I}{\partial y}-\frac{d}{dx}\left(\frac{\partial I}{\partial z}\right)\right]=0 \tag{A.46a}$$

$$y_x\frac{\partial I}{\partial y}-\frac{df}{dx}\frac{d}{dx}\left(\frac{\partial I}{\partial z}\right)=0 \tag{A.46b}$$

$$\left[\frac{dI_f}{dx}-\frac{\partial I}{\partial x}-f_{xx}\frac{\partial I}{\partial z}\right]-\left[\frac{d}{dx}\left(f'\frac{\partial I}{\partial z}\right)-\frac{d^2f}{dx^2}\frac{\partial I}{\partial z}\right]=0 \tag{A.46c}$$

$$\frac{dI_f}{dx}-\frac{d}{dx}\left(f'\frac{\partial I}{\partial z}\right)-\frac{\partial I}{\partial x}-\cancel{f_{xx}\frac{\partial I}{\partial z}}+\cancel{f_{xx}\frac{\partial I}{\partial z}} \tag{A.46d}$$

This form is know as the *Euler equation* associated with the variation minimization:

$$\frac{\partial I}{\partial x}-\frac{d}{dx}\left(I_f-f'\frac{\partial I}{\partial z}\right)\quad\text{or}\quad\boxed{\frac{\partial I}{\partial x}-\frac{d}{dx}\left(I-f'\frac{\partial I}{\partial f'}\right)} \tag{A.47}$$

Which, in the particular (but very common) case where I does not explicitly depends on x, further simplifies in:

$$I_f-f'\frac{\partial I}{\partial z}=\text{cste}\quad\text{or}\quad\boxed{I-f'\frac{\partial I}{\partial f'}=\text{cste}} \tag{A.48}$$

A.3.1.2 Single independent variable, multiple dependent variables

With the same notations, let us consider now a the case where the integral J depend on multiple dependent variables $(f_1,\cdots,f_n)\,t$ but still on a single dependent variable x (for instance the time t as a dependent variable and the coordinates and velocities $x(t),\dot{x}(t),y(t),\dot{y}(t),...$ as dependent variables):

$$J(f_1,\cdots,f_n)=\int_{x_1}^{x_2}I\left(x,f_1,f_1',\cdots,f_n,f_n'\right)dx \tag{A.49}$$

The minimization of the variations can still be written:

$$\int_{x_1}^{x_2}\delta_{\{F\}}I_{\{f\}}(x)\,dx=\int_{x_1}^{x_2}\delta I(x)\,dx=0 \tag{A.50}$$

Where $\{f\}=(f_1,\cdots,f_n)$ and $\{F\}=(F_1,\cdots,F_n)$ are sets of functions such as $\forall i\in[\![1,n]\!]$, F_i is admissible in regard to f_i. For the sake of clarity, we now omit the indexes when talking about the variations but they remain implicitly present. Likewise, for the differentiation we omit the usage of separate names for the variables of I (that are all independent from the point of view of I) and use directly the notation from the variables of $I_{\{f\}}$. The independence of the variables (and the dependency of the variables of $I_{\{f\}}$) also remain implicit for the differentiation. This time the variation of I (implicitly $I_{\{f\}}$) is:

$$\delta I=\left(\frac{\partial I}{\partial f_1}\right)_\delta f_1+\left(\frac{\partial I}{\partial f_1'}\right)_\delta f_1'+\cdots\left(\frac{\partial I}{\partial f_n}\right)_\delta f_n+\left(\frac{\partial I}{\partial f_n'}\right)_\delta f_n' \tag{A.51}$$

When calculating the integral Eq. (A.50) with the formula Eq. (A.51), the same integration by parts as in Eq. (A.44) can be performed to give $\forall i$:

$$\int_{x_1}^{x_2} \left(\delta f_i \frac{\partial I}{\partial f_i} + \frac{d}{dx} \left(\delta f_i \right) \frac{\partial I}{\partial f_i'} \right) dx = \int_{x_1}^{x_2} \delta f_i \left[\frac{\partial I}{\partial f_i} - \frac{d}{dx} \left(\frac{\partial I}{\partial f_i'} \right) \right] dx \tag{A.52}$$

In turn leading to the overall relation:

$$\int_{x_1}^{x_2} \left[\frac{\partial I}{\partial f_1} - \frac{d}{dx} \left(\frac{\partial I}{\partial f_1'} \right) \right] \delta f_1 \, dx + \cdots + \int_{x_1}^{x_2} \left[\frac{\partial I}{\partial f_n} - \frac{d}{dx} \left(\frac{\partial I}{\partial f_n'} \right) \right] \delta f_n \, dx = 0 \tag{A.53}$$

Given the nullity of the integral for any set of admissible functions $\{F\} = (F_1, \cdots, F_n)$ causing the variations $(\delta f_1, \cdots, \delta f_n)$, it leads to the nullity of every single "independent" integral and the Euler condition becomes:

$$\boxed{\forall i \in [\![1, n]\!], \qquad \frac{\partial I}{\partial f_i} - \frac{d}{dx} \left(\frac{\partial I}{\partial f_i'} \right) = 0} \tag{A.54}$$

A.3.1.3 Multiple independent variables

Single dependent variable

The case of multiple independent variables is worth mentioning for it appears in multi-dimensional stationary problem. Given the independent variables $(x_1, \cdots, x_n)$ and the the dependent variable f, with the same notations it comes:

$$\forall i \in [\![1, n]\!], \qquad f_{x_i} = \left(\frac{\partial f}{\partial x_i} \right)_{x_{j \neq i}} \tag{A.55}$$

The integral to minimize over $\mathcal{V} = \left[x_1^d, x_1^u\right] \times \cdots \times \left[x_n^d, x_n^u\right]$ is written:

$$J(f) = \int_{\mathcal{V}} I\left(x, f, f_{x_1}, \cdots, f_{x_n}\right) dx \tag{A.56}$$

And the corresponding Euler equation becomes:

$$\boxed{\frac{\partial I}{\partial f} - \frac{\partial}{\partial x_1} \left(\frac{\partial I}{\partial f_{x_1}} \right) \cdots - \frac{\partial}{\partial x_n} \left(\frac{\partial I}{\partial f_{x_n}} \right) = 0} \tag{A.57}$$

Multiple dependent variables

In the case of multiple independent variables $(x_1, \cdots, x_n)$ and multiple dependent variables $(f_1, \cdots, f_m)\, t$, using the notations it comes:

$$\forall i \in [\![1, n]\!], \ \forall j \in [\![1, m]\!], \qquad f_{j,x_i} = \left(\frac{\partial f_j}{\partial x_i} \right)_{x_{k \neq i}} \tag{A.58}$$

The integral is written:

$$J(f) = \int_{\mathcal{V}} I\left(x, f_1, f_{1,x_1}, \cdots, f_{1,x_m}, \cdot, f_n, f_{n,x_1}, \cdots, f_{n,x_m}\right) dx \tag{A.59}$$

And the Euler condition becomes:

$$\boxed{\forall j \in [\![1, m]\!], \qquad \frac{\partial I}{\partial f_j} - \frac{\partial}{\partial x_1}\left(\frac{\partial I}{\partial f_{j,x_1}}\right) \cdots - \frac{\partial}{\partial x_n}\left(\frac{\partial I}{\partial f_{j,x_n}}\right) = 0} \tag{A.60}$$

A.3.2 Cardan's method for 3^{rd} order equations

He we detail the method to solve a 3^{rd} order complex polynomial equation following the method established by G. Cardano (a.k.a. Cardan).
The starting equation is Eq. (A.61) where a, b, c, d are complex numbers with $a \neq 0$

$$\boxed{ax^3 + bx^2 + cx + d = 0} \tag{A.61}$$

The equation is modified into Eq. (A.62) with the introduction of the new unknown z and the new coefficients p and q from Eq. (A.63a).

$$z^3 + pz + q \tag{A.62}$$

$$z = x + \frac{z}{3a}, \qquad p = \frac{c}{y} - \frac{b^2}{3a^2}, \qquad q = \frac{2b^3}{27a^3} - \frac{bc}{3a^2} + \frac{d}{y} \tag{A.63a}$$

In the following $j = e^{\frac{2i\pi}{3}} = -\frac{1}{2} + i\frac{\sqrt{3}}{2}$

If $p = 0$ then the solutions are given by:

$$x_1 = \sqrt[3]{-q} - \frac{z}{3a} \quad x_2 = j.\sqrt[3]{-q} - \frac{z}{3a} \quad x_3 = j^2.\sqrt[3]{-q} - \frac{z}{3a} \tag{A.64}$$

Otherwise the discriminant of the equation is given by: $\Delta = q^2 + \frac{4p^3}{27}$

If $\Delta = 0$

$$x_1 = \frac{3q}{p} - \frac{z}{3a}, \quad x_2 = -\frac{3q}{2p} - \frac{z}{3a}, \quad x_3 = x_2 = -\frac{3q}{2p} - \frac{z}{3a} \tag{A.65}$$

If $\Delta > 0$, one defines $u = \sqrt[3]{\frac{-q + \sqrt{\Delta}}{2}}$ and $v = \sqrt[3]{\frac{-q - \sqrt{\Delta}}{2}}$ and the solutions are given by:

$$x_1 = u + v - \frac{z}{3a}, \quad x_2 = j.u + j^2 v - \frac{z}{3a}, \quad x_3 = j^2.u + jv - \frac{z}{3a} \tag{A.66}$$

If $\Delta < 0$, one defines $u = \sqrt[3]{\frac{-q + i\sqrt{-\Delta}}{2}}$ and $v = \sqrt[3]{\frac{-q - i\sqrt{-\Delta}}{2}}$ and the solutions are given by:

$$x_1 = u + v - \frac{z}{3a}, \quad x_2 = j.u + j^2.v - \frac{z}{3a}, \quad x_3 = j^2.u + j.v - \frac{z}{3a} \tag{A.67}$$

A.4 Usefull relationships

The following writing conventions are used:

- lowercase italic light letters for scalar fields (a, b, etc...)
- lowercase italic bold letters for vectorial fields ($\boldsymbol{u}$, $\boldsymbol{v}$, etc...)
- $\boldsymbol{M}$ is a matrix (second order tensor) field and $\mathbf{T}$ is tensorial field of order $\geqslant 1$

A.4.1 Linear/Tensorial algebra

$$(\boldsymbol{u} \otimes \boldsymbol{v}) \cdot \boldsymbol{w} = (\boldsymbol{v} \cdot \boldsymbol{w})\, \boldsymbol{u} \tag{A.68a}$$
$$(\boldsymbol{u} \otimes \boldsymbol{v}) : \mathbf{T} = \boldsymbol{u} \cdot (\boldsymbol{v} \cdot \mathbf{T}) \tag{A.68b}$$
$$\mathbf{T} : (\boldsymbol{u} \otimes \boldsymbol{v}) = (\mathbf{T} \cdot \boldsymbol{u})\, \boldsymbol{v} \tag{A.68c}$$
$$\boldsymbol{u} \cdot (\boldsymbol{v} \times \boldsymbol{w}) = \boldsymbol{v} \cdot (\boldsymbol{w} \times \boldsymbol{u}) = \boldsymbol{w} \cdot (\boldsymbol{u} \times \boldsymbol{v}) \tag{A.68d}$$
$$(\boldsymbol{u} \times \boldsymbol{v}) \cdot (\boldsymbol{w} \times \boldsymbol{t}) = (\boldsymbol{u} \cdot \boldsymbol{w})\, (\boldsymbol{v} \cdot \boldsymbol{t}) - (\boldsymbol{u} \cdot \boldsymbol{t})\, (\boldsymbol{v} \cdot \boldsymbol{w}) \tag{A.68e}$$
$$\boldsymbol{u} \times (\boldsymbol{v} \times \boldsymbol{w}) = (\boldsymbol{u} \cdot \boldsymbol{w})\, \boldsymbol{v} - (\boldsymbol{u} \cdot \boldsymbol{v})\, \boldsymbol{w} \tag{A.68f}$$

A.4.2 Differential operators

$$\boldsymbol{\nabla}\, (ab) = a \boldsymbol{\nabla} b + b \boldsymbol{\nabla} a \tag{A.69a}$$
$$\boldsymbol{\nabla}\, (a\mathbf{T}) = a \boldsymbol{\nabla} \mathbf{T} + \mathbf{T} \otimes \boldsymbol{\nabla} a \tag{A.69b}$$
$$\boldsymbol{\nabla}\, (\boldsymbol{u} \cdot \boldsymbol{v}) = \boldsymbol{u} \cdot \boldsymbol{\nabla} \boldsymbol{v} + \boldsymbol{v} \cdot \boldsymbol{\nabla} \boldsymbol{u} \tag{A.69c}$$
$$\boldsymbol{\nabla}\, (\boldsymbol{\nabla} \cdot \boldsymbol{u}) = \boldsymbol{\nabla} \cdot (\mathrm{tr}\, ((\boldsymbol{\nabla} \boldsymbol{u}))) \tag{A.69d}$$
$$(\boldsymbol{\nabla} \boldsymbol{u}) \cdot \boldsymbol{u} = \boldsymbol{\nabla} \left(u^2/2\right) + (\boldsymbol{\nabla} \times \boldsymbol{u}) \times \boldsymbol{u} \tag{A.69e}$$
$$\boldsymbol{\nabla} \cdot \mathbf{T} = \mathrm{tr}\, (\boldsymbol{\nabla} \mathbf{T}) \tag{A.69f}$$
$$\boldsymbol{\nabla} \cdot (\boldsymbol{\nabla} \times \boldsymbol{u}) = 0 \tag{A.69g}$$
$$\boldsymbol{\nabla} \cdot (a\mathbf{I}) = \boldsymbol{\nabla} a \tag{A.69h}$$
$$\boldsymbol{\nabla} \cdot (a\mathbf{T}) = a \boldsymbol{\nabla} \cdot \mathbf{T} + \mathbf{T} \cdot \boldsymbol{\nabla} a \tag{A.69i}$$
$$\boldsymbol{\nabla} \cdot (\mathbf{T} \otimes \boldsymbol{u}) = (\boldsymbol{\nabla} \cdot \boldsymbol{u})\, T + \boldsymbol{\nabla} \mathbf{T} \cdot \boldsymbol{u} \tag{A.69j}$$
$$\boldsymbol{\nabla} \cdot (\boldsymbol{u} \times \boldsymbol{v}) = \boldsymbol{v} \cdot \boldsymbol{\nabla} \times \boldsymbol{u} - \boldsymbol{u} \cdot \boldsymbol{\nabla} \times \boldsymbol{v} \tag{A.69k}$$
$$\boldsymbol{\nabla} \cdot (\boldsymbol{M} \cdot \boldsymbol{u}) = \boldsymbol{M} : \boldsymbol{\nabla} \boldsymbol{u} + \left(\boldsymbol{\nabla} \cdot \left(\boldsymbol{M}^{\mathrm{T}}\right)\right) \cdot \boldsymbol{u} \tag{A.69l}$$
$$\boldsymbol{\nabla} \times (\boldsymbol{\nabla} a) = 0 \tag{A.69m}$$
$$\boldsymbol{\nabla} \times (a\boldsymbol{u}) = a \boldsymbol{\nabla} \times \boldsymbol{u} + \boldsymbol{\nabla} a \times \boldsymbol{u} \tag{A.69n}$$
$$\boldsymbol{\nabla} \times (\boldsymbol{u} \times \boldsymbol{v}) = (\boldsymbol{\nabla} \cdot \boldsymbol{v})\, \boldsymbol{u} - (\boldsymbol{\nabla} \cdot \boldsymbol{u})\, \boldsymbol{v} + (\boldsymbol{\nabla} \boldsymbol{u}) \cdot \boldsymbol{v} - (\boldsymbol{\nabla} \boldsymbol{v}) \cdot \boldsymbol{u} \tag{A.69o}$$
$$\boldsymbol{\Delta} \mathbf{T} = \boldsymbol{\nabla} \cdot (\boldsymbol{\nabla} \mathbf{T}) \tag{A.69p}$$
$$\boldsymbol{\Delta} \boldsymbol{u} = \boldsymbol{\nabla}\, (\boldsymbol{\nabla} \cdot \boldsymbol{u}) - \boldsymbol{\nabla} \times (\boldsymbol{\nabla} \times \boldsymbol{u}) \tag{A.69q}$$
$$\boldsymbol{\Delta}\, (ab) = a \boldsymbol{\Delta} b + b \boldsymbol{\Delta} a + 2 \boldsymbol{\nabla} a \cdot \boldsymbol{\nabla} b \tag{A.69r}$$
$$\boldsymbol{\Delta}\, (a\boldsymbol{u}) = a \boldsymbol{\Delta} \boldsymbol{u} + (\boldsymbol{\Delta} a)\, \boldsymbol{u} + 2 \boldsymbol{\nabla} \boldsymbol{u} \cdot \boldsymbol{\nabla} a \tag{A.69s}$$
$$\boldsymbol{\Delta}\, (\boldsymbol{\nabla} a) = \boldsymbol{\nabla}\, (\boldsymbol{\Delta} a) \tag{A.69t}$$
$$\boldsymbol{\Delta}\, (\boldsymbol{\nabla} \cdot \boldsymbol{u}) = \boldsymbol{\nabla} \cdot (\boldsymbol{\Delta} \boldsymbol{u}) \tag{A.69u}$$
$$\boldsymbol{\Delta}\, (\boldsymbol{\nabla} \times \boldsymbol{u}) = \boldsymbol{\nabla} \times (\boldsymbol{\Delta} \boldsymbol{u}) \tag{A.69v}$$

A.4.3 Differential calculus

A.4.3.1 Partial derivatives

$$\left(\frac{\partial x}{\partial y}\right)_z \left(\frac{\partial y}{\partial x}\right)_z = \left(\frac{\partial x}{\partial z}\right)_y \left(\frac{\partial z}{\partial x}\right)_y = \left(\frac{\partial y}{\partial z}\right)_x \left(\frac{\partial z}{\partial y}\right)_x = 1 \tag{A.70a}$$

$$\left(\frac{\partial x}{\partial y}\right)_z \left(\frac{\partial y}{\partial z}\right)_x \left(\frac{\partial z}{\partial x}\right)_y = -1 \tag{A.70b}$$

$$\left(\frac{\partial A}{\partial x}\right)_y = \left(\frac{\partial A}{\partial x}\right)_z + \left(\frac{\partial A}{\partial z}\right)_x \left(\frac{\partial z}{\partial x}\right)_y \tag{A.70c}$$

A.4.3.2 Differential theorems

Stokes theorem [1] [2] and affiliated

$$\int_\Omega d\omega = \int_{\partial\Omega} \omega \qquad \textit{(Original Stokes theorem)} \tag{A.71a}$$

$$\int_{\mathcal{A}} (\boldsymbol{\nabla} \times \boldsymbol{u}) \cdot \boldsymbol{n}\, d\mathcal{A} = \oint_{\mathcal{J}} \boldsymbol{u} \cdot \boldsymbol{t}\, dl \qquad \textit{(Kelvin-Stokes theorem)} \tag{A.71b}$$

$$\int_{\mathcal{A}} \boldsymbol{n} \times \boldsymbol{\nabla} a\, d\mathcal{A} = \oint_{\mathcal{J}} a\boldsymbol{t}\, dl \tag{A.71c}$$

Green-Ostrogradsky theorem [1] and affiliated

$$\int_{\mathcal{V}} \boldsymbol{\nabla} \cdot \mathbf{T}\, d\mathcal{V} = \int_{\mathcal{A}} \mathbf{T} \cdot \boldsymbol{n}\, d\mathcal{A} \qquad \textit{(Green-Ostrogradsky/Gauss theorem)} \tag{A.72a}$$

$$\int_{\mathcal{V}} \boldsymbol{\nabla} a\, d\mathcal{V} = \int_{\mathcal{A}} a\, d\mathcal{A} \qquad \textit{(Gradient theorem)} \tag{A.72b}$$

$$\int_{\mathcal{V}} \boldsymbol{\nabla} \mathbf{T}\, d\mathcal{V} = \int_{\mathcal{A}} \mathbf{T} \cdot \boldsymbol{n}\, d\mathcal{A} \qquad \textit{(Gradient theorem (tensorial))} \tag{A.72c}$$

$$\int_{\mathcal{V}} \boldsymbol{\nabla} \times \boldsymbol{u}\, d\mathcal{V} = \int_{\mathcal{A}} \boldsymbol{n} \times \boldsymbol{u}\, d\mathcal{A} \qquad \textit{(Volumic Stokes-Kelvin formula)} \tag{A.72d}$$

$$\int_{\mathcal{V}} [\mathbf{T}\boldsymbol{\Delta} a - a\boldsymbol{\Delta}\mathbf{T}]\, d\mathcal{V} = \int_{\mathcal{A}} [\mathbf{T} \times \boldsymbol{\nabla} a - a\boldsymbol{\nabla}\mathbf{T}] \cdot \boldsymbol{n}\, d\mathcal{A} \qquad \textit{(Green's formula)} \tag{A.72e}$$

$$\int_{\mathcal{V}} (\boldsymbol{u} \cdot (\boldsymbol{\nabla} \times \boldsymbol{v}) - \boldsymbol{v} \cdot (\boldsymbol{\nabla} \times \boldsymbol{u}))\, d\mathcal{V} = \int_{\mathcal{A}} (\boldsymbol{u} \times \boldsymbol{v}) \cdot \boldsymbol{n}\, d\mathcal{A} \tag{A.72f}$$

[1] $\boldsymbol{n}$ is the outer normal vector to the considered surface and $\boldsymbol{t}$ is the tangent vector to the considered oriented line.

[2] ω is a differential form over the manifold Ω, $d\omega$ is its outer differential

A.4.3.3 Fluid dynamics

Lagrangian (particular) derivative [3]:

$$\frac{df}{dt} = \frac{\partial f}{\partial t} + \boldsymbol{\nabla} f \cdot \mathbf{v} \tag{A.73}$$

Transport theorems [3] [4]:

$$\frac{d}{dt} \int\limits_{\mathcal{V}_A(t)} f(t,\boldsymbol{x})\, d\mathcal{V} = \int\limits_{\mathcal{V}_A(t)} \frac{\partial f}{\partial t}(t,\boldsymbol{x})\, d\mathcal{V} + \int\limits_{\mathcal{A}_A(t)} f(t,\boldsymbol{x})\, \boldsymbol{w}_A(t) \cdot \boldsymbol{n}_A(t)\, d\mathcal{A} \tag{A.74a}$$

$$\frac{d}{dt} \int\limits_{\mathcal{V}_A(t)} f(t,\boldsymbol{x})\, d\mathcal{V} = \int\limits_{\mathcal{V}_A(t)} \left[\frac{\partial f}{\partial t}(t,\boldsymbol{x})\, \boldsymbol{\nabla} \cdot (f \boldsymbol{w}_A)\right] d\mathcal{V} \tag{A.74b}$$

$$\frac{d}{dt} \int\limits_{\mathcal{V}_M(t)} f(t,\boldsymbol{x})\, d\mathcal{V} = \int\limits_{\mathcal{V}_M(t)} \frac{\partial f}{\partial t}(t,\boldsymbol{x})\, d\mathcal{V} + \int\limits_{\mathcal{A}_M(t)} f(t,\boldsymbol{x})\, \mathbf{v}(t) \cdot \boldsymbol{n}(t)\, d\mathcal{A} \tag{A.74c}$$

$$\frac{d}{dt} \int\limits_{\mathcal{V}_M(t)} f(t,\boldsymbol{x})\, d\mathcal{V} = \int\limits_{\mathcal{V}_M(t)} \left[\frac{\partial f}{\partial t}(t,\boldsymbol{x}) + \boldsymbol{\nabla} \cdot (f\mathbf{v})\right] d\mathcal{V} \tag{A.74d}$$

$$\frac{d}{dt} \int\limits_{\mathcal{V}_M(t)} f(t,\boldsymbol{x})\, d\mathcal{V} = \frac{d}{dt} \int\limits_{\mathcal{V}_A(t)} f(t,\boldsymbol{x})\, d\mathcal{V} + \int\limits_{\mathcal{A}_A(t)} f(t,\boldsymbol{x})\, (\mathbf{v} - \boldsymbol{w}_A)(t) \cdot \boldsymbol{n}(t)\, d\mathcal{A} \tag{A.74e}$$

Reynolds formula [3] [4] ***(corollary)*** :

Integral formulation

$$\frac{d}{dt} \int\limits_{\mathcal{V}_M(t)} \rho(t,\boldsymbol{x})\, f(t,\boldsymbol{x})\, d\mathcal{V} = \int\limits_{\mathcal{V}_M(t)} \rho(t,\boldsymbol{x})\, \frac{df}{dt}(t,\boldsymbol{x})\, d\mathcal{V} \tag{A.75}$$

Local formulation:

$$\begin{aligned} \rho \frac{df}{dt} &= \frac{\partial \rho f}{\partial t} + \boldsymbol{\nabla} \cdot (f\mathbf{v}) && \textit{scalar} \\ \rho \frac{d\mathbf{f}}{dt} &= \frac{\partial \rho \mathbf{f}}{\partial t} + \boldsymbol{\nabla} \cdot (\mathbf{f} \otimes \mathbf{v}) && \textit{vectorial/tensorial} \end{aligned} \tag{A.76}$$

[3] All the formulas (except Eq. (A.76) as specified) still hold if f is a vectorial, matrix, tensorial function $\mathbf{f}$ as long as the order of the variables is not switched to match a particular case.

[4] See Sec. A.2.2.2 for the definitions of the notations $\mathcal{V}_A$, $\mathcal{A}_A$, $\boldsymbol{w}_A$, $\mathcal{V}_M$, $\mathcal{A}_M$, etc...

Appendix B

Complementary thermodynamic results

B.1 Brief results from general thermodynamics

B.1.1 Global functions

The Gibbs relationship allows to link the variations of the internal energy $\mathcal{E}_s$, the entropy $\mathcal{S}$, the volume $\mathcal{V}$ and the mass $\mathcal{M}$ for a system at equilibrium with:

$$d\mathcal{E}_s \;\hat{=}\; T\,d\mathcal{S} - P\,d\mathcal{V} + \mu\,d\mathcal{M} \tag{B.1}$$

The internal energy $\mathcal{E}_s$, which is an extensive variable, has a 1-homogeneity property with respect to $\mathcal{S}$, $\mathcal{V}$ and $\mathcal{M}$, extensive variables as well:

$$\forall \lambda > 0, \quad \mathcal{E}_s\left(\lambda\mathcal{S}, \lambda\mathcal{V}, \lambda\mathcal{M}\right) = \lambda\mathcal{E}_s\left(\mathcal{S}, \mathcal{V}, \mathcal{M}\right) \tag{B.2}$$

Thanks to Euler's theorem, one can write :

$$\mathcal{E}_s = T\mathcal{S} - P\mathcal{V} + \mu\mathcal{M} \tag{B.3}$$

and one gets at the same time :

$$\mathcal{S}\,dT - \mathcal{V}\,dP + \mathcal{M}\,d\mu = 0 \tag{B.4}$$

From that, one can define the other extensive variables and their differentials. The enthalpy $\mathcal{H}$, the free energy $\mathcal{F}$ and the free enthalpy $\mathcal{G}$ are defined by:

$$\mathcal{H} \;\hat{=}\; \mathcal{E}_s + P\mathcal{V} = T\mathcal{S} + \mu\mathcal{M} \tag{B.5}$$

$$\mathcal{F} \;\hat{=}\; \mathcal{E}_s - T\mathcal{S} = -P\mathcal{V} + \mu\mathcal{M} \tag{B.6}$$

$$\mathcal{G} \;\hat{=}\; \mathcal{E}_s - T\mathcal{V} + \mu\mathcal{M} = \mu\mathcal{M} \tag{B.7}$$

and their differentials are given by:

$$d\mathcal{H} = T\,d\mathcal{S} + \mu\,d\mathcal{M} \tag{B.8}$$

$$d\mathcal{F} = -P\,d\mathcal{V} + \mu\,d\mathcal{M} \tag{B.9}$$

$$d\mathcal{G} = \mu\,d\mathcal{M} \tag{B.10}$$

B.1.2 Volumetric functions

By dividing the extensive variables by the volume of the fluid $\mathcal{V}$, one can define the volumetric thermodynamic variables of which relationships are then given by :

$$E_s \hat{=} \frac{\mathcal{E}_s}{\mathcal{V}} = TS - P + \mu\rho \tag{B.11}$$

$$H \hat{=} \frac{\mathcal{H}}{\mathcal{V}} = TS - \mu\rho \tag{B.12}$$

$$F \hat{=} \frac{\mathcal{F}}{\mathcal{V}} = -P + \mu\rho \tag{B.13}$$

$$G \hat{=} \frac{\mathcal{G}}{\mathcal{V}} = \mu\rho \tag{B.14}$$

and dividing Eq. (B.4) by $\mathcal{V}$, one gets also gets $SdT - dP + \rho d\mu = 0$, what allows to write the derivatives :

$$dE_s = T\,dS + \mu\,d\rho \tag{B.15}$$

$$dH = T\,dS + dP + \mu\,d\rho \tag{B.16}$$

$$dF = -S\,dT + \mu\,d\rho \tag{B.17}$$

$$dG = -S\,dT + dP + \mu\,d\rho \tag{B.18}$$

B.1.3 Specific functions

B.1.3.1 Links between the density ρ and the specific volume v

The density of the fluid is defined as the ratio between the total mass of the fluid $\mathcal{M}$ and its total volume $\mathcal{V}$. Though this definition rely intrinsically on a macroscopic point of view, using an Eulerian description, the density can be defined locally by considering a reduced local portion of the fluid with a volume $\partial\mathcal{V}$, negligible in regard to the total volume $\mathcal{V}$, but which still contains enough particles to perform a statistical averaging. If the mass of this small portion of the fluid is $\partial\mathcal{M}$, the local density is given by the ratio $\rho_{\text{local}} = \partial\mathcal{M}/\partial\mathcal{V}$.
In some cases, it can be easier to work with the specific volume v which is the inverse of the density. The conversions from one variable to the other are given by:

$$\rho \hat{=} \frac{\mathcal{M}}{\mathcal{V}} \quad \text{and} \quad \mathrm{v} \hat{=} \frac{1}{\rho} \tag{B.19}$$

$$d\rho = -\frac{1}{\mathrm{v}^2}\,d\mathrm{v} \quad \text{and} \quad d\mathrm{v} = -\frac{1}{\rho^2}\,d\rho \tag{B.20}$$

$$\left(\frac{\partial *}{\partial \rho}\right)_X = -\mathrm{v}^2\left(\frac{\partial *}{\partial \mathrm{v}}\right)_X \quad \text{and} \quad \left(\frac{\partial *}{\partial \mathrm{v}}\right)_X = -\rho^2\left(\frac{\partial *}{\partial \rho}\right)_X \tag{B.21}$$

By dividing the extensive variables by the mass of the fluid $\mathcal{M}$ (or by dividing the volumetric variables by the fluid density ρ), one can define the specific thermodynamic variables of which relationships are then given by :

$$e_s = Ts - \tfrac{P}{\rho} + \mu = Ts - \mathrm{v}P + \mu \tag{B.22}$$

$$h = Ts + \mu \tag{B.23}$$

$$f = -\tfrac{P}{\rho} + \mu = -\mathrm{v}P + \mu \tag{B.24}$$

$$g = \mu \tag{B.25}$$

The specific version of Eq. (B.4) becomes $s\,dT - \frac{1}{\rho}\,dP + d\mu = 0$ which allows, once again, to write the derivatives:

$$de_s = \quad T\,ds + \frac{P}{\rho^2}\,d\rho \quad = T\,ds - P\,d\mathrm{v} \tag{B.26}$$

$$dh = \quad T\,ds + \frac{1}{\rho}\,dP \quad = T\,ds + \mathrm{v}\,dP \tag{B.27}$$

$$df = \quad -s\,dT + \frac{P}{\rho^2}\,d\rho \quad = -s\,dT - P\,d\mathrm{v} \tag{B.28}$$

$$dg = \quad -s\,dT + \frac{1}{\rho}\,dP \;\; (= d\mu) \quad = -s\,dT + \mathrm{v}\,dP \tag{B.29}$$

B.1.4 Maxwell's relations

Most of the time, all the thermodynamic potentials ($\mathcal{E}_s$, $\mathcal{H}$, etc..., E_s, H, etc... and e_s, h, etc...) are supposed to be at least two times derivable at any admissible thermodynamic point. Therefore, the Schwarz theorem can be applied to them leading to a set of equations called Maxwell's relations. The reader can find a non exhaustive list of such relations which are used, among many things, to derive the thermodynamic formulas for real gas equations of state.

from dE_s (B.15) $\quad \left(\frac{\partial \mu}{\partial S}\right)_\rho = \left(\frac{\partial T}{\partial \rho}\right)_S$ or $\left(\frac{\partial \mu}{\partial S}\right)_\mathrm{v} = -\mathrm{v}^2\left(\frac{\partial T}{\partial \mathrm{v}}\right)_S$ (B.30)

from dF (B.17) $\quad \left(\frac{\partial \mu}{\partial T}\right)_\rho = -S - \left(\frac{\partial S}{\partial \rho}\right)_T$ or $\left(\frac{\partial \mu}{\partial T}\right)_\mathrm{v} = -S - \mathrm{v}^2\left(\frac{\partial S}{\partial \mathrm{v}}\right)_T$ (B.31)

from de_s (B.26) $\quad \left(\frac{\partial T}{\partial \rho}\right)_s = \frac{1}{\rho^2}\left(\frac{\partial P}{\partial s}\right)_\rho$ or $\left(\frac{\partial T}{\partial \mathrm{v}}\right)_s = -\left(\frac{\partial P}{\partial s}\right)_\mathrm{v}$ (B.32)

from dh (B.27) $\quad \left(\frac{\partial T}{\partial P}\right)_s = -\frac{1}{\rho^2}\left(\frac{\partial \rho}{\partial s}\right)_P$ or $\left(\frac{\partial T}{\partial \mathrm{v}}\right)_s = \left(\frac{\partial \mathrm{v}}{\partial s}\right)_P$ (B.33)

from df (B.28) $\quad \left(\frac{\partial s}{\partial \rho}\right)_T = -\frac{1}{\rho^2}\left(\frac{\partial P}{\partial T}\right)_\rho$ or $\left(\frac{\partial s}{\partial \mathrm{v}}\right)_T = \left(\frac{\partial P}{\partial T}\right)_\mathrm{v}$ (B.34)

from dg (B.29) $\quad \left(\frac{\partial s}{\partial P}\right)_T = \frac{1}{\rho^2}\left(\frac{\partial \rho}{\partial T}\right)_P$ or $\left(\frac{\partial s}{\partial P}\right)_T = -\left(\frac{\partial \mathrm{v}}{\partial T}\right)_P$ (B.35)

B.1.5 Partial derivatives

Tables B.1 to B.6 compile the partial derivatives for the main thermodynamic variables ρ, T, P, e_s, h and s. The support variables defined hereafter are used to condense the notations.

$$\mathcal{T}_\alpha = T\alpha - 1; \quad \mathcal{P}_\beta = P\beta - 1; \quad \zeta = \rho\beta C_v; \quad \vartheta = P\alpha - \rho C_p; \quad \xi = P\left(\rho\beta C_v + \alpha\right) - \rho C_p$$

$d\rho$											
$-\rho\alpha$	dT	$+$	$\rho\beta$	dP	$\left(\frac{1}{c^2} + \frac{\alpha}{C_p}\right)$	dP	$+$	$\frac{-\rho\alpha}{C_p}$	dh
$\frac{\rho\zeta}{\mathcal{T}_\alpha - \mathcal{P}_\beta}$	dT	$+$	$\frac{\rho^2\beta}{\mathcal{P}_\beta - \mathcal{T}_\alpha}$	de_s	$\frac{1}{c^2}$	dP	$+$	$\frac{-T\alpha\rho}{C_p}$	ds
$\frac{\rho\left(\zeta+\alpha\right)}{\mathcal{T}_\alpha}$	dT	$+$	$\frac{-\rho^2\beta}{\mathcal{T}_\alpha}$	dh	$\frac{\rho^2\left(\zeta+\alpha\right)}{\xi}$	de_s	$+$	$\frac{\rho\zeta}{-\xi}$	dh
$\frac{\rho\rho\zeta}{T\alpha}$	dT	$+$	$\frac{-\rho^2\beta}{\alpha}$	ds	$\frac{\rho^2}{P}$	de_s	$+$	$\frac{-T\rho^2}{P}$	ds
$\frac{-\rho\zeta}{\vartheta}$	dP	$+$	$\frac{-\rho^2\alpha}{\vartheta}$	de_s	$\frac{\rho}{c^2}$	dh	$+$	$\frac{-\rho T\left(\zeta+\alpha\right)}{C_p}$	ds

Table B.1: *Partial derivatives table for the density ρ*

dT											
$\frac{\beta}{\alpha}$	dP	$+$	$\frac{-1}{\rho\alpha}$	$d\rho$	$\frac{\mathcal{T}_\alpha}{\rho\zeta+\alpha}$	$d\rho$	$+$	$\frac{\rho\beta}{\zeta+\alpha}$	dh
$\frac{\mathcal{P}_\beta - \mathcal{T}_\alpha}{\vartheta}$	dP	$+$	$\frac{-\rho}{\vartheta}$	de_s	$\frac{T\alpha}{\rho\zeta}$	$d\rho$	$+$	$\frac{T}{C_v}$	ds
$\frac{\mathcal{T}_\alpha}{\rho C_p}$	dP	$+$	$\frac{1}{C_p}$	dh	$\frac{\rho\mathcal{T}_\alpha}{\xi}$	de_s	$+$	$\frac{\rho\left(\mathcal{P}_\beta - \mathcal{T}_\alpha\right)}{\xi}$	dh
$\frac{T\alpha}{\rho C_p}$	dP	$+$	$\frac{T}{C_p}$	ds	$\frac{T\alpha}{P\beta C_v}$	de_s	$+$	$\frac{T\left(\mathcal{P}_\beta - \mathcal{T}_\alpha\right)}{P\beta C_v}$	ds
$\frac{\mathcal{T}_\alpha - \mathcal{P}_\beta}{\rho\zeta}$	$d\rho$	$+$	$\frac{1}{C_v}$	de_s	$\frac{T\alpha}{C_p}$	dh	$+$	$\frac{-T\mathcal{T}_\alpha}{C_p}$	ds

Table B.2: *Partial derivatives table for the temperature T*

dP											
$\frac{\alpha}{\beta}$	dT	$+$	$\frac{1}{\rho\beta}$	$d\rho$	$\frac{C_p}{\zeta+\alpha}$	$d\rho$	$+$	$\frac{\rho\alpha}{\zeta+\alpha}$	dh
$\frac{\vartheta}{\mathcal{P}_\beta - \mathcal{T}_\alpha}$	dT	$+$	$\frac{\rho}{\mathcal{P}_\beta - \mathcal{T}_\alpha}$	de_s	c^2	$d\rho$	$+$	$\frac{T\alpha}{\beta C_v}$	ds
$\frac{\rho C_p}{\mathcal{T}_\alpha}$	dT	$+$	$\frac{\rho}{-\mathcal{T}_\alpha}$	dh	$\frac{\rho^2 C_p}{\xi}$	de_s	$+$	$\frac{-\rho\vartheta}{\xi}$	dh
$\frac{\rho C_p}{t\alpha}$	dT	$+$	$\frac{-\rho}{\alpha}$	ds	$\frac{\rho^2 c^2}{P}$	de_s	$+$	$\frac{T\vartheta}{P\beta C_v}$	ds
$\frac{-\vartheta}{\rho\zeta}$	$d\rho$	$+$	$\frac{\alpha}{\beta C_v}$	de_s	ρ	dh	$+$	$-\rho T$	ds

Table B.3: *Partial derivatives table for the pressure P*

de_s										
$C_p - \frac{P\alpha}{\rho}$	dT	$+$	$\frac{\mathcal{P}_\beta - \mathcal{T}_\alpha}{\rho}$	dP	$\frac{1}{\rho}\left(\frac{P(\zeta+\alpha)}{\rho C_p} - 1\right)$	dP	$+$	$\left(1 - \frac{P\alpha}{\rho C_p}\right)$	dh
C_v	dT	$+$	$\frac{\mathcal{P}_\beta - \mathcal{T}_\alpha}{\rho^2\beta}$	$d\rho$	$\frac{P}{\rho^2 c^2}$	dP	$+$	$\frac{-T\vartheta}{\rho C_p}$	ds
$\frac{\xi}{\rho(\mathcal{P}_\beta - \mathcal{T}_\alpha)}$	dT	$+$	$\frac{\mathcal{T}_\alpha - \mathcal{P}_\beta}{\mathcal{T}_\alpha}$	dh	$\frac{1}{\rho\left(\frac{P}{\rho} - \frac{\beta C_p}{\zeta+\alpha}\right)}$	$d\rho$	$+$	$\frac{\zeta}{\zeta+\alpha}$	dh
$\frac{P\beta C_v}{T\alpha}$	dT	$+$	$\frac{\vartheta}{\rho^2\alpha}$	ds	$\frac{P}{\rho^2}$	$d\rho$	$+$	T	ds
$\frac{\beta C_v}{\alpha}$	dP	$+$	$\frac{-\mathcal{T}_\alpha}{\rho}$	$d\rho$	$\frac{P}{\rho c^2}$	dh	$+$	$T\left(1 - \frac{P}{\rho C_p}(\zeta+\alpha)\right)$	ds

Table B.4: *Partial derivatives table for the specific sensible energy e_s*

dh										
C_p	dT	$+$	$\frac{1 - T\alpha}{\rho}$	dP	$\frac{\xi}{\rho\vartheta}$	dP	$+$	$\frac{\rho - C_p}{\vartheta}$	de_s
$\left(C_v + \frac{\alpha}{\rho\beta}\right)$	dT	$+$	$\frac{-\mathcal{T}_\alpha}{\rho^2\beta}$	$d\rho$	$\frac{1}{\rho}$	dP	$+$	T	ds
$\frac{-\xi}{\rho(\mathcal{T}_\alpha - \mathcal{P}_\beta)}$	dT	$+$	$\frac{1 - T\alpha}{\mathcal{P}_\beta - \mathcal{T}_\alpha}$	de_s	$\frac{1}{\rho}\left(c^2 + \frac{P}{\rho} + \frac{P\alpha}{\rho\zeta}\right)$	$d\rho$	$+$	$1 + \frac{\alpha}{\zeta}$	de_s
$\frac{C_p}{T}$	dT	$+$	$\frac{T\alpha - 1}{\alpha}$	ds	$\frac{c^2}{\rho}$	$d\rho$	$+$	$T\left(1 + \frac{\alpha}{\zeta}\right)$	ds
$\left(\frac{\beta C_v}{\alpha} + \frac{1}{\rho}\right)$	dP	$+$	$\frac{-C_p}{\rho\alpha}$	$d\rho$	$\frac{\rho c^2}{P}$	de_s	$+$	$T\left(1 + \frac{\alpha}{\zeta} - \frac{\rho c^2}{P}\right)$	ds

Table B.5: *Partial derivatives table for the specific enthalpy h*

ds										
$\frac{C_p}{T}$	dT	$+$	$\frac{-\alpha}{\rho}$	dP	$\frac{P\beta C_v}{T\vartheta}$	dP	$+$	$\frac{-\rho C_p}{T\vartheta}$	de_s
$\frac{C_v}{T}$	dT	$+$	$\frac{-\alpha}{\rho^2\beta}$	$d\rho$	$\frac{-1}{\rho T}$	dP	$+$	$\frac{1}{T}$	dh
$\frac{P\beta C_v}{T(\mathcal{P}_\beta - \mathcal{T}_\alpha)}$	dT	$+$	$\frac{\alpha}{\mathcal{T}_\alpha - \mathcal{P}_\beta}$	de_s	$\frac{-P}{T\rho^2}$	$d\rho$	$+$	$\frac{1}{T}$	de_s
$\frac{C_p}{T(-\mathcal{T}_\alpha)}$	dT	$+$	$\frac{\alpha}{T\alpha - 1}$	dh	$\frac{-C_p}{\rho T(\zeta+\alpha)}$	$d\rho$	$+$	$\frac{\zeta}{T(\zeta+\alpha)}$	dh
$\frac{\beta C_v}{T\alpha}$	dP	$+$	$\frac{-C_p}{\rho T\alpha}$	$d\rho$	$\frac{-\rho C_p}{T\xi}$	de_s	$+$	$\frac{-\zeta}{T\xi}$	dh

Table B.6: *Partial derivatives table for the specific entropy s*

B.2 Definition and derivation for real gas thermodynamics

B.2.1 Residual values

B.2.1.1 Definitions

Residual value for a given pressure P ($\rho = \rho^{\text{EoS}}(P,T)$ and $\rho^0 = \dfrac{P}{rT}$)

$$\Delta^P \chi(T,P) = \chi^{\text{EoS}}(T,P) - \chi^0(T,P) = \int_0^P \left(\frac{\partial \chi^{\text{EoS}}}{\partial P_*}\right)_T - \left(\frac{\partial \chi^0}{\partial P_*}\right)_T dP_* \tag{B.36}$$

Residual value for a given density ρ ($P = P^{\text{EoS}}(\rho,T)$ and $P^0 = \rho r T$)

$$\Delta^\rho \chi(T,\rho) = \chi^{\text{EoS}}(T,\rho) - \chi^0(T,\rho) = \int_0^\rho \left(\frac{\partial \chi^{\text{EoS}}}{\partial \rho^*}\right)_T - \left(\frac{\partial \chi^0}{\partial \rho^*}\right)_T d\rho^* \tag{B.37}$$

B.2.1.2 Direct expressions for a given pressure P

Enthalpy

One can start with the differential $dh = T\,ds + \dfrac{1}{\rho}\,dP$

It allows to extract the partial derivative (with Eq. (A.30)) $\left(\dfrac{\partial h}{\partial P}\right)_T = \left(\dfrac{\partial h}{\partial P}\right)_s + \left(\dfrac{\partial h}{\partial s}\right)_P \left(\dfrac{\partial s}{\partial P}\right)_T$

Knowing from Eq. (B.35) that $\left(\dfrac{\partial s}{\partial P}\right)_T = \dfrac{1}{\rho^2}\left(\dfrac{\partial \rho}{\partial T}\right)_P$

It leads to $\left(\dfrac{\partial h}{\partial P}\right)_T = \dfrac{1}{\rho} + \dfrac{T}{\rho^2}\left(\dfrac{\partial \rho}{\partial T}\right)_P$

For a perfect gas $\rho = \dfrac{P}{rT}$ thus $\left(\dfrac{\partial \rho}{\partial T}\right)_P = \dfrac{-P}{rT^2} = \dfrac{-\rho}{T}$

Therefore $\left(\dfrac{\partial h^0}{\partial P}\right)_T = \dfrac{1}{\rho} - \dfrac{\cancel{T}}{\rho^{\cancel{2}}}\dfrac{\cancel{\rho}}{\cancel{T}} = \dfrac{\cancel{1}}{\rho} - \dfrac{\cancel{1}}{\rho} = 0$

$$\boxed{\Delta^P h(T,P) = \int_0^P \left[\frac{1}{\rho} - \frac{T}{\rho^2}\left(\frac{\partial \rho}{\partial T}\right)_{P_*}\right] dP_*} \tag{B.38}$$

Energy

The internal energy e_s and the enthalpy h are linked by $e_s = h - \dfrac{P}{\rho}$ and for a perfect gas $e_s = h - rT$

$$\boxed{\Delta^P e_s(T,P) = \int_0^P \left[\frac{1}{\rho} - \frac{T}{\rho^2}\left(\frac{\partial \rho}{\partial T}\right)_{P_*}\right] dP_* - \frac{P}{\rho} + rT} \tag{B.39}$$

Free enthalpy

One can start with the differential $dg = -s\,dT + \frac{1}{\rho}\,dP$, it allows to extract the partial derivative $\left(\frac{\partial g}{\partial P}\right)_T = \frac{1}{\rho}$, and for a perfect gas $\left(\frac{\partial g^0}{\partial P}\right)_T = \frac{1}{\rho} = \frac{rT}{P}$

$$\boxed{\Delta^P g\,(T,P) = \int_0^P \left[\frac{1}{\rho} - \frac{rT}{P_*}\right] dP_*} \tag{B.40}$$

Free energy

The free enthalpy g and the free energy are linked by $f = g - \frac{P}{\rho}$, for a perfect gas $f = g - rT$

$$\boxed{\Delta^P f\,(T,P) = \int_0^P \left[\frac{1}{\rho} - \frac{rT}{P_*}\right] dP_* + rT - \frac{P}{\rho}} \tag{B.41}$$

Entropy

From Eq. (B.35) one can express the partial derivative $\left(\frac{\partial s}{\partial P}\right)_T = \frac{1}{\rho^2}\left(\frac{\partial \rho}{\partial T}\right)_P$, for a perfect gas $\left(\frac{\partial s^0}{\partial P}\right)_T = \frac{1}{\rho^2}\frac{-P}{rT^2} = \frac{r}{P}$

$$\boxed{\Delta^P s\,(T,P) = \int_0^P \left[\frac{1}{\rho^2}\left(\frac{\partial \rho}{\partial T}\right)_{P_*} - \frac{r}{P_*}\right] dP_*} \tag{B.42}$$

B.2.1.3 Direct expressions for a given density ρ

Energy

One can start with the differential $de = T\,ds + \frac{P}{\rho^2}\,d\rho$

It allows to extract the partial derivative (with Eq. (A.30)) $\left(\frac{\partial e}{\partial \rho}\right)_T = \left(\frac{\partial e}{\partial \rho}\right)_s + \left(\frac{\partial e}{\partial s}\right)_\rho \left(\frac{\partial s}{\partial \rho}\right)_T$

Knowing from Eq. (B.34) that $\left(\frac{\partial s}{\partial \rho}\right)_T = -\frac{1}{\rho^2}\left(\frac{\partial P}{\partial T}\right)_\rho$

It leads to $\left(\frac{\partial e}{\partial \rho}\right)_T = \frac{P}{\rho^2} - \frac{T}{\rho^2}\left(\frac{\partial P}{\partial T}\right)_\rho$

For a perfect gas $\left(\frac{\partial P}{\partial T}\right)_\rho = \rho r$

Therefore $\left(\frac{\partial e^0}{\partial P}\right)_T = \frac{P}{\rho^2} - \frac{T}{\rho^2}\rho r = \frac{\cancel{rT}}{\cancel{\rho}} - \frac{\cancel{rT}}{\cancel{\rho}} = 0$

$$\boxed{\Delta^\rho e_s\left(T,\rho\right) = \int_0^\rho \left[\frac{P}{\rho_*^2} - \frac{T}{\rho_*^2}\left(\frac{\partial P}{\partial T}\right)_{\rho_*}\right] d\rho_*} \tag{B.43}$$

Enthalpy

The enthalpy h ans the internal energy e_s are linked by $h = e + \frac{P}{\rho}$ and for a perfect gas $h = e + rT$

$$\boxed{\Delta^\rho h\left(T,\rho\right) = \int_0^\rho \left[\frac{P}{\rho_*^2} - \frac{T}{\rho_*^2}\left(\frac{\partial P}{\partial T}\right)_{\rho_*}\right] d\rho_* + \frac{P}{\rho} - rT} \tag{B.44}$$

Free energy

One can start with the differential $df = -s\,dT + \frac{P}{\rho^2}\,d\rho$, it allows to extract the partial derivative $\left(\frac{\partial f}{\partial \rho}\right)_T = \frac{P}{\rho^2}$ and for a perfect gas $\left(\frac{\partial f^0}{\partial \rho}\right)_T = \frac{rT}{\rho}$

$$\boxed{\Delta^\rho f\left(T,\rho\right) = \int_0^\rho \left[\frac{P}{\rho_*^2} - \frac{rT}{\rho_*}\right] d\rho_*} \tag{B.45}$$

Free enthalpy

The free enthalpy g and the free energy f are linked by $g = f + \frac{P}{\rho}$ and for a perfect gas $g = f + rT$

$$\boxed{g^\rho_{\text{res}}\left(T,\rho\right) = \int_0^\rho \left[\frac{P}{\rho_*^2} - \frac{rT}{\rho_*}\right] d\rho_* + \frac{P}{\rho} - rT} \tag{B.46}$$

Entropy

From Eq. (B.34) one can express the partial derivative $\left(\frac{\partial s}{\partial \rho}\right)_T = -\frac{1}{\rho^2}\left(\frac{\partial P}{\partial T}\right)_\rho$, for a perfect gas $\left(\frac{\partial s^0}{\partial \rho}\right)_T = -\frac{1}{\rho^2} r\rho = -\frac{r}{\rho}$

$$\boxed{\Delta^\rho s\left(T,\rho\right) = \int_0^\rho \left[\frac{r}{\rho_*} - \frac{1}{\rho_*^2}\left(\frac{\partial P}{\partial T}\right)_{\rho_*}\right] d\rho_*} \tag{B.47}$$

B.2.1.4 Translation

Most of the time, the departure values are expressed for common temperature and pressure as these two variables are the easier to measure and often the one imposed for the system. However, in their primary expression, the pressure-defined departure variables require the calculation of an integral where the pressure is the integration variable. However, most equations of state (the cubic EoS in particular) are explicitly defined relatively to the temperature and the density. For more practicality, it is convenient the find a new expression for the departure values, maintaining their definition (pressure-defined) but making appear an integral where density is the integration variable, what is done in the following.
For a thermodynamic variable χ, by introducing the pressure $P^{\#}$ calculated with the ideal gas EoS ($P^{\#} = \rho^{\text{EoS}}(T,P)\,rT$) from the density given by the real gas EoS, one can write:

$$\Delta^P\chi(T,P) = \chi^{\text{EoS}}\left(T,P,\rho^{\text{EoS}}\right) - \chi^0\left(T,P,\rho^0\right) \tag{B.48}$$

$$\begin{aligned} &= \chi^{\text{EoS}}\left(T,P,\rho^{\text{EoS}}\right) - \chi^0\left(T,P^{\#},\rho^{\text{EoS}}\right) \\ &\quad + \chi^0\left(T,P^{\#},\rho^{\text{EoS}}\right) - \chi^0\left(T,P,\rho^*\right) \end{aligned} \tag{B.49}$$

One can notice that, by definition:

$$\begin{aligned} \chi^{\text{EoS}}\left(T,P,\rho^{\text{EoS}}\right) - \chi^0\left(T,P^{\#},\rho^{\text{EoS}}\right) &= \chi^{\text{EoS}}\left(T,P=P^{\text{EoS}}\left(\rho^{\text{EoS}},T\right),\rho^{\text{EoS}}\right) \\ &\quad - \chi^0\left(T,P^{\#}=\rho^{\text{EoS}}rT,\rho^{\text{EoS}}\right) \end{aligned} \tag{B.50a}$$

$$= \chi^{\rho}_{\text{res}}\left(T,\rho^{\text{EoS}}\right) \tag{B.50b}$$

But, more importantly, that :

$$\chi^0\left(T,P^{\#},\rho^{\text{EoS}}\right) - \chi^0\left(T,P,\rho^0\right) = \chi^0\left(T,\rho^{\text{EoS}}rT,\rho^{\text{EoS}}\right) - \chi^0\left(T,\rho^0rT,\rho^0\right) \tag{B.51a}$$

$$= \chi^0\left(T,\rho^{\text{EoS}}\right) - \chi^0\left(T,\rho^0\right) \tag{B.51b}$$

$$= \int_{\rho^0}^{\rho^{\text{EoS}}} \left(\frac{\partial\chi^0}{\partial\rho_*}\right)_T d\rho_* \tag{B.51c}$$

Finally

$$\boxed{\Delta^P\chi(T,P) = \Delta^\rho\chi\left(T,\rho^{\text{EoS}}\right) + \int_{\rho^0}^{\rho^{\text{EoS}}} \left(\frac{\partial\chi^0}{\partial\rho_*}\right)_T d\rho_*} \tag{B.52}$$

Sensible energy

For an ideal gas $\left(\frac{\partial {e_s}^0}{\partial\rho}\right)_T = 0$, then:

$$\boxed{\Delta^P e_s = \int_0^{\rho} \left[\frac{P}{\rho_*^2} - \frac{T}{\rho_*^2}\left(\frac{\partial P}{\partial T}\right)_{\rho_*}\right] d\rho_*} \tag{B.53}$$

Enthalpy

With $h = e_s + \dfrac{P}{\rho}$ ($h = e_s + rT$ for an ideal gas)

$$\boxed{\Delta^P h = \int_0^{\rho} \left[\frac{P}{\rho_*^2} - \frac{T}{\rho_*^2} \left(\frac{\partial P}{\partial T} \right)_{\rho_*} \right] d\rho_* + \frac{P}{\rho} - rT} \tag{B.54}$$

Free energy

For an ideal gas $\left(\dfrac{\partial f^0}{\partial \rho} \right)_T = \dfrac{P}{\rho^2} = \dfrac{rT}{\rho}$, thus:

$$\int_{\rho^0}^{\rho^{\mathrm{EoS}}} \left(\frac{\partial f^0}{\partial \rho_*} \right)_T d\rho_* = \int_{\rho^0}^{\rho^{\mathrm{EoS}}} \frac{rT}{\rho_*} \, d\rho_* = rT \ln \left(\frac{\rho^{\mathrm{EoS}}}{\rho^0} \right) = rT \ln \left(\frac{rT\rho^{\mathrm{EoS}}}{P} \right) \tag{B.55}$$

$$\boxed{\Delta^P f = \int_0^{\rho} \left[\frac{P}{\rho_*^2} - \frac{rT}{\rho_*} \right] d\rho_* - rT \ln \left(\frac{P}{\rho r T} \right)} \tag{B.56}$$

Free enthalpy

With $g = f + \dfrac{P}{\rho}$ ($g = f + rT$ for an ideal gas)

$$\boxed{\Delta^P g = \int_0^{\rho} \left[\frac{P}{\rho_*^2} - \frac{rT}{\rho_*} \right] d\rho_* - rT \ln \left(\frac{P}{\rho r T} \right) + \frac{P}{\rho} - rT} \tag{B.57}$$

Entropy

For an ideal gas $\left(\dfrac{\partial s^0}{\partial \rho} \right)_T = -\dfrac{1}{\rho^2} \left(\dfrac{\partial P}{\partial T} \right)_T = -\dfrac{1}{\rho^2} r\rho = -\dfrac{r}{\rho}$ leading to:

$$\int_{\rho^0}^{\rho^{\mathrm{EoS}}} \left(\frac{\partial s^0}{\partial \rho_*} \right)_T d\rho_* = -\int_{\rho^0}^{\rho^{\mathrm{EoS}}} \frac{r}{\rho_*} \, d\rho_* = -r \ln \left(\frac{\rho^{\mathrm{EoS}}}{\rho^0} \right) = rT \ln \left(\frac{P}{r\rho^{\mathrm{EoS}}} \right) \tag{B.58}$$

$$\boxed{\Delta^P s = \int_0^{\rho} \left[\frac{r}{\rho_*} - \frac{1}{\rho_*^2} \left(\frac{\partial P}{\partial T} \right)_{\rho_*} \right] d\rho_* + r \ln \left(\frac{P}{\rho r T} \right)} \tag{B.59}$$

Isochoric heat capacity

By definition $C_v = \left(\frac{\partial e_s}{\partial T}\right)_\rho$ therefore $\Delta C_v = \left(\frac{\partial \Delta e_s}{\partial T}\right)_\rho$ and since $\Delta^P e_s = \Delta^\rho e_s$ one has $\Delta^P C_v = \Delta^\rho C_v$.

$$\Delta^\rho C_v = \frac{\partial}{\partial T}\left(\int_0^\rho \left[\frac{P}{\rho_*^2} - \frac{T}{\rho_*^2}\left(\frac{\partial P}{\partial T}\right)_{\rho_*}\right] d\rho_*\right)_\rho \tag{B.60a}$$

$$= \int_0^\rho \frac{\partial}{\partial T}\left[\frac{P}{\rho_*^2} - \frac{T}{\rho_*^2}\left(\frac{\partial P}{\partial T}\right)_{\rho_*}\right]_{\rho_*} d\rho_* \tag{B.60b}$$

$$= \int_0^\rho \frac{\partial}{\partial T}\left[\cancel{\frac{1}{\rho_*^2}\left(\frac{\partial P}{\partial T}\right)_{\rho_*}} - \cancel{\frac{1}{\rho_*^2}\left(\frac{\partial P}{\partial T}\right)_{\rho_*}} - \frac{1}{\rho_*^2}\left(\frac{\partial P}{\partial T}\right)_{\rho_*}\right]_{\rho_*} d\rho_* \tag{B.60c}$$

$$\boxed{\Delta^P C_v = \Delta^\rho C_v = -\int_0^\rho \frac{T}{\rho_*^2}\left(\frac{\partial^2 P}{\partial T^2}\right)_{\rho_*} d\rho_*} \tag{B.61}$$

B.2.2 Other values

B.2.3 Heat capacities

By definition $C_v = \left(\frac{\partial e_s}{\partial T}\right)_\rho$ and $C_p = \left(\frac{\partial h}{\partial T}\right)_P$

One the one hand:

$$\left(\frac{\partial h}{\partial T}\right)_P = \frac{\partial}{\partial T}\left(e_s + \frac{P}{\rho}\right)_P = \left(\frac{\partial e_s}{\partial T}\right)_P - \frac{P}{\rho^2}\left(\frac{\partial \rho}{\partial T}\right)_P = \left(\frac{\partial e_s}{\partial T}\right)_P + \frac{P\alpha}{\rho} \tag{B.62}$$

On the other hand (with Eq. (A.30)):

$$\left(\frac{\partial e_s}{\partial T}\right)_P = \left(\frac{\partial e_s}{\partial T}\right)_\rho + \left(\frac{\partial e_s}{\partial \rho}\right)_T \left(\frac{\partial T}{\partial \rho}\right)_P \tag{B.63}$$

$$= C_v + \left(\left(\frac{\partial e_s}{\partial s}\right)_\rho + \left(\frac{\partial e_s}{\partial s}\right)_\rho \left(\frac{\partial s}{\partial \rho}\right)_T\right)(-\rho\alpha) \tag{B.64}$$

$$= C_v - \rho\alpha\left(\frac{P}{\rho^2} + T\frac{-\alpha}{\rho^2\beta}\right) \tag{B.65}$$

$$= C_v - \frac{P\alpha}{\rho} + \frac{T\alpha^2}{\rho\beta} \tag{B.66}$$

When joined together, it gives: $\left(\frac{\partial h}{\partial T}\right)_P = C_v - \cancel{\frac{P\alpha}{\rho}} + \frac{T\alpha^2}{\rho\beta} + \cancel{\frac{P\alpha}{\rho}} = C_v + \frac{T\alpha^2}{\rho\beta}$

$$\boxed{C_p = C_v + \frac{T\alpha^2}{\rho\beta}} \tag{B.67}$$

B.2.3.1 Sound speed

$$de_s = \left(\frac{\partial e_s}{\partial T}\right)_P dT + \left(\frac{\partial e_s}{\partial P}\right)_T dP \quad \text{and} \quad dT = -\frac{1}{\rho\alpha}\, d\rho + \frac{\beta}{\alpha}\, dP \tag{B.68}$$

From Eq. (B.62) $$\left(\frac{\partial e_s}{\partial T}\right)_P = C_p - \frac{P\alpha}{\rho}$$

Besides
$$\begin{aligned}
\left(\frac{\partial e_s}{\partial P}\right)_T &= \underbrace{\left(\frac{\partial h}{\partial P}\right)_T} - \frac{\partial}{\partial P}\left(\frac{P}{\rho}\right)_T \\
&= \underbrace{\left(\frac{\partial h}{\partial P}\right)_s + \left(\frac{\partial h}{\partial s}\right)_P \left(\frac{\partial s}{\partial P}\right)_T} - \left(\frac{1}{\rho} - \frac{P}{\rho^2}\left(\frac{\partial \rho}{\partial P}\right)_T\right) && \text{(B.69a)} \\
&= \cancel{\frac{1}{\rho}} + T\frac{1}{\rho^2}\left(\frac{\partial \rho}{\partial T}\right)_P - \cancel{\frac{1}{\rho}} + \frac{P}{\rho^2}\rho\beta && \text{(B.69b)} \\
&= \frac{P\beta}{\rho} - \frac{T\alpha}{\rho} && \text{(B.69c)}
\end{aligned}$$

$$\boxed{de_s = \left[C_p - \frac{P\alpha}{\rho}\right] dT + \left[\frac{P\beta}{\rho} - \frac{T\alpha}{\rho}\right] dP} \tag{B.70}$$

From (B.26) one also has $de_s = T\, ds + \dfrac{P}{\rho^2}\, d\rho$

$$\left[C_p - \frac{P\alpha}{\rho}\right] dT + \left[\frac{P\beta}{\rho} - \frac{T\alpha}{\rho}\right] dP = T\, ds + \frac{P}{\rho^2}\, d\rho \tag{B.71a}$$

$$\left[C_p - \frac{P\alpha}{\rho}\right] \left(-\frac{1}{\rho\alpha}\, d\rho + \frac{\beta}{\alpha}\, dP\right) + \left[\frac{P\beta}{\rho} - \frac{T\alpha}{\rho}\right] dP = T\, ds + \frac{P}{\rho^2}\, d\rho \tag{B.71b}$$

$$\left[-\frac{C_p}{\rho\alpha} + \frac{P\cancel{\alpha}}{\cancel{\rho^2}\alpha} - \frac{\cancel{P}}{\cancel{\rho^2}}\right] d\rho + \left[C_p\frac{\beta}{\alpha} - \frac{P\alpha}{\cancel{\rho}}\frac{\cancel{\beta}}{\alpha} + \frac{P\cancel{\beta}}{\cancel{\rho}} - \frac{T\alpha}{\rho}\right] dP = T\, ds \tag{B.71c}$$

$$-\frac{C_p}{\rho\alpha}\, d\rho + \frac{\beta}{\alpha}\left[C_p - \frac{T\alpha^2}{\beta\rho}\right] dP = T\, ds \tag{B.71d}$$

$$c^2 = \left(\frac{\partial P}{\partial \rho}\right)_s = \frac{\dfrac{C_p}{\rho\cancel{\alpha}}}{\dfrac{\beta}{\cancel{\alpha}}\left[C_p - \dfrac{T\alpha^2}{\rho\beta}\right]} = \frac{C_p}{\rho\cancel{\alpha}\dfrac{\beta}{\cancel{\alpha}}\left[C_p - \dfrac{T\alpha^2}{\rho\beta}\right]} \tag{B.72}$$

$$\boxed{c^2 = \frac{C_p}{\rho\beta\left(C_p - \dfrac{T\alpha^2}{\beta\rho}\right)} = \frac{C_p}{\rho\beta C_v}} \tag{B.73}$$

B.3 Definition and derivation for cubic equations of state

B.3.1 Departure values

B.3.1.1 Calculation tips

Cubic equation signature integral

The integral expressed Eq. (B.74) repeats throughout the derivation of the departure values expressions, its calculation is more easily carried out ba trading the density ρ for the specific volume $\mathrm{v} = 1/\rho$.

$$\mathcal{I}\left(e_1, e_2, \rho\right) = \int_0^{\rho} \frac{d\rho_*}{1 + e_1 b\rho_* + e_2 b^2 {\rho_*}^2} \tag{B.74}$$

Recalling that $d\rho = -\rho^2\, d\mathrm{v}$ the change of variable writes

$$\mathcal{I}\left(e_1, e_2, \rho\right) = \int_0^{\rho} \frac{d\rho_*}{1 + e_1 b\rho_* + e_2 b^2 {\rho_*}^2} = \int_{+\infty}^{\mathrm{v}} \frac{1}{\rho_*^2} \frac{-\rho_*^2\, d\mathrm{v}_*}{\frac{1}{\rho_*^2} + \frac{e_1 b}{\rho_*} + e_2 b^2} \tag{B.75a}$$

$$= \int_{\mathrm{v}}^{+\infty} \frac{d\mathrm{v}_*}{\mathrm{v}_*^2 + e_1 b\mathrm{v}_* + e_2 b^2} \tag{B.75b}$$

The discriminant and the roots of the cubic polynomial $\mathrm{v}_*^2 + e_1 b\mathrm{v}_* + e_2 b^2$ are given by:

$$\Delta = (e_1 b)^2 - 4e_2 b^2 = b^2\left(e_1^2 - 4e_2\right) \tag{B.76}$$

$$v_{+/-} = \frac{-e_1 b - \sqrt{\Delta}}{2} = \frac{b}{2}\left(-e_1 + /-\sqrt{{e_1}^2 - 4e_2}\right) \tag{B.77}$$

$$\mathcal{I}\left(e_1, e_2, \rho\right) = \frac{1}{v_+ - v_-} \ln\left(\frac{v - v_-}{v - v_+}\right) \tag{B.78}$$

$$\mathrm{v}_{+/-} = \frac{b}{2}\left(-e_1 + /-\sqrt{{e_1}^2 - 4e_2}\right) \tag{B.79}$$

The algebraic fraction in the integrand of $\mathcal{I}\left(e_1, e_2, \rho\right)$ can be written formally:

$$\frac{1}{\mathrm{v}^2 + e_1 b\mathrm{v} + e_2 b^2} = \frac{c_1}{\mathrm{v} - \mathrm{v}_+} + \frac{c_2}{\mathrm{v} - \mathrm{v}_-} \tag{B.80}$$

where the constants c_1 and c_2 must satisfy $c_1 + c_2 = 0$ and $c_1\mathrm{v}_- + c_2\mathrm{v}_+ = -1$ leading to:

$$c_1 = -c_2 = \frac{1}{\mathrm{v}_+ - \mathrm{v}_-} \tag{B.81}$$

Therefore $\mathcal{I}\left(e_1, e_2, \rho\right)$ can calculated with:

$$\mathcal{I}\left(e_1, e_2, \rho\right) = \int_{\mathrm{v}}^{+\infty} \frac{1}{\mathrm{v}_+ - \mathrm{v}_-}\left(\frac{1}{\mathrm{v}_* - \mathrm{v}_+} - \frac{1}{\mathrm{v}_* - \mathrm{v}_-}\right) d\mathrm{v}_* \tag{B.82a}$$

$$= \frac{1}{\mathrm{v}_+ - \mathrm{v}_-} \left(\int_{\mathrm{v}}^{+\infty} \frac{d\mathrm{v}_*}{\mathrm{v}_* - \mathrm{v}_+} - \int_{\mathrm{v}}^{+\infty} \frac{d\mathrm{v}_*}{\mathrm{v}_* - \mathrm{v}_-} \right) \tag{B.82b}$$

$$= \frac{1}{\mathrm{v}_+ - \mathrm{v}_-} \left(\left[\ln\left(\mathrm{v}_* - \mathrm{v}_+\right) \right]_{\mathrm{v}}^{+\infty} - \left[\ln\left(\mathrm{v}_* - \mathrm{v}_-\right) \right]_{\mathrm{v}}^{+\infty} \right) \tag{B.82c}$$

$$= \frac{1}{\mathrm{v}_+ - \mathrm{v}_-} \left[\ln\left(\frac{\mathrm{v}_* - \mathrm{v}_+}{\mathrm{v}_* - \mathrm{v}_-} \right) \right]_{\mathrm{v}}^{+\infty} \tag{B.82d}$$

Finally, given that $\lim_{\mathrm{v}\to+\infty} \ln\left(\mathrm{v}_* - \mathrm{v}_+\right)/\left(\mathrm{v}_* - \mathrm{v}_-\right) = \ln 1 = 0$, one obtains the final expression:

$$\boxed{\mathcal{I}\left(e_1, e_2, \rho\right) = \frac{1}{\mathrm{v}_+ - \mathrm{v}_-} \ln\left(\frac{\mathrm{v} - \mathrm{v}_-}{\mathrm{v} - \mathrm{v}_+} \right)} \tag{B.83}$$

Pressure derivatives

Successive partial derivatives with respect to the temperature also intervene in the departure values derivation. From the general expression of the pressure given in Eq. (1.17) one gets:

$$\left(\frac{\partial P}{\partial T} \right)_{\rho} = \frac{\rho r}{1 - b\rho} - \frac{da}{dT}\left(T\right) \frac{\rho^2}{1 + e_1 b\rho + e_2 b^2 \rho^2} \tag{B.84}$$

$$\left(\frac{\partial^2 P}{\partial T^2} \right)_{\rho} = -\frac{d^2 a}{dT^2}\left(T\right) \frac{\rho^2}{1 + e_1 b\rho + e_2 b^2 \rho^2} \tag{B.85}$$

B.3.1.2 Departure values expressions

Sensible energy

$$\Delta^P e_s = \int_0^{\rho} \left[\frac{P}{\rho_*^2} - \frac{T}{\rho_*^2} \left(\frac{\partial P}{\partial T} \right)_{\rho_*} \right] d\rho_* \tag{B.86a}$$

$$= \int_0^{\rho} \frac{1}{\rho_*^2} \left[\left(\frac{\rho_* r \cancel{T}}{\cancel{1 - b\rho_*}} - \frac{a\left(T\right)\rho_*^2}{1 + e_1 b\rho_* + e_2 b^2 \rho_*^2} \right) - \frac{T}{\rho_*^2} \left(\frac{\rho_* r}{\cancel{1 - b\rho_*}} - \frac{da}{dT}\left(T\right) \frac{\rho_*^2}{1 + e_1 b\rho_* + e_2 b^2 \rho_*^2} \right) \right] d\rho_* \tag{B.86b}$$

$$= \int_0^{\rho} \frac{1}{\cancel{\rho_*^2}} \left(-a\left(T\right) + T\frac{da}{dT}\left(T\right) \right) \frac{\cancel{\rho_*^2}}{1 + e_1 b\rho_* + e_2 b^2 \rho_*^2} d\rho_* \tag{B.86c}$$

$$= \left(T\frac{da}{dT}\left(T\right) - a\left(T\right) \right) \int_0^{\rho} \frac{d\rho_*}{1 + e_1 b\rho_* + e_2 b^2 \rho_*^2} \tag{B.86d}$$

$$\boxed{\Delta^P e_s = \left(T\frac{da}{dT}\left(T\right) - a\left(T\right) \right) \mathcal{I}\left(e_1, e_2, \rho\right)} \tag{B.87}$$

Free energy

$$\Delta^P f = \int_0^\rho \left[\frac{P}{\rho_*^2} - \frac{rT}{\rho_*}\right] d\rho_* - rT\ln\left(\frac{P}{\rho rT}\right) \tag{B.88a}$$

$$= \int_0^\rho \left[\frac{rT}{\rho_*\left(1-b\rho_*\right)} - \frac{a\left(T\right)}{1+e_1 b\rho_* + e_2 b^2\rho_*^2} - \frac{rT}{\rho_*}\right] d\rho_* - rT\ln\left(\frac{P}{\rho rT}\right) \tag{B.88b}$$

$$= \int_0^\rho rT\left(\frac{1}{\rho_*\left(1-b\rho_*\right)} - \frac{1}{\rho_*}\right) d\rho_* - a\left(T\right)\int_0^\rho \frac{d\rho_*}{1+e_1 b\rho_* + e_2 b^2\rho_*^2} - rT\ln\left(\frac{P}{\rho rT}\right) \tag{B.88c}$$

$$= \int_0^\rho rT\left(\frac{\cancel{1}}{\cancel{\rho_*}} + \frac{b}{1-b\rho_*} - \frac{\cancel{1}}{\cancel{\rho_*}}\right) d\rho_* - a\left(T\right)\mathcal{I}\left(e_1,e_2,\rho\right) - rT\ln\left(\frac{P}{\rho rT}\right) \tag{B.88d}$$

$$= -rT\int_0^\rho \frac{-b}{1-b\rho_*}\, d\rho_* - a\left(T\right)\mathcal{I}\left(e_1,e_2,\rho\right) - rT\ln\left(\frac{P}{\rho rT}\right) \tag{B.88e}$$

$$\boxed{\Delta^P f = -a\left(T\right)\mathcal{I}\left(e_1,e_2,\rho\right) - rT\ln\left(\frac{P\left(1-b\rho\right)}{\rho rT}\right)} \tag{B.89}$$

Entropy

$$\Delta^P s = \int_0^\rho \left[\frac{r}{\rho_*} - \frac{1}{\rho_*^2}\left(\frac{\partial P}{\partial T}\right)_{\rho_*}\right] d\rho_* + r\ln\left(\frac{P}{\rho rT}\right) \tag{B.90a}$$

$$= \int_0^\rho \left[\frac{r}{\rho_*} - \frac{r}{\rho_*\left(1-b\rho_*\right)} + \frac{da}{dT}\left(T\right)\frac{1}{1+e_1 b\rho_* + e_2 b^2\rho_*^2}\right] d\rho_* + r\ln\left(\frac{P}{\rho rT}\right) \tag{B.90b}$$

$$= \int_0^\rho r\left(\frac{1}{\rho_*} - \frac{1}{\rho_*\left(1-b\rho_*\right)}\right) d\rho_* + \frac{da}{dT}\left(T\right)\int_0^\rho \frac{d\rho_*}{1+e_1 b\rho_* + e_2 b^2\rho_*^2} + r\ln\left(\frac{P}{\rho rT}\right) \tag{B.90c}$$

$$= \int_0^\rho r\left(\frac{\cancel{1}}{\cancel{\rho_*}} - \frac{\cancel{1}}{\cancel{\rho_*}} - \frac{b}{1-b\rho_*}\right) d\rho_* + \frac{da}{dT}\left(T\right)\mathcal{I}\left(e_1,e_2,\rho\right) + r\ln\left(\frac{P}{\rho rT}\right) \tag{B.90d}$$

$$= r\int_0^\rho \frac{-b}{1-b\rho_*}\, d\rho_* + \frac{da}{dT}\left(T\right)\mathcal{I}\left(e_1,e_2,\rho\right) + r\ln\left(\frac{P}{\rho rT}\right) \tag{B.90e}$$

$$\boxed{\Delta^P s = \frac{da}{dT}\left(T\right)\mathcal{I}\left(e_1,e_2,\rho\right) + r\ln\left(\frac{P\left(1-b\rho\right)}{\rho rT}\right)} \tag{B.91}$$

Isochoric heat capacity

$$\Delta^P C_v = -\int_0^\rho \frac{T}{\rho_*^2}\left(\frac{\partial^2 P}{\partial T^2}\right)_{\rho_*} d\rho_* \tag{B.92a}$$

$$= -\int_0^\rho \frac{T}{\cancel{\rho_*^2}} - \frac{d^2a}{dT^2}(T)\frac{-\cancel{\rho_*^2}}{1+e_1 b\rho_* + e_2 b^2\rho_*^2} d\rho_* \tag{B.92b}$$

$$= T\frac{d^2a}{dT^2}(T)\int_0^\rho \frac{1}{1+e_1 b\rho_* + e_2 b^2\rho_*^2} d\rho_* \tag{B.92c}$$

$$\boxed{\Delta^P C_v = T\frac{d^2a}{dT^2}(T)\mathcal{I}(e_1, e_2, \rho)} \tag{B.93}$$

This last result could also have been obtained by a straightforward differentiation of Eq. (B.87) since $\mathcal{I}(e_1, e_2, \rho)$ is independent from the temperature.

B.4 Thermodynamic modifications for the Thickened Interface Method

Notations

Let χ be any thermodynamic variable, the following notations are used:

- $\chi^{\text{TIM}}(\rho, T)$ refers to the final thermodynamic variable as modified by the TIM
- $\chi^{\text{EoS}}(\rho, T)$ refers to the thermodynamic variable as derived directly from the EoS
- $\chi_l^{\text{sat}} = \chi^{\text{EoS}}(\rho_l(T), T)$ and $\chi_v^{\text{sat}} = \chi^{\text{EoS}}(\rho_v(T), T)$ refer to the thermodynamic variable as derived directly from the EoS, taken at saturation in the liquid "l" or vapor "v" phase
- $\underset{sat}{\Delta}(\chi)(T)$ defines the saturation gap value of χ between the liquid and the vapor phases, meaning that $\underset{sat}{\Delta}(\chi)(T) = \chi_l^{\text{sat}}(T) - \chi_v^{\text{sat}}(T)$
- $\chi^{\text{sat}}(T)$ is used to compress the notation when the thermodynamic variable χ satisfies the remarkable relation $\chi(\rho_l(T), T) = \chi(\rho_v(T), T)$, for instance $P(\rho_l(T), T) = P(\rho_v(T), T) = P^{\text{sat}}(T)$.
- $\bar{\chi}(T)$, conversely, can be equal either to the liquid or vapor saturation value of χ^{EoS} depending on the local equilibrium condition. For instance $\bar{\chi}(T) = \chi(\rho_l(T), T)$ if $y_l \geqslant 0.5$ and $\bar{\chi}(T) = \chi(\rho_v(T), T)$ if $y_l < 0.5$. The condition to discriminate between the liquid and vapor phases can be chosen arbitrarily bust must be conserved to calculate at once all the thermodynamic variables at a given point (the condition may however vary from one point to the other). One easily gets that $\bar{P}(T) = P^{\text{sat}}(T)$, $\bar{\mu}(T) = \mu^{\text{sat}}(T)$
- $\chi^\eta(\rho, T)$ is defined as equal to $\bar{\chi}(T) + \dfrac{\chi^{\text{EoS}}(\rho, T) - \bar{\chi}(T)}{\eta}$

B.4.1 Derivatives of saturation values

The derivation of a consistent TIM thermodynamics requires the expression of several thermodynamic variables. The notations in Sec. B.4 are used. Besides, the subscript $k \in \{l, v\}$ is used to refer to the liquid or vapor phase indifferently. Here, the saturation is defined by a thermal, mechanical and chemical equilibrium between the two phases, meaning that:

- $T_v^{\text{sat}} = T_l^{\text{sat}} = T^{\text{sat}}$
- $P^{\text{EoS}}\left(\rho_l\left(T\right), T\right) = P^{\text{EoS}}\left(\rho_v\left(T\right), T\right) = P^{\text{sat}}\left(T\right)$
- $\mu^{\text{EoS}}\left(\rho_l\left(T\right), T\right) = \mu^{\text{EoS}}\left(\rho_v\left(T\right), T\right) = \mu^{\text{sat}}\left(T\right)$

In particular, from these equilibrium conditions it comes that:

$$d\mu_l^{\text{sat}} = d\mu_v^{\text{sat}} = d\mu^{\text{sat}} \tag{B.94}$$

and

$$-s_l^{\text{sat}}\, dT + \frac{1}{\rho_l}\, dP^{\text{sat}} = -s_v^{\text{sat}}\, dT + \frac{1}{\rho_v}\, dP^{\text{sat}} \tag{B.95}$$

In addition, for a bivariate thermodynamic variable χ other than the pressure and the temperature, its partial derivative at saturation, relatively to the temperature, can be obtained using the following principle:

$$\frac{d\chi_k^{\text{sat}}}{dT} = \frac{d}{dT}\left(\chi_k^{\text{sat}}\left(T, P^{\text{sat}}\left(T\right)\right)\right) = \left(\frac{\partial \chi}{\partial T}\right)_P \left(\rho_k\left(T\right), T\right) + \left(\frac{\partial \chi}{\partial P}\right)_T \left(\rho_k\left(T\right), T\right) \frac{dP^{\text{sat}}}{dT}\left(T\right) \tag{B.96}$$

B.4.1.1 Saturation pressure derivative $\dfrac{dP^{\text{sat}}}{dT}$

From the Gibbs "saturation" equation Eq. (B.95), one gets:

$$-\left(s_l^{\text{sat}} - s_v^{\text{sat}}\right) dT = \left(\frac{1}{\rho_v} - \frac{1}{\rho_l}\right) dP^{\text{sat}} \tag{B.97}$$

Thus

$$\boxed{\frac{dP^{\text{sat}}}{dT} = \left(s_l^{\text{sat}} - s_v^{\text{sat}}\right)\left(\frac{1}{\rho_l} - \frac{1}{\rho_v}\right)^{-1}} \tag{B.98}$$

or

$$\frac{dP^{\text{sat}}}{dT} = -\frac{\left(s_l^{\text{sat}} - s_v^{\text{sat}}\right)\rho_l \rho_v}{\rho_l - \rho_v} \tag{B.99}$$

Additionally, from the relation $h = \mu + Ts$ and the chemical equilibrium it comes:

$$s_l^{\text{sat}} - s_v^{\text{sat}} = \frac{1}{T}\left(h_l^{\text{sat}} - h_v^{\text{sat}}\right) = \frac{\mathcal{L}^{\text{vap}}}{T} \tag{B.100}$$

thus

$$\boxed{\frac{dP^{\text{sat}}}{dT} = -\frac{\mathcal{L}^{\text{vap}}\rho_l\rho_v}{T\left(\rho_l - \rho_v\right)}} \tag{B.101}$$

The second order saturation pressure derivative can also be expressed. From Eq. (B.98) it comes:

$$\frac{d^2P^{\text{sat}}}{dT^2} = \frac{d}{dT}\left(\frac{s_l^{\text{sat}} - s_v^{\text{sat}}}{1/\rho_l - 1/\rho_v}\right) = \frac{d}{dT}\left(\frac{\underset{sat}{\Delta}(s)}{\underset{sat}{\Delta}\left(\frac{1}{\rho}\right)}\right) \tag{B.102}$$

The derivation gives:

$$\frac{d^2P^{\text{sat}}}{dT^2} = \frac{1}{\left(\underset{sat}{\Delta}\left(\frac{1}{\rho}\right)\right)^2}\left[\frac{d\underset{sat}{\Delta}(s)}{dT}\underset{sat}{\Delta}\left(\frac{1}{\rho}\right) - \underset{sat}{\Delta}(s)\frac{d}{dT}\left(\underset{sat}{\Delta}\left(\frac{1}{\rho}\right)\right)\right] \tag{B.103}$$

Using Eq. (B.114) one can write:

$$\frac{d\underset{sat}{\Delta}(s)}{dT} = \frac{\underset{sat}{\Delta}(C_P)}{T} - \underset{sat}{\Delta}\left(\frac{\alpha}{\rho}\right)\frac{dP^{\text{sat}}}{dT} \tag{B.104}$$

And from Eq. (B.111) one gets:

$$\frac{d}{dT}\left(\underset{sat}{\Delta}\left(\frac{1}{\rho}\right)\right) = \underset{sat}{\Delta}\left(\frac{\alpha}{\rho}\right) - \underset{sat}{\Delta}\left(\frac{\beta}{\rho}\right)\frac{dP^{\text{sat}}}{dT} \tag{B.105}$$

When injected into Eq. (B.102) it eventually leads to:

$$\boxed{\frac{d^2P^{\text{sat}}}{dT^2} = \frac{1}{\underset{sat}{\Delta}\left(\frac{1}{\rho}\right)}\left[\frac{\underset{sat}{\Delta}(C_P)}{T} - \frac{dP^{\text{sat}}}{dT}\left(2\underset{sat}{\Delta}\left(\frac{\alpha}{\rho}\right) - \frac{dP^{\text{sat}}}{dT}\underset{sat}{\Delta}\left(\frac{\beta}{\rho}\right)\right)\right]} \tag{B.106}$$

B.4.1.2 Saturation free enthalpy derivative $\frac{d\mu^{\text{sat}}}{dT}$

From the chemical equilibrium, Eq. (B.94) and Gibbs "saturation' equation Eq. (B.95) it comes that one can chose indifferently:

$$\frac{d\mu^{\text{sat}}}{dT} = -s_l^{\text{sat}} + \frac{1}{\rho_l}\frac{dP^{\text{sat}}}{dT} = -s_v^{\text{sat}} + \frac{1}{\rho_v}\frac{dP^{\text{sat}}}{dT} \tag{B.107}$$

This allows to write:

$$\boxed{\frac{d\mu^{\text{sat}}}{dT} = -\bar{s} + \frac{1}{\bar{\rho}}\frac{dP^{\text{sat}}}{dT}} \tag{B.108}$$

Given that $\mu^{\text{sat}} = \bar{\mu}$, it also ensues that:

$$\frac{d\bar{\mu}}{dT} = -\bar{s} + \frac{1}{\bar{\rho}}\frac{dP^{\text{sat}}}{dT} \tag{B.109}$$

B.4.1.3 Saturation density derivative $\frac{d\rho_k}{dT}$

Eq. (B.96) can be used noticing that $\left(\frac{\partial \rho}{\partial T}\right)_P = -\rho\alpha$ and $\left(\frac{\partial \rho}{\partial T}\right)_P = -\rho\alpha$ to get:

$$\boxed{\frac{d\rho_k}{dT} = \rho_k\left(\beta_k^{\text{sat}}\frac{dP^{\text{sat}}}{dT} - \alpha_k^{\text{sat}}\right)} \tag{B.110}$$

and

$$\frac{d}{dT}\left(\frac{1}{\rho_k}\right) = \frac{1}{\rho_k}\left(\alpha_k^{\text{sat}} - \beta_k^{\text{sat}}\frac{dP^{\text{sat}}}{dT}\right) \tag{B.111}$$

It also ensues that:

$$\boxed{\frac{d\bar{\rho}}{dT} = \frac{1}{\bar{\rho}}\left(\bar{\beta}\frac{dP^{\text{sat}}}{dT} - \bar{\alpha}\right)} \tag{B.112}$$

and

$$\frac{d}{dT}\left(\frac{1}{\bar{\rho}}\right) = \frac{1}{\bar{\rho}}\left(\bar{\alpha} - \bar{\beta}\frac{dP^{\text{sat}}}{dT}\right) \tag{B.113}$$

B.4.1.4 Saturation entropy derivative $\frac{ds_k^{\text{sat}}}{dT}$

Eq. (B.96) can be used noticing that $\left(\frac{\partial s}{\partial T}\right)_P = \frac{C_P}{T}$ and $\left(\frac{\partial s}{\partial T}\right)_P = -\frac{\alpha}{\rho}$ to get:

$$\boxed{\frac{ds_k^{\text{sat}}}{dT} = \frac{C_{P_k}^{\text{sat}}}{T} - \frac{\alpha_k^{\text{sat}}}{\rho_k}\frac{dP^{\text{sat}}}{dT}} \tag{B.114}$$

It also ensues that:

$$\boxed{\frac{d\bar{s}}{dT} = \frac{\bar{C_P}}{T} - \frac{\bar{\alpha}}{\bar{\rho}}\frac{dP^{\text{sat}}}{dT}} \tag{B.115}$$

B.4.1.5 Main derivatives summary

$$\frac{dP^{\text{sat}}}{dT} = \left(s_l^{\text{sat}} - s_v^{\text{sat}}\right)\left(\frac{1}{\rho_l} - \frac{1}{\rho_v}\right)^{-1} = -\frac{\mathcal{L}^{\text{vap}}\rho_l\rho_v}{T\left(\rho_l - \rho_v\right)} \tag{B.116}$$

$$\frac{d^2P^{\text{sat}}}{dT^2} = \frac{1}{\underset{sat}{\Delta}\left(\frac{1}{\rho}\right)}\left[\frac{\underset{sat}{\Delta}\left(C_P\right)}{T} - 2\underset{sat}{\Delta}\left(\frac{\alpha}{\rho}\right)\frac{dP^{\text{sat}}}{dT} + \underset{sat}{\Delta}\left(\frac{\beta}{\rho}\right)\left(\frac{dP^{\text{sat}}}{dT}\right)^2\right] \tag{B.117}$$

$$\frac{d\rho_k}{dT} = \rho_k\left(\beta_k^{\text{sat}}\frac{dP^{\text{sat}}}{dT} - \alpha_k^{\text{sat}}\right) \tag{B.118}$$

$$\frac{d\mu^{\text{sat}}}{dT} = -\bar{s} + \frac{1}{\bar{\rho}}\frac{dP^{\text{sat}}}{dT} \tag{B.119}$$

$$\frac{ds_k^{\text{sat}}}{dT} = \frac{C_{P_k}^{\text{sat}}}{T} - \frac{\alpha_k^{\text{sat}}}{\rho_k}\frac{dP^{\text{sat}}}{dT} \tag{B.120}$$

Appendix C

Additional developments on the Second Gradient theory

C.1 Virtual power principle for the Second Gradient theory

To derive the equations of the fluid motion in the Second Gradient theory, two main methods can be used. The first one relies on a Hamiltonian approach and has been developed by Casal and Gouin in Casal (1972), Casal and Gouin (1985), Casal and Gouin (1989). The second one, which will be described in the following paragraphs, is based on the virtual power principle as demonstrated in Germain (1972), Frémond (2013), Yu (2014) and has been expanded on in Germain (1972), Seppecher (1987) and Jamet (1998).
The virtual power principle is used to derive the equations of smooth motions for systems where no shocks occur. It can be shown (see Antman (1995)) that describing indirectly the internal forces using their virtual power is equivalent to describing them directly through a momentum equation. Starting from a general framework, the fluid motion satisfies the Cauchy's law:

$$\rho \frac{d\mathbf{v}}{dt} = \boldsymbol{\nabla} \cdot \underline{\underline{\boldsymbol{\tau}}} + \rho \boldsymbol{g} \tag{C.1}$$

where ρ is the density of the fluid, $\mathbf{v}$ its actual velocity, $\underline{\underline{\boldsymbol{\tau}}}$ is the stress tensor and $\rho \boldsymbol{g}$ are the body forces. The idea behind the virtual power principle is to notice that the power produced by the different forces (stress tensor and body forces, whether internal or external) corresponding *a priori* to the real motion represented by the velocity field $\mathbf{v}$, can still be defined for an arbitrary motion, called a "virtual" motion, described by the "virtual" velocity field $\mathbf{v}^*$. In this section, the virtual power principle is explained in its classic form as done in Frémond (2013). This better allows to grasp its inherent meaning and its consequences without the additional complexity linked to the Second Gradient theory in itself.

The fluid, in the domain Ω, is described by the usual continuum mechanics quantities such as the pressure P, the density ρ, the temperature T , etc. and the quantities describing its motion and deformation $\mathbf{v}$, $\boldsymbol{\nabla}\mathbf{v}$, etc. but also by an other characteristic quantities c to ensure prescribed precision and complexity in the desired description of the fluid dynamics. For instance c can be a volume fraction of one of the component in a mixture, the volume fraction of one of the phase in a two-phase flow or can be as sophisticated as the volume density of active bounds between the microscopic components of the fluid. Whatever the choice of c, the

important idea is that its evolution is a consequence of microscopic actions and movements that do not necessarily result in a macroscopic motion of the fluid. From c, one can define a microscopic rate of change $\nu = dc/dt$ representing the motion velocity at a microscopic scale. Given these definitions, a localized virtual motion will be defined as a triplet $(\mathcal{V}, \mathbf{v}^*, \nu^*)$ where $\mathcal{V}$ is a portion of the domain Ω containing the fluid and $\mathcal{A}$ its boundary, $\mathbf{v}^*$ a virtual (macroscopic) velocity field and ν^* a virtual microscopic rate of change for the fluid in $\mathcal{V}$. The set containing all the localized virtual motions will be noted $\mathbb{M}^*$.

C.1.1 Virtual power of the internal forces

For any localized virtual motion $(\mathcal{V}, \mathbf{v}^*, \nu^*) \in \mathbb{M}^*$ in Ω, the virtual power $\mathcal{P}_{(i)}$ of the internal forces acting on the fluid in $\mathcal{V}$ is given by:

$$\mathcal{P}_{(i)} = -\int_{\mathcal{V}} \left[\boldsymbol{\nabla}\mathbf{v}^* : \underline{\underline{\boldsymbol{\tau}}} + \epsilon\nu^* + \boldsymbol{f}_\epsilon \cdot \boldsymbol{\nabla}\nu^* \right] d\mathcal{V} \tag{C.2}$$

The different contributions can be, from a physical point of view,, interpreted as follows: $\boldsymbol{\nabla}\mathbf{v}^* : \underline{\underline{\boldsymbol{\tau}}}$ represents the power of internal forces related to macroscopic motions, ϵ is a volume density of energy by unit of ν^* and $\boldsymbol{f}_\epsilon$ is a volume density of energy flux by unit of ν^*. In fact, $\int_{\mathcal{V}} [\epsilon\rho + \boldsymbol{f}_\epsilon \cdot \boldsymbol{\nabla}\nu^*] \, d\mathcal{V}$ accounts for the power of internal forces that do not induce a macroscopic motion of the fluid while causing movement at a microscopic scale.

C.1.2 Virtual power of the external forces

For any localized virtual motion $(\mathcal{V}, \mathbf{v}^*, \nu^*) \in \mathbb{M}^*$ in Ω, the virtual power $\mathcal{P}_{(e)}$ of the external forces acting on the fluid in $\mathcal{V}$ is given by:

$$\mathcal{P}_{(e)} = \int_{\mathcal{V}} [\mathbf{v}^* \cdot \boldsymbol{g} + \mathcal{E}\nu^*] \, d\mathcal{V} + \int_{\mathcal{A}} [\mathbf{v}^* \cdot \boldsymbol{t} + \varepsilon\nu^*] \, d\mathcal{A} \tag{C.3}$$

This time the contributions are separated in two categories: firstly the power of the external forces applied at distance over the volume of fluid $\mathcal{V}$ and secondly the power of the external forces applied by contact over the boundary $\mathcal{A}$. Regarding the first integral, the two contributions are interpreted as follows: $\mathbf{v}^* \cdot \boldsymbol{g}$ represents the power of external body forces, at distance, related to macroscopic motions and $\mathcal{E}$ is a volume density of energy accounting for the power of external body forces at distance only resulting on microscopic motions. The same interpretations arise for the second integral: $\mathbf{v}^* \cdot \boldsymbol{t}$ accounts for the power of contact forces resulting in macroscopic motions and ε is a volume density of energy accounting for the power of contact forces only resulting in microscopic motions.

C.1.3 Virtual power of the acceleration forces

From Cauchy's law, the acceleration of the fluid can be interpreted as a force $\boldsymbol{\gamma}$ of which elementary expression is:

$$\boldsymbol{\gamma} = \rho \frac{d\mathbf{v}}{dt} \tag{C.4}$$

From that, for any localized virtual motion $(\mathcal{V}, \mathbf{v}^*, \nu^*) \in \mathbb{M}^*$ in Ω, the virtual power $\mathcal{P}_{(a)}$ of the acceleration forces acting on the fluid in $\mathcal{V}$ is given by:

$$\mathcal{P}_{(a)} = \int_{\mathcal{V}} \mathbf{v}^* \cdot \boldsymbol{\gamma} \, d\mathcal{V} = \int_{\mathcal{V}} \rho \mathbf{v}^* \cdot \frac{d\mathbf{v}}{dt} \, d\mathcal{V} \tag{C.5}$$

C.1.4 Virtual power theorems

Given all the previous definitions, one can now formulate the virtual power principle:

For any localized virtual motion $(\mathcal{V}, \boldsymbol{v}^*, \nu^*) \in \mathbb{M}^*$ in Ω, the sum of the virtual power of the internal forces $\mathcal{P}_{(i)}$ and the virtual power of the external forces $\mathcal{P}_{(e)}$ in $\mathcal{V}$ equals the virtual power of the acceleration forces $\mathcal{P}_{(a)}$ in $\mathcal{V}$.

$$\forall\, (\mathcal{V}, \mathbf{v}^*, \nu^*) \in \mathbb{M}^*, \quad \mathcal{P}_{(a)} = \mathcal{P}_{(i)} + \mathcal{P}_{(e)} \tag{C.6}$$

A prerequisite to the virtual power principle as obtained in Eq. (C.6) is the axiom of the virtual power principle for internal forces which states:

*For any localized virtual motion $(\mathcal{V}, \boldsymbol{v}^*, \nu^*) \in \mathbb{M}^*$ in Ω that causes a **rigid body motion** for the fluid in $\mathcal{V}$, the virtual power of the internal forces $\mathcal{P}_{(i)}$ in $\mathcal{V}$ equals to zero.*

For the interested reader, a more in-depth description is given in Yu (2014) about the microscopic rate of change c and the different posssible sourcess for the microscopic power term $\epsilon, \mathcal{E}, \varepsilon$.

C.1.5 Equations of motion

Since Eq. (C.6) holds for any $(\mathcal{V}, \mathbf{v}^*, \nu^*) \in \mathbb{M}^*$, one can choose localized virtual motions such as $\mathbf{v}^* = \mathbf{0}$ leading to Eqs. (C.7a) and (C.7b), and then localized virtual motions such as $\nu^* = 0$ leading to Eqs. (C.8a) and (C.8b).

$$\rho \frac{d\mathbf{v}}{dt} = \boldsymbol{\nabla} \cdot \underline{\underline{\boldsymbol{\tau}}} + \boldsymbol{g} \quad \text{in } \mathcal{V} \tag{C.7a}$$

$$\underline{\underline{\boldsymbol{\tau}}} \cdot \boldsymbol{n} = \boldsymbol{t} \quad \text{on } \mathcal{A} \tag{C.7b}$$

$$\boldsymbol{\nabla} \cdot \boldsymbol{f}_\epsilon = \mathcal{E} - \epsilon \quad \text{in } \mathcal{V} \tag{C.8a}$$

$$\boldsymbol{f}_\epsilon \cdot \boldsymbol{n} = 0 \quad \text{on } \mathcal{A} \tag{C.8b}$$

The virtual work principle has been presented in its native form, completing the description of the fluid motion by adding a microscopic characteristic quantity c and the corresponding microscopic motion velocity $\nu = dc/dt$. It has allowed to retrieve a classic set of motion equations. However, another way to refine the definition of the fluid can be to consider a specific subset of virtual motions with corresponding virtual velocity fields $\mathbf{v}^*$ at least two times differentiable, as explained in Germain (1972). This different approach is used Sec. 5.1.1 more specifically to derive the motion equations for the Second Gradient theory. For the sake of simplicity and since such a level of refinement is not proven to be useful and pertinent, the microscopic motion represented by ν^* will not be considered in this framework.

C.2 Gibbs equation

In this section, we derive the new form of the Gibbs equation for a fluid endowed with capillarity. The starting assumption is that the volumetric free energy F of the fluid can be written like in Eq. (5.47):

$$F\left(T,\rho,\boldsymbol{\nabla}\rho\right)=F_0\left(T,\rho\right)+F_1\left(T,\rho,\boldsymbol{\nabla}\rho\right) \tag{C.9}$$

The thermodynamic variables have a dependency on two classic intensive variables, here we chose T ans ρ for convenience, and on the density gradient $\boldsymbol{\nabla}\rho$. The differential of the specific internal energy is written:

$$de_s=\left(\frac{\partial e_s}{\partial s}\right)_{\rho,\boldsymbol{\nabla}\rho}ds+\left(\frac{\partial e_s}{\partial \rho}\right)_{s,\boldsymbol{\nabla}\rho}d\rho+\left(\frac{\partial e_s}{\partial \boldsymbol{\nabla}\rho}\right)_{s,\rho}\cdot d\boldsymbol{\nabla}\rho \tag{C.10}$$

The temperature definition should not be impacted by the capillary description, therefore:

$$T\hat{=}\left(\frac{\partial e_s}{\partial s}\right)_{\rho,\boldsymbol{\nabla}\rho} \tag{C.11}$$

Remembering that $e_s=f-Ts=F/\rho-Ts$, one can write:

$$\left(\frac{\partial e_s}{\partial \rho}\right)_{s,\boldsymbol{\nabla}\rho}=\frac{\partial}{\partial\rho}\left(\frac{F}{\rho}-Ts\right)_{s,\boldsymbol{\nabla}\rho} \tag{C.12a}$$

$$=\frac{1}{\rho}\left(\frac{\partial F}{\partial\rho}\right)_{s,\boldsymbol{\nabla}\rho}-\frac{F}{\rho^2}-s\left(\frac{\partial T}{\partial\rho}\right)_{s,\boldsymbol{\nabla}\rho} \tag{C.12b}$$

Thanks to Eq. (A.30) and Eq. (B.17), one can also write:

$$\left(\frac{\partial F}{\partial\rho}\right)_{s,\boldsymbol{\nabla}\rho}=\left(\frac{\partial F}{\partial\rho}\right)_{T,\boldsymbol{\nabla}\rho}+\left(\frac{\partial F}{\partial T}\right)_{\rho,\boldsymbol{\nabla}\rho}\left(\frac{\partial T}{\partial\rho}\right)_{s,\boldsymbol{\nabla}\rho}=\left(\frac{\partial F}{\partial\rho}\right)_{T,\boldsymbol{\nabla}\rho}+S\left(\frac{\partial T}{\partial\rho}\right)_{s,\boldsymbol{\nabla}\rho} \tag{C.13}$$

Eventually, with the definition of the thermodynamic pressure Eq. (5.54), one gets:

$$\left(\frac{\partial e_s}{\partial \rho}\right)_{s,\boldsymbol{\nabla}\rho}=\frac{1}{\rho}\left(\frac{\partial F}{\partial\rho}\right)_{T,\boldsymbol{\nabla}\rho}+\cancel{\frac{S}{\rho}\left(\frac{\partial T}{\partial\rho}\right)_{s,\boldsymbol{\nabla}\rho}}-\frac{F}{\rho^2}-\cancel{s\left(\frac{\partial T}{\partial\rho}\right)_{s,\boldsymbol{\nabla}\rho}} \tag{C.14a}$$

$$=\frac{1}{\rho^2}\left(\rho\left(\frac{\partial F}{\partial\rho}\right)_{T,\boldsymbol{\nabla}\rho}-F\right) \tag{C.14b}$$

$$=\frac{P}{\rho^2} \tag{C.14c}$$

Besides, with the definition Eq. (5.53), one also gets:

$$\left(\frac{\partial e_s}{\partial \boldsymbol{\nabla}\rho}\right)_{s,\rho}=\frac{\partial}{\partial\boldsymbol{\nabla}\rho}\left(\frac{F}{\rho}-Ts\right)_{s,\rho}=\frac{1}{\rho}\left(\frac{\partial F}{\partial\boldsymbol{\nabla}\rho}\right)_{s,\rho}-\cancel{s\left(\frac{\partial T}{\partial\boldsymbol{\nabla}\rho}\right)_{s,\rho}}=\frac{1}{\rho}\boldsymbol{\mathcal{F}} \tag{C.15}$$

Combining all the previous results, one can write the new Gibbs equation:

$$\boxed{de_s=T\,ds+\frac{P}{\rho^2}\,d\rho+\frac{1}{\rho}\boldsymbol{\mathcal{F}}\cdot d\boldsymbol{\nabla}\rho} \tag{C.16}$$

C.3 Entropy balance

In this section we derive an expression for the volumetric entropy production term using the relations obtained trough the application of the two fundamental thermodynamic principles and the virtual powers principle. This volumetric entropy production allows, in turn, to express the internal fluxes and derive the fluid motion equations for the Second Gradient theory. The starting set of equationsis:

(1) $\dfrac{\partial \rho}{\partial t} = -\boldsymbol{\nabla} \cdot (\rho \mathbf{v})$

(2) $\rho \dfrac{de_s}{dt} = \boldsymbol{\nabla}\mathbf{v} : \underline{\underline{\boldsymbol{\varsigma}}} + \boldsymbol{\nabla}\boldsymbol{\nabla}\mathbf{v} \vdots \underline{\underline{\underline{\mathbf{C}}}} - \boldsymbol{\nabla} \cdot \boldsymbol{q}$

(3) $\dfrac{de_s}{dt} = T\dfrac{ds}{dt} + \dfrac{P}{\rho^2}\dfrac{d\rho}{dt} + \dfrac{1}{\rho}\boldsymbol{\mathcal{F}} \cdot \dfrac{d\boldsymbol{\nabla}\rho}{dt}$

(4) $\rho \dfrac{ds}{dt} = \phi_S - \boldsymbol{\nabla} \cdot \left(\dfrac{\boldsymbol{q}}{T}\right)$

Applying the particular derivative Eq. (A.73) to ρ and injecting (1), one gets:

$$\frac{d\rho}{dt} = \frac{\partial \rho}{\partial t} + \boldsymbol{\nabla}\rho \cdot \mathbf{v} = -\boldsymbol{\nabla} \cdot (\rho \mathbf{v}) + \boldsymbol{\nabla}\rho \cdot \mathbf{v} = -\rho \boldsymbol{\nabla} \cdot \mathbf{v} \tag{C.17}$$

Likewise, the particular derivative Eq. (A.73) applied to the density gradient $\boldsymbol{\nabla}\rho$ can be expressed:

$$\begin{aligned}
\frac{d\boldsymbol{\nabla}\rho}{dt} &= \frac{\partial(\boldsymbol{\nabla}\rho)}{\partial t} + \boldsymbol{\nabla}\boldsymbol{\nabla}\rho \cdot \mathbf{v} && \text{(C.18a)}\\
&= \boldsymbol{\nabla}\left(\frac{\partial \rho}{\partial t}\right) + \boldsymbol{\nabla}\boldsymbol{\nabla}\rho \cdot \mathbf{v} && \text{(C.18b)}\\
&= -\boldsymbol{\nabla}\left(\boldsymbol{\nabla} \cdot (\rho \mathbf{v})\right) + \boldsymbol{\nabla}\boldsymbol{\nabla}\rho \cdot \mathbf{v} && \text{(C.18c)}\\
&= -\boldsymbol{\nabla}\left(\rho \boldsymbol{\nabla} \cdot \mathbf{v} + \boldsymbol{\nabla}\rho \cdot \mathbf{v}\right) + \boldsymbol{\nabla}\boldsymbol{\nabla}\rho \cdot \mathbf{v} && \text{(C.18d)}\\
&= -\rho \boldsymbol{\nabla}\left(\boldsymbol{\nabla} \cdot \mathbf{v}\right) - \boldsymbol{\nabla}\rho \boldsymbol{\nabla} \cdot \mathbf{v} + \boldsymbol{\nabla}\rho \cdot \boldsymbol{\nabla}\mathbf{v} - \mathbf{v} \cdot \boldsymbol{\nabla}\boldsymbol{\nabla}\rho + \boldsymbol{\nabla}\boldsymbol{\nabla}\rho \cdot \mathbf{v} && \text{(C.18e)}\\
&= -\rho \boldsymbol{\nabla}\left(\boldsymbol{\nabla} \cdot \mathbf{v}\right) - \boldsymbol{\nabla}\rho \boldsymbol{\nabla} \cdot \mathbf{v} + \boldsymbol{\nabla}\rho \cdot \boldsymbol{\nabla}\mathbf{v} - \boldsymbol{\nabla}\boldsymbol{\nabla}\rho^{\mathrm{T}} \cdot \mathbf{v} + \boldsymbol{\nabla}\boldsymbol{\nabla}\rho \cdot \mathbf{v} && \text{(C.18f)}
\end{aligned}$$

The tensor $\boldsymbol{\nabla}\boldsymbol{\nabla}\rho$ being symmetrical, one gets:

$$\frac{d\boldsymbol{\nabla}\rho}{dt} = -\left(\rho \boldsymbol{\nabla}\left(\boldsymbol{\nabla} \cdot \mathbf{v}\right) + \boldsymbol{\nabla}\rho \boldsymbol{\nabla} \cdot \mathbf{v} + \boldsymbol{\nabla}\rho \cdot \boldsymbol{\nabla}\mathbf{v}\right) \tag{C.19}$$

By noting $q_T = \boldsymbol{q} \cdot \boldsymbol{\nabla}T/T$, one can express $T \times$ (4) with:

$$\rho T \frac{ds}{dt} = T\phi_S - T\left(\frac{1}{T}\boldsymbol{q} - \frac{1}{T^2}\boldsymbol{q} \cdot \boldsymbol{\nabla}T\right) = T\phi_S - \boldsymbol{\nabla} \cdot \boldsymbol{q} + q_T \tag{C.20}$$

Finally, one can equalize (2) and $\rho \times$ (3) to get:

$$\rho T \frac{ds}{dt} + \frac{P}{\rho}\frac{d\rho}{dt} + \boldsymbol{\mathcal{F}} \cdot \frac{d\boldsymbol{\nabla}\rho}{dt} = \boldsymbol{\nabla}\mathbf{v} : \underline{\underline{\boldsymbol{\varsigma}}} + \boldsymbol{\nabla}\boldsymbol{\nabla}\mathbf{v} \vdots \underline{\underline{\underline{\mathbf{C}}}} - \boldsymbol{\nabla} \cdot \boldsymbol{q} \tag{C.21}$$

The left-hand side particular derivative can be replaced by the expressions in Eq. (C.17), Eq. (C.19), Eq. (C.20) to obtain:

$$\begin{aligned} T\phi_S - &\boldsymbol{\nabla}\cdot\boldsymbol{q} + q_T - P\boldsymbol{\nabla}\cdot\mathbf{v} - \boldsymbol{\mathcal{F}}\cdot\left(\rho\boldsymbol{\nabla}\left(\boldsymbol{\nabla}\cdot\mathbf{v}\right) + \boldsymbol{\nabla}\rho\boldsymbol{\nabla}\cdot\mathbf{v} + \boldsymbol{\nabla}\rho\cdot\boldsymbol{\nabla}\mathbf{v}\right) \\ &= \boldsymbol{\nabla}\mathbf{v} : \underline{\underline{\varsigma}} + \boldsymbol{\nabla}\boldsymbol{\nabla}\mathbf{v} \vdots \underline{\underline{\underline{\mathbf{C}}}} - \boldsymbol{\nabla}\cdot\boldsymbol{q} \end{aligned} \tag{C.22}$$

And eventually the volumetric entropy production is written:

$$T\phi_S = P\boldsymbol{\nabla}\cdot\mathbf{v} + \boldsymbol{\mathcal{F}}\cdot\left(\rho\boldsymbol{\nabla}\left(\boldsymbol{\nabla}\cdot\mathbf{v}\right) + \boldsymbol{\nabla}\rho\boldsymbol{\nabla}\cdot\mathbf{v} + \boldsymbol{\nabla}\rho\cdot\boldsymbol{\nabla}\mathbf{v}\right) + \boldsymbol{\nabla}\mathbf{v} : \underline{\underline{\varsigma}} + \boldsymbol{\nabla}\boldsymbol{\nabla}\mathbf{v} \vdots \underline{\underline{\underline{\mathbf{C}}}} - q_T \tag{C.23}$$

Using the Einstein notation, Eq. (C.23) can be written with indexes:

$$\begin{aligned} T\phi_S =& P\frac{\partial \mathbf{v}_i}{\partial x_i} + \boldsymbol{\mathcal{F}}_j\left(\rho\frac{\partial^2\mathbf{v}_i}{\partial x_i\partial x_j} + \frac{\partial\rho}{\partial x_j}\frac{\partial\mathbf{v}_i}{\partial x_i} + \frac{\partial\rho}{\partial x_i}\frac{\partial\mathbf{v}_i}{\partial x_j}\right) \\ &+ \varsigma ji\frac{\partial\mathbf{v}_i}{\partial x_j} + \mathrm{C}_{kji}\frac{\partial^2\mathbf{v}_i}{\partial x_j\partial x_k} - q_T \end{aligned} \tag{C.24a}$$

$$\begin{aligned} T\phi_S =& P\frac{\partial \mathbf{v}_i}{\partial x_i} + \rho\boldsymbol{\mathcal{F}}_k\delta_{ik}\frac{\partial^2\mathbf{v}_i}{\partial x_k\partial x_j} + \boldsymbol{\mathcal{F}}_k\frac{\partial\rho}{\partial x_k}\delta_{ij}\frac{\partial\mathbf{v}_i}{\partial x_j} + \boldsymbol{\mathcal{F}}_j\frac{\partial\rho}{\partial x_i}\frac{\partial\mathbf{v}_i}{\partial x_j} \\ &+ \varsigma ji\frac{\partial\mathbf{v}_i}{\partial x_j} + \mathrm{C}_{kji}\frac{\partial^2\mathbf{v}_i}{\partial x_j\partial x_k} \end{aligned} \tag{C.24b}$$

To finally get the condensed relation:

$$T\phi_S = -q_T + \left[\varsigma_{ji} + \frac{\partial\rho}{\partial x_i}\mathcal{F}_j + \left(P + \frac{\partial\rho}{\partial x_k}\mathcal{F}_k\right)\delta_{ij}\right]\frac{\partial\mathbf{v}_i}{\partial x_j} + \left[\mathrm{C}_{kji} + \rho\mathcal{F}_k\delta_{ik}\right]\frac{\partial^2\mathbf{v}_i}{\partial x_j\partial x_k} \tag{C.25}$$

Given the hypothesis that the second gradient of the velocity does not contribute to the entropy intrinsic creation and the fact that $\underline{\underline{\underline{\mathbf{C}}}}$ is symmetrical in its two first indexes, one gets:

$$\mathrm{C}_{kji} + \rho\mathcal{F}_k\delta_{ik} = 0 \Rightarrow \mathrm{C}_{ijk} = \frac{1}{2}\rho\left(\delta_{ik}\mathcal{F}_k + \delta_{jk}\mathcal{F}_i\right) \tag{C.26}$$

Besides, knowing that $\underline{\underline{\varsigma}}$ is symmetrical, it can be expressed using the relation $\underline{\underline{\varsigma}} = \underline{\underline{\boldsymbol{\tau}}} + \boldsymbol{\nabla}\cdot\underline{\underline{\underline{\boldsymbol{\mathcal{C}}}}}$ with $\mathcal{C}_{ijk} = \mathrm{C}_{kji}$ (from App. C.1):

$$\begin{aligned} \left(\boldsymbol{\nabla}\cdot\underline{\underline{\underline{\boldsymbol{\mathcal{C}}}}}\right)_{ij} = \frac{\partial\mathcal{C}_{ijk}}{\partial x_k} = \frac{\partial\mathrm{C}_{kji}}{\partial x_k} &= -\frac{1}{2}\left[\frac{\partial(\rho\delta_{ik}\mathcal{F}_j)}{\partial x_k} + \frac{\partial(\rho\delta_{ij}\mathcal{F}_k)}{\partial x_k}\right] \\ &= -\frac{1}{2}\left[\frac{\partial(\rho\mathcal{F}_j)}{\partial x_i} + \delta ij\frac{\partial(\rho\mathcal{F}_k)}{\partial x_k}\right] \end{aligned} \tag{C.27}$$

$$\underline{\underline{\varsigma}} = \underline{\underline{\boldsymbol{\tau}}} - \frac{1}{2}\boldsymbol{\nabla}\left(\rho\boldsymbol{\mathcal{F}}\right) - \frac{1}{2}\boldsymbol{\nabla}\cdot\left(\rho\boldsymbol{\mathcal{F}}\right)\underline{\underline{\mathbf{I}}} \tag{C.28}$$

With that, the volume entropy production is eventually given by:

$$T\phi_S = -q_T + \left[\tau^d_{ij} + \tau^n_{ij} - \frac{1}{2}\frac{\partial(\rho\mathcal{F}_j)}{\partial x_i} + \frac{\partial\rho}{\partial x_i}\mathcal{F}_j + \left(P + \frac{\partial\rho}{\partial x_k}\mathcal{F}_k - \frac{1}{2}\frac{\partial(\rho\mathcal{F}_k)}{\partial x_k}\right)\delta_{ij}\right]\frac{\partial\mathbf{v}_i}{\partial x_j} \tag{C.29}$$

or using tensorial notations:

$$T\phi_S = -q_T + \left[\underline{\underline{\boldsymbol{\tau}}} + \boldsymbol{\nabla}\rho\otimes\boldsymbol{\mathcal{F}} - \frac{1}{2}\boldsymbol{\nabla}\left(\rho\boldsymbol{\mathcal{F}}\right)\right] : \boldsymbol{\nabla}\mathbf{v} + \left[P + \boldsymbol{\nabla}\rho\cdot\boldsymbol{\mathcal{F}} - \frac{1}{2}\boldsymbol{\nabla}\cdot\left(\rho\boldsymbol{\mathcal{F}}\right)\right]\boldsymbol{\nabla}\cdot\mathbf{v} \tag{C.30}$$

C.4 Equilibrium conditions for an isothermal interface

The study of an isothermal interface at equilibrium is a usefull method to qualify the Second Gradient theory behavior and try to retrieve known results of fluid mechanics regarding surface tension by stuying planar, circular or spherical interfaces. In this section, the reader can find a condensed equation that define said equilibrium and which solely depends on the expression chosen for the volumetric free enthalpy F.

In the framework of the Second Gradient theory, the differential of the volumetric free energy F is written:

$$dF = \left(\frac{\partial F}{\partial T}\right)_{\rho,\boldsymbol{\nabla}\rho} dT + \left(\frac{\partial F}{\partial \rho}\right)_{T,\boldsymbol{\nabla}\rho} d\rho + \boldsymbol{\mathcal{F}} \cdot d\boldsymbol{\nabla}\rho \tag{C.31}$$

In particular, when looking to a spatial partial derivative, it lands:

$$\frac{dF}{dx_i} = \left(\frac{\partial F}{\partial T}\right)_{\rho,\boldsymbol{\nabla}\rho} \frac{\partial T}{\partial x_i} + \left(\frac{\partial F}{\partial \rho}\right)_{T,\boldsymbol{\nabla}\rho} \frac{\partial \rho}{\partial x_i} + \boldsymbol{\mathcal{F}} \cdot \frac{\partial \boldsymbol{\nabla}\rho}{\partial x_i} \tag{C.32}$$

where the last term can be expressed as:

$$\boldsymbol{\mathcal{F}} \cdot \frac{\partial \boldsymbol{\nabla}\rho}{\partial x_i} = \mathcal{F}_j \frac{\partial (\boldsymbol{\nabla}\rho)_j}{\partial x_i} = \frac{\partial^2 \rho}{\partial x_i \partial x_j} \mathcal{F}_j = (\boldsymbol{\nabla}\boldsymbol{\nabla}\rho)_{ij} \mathcal{F}_j \tag{C.33}$$

Therefore one obtains:

$$\boldsymbol{\nabla} F = \boldsymbol{\nabla} T \left(\frac{\partial F}{\partial T}\right)_{\rho,\boldsymbol{\nabla}\rho} + \boldsymbol{\nabla}\rho \left(\frac{\partial F}{\partial \rho}\right)_{T,\boldsymbol{\nabla}\rho} + \boldsymbol{\nabla}\boldsymbol{\nabla}\rho \cdot \boldsymbol{\mathcal{F}} \tag{C.34}$$

When considering an isothermal interface at equilibrium, the velocity and the temperature gradient are null. Therefore, only the momentum equation is to be considered among the different motion equations given Eqs. (5.86) and the gradient of the volumetric free enrgy given Eq. (C.34) simplifies to give the reduced set of equations:

$$\boldsymbol{\nabla} p + \boldsymbol{\nabla} \cdot (\boldsymbol{\nabla}\rho \otimes \boldsymbol{\mathcal{F}}) = 0 \tag{C.35}$$

$$\boldsymbol{\nabla} F = \boldsymbol{\nabla}\rho \left(\frac{\partial F}{\partial \rho}\right)_{T,\boldsymbol{\nabla}\rho} + \boldsymbol{\nabla}\boldsymbol{\nabla}\rho \cdot \boldsymbol{\mathcal{F}} \tag{C.36}$$

where the expressions of the mechanical pressure and the thermodynamic pressure are by Eq. (5.73) and Eq. (5.54). The momentum equation Eq. (C.35) can then be simplified:

$$\boldsymbol{\nabla} p + \boldsymbol{\nabla} \cdot (\boldsymbol{\nabla}\rho \otimes \boldsymbol{\mathcal{F}}) = \boldsymbol{\nabla} \left(\rho \left(\frac{\partial F}{\partial \rho}\right)_{T,\boldsymbol{\nabla}\rho} - F - \rho \boldsymbol{\nabla} \cdot \boldsymbol{\mathcal{F}} \right) + \boldsymbol{\nabla} \cdot (\boldsymbol{\nabla}\rho \otimes \boldsymbol{\mathcal{F}}) \tag{C.37a}$$

$$\begin{aligned} &= \boldsymbol{\nabla}\rho \left(\frac{\partial F}{\partial \rho}\right)_{T,\boldsymbol{\nabla}\rho} + \rho \boldsymbol{\nabla} \left[\left(\frac{\partial F}{\partial \rho}\right)_{T,\boldsymbol{\nabla}\rho} \right] - \boldsymbol{\nabla} F \\ &\quad - \cancel{\boldsymbol{\nabla}\rho \boldsymbol{\nabla} \cdot \boldsymbol{\mathcal{F}}} - \rho \boldsymbol{\nabla} (\boldsymbol{\nabla} \cdot \boldsymbol{\mathcal{F}}) + \cancel{\boldsymbol{\nabla}\rho \boldsymbol{\nabla} \cdot \boldsymbol{\mathcal{F}}} + \boldsymbol{\nabla}\boldsymbol{\nabla}\rho \cdot \boldsymbol{\mathcal{F}} \end{aligned} \tag{C.37b}$$

One can recognize the gradient of the volumetric free energy:

$$\boldsymbol{\nabla} p + \boldsymbol{\nabla} \cdot (\boldsymbol{\nabla}\rho \otimes \boldsymbol{\mathcal{F}}) = \underbrace{\left[\boldsymbol{\nabla}\rho \left(\frac{\partial F}{\partial \rho}\right)_{T,\boldsymbol{\nabla}\rho} + \boldsymbol{\nabla}\boldsymbol{\nabla}\rho \cdot \boldsymbol{\mathcal{F}}\right]}_{\boldsymbol{\nabla} F} - \boldsymbol{\nabla} F + \rho \boldsymbol{\nabla}\left[\left(\frac{\partial F}{\partial \rho}\right)_{T,\boldsymbol{\nabla}\rho} - \boldsymbol{\nabla}\cdot\boldsymbol{\mathcal{F}}\right] \tag{C.38a}$$

$$= \rho \boldsymbol{\nabla}\left[\left(\frac{\partial F}{\partial \rho}\right)_{T,\boldsymbol{\nabla}\rho} - \boldsymbol{\nabla}\cdot\boldsymbol{\mathcal{F}}\right] \tag{C.38b}$$

Finally the equilibrium condition is expressed as:

$$\boxed{\left(\frac{\partial F}{\partial \rho}\right)_{T,\boldsymbol{\nabla}\rho} - \boldsymbol{\nabla}\cdot\left(\left(\frac{\partial F}{\partial \boldsymbol{\nabla}\rho}\right)_{T,\rho}\right) = \text{cste}} \tag{C.39}$$

Résumé en Francais

Les systèmes d'injection liquide sont pléthores dans l'industrie, en particulier celle du transport, que ce soit à travers les moteurs Diesel, les moteurs aéronautiques ou encore certains moteurs-fusées. Au cours de leur fonctionnement, ces systèmes sont confrontés à une large gamme de températures et en particulier de pressions, qui peuvent entrainer une modification du régime thermodynamique lorsque les conditions critiques du fluide sont franchies.
A faible pression, il est commun de retrouver un écoulement mêlant des phases liquide et vapeur distinctes, on parle alors de régime diphasique. Au-delà de la pression critique, la distinction entre les deux phases n'est plus possible et l'on parle alors d'écoulement transcritique, voire supercritique. C'est un phénomène particulièrement marqué dans les moteurs-fusées cryogéniques, notamment au moment de leur allumage. Ce changement de régime thermodynamique a un impact très important sur la topologie du jet liquide au cours de l'injection, ce qui, à son tour, aura de forts impacts sur les conditions d'atomisation dudit jet, sur les phénomènes de mélange ainsi que sur le comportement de la flamme éventuelle. Si le traitement des écoulements diphasiques d'un côté et des écoulements trans/supercritiques de l'autre, jouissent respectivement de nombreux résultats tant expérimentaux que numériques, les cadres de description englobant ces deux domaines restent aujourd'hui très rares.

L'objectif de cette thèse est donc d'étudier un modèle physique original, dit du Second Gradient, qui semble a priori permettre la description des écoulements fluides dans les différents régimes de fonctionnement de manière unifiée, et d'évaluer sa pertinence en tant qu'outil de simulation numérique. Pour ce faire, ce manuscrit s'articule autour de trois axes principaux qui ont rythmé ces travaux de thèse.

Il propose dans un premier temps une revue approfondie des méthodes classiques de modélisation des écoulements diphasiques dans lesquels il y a présence, par définition, d'interfaces liquide-vapeur. Généralement séparées en deux grandes familles, elles se distinguent les unes des autres par le point de vue qu'elles utilisent pour représenter l'interface. Les méthodes d'interface raide (Sharp Interface) vont traiter les interfaces comme des discontinuités à travers lesquelles les grandeurs thermodynamiques subissent un saut. Réciproquement, les méthodes d'interface diffuse (Diffuse Interface) vont traiter les interfaces comme des régions de l'espace, d'épaisseur faible mais non nulle, à travers lesquelles les grandeurs thermodynamiques vont subir des variations, certes rapides, mais néanmoins continues. Cette étude bibliographique permet de mettre en lumière les éléments clés qui ont motivé le choix du Second Gradient, modèle d'interface diffuse, pour nos travaux.
Cette présentation théorique des différentes méthodes de traitement d'interface, Second Gradient compris, est complétée par une description des enjeux thermodynamiques de la modéli-

sation des écoulements à haute pression, sur laquelle le modèle final qui est utilisé s'appuie largement. On montre en particulier comment le modèle du gaz parfait n'est plus adapté dans de telles conditions et on présente les modifications qu'il est nécessaire d'y apporter pour prendre en compte les interactions complexes régnant dans les écoulements d'une telle nature.

La seconde partie du manuscrit se focalise sur la validation numérique de ce modèle en passant plus particulièrement par son implémentation au sein d'un solveur numérique semi-industriel, AVBP, conçut pour simuler des configurations complexes multidimensionnelles dans un contexte hautement parallèle. Les aspects essentiels d'AVBP sont exposés dans un chapitre dédié. Les nouvelles équations décrivant le comportement d'un fluide dans le cadre du Second Gradient font apparaitre des nouveaux termes impliquant des dérivées d'ordres élevés de la masse volumique. La question délicate de la discrétisation de ces termes est largement traitée afin de valider leur interaction avec les méthodes numériques nativement présentes dans AVBP, a priori non prévues pour prendre en compte de telles dérivées dans les flux.
Suite à cette étude approfondie, le modèle est utilisé pour simuler, avec succès, des configurations canoniques en une dimension (interfaces advectées, déformées, évaporantes ou condensées) et en deux dimensions (interfaces planes oscillantes, gouttes déformées oscillantes) en considérant exhaustivement des cadres isothermes et non isothermes ainsi que visqueux et non-visqueux.

Malgré ces résultat encourageants, le modèle souffre d'une limitation majeure issue du fait que les épaisseurs des interfaces, telles que prédites par la formulation native du Second Gradient, demeurent plusieurs ordres de grandeurs en deçà des tailles de maillage actuellement accessibles pour des couts de calcul raisonnables. Afin d'y remédier, une nouvelle méthode d'épaississement d'interface dans le cadre du Second Gradient est introduite dans la troisième partie de ce manuscrit.
Après un bref rappel des méthodes d'épaississement déjà proposées dans le passé, les fondements théoriques de la méthode, appelée Thickened Interface Method (TIM), sont méticuleusement exposés. La TIM est ensuite soumisse aux même séries de tests que celles subi par le Second Gradient dans sa forme originelle et, au prix de certains ajustements, démontre des comportements conformes à l'attendu. Finalement, la méthode est appliquée à des configurations plus complexes et en lien direct avec le sujet des moteurs-fusées liquides. Dans un premier temps, des collisions frontales de gouttes tridimensionnelles d'oxygène dans leur vapeur sont simulées et les résultats mènent à des comparaisons satisfaisantes avec les résultats expérimentaux. Ensuite, la déstabilisation d'un jet liquide d'azote dans sa vapeur est étudiée en deux dimensions, à différentes vitesses, et permet avec succès de retrouver les différents régimes d'atomisation obtenus par expérience.

Ainsi donc, ce travail de thèse a permis d'introduire une nouvelle méthode innovante de modélisation diphasique dans un contexte de gaz réel, dont la cohérence thermodynamique a été particulièrement travaillée, afin d'épaissir les interfaces prédites par la théorie du Second Gradient jusqu'à atteindre des échelles de maillage typiques de Simulations Numériques Directes, au sens de le turbulence. La méthode, TIM, a pu être appliquée avec succès à des configurations canoniques en une et deux dimensions, démontrant un accord important avec la théorie, mais surtout à des configurations académiques en deux et trois dimensions, menant à des comparaisons particulièrement probantes avec les résultats expérimentaux.

Bibliography

Abels, H. (2009a). Existence of weak solutions for a diffuse interface model for viscous, incompressible fluids with general densities. *Communications in Mathematical Physics 289*(1), 45. *(p. 144)*

Abels, H. (2009b). On a diffuse interface model for two-phase flows of viscous, incompressible fluids with matched densities. *Archive for rational mechanics and analysis 194*(2), 463–506. *(p. 143)*

Abels, H., D. Depner, and H. Garcke (2013a). Existence of weak solutions for a diffuse interface model for two-phase flows of incompressible fluids with different densities. *Journal of Mathematical Fluid Mechanics 15*(3), 453–480. *(p. 123, 144)*

Abels, H., D. Depner, and H. Garcke (2013b). On an incompressible navier-stokes/cahn-hilliard system with degenerate mobility. In *Annales de l'IHP Analyse non linéaire*, Volume 30, pp. 1175–1190. *(p. 144)*

Abels, H. and E. Feireisl (2008). On a diffuse interface model for a two-phase flow of compressible viscous fluids. *Indiana University mathematics journal*, 659–698. *(p. 141)*

Abels, H., H. Garcke, and G. Grün (2012). Thermodynamically consistent, frame indifferent diffuse interface models for incompressible two-phase flows with different densities. *Mathematical Models and Methods in Applied Sciences 22*(03), 1150013. *(p. 123)*

Abels, H., H. Garcke, G. Grün, and S. Metzger (2017). Diffuse interface models for incompressible two-phase flows with different densities. In *Transport Processes at Fluidic Interfaces*, pp. 203–229. Springer. *(p. 144)*

Abgrall, R. and R. Saurel (2003). Discrete equations for physical and numerical compressible multiphase mixtures. *Journal of Computational Physics 186*(2), 361–396. *(p. 151)*

Adalsteinsson, D. and J. A. Sethian (1995). A fast level set method for propagating interfaces. *Journal of computational physics 118*(2), 269–277. *(p. 100, 104, 105, 109)*

Adalsteinsson, D. and J. A. Sethian (1999). The fast construction of extension velocities in level set methods. *Journal of Computational Physics 148*(1), 2–22. *(p. 74, 100, 109)*

Adam, J., N. Lindblad, and C. Hendricks (1968). The collision, coalescence, and disruption of water droplets. *Journal of Applied Physics 39*(11), 5173–5180. *(p. 350)*

Adams, N. A. and S. Stolz (2002). A subgrid-scale deconvolution approach for shock capturing. *Journal of Computational Physics 178*(2), 391–426. *(p. 216)*

Akhatov, I. S. and P. Vainshtein (1984). Transition of porous explosive combustion into detonation. *Combustion, Explosion and Shock Waves 20*(1), 63–69. *(p. 149)*

Alikakos, N., P. W. Bates, and G. Fusco (1991). Slow motion for the cahn-hilliard equation in one space dimension. *Journal of differential equations 90*(1), 81–135. *(p. 122)*

Alikakos, N. D., P. W. Bates, and X. Chen (1994). Convergence of the cahn-hilliard equation to the hele-shaw model. *Archive for rational mechanics and analysis 128*(2), 165–205. *(p. 122)*

Allaire, G., S. Clerc, and S. Kokh (2002). A five-equation model for the simulation of interfaces between compressible fluids. *Journal of Computational Physics 181*(2), 577–616. *(p. 149, 151)*

Allen, S. M. and J. W. Cahn (1979). A microscopic theory for antiphase boundary motion and its application to antiphase domain coarsening. *Acta Metallurgica 27*(6), 1085–1095. *(p. 121, 129)*

Ambrosio, L., N. Gigli, and G. Savaré (2004). Gradient flows with metric and differentiable structures, and applications to the wasserstein space. *Atti Accad. Naz. Lincei Cl. Sci. Fis. Mat. Natur. Rend. Lincei (9) Mat. Appl 15*(3-4), 327–343. *(p. 136)*

Ambrosio, L., N. Gigli, and G. Savaré (2008). *Gradient flows: in metric spaces and in the space of probability measures*. Springer Science & Business Media. *(p. 136)*

Amiri, H. A. and A. A. Hamouda (2013). Evaluation of level set and phase field methods in modeling two phase flow with viscosity contrast through dual-permeability porous medium. *International Journal of Multiphase Flow 52*, 22–34. *(p. 122)*

Amsden, A. A. (1966). Particle-in-cell method for the calculation of the dynamics of compressible fluids. Technical report, Los Alamos Scientific Lab., Univ. of California, N. Mex. *(p. 51)*

Amsden, A. A. and F. H. Harlow (1970). The smac method: a numerical technique for calculating incompressible fluid flows. Technical report, Los Alamos Scientific Lab., N. Mex. *(p. xvii, 12, 54, 59, 60)*

Anderson, C. R. (1985). A vortex method for flows with slight density variations. *Journal of Computational Physics 61*(3), 417–444. *(p. 51)*

Anderson, D. and G. B. McFadden (1997). A diffuse-interface description of internal waves in a near-critical fluid. *Physics of Fluids (1994-present) 9*(7), 1870–1879. *(p. 122)*

Antanovskii, L. K. (1995). A phase field model of capillarity. *Physics of Fluids (1994-present) 7*(4), 747–753. *(p. 122, 143, 148)*

Antman, S. S. (1995). *Background*, pp. 1–10. New York, NY: Springer New York. *(p. 169, 172, 423)*

Ashgriz, N. and J. Poo (1990). Coalescence and separation in binary collisions of liquid drops. *Journal of Fluid Mechanics 221*, 183–204. *(p. xviii, xxviii, xxix, 110, 111, 350, 352, 353, 355, 356, 357, 358, 359, 360, 361)*

Ashgriz, N. and J. Poo (1991). Flair: Flux line-segment model for advection and interface reconstruction. *Journal of computational physics 93*(2), 449–468. *(p. 81, 85, 87)*

Aslam, T. D., J. B. Bdzil, and D. S. Stewart (1996). Level set methods applied to modeling detonation shock dynamics. *Journal of Computational Physics 126*(2), 390–409. *(p. 99)*

Audiard, C. (2010). *Problemès aux limites dispersifs linéaires non homogènes, application au système d'Euler-Korteweg*. Ph. D. thesis, Université Claude Bernard-Lyon I. *(p. 236)*

Badalassi, V., H. Ceniceros, and S. Banerjee (2003). Computation of multiphase systems with phase field models. *Journal of Computational Physics 190*(2), 371–397. *(p. 143, 144)*

Baer, M. and J. Nunziato (1986). A two-phase mixture theory for the deflagration-to-detonation transition (ddt) in reactive granular materials. *International journal of multiphase flow 12*(6), 861–889. *(p. 149)*

Banuti, D. T. and K. Hannemann (2014). Supercritical pseudo-boiling and its relevance for transcritical injection. In *50th AIAA/ASME/SAE/ASEE Joint Propulsion Conference*, pp. 3571. *(p. 10)*

Barles, G., H. M. Soner, and P. E. Souganidis (1993). Front propagation and phase field theory. *SIAM Journal on Control and Optimization 31*(2), 439–469. *(p. 107)*

Barrett, J. W., J. F. Blowey, and H. Garcke (1999). Finite element approximation of the cahn–hilliard equation with degenerate mobility. *SIAM Journal on Numerical Analysis 37*(1), 286–318. *(p. 128)*

Batchelor, G. K. (1969). Computation of the energy spectrum in homogeneous two-dimensional turbulence. *The Physics of Fluids 12*(12), II–233. *(p. 365)*

Bates, P. W. and P. C. Fife (1993). The dynamics of nucleation for the cahn–hilliard equation. *SIAM Journal on Applied Mathematics 53*(4), 990–1008. *(p. 122)*

Bayareh, M. and S. Mortazavi (2011). Binary collision of drops in simple shear flow at finite reynolds numbers: Geometry and viscosity ratio effects. *Advances in Engineering Software 42*(8), 604–611. *(p. 75)*

Beckermann, C., H.-J. Diepers, I. Steinbach, A. Karma, and X. Tong (1999). Modeling melt convection in phase-field simulations of solidification. *Journal of Computational Physics 154*(2), 468–496. *(p. 122, 137, 139)*

Bellan, J. (2000). Supercritical (and subcritical) fluid behavior and modeling: drops, streams, shear and mixing layers, jets and sprays. *Progress in energy and combustion science 26*(4), 329–366. *(p. 15)*

Bellan, J. (2006). Theory, modeling and analysis of turbulent supercritical mixing. *Combustion Science and Technology 178*(1-3), 253–281. *(p. 15, 16)*

Benedict, M., G. B. Webb, and L. C. Rubin (1940). An empirical equation for thermodynamic properties of light hydrocarbons and their mixtures i. methane, ethane, propane and n-butane. *The Journal of Chemical Physics 8*(4), 334–345. *(p. 26)*

Beneš, M., V. Chalupeckỳ, and K. Mikula (2004). Geometrical image segmentation by the allen–cahn equation. *Applied Numerical Mathematics 51*(2-3), 187–205. *(p. 122)*

Benzoni-Gavage, S. (2010). Spectral transverse instability of solitary waves in korteweg fluids. *Journal of Mathematical Analysis and Applications 361*(2), 338–357. *(p. 236)*

Benzoni-Gavage, S., R. Danchin, and S. Descombes (2006). Well-posedness of one-dimensional korteweg models. *Electronic Journal of Differential Equations (EJDE)[electronic only] 2006*, Paper–No. *(p. 191, 236)*

Benzoni-Gavage, S., R. Danchin, and S. Descombes (2007). On the well-posedness for the euler-korteweg model in several space dimensions. *Indiana University Mathematics Journal*, 1499–1579. *(p. 191, 236)*

Benzoni-Gavage, S., R. Danchin, S. Descombes, and D. Jamet (2007). Stability issues in the euler-korteweg model. *Contemporary Mathematics 426*, 103. *(p. 236)*

Benzoni-Gavage, S., S. Descombes, D. Jamet, and L. Mazet (2005). Structure of korteweg models and stability of diffuse interfaces. *Interfaces and free boundaries 7*(4), 371–414. *(p. 191)*

Bidone, G. (1829). *Expériences sur la forme et sur la direction des veines et des courans d'eau lancés par diverses ouvertures. Par Georges Bidone.* De l'Imprimerie royale. *(p. 7)*

Birkhoff, G. (1955). Taylor instability : appendixes to report la-1862. Technical report. *(p. 52, 54)*

Birkhoff, G. (1962). Helmholtz and taylor instability. In *Proceedings of Symposia in Applied Mathematics*, Volume 13, pp. 55–76. *(p. 52, 54)*

Birkhoff, G. and J. Fisher (1959). Do vortex sheets roll up? *Rendiconti del Circolo matematico di Palermo 8*(1), 77–90. *(p. 52, 54)*

Blesgen, T. (1999). A generalization of the navier-stokes equations to two-phase flows. *Journal of Physics D: Applied Physics 32*(10), 1119. *(p. 122, 141)*

Blowey, J. F. and C. M. Elliott (1991). The cahn–hilliard gradient theory for phase separation with non-smooth free energy part i: Mathematical analysis. *European Journal of Applied Mathematics 2*(3), 233–280. *(p. 122)*

Bo, W. and J. W. Grove (2014). A volume of fluid method based ghost fluid method for compressible multi-fluid flows. *Computers & Fluids 90*(Supplement C), 113 – 122. *(p. 71)*

Bo, W., X. Liu, J. Glimm, and X. Li (2011). A robust front tracking method: verification and application to simulation of the primary breakup of a liquid jet. *SIAM Journal on Scientific Computing 33*(4), 1505–1524. *(p. xv, xvii, 12, 13, 63, 67, 71, 72, 73)*

Boettinger, W. J., J. A. Warren, C. Beckermann, and A. Karma (2002). Phase-field simulation of solidification. *Annual review of materials research 32*(1), 163–194. *(p. 122, 127, 139)*

Boileau, M. (2007). *Simulation aux grandes échelles de l'allumage diphasique des foyers aéronautiques.* Ph. D. thesis, Institut National Polytechnique de Toulouse. *(p. 204)*

Boyer, F. (1999). Mathematical study of multi-phase flow under shear through order parameter formulation. *Asymptotic analysis 20*(2), 175–212. *(p. 143)*

Boyer, F. (2002). A theoretical and numerical model for the study of incompressible mixture flows. *Computers & fluids 31*(1), 41–68. *(p. 143, 144)*

Brackbill, J. and H. Ruppel (1986). Flip: A method for adaptively zoned, particle-in-cell calculations of fluid flows in two dimensions. *Journal of Computational physics 65*(2), 314–343. *(p. 51)*

Brackbill, J. U., D. B. Kothe, and C. Zemach (1992, June). A continuum method for modeling surface tension. *J. Comput. Phys. 100*(2), 335–354. *(p. 126, 253)*

Branam, R. and W. Mayer (2002). Length scales in cryogenic injection at supercritical pressure. *Experiments in fluids 33*(3), 422–428. *(p. 306)*

Brassel, M. and E. Bretin (2011). A modified phase field approximation for mean curvature flow with conservation of the volume. *Mathematical Methods in the Applied Sciences 34*(10), 1157–1180. *(p. xix, 122, 128, 129, 131, 132)*

Brenn, G. (2011). Droplet collision. In *Handbook of Atomization and Sprays*, pp. 157–181. Springer. *(p. xxviii, 351)*

Brenn, G., S. Kalenderski, and I. Ivanov (1997). Investigation of the stochastic collisions of drops produced by rayleigh breakup of two laminar liquid jets. *Physics of fluids 9*(2), 349–364. *(p. 350)*

Bresch, D., B. Desjardins, M. Gisclon, and R. Sart (2008). Instability results related to compressible korteweg system. *Annali dell'Universita di Ferrara 54*(1), 11–36. *(p. 236)*

Bronsard, L. and B. Stoth (1997). Volume-preserving mean curvature flow as a limit of a nonlocal ginzburg-landau equation. *SIAM Journal on Mathematical Analysis 28*(4), 769–807. *(p. 122)*

Butler, P. B., M. Lembeck, and H. Krier (1982). Modeling of shock development and transition to detonation initiated by burning in porous propellant beds. *Combustion and Flame 46*, 75–93. *(p. 149)*

Caginalp, G. (1989). Stefan and hele-shaw type models as asymptotic limits of the phase-field equations. *Physical Review A 39*(11), 5887. *(p. 127)*

Cahn, J. and A. Novick-Cohen (1994). Evolution equations for phase separation and ordering in binary alloys. *Journal of statistical physics 76*(3-4), 877–909. *(p. 122)*

Cahn, J. W. (1959). Free energy of a nonuniform system. ii. thermodynamic basis. *The Journal of Chemical Physics 30*(5), 1121–1124. *(p. 121, 169)*

Cahn, J. W. (1961). On spinodal decomposition. *Acta metallurgica 9*(9), 795–801. *(p. 121, 128)*

Cahn, J. W., C. M. Elliott, and A. Novick-Cohen (1996). The cahn–hilliard equation with a concentration dependent mobility: motion by minus the laplacian of the mean curvature. *European journal of applied mathematics 7*(3), 287–301. *(p. 135)*

Cahn, J. W. and J. E. Hilliard (1958). Free energy of a nonuniform system. i. interfacial free energy. *The Journal of Chemical Physics 28*(2), 258–267. *(p. 17, 121, 123, 124, 127, 160, 167, 180, 191, 199)*

Cahn, J. W. and J. E. Hilliard (1959). Free energy of a nonuniform system. iii. nucleation in a two-component incompressible fluid. *The Journal of Chemical Physics 31*(3), 688–699. *(p. 121, 169)*

Cahn, J. W. and J. E. Hilliard (1971). Spinodal decomposition: A reprise. *Acta Metallurgica 19*(2), 151–161. *(p. 121, 128)*

Cahn, J. W. and R. Kikuchi (1966). Theory of domain walls in ordered structures-iii: Effect of substitutional deviations from stoichiometry. *Journal of Physics and Chemistry of Solids 27*(8), 1305–1317. *(p. 121)*

Candel, S., G. Herding, R. Snyder, P. Scouflaire, J.-C. Rolon, L. Vingert, M. Habiballah, F. Grisch, M. Pealat, P. Bouchardy, et al. (1998). Experimental investigation of shear coaxial cryogenic jet flames. *Journal of Propulsion and Power 14*(5), Pages–826. *(p. 16)*

Candel, S., M. Juniper, G. Singla, P. Scouflaire, and C. Rolon (2006). Structure and dynamics of cryogenic flames at supercritical pressure. *Combustion Science and Technology 178*(1-3), 161–192. *(p. xi, 16, 17)*

Carey, V. (2007). *Liquid Vapor Phase Change Phenomena: An Introduction to the Thermophysics of Vaporization and Condensation Processes in Heat Transfer Equipment, Second Edition*. Taylor & Francis. *(p. 191)*

Carr, J. and R. L. Pego (1989). Metastable patterns in solutions of $u_t = \epsilon u_{xx}^2 - f(u)$. *Communications on pure and applied mathematics 42*(5), 523–576. *(p. 122)*

Casal, P. (1972). Theory of second gradient and capillarity. *Comptes rendus hebdomadaire de l'Academie des Science A 274*(22), 1571–1574. *(p. 169, 423)*

Casal, P. and H. Gouin (1989). *Invariance properties of inviscid fluids of grade n*, pp. 85–98. Berlin, Heidelberg: Springer Berlin Heidelberg. *(p. 169, 423)*

Casal, P. e. and H. Gouin (1985). Relation entre l'équation de l'énergie et l'équation du mouvement en théorie de korteweg de la capillarité. *Comptes-rendus des séances de l'Académie des sciences. Série 2, Mécanique-physique, chimie, sciences de l'univers, sciences de la terre 300*(7), 231–234. *(p. 121, 159, 163, 169, 180, 423)*

Ceniceros, H. D., R. L. Nós, and A. M. Roma (2010). Three-dimensional, fully adaptive simulations of phase-field fluid models. *Journal of computational physics 229*(17), 6135–6155. *(p. 128, 143)*

Cessou, A., P. Colin, and D. Stepowski (1998). Statistical investigation of the turbulent flame geometrical structures in a liquid oxygen/gaseous hydrogen shear-coaxial jet. In *Symposium (International) on Combustion*, Volume 27, pp. 1039–1045. Elsevier. *(p. 16)*

Chai, Z., D. Sun, H. Wang, and B. Shi (2018). A comparative study of local and nonlocal allen-cahn equations with mass conservation. *International Journal of Heat and Mass Transfer 122*, 631–642. *(p. 122, 139)*

Chan, R. K. C., R. L. Street, and J. E. Fromm (1971). *The digital simulation of water waves — An evaluation of SUMMAC*, pp. 429–434. Berlin, Heidelberg: Springer Berlin Heidelberg. *(p. 54)*

Chandrasekhar, S. (1959). The oscillations of a viscous liquid globe. *Proceedings of the London Mathematical Society 3*(1), 141–149. *(p. 295)*

Chang, Y.-C., T. Hou, B. Merriman, and S. Osher (1996). A level set formulation of eulerian interface capturing methods for incompressible fluid flows. *Journal of computational Physics 124*(2), 449–464. *(p. 100, 109, 110)*

Chapman, S. (1954, July). The Viscosity and Thermal Conductivity of a Completely Ionized Gas. *Astrophysical Journal 120*, 151–155. *(p. 31)*

Chapman, S. and T. Cowling (1970). *The Mathematical Theory of Non-uniform Gases: An Account of the Kinetic Theory of Viscosity, Thermal Conduction and Diffusion in Gases*. Cambridge Mathematical Library. Cambridge University Press. *(p. 31)*

Charve, F. and B. Haspot (2013). Existence of a global strong solution and vanishing capillarity-viscosity limit in one dimension for the korteweg system. *SIAM Journal on Mathematical Analysis 45*(2), 469–494. *(p. 236)*

Chehroudi, B., R. Cohn, D. Talley, and A. Badakhshan (2000). Raman scattering measurements in the initial region of sub-and supercritical jets. In *36th AIAA/ASME/SAE/ASEE Joint Propulsion Conference and Exhibit*, pp. 3392. *(p. 10)*

Chehroudi, B. and D. Talley (2002). Interaction of acoustic waves with a cryogenic nitrogen jet at sub-and supercritical pressures. In *40th AIAA Aerospace Sciences Meeting & Exhibit*, pp. 342. *(p. 10)*

Chehroudi, B., D. Talley, and E. Coy (1999). Initial growth rate and visual characteristics of a round jet into a sub-to supercritical environment of relevance to rocket, gas turbine, and diesel engines. In *37th Aerospace Sciences Meeting and Exhibit*, pp. 206. *(p. 10)*

Chehroudi, B., D. Talley, and E. Coy (2002). Visual characteristics and initial growth rates of round cryogenic jets at subcritical and supercritical pressures. *Physics of Fluids 14*(2), 850–861. *(p. xv, 10, 11)*

Chella, R. and J. Viñals (1996). Mixing of a two-phase fluid by cavity flow. *Physical Review E 53*(4), 3832. *(p. 128, 143)*

Chen, L.-Q. (2002). Phase-field models for microstructure evolution. *Annual review of materials research 32*(1), 113–140. *(p. 122)*

Chen, M. and X. Guo (2017). Global large solutions for a coupled compressible navier-stokes/allen-cahn system with initial vacuum. *Nonlinear Analysis: Real World Applications 37*, 350–373. *(p. 122, 142)*

Chen, S., D. B. Johnson, P. E. Raad, and D. Fadda (1997). The surface marker and micro cell method. *International Journal for Numerical Methods in Fluids 25*(7), 749–778. *(p. 61, 106)*

Chen, S., B. Merriman, S. Osher, and P. Smereka (1997). A simple level set method for solving stefan problems. *Journal of Computational Physics 135*(1), 8–29. *(p. 99, 100)*

Chen, X. (1992). Generation and propagation of interfaces for reaction-diffusion equations. *Journal of Differential equations 96*(1), 116–141. *(p. 122)*

Chen, Y., Q. He, M. Mei, and X. Shi (2018). Asymptotic stability of solutions for 1-d compressible navier–stokes–cahn–hilliard system. *Journal of Mathematical Analysis and Applications 467*(1), 185–206. *(p. 142)*

Chen, Y. and J. Shen (2016). Efficient, adaptive energy stable schemes for the incompressible cahn-hilliard navier-stokes phase-field models. *Journal of Computational Physics 308*, 40–56. *(p. 122)*

Cheng, G. C. and R. Farmer (2006). Real fluid modeling of multiphase flows in liquid rocket engine combustors. *Journal of propulsion and power 22*(6), 1373–1381. *(p. 16)*

Chiapolino, A., P. Boivin, and R. Saurel (2017a). A simple and fast phase transition relaxation solver for compressible multicomponent two-phase flows. *Computers & Fluids 150*, 31–45. *(p. xix, 14, 155, 156)*

Chiapolino, A., P. Boivin, and R. Saurel (2017b). A simple phase transition relaxation solver for liquid–vapor flows. *International Journal for Numerical Methods in Fluids 83*(7), 583–605. *(p. 17, 150, 155)*

Chiodi, R. and O. Desjardins (2017). A reformulation of the conservative level set reinitialization equation for accurate and robust simulation of complex multiphase flows. *Journal of Computational Physics 343*, 186–200. *(p. 117)*

Chiu, P.-H. and Y.-T. Lin (2011). A conservative phase field method for solving incompressible two-phase flows. *Journal of Computational Physics 230*(1), 185–204. *(p. xix, 147, 148)*

Chiu, P.-H. and T. W. Sheu (2009). On the development of a dispersion-relation-preserving dual-compact upwind scheme for convection-diffusion equation. *Journal of Computational Physics 228*(10), 3640–3655. *(p. 147)*

Choi, J.-W., H. G. Lee, D. Jeong, and J. Kim (2009). An unconditionally gradient stable numerical method for solving the allen–cahn equation. *Physica A: Statistical Mechanics and its Applications 388*(9), 1791–1803. *(p. 130)*

Chopp, D. L. (1991). *Computing Minimal Surfaces Via Level Set Curvature Flow*. phdthesis, Lawrence Berkeley National Laboratory, University of California Berkeley. *(p. 100, 105)*

Chopp, D. L. (1993). Computing minimal surfaces via level set curvature flow. *Journal of Computational Physics 106*(1), 77–91. *(p. 107)*

Chopp, D. L. (2009). Another look at velocity extensions in the level set method. *SIAM Journal on Scientific Computing 31*(5), 3255–3273. *(p. 110, 112)*

Chorin, A. J. (1976). Random choice solution of hyperbolic systems. *Journal of Computational Physics 22*(4), 517–533. *(p. 63)*

Christian, J. W. (2002). *The theory of transformations in metals and alloys*. Newnes. *(p. 128, 135)*

Chung, T. H., M. Ajlan, L. L. Lee, and K. E. Starling (1988). Generalized multiparameter correlation for nonpolar and polar fluid transport properties. *Industrial & engineering chemistry research 27*(4), 671–679. *(p. 26, 32, 33, 34, 262, 268, 274, 285, 298, 361, 364)*

Clausius, R. (1870). Ueber einen auf die wärme anwendbaren mechanischen satz. *Annalen der Physik 217*(9), 124–130. *(p. 20)*

Comminal, R., J. Spangenberg, and J. H. Hattel (2015). Cellwise conservative unsplit advection for the volume of fluid method. *Journal of Computational Physics 283*, 582–608. *(p. 89)*

Cottet, G.-H. and P. Poncet (2004). Advances in direct numerical simulations of 3d wall-bounded flows by vortex-in-cell methods. *Journal of Computational Physics 193*(1), 136–158. *(p. 51)*

Couet, B., O. Buneman, and A. Leonard (1981). Simulation of three-dimensional incompressible flows with a vortex-in-cell method. *Journal of Computational Physics 39*(2), 305–328. *(p. 51)*

Cowan, C. (2005). *The Cahn-Hilliard equation as a gradient flow*. Ph. D. thesis, Department of Mathematics-Simon Fraser University. *(p. 136)*

Crandall, M. G., L. C. Evans, and P.-L. Lions (1984). Some properties of viscosity solutions of hamilton-jacobi equations. *Transactions of the American Mathematical Society 282*(2), 487–502. *(p. 99)*

Crandall, M. G. and P.-L. Lions (1983). Viscosity solutions of hamilton-jacobi equations. *Transactions of the American mathematical society 277*(1), 1–42. *(p. 99)*

Crandall, M. G. and P.-L. Lions (1984a). On existence and uniqueness of solutions of hamilton-jacobi equations. Technical report, WISCONSIN UNIV-MADISON MATHEMATICS RESEARCH CENTER. *(p. 99)*

Crandall, M. G. and P.-L. Lions (1984b). Two approximations of solutions of hamilton-jacobi equations. *Mathematics of computation 43*(167), 1–19. *(p. 99)*

Curl, R. F. and K. Pitzer (1958). Volumetric and thermodynamic properties of fluids - enthalpy, free energy, and entropy. *Industrial & Engineering Chemistry 50*(2), 265–274. *(p. 197)*

Dahms, R. N. (2015). Gradient theory simulations of pure fluid interfaces using a generalized expression for influence parameters and a helmholtz energy equation of state for fundamentally consistent two-phase calculations. *Journal of colloid and interface science 445*, 48–59. *(p. 17, 197)*

Dahms, R. N. and J. C. Oefelein (2013). On the transition between two-phase and single-phase interface dynamics in multicomponent fluids at supercritical pressures. *Physics of Fluids 25*(9), 092103. *(p. xv, 17, 23)*

Dal Passo, R., L. Giacomelli, and A. Novick-Cohen (1999). Existence for an allen-cahn/cahn-hilliard system with degenerate mobility. *Interfaces and free boundaries 1*(2), 199–226. *(p. 122)*

Daly, B. J. (1969). Numerical study of the effect of surface tension on interface instability. *The Physics of Fluids 12*(7), 1340–1354. *(p. 63)*

Daly, B. J. and W. E. Pracht (1968). Numerical study of density-current surges. *The Physics of Fluids 11*(1), 15–30. *(p. 63)*

Darwish, M. and F. Moukalled (2006). Convective schemes for capturing interfaces of free-surface flows on unstructured grids. *Numerical heat transfer, part B: Fundamentals 49*(1), 19–42. *(p. 81, 97)*

Davis, D. W. and B. Chehroudi (2007). Measurements in an acoustically driven coaxial jet under sub-, near-, and supercritical conditions. *Journal of Propulsion and Power 23*(2), 364–374. *(p. 10)*

de Groot, S. R. and P. Mazur (1954). Extension of onsager's theory of reciprocal relations. i. *Physical Review 94*(2), 218. *(p. 169)*

de Groot, S. R. and P. Mazur (1984). *Non-equilibrium Thermodynamics*. Dover Publication. *(p. 128, 169)*

De Laplace, P. S. (1806). Supplément au livre x du traitée de mécanique céleste. *Couvreier, Paris*. *(p. 119)*

De Laplace, P. S. (1807). Supplément à la théorie de l'action capillaire. *Couvreier, Paris*. *(p. 119)*

de Mottoni, P. and M. Schatzman (1990). Development of interfaces in $\mathbb{R}^n$. *Proceedings of the Royal Society of Edinburgh Section A: Mathematics 116*(3-4), 207–220. *(p. 122)*

de Niem, D., E. Kührt, and U. Motschmann (2007). A volume-of-fluid method for simulation of compressible axisymmetric multi-material flow. *Computer physics communications 176*(3), 170–190. *(p. 81)*

De Rosa, M., J. Sender, H. Zimmermann, and M. Oschwald (2006). Cryogenic spray ignition at high altitude conditions. In *42nd AIAA/ASME/SAE/ASEE Joint Propulsion Conference & Exhibit*, pp. 4539. *(p. 16)*

De Sousa, F., N. Mangiavacchi, L. Nonato, A. Castelo, M. F. Tomé, V. Ferreira, J. Cuminato, and S. McKee (2004). A front-tracking/front-capturing method for the simulation of 3d multi-fluid flows with free surfaces. *Journal of Computational Physics 198*(2), 469–499. *(p. xvii, 55, 60, 61)*

DeBar, R. (1974). *Fundamentals of the KRAKEN code. [Eulerian hydrodynamics code for compressible nonviscous flow of several fluids in two-dimensional (axially symmetric) region]*. *(p. 83, 85, 87)*

Debussche, A. and L. Dettori (1995). On the cahn-hilliard equation with a logarithmic free energy. *Nonlinear Analysis: Theory, Methods & Applications 24*(10), 1491–1514. *(p. 122)*

Desjardins, O., V. Moureau, and H. Pitsch (2008). An accurate conservative level set/ghost fluid method for simulating turbulent atomization. *Journal of Computational Physics 227*(18), 8395 – 8416. *(p. xv, xviii, 13, 15, 101, 114, 115, 116)*

Desjardins, O. and H. Pitsch (2009). A spectrally refined interface approach for simulating multiphase flows. *Journal of computational physics 228*(5), 1658–1677. *(p. 112)*

Deuflhard, P. (1991). Global inexact newton methods for very large scale nonlinear problems. *IMPACT of Computing in Science and Engineering 3*(4), 366–393. *(p. 257)*

Diepers, H.-J., C. Beckermann, and I. Steinbach (1999). Simulation of convection and ripening in a binary alloy mush using the phase-field method. *Acta Materialia 47*(13), 3663–3678. *(p. 122)*

Ding, H., P. D. Spelt, and C. Shu (2007). Diffuse interface model for incompressible two-phase flows with large density ratios. *Journal of Computational Physics 226*(2), 2078–2095. *(p. 123)*

Ding, S., Y. Li, and W. Luo (2013). Global solutions for a coupled compressible navier-stokes/allen-cahn system in 1d. *Journal of Mathematical Fluid Mechanics 15*(2), 335–360. *(p. 122, 142, 143)*

Diwakar, S., S. K. Das, and T. Sundararajan (2009). A quadratic spline based interface (quasi) reconstruction algorithm for accurate tracking of two-phase flows. *Journal of Computational Physics 228*(24), 9107–9130. *(p. 81, 86)*

Dobrushin, R. L. (1970). Prescribing a system of random variables by conditional distributions. *Theory of Probability & Its Applications 15*(3), 458–486. *(p. 136)*

Donea, J. (1984). A taylor–galerkin method for convective transport problems. *International Journal for Numerical Methods in Engineering 20*(1), 101–119. *(p. 209, 210)*

Donea, J., L. Quartapelle, and V. Selmin (1987). An analysis of time discretization in the finite element solution of hyperbolic problems. *Journal of Computational Physics 70*(2), 463–499. *(p. 210)*

Drew, D. A. (1983). Mathematical modeling of two-phase flow. *Annual review of fluid mechanics 15*(1), 261–291. *(p. 149)*

Drew, D. A. and L. A. Segel (1971). Averaged equations for two-phase flows. *Studies in Applied Mathematics 50*(3), 205–231. *(p. 149)*

Du, J., B. Fix, J. Glimm, X. Jia, X. Li, Y. Li, and L. Wu (2006). A simple package for front tracking. *Journal of Computational Physics 213*(2), 613–628. *(p. 63)*

Du, Q., M. Li, and C. Liu (2007). Analysis of a phase field navier-stokes vesicle-fluid interaction model. *Discrete and Continuous Dynamical Systems Series B 8*(3), 539. *(p. 144)*

Du, Q. and R. A. Nicolaides (1991). Numerical analysis of a continuum model of phase transition. *SIAM Journal on Numerical Analysis 28*(5), 1310–1322. *(p. 122)*

Dyadechko, V. and M. Shashkov (2005). Moment-of-fluid interface reconstruction. *Los Alamos Report LA-UR-05-7571*. *(p. 112)*

Dymond, J. H. and E. B. Smith (1980). Virial coefficients of pure gases and mixtures. a critical compilation. *(p. 21)*

Easton, C. (1972). Homogeneous boundary conditions for pressure in the mac method. *Journal of Computational Physics 9*(2), 375–379. *(p. 54)*

Edwards, D. A., H. Brenner, and D. T. Wasan (1991). {CHAPTER} 15 - a surface-excess theory of interfacial transport processes. In D. A. Edwards, H. Brenner, and D. T. Wasan (Eds.), *Interfacial Transport Processes and Rheology*, pp. 370 – 432. Boston: Butterworth-Heinemann. *(p. 126, 192)*

Elder, K., F. Drolet, J. Kosterlitz, and M. Grant (1994). Stochastic eutectic growth. *Physical review letters 72*(5), 677. *(p. 122)*

Elliott, C. M. (1989). The cahn-hilliard model for the kinetics of phase separation. In *Mathematical models for phase change problems*, pp. 35–73. Springer. *(p. 122, 124)*

Elliott, C. M. and H. Garcke (1996). On the cahn-hilliard equation with degenerate mobility. *Siam journal on mathematical analysis 27*(2), 404–423. *(p. 135)*

Elmore, W. C. and M. A. Heald (1985). *Physics of Waves*. Dover. *(p. 253)*

Enright, D., R. Fedkiw, J. Ferziger, and I. Mitchell (2002). A hybrid particle level set method for improved interface capturing. *Journal of Computational Physics 183*(1), 83 – 116. *(p. 100, 112)*

Enright, D., F. Losasso, and R. Fedkiw (2005). A fast and accurate semi-lagrangian particle level set method. *Computers & structures 83*(6-7), 479–490. *(p. 112)*

Esmaeeli, A. and G. Tryggvason (2004). Computations of film boiling. part ii: multi-mode film boiling. *International Journal of Heat and Mass Transfer 47*(25), 5463–5476. *(p. xvii, 76, 77)*

Estrade, J.-P., H. Carentz, G. Lavergne, and Y. Biscos (1999). Experimental investigation of dynamic binary collision of ethanol droplets–a model for droplet coalescence and bouncing. *International Journal of Heat and Fluid Flow 20*(5), 486–491. *(p. 350)*

Evans, L. C. and J. Spruck (1992a). Motion of level sets by mean curvature. ii. *Transactions of the american mathematical society 330*(1), 321–332. *(p. 100, 104)*

Evans, L. C. and J. Spruck (1992b). Motion of level sets by mean curvature iii. *The Journal of Geometric Analysis 2*(2), 121–150. *(p. 100, 104)*

Evans, L. C. and J. Spruck (1995). Motion of level sets by mean curvature iv. *The Journal of Geometric Analysis 5*(1), 77–114. *(p. 100, 104)*

Evans, L. C., J. Spruck, et al. (1991). Motion of level sets by mean curvature. i. *Journal of Differential Geometry 33*(3), 635–681. *(p. 100, 104)*

Eyre, D. J. (1998). Unconditionally gradient stable time marching the cahn-hilliard equation. *MRS online proceedings library archive 529*. *(p. 128)*

Faeth, G. (1991). Structure and atomization properties of dense turbulent sprays. In *Symposium (International) on Combustion*, Volume 23, pp. 1345–1352. Elsevier. *(p. 7)*

Faeth, G. (1996). Spray combustion phenomena. In *Symposium (international) on combustion*, Volume 26, pp. 1593–1612. Elsevier. *(p. 7)*

Favre-Marinet, M. and E. C. Schettini (2001). The density field of coaxial jets with large velocity ratio and large density differences. *International journal of heat and mass transfer 44*(10), 1913–1924. *(p. 8)*

Fedkiw, R. P. (2002). Coupling an eulerian fluid calculation to a lagrangian solid calculation with the ghost fluid method. *Journal of Computational Physics 175*(1), 200–224. *(p. 67, 74, 103)*

Fedkiw, R. P., T. Aslam, B. Merriman, and S. Osher (1999). A non-oscillatory eulerian approach to interfaces in multimaterial flows (the ghost fluid method). *Journal of computational physics 152*(2), 457–492. *(p. 67, 100, 103)*

Fedkiw, R. P., A. Marquina, and B. Merriman (1999). An isobaric fix for the overheating problem in multimaterial compressible flows. *Journal of Computational Physics 148*(2), 545–578. *(p. 67, 71)*

Feireisl, E., H. Petzeltová, E. Rocca, and G. Schimperna (2010). Analysis of a phase-field model for two-phase compressible fluids. *Mathematical Models and Methods in Applied Sciences 20*(07), 1129–1160. *(p. 142)*

Feng, X. and A. Prohl (2003). Numerical analysis of the allen-cahn equation and approximation for mean curvature flows. *Numerische Mathematik 94*(1), 33–65. *(p. 122)*

Fife, P. C. (1988). Dynamics of internal layers and diffusive interfaces. In *CBMS-NSF Regional Conf. Ser. in Appl. Math.* SIAM. *(p. 122)*

Fink, P. and W. Soh (1976). Calculation of vortex sheets in unsteady flow and applications in ship hydrodynamics. In *Symposium on Naval Hydrodynamics, 10th, Proceedings, Pap and Discuss, Cambridge, Massachusetts, June 24-28, 1974.*, Number Proceeding. *(p. 54)*

Folch, R., J. Casademunt, A. Hernández-Machado, and L. Ramirez-Piscina (1999). Phase-field model for hele-shaw flows with arbitrary viscosity contrast. i. theoretical approach. *Physical Review E 60*(2), 1724. *(p. 122, 137, 138, 139)*

Fouillet, C. (2003). *Généralisation à des mélanges binaires de la méthode du second gradient et application à la simulation numérique directe de l'ébulition nucléée.* Ph. D. thesis, Ecole Centrale Paris. *(p. 310, 321, 322)*

Freistühler, H. and M. Kotschote (2017). Phase-field and korteweg-type models for the time-dependent flow of compressible two-phase fluids. *Archive for Rational Mechanics and Analysis 224*(1), 1–20. *(p. 144, 236)*

Frémond, M. (2013). *Non-smooth thermomechanics*. Springer Science & Business Media. *(p. 169, 423)*

Frisch, U. and A. N. Kolmogorov (1995). *Turbulence: the legacy of AN Kolmogorov*. *(p. 365)*

Fuster, D., A. Bagué, T. Boeck, L. Le Moyne, A. Leboissetier, S. Popinet, P. Ray, R. Scardovelli, and S. Zaleski (2009). Simulation of primary atomization with an octree adaptive mesh refinement and vof method. *International Journal of Multiphase Flow 35*(6), 550–565. *(p. xv, xviii, 14, 92)*

Fyfe, D., E. Oran, and M. Fritts (1988). Surface tension and viscosity with lagrangian hydrodynamics on a triangular mesh. *Journal of Computational Physics 76*(2), 349 – 384. *(p. 277)*

Gaillard, P. (2015). *Interfaces diffuses et flammes transcritiques LOX/H2*. Ph. D. thesis, Université Pierre et Marie Curie-Paris VI. *(p. 6, 14, 19, 169, 176, 181, 182, 196, 197, 388)*

Gaillard, P., V. Giovangigli, and L. Matuszewski (2016). A diffuse interface lox/hydrogen transcritical flame model. *Combustion Theory and Modelling 20*(3), 486–520. *(p. xix, 17, 150, 153, 154)*

Gal, C. G., M. Grasselli, and A. Miranville (2016). Cahn-hilliard-navier-stokes systems with moving contact lines. *Calculus of Variations and Partial Differential Equations 55*(3), 50. *(p. 144)*

Gal, C. G., M. Grasselli, and H. Wu (2019). Global weak solutions to a diffuse interface model for incompressible two-phase flows with moving contact lines and different densities. *Archive for Rational Mechanics and Analysis 234*(1), 1–56. *(p. 144)*

Garcke, H., B. Nestler, B. Stinner, and F. Wendler (2008). Allen-cahn systems with volume constraints. *Mathematical Models and Methods in Applied Sciences 18*(08), 1347–1381. *(p. 122)*

Gaskell, P. and A. Lau (1988). Curvature-compensated convective transport: Smart, a new boundedness-preserving transport algorithm. *International journal for numerical methods in fluids 8*(6), 617–641. *(p. 94)*

Gauss, C. F. (1877). Principia generalia theoriae figurae fluidorum in statu aequilibrii. In *Werke*, pp. 29–77. Springer. *(p. 119)*

Gavrilyuk, S. and H. Gouin (1998). Symmetric form of governing equations for capillary fluids. *Trends in applications of mathematics to mechanics (Nice, 1998) 106*, 306–311. *(p. 235)*

Gawain, T. and J. Pritchett (1970). A unified heuristic model of fluid turbulence. *Journal of Computational Physics 5*(3), 383–405. *(p. 54)*

Germain, P. (1972). Sur l'application de la méthode des puissances virtuelles en mécanique des milieux continus. *Comptes rendus hebdomadaire de l'Académie des Sciences A 274*(22), 1051–1055. *(p. 121, 159, 163, 169, 170, 423, 425)*

Gibbs, J. W. (1874-1878). On the equilibrium of heterogeneous substances. In *Transactions of the Connecticut Academy of Arts and Sciences*, Volume III, pp. 108–248,343–524. *(p. 120, 121, 124, 126)*

Gicquel, P., L. Vingert, L. Lecourt, and M. Barat (2001). Etudes expérimentales des sprays cryogéniques en combustion dans des conditions sub-et supercritiques. *Proceedings Combustion dans les moteurs fusées*, 359–369. *(p. xix, 10, 154, 155, 157)*

Ginzburg, V. L. and L. D. Landau (1950). On the theory of superconductivity. *Zh. Eksp. Teor. Fiz. 20*, 1064–1082. *(p. 121, 123, 133)*

Giovangigli, V. and L. Matuszewski (2012). Supercritical fluid thermodynamics from equations of state. *Physica D: Nonlinear Phenomena 241*(6), 649–670. *(p. 43)*

Glansdorff, P. and I. Prigogine (1954). Sur les propriétés différentielles de la production d'entropie. *Physica 20*(7-12), 773–780. *(p. 169)*

Glansdorff, P. and I. Prigogine (1971). *Thermodynamic theory of structure, stability and fluctuations*. J. Willey & Sons. *(p. 169)*

Glimm, J., J. Grove, X. Li, W. Oh, and D. Sharp (2001). A critical analysis of rayleigh–taylor growth rates. *Journal of Computational Physics 169*(2), 652–677. *(p. xvii, 70, 72)*

Glimm, J., J. Grove, B. Lindquist, O. A. McBryan, and G. Tryggvason (1988). The bifurcation of tracked scalar waves. *SIAM Journal on Scientific and Statistical Computing 9*(1), 61–79. *(p. 63)*

Glimm, J., J. W. Grove, X. L. Li, K.-m. Shyue, Y. Zeng, and Q. Zhang (1998). Three-dimensional front tracking. *SIAM Journal on Scientific Computing 19*(3), 703–727. *(p. 63)*

Glimm, J., E. Isaacson, D. Marchesin, and O. McBryan (1981). Front tracking for hyperbolic systems. *Advances in Applied Mathematics 2*(1), 91–119. *(p. 12, 63, 67)*

Glimm, J., C. Klingenberg, O. McBryan, B. Plohr, D. Sharp, and S. Yaniv (1985). Front tracking and two-dimensional riemann problems. *Advances in Applied Mathematics 6*(3), 259–290. *(p. 63, 71)*

Glimm, J., X. Li, Y. Liu, Z. Xu, and N. Zhao (2003). Conservative front tracking with improved accuracy. *SIAM Journal on Numerical Analysis 41*(5), 1926–1947. *(p. 63, 72)*

Glimm, J., X. L. Li, and Y. Liu (2002). Conservative front tracking in one space dimension. *Contemporary Mathematics 295*, 253–264. *(p. 72)*

Glimm, J., X. L. Li, Y. Liu, and N. Zhao (2001). Conservative front tracking and level set algorithms. *Proceedings of the National Academy of Sciences 98*(25), 14198–14201. *(p. 72)*

Glimm, J., D. Marchesin, E. Isaacson, and O. McBryan (1980). A shock tracking method for hyperbolic systems. In *Proceedings of the 1980 Army Numerical Analysis and Computers Conference (NASA Res. Center, Moffett Field, Calif., 1980)*, pp. 1. *(p. 63)*

Glimm, J., D. Marchesin, and O. McBryan (1980). Subgrid resolution of fluid discontinuities, ii. *Journal of Computational Physics 37*(3), 336–354. *(p. 63)*

Glimm, J., D. Marchesin, and O. McBryan (1981). A numerical method for two phase flow with an unstable interface. *Journal of Computational Physics 39*(1), 179–200. *(p. 63)*

Glimm, J. and O. A. Mcbryan (1985). A computational model for interfaces. *Advances in Applied Mathematics 6*(4), 422–435. *(p. 63)*

Gokieli, M. and L. Marcinkowski (2003). Discrete approximation of the cahn-hilliard/allen-cahn system with logarithmic entropy. *Japan journal of industrial and applied mathematics 20*(3), 321. *(p. 122)*

Gough, P. and F. Zwarts (1979). Modeling heterogeneous two-phase reacting flow. *AIAA Journal 17*(1), 17–25. *(p. 149)*

Gouin, H. (1988). *Utilization of the Second Gradient Theory in Continuum Mechanics to Study the Motion and Thermodynamics of Liquid-Vapor Interfaces*, pp. 667–682. Boston, MA: Springer US. *(p. 176)*

Gourdain, N., L. Gicquel, M. Montagnac, O. Vermorel, M. Gazaix, G. Staffelbach, M. Garcia, J. Boussuge, and T. Poinsot (2009). High performance parallel computing of flows in complex geometries: I. methods. *Computational Science & Discovery 2*(1), 015003. *(p. 204)*

Gourdain, N., L. Gicquel, G. Staffelbach, O. Vermorel, F. Duchaine, J. Boussuge, and T. Poinsot (2009). High performance parallel computing of flows in complex geometries: Ii. applications. *Computational Science & Discovery 2*(1), 015004. *(p. 204)*

Gueyffier, D., J. Li, A. Nadim, R. Scardovelli, and S. Zaleski (1999). Volume-of-fluid interface tracking with smoothed surface stress methods for three-dimensional flows. *Journal of Computational physics 152*(2), 423–456. *(p. 87)*

Guillén-González, F. and G. Tierra (2014). Splitting schemes for a navier-stokes/cahn-hilliard model for two fluids with different densities. *Journal of Computational Mathematics 32*(6), 643–664. *(p. 143)*

Guo, Z. and P. Lin (2015). A thermodynamically consistent phase-field model for two-phase flows with thermocapillary effects. *Journal of Fluid Mechanics 766*, 226–271. *(p. 123)*

Gurliat, O., V. Schmidt, O. Haidn, and M. Oschwald (2003). Ignition of cryogenic h2/lox sprays. *Aerospace Science and Technology 7*(7), 517–531. *(p. 16)*

Gurtin, M. E., D. Polignone, and J. Vinals (1996). Two-phase binary fluids and immiscible fluids described by an order parameter. *Mathematical Models and Methods in Applied Sciences 6*(06), 815–831. *(p. 122, 142, 143, 144)*

Haase, R. (1951). Zur thermodynamik der irreversiblen prozesse i. *Zeitschrift für Naturforschung A 6*(8), 420–437. *(p. 169)*

Haberzettl, A., D. Gundel, K. Bahlmann, J. Thomas, J. Kretschmer, and P. Vuillermoz (2000). European research and technology test bench p8 for high pressure liquid rocket propellants. In *36th AIAA/ASME/SAE/ASEE Joint Propulsion Conference and Exhibit*, pp. 3307. *(p. 9)*

Habiballah, M., L. Vingert, J. Traineau, and P. Vuillermoz (1996). Mascotte- a test bench for cryogenic combustion research. In *IAF, International Astronautical Congress, 47 th, Beijing, China*. *(p. xix, 10, 154, 155, 157)*

Haidn, O. J. (2008). Advanced rocket engines. *Advances on Propulsion Technology for High-Speed Aircraft 1*, 6–1. *(p. xv, 4)*

Hall, M. (1984). Cell vertex multigrid solution of the euler equations for transonic flow past aerofoils. *Rapport technique, Royal Aerospace Establishment*, 26. *(p. 209)*

Hama, F. R. and E. R. Burke (1960). *On the rolling-up of a vortex sheet.* University of Maryland, Institute for Fluid Dynamics and Applied Mathematics. *(p. 54)*

Harlow, F. H. (1964). The particle-in-cell computing method for fluid dynamics. *Methods Comput. Phys. 3*, 319–343. *(p. 51)*

Harlow, F. H., J. E. Welch, et al. (1965). Numerical calculation of time-dependent viscous incompressible flow of fluid with free surface. *Physics of fluids 8*(12), 2182. *(p. 12, 54)*

Hartmann, D., M. Meinke, and W. Schröder (2008). Differential equation based constrained reinitialization for level set methods. *Journal of Computational Physics 227*(14), 6821–6845. *(p. 110)*

Hartmann, D., M. Meinke, and W. Schröder (2010). The constrained reinitialization equation for level set methods. *Journal of computational physics 229*(5), 1514–1535. *(p. 110)*

Haspot, B. (2008). Weak solution for compressible fluid models of korteweg type. *arXiv preprint arXiv:0803.1925*. *(p. 191, 236)*

He, Q., R. Glowinski, and X.-P. Wang (2011). A least-squares/finite element method for the numerical solution of the navier-stokes/cahn-hilliard system modeling the motion of the contact line. *Journal of Computational Physics 230*(12), 4991–5009. *(p. 143)*

He, Q. and N. Kasagi (2008). Phase-field simulation of small capillary-number two-phase flow in a microtube. *Fluid dynamics research 40*(7-8), 497. *(p. 143)*

Heida, M., J. Málek, and K. Rajagopal (2012a). On the development and generalizations of allen-cahn and stefan equations within a thermodynamic framework. *Zeitschrift für angewandte Mathematik und Physik 63*(4), 759–776. *(p. 122, 141)*

Heida, M., J. Málek, and K. R. Rajagopal (2012b). On the development and generalizations of cahn–hilliard equations within a thermodynamic framework. *Zeitschrift für angewandte Mathematik und Physik 63*(1), 145–169. *(p. 122, 141)*

Hejazialhosseini, B., D. Rossinelli, and P. Koumoutsakos (2013). Vortex dynamics in 3d shock-bubble interaction. *Physics of Fluids 25*(11), 110816. *(p. xix, 153)*

Helfand, E. and G. H. Fredrickson (1989). Large fluctuations in polymer solutions under shear. *Physical review letters 62*(21), 2468. *(p. 122)*

Henry, D. (2006). *Geometric theory of semilinear parabolic equations*, Volume 840. Springer. *(p. 121)*

Herding, G., R. Snyder, C. Rolon, and S. Candel (1998). Investigation of cryogenic propellant flames using computerized tomography of emission images. *Journal of propulsion and power 14*(2), 146–151. *(p. 16)*

Herding, G., R. Snyder, P. Scouflaire, C. Rollin, and S. Candel (1995). Emission and laser induced fluorescence imaging of cryogenic propellant combustion. In *Proceedings of the Conference on Propulsive Flow in Space Transportation Systems, Bordeaux, France*, pp. 1–14. *(p. 16)*

Herding, G., R. Snyder, P. Scouflaire, C. Rolon, and S. Candel (1996). Flame stabilization in cryogenic propellant combustion. In *Symposium (International) on Combustion*, Volume 26, pp. 2041–2047. Elsevier. *(p. 16)*

Herrmann, M. (2008). A balanced force refined level set grid method for two-phase flows on unstructured flow solver grids. *Journal of computational physics 227*(4), 2674–2706. *(p. 112)*

Heyns, J. A., A. Malan, T. Harms, and O. F. Oxtoby (2013). Development of a compressive surface capturing formulation for modelling free-surface flow by using the volume-of-fluid approach. *International Journal for Numerical Methods in Fluids 71*(6), 788–804. *(p. 99)*

Hieber, S. E. and P. Koumoutsakos (2005). A lagrangian particle level set method. *Journal of Computational Physics 210*(1), 342–367. *(p. 112)*

Hirsch, C. (2007). *Numerical computation of internal and external flows: The fundamentals of computational fluid dynamics*. Butterworth-Heinemann. *(p. 211, 236)*

Hirt, C. and F. H. Harlow (1967). A general corrective procedure for the numerical solution of initial-value problems. *Journal of Computational Physics 2*(2), 114–119. *(p. 58)*

Hirt, C. W. and B. D. Nichols (1981). Volume of fluid (vof) method for the dynamics of free boundaries. *Journal of computational physics 39*(1), 201–225. *(p. 12, 80, 81, 83, 95, 96)*

Hohenberg, P. C. and B. I. Halperin (1977). Theory of dynamic critical phenomena. *Reviews of Modern Physics 49*(3), 435. *(p. 122, 140, 142)*

Hopfinger, E. (1998). Liquid jet instability and atomization in a coaxial gas stream. In *Advances in Turbulence VII*, pp. 69–78. Springer. *(p. 7)*

Hopfinger, E. and J. C. Lasheras (1994). Breakup of a water jet in high velocity co-flowing air. In *Proc. of the 6th Int. Conference on Liquid Atomization, Rouen, France*. *(p. 7, 8)*

Houim, R. W. and K. K. Kuo (2013). A ghost fluid method for compressible reacting flows with phase change. *Journal of Computational Physics 235*, 865–900. *(p. 72, 100)*

Höwing, J. (2011). Stability of large-and small-amplitude solitary waves in the generalized korteweg–de vries and euler–korteweg/boussinesq equations. *Journal of Differential Equations 251*(9), 2515–2533. *(p. 236)*

Hoyt, J. and J. Taylor (1977a). Turbulence structure in a water jet discharging in air. *The Physics of Fluids 20*(10), S253–S257. *(p. 7)*

Hoyt, J. W. and J. Taylor (1977b). Waves on water jets. *Journal of Fluid Mechanics 83*(1), 119–127. *(p. 7)*

Hsiang, L.-P. and G. M. Faeth (1992). Near-limit drop deformation and secondary breakup. *International Journal of Multiphase Flow 18*(5), 635–652. *(p. 7)*

Hsiang, L.-P. and G. M. Faeth (1993). Drop properties after secondary breakup. *International Journal of Multiphase Flow 19*(5), 721–735. *(p. 7)*

Hu, X., B. Khoo, N. Adams, and F. Huang (2006). A conservative interface method for compressible flows. *Journal of Computational Physics 219*(2), 553 – 578. *(p. 100)*

Hu, X. Y. and B. C. Khoo (2004). An interface interaction method for compressible multifluids. *Journal of Computational Physics 198*(1), 35–64. *(p. 67, 71, 72)*

Hua, J., J. F. Stene, and P. Lin (2008). Numerical simulation of 3d bubbles rising in viscous liquids using a front tracking method. *Journal of Computational Physics 227*(6), 3358–3382. *(p. 75)*

Huang, M., B. Chen, and L. Wu (2010). A slic–vof method based on unstructured grid. *Microgravity Science and Technology 22*(3), 305–314. *(p. 84)*

Inamuro, T., T. Ogata, S. Tajima, and N. Konishi (2004). A lattice boltzmann method for incompressible two-phase flows with large density differences. *Journal of Computational physics 198*(2), 628–644. *(p. 128)*

Irfan, M. and M. Muradoglu (2017). A front tracking method for direct numerical simulation of evaporation process in a multiphase system. *Journal of Computational Physics 337*(Supplement C), 132–153. *(p. 76)*

Irfan, M. and M. Muradoglu (2018). A front tracking method for particle-resolved simulation of evaporation and combustion of a fuel droplet. *Computers & Fluids 174*, 283–299. *(p. 76)*

Issakhov, A. and M. Imanberdiyeva (2019). Numerical simulation of the movement of water surface of dam break flow by vof methods for various obstacles. *International Journal of Heat and Mass Transfer 136*, 1030–1051. *(p. xviii, 98)*

Ivancic, B. and W. Mayer (2002). Time-and length scales of combustion in liquid rocket thrust chambers. *Journal of propulsion and power 18*(2), 247–253. *(p. 306)*

Ivey, C. B. and P. Moin (2015). Accurate interface normal and curvature estimates on three-dimensional unstructured non-convex polyhedral meshes. *Journal of Computational Physics 300*, 365–386. *(p. 85)*

Ivey, C. B. and P. Moin (2017). Conservative and bounded volume-of-fluid advection on unstructured grids. *Journal of Computational Physics 350*(Supplement C), 387 – 419. *(p. 81, 85, 87, 89, 91)*

Izbassarov, D. and M. Muradoglu (2015). A front-tracking method for computational modeling of viscoelastic two-phase flow systems. *Journal of Non-Newtonian Fluid Mechanics 223*(Supplement C), 122–140. *(p. 64)*

Jacqmin, D. (1995). Three-dimensional computations of droplet collisions, coalescence, and droplet/wall interactions using a continuum surface-tension method. *AIAA paper* (95-0883). *(p. 122)*

Jacqmin, D. (1999). Calculation of two-phase navier–stokes flows using phase-field modeling. *Journal of Computational Physics 155*(1), 96–127. *(p. 122, 128, 143, 144)*

Jacqmin, D. (2000). Contact-line dynamics of a diffuse fluid interface. *Journal of Fluid Mechanics 402*, 57–88. *(p. 143, 144)*

Jamet, D. (1998). *Etude des potentialités de la théorie du second gradient pour la simulation numérique directe des écoulements liquide-vapeur avec changement de phase*. Ph. D. thesis, Ecole Centrale Paris. *(p. 159, 169, 170, 171, 172, 175, 176, 183, 185, 189, 196, 305, 308, 310, 322, 388, 423)*

Jamet, D. (2010). Diffuse interface models in fluid mechanics. *GdR CNRS documentation*. *(p. 126, 169)*

Jamet, D., O. Lebaigue, N. Coutris, and J. Delhaye (2001). The second gradient method for the direct numerical simulation of liquid–vapor flows with phase change. *Journal of Computational Physics 169*(2), 624–651. *(p. 313, 321)*

Jamet, D., O. Lebaigue, J.-M. Delhaye, and N. Coutris (1995). A numerical description of a liquid-vapor interface based on the second gradient theory. *International Journal of Fluid Mechanics Research 22*(1), 1–14. *(p. 194)*

Jasak, H. (1996). *Error analysis and estimation for the finite volume method with applications to fluid flows.* Ph. D. thesis, Imperial College London. *(p. 81, 97)*

Jasnow, D. and J. Vinals (1995). Coarse-grained description of thermo-capillary flow. *Physics of Fluids 8*(3), 660–669. *(p. 143, 144)*

Jasnow, D. and J. Vinals (1996). Coarse-grained description of thermo-capillary flow. *Physics of Fluids (1994-present) 8*(3), 660–669. *(p. 148)*

Jemison, M., E. Loch, M. Sussman, M. Shashkov, M. Arienti, M. Ohta, and Y. Wang (2013). A coupled level set-moment of fluid method for incompressible two-phase flows. *Journal of Scientific Computing 54*(2-3), 454–491. *(p. 112)*

Jeong, D. and J. Kim (2017). Conservative allen-cahn-navier-stokes system for incompressible two-phase fluid flows. *Computers & Fluids 156*, 239–246. *(p. 130, 143)*

Jessop, P. G. and W. Leitner (2008). *Chemical synthesis using supercritical fluids.* John Wiley & Sons. *(p. xv, 23)*

Jiang, Y., A. Umemura, and C. K. Law (1992). An experimental investigation on the collision behaviour of hydrocarbon droplets. *Journal of Fluid Mechanics 234*, 171–190. *(p. xxviii, xxix, 350, 351, 356, 357)*

Jofre, L. and J. Urzay (2016). On interfacial transport in transcritical flows of liquid fuels into high-pressure combustors. *Center for Turbulence Research Annual Research Briefs*, 193–207. *(p. 181)*

Johnson, W. (1970). Development and application of computer programs related to hypervelocity impact. *Systems Science, and Software Report*. *(p. 96)*

Juniper, M., A. Tripathi, P. Scouflaire, C. Rolon, and S. Candel (2001a). Stabilisation des flammes cryotechniques et effets du retrait. In *Actes du Colloque de Synthèse du Groupe de Recherche CNES/CNRS/ONERA/SNECMA «Combustion dans les Moteurs-Fusées», Cépaduès Éditions*, pp. 221–231. *(p. 16)*

Juniper, M., A. Tripathi, P. Scouflaire, J. Rolon, and S. Candel (2001b). The structure of cryogenic flames and subcritical and supercritical pressures. *(p. 16)*

Juniper, M., A. Tripathi, P. Scouflaire, J.-C. Rolon, and S. Candel (2000). Structure of cryogenic flames at elevated pressures. *Proceedings of the Combustion Institute 28*(1), 1103–1109. *(p. 16)*

Juric, D. and G. Tryggvason (1998). Computations of boiling flows. *International Journal of Multiphase Flow 24*(3), 387–410. *(p. 63)*

Kapila, A., R. Menikoff, J. Bdzil, S. Son, and D. S. Stewart (2001). Two-phase modeling of deflagration-to-detonation transition in granular materials: Reduced equations. *Physics of fluids 13*(10), 3002–3024. *(p. 149, 151, 152)*

Karma, A., D. A. Kessler, and H. Levine (2001). Phase-field model of mode iii dynamic fracture. *Physical Review Letters 87*(4), 045501. *(p. 122)*

Karma, A. and W.-J. Rappel (1998). Quantitative phase-field modeling of dendritic growth in two and three dimensions. *Physical review E 57*(4), 4323. *(p. 137, 139)*

Kashiwa, B. A. (1986). A generalized mac method for incompressible fluid flow. Technical report, Los Alamos, N.M. : Springfield, VA. *(p. 55)*

Kassner, K., C. Misbah, J. Müller, J. Kappey, and P. Kohlert (2001). Phase-field modeling of stress-induced instabilities. *Physical Review E 63*(3), 036117. *(p. 138)*

Kay, D., V. Styles, and E. Süli (2009). Discontinuous galerkin finite element approximation of the cahn–hilliard equation with convection. *SIAM Journal on Numerical Analysis 47*(4), 2660–2685. *(p. xix, 128, 129, 131)*

Kellogg, O. D. (1929). *Foundations of potential theory*, Volume 31. Springer Science & Business Media. *(p. 52)*

Kelly, D. M., Q. Chen, and J. Zang (2015). Picin: a particle-in-cell solver for incompressible free surface flows with two-way fluid-solid coupling. *SIAM Journal on Scientific Computing 37*(3), B403–B424. *(p. 51)*

Kendrick, D., G. Herding, P. Scouflaire, C. Rolon, and S. Candel (1998). Effet du retrait sur la stabilisation des flammes cryotechniques. *Comptes Rendus de l'Académie des Sciences-Series IIB-Mechanics-Physics-Chemistry-Astronomy 326*(2), 111–116. *(p. 16)*

Kendrick, D., G. Herding, P. Scouflaire, C. Rolon, and S. Candel (1999). Effects of a recess on cryogenic flame stabilization. *Combustion and Flame 118*(3), 327–339. *(p. 16)*

Kikuchi, R. and J. W. Cahn (1962). Theory of domain walls in ordered structures-ii: Pair approximation for nonzero temperatures. *Journal of Physics and Chemistry of Solids 23*(1-2), 137–151. *(p. 121)*

Kim, D. and P. Moin (2011). Numerical simulation of the breakup of a round liquid jet by a coaxial flow of gas with a subgrid lagrangian breakup model. *Center for Turbulence Research, Annual Research Briefs*, 15–30. *(p. 16)*

Kim, H. and M.-S. Liou (2011). Accurate adaptive level set method and sharpening technique for three dimensional deforming interfaces. *Computers & Fluids 44*(1), 111–129. *(p. 112)*

Kim, J. (2005). A continuous surface tension force formulation for diffuse-interface models. *Journal of Computational Physics 204*(2), 784–804. *(p. 142, 143)*

Kim, J. (2012). Phase-field models for multi-component fluid flows. *Communications in Computational Physics 12*(03), 613–661. *(p. 122)*

Kim, J., K. Kang, and J. Lowengrub (2004). Conservative multigrid methods for cahn-hilliard fluids. *Journal of Computational Physics 193*(2), 511–543. *(p. 143)*

Kim, J. and H. G. Lee (2017). A new conservative vector-valued allen–cahn equation and its fast numerical method. *Computer Physics Communications 221*, 102–108. *(p. xix, 132, 133, 143)*

Kim, J., S. Lee, Y. Choi, S.-M. Lee, and D. Jeong (2016). Basic principles and practical applications of the cahn-hilliard equation. *Mathematical Problems in Engineering 2016*. *(p. xix, 129, 130)*

Kim, S.-O. and H. C. No (1998). Second-order model for free surface convection and interface reconstruction. *International Journal for Numerical Methods in Fluids 26*(1), 79–100. *(p. 81, 85)*

Ko, G. H. and H. S. Ryou (2005). Modeling of droplet collision-induced breakup process. *International Journal of Multiphase Flow 31*(6), 723–738. *(p. xiii, 359, 360, 361)*

Kobayashi, R. (1991). Mathematical models of phase transition and interfacial motion. *Bull Jpn Soc Ind Appl Math 1*, 22–33. *(p. 127)*

Koff, B. L. (2004). Gas turbine technology evolution: A designers perspective. *Journal of propulsion and power 20*(4), 577–595. *(p. 1)*

Koga, T. and K. Kawasaki (1991). Spinodal decomposition in binary fluids: Effects of hydrodynamic interactions. *Physical Review A 44*(2), R817. *(p. 122)*

Kohn, R. V., F. Otto, M. G. Reznikoff, and E. Vanden-Eijnden (2007). Action minimization and sharp-interface limits for the stochastic allen-cahn equation. *Communications on Pure and Applied Mathematics: A Journal Issued by the Courant Institute of Mathematical Sciences 60*(3), 393–438. *(p. 122)*

Kohn, R. V., M. G. Reznikoff, and Y. Tonegawa (2006). Sharp-interface limit of the allen-cahn action functional in one space dimension. *Calculus of variations and partial differential equations 25*(4), 503–534. *(p. 122)*

Korteweg, D. J. (1901). Sur la forme que prennent les équations du mouvement des fluides si l'on tient compte des forces capillaires causées par des variations de densitćonsidérables mais continues et sur la thórie de la capillarité dans l'hypothese d'une variation continue de la densité. *Archives Nérlandaises des Sciences exactes et naturelles 6*(1), 265. *(p. 17, 121, 160, 163, 164, 165, 166, 180)*

Koschel, W. W. and O. J. Haidn (1998). P8-the new french/german test facility for h2o2 high pressure rocket engine combustion research. *International journal of hydrogen energy 23*(8), 683–694. *(p. 9)*

Kotschote, M. (2014). Existence and time-asymptotics of global strong solutions to dynamic korteweg models. *Indiana Univ. Math. J 63*(1), 21–51. *(p. 236)*

Kotschote, M. and R. Zacher (2015). Strong solutions in the dynamical theory of compressible fluid mixtures. *Mathematical Models and Methods in Applied Sciences 25*(07), 1217–1256. *(p. 141)*

Kou, J. and S. Sun (2014). An adaptive finite element method for simulating surface tension with the gradient theory of fluid interfaces. *Journal of Computational and Applied Mathematics 255*, 593–604. *(p. 123)*

Kou, J. and S. Sun (2016). Unconditionally stable methods for simulating multi-component two-phase interface models with peng–robinson equation of state and various boundary conditions. *Journal of Computational and Applied Mathematics 291*, 158–182. *(p. 123)*

Kou, J., S. Sun, and X. Wang (2015). Efficient numerical methods for simulating surface tension of multi-component mixtures with the gradient theory of fluid interfaces. *Computer Methods in Applied Mechanics and Engineering 292*, 92–106. *(p. 123)*

Koynov, A., J. G. Khinast, and G. Tryggvason (2005). Mass transfer and chemical reactions in bubble swarms with dynamic interfaces. *AIChE Journal 51*(10), 2786–2800. *(p. 63)*

Kraichnan, R. H. (1967). Inertial ranges in two-dimensional turbulence. *The Physics of Fluids 10*(7), 1417–1423. *(p. 365)*

Kraichnan, R. H. (1971). Inertial-range transfer in two-and three-dimensional turbulence. *Journal of Fluid Mechanics 47*(3), 525–535. *(p. 365)*

Krier, H. and S. Gokhale (1978). Modeling of convective mode combustion through granulated propellant to predict detonation transition. *AIAA journal 16*(2), 177–183. *(p. 149)*

Krill Iii, C. and L.-Q. Chen (2002). Computer simulation of 3-d grain growth using a phase-field model. *Acta materialia 50*(12), 3059–3075. *(p. 122)*

Kuo, K. and M. Summerfield (1975). High speed combustion of mobile granular solid propellants: Wave structure and the equivalent rankine-hugoniot relation. In *Symposium (International) on Combustion*, Volume 15, pp. 515–527. Elsevier. *(p. 149)*

Kurganov, A. and E. Tadmor (2002). Solution of two-dimensional riemann problems for gas dynamics without riemann problem solvers. *Numerical Methods for Partial Differential Equations: An International Journal 18*(5), 584–608. *(p. 71)*

Lafaurie, B., C. Nardone, R. Scardovelli, S. Zaleski, and G. Zanetti (1994). Modelling merging and fragmentation in multiphase flows with surfer. *Journal of Computational Physics 113*(1), 134–147. *(p. 81, 95, 96, 97)*

Lamarque, N. (2007). *Schémas numériques et conditions limites pour la simulation aux grandes échelles de la combustion diphasique dans les foyers d'hélicoptère.* Ph. D. thesis, Institut National Polytechnique de Toulouse-INPT. *(p. 204, 206, 211, 213, 275)*

Lamb, H. (1916). *Hydrodynamics.* *(p. 295)*

Lamb, H. (1975). *Hydrodynamics.* *(p. 52, 291)*

Landau, L. D. (1937). On the theory of phase transitions. *Ukr. J. Phys. 11*, 19–32. *(p. 121, 123, 133)*

Langer, J. and R. Sekerka (1975). Theory of departure from local equilibrium at the interface of a two-phase diffusion couple. *Acta Metallurgica 23*(10), 1225–1237. *(p. 121)*

Lasheras, J. and E. Hopfinger (2000). Liquid jet instability and atomization in a coaxial gas stream. *Annual Review of Fluid Mechanics 32*(1), 275–308. *(p. xv, 7, 8, 9)*

Lasheras, J., E. Villermaux, and E. Hopfinger (1998). Break-up and atomization of a round water jet by a high-speed annular air jet. *Journal of Fluid Mechanics 357*, 351–379. *(p. 7, 8, 9)*

Lax, P. D. and X.-D. Liu (1998). Solution of two-dimensional riemann problems of gas dynamics by positive schemes. *SIAM Journal on Scientific Computing 19*(2), 319–340. *(p. 71)*

Layes, G. and O. Le Métayer (2007). Quantitative numerical and experimental studies of the shock accelerated heterogeneous bubbles motion. *Physics of fluids 19*(4), 042105. *(p. xix, 152)*

Le Chenadec, V. and H. Pitsch (2013). A monotonicity preserving conservative sharp interface flow solver for high density ratio two-phase flows. *Journal of Computational Physics 249*, 185–203. *(p. xviii, 93)*

Le Martelot, S., R. Saurel, and B. Nkonga (2014). Towards the direct numerical simulation of nucleate boiling flows. *International Journal of Multiphase Flow 66*, 62–78. *(p. 150, 155)*

Le Métayer, O., J. Massoni, and R. Saurel (2005). Modelling evaporation fronts with reactive riemann solvers. *Journal of Computational Physics 205*(2), 567–610. *(p. 150)*

Lebedev, V. I. (1964). Difference analogues of orthogonal decompositions, basic differential operators and some boundary problems of mathematical physics. i. *USSR Computational Mathematics and Mathematical Physics 4*(3), 69–92. *(p. 54)*

Lee, D. and J. Kim (2016). Comparison study of the conservative allen–cahn and the cahn-hilliard equations. *Mathematics and Computers in Simulation 119*, 35–56. *(p. 123, 128, 130, 134, 135)*

Lee, H. G., J.-W. Choi, and J. Kim (2012). A practically unconditionally gradient stable scheme for the n-component cahn–hilliard system. *Physica A: Statistical Mechanics and its Applications 391*(4), 1009–1019. *(p. 123)*

Lee, H. G. and J. Kim (2015). An efficient numerical method for simulating multiphase flows using a diffuse interface model. *Physica A: Statistical Mechanics and its Applications 423*, 33–50. *(p. 123)*

Leith, C. E. (1968). Diffusion approximation for two-dimensional turbulence. *The Physics of Fluids 11*(3), 671–672. *(p. 365)*

Li, J. (1995, 01). Piecewise linear interface calculation[calcul d'interface affine par morceaux]. *320*, 391–396. *(p. 87)*

Li, Y., J.-I. Choi, and J. Kim (2016). A phase-field fluid modeling and computation with interfacial profile correction term. *Communications in Nonlinear Science and Numerical Simulation 30*(1), 84 – 100. *(p. 123)*

Li, Y. and M. Huang (2018). Strong solutions for an incompressible navier-stokes/allen-cahn system with different densities. *Zeitschrift für angewandte Mathematik und Physik 69*(3), 68. *(p. 144)*

Liang, H., B. Shi, Z. Guo, and Z. Chai (2014). Phase-field-based multiple-relaxation-time lattice boltzmann model for incompressible multiphase flows. *Physical Review E 89*(5), 053320. *(p. xix, 143, 145, 146)*

Lin, H., Y.-Y. Duan, and Q. Min (2007). Gradient theory modeling of surface tension for pure fluids and binary mixtures. *Fluid Phase Equilibria 254*(12), 75 – 90. *(p. 197, 199)*

Linstrom, P. J. and W. G. Mallard (2001). *The NIST Chemistry WebBook: A chemical data resource on the internet*. National Institute of Standards and Technology. *(p. xv, xvi, 24, 32, 35, 36, 37, 38, 39, 40, 41, 42, 47)*

Liu, T., B. Khoo, and C. Wang (2005). The ghost fluid method for compressible gas-water simulation. *Journal of Computational Physics 204*(1), 193–221. *(p. 71)*

Liu, T., B. Khoo, and K. Yeo (2003). Ghost fluid method for strong shock impacting on material interface. *Journal of Computational Physics 190*(2), 651–681. *(p. 128, 142, 143, 144)*

Liu, W., A. Bertozzi, and T. Kolokolnikov (2012). Diffuse interface surface tension models in an expanding flow. *Communications in Mathematical Sciences 10*(1), 387–418. *(p. 144)*

López, J., J. Hernández, P. Gómez, and F. Faura (2004). A volume of fluid method based on multidimensional advection and spline interface reconstruction. *Journal of Computational Physics 195*(2), 718–742. *(p. xviii, 81, 86, 90, 91, 92)*

Losasso, F., R. Fedkiw, and S. Osher (2006). Spatially adaptive techniques for level set methods and incompressible flow. *Computers & Fluids 35*(10), 995–1010. *(p. 112)*

Lovett, R., P. W. DeHaven, J. J. Vieceli Jr, and F. P. Buff (1973). Generalized van der waals theories for surface tension and interfacial width. *The Journal of Chemical Physics 58*(5), 1880–1885. *(p. 196)*

Lowengrub, J. and L. Truskinovsky (1998). Quasi–incompressible cahn–hilliard fluids and topological transitions. *Proceedings of the Royal Society of London. Series A: Mathematical, Physical and Engineering Sciences 454*(1978), 2617–2654. *(p. 122, 134, 141, 143)*

Lu, H., N. Zhao, and D. Wang (2016). A front tracking method for the simulation of compressible multimedium flows. *Communications in Computational Physics 19*(1), 124–142. *(p. 75)*

Luo, K., C. Shao, Y. Yang, and J. Fan (2015). A mass conserving level set method for detailed numerical simulation of liquid atomization. *Journal of Computational Physics 298*(Supplement C), 495 – 519. *(p. 101)*

Ma, L., R. Chen, X. Yang, and H. Zhang (2017). Numerical approximations for allen-cahn type phase field model of two-phase incompressible fluids with moving contact lines. *Communications in Computational Physics 21*(3), 867–889. *(p. 122, 143)*

Malladi, R., J. A. Sethian, and B. C. Vemuri (1994). Shape modeling with front propagation: A level set approach. *(p. 100, 105)*

Malladi, R., J. A. Sethian, and B. C. Vemuri (1995). Shape modeling with front propagation: A level set approach. *IEEE TRANSACTIONS ON PATTERN ANALYSIS AND MACHINE INTELLIGENCE 17*(2). *(p. 99)*

Mangiavacchi, N., A. Castelo, M. F. Tomé, J. A. Cuminato, M. L. B. de Oliveira, and S. McKee (2005). An effective implementation of surface tension using the marker and cell method for axisymmetric and planar flows. *SIAM Journal on Scientific Computing 26*(4), 1340–1368. *(p. 55, 60)*

Marmottant, P. and E. Villermaux (2003). Atomisation primaire dans les jets coaxiaux. *Combustion. Revue des Sciences et Techniques de Combustion 2*(2), 89–125. *(p. 7)*

Marmottant, P. and E. Villermaux (2004). On spray formation. *Journal of fluid mechanics 498*, 73–111. *(p. xv, 7, 8)*

Matheis, J. and S. Hickel (2018). Multi-component vapor-liquid equilibrium model for les of high-pressure fuel injection and application to ecn spray a. *International Journal of Multiphase Flow 99*, 294–311. *(p. 150)*

Mathew, J., R. Lechner, H. Foysi, J. Sesterhenn, and R. Friedrich (2003). An explicit filtering method for large eddy simulation of compressible flows. *Physics of fluids 15*(8), 2279–2289. *(p. 216)*

Mayer, W., B. Ivancic, A. Schik, and U. Hornung (1998). Propellant atomization in lox/gh2 rocket engines. In *34th AIAA/ASME/SAE/ASEE Joint Propulsion Conference and Exhibit*, pp. 3685. *(p. 10, 16)*

Mayer, W., A. Schik, M. Sch-aring, ffler, and H. Tamura (2000). Injection and mixing processes in high-pressure liquid oxygen/gaseous hydrogen rocket combustors. *Journal of Propulsion and Power 16*(5), 823–828. *(p. 10)*

Mayer, W., A. Schik, C. Schweitzer, and M. Schaeffler (1996). Injection and mixing processes in high pressure lox/gh2 rocket combustors. In *32nd Joint Propulsion Conference and Exhibit*, pp. 2620. *(p. 9, 10)*

Mayer, W. and H. Tamura (1996). Propellant injection in a liquid oxygen/gaseous hydrogen rocket engine. *Journal of Propulsion and Power 12*(6), 1137–1147. *(p. 16)*

Mayer, W., J. Telaar, R. Branam, G. Schneider, and J. Hussong (2003). Raman measurements of cryogenic injection at supercritical pressure. *Heat and Mass Transfer 39*(8-9), 709–719. *(p. 10, 16)*

Mayer, W. O. H., B. Ivancic, A. Schik, and U. Hornung (2001). Propellant atomization and ignition phenomena in liquid oxygen/gaseous hydrogen rocket combustors. *Journal of Propulsion and Power 17*(4), 794–799. *(p. 10, 16)*

Mayer, W. O. H., A. H. A. Schik, B. Vielle, C. Chauveau, I. Gökalp, D. G. Talley, and R. D. Woodward (1998). Atomization and breakup of cryogenic propellants under high-pressure subcritical and supercritical conditions. *Journal of Propulsion and Power 14*(5), 835–842. *(p. xv, 12)*

McBride, B. J., M. J. Zehe, and S. Gordon (2002). Nasa glenn coefficients for calculating thermodynamic properties of individual species. *(p. 35)*

Mccaslin, J. O. and O. Desjardins (2014). A localized re-initialization equation for the conservative level set method. *Journal of Computational Physics 262*, 408–426. *(p. xviii, 101, 116)*

McCoy, B., L. Scriven, and H. Davis (1981). Comparison of molecular models of the liquid–vapor interface. *The Journal of Chemical Physics 75*(9), 4719–4726. *(p. 199)*

McKee, S., M. Tomé, V. Ferreira, J. Cuminato, A. Castelo, F. Sousa, and N. Mangiavacchi (2008). The mac method. *Computers & Fluids 37*(8), 907 – 930. *(p. 55, 60)*

Mehrabian, H. (2014). *Simulation of selected interfacial dynamic problems using Cahn-Hilliard diffuse-interface method*. Ph. D. thesis, University of British Columbia. *(p. 122, 123)*

Meixner, J., S. de Groot, and P. Mazur (1962). *Non-equilibrium thermodynamics*. North-Holland Publishing Company, Amsterdam. *(p. 169)*

Meng, J. and J. Thomson (1978). Numerical studies of some nonlinear hydrodynamic problems by discrete vortex element methods. *Journal of Fluid Mechanics 84*(3), 433–453. *(p. 51)*

Michelsen, M. L., J. Mollerup, and M. P. Breil (2008). Thermodynamic models: Fundamental & computational aspects. In *Thermodynamic Models: Fundamental & Computational Aspects*. Tie-Line Publications. *(p. 27)*

Modica, L. (1987). The gradient theory of phase transitions and the minimal interface criterion. *Archive for Rational Mechanics and Analysis 98*(2), 123–142. *(p. 122, 124, 135)*

Moin, P. and K. Mahesh (1998). Direct numerical simulation: a tool in turbulence research. *Annual review of fluid mechanics 30*(1), 539–578. *(p. 306)*

Monge, G. (1787). Mémoire sur quelques effets d'attraction ou de répulsion apparente entre les molécules de matière. *Mémoire de l'Académie Royale des Sciences*, 506–529. *(p. 119)*

Moretti, G. (1987). Computation of flows with shocks. *Annual Review of Fluid Mechanics 19*(1), 313–337. *(p. 64)*

Morin, A. and T. Flåtten (2016). A two-fluid four-equation model with instantaneous thermodynamical equilibrium. *ESAIM: Mathematical Modelling and Numerical Analysis 50*(4), 1167–1192. *(p. 150)*

Mulder, W., S. Osher, and J. A. Sethian (1992). Computing interface motion in compressible gas dynamics. *Journal of Computational Physics 100*(2), 209–228. *(p. 100)*

Mullins, W. W. and R. Sekerka (1964). Stability of a planar interface during solidification of a dilute binary alloy. *Journal of applied physics 35*(2), 444–451. *(p. 135)*

Muradoglu, M. and G. Tryggvason (2008). A front-tracking method for computation of interfacial flows with soluble surfactants. *Journal of computational physics 227*(4), 2238–2262. *(p. 75)*

Murrone, A. and H. Guillard (2005). A five equation reduced model for compressible two phase flow problems. *Journal of Computational Physics 202*(2), 664–698. *(p. 151)*

Muzaferija, S. and M. Peric (1997). Computation of free-surface flows using the finite-volume method and moving grids. *Numerical heat transfer 32*(4), 369–384. *(p. xviii, 95, 97)*

Neufeld, P. D., A. Janzen, and R. Aziz (1972). Empirical equations to calculate 16 of the transport collision integrals ω (l, s)* for the lennard-jones (12–6) potential. *The Journal of Chemical Physics 57*(3), 1100–1102. *(p. 32)*

Newman, J. A. and T. Brzustowski (1971). Behavior of a liquid jet near the thermodynamic critical region. *AIAA journal 9*(8), 1595–1602. *(p. 9)*

Nguyen, V.-T. and W.-G. Park (2017). A volume-of-fluid (vof) interface-sharpening method for two-phase incompressible flows. *Computers & Fluids 152*(Supplement C), 104 – 119. *(p. xviii, 99)*

Ni, R.-H. (1981). A multiple grid scheme for solving the euler equations. In *5th Computational Fluid Dynamics Conference*, pp. 1025. *(p. 209)*

Nichols, B. and C. Hirt (1971). Improved free surface boundary conditions for numerical incompressible-flow calculations. *Journal of Computational Physics 8*(3), 434–448. *(p. 54)*

Nichols, B. and C. Hirt (1975). Methods for calculating multidimensional, transient free surface flows past bodies. In *Proc., 1st Int. Conf. Ship Hydrodynamics*, pp. 253–277. Naval Ship Research and Development Center, Bethesda, Md. *(p. 80)*

Nobari, M., Y.-J. Jan, and G. Tryggvason (1996). Head-on collision of drops-a numerical investigation. *Physics of Fluids 8*(1), 29–42. *(p. xvii, 75, 76)*

Noh, W. F. and P. Woodward (1976). Slic (simple line interface calculation). In *Proceedings of the Fifth International Conference on Numerical Methods in Fluid Dynamics June 28–July 2, 1976 Twente University, Enschede*, pp. 330–340. Springer. *(p. 80, 81, 83, 84)*

Nourgaliev, R., S. Wiri, N. Dinh, and T. Theofanous (2005). On improving mass conservation of level set by reducing spatial discretization errors. *International journal of multiphase flow 31*(12), 1329–1336. *(p. 112)*

Novick-Cohen, A. (1998). The cahn-hilliard equation: Mathematical and modeling perspectives. *Advances in Mathematical Sciences and Applications 8*, 965–985. *(p. 122)*

Novick-Cohen, A. (2000). Triple-junction motion for an allen–cahn/cahn–hilliard system. *Physica D: Nonlinear Phenomena 137*(1-2), 1–24. *(p. 122, 135)*

Novick-Cohen, A. and L. A. Segel (1984). Nonlinear aspects of the cahn-hilliard equation. *Physica D: Nonlinear Phenomena 10*(3), 277–298. *(p. 122)*

Oefelein, J. C. (2005). Thermophysical characteristics of shear-coaxial lox–h 2 flames at supercritical pressure. *Proceedings of the Combustion Institute 30*(2), 2929–2937. *(p. 307)*

Oefelein, J. C. and V. Yang (1998). Modeling high-pressure mixing and combustion processes in liquid rocket engines. *Journal of Propulsion and Power 14*(5), 843–857. *(p. 15)*

Ohtsuka, T., Y.-H. Tsai, and Y. Giga (2015). A level set approach reflecting sheet structure with single auxiliary function for evolving spirals on crystal surfaces. *Journal of Scientific Computing 62*(3), 831–874. *(p. 99)*

Oishi, C., V. Ferreira, J. Cuminato, A. Castelo, M. Tomé, and N. Mangiavacchi (2004). Implementing implicit schemes in gensmac. *Trends in Applied and Computational Mathematics 5*(2), 259–268. *(p. 55, 60)*

Okong'o, N. A. and J. Bellan (2002). Direct numerical simulation of a transitional supercritical binary mixing layer: heptane and nitrogen. *Journal of Fluid Mechanics 464*, 1–34. *(p. 15)*

Olsson, E. and G. Kreiss (2005). A conservative level set method for two phase flow. *Journal of computational physics 210*(1), 225–246. *(p. 101, 113, 114)*

Olsson, E., G. Kreiss, and S. Zahedi (2007). A conservative level set method for two phase flow ii. *Journal of Computational Physics 225*(1), 785–807. *(p. 101, 114)*

Onuki, A. and K. Kawasaki (1979). Nonequilibrium steady state of critical fluids under shear flow: A renormalization group approach. *Annals of Physics 121*(1-2), 456–528. *(p. 122)*

Oono, Y. and S. Puri (1988). Study of phase-separation dynamics by use of cell dynamical systems. i. modeling. *Physical Review A 38*(1), 434. *(p. 126)*

Ornstein, L. and F. Zernike (1914). Accidental deviations of density and opalescence at the critical point of a single substance. *Proc. Akad. Sci. 17*, 793. *(p. 196)*

Osher, S. and R. Fedkiw (2006). *Level set methods and dynamic implicit surfaces*, Volume 153. Springer Science & Business Media. *(p. 99)*

Osher, S. and J. A. Sethian (1988). Fronts propagating with curvature-dependent speed: algorithms based on hamilton-jacobi formulations. *Journal of computational physics 79*(1), 12–49. *(p. 13, 99, 100, 104)*

Ovsyannikov, A., V. Sabelnikov, and M. Gorokhovski (2012). A new level set equation and its numerical assessments. In *Proceedings of the Summer Program*, pp. 315. *(p. 113)*

Owen, N. C. and P. Sternberg (1992). Gradient flow and front propagation with boundary contact energy. *Proceedings of the Royal Society of London. Series A: Mathematical and Physical Sciences 437*(1901), 715–728. *(p. 122)*

Owkes, M. and O. Desjardins (2013). A discontinuous galerkin conservative level set scheme for interface capturing in multiphase flows. *Journal of Computational Physics 249*, 275–302. *(p. 101, 112)*

Owkes, M. and O. Desjardins (2014). A computational framework for conservative, three-dimensional, unsplit, geometric transport with application to the volume-of-fluid (vof) method. *Journal of Computational Physics 270*, 587–612. *(p. 12, 81)*

Paciorri, R. and A. Bonfiglioli (2009). A shock-fitting technique for 2d unstructured grids. *Computers & Fluids 38*(3), 715–726. *(p. 64)*

Paddick, M. (2017). Transverse nonlinear instability of euler-korteweg solitons. *Annales de la Faculté des Sciences de Toulouse. Mathématiques. Série 6 26*(1), 23–48. *(p. 236)*

Pai, M., H. Pitsch, and O. Desjardins (2009). Detailed numerical simulations of primary atomization of liquid jets in crossflow. In *47th AIAA Aerospace Sciences Meeting Including the New Horizons Forum and Aerospace Exposition*, pp. 373. *(p. 110)*

Pan, Y. and K. Suga (2005). Numerical simulation of binary liquid droplet collision. *Physics of Fluids 17*(8), 082105. *(p. 355)*

Park, R. W. (1970). Behavior of water drops colliding in humid nitrogen. *(p. 350)*

Parker, B. and D. Youngs (1992). *Two and three dimensional Eulerian simulation of fluid flow with material interfaces*. Atomic Weapons Establishment. *(p. 81, 85)*

Patel, J. K. and G. Natarajan (2015). A generic framework for design of interface capturing schemes for multi-fluid flows. *Computers & Fluids 106*, 108–118. *(p. 81, 97)*

Pego, R. L. (1989). Front migration in the nonlinear cahn-hilliard equation. *Proceedings of the Royal Society of London. A. Mathematical and Physical Sciences 422*(1863), 261–278. *(p. 122, 135)*

Pelletier, M. (2019). *Diffuse interface models and adapted numerical schemes for the simulation of subcritical to supercritical flows*. Ph. D. thesis, Paris Saclay. *(p. xix, 17, 19, 150, 155, 157, 322)*

Pelletier, M., T. Schmitt, and S. Ducruix (2020). A multifluid taylor-galerkin methodology for the simulation of compressible multicomponent separate two-phase flows from subcritical to supercritical states. *Computers & Fluids*, 104588. *(p. 155)*

Peng, D., B. Merriman, S. Osher, H. Zhao, and M. Kang (1999). A pde-based fast local level set method. *Journal of computational physics 155*(2), 410–438. *(p. 108, 109)*

Peng, D.-Y. and D. B. Robinson (1976). A new two-constant equation of state. *Industrial & Engineering Chemistry Fundamentals 15*(1), 59–64. *(p. 27)*

Penrose, O. and P. C. Fife (1990). Thermodynamically consistent models of phase-field type for the kinetic of phase transitions. *Physica D: Nonlinear Phenomena 43*(1), 44–62. *(p. 122, 127)*

Peskin, C. S. (1977). Numerical analysis of blood flow in the heart. *Journal of computational physics 25*(3), 220–252. *(p. 63, 67, 73)*

Peskin, C. S. (2002). The immersed boundary method. *Acta numerica 11*, 479–517. *(p. 67, 69, 73)*

Peskin, C. S. and D. M. McQueen (1989). A three-dimensional computational method for blood flow in the heart i. immersed elastic fibers in a viscous incompressible fluid. *Journal of Computational Physics 81*(2), 372–405. *(p. 67, 73)*

Pilliod, J. E. (1992). *An analysis of piecewise linear interface reconstruction algorithms for volume-of-fluid methods*. Ph. D. thesis. *(p. 81, 85)*

Pilliod, J. E. and E. G. Puckett (2004). Second-order accurate volume-of-fluid algorithms for tracking material interfaces. *Journal of Computational Physics 199*(2), 465–502. *(p. 85)*

Pismen, L. (2001). Nonlocal diffuse interface theory of thin films and the moving contact line. *Physical Review E 64*(2), 021603. *(p. 182)*

Pitzer, K. S. (1995). Ionic fluids: Near-critical and related properties. *The Journal of Physical Chemistry 99*(35), 13070–13077. *(p. 26)*

Pitzer, K. S. and R. F. Curl Jr (1957). The volumetric and thermodynamic properties of fluids. iii. empirical equation for the second virial coefficient1. *Journal of the American Chemical Society 79*(10), 2369–2370. *(p. 26)*

Pitzer, K. S., D. Z. Lippmann, R. F. Curl, C. M. Huggins, and D. E. Petersen (1955). The volumetric and thermodynamic properties of fluids. ii. compressibility factor, vapor pressure and entropy of vaporization. *Journal of the American Chemical Society 77*(13), 3433–3440. *(p. 26)*

Plateau, J. (1873). *Statique expérimentale et théorique des liquides soumis aux seules forces moléculaires*, Volume 2. Gauthier-Villars. *(p. 7)*

Podvysotsky, A. and A. Shraiber (1984). Coalescence and break-up of drops in two-phase flows. *International journal of multiphase flow 10*(2), 195–209. *(p. 350)*

Poinsot, T. J. and S. K. Lele (1992, July). Boundary conditions for direct simulations of compressible viscous flows. *Journal of Computational Physics 101*, 104–129. *(p. 204, 219)*

Poisson, S.-D. (1831). *Nouvelle théorie de l'action capillaire*. Bachelier père et fils. *(p. 120)*

Poling, B., J. Prausnitz, and J. O'Connell (2001). The properties of gases and liquids. 5-th edition, mcgrow-hill. *New York*. *(p. 25, 26, 27, 32)*

Poo, J. and N. Ashgriz (1989). A computational method for determining curvatures. *Journal of Computational Physics 84*(2), 483–491. *(p. 81, 85, 86)*

Price, G., G. Reader, R. Rowe, and J. Bugg (1998). A piecewise parabolic interface calculation for volume tracking. In *Proc of 6th Annual Conf of the Computational Fluid Dynamics Society of Canada*. *(p. 81, 85, 86)*

Price, G. R. (1998). *A piecewise parabolic interface calculation for volume tracking*. Ph. D. thesis. *(p. 81, 85)*

Pritchett, J. W. (1970). The macyl6 hydrodynamic code: A numerical method for calculating incompressible axisymmetric time-dependent free-surface fluid flows at high reynolds number. Technical report, INFORMATION RESEARCH ASSOCIATES INC BERKELEY CA. *(p. 54)*

Prosperetti, A. (1976). Viscous effects on small-amplitude surface waves. *The Physics of Fluids 19*(2), 195–203. *(p. 281, 286)*

Prosperetti, A. (1980). Free oscillations of drops and bubbles: the initial-value problem. *Journal of Fluid Mechanics 100*(2), 333–347. *(p. 295)*

Prosperetti, A. (1981). Motion of two superposed viscous fluids. *The Physics of Fluids 24*(7), 1217–1223. *(p. 281, 286, 288, 340)*

Puckett, E. and J. Saltzman (1992). A 3d adaptive mesh refinement algorithm for multimaterial gas dynamics. *Physica D: Nonlinear Phenomena 60*(1-4), 84–93. *(p. 81, 85)*

Puckett, E. G. (1991). A volume-of-fluid interface tracking algorithm with applications to computing shock wave refraction. In *Proceedings of the Fourth International Symposium on Computational Fluid Dynamics*, pp. 933–938. *(p. 81, 85)*

Qian, J. and C. K. Law (1997). Regimes of coalescence and separation in droplet collision. *Journal of Fluid Mechanics 331*, 59–80. *(p. 350, 357)*

Qian, J., G. Tryggvason, and C. Law (1998). A front tracking method for the motion of premixed flames. *Journal of Computational Physics 144*(1), 52–69. *(p. 63)*

Qin, R. and H. Bhadeshia (2010). Phase field method. *Materials science and technology 26*(7), 803–811. *(p. 135)*

Raad, P. E. and R. Bidoae (2005). The three-dimensional eulerian–lagrangian marker and micro cell method for the simulation of free surface flows. *Journal of Computational Physics 203*(2), 668–699. *(p. xvii, 61, 62)*

Rabe, C., J. Malet, and F. Feuillebois (2010). Experimental investigation of water droplet binary collisions and description of outcomes with a symmetric weber number. *Physics of fluids 22*(4), 047101. *(p. 350)*

Ramshaw, J. D. and J. A. Trapp (1976). A numerical technique for low-speed homogeneous two-phase flow with sharp interfaces. *Journal of Computational Physics 21*(4), 438–453. *(p. 80, 83)*

Rayleigh, L. (1878). On the instability of jets. *Proceedings of the London Mathematical Society s1-10*(1), 4–13. *(p. 7)*

Rayleigh, L. (1879). On the Capillary Phenomena of Jets. *Proceedings of the Royal Society of London Series I 29*, 71–97. *(p. 7, 120)*

Razizadeh, M., S. Mortazavi, and H. Shahin (2018). Drop breakup and drop pair coalescence using front-tracking method in three dimensions. *Acta Mechanica 229*(3), 1021–1043. *(p. xvii, 75, 76, 77)*

Redlich, O. and J. N. S. Kwong (1949). On the thermodynamics of solutions. v. an equation of state. fugacities of gaseous solutions. *Chemical Reviews 44*(1), 233–244. PMID: 18125401. *(p. 19, 27)*

Reitz, R. D. (1978). Atomization and other breakup regimes of a liquid jet. *PhDT*. *(p. 362, 381)*

Renardy, Y. and M. Renardy (2002). Prost: a parabolic reconstruction of surface tension for the volume-of-fluid method. *Journal of computational physics 183*(2), 400–421. *(p. 81, 86)*

Rhee, C., L. Talbot, and J. A. Sethian (1995). Dynamical behaviour of a premixed turbulent open v-flame. *Journal of Fluid Mechanics 300*, 87–115. *(p. 100)*

Richtmyer, R. D. and K. W. Morton (1967). *Difference methods for initial-value problems.* *(p. 62)*

Rider, W. J. and D. B. Kothe (1998). Reconstructing volume tracking. *Journal of Computational Physics 141*(2), 112 – 152. *(p. 90)*

Rieber, M. and A. Frohn (1997). Navier-stokes simulation of droplet collision dynamics. In *Proc. 7th Int. Symp. On Comp. Fluid Dynamics,(ed. by Zhuang, FG) Beijing, China*, pp. 520–525. *(p. 355)*

Rocard, Y. (1952). *Thermodynamique.* Masson et Ode. *(p. 121)*

Rocard, Y. (1967). *Thermodynamique II.* Masson et Ode. *(p. 160, 161, 162, 163, 196)*

Rocchi, J.-P. (2014). *Simulations aux grandes échelles de la phase d'allumage dans un moteur fusée cryotechnique.* Ph. D. thesis, Université de Toulouse. *(p. xi, 16, 17)*

Rosenhead, L. (1931). The formation of vortices from a surface of discontinuity. *Proceedings of the Royal Society of London A: Mathematical, Physical and Engineering Sciences 134*(823), 170–192. *(p. xvii, 52, 53)*

Rouy, E. and A. Tourin (1992). A viscosity solutions approach to shape-from-shading. *SIAM Journal on Numerical Analysis 29*(3), 867–884. *(p. 108)*

Rowlinson, J. and B. Widom (1982). Molecular theory of capillarity. the international series of monographs on chemistry. *(p. 182, 183)*

Roy, D. and G. Thodos (1968). Thermal conductivity of gases. hydrocarbons at normal pressures. *Industrial & Engineering Chemistry Fundamentals 7*(4), 529–534. *(p. 26)*

Rubinstein, J. and P. Sternberg (1992). Nonlocal reaction-diffusion equations and nucleation. *IMA Journal of Applied Mathematics 48*(3), 249–264. *(p. 121, 122, 131)*

Rubinstein, J., P. Sternberg, and J. B. Keller (1989). Fast reaction, slow diffusion, and curve shortening. *SIAM Journal on Applied Mathematics 49*(1), 116–133. *(p. 122)*

Ruiz, A. (2012). *Unsteady Numerical Simulations of Transcritical Turbulent Combustion in Liquid Rocket Engines.* Ph. D. thesis, Toulouse, INPT. *(p. 16, 17, 307)*

Ruiz, A. M., G. Lacaze, J. C. Oefelein, R. Mari, B. Cuenot, L. Selle, and T. Poinsot (2015). Numerical benchmark for high-reynolds-number supercritical flows with large density gradients. *AIAA Journal 54*(5), 1445–1460. *(p. 307)*

Rüschendorf, L. (1985). The wasserstein distance and approximation theorems. *Probability Theory and Related Fields 70*(1), 117–129. *(p. 136)*

Russo, G. and P. Smereka (2000). A remark on computing distance functions. *Journal of Computational Physics 163*(1), 51–67. *(p. 109)*

Sabelnikov, V., A. Y. Ovsyannikov, and M. Gorokhovski (2014). Modified level set equation and its numerical assessment. *Journal of Computational Physics 278*(Supplement C), 1 – 30. *(p. 113)*

Salih, A. and S. G. Moulic (2009). Some numerical studies of interface advection properties of level set method. *Sadhana 34*(2), 271–298. *(p. 112)*

Santambrogio, F. (2017). {Euclidean, metric, and Wasserstein} gradient flows: an overview. *Bulletin of Mathematical Sciences 7*(1), 87–154. *(p. 136)*

Sato, Y. and B. Ničeno (2013). A sharp-interface phase change model for a mass-conservative interface tracking method. *Journal of Computational Physics 249*, 127–161. *(p. xvii, 78)*

Saurel, R. and R. Abgrall (1999a). A multiphase godunov method for compressible multifluid and multiphase flows. *Journal of Computational Physics 150*(2), 425–467. *(p. 149, 150, 151)*

Saurel, R. and R. Abgrall (1999b). A simple method for compressible multifluid flows. *SIAM Journal on Scientific Computing 21*(3), 1115–1145. *(p. 149)*

Saurel, R., S. Gavrilyuk, and F. Renaud (2003). A multiphase model with internal degrees of freedom: application to shock-bubble interaction. *Journal of Fluid Mechanics 495*, 283. *(p. 149)*

Saurel, R., F. Petitpas, and R. Abgrall (2008). Modelling phase transition in metastable liquids: Application to cavitating and flashing flows. *(p. 150, 152, 155)*

Saurel, R., F. Petitpas, and R. A. Berry (2009). Simple and efficient relaxation methods for interfaces separating compressible fluids, cavitating flows and shocks in multiphase mixtures. *journal of Computational Physics 228*(5), 1678–1712. *(p. xix, 149, 151, 152)*

Scardovelli, R. and S. Zaleski (2003). Interface reconstruction with least-square fit and split eulerian–lagrangian advection. *International Journal for Numerical Methods in Fluids 41*(3), 251–274. *(p. 81, 85, 87)*

Schmidt, V., D. Klimenko, O. Haidn, M. Oschwald, A. Nicole, G. Ordonneau, and M. Habiballah (2003). Experimental investigation and modeling of the ignition transient of a coaxial o2/h2 injector. *(p. 16)*

Schmidt, V., U. Wepler, O. Haidn, and M. Oschwald (2004). Characterization of the primary ignition process of a coaxial gh2/lox spray. In *42nd AIAA Aerospace Sciences Meeting and Exhibit*, pp. 1167. *(p. 16)*

Schmitt, T. (2009). *Simulation des Grandes Echelles de la combustion turbulente à pression supercritique*. Ph. D. thesis, Toulouse, INPT. *(p. 17, 204, 209)*

Schmitt, T. (2020). Large-eddy simulations of the mascotte test cases operating at supercritical pressure. *Flow, Turbulence and Combustion*, 1–31. *(p. xx, 216, 217)*

Schmitt, T., J. Rodriguez, I. Leyva, and S. Candel (2012). Experiments and numerical simulation of mixing under supercritical conditions. *Physics of Fluids 24*(5), 055104. *(p. 16)*

Schmitt, T., L. Selle, A. Ruiz, and B. Cuenot (2010). Large-eddy simulation of supercritical-pressure round jets. *AIAA journal 48*(9), 2133–2144. *(p. 16)*

Schönfeld, T. and M. Rudgyard (1999). Steady and unsteady flow simulations using the hybrid flow solver avbp. *AIAA journal 37*(11), 1378–1385. *(p. 204, 216)*

Sengupta, T. K. (2004). *Fundamentals of computational fluid dynamics*, Volume 364. Universities Press Hyderabad (India). *(p. 211, 275)*

Seppecher, P. (1987). *Etude d'une modelisation des zones capillaires fluides: interfaces et lignes de contact*. Ph. D. thesis, Ecole Nationale Superieure de Techniques Avancees. *(p. 159, 169, 170, 172, 175, 176, 423)*

Sethian, J. (1982). *An analysis of flow propagation*. Ph. D. thesis, PhD thesis, University of California. *(p. 99, 104)*

Sethian, J. (1984). Turbulent combustion in open and closed vessels. *Journal of computational physics 54*(3), 425–456. *(p. 99, 104)*

Sethian, J. A. (1985). Curvature and the evolution of fronts. *Communications in Mathematical Physics 101*(4), 487–499. *(p. 99, 104)*

Sethian, J. A. (1987). Numerical methods for propagating fronts. In *Variational methods for free surface interfaces*, pp. 155–164. Springer. *(p. 99)*

Sethian, J. A. (1996). A fast marching level set method for monotonically advancing fronts. *Proceedings of the National Academy of Sciences 93*(4), 1591–1595. *(p. 74, 100, 109)*

Sethian, J. A. (2001). Evolution, implementation, and application of level set and fast marching methods for advancing fronts. *Journal of computational physics 169*(2), 503–555. *(p. 11)*

Sethian, J. A. and J. Straint (1992). Crystal growth and dendritic solidification. *Journal of Computational Physics 98*(2), 231–253. *(p. 99, 100)*

Shen, J. and X. Yang (2009). An efficient moving mesh spectral method for the phase-field model of two-phase flows. *Journal of computational physics 228*(8), 2978–2992. *(p. 130)*

Shen, J. and X. Yang (2014). Decoupled energy stable schemes for phase-field models of two-phase complex fluids. *SIAM Journal on Scientific Computing 36*(1), B122–B145. *(p. xix, 143, 145, 146)*

Shepel, S. V. and B. L. Smith (2006). New finite-element/finite-volume level set formulation for modelling two-phase incompressible flows. *Journal of Computational Physics 218*(2), 479–494. *(p. 100)*

Shimasaki, S. and S. Taniguchi (2011). Formation of uniformly sized metal droplets from a capillary jet by electromagnetic force. *Applied Mathematical Modelling 35*(4), 1571–1580. *(p. xxix, 362, 363)*

Shinjo, J. and A. Umemura (2010). Simulation of liquid jet primary breakup: Dynamics of ligament and droplet formation. *International Journal of Multiphase Flow 36*(7), 513–532. *(p. xv, 15)*

Shukla, R. K. (2014). Nonlinear preconditioning for efficient and accurate interface capturing in simulation of multicomponent compressible flows. *Journal of Computational Physics 276*, 508–540. *(p. xviii, 117)*

Siggia, E., B. Halperin, and P. Hohenberg (1976). Renormalization-group treatment of the critical dynamics of the binary-fluid and gas-liquid transitions. *Physical Review B 13*(5), 2110. *(p. 122)*

Singla, G., P. Scouflaire, C. Rolon, and S. Candel (2005). Transcritical oxygen/transcritical or supercritical methane combustion. *Proceedings of the combustion institute 30*(2), 2921–2928. *(p. 16)*

Singla, G., P. Scouflaire, C. Rolon, and S. Candel (2006). Planar laser-induced fluorescence of oh in high-pressure cryogenic lox/gh 2 jet flames. *Combustion and Flame 144*(1), 151–169. *(p. 16)*

Smith, J. J. (2007). *High Pressure LOx/H2 rocket engine combustion*. Ph. D. thesis, University of Adelaide, School of Mechanical Engineering. *(p. 16)*

Smoluchowski, R. (1951). Theory of grain boundary motion. *Physical Review 83*(1), 69. *(p. 121)*

Snyder, R., G. Herding, J. C. Rolon, and S. Candel (1997). Analysis of flame patterns in cryogenic propellant combustion. *Combustion science and technology 124*(1-6), 331–370. *(p. 16)*

Soave, G. (1972). Equilibrium constants from a modified redlich-kwong equation of state. *Chemical Engineering Science 27*(6), 1197 – 1203. *(p. 19, 27)*

Son, G. and V. Dhir (1998). Numerical simulation of film boiling near critical pressures with a level set method. *TRANSACTIONS-AMERICAN SOCIETY OF MECHANICAL ENGINEERS JOURNAL OF HEAT TRANSFER 120*, 183–192. *(p. 99)*

Sousa, F., A. Castelo, L. Nonato, N. Mangiavacchi, and J. Cuminato (2007). Local volume-conserving free surface smoothing. *International Journal for Numerical Methods in Biomedical Engineering 23*(2), 109–120. *(p. 66)*

Starovoitov, V. (1994). Model of the motion of a two-component liquid with allowance of capillary forces. *Journal of applied mechanics and technical physics 35*(6), 891–897. *(p. 143)*

Starovoitov, V. N. (1997). The dynamics of a two-component fluid in the presence of capillary forces. *Mathematical Notes 62*(2), 244–254. *(p. 143)*

Sternberg, P. (1988). The effect of a singular perturbation on nonconvex variational problems. *Archive for Rational Mechanics and Analysis 101*(3), 209–260. *(p. 122)*

Sternfeld, H. J., O. J. Haidn, B. Potier, P. Vuillermoz, and M. Popp (1995). International cooperation on hydrogenoxygen high pressure combustion. *Acta Astronautica 37*, 487–496. *(p. 9)*

Stewart, D. S., T. Aslam, J. Yao, and J. B. Bdzil (1995). Level-set techniques applied to unsteady detonation propagation. In *Modeling in Combustion Science*, pp. 352–369. Springer. *(p. 99)*

Stolz, S. and N. A. Adams (1999). An approximate deconvolution procedure for large-eddy simulation. *Physics of Fluids 11*(7), 1699–1701. *(p. 216)*

Strain, J. (1999). Semi-lagrangian methods for level set equations. *Journal of Computational Physics 151*(2), 498–533. *(p. 112)*

Strait, M. E. et al. (2017). Phase field models of two-fluid flow in a capillary tube and hele-shaw cell. *(p. 123)*

Sun, D. and W. Tao (2010). A coupled volume-of-fluid and level set (voset) method for computing incompressible two-phase flows. *International Journal of Heat and Mass Transfer 53*(4), 645 – 655. *(p. 80, 112)*

Sun, Y. and C. Beckermann (2007). Sharp interface tracking using the phase-field equation. *Journal of Computational Physics 220*(2), 626–653. *(p. 122, 138, 139)*

Sussman, M. (2003). A second order coupled level set and volume-of-fluid method for computing growth and collapse of vapor bubbles. *Journal of Computational Physics 187*(1), 110–136. *(p. 99)*

Sussman, M., A. S. Almgren, J. B. Bell, P. Colella, L. H. Howell, and M. L. Welcome (1999). An adaptive level set approach for incompressible two-phase flows. *Journal of Computational Physics 148*(1), 81–124. *(p. xviii, 109, 111, 112)*

Sussman, M., E. Fatemi, P. Smereka, and S. Osher (1998). An improved level set method for incompressible two-phase flows. *Computers & Fluids 27*(5), 663–680. *(p. 110)*

Sussman, M. and E. G. Puckett (2000). A coupled level set and volume-of-fluid method for computing 3d and axisymmetric incompressible two-phase flows. *Journal of computational physics 162*(2), 301–337. *(p. 80, 112)*

Sussman, M., P. Smereka, and S. Osher (1994). A level set approach for computing solutions to incompressible two-phase flow. *Journal of Computational physics 114*(1), 146–159. *(p. 13, 100, 108)*

Takada, N., J. Matsumoto, and S. Matsumoto (2013). Phase-field model-based simulation of motions of a two-phase fluid on solid surface. *Journal of Computational Science and Technology 7*(2), 322–337. *(p. xix, 122, 138, 139, 145)*

Tan, Z., K. M. Lim, and B. C. Khoo (2007). An adaptive mesh redistribution method for the incompressible mixture flows using phase-field model. *Journal of Computational Physics 225*(1), 1137–1158. *(p. 145)*

Tanguy, S. and A. Berlemont (2005). Application of a level set method for simulation of droplet collisions. *International journal of multiphase flow 31*(9), 1015–1035. *(p. xviii, 110, 111, 355)*

Tanguy, S., T. MÃ©nard, and A. Berlemont (2007). A level set method for vaporizing two-phase flows. *Journal of Computational Physics 221*(2), 837 – 853. *(p. 99, 100)*

Terashima, H. and G. Tryggvason (2009). A front-tracking/ghost-fluid method for fluid interfaces in compressible flows. *Journal of Computational Physics 228*(11), 4012 – 4037. *(p. xvii, 63, 67, 72, 73, 74, 75)*

Terashima, H. and G. Tryggvason (2010). A front-tracking method with projected interface conditions for compressible multi-fluid flows. *Computers & Fluids 39*(10), 1804–1814. *(p. 75)*

Teukolsky, S. A., B. P. Flannery, W. Press, and W. Vetterling (1992). Numerical recipes in c. *SMR 693*(1), 59–70. *(p. 257)*

Tomé, M., A. Castelo, J. Murakami, J. Cuminato, R. Minghim, M. Oliveira, N. Mangiavacchi, and S. McKee (2000). Numerical simulation of axisymmetric free surface flows. *Journal of Computational Physics 157*(2), 441–472. *(p. 55, 60)*

Tomé, M. F., B. Duffy, and S. McKee (1996). A numerical technique for solving unsteady non-newtonian free surface flows. *Journal of non-newtonian fluid mechanics 62*(1), 9–34. *(p. 55)*

Tomé, M. F. and S. McKee (1994). Gensmac: A computational marker and cell method for free surface flows in general domains. *Journal of Computational Physics 110*(1), 171 – 186. *(p. 54, 55, 60)*

Tornberg, A.-K. and B. Engquist (2000). A finite element based level-set method for multiphase flow applications. *Computing and Visualization in Science 3*(1-2), 93–101. *(p. 110)*

Toutant, A., B. Mathieu, and O. Lebaigue (2012). Volume-conserving mesh smoothing for front-tracking methods. *Computers & Fluids 67*(Supplement C), 16 – 25. *(p. 66)*

Tripathi, A., M. Juniper, P. Scouflaire, J.-C. Rolon, D. Durox, and S. Candel (1999). Lox tube recess in cryogenic flames investigated using oh and h2o emission. In *35th Joint Propulsion Conference and Exhibit*, pp. 2490. *(p. 16)*

Truesdell, C. and R. Toupin (1960). The classical field theories. In *Principles of classical mechanics and field theory/Prinzipien der Klassischen Mechanik und Feldtheorie*, pp. 226–858. Springer. *(p. 149)*

Truskinovsky, L. (1993). Kinks versus shocks. In *Shock induced transitions and phase structures in general media*, pp. 185–229. Springer. *(p. 140, 141)*

Tryggvason, G., B. Bunner, A. Esmaeeli, D. Juric, N. Al-Rawahi, W. Tauber, J. Han, S. Nas, and Y.-J. Jan (2001). A front-tracking method for the computations of multiphase flow. *Journal of Computational Physics 169*(2), 708 – 759. *(p. 63, 75)*

Tryggvason, G., A. Esmaeeli, J. Lu, and S. Biswas (2006). Direct numerical simulations of gas/liquid multiphase flows. *Fluid dynamics research 38*(9), 660–681. *(p. 75)*

Tryggvason, G., R. Scardovelli, and S. Zaleski (2011). *Direct numerical simulations of gas–liquid multiphase flows*. Cambridge University Press. *(p. 68, 69, 85)*

Tsui, Y.-Y., S.-W. Lin, T.-T. Cheng, and T.-C. Wu (2009). Flux-blending schemes for interface capture in two-fluid flows. *International Journal of Heat and Mass Transfer 52*(23), 5547–5556. *(p. 81, 97)*

Turnbull, D. (1952). Theory of grain boundary migration rates. *Trans. Aime 191*(8), 661–65. *(p. 121)*

Ubbink, O. (1997). *Numerical prediction of two fluid systems with sharp interfaces*. Ph. D. thesis, University of London PhD Thesis. *(p. 95, 96)*

Ubbink, O. and R. Issa (1999). A method for capturing sharp fluid interfaces on arbitrary meshes. *Journal of Computational Physics 153*(1), 26–50. *(p. 81, 97)*

Udaykumar, H., H.-C. Kan, W. Shyy, and R. Tran-Son-Tay (1997). Multiphase dynamics in arbitrary geometries on fixed cartesian grids. *Journal of Computational Physics 137*(2), 366–405. *(p. 64)*

Udaykumar, H., R. Mittal, and W. Shyy (1999). Computation of solid–liquid phase fronts in the sharp interface limit on fixed grids. *Journal of computational physics 153*(2), 535–574. *(p. 64)*

Udaykumar, H., W. Shyy, and M. Rao (1996). Elafint: a mixed eulerian–lagrangian method for fluid flows with complex and moving boundaries. *International journal for numerical methods in fluids 22*(8), 691–712. *(p. 64)*

Unverdi, S. O. and G. Tryggvason (1992). A front-tracking method for viscous, incompressible, multi-fluid flows. *Journal of computational physics 100*(1), 25–37. *(p. 12, 63, 126)*

Van der Pijl, S., A. Segal, C. Vuik, and P. Wesseling (2005). A mass-conserving level-set method for modelling of multi-phase flows. *International journal for numerical methods in fluids 47*(4), 339–361. *(p. 80, 112)*

van der Waals, J. D. (1873). *La continuité des états gazeux et liquides (1894)*. Ph. D. thesis. *(p. 20, 25, 27, 162)*

van der Waals, J. D. (1891). Théorie moléculaire d'une substance composée de deux matières différentes. *Archives Néerlandaises des Sciences exactes et naturelles, Série I 24*(1), 1–56. *(p. 120)*

van der Waals, J. D. (1893, February). The thermodynamic theory of capillarity under the hypothesis of a continuous variation of density (Verhandel/Konink. Akad. Weten., 1893, vol. 1, English Translation). *Journal of Statistical Physics 20*, 200–244. *(p. 17, 120, 167, 192)*

Vasconcelos, D., A. Rossa, and A. Coutinho (2014). A residual-based allen–cahn phase field model for the mixture of incompressible fluid flows. *International Journal for Numerical Methods in Fluids 75*(9), 645–667. *(p. 130, 143, 145)*

Vidal, J. (1997). *Thermodynamique: application au génie chimique et à l'industrie pétrolière*. Editions Technip. *(p. 29)*

Viecelli, J. (1969). A method for including arbitrary external boundaries in the mac incompressible fluid computing technique. *Journal of Computational Physics 4*(4), 543 – 551. *(p. 54)*

Vingert, L., M. Habiballah, and J. Traineau (1999). Mascotte, a research test facility for high pressure combustion of cryogenic propellants. In *AAAF/CEAS, European Aerospace Conference, 12 th, Paris, France, Nov. 29-Dec. 1, 1999, ONERA, TP*, Number 2000-15. *(p. xix, 10, 154, 155, 157)*

Wacławczyk, T. (2015). A consistent solution of the re-initialization equation in the conservative level-set method. *Journal of Computational Physics 299*, 487–525. *(p. 117)*

Wang, S.-L., R. Sekerka, A. Wheeler, B. Murray, S. Coriell, R. Braun, and G. McFadden (1993). Thermodynamically-consistent phase-field models for solidification. *Physica D: Nonlinear Phenomena 69*(1-2), 189–200. *(p. 127)*

Wang, X. and V. Yang (2016). Supercritical mixing and combustion of liquid-oxygen/kerosene bi-swirl injectors. *Journal of Propulsion and Power 33*(2), 316–322. *(p. 307)*

Wang, Y., Y. Jin, A. Cuitino, and A. Khachaturyan (2001). Phase field microelasticity theory and modeling of multiple dislocation dynamics. *Applied Physics Letters 78*(16), 2324–2326. *(p. 126)*

Ward, M. J. (1996). Metastable bubble solutions for the allen-cahn equation with mass conservation. *SIAM Journal on Applied Mathematics 56*(5), 1247–1279. *(p. 122)*

Welch, J., F. Harlow, J. Shannon, and B. Daly (1965). The mac method - a computing technique for solving viscous, incompressible, transient fluid-flow problems involving free surfaces. Technical report, Los Alamos Scientific Lab., Univ. of California, N. Mex. *(p. xvii, 12, 54, 57, 59)*

Wemmenhove, R., R. Luppes, A. E. Veldman, and T. Bunnik (2015). Numerical simulation of hydrodynamic wave loading by a compressible two-phase flow method. *Computers & Fluids 114*, 218–231. *(p. 81)*

Wheeler, A. A., B. T. Murray, and R. J. Schaefer (1993). Computation of dendrites using a phase field model. *Physica D: Nonlinear Phenomena 66*(1-2), 243–262. *(p. 122)*

Witterstein, G. (2008). On the existence of a solution for a model of stem cell differentiation. *Mathematical methods in the applied sciences 31*(16), 1972–1995. *(p. 142)*

Witteveen, J. A. (2010). Second order front tracking for the euler equations. *Journal of Computational Physics 229*(7), 2719–2739. *(p. 64)*

Witteveen, J. A. S., B. Koren, and P. Bakker (2007). An improved front tracking method for the euler equations. *Journal of Computational Physics 224*(2), 712–728. *(p. 64)*

Wu, F. Y. and R. Aaron (2015). The virial expansion re-visited: A new interpretation. *Modern Physics Letters B 29*(34), 1530014. *(p. 21)*

Wu, P.-K. and G. Faeth (1993). Aerodynamic effects on primary breakup of turbulent liquids. *Atomization and Sprays 3*(3). *(p. 7)*

Wu, Y. and C. He (2015). A convex variational level set model for image segmentation. *Signal Processing 106*, 123–133. *(p. 99)*

Xia, Y., Y. Xu, and C.-W. Shu (2009). Application of the local discontinuous galerkin method for the allen-cahn/cahn-hilliard system. *Communications in Computational Physics 5*(2-4), 821–83. *(p. 130)*

Xiao, F., M. Dianat, and J. J. McGuirk (2013). Large eddy simulation of liquid-jet primary breakup in air crossflow. *AIAA journal 51*(12), 2878–2893. *(p. 13)*

Xiao, F., M. Dianat, and J. J. McGuirk (2014). Les of turbulent liquid jet primary breakup in turbulent coaxial air flow. *International Journal of Multiphase Flow 60*, 103–118. *(p. 13)*

Xu, X., L. Zhao, and C. Liu (2010). Axisymmetric solutions to coupled navier–stokes/allen–cahn equations. *SIAM journal on mathematical analysis 41*(6), 2246–2282. *(p. 144)*

Yang, A. J. M., P. D. Fleming, and J. H. Gibbs (1976). Molecular theory of surface tension. *The Journal of Chemical Physics 64*(9), 3732–3747. *(p. 196)*

Yang, S.-D., H. G. Lee, and J. Kim (2010). A phase-field approach for minimizing the area of triply periodic surfaces with volume constraint. *Computer Physics Communications 181*(6), 1037–1046. *(p. 129)*

Yang, V. (2000). Modeling of supercritical vaporization, mixing, and combustion processes in liquid-fueled propulsion systems. *Proceedings of the Combustion Institute 28*(1), 925–942. *(p. 15)*

Yang, X., J. J. Feng, C. Liu, and J. Shen (2006). Numerical simulations of jet pinching-off and drop formation using an energetic variational phase-field method. *Journal of Computational Physics 218*(1), 417–428. *(p. 122, 143, 145)*

Yang, X. and L. Ju (2017). Linear and unconditionally energy stable schemes for the binary fluid–surfactant phase field model. *Computer Methods in Applied Mechanics and Engineering 318*, 1005–1029. *(p. 123)*

Yap, Y., H. Li, J. Lou, L. Pan, and Z. Shang (2017). Numerical modeling of three-phase flow with phase change using the level-set method. *International Journal of Heat and Mass Transfer 115*, 730–740. *(p. 99)*

Young, T. (1805). Iii. an essay on the cohesion of fluids. *Philosophical transactions of the royal society of London* (95), 65–87. *(p. 119)*

Youngs, D. L. (1982, 01). Time-dependent multi-material flow with large fluid distortion. *Numerical methods for fluid dynamics 24*, 273–285. *(p. 12, 81, 84, 85)*

Yu, Y. (2014). The virtual power principle in fluid mechanics. *Journal of Fluid Mechanics 744*, 310–328. *(p. 169, 423, 425)*

Yue, P., J. J. Feng, C. Liu, and J. Shen (2004). A diffuse-interface method for simulating two-phase flows of complex fluids. *Journal of Fluid Mechanics 515*, 293–317. *(p. 122, 142, 143)*

Zalosh, R. G. (1976). Discretized simulation of vortex sheet evolution with buoyancy and surface tension effects. *AIAA J 14*(11), 1517–1523. *(p. 54)*

Zhang, J. and Q. Du (2009). Numerical studies of discrete approximations to the allen–cahn equation in the sharp interface limit. *SIAM Journal on Scientific Computing 31*(4), 3042–3063. *(p. 122)*

Zhang, K., L. Zhang, H. Song, and W. Zhou (2010). Active contours with selective local or global segmentation: a new formulation and level set method. *Image and Vision computing 28*(4), 668–676. *(p. 99)*

Zhao, H.-K., T. Chan, B. Merriman, and S. Osher (1996). A variational level set approach to multiphase motion. *Journal of computational physics 127*(1), 179–195. *(p. 109)*

Zhao, J., H. Li, Q. Wang, and X. Yang (2017). Decoupled energy stable schemes for a phase field model of three-phase incompressible viscous fluid flow. *Journal of Scientific Computing 70*(3), 1367–1389. *(p. xix, 147)*

Zhao, J., Q. Wang, and X. Yang (2016). Numerical approximations to a new phase field model for two phase flows of complex fluids. *Computer Methods in Applied Mechanics and Engineering 310*, 77–97. *(p. 143)*

Zhao, L., X. Bai, T. Li, and J. Williams (2014). Improved conservative level set method. *International Journal for Numerical Methods in Fluids 75*(8), 575–590. *(p. 101)*

Zhao, L., B. Guo, and H. Huang (2011). Vanishing viscosity limit for a coupled navier–stokes/allen–cahn system. *J. Math. Anal. Appl 384*, 232–245. *(p. 144)*

Zheng, Y. (2012). *Systems of conservation laws: two-dimensional Riemann problems*, Volume 38. Springer Science & Business Media. *(p. 71)*

Zong, N., H. Meng, S.-Y. Hsieh, and V. Yang (2004). A numerical study of cryogenic fluid injection and mixing under supercritical conditions. *Physics of Fluids 16*(12), 4248–4261. *(p. 16)*

Zong, N. and V. Yang (2005). Numerical study of high-pressure oxygen/methane mixing and combustion of a shear coaxial injector. In *43rd AIAA Aerospace Sciences Meeting and Exhibit*, pp. 152. *(p. 16)*

Zong, N. and V. Yang (2006). Cryogenic fluid jets and mixing layers in transcritical and supercritical environments. *Combustion Science and Technology 178*(1-3), 193–227. *(p. 16)*

université PARIS-SACLAY

ÉCOLE DOCTORALE
Sciences mécaniques et énergétiques, matériaux et géosciences (SMEMAG)

Titre: Simulations instationnaires d'interfaces liquide/gaz dans les écoulements gaz réels en utilisant la théorie du Second Gradient

Mots clés: Second Gradient, Interfaces, Écoulements Diphasiques, Gaz réels, AVBP

Résumé: L'objectif de cette thèse est d'évaluer la théorie du second gradient pour la simulation d'écoulements de fluides de gaz réels diphasiques instationnaires. L'implémentation du modèle a été validée sur des configurations canoniques. Une investigation numérique systématique a permis de dévoiler les paramètres clés nécessaires pour assurer la stabilité des simulations, comme la condition du pas de temps ou la résolution minimale nécessaire pour les interfaces. Des interfaces planaires oscillantes bidimensionnelles et des gouttes déformées ont été simulées avec succès en résolvant l'ensemble complet des équations de Navier-Stokes compressibles, ce qui n'avait jamais été fait avec ce modèle, au meilleur de nos connaissances. Le modèle SG dans sa formulation native prédit des largeurs d'interface de plusieurs ordres de grandeur inférieures aux tailles de maillage typiques utilisées pour des applications pratiques, même dans des configurations DNS. Pour surmonter cet obstacle, la méthode d'interface épaissie (TIM) a été dérivée pour épaissir une interface d'une manière thermodynamiquement cohérente tout en maintenant sa tension superficielle. La méthode TIM a été soumise aux mêmes tests systématiques que ceux appliqués au modèle SG natif et a répondu avec le comportement attendu sur les cas simplifiés. De plus, des comparaisons quantitatives ont permis de confirmer que la méthode préserve bien la tension superficielle et le comportement macroscopique de l'interface. Enfin, la méthode a été utilisée pour simuler des configurations plus pratiques: jets périodiques bidimensionnels et gouttes en collision tridimensionnelles. Les résultats pour différents nombres de Weber ont montré un bon accord avec les résultats expérimentaux.

Title: Unsteady simulations of liquid/gas interfaces in real gas flows using the Second Gradient theory

Keywords: Second Gradient, Interfaces, Two-phase flows, Real gas, AVBP

Abstract: The objective of this thesis is to assess the ability of the Second Gradient theory to allow unsteady two-phase flow simulations with real-gas fluids. The implementation of the model has been validated on canonical configurations. A systematic numerical investigation has permitted to unveil key parameters needed to ensure the stability of the simulations, such as the time step condition or the minimal resolution needed for the interfaces. Two-dimensional oscillating planar interfaces and deformed droplets have been successfully simulated solving the full set of compressible Navier-Stokes equations, which had never been done using this model so far, to the best of our knowledge. The SG model in its native formulation predicted interface widths of multiple orders of magnitude lower than the typical mesh sizes used for practical applications, even in DNS configurations. To address this hurdle, the Thickened Interface Method (TIM) has been derived to thicken an interface in a thermodynamically consistent manner while maintaining its surface tension. The TIM has been submitted to the same systematic testing applied to the native SG model and invariably responded with the expected behavior on simplified cases. Furthermore, quantitative comparisons which have allowed to confirm that the method indeed preserves the surface tension and the macroscopic behavior of the interface. Finally, the method has been used to simulate more practical configurations: two dimensional periodic jets and three-dimensional colliding droplets. The results for different Weber numbers showed a good agreement with experimental results.

Université Paris-Saclay
Espace Technologique / Immeuble Discovery
Route de l'Orme aux Merisiers RD 128 / 91190 Saint-Aubin, France